coatings

Special Issue Reprint

Laser-Assisted Coating Techniques and Surface Modifications

Edited by
Haiying Song, Shibing Liu and Xuewu Li

mdpi.com/journal/coatings

MDPI

Laser-Assisted Coating Techniques and Surface Modifications

Laser-Assisted Coating Techniques and Surface Modifications

Guest Editors

Haiying Song
Shibing Liu
Xuewu Li

MDPI

Basel • Beijing • Wuhan • Barcelona • Belgrade • Novi Sad • Cluj • Manchester

Guest Editors

Haiying Song
School of Physics and Optoelectronic Engineering
Beijing University of Technology
Beijing
China

Shibing Liu
School of Physics and Optoelectronic Engineering
Beijing University of Technology
Beijing
China

Xuewu Li
College of Mechanical Engineering
Xi'an University of Science & Technology
Xi'an
China

Editorial Office
MDPI AG
Grosspeteranlage 5
4052 Basel, Switzerland

This is a reprint of the Special Issue, published open access by the journal *Coatings* (ISSN 2079-6412), freely accessible at: https://www.mdpi.com/journal/coatings/special_issues/Laser_assisted_coating.

For citation purposes, cite each article independently as indicated on the article page online and as indicated below:

Lastname, A.A.; Lastname, B.B. Article Title. *Journal Name* **Year**, *Volume Number*, Page Range.

ISBN 978-3-7258-9109-2 (Hbk)
ISBN 978-3-7258-9110-8 (PDF)
https://doi.org/10.3390/books978-3-7258-9110-8

© 2026 by the authors. Articles in this reprint are Open Access and distributed under the Creative Commons Attribution (CC BY) license. The reprint as a whole is distributed by MDPI under the terms and conditions of the Creative Commons Attribution-NonCommercial-NoDerivs (CC BY-NC-ND) license (https://creativecommons.org/licenses/by-nc-nd/4.0/).

Contents

Haiying Song, Liang Wang and Shibing Liu
Metasurface Properties Obtained via Laser-Assisted Surface Technology
Reprinted from: *Coatings* **2023**, *13*, 251, https://doi.org/10.3390/coatings13020251 . . . . . **1**

Haiying Song and Fujiang Tao
Special Issue: "Laser-Assisted Coating Techniques and Surface Modifications"
Reprinted from: *Coatings* **2026**, *16*, 430, https://doi.org/10.3390/coatings16040430 . . . . . **4**

Yuan Lv, Mengen Dong, Xixiang Pan, Cong Yi and Jiaqi Su
Surface Mechanical Properties and Micro-Structure Evolution of 7075 Aluminum Alloy Sheet for 2-Dimension Ellipse Ultrasonic Vibration Incremental Forming: A Pretreatment for Laser Shock Peening
Reprinted from: *Coatings* **2022**, *12*, 1914, https://doi.org/10.3390/coatings12121914 . . . . . **9**

Jun Zhang, Yuncai Zhao, Yang He, Cheng Meng, Xinyu Zhang and Shilei Zhang
Effect of High-Temperature-Assisted Ultrasonic Deep Rolling on Microstructure and Tribological Properties of Ni-WC Coatings
Reprinted from: *Coatings* **2023**, *13*, 499, https://doi.org/10.3390/coatings13030499 . . . . . **23**

Kaijin Huang and Xianchao Han
High-Temperature Oxidation Properties of Ti-Hf-Mo-Ta-Nb-B Composite Coating Deposited on Ti60 Alloy with Laser Cladding
Reprinted from: *Coatings* **2023**, *13*, 1646, https://doi.org/10.3390/coatings13091646 . . . . . **39**

Seong Ju Park and Chanwoo Yang
Flexible Finely and Directly Patternable Liquid Metal Electrodes via Selective Surface Wetting Technique
Reprinted from: *Coatings* **2023**, *13*, 1922, https://doi.org/10.3390/coatings13111922 . . . . . **57**

Xinyi Feng, Xiao Li, Fei Wang, Zengzhi Liu and Wenping Wang
Effect of Spherical WC Content on the Microstructure and Properties of SiCp Aluminium Composite Material
Reprinted from: *Coatings* **2023**, *13*, 1935, https://doi.org/10.3390/coatings13111935 . . . . . **68**

Tianyi Lv, Wenkai Zou, Jiaqi He, Xiang Ju and Chuanbo Zheng
Study on the Microstructure and Properties of FeCoNiCrAl High-Entropy Alloy Coating Prepared by Laser Cladding-Remelting
Reprinted from: *Coatings* **2023**, *14*, 49, https://doi.org/10.3390/coatings14010049 . . . . . **91**

Jacek Górka, Aleksandra Lont, Damian Janicki, Tomasz Poloczek and Agnieszka Rzeźnikiewicz
Comparison of the Erosive Wear Resistance of Ductile Cast Iron Following Laser Surface Melting and Alloying
Reprinted from: *Coatings* **2024**, *14*, 646, https://doi.org/10.3390/coatings14050646 . . . . . **107**

Ladislav Záhon, Jiří Kuchař, Jakub Horník, Jan Krčil and Jan Kudláček
Laser Surface Hardening of Austempered Ductile Iron (ADI)
Reprinted from: *Coatings* **2024**, *14*, 958, https://doi.org/10.3390/coatings14080958 . . . . . **122**

Andrea Sütőová, Róbert Kočiško, Patrik Petroušek, Martin Kotus, Ivan Petryshynets and Andrii Pylypenko
Study of PVD-Coated Inserts' Lifetime in High-Pressure Die Casting Regarding the Requirements for Surface Quality of Castings
Reprinted from: *Coatings* **2024**, *14*, 1043, https://doi.org/10.3390/coatings14081043 . . . . . **143**

Ruxue Guo, Ping Zhou, Wanyun Zhang, Haiying Song and Shibing Liu
Study on the Thermal Radiation Characteristics of Tungsten Surface Grating Structures Prepared by Femtosecond Laser Direct Writing
Reprinted from: *Coatings* **2024**, *14*, 1045, https://doi.org/10.3390/coatings14081045 . . . . . **154**

Kaijin Huang and Xianchao Han
Laser Cladding of a Ti–Zr–Mo–Ta–Nb–B Composite Coating on Ti60 Alloy to Improve Wear Resistance
Reprinted from: *Coatings* **2024**, *14*, 1247, https://doi.org/10.3390/coatings14101247 . . . . . **170**

J. Apolinar Muñoz Rodríguez
Microsurface Defect Recognition via Microlaser Line Projection and Affine Moment Invariants
Reprinted from: *Coatings* **2025**, *15*, 385, https://doi.org/10.3390/coatings15040385 . . . . . **186**

coatings

MDPI

Editorial

Metasurface Properties Obtained via Laser-Assisted Surface Technology

Haiying Song [1,2,*], Liang Wang [1,2] and Shibing Liu [1,2]

[1] Strong-Field and Ultrafast Photonics Lab, Faculty of Materials and Manufacturing, Beijing University of Technology, Beijing 100124, China
[2] Key Laboratory of Trans-Scale Laser Manufacturing Technology, Ministry of Education, Beijing University of Technology, Beijing 100124, China
* Correspondence: hysong@bjut.edu.cn

Lasers as sources of heat or light energy have become a "universal tool" in the advanced manufacturing industry [1]. With the rapid development of high-precision mechanical manufacturing, high-performance surface devices are needed in many surface application fields. Laser-assisted surface technology (LAST, including coatings and modification) plays a vital role in several surface engineering fields [2–5]. LAST has been used to obtain many different surface properties on solid surfaces, such as super-hydrophobic, super-hydrophilic, super-interface, ultra-hydromechanical, ultra-tribological, and super-color characteristics [6–8]. Due to the higher performance requirements of structural parts in the high-end equipment manufacturing industry, single-surface technology cannot completely solve the problems of surface micro-defects and macro-deformation. Therefore, LAST combined with other surface engineering technologies has become more important and is receiving much attention.

Additive manufacturing-processed structures have an exemplary internal structure, excellent mechanical properties, and gradient materials. For example, by using laser-engineered net-shaping technology to deposit coatings on the surface of Ti-based implants, the wear resistance, corrosion resistance [9], and biocompatibility [10] have been improved significantly. A copolymer wire blended with carbon material was used as a raw material to construct a pyramid-shaped absorbing array, which achieved an absorption rate of more than 90% in the frequency range of 5.3–18 GHz [11]. Laser-based phase transformation hardening (LPTH) uses a high-energy laser to quickly scan a workpiece so that the surface temperature rapidly rises to the phase transition point. Subsequently, self-cooling quenching is carried out via rapid cooling, and the surface hardness of the workpiece is greatly improved. For example, Lesyk et al. [12] combined LPTH and ultrasonic impact hardening to treat medium-carbon steel AISI 1045, which rendered its surface wear 84 % lower than that of steel treated using a single technology (laser-ultrasonic composite surface treatment). Laser-shock processing uses a short-pulse high-power-density laser ($>10^8$ W/cm^2) to radiate the surface of the workpiece so that it rapidly vaporizes to produce a shock wave with a pressure of 10^4 Pa, resulting in robust and ductile deformation of the metal surface. Yang et al. [13] found that laser-shock hardening can significantly improve the corrosion resistance and wettability of a Ti-Cu alloy. Laser surface cladding involved the formation of a heterogeneous cladding layer with a certain thickness on the surface of an alloy using high-energy-laser rapid melting and solidification. Hu et al. [14] deposited nickel-based tungsten carbide composite powder on a tunnel-boring-machine cutter ring surface via laser cladding. The wear resistance of the coating with carbide particles was improved by about seven times. Arthanari et al. [15] deposited coatings sequentially on the surface of rare Earth magnesium alloy treated with laser melting cladding technology, and an excellent combination of hardness and corrosion resistance was obtained.

Laser molecular beam epitaxy (LMBE) is a thin-film deposition method that can precisely monitor the epitaxial growth of thin films at an atomic scale to prepare multi-element, high melting points and complex, layered structures. Krichevtsov et al. [16] prepared nano-sized magnetic NFO thin films using LMBE, which has an anti-spinel crystal structure and exhibits a magnetization reversal phenomenon. Laser chemical vapor deposition (LCVD) uses a focused laser beam to locally heat the substrate to drive the CVD reaction. The film exhibits excellent adhesion, conductivity, hardness, and smoothness [17]. Pulsed laser deposition (PLD) uses a high-power-density laser beam to ablate the target surface, with a high-speed plasma plume perpendicularly sputtering out on the target surface and forming high-performance thin films with complex compositions. Haroon et al. [18] used PLD to prepare a ZnO saturable absorber and coupled it to an erbium-doped fiber laser ring cavity. The peak power and pulse energy of the laser were significantly improved. Dong et al. [19] directly graphitized the surface of a Si substrate via femtosecond laser sputtering deposition, and multi-layer and layer-controlled graphene films were prepared on a Si substrate.

Laser surface micro-structuring uses the high-energy peak intensity and nonlinear absorption characteristics of lasers to prepare super-hydrophobic, super-hydrophilic, super-color, and antifriction micro-nano-scale structures on the surface of solid materials. Using laser ablation, Zhang et al. [20] formed a conical non-spherical microstructure on a metal surface, and a super-hydrophobic surface of a nano-pyramid structure with a contact angle of 160° was obtained. Li et al. [21] prepared composite nanostructures composed of random nanopores and nano-protrusions on the surface of GaAs/Ge solar cells using a liquid-phase femtosecond laser. The structure suppressed the surface reflectivity at 8.9% in the range of 300~1200 nm, and improved the battery surface's antireflection property. Meng et al. [22,23] prepared jungle-like black silicon structures using a femtosecond laser in an alkaline solution. The structures were able to reduce the average minimum reflectivity of the silicon surface in the whole visible light region to about 5.6%.

In summary, the protective layer and modified surface obtained via LAST can significantly improve the surface properties of solid materials. It can be widely used in fields such as aerospace, machinery manufacturing, petrochemical, shipbuilding, metallurgy, electronics, and information, and plays an increasingly important role in reducing weight, remanufacturing, energy saving, and environmental protection.

Funding: The authors acknowledge financial support from the National Natural Science Foundation of China (No. 51875006).

Conflicts of Interest: The authors declare no conflict of interest.

References

1. Fotovvati, B.; Dehghanghadikolaei, A.; Namdari, N. Laser-Assisted Coating Techniques and Surface Modifications: A Short Review. *Part. Sci. Technol.* **2021**, *39*, 738–747. [CrossRef]
2. Etsion, I. State of the Art in Laser Surface Texturing. *J. Trib.* **2005**, *127*, 248–253. [CrossRef]
3. Kurella, A.; Dahotre, N.B. Surface Modification for Bioimplants: The Role of Laser Surface Engineering. *J. Biomater. Appl.* **2005**, *20*, 5–50. [CrossRef] [PubMed]
4. Dinesh Babu, P.; Balasubramanian, K.R.; Buvanashekaran, G. Laser Surface Hardening: A Review. *Int. J. Surf. Sci. Eng.* **2011**, *5*, 131–151. [CrossRef]
5. Vorobyev, A.Y.; Guo, C. Direct Femtosecond Laser Surface Nano/Microstructuring and Its Applications. *Laser Photonics Rev.* **2013**, *7*, 385–407. [CrossRef]
6. Min, T. *Design & Fabrication of Super-Hydrophobic Surfaces by Laser Micro/Nanoprocessing*; National University of Singapore: Singapore, 2012.
7. Sun, Q.; Yang, J.; Tian, R.; Fan, X.; Liao, Z.; Zhu, M. Enhanced Corrosion and Wear Resistances in a Precipitate-Hardened Magnesium Alloy by Laser Surface Remelting. *Mater. Charact.* **2022**, *193*, 112306. [CrossRef]
8. Hu, H.-L.; Pham, A.; Tilley, R.; Zeng, R.; Tan, T.T.; Kong, C.-H.C.; Webster, R.; Wang, D.; Li, S. Largely Enhanced Mobility in Trilayered $LaAlO_3$ /$SrTiO_3$ /$LaAlO_3$ Heterostructures. *ACS Appl. Mater. Interfaces* **2018**, *10*, 20950–20958. [CrossRef] [PubMed]
9. Balla, V.K.; Xue, W.; Bose, S.; Bandyopadhyay, A. Laser-Assisted Zr/ZrO2 Coating on Ti for Load-Bearing Implants. *Acta Biomater.* **2009**, *5*, 2800–2809. [CrossRef] [PubMed]

10. Roy, M.; Bandyopadhyay, A.; Bose, S. In Vitro Antimicrobial and Biological Properties of Laser Assisted Tricalcium Phosphate Coating on Titanium for Load Bearing Implant. *Mater. Sci. Eng. C* **2009**, *29*, 1965–1968. [CrossRef] [PubMed]
11. Chen, X.; Wu, Z.; Zhang, Z.; Zou, Y. Ultra-Broadband and Wide-Angle Absorption Based on 3D-Printed Pyramid. *Opt. Laser Technol.* **2020**, *124*, 105972. [CrossRef]
12. Lesyk, D.A.; Martinez, S.; Mordyuk, B.N.; Dzhemelinskyi, V.V.; Lamikiz, A.; Prokopenko, G.I.; Iefimov, M.O.; Grinkevych, K.E. Combining Laser Transformation Hardening and Ultrasonic Impact Strain Hardening for Enhanced Wear Resistance of AISI 1045 Steel. *Wear* **2020**, *462*, 203494. [CrossRef]
13. Yang, Y.; Lu, Y.; Shi, W.; Hou, B.; Qiao, H.; Qi, J.; Zhang, E.; Qin, G. Improvement of Biocorrosion Resistance and Antibacterial Performance of Ti-3Cu Alloy Subjected to Laser Shock Peening. *Opt. Laser Technol.* **2023**, *158*, 108794. [CrossRef]
14. Hu, D.; Liu, Y.; Chen, H.; Wang, M. Microstructure and Wear Resistance of Ni-Based Tungsten Carbide Coating by Laser Cladding on Tunnel Boring Machine Cutter Ring. *Surf. Coat. Technol.* **2020**, *404*, 126432. [CrossRef]
15. Arthanari, S.; Li, Y.; Nie, L.; Guan, Y.; Yang, S. Microstructural Evolution and Properties Analysis of Laser Surface Melted and Al/SiC Cladded Magnesium-Rare Earth Alloys. *J. Alloy. Compd.* **2020**, *848*, 156598. [CrossRef]
16. Krichevtsov, B.; Gastev, S.; Mashkov, K.; Kaveev, A.; Korovin, A.; Lutsev, L.; Suturin, S.; Lobov, I.; Telegin, A.; Lomov, A.; et al. Magnetization Reversal in $NiFe_2$ O4/$SrTiO_3$ Nanoheterostructures Grown by Laser Molecular Beam Epitaxy. *J. Phys. Conf. Ser.* **2019**, *1389*, 012106. [CrossRef]
17. Allen, S.D. Laser Chemical Vapor Deposition: A Technique for Selective Area Deposition. *J. Appl. Phys.* **1981**, *52*, 6501–6505. [CrossRef]
18. Asghar, H.; Ahmed, R.; Ajmal, R.; Umar, Z.A.; McInerney, J.; Baig, M.A. Ameliorating the Stability of Erbium-Doped Fiber Laser Using Saturable Absorber Fabricated by the Pulsed Laser Deposition Technique. *Sci. Rep.* **2022**, *12*, 20267. [CrossRef] [PubMed]
19. Dong, X.; Liu, S.; Song, H.; Gu, P. Growth of Large-Area, Few-Layer Graphene by Femtosecond Pulsed Laser Deposition with Double-Layer Ni Catalyst. *J. Mater. Sci.* **2017**, *52*, 2060–2065. [CrossRef]
20. Zhang, Z.; Gu, Q.; Jiang, W.; Zhu, H.; Xu, K.; Ren, Y.; Xu, C. Achieving of Bionic Super-Hydrophobicity by Electrodepositing Nano-Ni-Pyramids on the Picosecond Laser-Ablated Micro-Cu-Cone Surface. *Surf. Coat. Technol.* **2019**, *363*, 170–178. [CrossRef]
21. Li, Z.; Guan, X.; Hua, Y.; Hui, S. Composite Nanostructures Induced by Water-Confined Femtosecond Laser Pulses Irradiation on GaAs/Ge Solar Cell Surface for Anti-Reflection. *Opt. Laser Technol.* **2018**, *106*, 222–227. [CrossRef]
22. Meng, J.; Song, H.; Li, X.; Liu, S. Femtosecond Laser Fabricating Black Silicon in Alkaline Solution. *Appl. Phys. A* **2015**, *118*, 1197–1203. [CrossRef]
23. Meng, J.; Song, H.; Li, X.; Liu, S. Influence of Femtosecond Laser Pulse Energy on the Surface Reflection of Black Silicon in Alkaline Solution. *J. Laser Appl.* **2016**, *28*, 012005. [CrossRef]

Disclaimer/Publisher's Note: The statements, opinions and data contained in all publications are solely those of the individual author(s) and contributor(s) and not of MDPI and/or the editor(s). MDPI and/or the editor(s) disclaim responsibility for any injury to people or property resulting from any ideas, methods, instructions or products referred to in the content.

coatings

MDPI

Editorial

Special Issue: "Laser-Assisted Coating Techniques and Surface Modifications"

Haiying Song [1,2,*] and Fujiang Tao [1,2]

[1] Strong-Field and Ultrafast Photonics Laboratory, School of Physics and Optoelectronic Engineering, Beijing University of Technology, Beijing 100124, China; fjtao@emails.bjut.edu.cn
[2] Key Laboratory of Trans-Scale Laser Manufacturing Technology, Ministry of Education, Beijing University of Technology, Beijing 100124, China
* Correspondence: hysong@bjut.edu.cn

1. Introduction

With its outstanding directionality, high energy density, and flexible controllability, laser technology has become a key and multifunctional core tool in advanced manufacturing systems [1–3]. As a highly localized and precisely controllable heat source, lasers have driven the development of a wide range of material processing technologies, including surface modification [4], coating fabrication [5], and micro- and nanoscale manufacturing [6], thereby giving rise to the broad and evolving field of Laser-assisted coating techniques and surface modifications (LACT & SM). From the perspective of surface performance enhancement, technologies such as laser shock peening [7] and laser surface hardening [8] have demonstrated great potential in improving wear resistance, corrosion resistance, and service reliability. In coating fabrication, laser cladding enables the formation of coating systems with strong metallurgical bonding and controllable microstructures on substrate surfaces [9], while laser remelting [10] can further improve coating density and uniformity. In addition, laser alloying [11] emphasizes elemental incorporation and localized compositional reconstruction, allowing for the tailored design of surface microstructures and properties. Together, these laser-enabled coating and modification technologies provide critical support for enhancing oxidation resistance, wear resistance, and overall service performance. At the micro- and nanoscale, laser surface texturing [12] has shown broad application prospects in regulating surface wettability, improving tribological behavior, and optimizing photothermal radiation characteristics. Meanwhile, as an efficient coherent light source, lasers are also widely applied in precision metrology [13], material characterization [14], and intelligent inspection [15]. Owing to these unique advantages, LACT & SM play an indispensable role in the manufacturing of high-end equipment, precision engineering components, and advanced functional materials, thereby continuously advancing modern manufacturing capabilities [3,16].

This Special Issue has systematically compiled the latest advances in LACT & SM, covering a broad range of processing techniques, fundamental mechanisms, and material systems, and highlights the emerging trend of multi-technology integration and interdisciplinary development aimed at enhancing surface performance [17].

2. Statistics of the Special Issue

This issue consists of 13 full-text articles written by 48 authors. The geographical distribution of the authors is shown in Figure 1. The authors come from six countries across three continents: Europe, Asia, and North America. On average, each paper has approximately four authors.

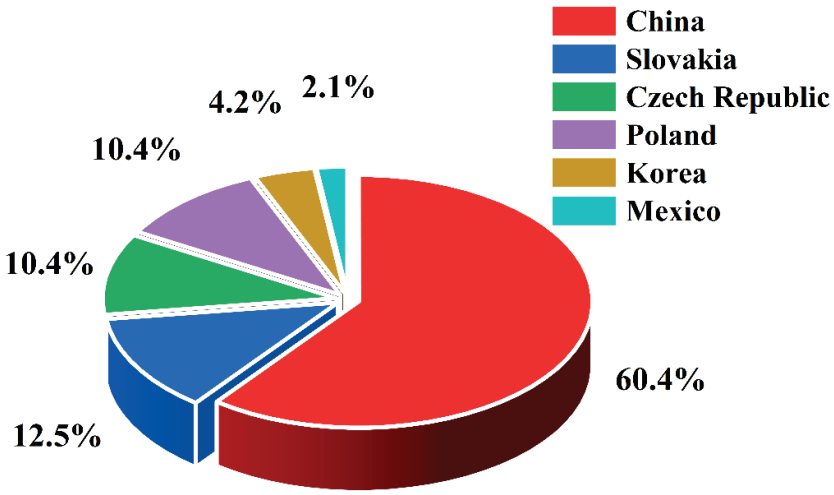


Figure 1. The distribution of authors by country.

3. Brief Overview of the Contributions to This Special Issue

Lv et al. [18] proposed a two-dimensional elliptical ultrasonic vibration incremental forming process for laser shock peening pretreatment. This process significantly improves the surface microhardness of 7075 aluminum alloy plates through a dual mechanism that promotes internal softening during material deformation and surface strengthening, thereby improving the surface mechanical properties of the sheet. At the same time, it creates a strengthening coating with excellent mechanical properties and a residual compressive stress field on the surface, showing potential value in manufacturing aircraft panels with complex shapes and excellent surface properties. Záhon et al. [19] studied the changes in tribological properties of Austempered ductile iron (ADI) under laser surface strengthening at different isothermal holding temperatures. The results showed that the laser process achieved a homogeneous martensitic layer on the surface, and its hardness and wear resistance were significantly improved compared with the non-laser-hardened surface. This phenomenon supports the theory of a possible martensitic-phase transformation of high-carbon austenite contained in the structure of ADI castings. Huang et al. [20] found that the high-temperature oxidation performance of Ti_{60} alloy after laser cladding of a Ti-Hf-Mo-Ta-Nb-B composite coating was significantly improved, and they systematically explored the microstructure and oxidation behavior of the material, as well as the potential mechanism of the coating's high-temperature oxidation resistance. Following the work in reference [20], to improve the wear resistance of Ti_{60} alloy, Huang et al. [21] obtained a composite coating containing a high-entropy $(Ti_{0.2}Zr_{0.2}Mo_{0.2}Ta_{0.2}Nb_{0.2})B_2$ boride phase by laser cladding. When the surface of Ti_{60} alloy was coated with a high-entropy phase of 34.17 wt.%, the hardness of the composite coating was about 2.9 times that of the Ti_{60} alloy substrate, and the mass wear rate was about 1/11 of that of the Ti_{60} alloy substrate. Zhang et al. [22] reported a new surface microcrystallization technique for post-treatment of cermet coatings using high-temperature-assisted ultrasonic deep rolling (HT+UDR). They systematically studied the microstructure and tribological properties of Ni-WC coatings and achieved improvements in coating surface quality, hardness, and wear resistance, providing a reference for the field of high-temperature ultrasonic rolling of cermet coatings. To address the lack of research on laser modification technology for improving high-entropy alloy coatings by laser remelting, Lv et al. [23] used laser remelting to treat FeCoNiCrAl high-entropy alloy coatings prepared by laser cladding technology and discussed the effects of laser remelting on the phase composition, microstructure, wear resistance, and corrosion resistance of the coating. In the corrosion resistance study, they also used Scanning Vibration Electrode Technology, which was rarely used in previous studies, to accurately show

https://doi.org/10.3390/coatings16040430

the effect of laser remelting on the corrosion resistance of the coating. Górka et al. [24] compared the erosive wear resistance of ductile cast irons (DCIs) after laser surface melting (LSM) and laser surface alloying (LSA) treatments. They analyzed the effects of the process environment (argon and nitrogen), structural composition (TiC/TiCN fraction, cementite fraction), and hardness on the erosive wear resistance, as well as the erosion mechanisms. The results showed that laser melting and alloying processes with titanium powder had a positive effect on the hardness and erosive wear resistance of DCI surfaces. In response to the requirements for surface quality in High-Pressure Die Casting (HPDC), Sütőová et al. [25] investigated the lifetime of PVD-coated inserts and uncoated inserts, as well as inserts coated with three different nitride-based PVD coatings (TiN, TiAlN, and CrAlSiN) under actual mass production conditions. Compared with untreated mold inserts, mold inserts with deposited coatings had higher hardness and longer lifetime, with TiN coating achieving the longest lifetime.

In the paper by Park et al. [26], a laser-induced selective surface wetting technique (SSWT) was used to prepare patterned eutectic gallium-indium (EGaIn) flexible liquid metal electrodes. By establishing a perfluorinated self-assembled monolayer to impart superhydrophobicity, followed by selective ultraviolet (UV) pulsed laser ablation to generate hydrophilic regions at predefined surface sites, liquid metal patterns with a linewidth of approximately 50 μm, superior flexibility, and simple fabrication were achieved. It is expected to be applied in the promising field of wearable and stretchable electronics with high flexibility when combined with a passivation layer to protect the liquid metal electrodes. Feng et al. [27] prepared SiCp aluminum matrix composites with different spherical WC contents by laser cladding. They analyzed the influence of various factors on the coating quality through single-factor experiments, and systematically studied the effects of different laser power, powder feeding rate, and scanning rate on melt width and dilution rate, micromorphology, phase composition, elemental distribution, microhardness, and wear performance. They determined the spherical WC content with the best comprehensive coating performance. Guo et al. [28] studied the application of femtosecond laser direct writing in the preparation of tungsten surface gratings and the modulation of their thermal radiation spectrum. They reported the effects of femtosecond lasers with different laser fluence on grating depth, direct-writing width, and nanostructured regions. The thermal radiation enhancement phenomenon caused by adjusting parameters such as structural period and temperature is expected to be applied to infrared remote sensing, infrared detection, and infrared guidance in the aerospace field. In laser manufacturing technologies such as additive manufacturing, advanced non-destructive technologies play an important role in detecting surface defects. In the study of Rodríguez et al. [29], a microsurface defect identification method based on microlaser line projection and affine moment invariants was proposed. Compared with traditional optical microscope imaging systems, which typically have a relative identification error exceeding 3%, this method exhibits higher accuracy, achieving a relative identification error of 0.721%.

4. Conclusions

Laser surface engineering is a vast subject, encompassing diverse processes, methods, materials, and applications. The field boasts a wealth of literature, including numerous reviews and specialized studies. In our Special Issue, we have collected recent works, in accordance with the authors' choices, covering novel schemes for coating preparation and surface modification of advanced manufacturing materials. All of them are aimed at significantly enhancing the surface properties of devices using advanced laser technologies and bridging the gap between surface structure design and practical applications. While no research papers on the latest machine learning and AI-driven optimization methods

https://doi.org/10.3390/coatings16040430

for laser processing have yet emerged, our Special Issue clearly demonstrates the steadily growing interest among researchers in laser-assisted surface technologies for coatings and surface modification. We hope readers will find the published papers interesting and helpful.

Conflicts of Interest: The authors declare no conflicts of interest.

References

1. Huang, Y.; Yang, R.; Li, M.G. Recent Advances in Laser Manufacturing: Multifunctional Integrative Sensing Systems for Human Health and Gas Monitoring. *Adv. Funct. Mater.* **2024**, *34*, 2407503. [CrossRef]
2. Lian, R.; Xu, X.; Zhao, K.; Fei, X.; Cao, W.; Zhu, J. Advancements in Laser Processes for Additive Manufacturing: Techniques and Future Directions. *J. Mater. Res. Technol.* **2026**, *41*, 2428–2451. [CrossRef]
3. Gao, B.; Tang, K.; Deng, Z.; Chen, Z.; Yuan, L.; Wang, W. A review of laser-assisted cutting of hard and brittle materials: Tools, devices and mechanisms. *Opt. Laser Technol.* **2025**, *189*, 113105. [CrossRef]
4. Sypniewska, J.; Szkodo, M.; Majkowska-Marzec, B.; Pawłowski, Ł.; Mirowska, A.; Ryl, J.; Mielewczyk-Gryń, A.; Gaweł, G.Ł.; Campos, E.M.; Hernán, J.P.F. Hybrid laser-micro-arc oxidation techniques for enhanced biocompatibility and surface modification of $Ti_{13}Nb_{13}Zr$ alloy in biomedical applications. *Appl. Surf. Sci.* **2025**, *698*, 163136. [CrossRef]
5. Sun, G.; Cong, X.; Du, W.; Chen, C. Preparation of near iso-atomic ratio aluminium-based high-entropy alloyed high-performance coatings by laser multiple remelting process. *Opt. Laser Technol.* **2025**, *191*, 113285. [CrossRef]
6. Li, M.; Chen, W.; Deng, C.; Li, D.; Ning, Z.; Hu, H.; Wang, W.; Gao, H.; Deng, L.; Xiong, W. Recent advances in femtosecond direct laser writing of micro-optical imaging components. *Int. J. Extreme Manuf.* **2026**, *8*, 022011. [CrossRef]
7. Sahu, A.; Tewari, M.; Yarramilli, V.A.; Raj, S.; Rai, S.; Maharjan, N.; Kumar, S.; Bhatnagar, N.; Bhowmik, A. Modification of superficial microstructure of D2205 duplex stainless steel for improvement of mechanical properties and biocompatibility of surfaces by laser shock peening. *Appl. Surf. Sci.* **2026**, *715*, 164568. [CrossRef]
8. Kluczyński, J.; Jasik, K.; Łuszczek, J.; Pokropek, J. Laser Surface Hardening of Carburized Steels: A Review of Process Parameters and Application in Gear Manufacturing. *Materials* **2025**, *18*, 3623. [CrossRef]
9. Sun, J.; Zhang, Y.; Sun, Z.; Yu, T.; Wang, G. Microstructure and tribological property of laser cladding Stellite 6 alloy by laser remelting and ultrasonic surface rolling. *Surf. Coat. Technol.* **2025**, *495*, 131560. [CrossRef]
10. Jiang, X.; Du, Y.; Peng, Y.; Chen, H.; Lei, X. Laser remelting post-treatment: Improving microstructure and tribological properties of laser cladded Stellite6 coating on 2507 duplex stainless steel. *Opt. Laser Technol.* **2026**, *193*, 114236. [CrossRef]
11. Pulluru, S.K.; Birru, A.K.; Sharma, F.; Dixit, U.S. Laser surface alloying of 7075 aluminum alloy with Cr, SiC, and carbon nanotube powders. *J. Mater. Eng. Perform.* **2025**, *34*, 13941–13955. [CrossRef]
12. Ince, F.D.; Özel, T. Laser surface texturing of materials for surface functionalization: A holistic review. *Surf. Coat. Technol.* **2025**, *498*, 131818. [CrossRef]
13. Zhao, F.; Tang, H.; Zou, X.; Li, X. A Review of Optical Metrology Techniques for Advanced Manufacturing Applications. *Micromachines* **2025**, *16*, 1224. [CrossRef] [PubMed]
14. Xu, L.; Tang, J.; Xiang, H.; Wu, X.; Hou, C.; Gan, Q.; Nie, Z.; Lan, P.; Lu, P. Single-shot characterization of ultrashort laser pulses on wide-bandgap solid material. *Opt. Lett.* **2025**, *50*, 932–935. [CrossRef]
15. An, Z.; Pei, Y. Research on Power Laser Inspection Technology Based on High-Precision Servo Control System. *Photonics* **2025**, *12*, 944. [CrossRef]
16. Yang, C.; Ji, C.; Feng, S.; Liu, Y.; Wei, W.; Long, Y. Ultrafast laser-matter interaction mechanisms and applications in functional device fabrication: Recent advances and perspectives. *Appl. Phys. Rev.* **2025**, *12*, 03325. [CrossRef]
17. Song, H.; Wang, L.; Liu, S. Metasurface Properties Obtained via Laser-Assisted Surface Technology. *Coatings* **2023**, *13*, 251. [CrossRef]
18. Lv, Y.; Dong, M.; Pan, X.; Yi, C.; Su, J. Surface Mechanical Properties and Micro-Structure Evolution of 7075 Aluminum Alloy Sheet for 2-Dimension Ellipse Ultrasonic Vibration Incremental Forming: A Pretreatment for Laser Shock Peening. *Coatings* **2022**, *12*, 1914. [CrossRef]
19. Záhon, L.; Kuchař, J.; Horník, J.; Krčil, J.; Kudláček, J. Laser Surface Hardening of Austempered Ductile Iron (ADI). *Coatings* **2024**, *14*, 958. [CrossRef]
20. Huang, K.; Han, X. High-Temperature Oxidation Properties of Ti-Hf-Mo-Ta-Nb-B Composite Coating Deposited on Ti_{60} Alloy with Laser Cladding. *Coatings* **2023**, *13*, 1646.
21. Huang, K.; Han, X. Laser Cladding of a Ti–Zr–Mo–Ta–Nb–B Composite Coating on Ti_{60} Alloy to Improve Wear Resistance. *Coatings* **2024**, *14*, 1247. [CrossRef]

22. Zhang, J.; Zhao, Y.; He, Y.; Meng, C.; Zhang, X.; Zhang, S. Effect of High-Temperature-Assisted Ultrasonic Deep Rolling on Microstructure and Tribological Properties of Ni-WC Coatings. *Coatings* **2023**, *13*, 499. [CrossRef]
23. Lv, T.; Zou, W.; He, J.; Ju, X.; Zheng, C. Study on the Microstructure and Properties of FeCoNiCrAl High-Entropy Alloy Coating Prepared by Laser Cladding-Remelting. *Coatings* **2024**, *14*, 49. [CrossRef]
24. Górka, J.; Lont, A.; Janicki, D.; Poloczek, T.; Rzeźnikiewicz, A. Comparison of the Erosive Wear Resistance of Ductile Cast Iron Following Laser Surface Melting and Alloying. *Coatings* **2024**, *14*, 646. [CrossRef]
25. Sütőová, A.; Kočiško, R.; Petroušek, P.; Kotus, M.; Petryshynets, I.; Pylypenko, A. Study of PVD-Coated Inserts' Lifetime in High-Pressure Die Casting Regarding the Requirements for Surface Quality of Castings. *Coatings* **2024**, *14*, 1043. [CrossRef]
26. Park, S.J.; Yang, C. Flexible Finely and Directly Patternable Liquid Metal Electrodes via Selective Surface Wetting Technique. *Coatings* **2023**, *13*, 1922. [CrossRef]
27. Feng, X.; Li, X.; Wang, F.; Liu, Z.; Wang, W. Effect of Spherical WC Content on the Microstructure and Properties of SiCp Aluminium Composite Material. *Coatings* **2023**, *13*, 1935. [CrossRef]
28. Guo, R.; Zhou, P.; Zhang, W.; Song, H.; Liu, S. Study on the Thermal Radiation Characteristics of Tungsten Surface Grating Structures Prepared by Femtosecond Laser Direct Writing. *Coatings* **2024**, *14*, 1045. [CrossRef]
29. Rodríguez, J.A.M. Microsurface Defect Recognition via Microlaser Line Projection and Affine Moment Invariants. *Coatings* **2025**, *15*, 385. [CrossRef]

Disclaimer/Publisher's Note: The statements, opinions and data contained in all publications are solely those of the individual author(s) and contributor(s) and not of MDPI and/or the editor(s). MDPI and/or the editor(s) disclaim responsibility for any injury to people or property resulting from any ideas, methods, instructions or products referred to in the content.

coatings

Article

Surface Mechanical Properties and Micro-Structure Evolution of 7075 Aluminum Alloy Sheet for 2-Dimension Ellipse Ultrasonic Vibration Incremental Forming: A Pretreatment for Laser Shock Peening

Yuan Lv *, Mengen Dong, Xixiang Pan, Cong Yi and Jiaqi Su

College of Mechanical Engineering, Xi'an University of Science and Technology, Xi'an 710054, China
* Correspondence: lvyuan@xust.edu.cn; Tel.: +86-135-7219-9684

Abstract: In this paper, a composite technique of ultrasonic incremental forming and laser shock peeing is proposed. The former process is mainly used for the manufacturing of complex-shaped sheet and strengthening coating that is prepared for subsequent laser treatment. The latter is applied for secondary surface reinforcement with ultra-high energy. This work focused on the novel ultrasonic incremental forming method and its effects on surface mechanical properties and micro-structure of a 7075 aluminum alloy. First, a kind of 2-dimension ellipse ultrasonic vibration incremental forming process and the unique double-mechanism method of sectionalized cooperative control of plastic deformation and mechanical performance were designed. Second, the single-point incremental forming, the longitudinal ultrasonic vibration incremental forming, and the 2 dimension ellipse ultrasonic vibration incremental forming were performed for the manufacture of conical components of 7075 aluminum alloy. Third, the Vickers micro-hardness testing results and images of the fracture morphology of the machined part for the novel technique confirm that softening mechanisms become dominant inside the metal sheet. Furthermore, a strengthening coating with excellent mechanical properties and a residual compressive stress field were created on its surface simultaneously. In a word, the research shows potential values of the proposed technique for the manufacture of aircraft panels of complex shape and excellent surface properties.

Keywords: ultrasonic incremental forming; laser shock peening; aluminum alloys; surface strengthening coating; fracture morphology

1. Introduction

In the aviation industry, great attention has been paid to high-strength aluminum alloys and thin-walled integral panels, which is a crucial component of large aircraft. Therefore, the forming technology of key panels is one of the critical issues [1]. At present, several kinds of developing technology are suitable for manufacturing essential boards such as stretch forming, shot-peening, incremental forming, creep age forming, and laser forming [2]. Single-point incremental forming (SPIF) is a sheet metal forming method that has gained considerable interest in the research field due to its good formability, high flexibility, and low cost. Researchers have mainly studied the deformation mechanism, process optimization, and finite element modeling (FEM) simulation to resolve the forming accuracy and quality problems. Malhotra [3] used a new fracture model combined with finite element analyses to predict the occurrence of fracture in the SPIF process. Aerens [4] established practical formulae to predict forming forces based on a large set of systematic experiments. Vanhove and Pereira [5,6] studied the influence of an increasing feed rate on forming forces, temperature, and formability. Azevedo [7] evaluated the influence of the type of lubricant on the surface quality of incremental forming parts of aluminum 1050 and DP780 steel sheets. Trzepieciński [8] analyzed the interactions between the SPIF process

parameters and the main roughness parameters of stiffened ribs fabricated in aluminum alloy panels. In Bansal's work, a modified model was given to accurately predict the formed component thickness, contact area, and forming forces during single and multi-stage incremental forming [9]. In addition, a great number of research has also facilitated the rapid development of the SPIF technique. However, it still has some weaknesses such as severe sheet thinning, long processing cycle, and fracture. These problems impede the application of the SPIF process in industrial practice [10].

In recent years, numerous studies have indicated that the input of auxiliary energy is helpful for an improvement in the forming limit and qualities and the reduction in the forming force. Then, powerful energy such as electricity, magnetism, and ultrasonic wave has been widely applied to the plastic forming field and machining field [11–14]. Ultrasonic vibration incremental forming has been the one of the most promising technologies. To study its unique forming mechanism, the ultrasonic volume effect containing multi-mechanisms of stress superposition, acoustic softening, and dynamic impact has been investigated [15–18]. Li [19] explored the influence of the superposition of ultrasonic vibration on the contact behavior and material deformation mechanism during the forming process. Zhai [20] conducted a series of experiments to explore the impacts of the step-down size, the sheet thickness, and the rotation speed on the ultrasonic softening effect. Based on the conversion of ultrasonic vibration to heat, Sakhtemanian [21] established a new theoretical model to investigate the material behavior in the finite element simulation of the ultrasonic assisted SPIF process. In fact, a complicated ultrasonic effect involves a multi-coupling action of the ultrasonic softening effect, ultrasonic hardening effect, work hardening, heat softening, and stress superposition. The simple heat-conversion theory is insufficient to completely explore the ultrasonic forming mechanism and satisfactorily explain the ultrasonic-induced material behaviors. In addition to these mechanism studies, technique rules and parameter optimization have also been the focus of research. Sun [22] established a series of experiments to explore the influence of ultrasonic vibration on the surface property and springback effect of a symmetrical aluminum alloy sheet. Li [23] investigated the effect of the ultrasonic vibration on the material flow characteristics and the plastic deformation mechanism during the forming of a straight groove. Amini [24] analyzed the impacts of process parameters including the sheet material, ultrasonic power, feeding speed, and tool diameter on the force reduction and temperature increment. Li and Cheng [25] built a theoretical model describing the relationship between the stress and strain during the ultrasonic-assisted incremental sheet forming to facilitate an accurate prediction. However, the modified model only considering the softening effect is insufficient and provides limited improvement in the prediction accuracy.

All of the current published research has mainly paid attention to the ultrasonic effect and technical optimization based on the unidirectional ultrasonic vibration incremental forming process. The one-way vibration device only provides inadequate ultrasonic energy and single high-frequency impact for processing high-strength alloys. The ultrasonic softening effect is limited to reduce the forming force and improve the formability of high-strength metals. Furthermore, it is well-known that a series of aircraft disasters were induced by fatigue failures of the airplane panels because of vibration, aerodynamic noise, a corrosive environment, and high temperature. This demands aircraft panels of a complex and accurate shape, outstanding superficial mechanical properties, and remarkable anti-fatigue performance. The existing forming technology cannot meet the strict and paradoxical manufacturing requirements of excellent formability, good flexibility, and valid surface-strengthening simultaneously. To satisfy the increasingly common and challenging needs, a composite technique of 2-dimension ultrasonic incremental forming and laser shock peening was proposed in this paper. The former method was suitable for the manufacturing of a complex-shaped sheet and strengthening coating, which was prepared for subsequent laser treatment. The latter was applied for secondary surface reinforcement with ultra-high energy. This work focused on the design of a type of 2-dimension ultrasonic vibration incremental forming method and its effects on the surface

mechanical property and micro-structure of 7075 aluminum alloy. The traditional single-point incremental forming tests, the longitudinal ultrasonic vibration incremental forming tests, and 2D ellipse ultrasonic vibration incremental forming tests were conducted on the designed special ultrasonic incremental forming equipment. Classic conical sheets of the 7075 aluminum alloy were manufactured with the above techniques to verify the effectiveness of the novel method and study its influence on the mechanical properties and micro structural evolution of high strength alloys.

2. Materials and Methods

2.1. Experimental Material

The experimental material was the 7075 (T651) aluminum alloy (ALNAN Aluminium Industry Company, Nanning, China) of the Al-Zn-Mg-Cu series, which was used for the manufacturing of aircraft due to its ultra-high-strength and lightweight. Its chemical composition is shown in Table 1.

Table 1. Chemical composition of the 7075 aluminum alloy.

Si	Fe	Cu	Mn	Mg	Cr	Zn	Ti	Al
≤0.4	≤0.5	1.2–2.0	≤0.3	2.1–2.9	0.18–0.28	5.1–6.1	≤0.2	Bal.

2.2. Preparation of Specimen and Tooling

Aluminum alloys are one of the most essential metals due to its good plasticity, high specific strength, excellent corrosion resistance, and low cost. The 7075 aluminum alloy with the highest strength has been widely applied to aerospace, automobile, ship, and die machining, mainly including girder, bulkhead, junction, and integral panels, which are the main load-carrying structure of planes. While it has a large application in industry, engineers face significant manufacturing problems of the low processing properties caused by the high mechanical strength and efficient cooperation of plastic forming and surface strengthening of the 7075 aluminum alloy. To investigate this further, a 2D ellipse ultrasonic vibration incremental forming test of the thin-walled panel of the 7075 aluminum alloy was designed in this paper. Thin-walled specimens of the 7075 aluminum alloy used for 2D ellipse ultrasonic vibration incremental forming tests to investigate the macroscopic mechanical properties and micro-structure evolution under different conditions of ultrasonic vibration are shown in Figure 1a. The specimens were machined with a wire-cut electrical discharge machine.

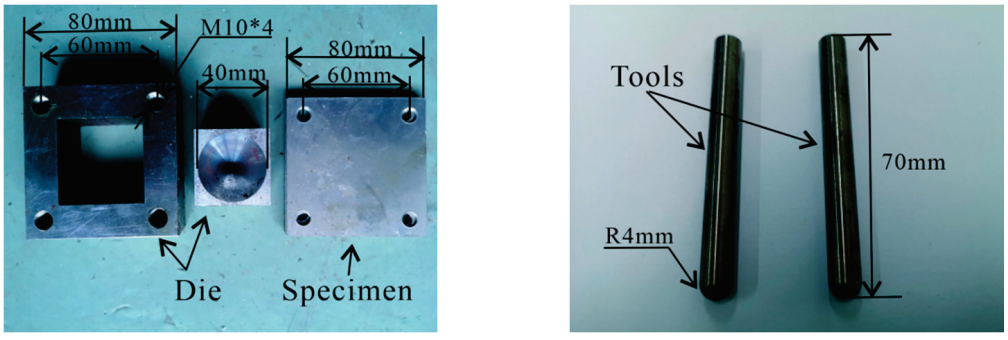


Figure 1. Devices for incremental forming. (**a**) Specimen and die. (**b**) Forming tools.

Unlike the traditional punching process, the single-point incremental forming process of curve surface sheet metal mainly relies on the layered forming path of the single-point tool instead of the conventional punching die. It is obvious that the single-point forming tool suffers more strike, friction, and heat than the incremental forming die, which plays a vital role in improving the quality and geometrical accuracy of the forming

sheet by supporting and fastening it. Therefore, the single-point forming tools were made of high-temperature cemented carbide K25, which features a high-temperature abrasion resistance and long service life because of the high-temperature area of up to 200–800 °C that occurs at the ends of the tool. The tool works under conditions of intense friction and ultrasonic vibration. The single-point forming tool and die are shown in Figure 1a,b.

2.3. Method of Experiment

2.3.1. Design of Principle

As known, the most remarkable characteristic of the single-point incremental forming is that the metal sheet is extruded by the rolling tool point by point, according to the layered forming paths, which are a series of contour lines of the designed production. In Figure 2a, as the principle image of the single-point incremental forming shows, regional materials that contact the half-spherical head of the forming tool deforms permanently as the tool feeds horizontally or vertically. Compared to the traditional stamping process, this unique processing mode reduces the forming force and tremendously improves the manufacturing flexibility. At the same time, it causes the heterogeneous deformation and flow of materials. The severe problem of the thinning rate of the forming sheet hampers the application of the traditional incremental forming in manufacturing fields. Furthermore, it is difficult to utilize this technique to manufacture high-strength alloys. Rupture phenomena always occurs on metal sheets that are deformed beyond their forming limit. To conquer these challenging difficulties, ultrasonic energy is used in the softening of difficult-to-deform materials. In recent years, longitudinal ultrasonic vibration incremental forming has become a research hot spot due to some of its advantages. As Figure 2b shows, the sheet driven by a one-way ultrasonic device vertically vibrates relative to the forming tool. Then, the feeding and rolling tool impacts the sheet surface while it extrudes the deformed sheet. The half-spherical affected field caused by the impact actions marked as a shadow is present in Figure 2b. The longitudinal ultrasonic vibration incremental forming process features a special phenomenon of high frequency periodic contact–detach conditions of the sheet and the tool. The working mechanism causing a coupling action of ultrasonic effect, work hardening, heat softening, and stress superposition has been investigated. Moreover, the periodic extrusion ameliorates the intense friction condition between the sheet and the tool. This is beneficial to the improvement in the surface qualities of the forming sheet. However, the unidirectional ultrasonic vibration design only provides limited energy for material softening. The manufacture of complex thin-walled panels of high-strength alloys is still a challenging engineering problems. In addition, current technologies cannot fulfil the industry's need for the surface strengthening and fatigue resistance of thin-walled parts. The bidirectional ultrasonic vibration device, which was successfully applied to other manufacturing fields, has never been used for incremental forming. In this work, a unique 2-dimension ellipse ultrasonic vibration method and device were designed. As Figure 2c shows, the forming sheet driven by the designed 2-dimension ellipse ultrasonic device vibrates in an ellipse path relative to the forming tool. Compared to the second process, it dramatically increases the contact areas between the sheet and the tool. This affected area, marked as an ellipsoid shadow in Figure 2c, is divided into two parts. One part is located in the processing region. Materials in this area deform and flow under the extrusion action and ultrasonic effect of the rolling and vibrating tool. A coupling action of the ultrasonic softening effect, ultrasonic hardening effect, thermal softening effect, work hardening, refined crystalline strengthening, and stress superposition affects the micro-structure evolution and the mechanical behaviors of metal materials. It was deduced that the reinforced softening effects dominated in this process, which tremendously improved the forming limit of difficult-to-deform materials such as the 7075 aluminum alloy. The other part of the affected area was located in the adjacent processed region on the side wall of the sheet. Materials restricted by

the supporting mold in this area cannot flow. This process, similar to shot-peening, created a huge number of impact craters and a layer of strengthening coating with the residual compressive stress field. Obviously, hardening effects play a leading role in this area. In other words, the most outstanding innovation of this work is that the proposed 2-dimension ellipse ultrasonic vibration incremental forming process and the unique double-mechanism method of sectionalized cooperative control of forming deformation and mechanical performance including an internal softening mechanism, which promotes the deformation of materials and a surface strengthening mechanism that improves superficial mechanical properties of the sheet. Therefore, this new technique could meet the challenging demands on aircraft panels of complex shape and strengthening surface. Micro-hardness tests, scanning electron microscope (SEM) (TESCON Company, Brno, Czech Republic) tests of the micro-structure, and residual stress tests were performed to prove the above assumptions.

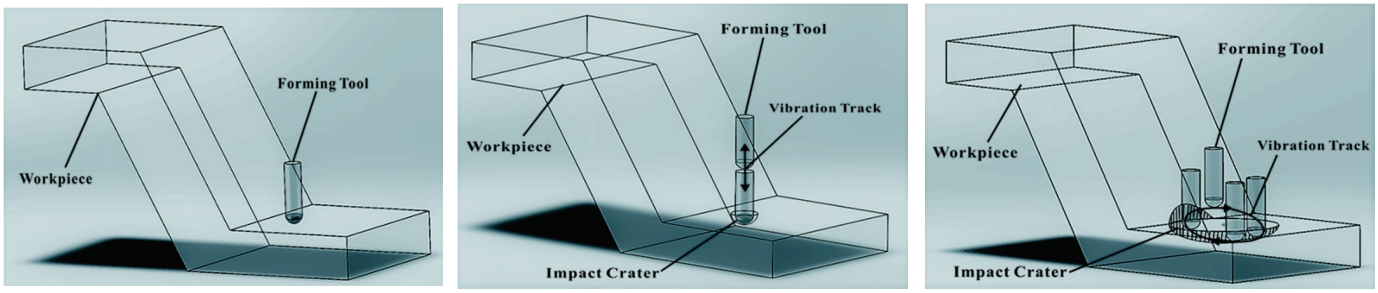


Figure 2. Ultrasonic vibration mode of progressive forming. (**a**) Without ultrasonic vibration; (**b**) vertical ultrasonic vibration; (**c**) 2D ultrasonic vibration.

2.3.2. Design of Equipment

To accomplish the above goals, it was significant and necessary to design and manufacture the 2D ellipse ultrasonic vibration system. This vibration system was installed on the workbench of the numerical control milling machine, which turned out to be a type of specialized equipment for the 2D ellipse ultrasonic vibration incremental forming tests. As Figure 3a shows, the two ultrasonic vibration devices with the same frequency (20 KHz) and amplitude (10 μm) were fixed on the workbench. They both contained a supersonic generator, filter, phase shifter, energy converter, and amplitude transformer. The amplitude transformer of the named *X*-axis vibration device was connected to the left profile of the vibration platform. One of the *Z*-axis devices was joined with the bottom of the vibration platform. The exact frequency and the phase difference of a quarter of the two ultrasonic vibration systems driving the platform vibrated in a 2D ellipse path. The long-axis and the short-axis of the ellipse path were equal to the vibration amplitude of the two devices, respectively.

Three kinds of forming experiments—single-point incremental forming process, longitudinal ultrasonic vibration incremental forming process, and 2D ellipse ultrasonic vibration incremental forming process—were performed on the specialized ultrasonic equipment. The die installed above the vibration platform of the equipment was used to fix the part and assist in forming. The spherical tool with a rolling speed of 500 r/min adopted movements of horizontal feeding at a constant velocity of 500 mm/min and vertical feeding at a layered depth of 0.1 mm, once each time. The specialized ultrasonic equipment, conical specimens, and processing procedure are shown in Figure 3b–d.

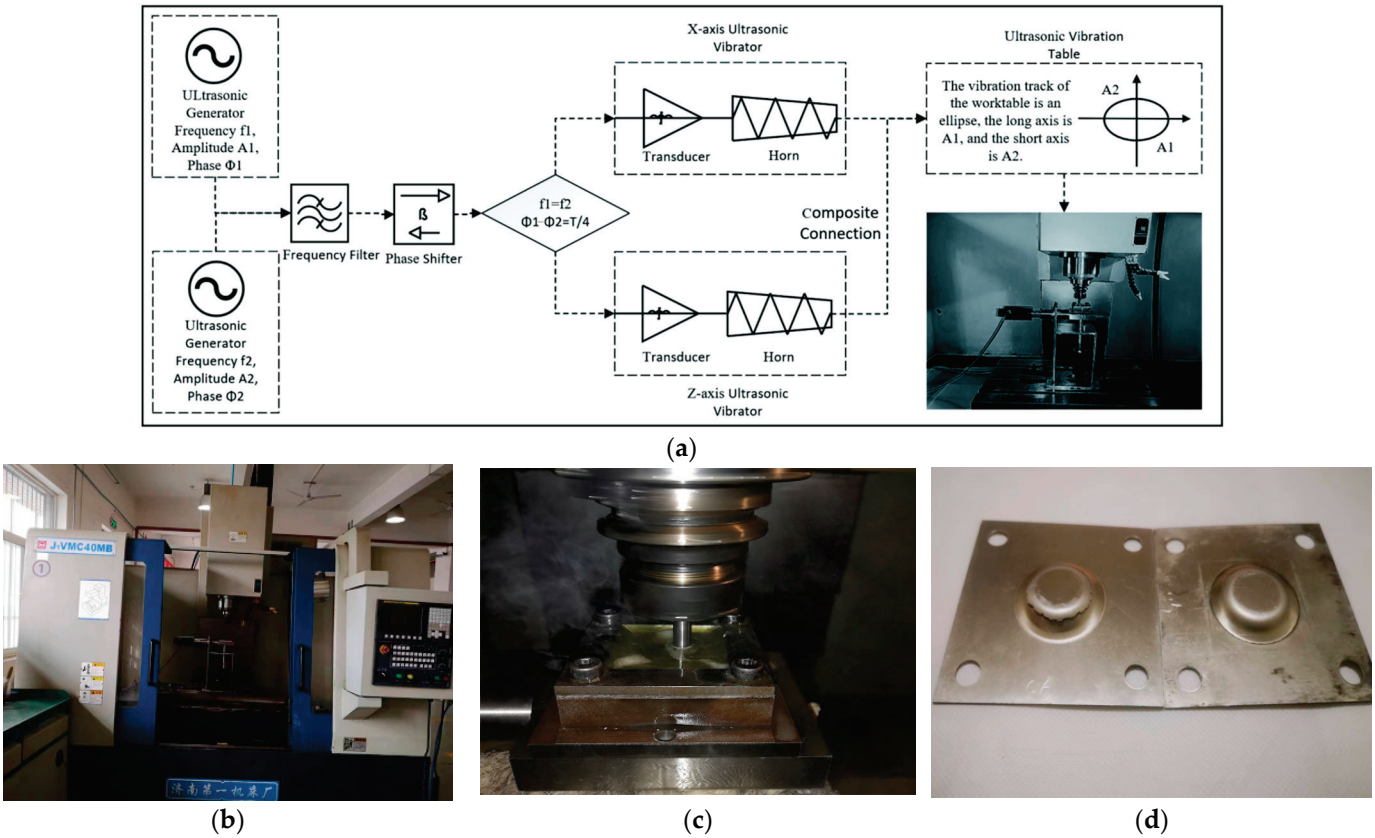


Figure 3. The 2D ultrasonic vibration incremental forming system. (**a**) Design of the 2D ultrasonic vibration system; (**b**) specialized equipment; (**c**) processing procedure; (**d**) processed specimens.

3. Results and Discussion

3.1. Mechanical Property

After single-point incremental forming tests, longitudinal ultrasonic vibration incremental forming tests and 2D ellipse ultrasonic vibration incremental forming tests, five groups of the Vickers micro-hardness tests were performed on the HMAS automatic hardness testing and analysis system with a testing force of 1000 g and testing time of 20 s to research the effect of ultrasonic vibration on the mechanical property of the 7075 aluminum alloy. The hardness tests were independently conducted on the surface of the unprocessed 7075 aluminum alloy sheet, the single-point incremental forming part, the longitudinal ultrasonic vibration incremental forming part, and the 2D ellipse ultrasonic vibration incremental forming part and cross-section of the 2D ellipse ultrasonic vibration incremental forming part. As Figure 4a shows, five isometric testing points on the conical part were uniformly distributed along the depth direction. To confirm the accurate results of the hardness experiments, the specimen was measured repeatedly five times at each testing point. The average value of the five measurement values was the final hardness value of the testing point. Figure 4b shows the Vickers micro-hardness curves of five groups of testing points. It could be found that compared to the unprocessed sheet of the 7075 aluminum alloy, the surface micro-hardness of the SPIF part increased by 17.67%, the surface micro-hardness of the longitudinal ultrasonic vibration incremental forming part increased by 38.2%, and the surface micro-hardness of the 2D ellipse ultrasonic vibration incremental forming part increased by 50.12%. Particularly, the cross-sectional micro-hardness of the 2D ellipse ultrasonic vibration incremental forming part only increased by 6.87%. The experimental results imply that the proposed 2D ellipse ultrasonic vibration incremental forming process produces a more powerful surface strengthening effect on the surface of the 7075 aluminum alloy sheet than the other two techniques. It could be deduced that work hardening and ultrasonic hardening play a leading role in this region. In addition,

the testing results also showed that the mechanical properties of the core materials of the sheet for 2D ellipse ultrasonic vibration incremental forming were similar to or even lower than that of raw materials of the 7075 aluminum alloy. As known, a coupling mechanism of ultrasonic softening, ultrasonic hardening, thermal softening, work hardening, refined crystal strengthening, and superposition stress occurs in the ultrasonic forming process. Obviously, it is easily inferred that the softening effects merely counteract the hardening effects inside the sheet for the 2D ellipse ultrasonic incremental forming. In brief, the hardness experimental results totally confirm the double-mechanism assumption.

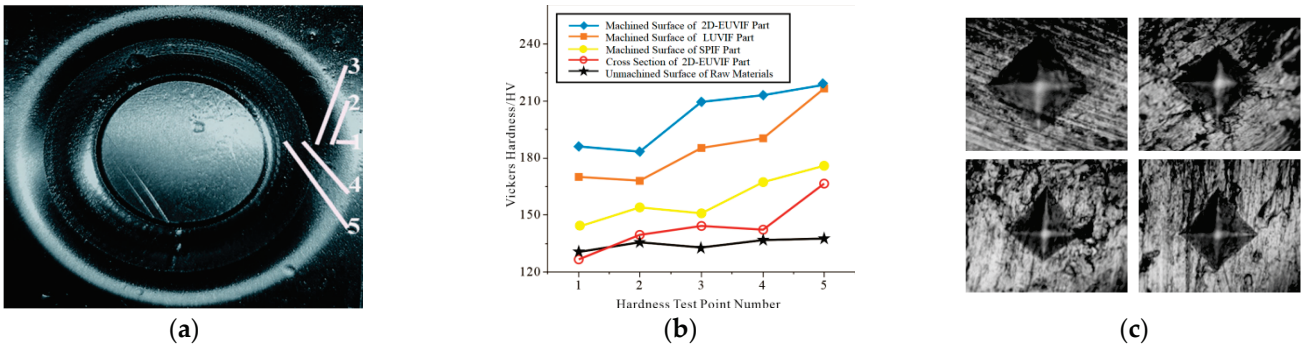


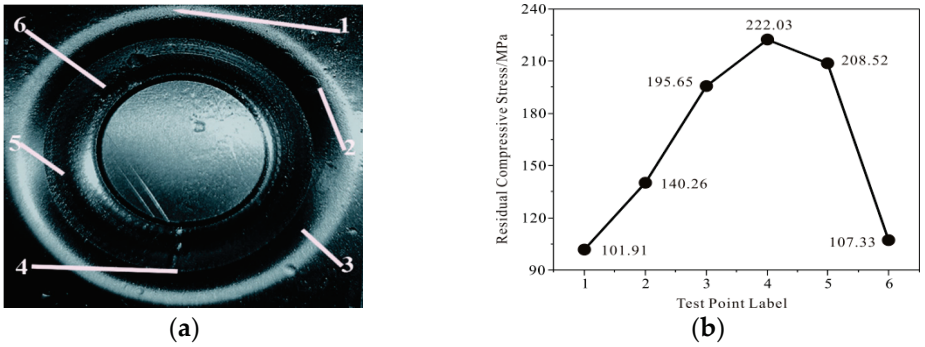
Figure 4. Micro-hardness tests of samples for various forming techniques. (**a**) Hardness testing points; (**b**) hardness curves; (**c**) micro-hardness test images (from upper left to lower right: 7075 aluminum alloy raw material, incremental forming sample, vertical vibrating ultrasonic incremental forming sample, and elliptic vibrating ultrasonic incremental forming sample. Notes: 2D-EUVIF is the abbreviation for 2D ellipse ultrasonic vibration incremental forming; LUVIF is the abbreviation for longitudinal ultrasonic vibration incremental forming; SPIF is the abbreviation for single-point incremental forming). (Notes: The numbers 1–5 in Figure 4a represent accordingly five testing points located equidistantly on the inside wall of the conical part.)

3.2. Residual Stress

To investigate the residual stress field of the 7075 aluminum alloy parts induced by 2D ellipse ultrasonic vibration incremental forming, residual stress tests were carried out on the i-XRD residual stress test and analysis system produced by the PROTO company in Canada (Aaugha). Testing standards of ASTM E915-2010 [26] and EN 15305-2008 [27] were conducted in residual stress tests. The testing conditions are listed as follows: tube voltage of 20 KV, tube current of 4 mA, radiation of CrKα, the wavelength of 2.291 m, diffraction crystal plane of (FCC, (311)), X-ray elastic constant of (1/2) S2 = 19.54×10^{-6} MPa^{-1}, and S1 = -5.11×10^{-6} MPa^{-1}.

According to the principle of equal angle in the circumferential direction and equal distance in the depth direction, six points distributed on a spiral line shown in Figure 5a were selected to test the residual stress. Figure 5b shows the residual stress values of the testing points on the conical part for the 2D ellipse ultrasonic vibration incremental forming. The negative stress values of the six sampled points indicate that the 2D ellipse ultrasonic vibration incremental forming could produce a residual compressive stress field on the surface of the conical part. The minimum absolute value of residual stress of -101.91 and -107.33 MPa occurred at the top and bottom of the conical part, respectively. The maximum absolute value of residual stress of -222.03 MPa appeared in the middle of the sidewall of the conical portion. Moreover, similar measuring results were probed at locations of No. 3 and No. 4. From this evidence, it was deduced that there was a significant gap between testing points at various depths, but fewer differences occurred in the circumferential direction. This was mainly due to the lack of enough support at the top and the bottom of the conical part. Elastic recovery and deformation led to a decrease in residual stress. Obviously, to obtain homogeneous residual compressive stress on the surface of the forming part and improve its fatigue resistance performance, it is necessary

to facilitate its supporting conditions through optimized processing planning during the 2D ellipse ultrasonic vibration incremental forming procedure.



(**a**) (**b**)

Figure 5. Residual compressive stress of the 2D-UVIF part. (**a**) Locations of residual stress testing points. (**b**) Residual compressive stress curve. 2D-EUVIF is the abbreviation for 2D ellipse ultrasonic vibration incremental forming. (Notes: The numbers 1–6 accordingly represent six testing points located on the inside wall of the conical part.).

3.3. Micro-Structures and Fracture Features

Three metal sheets of 7075 aluminum alloy were processed separately with single-point incremental forming, longitudinal ultrasonic vibration incremental forming, and 2D ellipse ultrasonic vibration incremental forming until fracture occurred. Then, their machined surfaces and fracture morphology were observed on a scanning electron microscope. Some comparative analyses were performed to identify their surface morphology and fracture features and to study the effect of ultrasonic vibration on the mechanisms of deformation and fracture of the high strength aluminum alloy materials from a microscopic perspective.

In incremental forming, the metal sheet is deformed under an extruding force and frictional force is provided by the rolling single-point tool with feeding movement. When the metal sheet is in contact with the forming tool, it is inevitable that its surface will be scratched by the ultra-hard tool. Local material is deformed and departs from the sheet surface, then it becomes metal debris, which further aggravates its surface quality. Figure 6a shows that a mass of apparent and dense scratches and layered lacerations were created on the surface of the sheet. Some small flake debris almost peeling from the sheet surface were observed in Figure 6b. This was mainly due to the constant extrusion effect on its surface implemented by the tool, which produced severe deformation and strong friction during the traditional single-point incremental forming process. The longitudinal ultrasonic vibration incremental forming process could decrease the forming force and improve the contact condition between the sheet and the tool because the aided ultrasonic vibration device reduced their contact area and time. As Figure 6c shows, there were more light and superficial scratches and lacerations on the sheet surface than in Figure 6a. However, a large number of circular cavities with a diameter of about 10 μm was observed in Figure 6d. It is easy to deduce that a few micro-debris might get into the processing area when the tool is briefly apart from the sheet surface driven by the longitudinal ultrasonic vibration device, and then the one located at the central axis of the spherical-top tool becomes a piece of sharp and hard abrasive, which drills a circular cavity with the device falling and revolving in high-speed. This clearly explains the formation of these circular cavities with regular shapes and similar sizes. Moreover, the holes could undermine the surface integrity of the product. The 2D ellipse ultrasonic vibration incremental forming proposed in this paper adopted a kind of unique mode of ultrasonic vibration, which drives the forming tool to move in an ellipse path relative to the sheet. On one hand, this kind of high frequency and intermittent extruding action also reduce the forming force and improves friction condition. Figure 6e displays a few slight scratches on its surface. On the other hand, the tool vibrating in a 2D ellipse path fiercely impacted the sheet surface. Then,

some big-flake lacerations were produced as well as the strengthening layer because of the compound vibration.

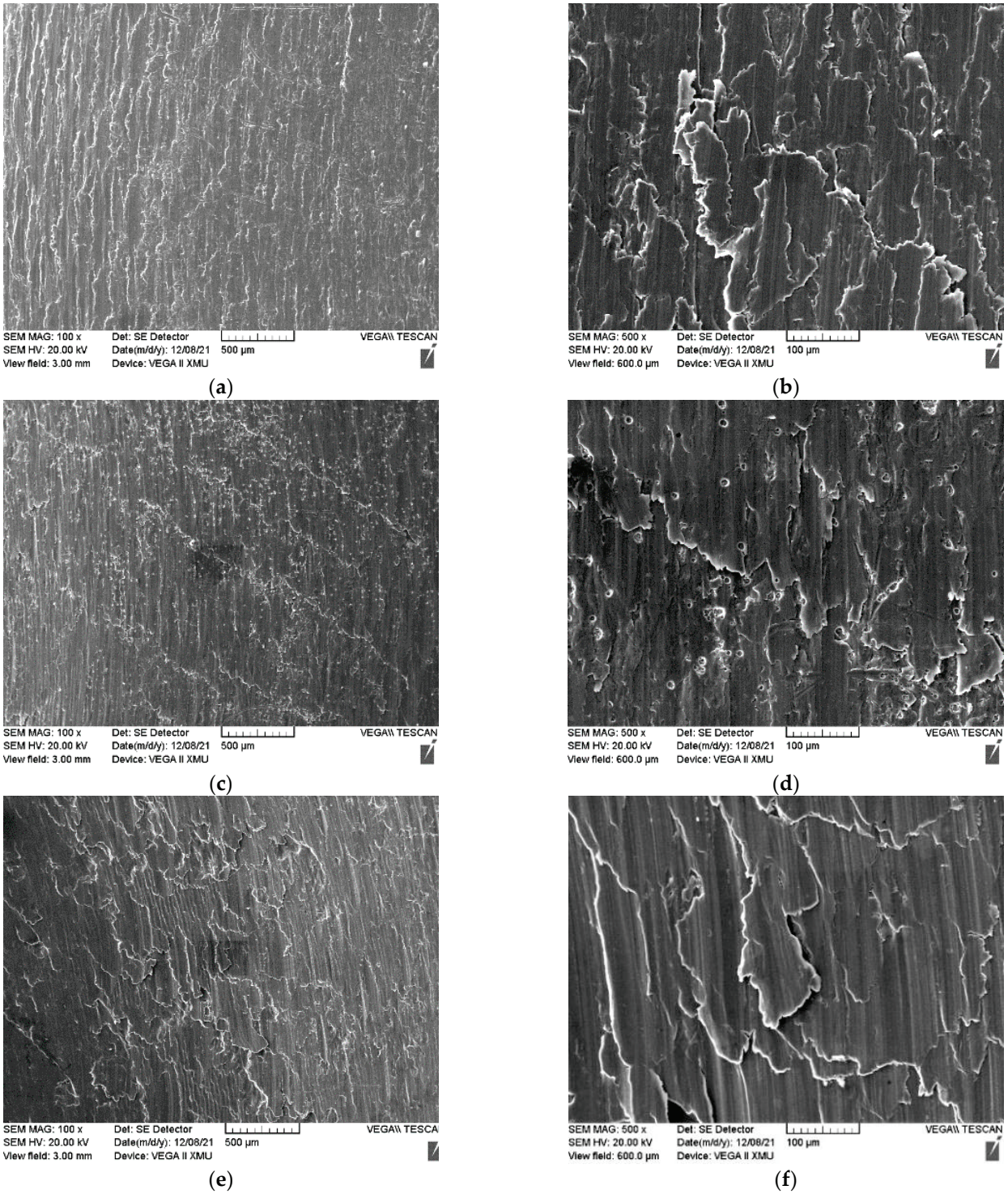


Figure 6. Surface morphology of specimens for SPIF, LUVIF and 2D-EUVIF. (**a**) 100×, SPIF; (**b**) 500×, SPIF; (**c**) 100×, LUVIF; (**d**) 500×, LUVIF; (**e**) 100×, 2D-EUVIF; (**f**) 500×, 2D-EUVIF; 2D-EUVIF is the abbreviation for 2D ellipse ultrasonic vibration incremental forming; LUVIF is the abbreviation for longitudinal ultrasonic vibration incremental forming; SPIF is the abbreviation for single-point incremental forming.

As known, fracture morphology is important and necessary for material analysis. It always clearly signifies how the micro-structure of the metal evolved and what kind of fracture characteristic it is. (1) As Figure 7a shows, the fracture surface of the specimen processed by the SPIF method was flat, with only a few dimples and some shallow pits were distributed on it. Figure 7b,c displays the back-scattered electron image (BEI) and the secondary electron image (SEI) of the sample surface topography in the same position. It is easy to see that the distribution of dimples and the location of strengthening phases and impurities in the 7075 aluminum alloy was highly identical. This was mainly due to the weakness of adhesion between the strengthening phases or impurities and the metal substrate. Then, some cavities were formed preferentially at the location of those secondary phases. The growing and aggregating adjacent cavities tended to become big dimples by annexing small dimples nearby. However, the 7075 aluminum alloy, which possesses high strength and poor plastic forming capacity at room temperature, only created tiny plastic deformation under loading. The cracks rapidly grew, causing flat dimples. (2) Figure 7d revealed distinct roughness of fracture surface of 45 degrees. At first, the nucleation, growth, and connection of a small number of tiny dimples occurred nearby the strengthening phases. These shear dimples that occurred in Figure 7e signifies an obvious directional consistency. By magnifying the object 2000 times, a considerable volume of extremely tiny dimples hiding in larger dimples could clearly be seen in Figure 7f. A few strengthening phase particles appeared in these larger dimples. It could be deduced that parts of the strengthening phases cracked under the huge shearing load. One part of these heterogeneous particles started to fall from the original position, but the other part of the strengthening phases still stayed in the original location. Due to the plastic deformation limit of the 7075 aluminum alloy, dimples stopped forming and growing. Then, a large number of tearing ridges appeared and extended in the ways of connecting contiguous dimples. Each two adjacent tearing ridges expanded to become a cleavage plane. There was no time for a mass of micro-dimples to grow, which were distributed on the nearby tearing ridge or on the planes. Therefore, the whole micro-topography of the fracture surface presented a beach-like appearance. The phenomenon of the coexisting tearing ridge and dimple indicates a typical complex pattern of quasi-cleavage fracture and ductile fracture. In contrast with the former SPIF sample, the micro-topography characteristic of the longitudinal ultrasonic vibration incremental forming sample showed that the plasticity and flexibility of the high-strength 7075 aluminum alloy showed a certain improvement with the action of one dimension ultrasonic vibration. However, a deficiency in the plastic deformation of this alloy material was induced by the improper design of the one-dimension ultrasonic device and lack of sufficient ultrasonic energy. (3) Unlike the longitudinal ultrasonic vibration incremental forming, the two-dimension ellipse ultrasonic vibration device derives a forming tool to strike the sheet surface at an inclining angle. At the same time, this double-vibration design increased the ultrasonic energy greatly to reinforce the sheet surface and soften its interior material. Figure 7g shows that the image of the fracture surface morphology of the 7075 alloy sheet processed by the 2D ellipse ultrasonic vibration incremental forming method confirms this assumption. As Figure 7g shows, it is easy to divide the whole fracture surface into two distinct areas according to its magnifying micro-morphology characteristic. The upper area with a thickness of about 200 μm nearby the machined surface showed fewer patterns and was smoother. The lower area, far from the machined surface, displayed abundant and density toughness fracture features. Figure 7h–j presents images of amplifying the marked area 1, area 2, and area 3 in Figure 7g 500 times. In Figure 7h, a mass of large and deep dimples was distributed uniformly in this area. It is reasonable to deduce that multiple coupling actions of ultrasonic softening, ultrasonic hardening, work hardening, stress superposition and heating softening were induced by the strong 2D ultrasonic vibration. Moreover, softening mechanisms played a dominant role in the forming process. Therefore, great dimples were generated and kept growing quickly along with

the increase in the forming stress and the plastic deformation. While the softening alloy material was getting close to its plastic limit, the formed dimples and the forming ones began to tear. In particular, materials around those dimples deformed heavily before a bright tearing ridge appeared. Therefore, the petal-shaped micro-topography containing a mass of great dimples and micro ones, as shown in Figure 7h, proved the assumption of a material-softening-dominant mechanism in the 2D ellipse ultrasonic vibration incremental forming process. Comparing Figure 7h with Figure 7i, it is easy to see that more quasi-cleavage planes appeared in area 2, which was far away from the source of ultrasonic vibration due to the attenuation of the material-softening mechanism and a reduction in plastic deformation. A long-distance softening mechanism could probably be realized by the design of a new 3D ellipse ultrasonic vibration incremental forming method and the optimization of process parameters including the amplitude, power, and frequency of the ultrasonic vibration system. Figure 7j clearly displays the contrast of the fracture topography between the superficial strengthening layer and the internal softening-layer. The magnifying images of the marked areas 4 and 5 are shown in Figure 7k,l. A trans-granular crack with an angle of 45 degrees almost penetrated the whole strengthening layer. Nevertheless, there were a few short inter-granular cracks observed in the softening layer. Large crushed secondary-phase particles were left in the dimples. Part of those strengthening phases was crushed badly under the forming load and shearing force that formed during the fracture process. It proved that these dimples tended to nucleate first at the location of secondary phases, which were also the source of the short cracks. Furthermore, a considerable volume of micro-dimples of about 5 μm in diameter were observed surrounding the large ones. This indicates that the metal sheet fractured too early before those micro-dimples grew larger. Therefore, the softening-alloy deformed vastly, but still insufficiently. This phenomenon is consistent with the multiple coupling action of softening and hardening in the 2D ellipse ultrasonic vibration incremental forming process. On one hand, the softening effect generated many great dimples. On the other hand, the hardening mechanism restrained the size growth of the micro-dimples. At the same time, it was clearly stated that these great dimples were caused by a plastic slip of fibrous particles instead of detachment or the rupture of a single huge secondary phase. As Figure 7l shows, the delicate fiber-shape micro-structure was evenly distributed on the fracture surface of the hardening layer. The micro-hardness testing results prove that the surface hardness was improved significantly by the 2D ellipse ultrasonic vibration incremental forming process. This was closely related to the strengthening coating of the fibrous micro-structure caused by work-hardening and ultrasonic hardening. Probing the fracture surface carefully, some stretched dimples hiding between the fibers were observed. Aside from the secondary effects of the multiple softening, it was reasonable to conclude that the hardening mechanism plays an important role in the evolution of the micro-structure and properties of the surface layer.

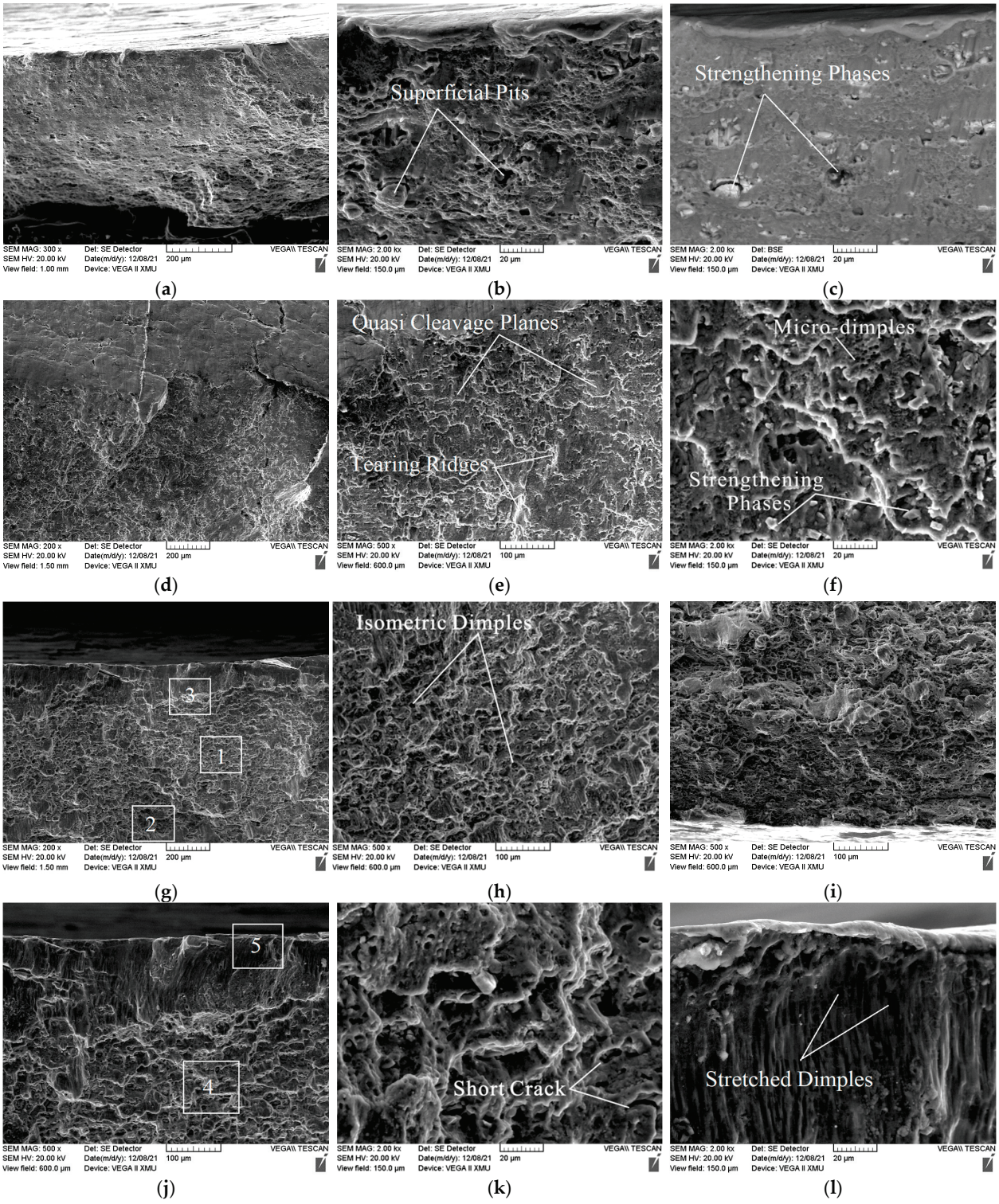


Figure 7. The fracture morphology of the processed specimens for SPIF, LUVIF, and 2D-UVIF (SEM images of SE (secondary electrons) and BSE (backscatter electrons)). (**a**) SPIF, SE, 200×; (**b**) SPIF, SE, 2KX; (**c**) SPIF, BSE, 2KX; (**d**) LUVIF, SE, 200X; (**e**) LUVIF, SE, 500×; (**f**) LUVIF, SE, 2KX; (**g**) 2D-UVIF, SE, 200×; (**h**) 2D-UVIF, SE, 500X, District 1; (**i**) 2D-UVIF, SE, 500×, District 2; (**j**) 2D-UVIF, SE, 500×, District 3; (**k**) 2D-UVIF, SE, 2KX, District 4; (**l**) 2D-UVIF, SE, 2KX, District 5; 2D-EUVIF is the abbreviation for 2D ellipse ultrasonic vibration incremental forming; LUVIF is the abbreviation for longitudinal ultrasonic vibration incremental forming; SPIF is the abbreviation for single-point incremental forming. Notes: The numbers 1–5 with white boxes in (**g**,**j**) represent five testing areas and their magnified im-ages are accordingly showed in (**h**–**l**).

4. Conclusions

1. In this work, a type of 2-dimension ellipse ultrasonic vibration incremental forming process and its unique double-mechanism method of the sectionalized cooperative control of deformation formation and mechanical performance including the internal softening mechanism, which promotes the deformation of materials, and the surface strengthening mechanism, which improves the superficial mechanical properties of sheet, were designed. This innovative technique aims to meet the challenging industry demands on the manufacture of thin-walled aircraft panels of a high-strength aluminum alloy with a complex shape and surface strengthening coating.
2. The experimental results showed that the mean value of the surface micro-hardness of the conical sheets processed by single-point incremental forming, longitudinal ultrasonic vibration incremental forming, and 2D ellipse ultrasonic vibration incremental forming were increased accordingly by 17.67%, 38.2%, and 50.13% compared to that of the raw materials of the 7075 aluminum ally. However, the mean value of the cross-sectional micro-hardness of the 2D ellipse ultrasonic vibration incremental forming sheet increased by only 6.87%. The experimental results demonstrated that the mechanical properties of the core materials of the part were nearly the same as or even lower than that of the raw materials. The SEM images of the fracture surface of the sheet for the novel forming technique showed distinct features of the surface strengthening coating with about a 200 μm fibrous-structure thickness and ductile fracture with a great number of dimples induced by softening effects. The testing results totally confirmed the double-mechanism assumption of internal softening and surface strengthening. In addition, a residual compressive stress field located on the surface of the sheet for the novel forming method could improve its fatigue resistance.
3. The SEM images of the fracture surface of the sheet for the novel technique showed that the ductile feature of the isometric dimples decreased along the depth and more quasi-cleavage planes appeared far from the source of ultrasonic vibration. Obviously, these phenomena were closely related to the affecting range of ultrasonic vibration. Although the double-mechanism method was proven to be feasible, the conditions for the motivating softening effects or hardening effects that play a leading role are still unknown. The precise quantification of ultrasonic softening, ultrasonic hardening, thermal softening, work hardening, refined crystalline strengthening, and stress superposition is challenging but vital for application of the 2D ellipse ultrasonic vibration incremental forming process and the double-mechanism method in industry.

Author Contributions: Conceptualization, Y.L.; Methodology, Y.L.; Investigation, Y.L.; Writing-Original Draft, Y.L.; Supervision, Y.L.; Funding acquisition, Y.L.; Data Curation, M.D.; Visualization, M.D.; Writing-Review & Editing, Y.L. and M.D.; Resources, X.P.; Project administration, C.Y. and J.S. All authors have read and agreed to the published version of the manuscript.

Funding: This research was funded by the National Natural Science Foundation of China (Grant Number 52005399), the Natural Science Basic Research Plan in Shaanxi Province of China (Grant Number 2016JQ5054), and the Special Scientific Research Program of the Shaanxi Provincial Department of Education (Grant Number 20JK0772).

Institutional Review Board Statement: Not applicable.

Informed Consent Statement: Not applicable.

Data Availability Statement: All the data are available within the manuscript.

Conflicts of Interest: The authors declare no conflict of interest.

References

1. Liu, C.; Zhao, Z.; Zhang, X.; Wang, J. A progressive approach to predict shot peening process parameters for forming integral panel of Al7050-T7451. *Chin. J. Aeronaut.* **2021**, *34*, 617–627. [CrossRef]
2. Wang, D.; Xu, F.; Yuan, L.; Zhang, D.; Liu, J.; Hu, Y.; Kang, H.; Ma, Q.; Tong, Y.; Han, W. Brief introduction and recent development on the manufacture of aluminium alloy integral panels in aerospace applications. *Int. J. Mater. Struct. Integr.* **2021**, *14*, 299–318. [CrossRef]
3. Malhotra, R.; Xue, L.; Belytschko, T.; Cao, J. Mechanics of fracture in single point incremental forming. *J. Mater. Process. Technol.* **2012**, *212*, 1573–1590. [CrossRef]
4. Aerens, R.; Eyckens, P.; Van Bael, A.; Duflou, J.R. Force prediction for single point incremental forming deduced from experimental and FEM observations. *Int. J. Adv. Manuf. Technol.* **2010**, *46*, 969–982. [CrossRef]
5. Vanhove, H.; Mohammadi, A.; Guo, Y.S.; Duflou, J.R. High-Speed Single Point Incremental Forming of an Automotive Aluminium Alloy. *Key Eng. Mater.* **2014**, *622–623*, 433–439. [CrossRef]
6. Bastos, R.N.P.; De Sousa, R.J.A.; Ferreira, J.A.F. Enhancing time efficiency on single point incremental forming processes. *Int. J. Mater. Form.* **2016**, *9*, 653–662. [CrossRef]
7. Azevedo, N.G.; Farias, J.S.; Bastos, R.P.; Teixeira, P.; Davim, J.P.; de Sousa, R.J.A. Lubrication aspects during Single Point Incremental Forming for steel and aluminum materials. *Int. J. Precis. Eng. Manuf.* **2015**, *16*, 589–595. [CrossRef]
8. Trzepieciński, T.; Kubit, A.; Dzierwa, A.; Krasowski, B.; Jurczak, W. Surface Finish Analysis in Single Point Incremental Sheet Forming of Rib-Stiffened 2024-T3 and 7075-T6 Alclad Aluminium Alloy Panels. *Materials* **2021**, *14*, 1640. [CrossRef]
9. Bansal, A.; Lingam, R.; Yadav, S.K.; Reddy, N.V. Prediction of forming forces in single point incremental forming. *J. Manuf. Process.* **2017**, *28*, 486–493. [CrossRef]
10. Zhang, H.; Lu, B.; Chen, J.; Feng, S.; Li, Z.; Long, H. Thickness control in a new flexible hybrid incremental sheet forming process. *Proc. Inst. Mech. Eng. Part B J. Eng. Manuf.* **2017**, *231*, 779–791. [CrossRef]
11. Liu, S.; Shan, X.; Guo, K.; Yang, Y.; Xie, T. Experimental study on titanium wire drawing with ultrasonic vibration. *Ultrasonics* **2018**, *83*, 60–67. [CrossRef]
12. Zhou, H.; Cui, H.; Qin, Q.H. Influence of ultrasonic vibration on the plasticity of metals during compression process. *J. Mater. Process. Technol.* **2018**, *251*, 146–159. [CrossRef]
13. Tao, G.; Ma, C.; Bai, L.; Shen, X.; Zhang, J. Feed-direction ultrasonic vibration−assisted milling surface texture formation. *Mater. Manuf. Process.* **2017**, *32*, 193–198. [CrossRef]
14. Sun, S.; Tang, J.; Shao, W.; Chen, C.; Liu, Y. Research on the matching relationship between ultrasonic-assisted grinding parameters and workpiece surface roughness. *Int. J. Adv. Manuf. Technol.* **2019**, *102*, 487–496. [CrossRef]
15. Hu, J.; Shimizu, T.; Yang, M. Investigation on ultrasonic volume effects: Stress superposition, acoustic softening and dynamic impact. *Ultrason. Sonochem.* **2018**, *48*, 240–248. [CrossRef] [PubMed]
16. Siddiq, A.; El Sayed, T. Ultrasonic-assisted manufacturing processes: Variational model and numerical simulations. *Ultrasonics* **2012**, *52*, 521–529. [CrossRef] [PubMed]
17. Deshpande, A.; Hsu, K. Acoustic energy enabled dynamic recovery in aluminium and its effects on stress evolution and post-deformation microstructure. *Mater. Sci. Eng. A* **2018**, *711*, 62–68. [CrossRef]
18. Hu, J.; Shimizu, T.; Yoshino, T.; Shiratori, T.; Yang, M. Ultrasonic dynamic impact effect on deformation of aluminum during micro-compression tests. *J. Mater. Process. Technol.* **2018**, *258*, 144–154. [CrossRef]
19. Li, Y.; Chen, X.; Sun, J.; Li, J.; Zhao, G. Effects of ultrasonic vibration on deformation mechanism of incremental point-forming process. *Procedia Eng.* **2017**, *207*, 777–782. [CrossRef]
20. Zhai, W.; Li, Y.; Cheng, Z.; Sun, L.; Li, F.; Li, J. Investigation on the forming force and surface quality during ultrasonic-assisted incremental sheet forming process. *Int. J. Adv. Manuf. Technol.* **2020**, *106*, 2703–2719. [CrossRef]
21. Sakhtemanian, M.R.; Honarpisheh, M.; Amini, S. A novel material modeling technique in the single-point incremental forming assisted by the ultrasonic vibration of low carbon steel/commercially pure titanium bimetal sheet. *Int. J. Adv. Manuf. Technol.* **2019**, *102*, 473–486. [CrossRef]
22. Sun, Y.; Lu, Z.; Li, C.; Wang, R.; Zhai, W. Study on the Springback Effect and Surface Property for Ultrasonic-Assisted Incremental Sheet Forming of Aluminum Alloy. *Symmetry* **2021**, *13*, 1217. [CrossRef]
23. Li, Y.; Zhai, W.; Wang, Z.; Li, X.; Sun, L.; Li, J.; Zhao, G. Investigation on the material flow and deformation behavior during ultrasonic-assisted incremental forming of straight grooves. *J. Mater. Res. Technol.* **2020**, *9*, 433–454. [CrossRef]
24. Amini, S.; Gollo, A.H.; Paktinat, H. An investigation of conventional and ultrasonic-assisted incremental forming of annealed AA1050 sheet. *Int. J. Adv. Manuf. Technol.* **2016**, *90*, 1569–1578. [CrossRef]
25. Li, Y.; Cheng, Z.; Chen, X.; Long, Y.; Li, X.; Li, F.; Li, J.; Twiefel, J. Constitutive modeling and deformation analysis for the ultrasonic-assisted incremental forming process. *Int. J. Adv. Manuf. Technol.* **2019**, *104*, 2287–2299. [CrossRef]
26. *ASTM E915-2010*; Standard Test Method for Verifying the Alignment of X-ray Diffraction Instrumentation for Residual Stress Measurement. ASTM International: West Conshohocken, PA, USA, 2010. Available online: https://www.mendeley.com/catalogue/0dc87e11-4cd6-33f1-b58d-498da3460460/ (accessed on 3 November 2022).
27. *EN 15305-2008*; Non-Destructive Testing-Test Method for Residual Stress Analysis by X-ray Diffraction. Beuth GmbH: Berlin, Germany, 2009. Available online: https://www.antpedia.com/standard/pdf/H26/1702/BS%20EN%2015305-2008_1875.pdf (accessed on 3 November 2022).

coatings

MDPI

Article

Effect of High-Temperature-Assisted Ultrasonic Deep Rolling on Microstructure and Tribological Properties of Ni-WC Coatings

Jun Zhang, Yuncai Zhao *, Yang He, Cheng Meng, Xinyu Zhang and Shilei Zhang

School of Mechanical and Electrical Engineering, Jiangxi University of Science and Technology, Ganzhou 341000, China
* Correspondence: zhaoyuncai@126.com

Abstract: Cermet coatings are post-treated by a new surface microcrystallization technology, namely high-temperature-assisted ultrasonic deep rolling (HT + UDR). The process parameters of ultrasonic deep rolling significantly affect the microstructure and tribological properties of the Ni-WC coatings. In this paper, the samples were treated with different preloading depths (0.20 mm, 0.25 mm, and 0.30 mm), and the microstructure and properties of the coatings were characterized by SEM, EDS, X-ray stress analysis, and micro-Vickers hardness testing. An MMW-1A-type friction and wear tester was used for the dry friction and wear test at room temperature, respectively. Compared with the untreated sample, plastic rheology occurred on the surface of the coatings after HT + UDR, showing a phenomenon of "cutting peaks and filling valleys". In the treated coatings, visible cracks were eliminated, and the inside of the coating was denser. The surface hard phase was increased as a "skeleton" and embedded with the soft phase, which played a role in strong and tough bonding. After HT + UDR + 0.25 mm treatment, the surface roughness increased by 68%, the microhardness of the surface layer reached a maximum of 726.3 $HV_{0.1}$, and the residual tensile stress changed from 165.5 MPa to −337.9 MPa, which inhibited the germination and propagation of cracks. HT + UDR improved the wear resistance of the coating in many aspects. The coating after the 0.25 mm preloading depth treatment possessed the smallest friction coefficient and the lowest wear amount, which is 0.04 and 4.5 mg, respectively. The wear form was abrasive wear, and the comprehensive tribological performance is the best.

Keywords: preloading depth; plastic flow; microhardness; residual stress; tribological property

1. Introduction

The cermet coatings are deposited on the surface of the metal materials by plasma spraying technology. Ceramic materials (such as WC, Cr_3C_2, TiC, and TiB_2) serve as hard phases, and metal materials (such as Ni, Fe, and Co) work as soft phases, thus generating strong and cohesive coatings [1–4]. Currently, traditional plasma-sprayed cermet coatings have insurmountable shortcomings, such as poor quality of the coating surface, internal defects, and the uneven distribution of ceramic grains in the coatings [5]. The grain distribution in the coating cannot be improved by optimizing spray process parameters alone [6]. On the one hand, the cermet coating has high porosity, multiple cracks, and a coarse layered structure in the presence of large ceramic particles, and the interface bonding strength of each layer is weak [7]. On the other hand, the thermal expansion coefficient and elastic modulus of the ceramic particles are quite different from those of the alloy powders, resulting in high amplitude and residual gradient stress in the coating interior and at the substrate-coating interface. These two aspects seriously affect the overall performance and wear resistance of the coatings [8]. Xiaoqin Zhao et al. deposited conventional and nanoscale WC-12%Co coatings on a 1Cr18Ni9Ti stainless steel substrate by plasma spraying technology, wherein the nanoscale WC-12%Co coating exhibited higher hardness and finer microstructure [9]. However, the preparation of nanocoatings cannot solve the

large residual tensile stress. Residual stress further promotes interface delamination and cohesive delamination, which requires appropriate post-treatment [10].

Numerous studies have shown that strong plastic deformation (SPD) causes grain refinement [11,12] and work hardening [13,14] on the surface of the materials and introduces large residual compressive stress, which plays an important role in reducing the growth rate and germination of crack [15,16]. SPD technologies include surface mechanical grinding (SMAT) [17], shot peening (SP) [18], deep drawing (DR) [19], low plastic polishing (LSP) [20], etc. Different surface states of treated materials may generate surface defects and affect fatigue strength. Ultrasonic deep rolling (UDR) utilized both ultrasonic frequency and static pressure to reduce surface damage, showing excellent results [21]. For materials with high hardness and poor toughness, UDR treatment leads to excessive work hardening of the material and is not easy to produce a large plastic deformation layer. Metal materials have good ductility at high temperatures and are more prone to plastic deformation [22]. Xuehui Shen et al. [23] conducted ultrasonic roller burnishing (URB) and ultrasonic roller burnishing combined with heat treatment (URB/HT) on Inconel 718 alloy. After URB/HT treatment, the sample surface roughness was lower, the microhardness was further improved, and the residual compressive stress distribution was more uniform. Auezhan et al. [24] performed ultrasonic nanocrystalline surface modification (UNSM) on the basis of local high-temperature heating (LHT) for Ti-6Al-4V, in which the surface hardness was increased by a maximum of 34.3%, forming a high work hardening layer on the surface. The surface roughness and friction coefficient decreased, and LHT (800 °C) and UNSM exhibited the highest residual compressive stress and the best wear resistance. S G MacLeod et al. [25] also treated Ti-6Al-4V at high temperatures and high pressures, and Ti-6Al-4V existed stably in a hexagonal structure at 30 GPa and 886 K. Numerous studies have confirmed that the comprehensive properties of the materials were improved under high-temperature and high-pressure treatment.

Many researchers have mainly applied this technology to metal materials with low hardness and good toughness, greatly improving fatigue life and wear resistance. There are few studies on HT + UDR (high temperature and ultrasonic deep rolling) Ni-WC coatings because WC particles have high hardness and high brittleness. In this paper, the surface morphology, microstructure, mechanical properties, and wear resistance of Ni-WC coatings treated with different process parameters under HT + UDR were investigated. It provides a reference for high-temperature ultrasonic deep rolling metal-ceramic coating and is of great significance to the development of coating post-treatment technology.

2. Experimental Materials and Methods

2.1. Experimental Materials and Equipment

First, the base body was pretreated. 45 steel served as the base body material, which was processed into a ring shape with an outer diameter of 54 mm, an inner diameter of 38 mm, and a ring thickness of 8 mm. The chemical composition and mechanical properties of 45 steel are shown in Tables 1 and 2. The samples were polished with metallographic sandpaper, cleaned with acetone to remove impurities, and sandblasted for roughening. Ni60 and 15 WC cermet powder produced by China Chengdu Zhenxing Metal Powder Co., Ltd. was used as the plasma spraying material, with a powder particle size and particle size of 53 μm. The chemical composition is shown in Table 3. Ni60 and 15 WC cermet powder was sprayed on the surface of 45 steel with a thickness of 0.45 mm through a JP-8000 automatic spraying system (TAFA Corporation, Concord, NH, USA). The parameters were set as a barrel size of 10/cm, oxygen flow rate of 837/L·min^{-1}, powder feeding gas flow rate of 11.8/L·min^{-1}, powder feeding pressure of 0.34/MPa, powder feeding rate of 100/g·min^{-1}, spraying distance of 350/mm, and natural cooling in air.

Table 1. Chemical composition of 45 steel (mass fraction, %).

Element	C	Si	Mn	Cr	Ni	Cu	Fe
45 steel	0.42∼0.50	0.18∼0.3	0.50∼0.80	≤0.25	≤0.30	≤0.25	Bal.

Table 2. Mechanical properties of 45 steel.

Yield Strength/MPa	Tensile Strength/MPa	Section Shrinkage/%	Elongation after Fracture/%	Hardness/HRC
≥355	≥600	≥40	≥25	45

Table 3. Chemical composition of nickel tungsten carbide powder Ni60 + 15 WC (mass fraction, %).

Element	Cr	B	Si	C	Fe	Ni	WC
Ni60 + 15 WC	15∼20	3.0∼4.5	3.5∼5.5	0.5∼1.1	≤10	Bal.	15

The coatings were softened by absorbing high heat provided with induction heating equipment, an Al-518 artificial intelligence temperature controller, auxiliary induction heating, and other modular system devices at 800 °C. The coatings exhibited a large surface roughness after heating treatment, and direct ultrasonic rolling caused the peeling of the coating due to the high friction between the ball and the coating contact surface. Therefore, ultrasonic deep rolling surface strengthening treatment on the coating was carried out using an ultrasonic rolling strengthening horizontal lathe (Shandong Huayun Haukeng equipment C616-10 series, Jinan, China) after grinding. The ultrasonic deep rolling process is shown in Figure 1. The deep rolling force was 0.3 MPa, the feed rate was 0.15 r/min, the spindle speed was 248 r/min, the ultrasonic frequency was 20 kHz, the amplitude was 10 μm, and the preloading depths were 0.20 mm, 0.25 mm, and 0.30 mm. Samples were labeled as follows: Untreated, HT + UDR + 0.20 mm, HT + UDR + 0.25 mm, and HT + UDR + 0.30 mm.

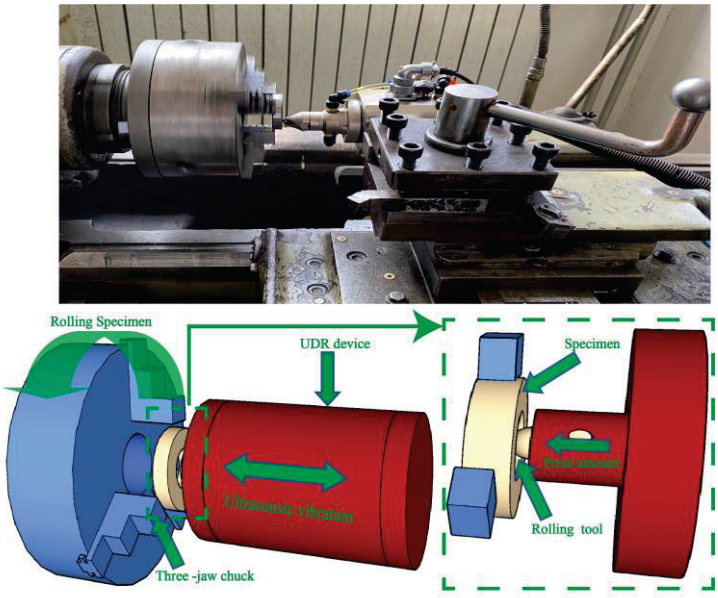


Figure 1. Diagram of the ultrasonic deep rolling process.

2.2. Analysis and Characterization

A wire cutting machine was used to process the large sample of the ring into a small sample of 10 mm × 9 mm × 6 mm, and 500, 800, 1000, 1500, and 2000 grit sandpaper

was used on the YM-2A metallographic sample pre-grinder in turn. The samples were polished to the mirror effect by the PG-2D metallographic polishing machine with 0.5 W and 0.25 W diamond abrasive paste. After washing with absolute ethanol, the section of the small sample was etched with 4% nitric acid alcohol for 10 s, quickly cleaned, and dried for further observation.

The microstructure of the cermet coating was observed by electron microscopy (ZEISS Sigma, Jena, Germany), and the surface elements of the coating were analyzed by energy dispersive spectrometry (EDS), as shown in Figure 2. The JB-6C inductive surface roughness tester was used to randomly measure the surface roughness of the coating in three regions of the sample, and the average value was taken to reduce the error. The gradient microhardness of the cermet coating was tested by a CHV-1000A microhardness tester with an experimental load of 100 g and an application time of 15 s. Ten regions were selected for each position, and the average value was taken. The residual stress test of the coating surface was carried out by an X-350A X-ray stress analyzer, and the Cu target Kα line was selected and measured by the roll fixed ψ method. The principle is that the residual stress changes the crystal structure of the material, the diffraction peak is displaced, the diffraction line displacement is used as the original data, and the measured result is the residual strain. Then, the residual stress was calculated by Hooke's law, as shown in Formula (1):

$$\sigma = -\frac{E}{2(1+\mu)} \cot\theta_0 \frac{\pi}{180} \frac{\partial(2\theta_\psi)}{\partial \sin^2\psi} \quad (1)$$

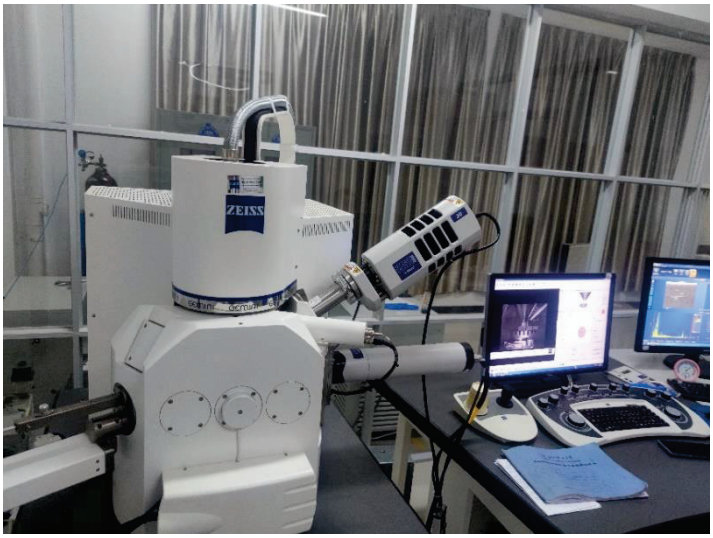


Figure 2. Electron microscope (ZEISS Sigma) with spectrometer.

In Formula (1), σ is the residual stress, E is the elastic modulus of the material, μ Poisson's ratio for the material, θ_0 is the Bragg angle without stress, θ_ψ is the Bragg angle when stressed, and ψ is the normal angle with the surface of the specimen. Each specimen surface was randomly tested for 5 points, and the average value was taken.

A large pin plate wear test on the surface of the sample was performed at room temperature using an MMW-1A friction and wear testing machine (Jinan Chenda Testing Machine Manufacturing Co., Ltd., Jinan, China). As shown in Figure 3. The friction pair material was 45 steel with φ 4 mm × 12 mm, and the hardness was HRC40-HRC45. The friction and wear test parameters are listed in Table 4.

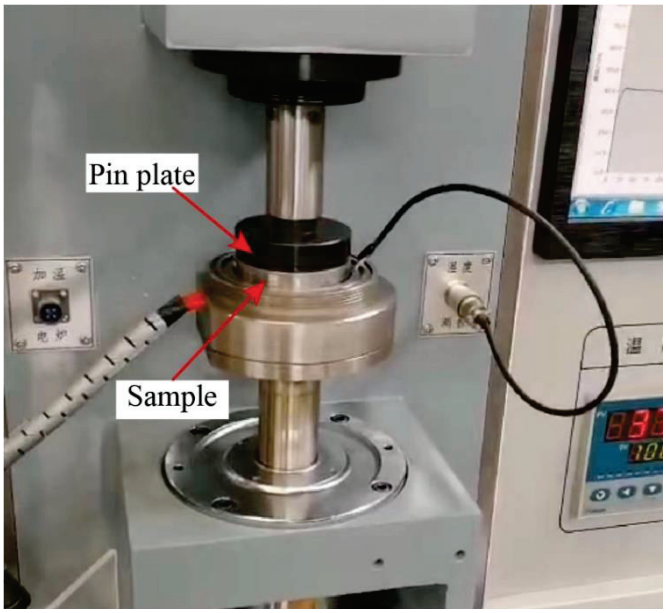


Figure 3. MMW-1A friction and wear testing machine.

Table 4. Parameters of the friction-wear test.

Normal Load/N	Rotating Speed of Pair/(r·min^{-1})	Wear Time/s	Test Temperature/°C
300	200	1500	25

3. Results and Discussion

3.1. Analysis of Organizational Structure and Surface Topography

3.1.1. Organizational Structure Analysis

Figure 4 shows the SEM (scanning electron microscope) images of the cross-section of the cermet coatings. Figure 4a indicates that Untreated coating possessed a low density and high surface roughness. A large number of cracks and holes were mainly distributed in the middle and upper parts of the coating, and a mass of unmelted silver–white WC particles were aggregated and unevenly distributed [26]. Plasma spraying heated the metal and ceramic material particles to a high temperature in a very short time, making the materials in a molten and semi-molten state. After spraying to the surface of the substrate, they were solidified by rapid cooling in air. The thermal expansion coefficient and elastic modulus of the metal powder and ceramic particles in the coating were quite different, and the residual stress distribution in the coating and the bonding area between the coating and the substrate exhibited a high amplitude and a large gradient [9], which resulted in cracks and pores in the coating, mainly occurring around the WC ceramic particles with a small thermal expansion coefficient. In Figure 4b, HT + UDR + 0.20 mm coating comprised a higher density, obvious cracks were eliminated, the surface roughness was reduced, the upper pores were eliminated by the flowing material, and the unmelted WC particles were embedded in the coating. The layer was evenly distributed and stretched in a wavy shape along the deep rolling direction. The surface roughness of untreated and HT + UDR treated samples were 1.36, 0.466, 0.335, and 0.387 μm, respectively, as shown in Table 5. Under HT + UDR processing, the coating absorbed enough heat to soften, the atomic spacing increased, the metal bonds became weaker and broken, and plastic deformation was more likely to occur. In addition, the micro peaks were squeezed to flow, and the pits were filled with the material flowing in the micro peaks. The surface cracks were also eliminated, and the internal cracks of the coating were bridged under the action of plastic rheology, which inhibited the large-area expansion of the cracks and the surface cracking. The hardness

and brittleness of WC particles decreased, and the tensile deformation in the deep rolling direction exhibited a wavy shape.

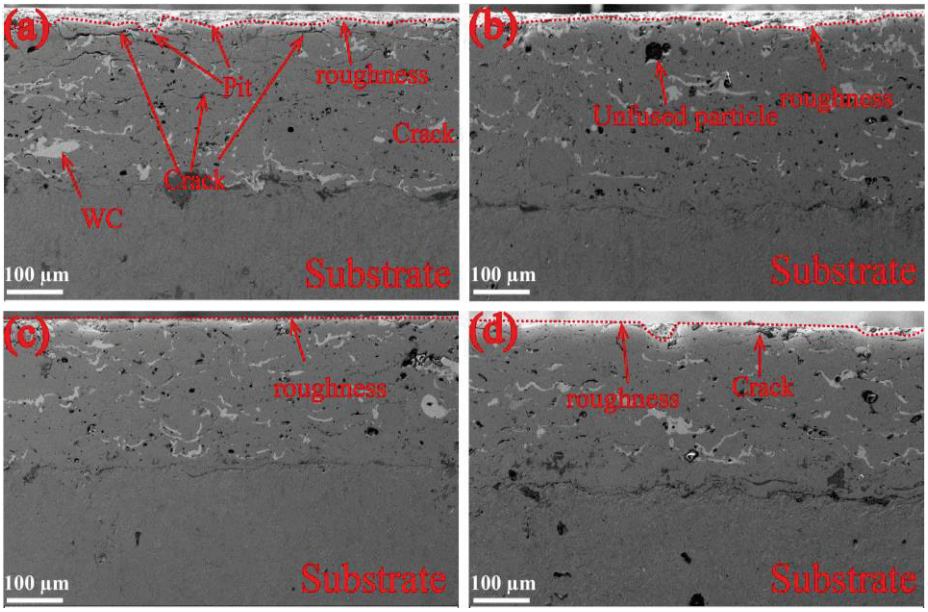


Figure 4. The structure of different preloading depths: (**a**) Untreated; (**b**) HT + UDR + 0.20 mm; (**c**) HT + UDR + 0.25 mm; (**d**) HT + UDR + 0.30 mm.

Table 5. Surface roughness of untreated and HT + UDR processed samples.

Sample	Untreated	0.20 mm	0.25 mm	0.30 mm
Surface roughness/μm	1.36	0.466	0.335	0.387

In Figure 4c,d, the surface pits of the HT + UDR + 0.25 mm and HT + UDR + 0.30 mm coatings were eliminated, and the porosity was gradually reduced. HT + UDR + 0.25 mm coating possessed the highest surface flatness, in which coating cracks and pores were basically eliminated. With the increase in the preloading depth, the slip [27,28] and dislocation of the grains became large under the action of high-temperature heating and ultrasonic deep rolling. The deformation degree of the coating was also increased, the effect was deepened, and the dislocation slip rate of the unit cell gradually changed. The large dislocation density led to the entanglement phenomenon, and annihilation and recombination were generated near the dislocation wall, forming a new grain boundary layer and refining the grains [29]. However, the bottom layer cracked when the preloading depth was 0.3 mm. When the grains were refined to the limit of the material, the more grains per unit volume increased, the grain boundary area became larger, which prevented dislocation and intergranular slip. The ability to resist plastic deformation became stronger, and excessive preloading depth destroyed the internal stress balance, causing the coating grains to break and fall off.

Figure 5 shows the energy spectrum line scanning diagram of the interface of the coating treated by high-temperature ultrasonic deep rolling. The scanning direction was from the coating to the substrate, and the different color curves indicate the changes of the main elements Fe, W, Ni and Cr at the interface. The content of Fe and Cr elements in the transition interface from the coating to the substrate gradually increased, and the content of Ni and W elements gradually decreased at the interface junction. It can be concluded that the element diffusion phenomenon occurred at the interface between the coating and the substrate after the coupling treatment, mainly Fe and Cr diffused from the substrate to the deep rolling coating, and Ni and W diffused from the coating to the substrate. The interface between the coating and the substrate was clear and in the form of occlusion, and

the main bonding mode was mechanical bonding [29,30]. After HT + UDR, the lower part of the coating was embedded with the substrate under the action of temperature field and ultrasonic extrusion pressure, which improves its bonding strength.

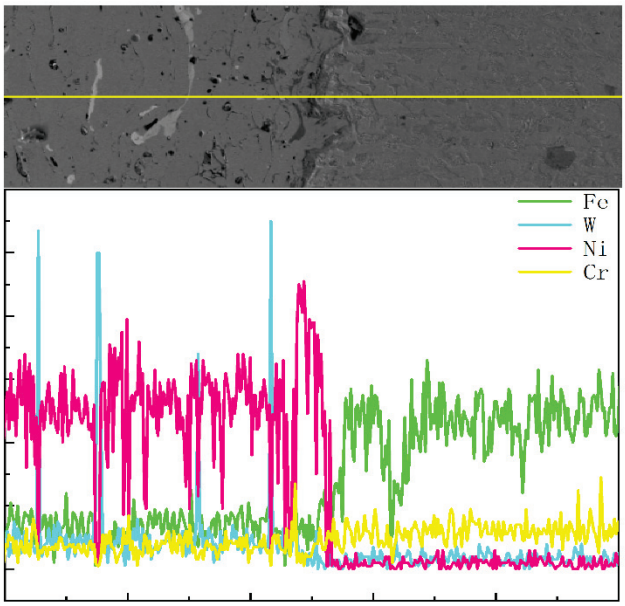


Figure 5. Line scanning results of HT + UDR + 0.25 mm coating interface.

3.1.2. Surface Topography Analysis

Figure 6 shows the surface morphologies of all coatings. The surface of the Untreated coating (Figure 6a) was continuous and uneven, similar to a hill. The melting point of WC powder particles is much higher than that of Ni-based powder particles, and the incompletely melted WC particles accumulated on the surface of the coating, resulting in the diffusion, accumulation, and solidification of droplets after high-speed impact. After the HT + UDR + 0.20 mm processing (Figure 6b), the distance between the surface microgrooves and pits of the coating was equal. Surface grinding was performed before HT + UDR to leave grooves. To avoid cracks, shedding and cracking of the coating occurred under the action of ultrasonic deep rolling, which was due to the large contact friction between the ball and the coating surface. Subsequently, the material underwent plastic flow to fill the grooves, forming microgrooves and pits. Figure 6c shows that both grooves and pits on the surface of the HT + UDR + 0.25 mm coating basically disappeared. With better plastic rheology, enough materials were available to fill pits to obtain better surface quality. In Figure 6d, the grooves on the surface of the HT + UDR + 0.30 mm coating disappeared completely, leaving a large area of potholes. The larger preloading depth generated a more intense deep rolling force impact on the coating surface, exceeding the strength limit of the material itself. The excessive slip of local metal particles produced more significant compressive stress, severe lattice and grain damage distortion, and the falling-off material and fine lines on the coating surface.

There were a large number of "silvery white" areas on the surface of the HT + UDR coatings, which points 1–4 were analyzed by EDS, as shown in Figure 7. The gray position points 1 and 2 showed that the enrichment of Ni was the most significant, and the peak intensity of Cr and W on the surface of HT + UDR was improved. Cr and C easily formed hard phases at high temperatures, such as Cr_7C_3 and $Cr_{23}C_7$ compounds [30], which played an important role in improving the strength and hardness of the coatings. The W element was enriched in Point 3 and Point 4 with a silver–white color, which was composed of WC and W_2C. WC particles were crushed under the action of the UDR surface. The brittle fracture occurred, which was attributed to the softening of the coating at high temperatures and the embedding of particles on the coating surface under ultrasonic impact. Therefore,

the surface quality of the coating was improved under HT + UDR, and more hard phases were generated on the surface, which comprehensively improved its wear resistance.

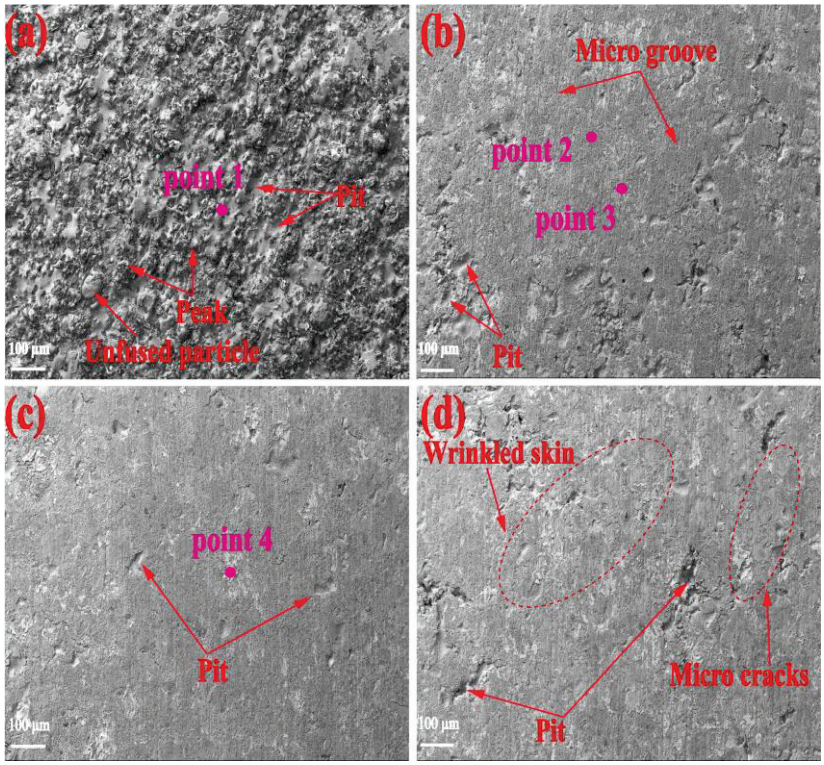


Figure 6. Surface morphology of preloading depth: (**a**) Untreated; (**b**) HT + UDR + 0.20 mm; (**c**) HT + UDR + 0.25 mm; (**d**) HT + UDR + 0.30 mm.

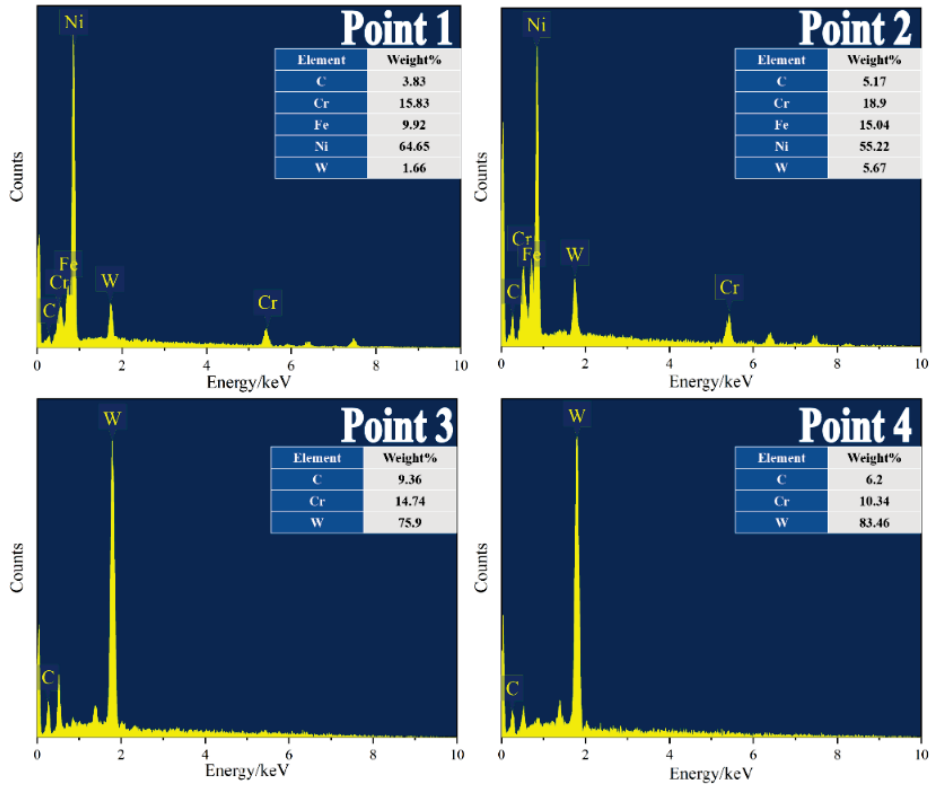


Figure 7. EDS results of the corresponding points of Points 1–4 in Figure 6.

3.2. Coating Performance Analysis

3.2.1. Microhardness Analysis

In this study, the hardness of the coating was significantly improved after HT + UDR treatment. Under the action of the high-frequency deep rolling impact coating surface, the coating was extruded and deformed, the cracks and pores were compressed, and the bonding was closer. The surface grains were extruded and deformed gradually with the depth, resulted in changes in the microstructure. As shown in Figure 8, the maximum microhardness was not on the surface, which occurred at 25 μm from the surface. The maximum surface microhardness of the Untreated, HT + UDR + 0.20 mm, HT + UDR + 0.25 mm, and HT + UDR + 0.30 mm groups was 450.9 $HV_{0.1}$, 610.5 $HV_{0.1}$, 726.3 $HV_{0.1}$, and 685.3 $HV_{0.1}$, respectively. In the process of HT + UDR, the surface grains were refined under the action of deep rolling force [11,31,32], and the surface grains underwent elastic recovery after deep rolling. Meanwhile, the heat generated by the contact between the deep ball and the coating surface and the residual heat generated by high-temperature heating promoted grain growth. The grains in the subsurface layer were prevented from elastic recovery by the coating surface, and the heat transmitted to this area was also small, so the grains occurred permanent plastic deformation. The microhardness decreased with increasing grain size, which was ascribed to the refinement of grains under the ultrasonic deep rolling impact, and the strength (or hardness) was calculated by the Formula (2) [33]:

$$\sigma_f = \sigma_0 + k\left(d_{fp}\right)^{-1/2} + \alpha G b \rho^{1/2} \quad (2)$$

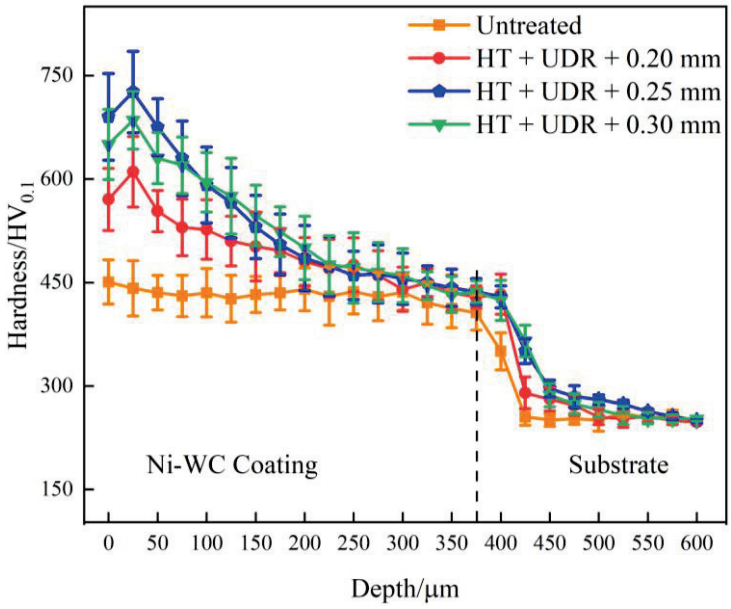


Figure 8. Distribution of hardness along with depth under different preloading depths.

In Formula (2), σ_f is the strength, σ_0 is the frictional stress, k is the Hall–Petch constant, d_{fp} is the mean free path of dislocation, α is the constant, G is the shear modulus, b is the Burgess vector, and ρ is the dislocation density.

According to the formula, with the decrease in the mean free path of dislocations and the increase in dislocation density, the grain size decreased, and the microhardness increased. The hardness of the Untreated coating varied with different preloading depths, which was less than that of HT + UDR. However, the hardness did not increase with increasing preloading depth, it increased between 0.20 mm and 0.25 mm and then decreased from 0.25 mm to 0.30 mm. Combined with the analysis of the microstructure of the coating, the impact stress on the surface of the cermet coating was more significant when the preloading depth was too high, resulting in wrinkling and micro-cracks on the surface of

the coating, and the surface roughness will increase, which had a particular influence on the uniformity of the microhardness. With the increase in the preloading depth, the plastic change layer and work hardening layer of the coating were improved. When the depth was more than 0.25 mm, the maximum microhardness no longer increased, the depth of strengthening also gradually became slow, and the hardness tended to be consistent after reaching the substrate.

3.2.2. Residual Stress Analysis

The residual stress in the thermal spraying coating is mostly tensile stress, which has an adverse effect on the comprehensive performance of the coating. The main sources are quenching stress, thermal stress, and structural stress [10]. Figure 9 shows the residual stress of the Untreated, HT + UDR + 0.20 mm, HT + UDR + 0.25 mm, and HT + UDR + 0.30 mm coatings were 165.5 MPa, −290.9 MPa, −337.9 MPa, and −308.6 MPa, respectively. Considering the large error bar, the residual stress after treatment was relatively close. Uneven plastic deformation occurred on the surface layer under UDR, resulting in lattice distortion and residual compressive stress on the surface layer. The maximum value reached −337.9 MPa with a preloading depth of 0.25 mm. The residual compressive stress on the surface of the HT + UDR + 0.30 mm treated coating was reduced. However, the plastic deformation of the coating became more severe with increasing preloading depth, resulting in a change in residual stress. With the continuous increase in preloading depth, the dynamic recrystallization behavior of the surface was intensified, and the dislocation density decreased and released residual stress. The transformation of residual tensile stress into residual compressive stress on the surface increased the fatigue resistance and plastic deformation resistance of the coating, thus effectively improving the wear resistance of the material [31,34].

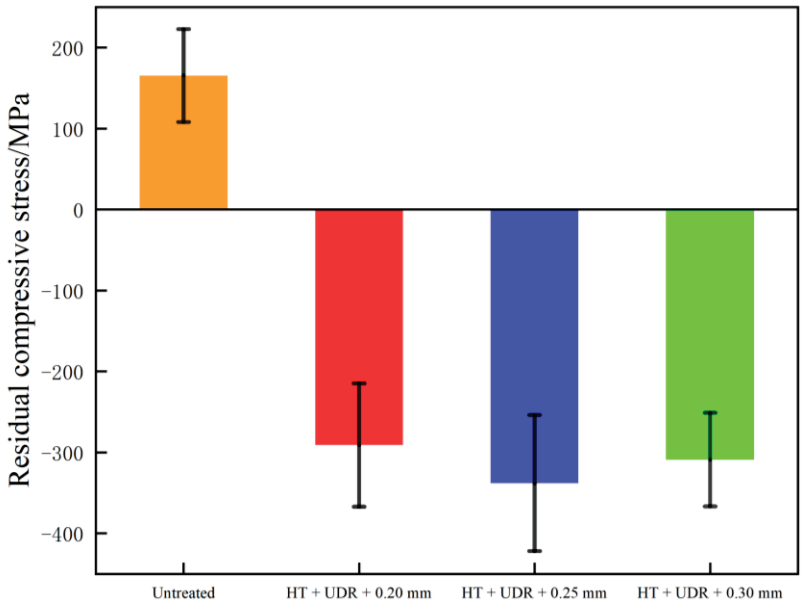


Figure 9. Residual stress of the coating under different preloading depths.

3.3. Tribological Performance Analysis

3.3.1. Analysis of the Friction Coefficient and Wear Loss

Figure 10 shows the friction coefficient curves of the samples after different preloading depth treatments. In the initial stage of friction and wear, the friction coefficients showed a sharp rise trend and then gradually decreased to a stable stage. In the initial stage, the soft base was first worn off by the surface of the friction pair to produce scratches, furrows, or fragments, and the remaining hard points formed a prominent surface to rub against the surface of the friction pair, leading to a large friction coefficient. As the friction and

wear entered the second stage, the wear contact part of the coating began to peel off, and oxidation continued to increase. At this time, the wear contact interface was micro peak and chip layer, and the friction coefficient decreased. When the wear entered the third stage, the friction coefficient gradually stabilized. Mechanical meshing and molecular attraction were involved in the coating wear process. According to the tribology principle, the calculation formula of the friction coefficient is as follows:

$$\mu = \frac{F}{W} = \frac{SA}{W} \tag{3}$$

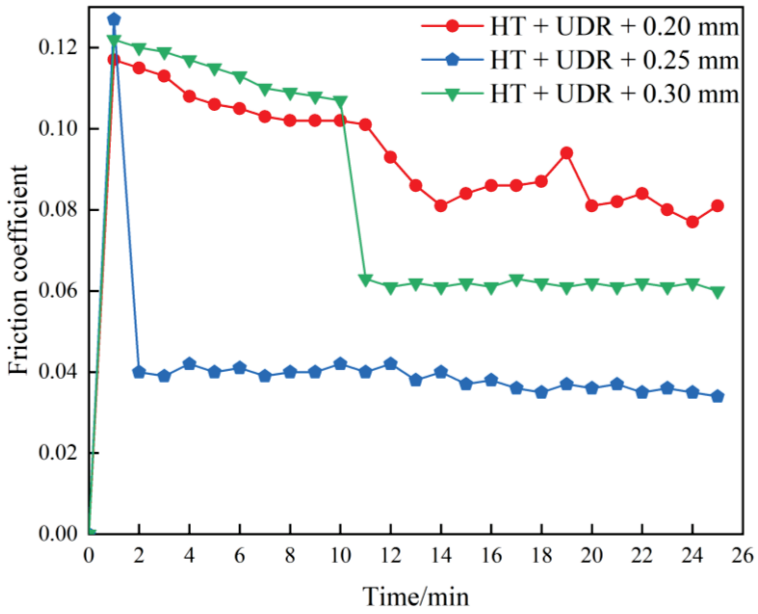


Figure 10. Friction coefficient of the coating under different preloading depths.

In Formula (3), μ is the friction coefficient, F is the friction test force, W is the normal load, A is the actual contact area, and S is the shear stress.

The initial friction coefficient of HT + UDR + 0.20 mm was the smallest, and it fluctuated more. The initial friction coefficient of HT + UDR + 0.25 mm was the largest, but it quickly reached the stable stage. The initial friction coefficient of HT + UDR + 0.30 mm was in the middle, then gradually decreased, then dropped sharply at 10 min, and gradually fluctuated steadily. The surface quality under the 0.20 mm preloading depth was relatively poor with pits and grooves, which resulted in contact stress concentration, local friction heat, high adhesion, and oxide, promoting the friction coefficient to fluctuate in an unstable way. Tribology mentioned in molecular mechanical theory that there were many tiny bumps on the smooth surface from the atomic scale. When the normal pressure was more than the elastic limit of the material, the bump at the top of the plastic deformation happened, crushed into a flat, and then touched each other. The distance between two objects decreased, with small molecular attraction to the scope of work, and atomic bonding occurred between two compressed surfaces. Therefore, the initial friction coefficient was the largest under 0.25 mm. After the preloading depth HT + UDR + 0.30 mm treatment, microcracks and pits appeared on the surface of the coating, which needed a long period of wear in the first and second stages before entering the stable wear stage.

As shown in Figure 11, the average friction coefficients of the coatings under different preloading depths of 0.20 mm, 0.25 mm, and 0.30 mm were 0.09, 0.04, and 0.08, respectively, with the wear amounts of 7.8 mg, 4.5 mg, and 5.4 mg, respectively. In addition, the friction coefficient is related to the hardness and residual stress of the material. The residual compressive stress generated on the surface can offset the contact stress suffered by some samples. The microhardness and residual compressive stress of the coatings increased with

increasing preloading depth. When the preloading depth reached 0.30 mm, microcracks appeared on the coating surface and the residual compressive stress was reduced.

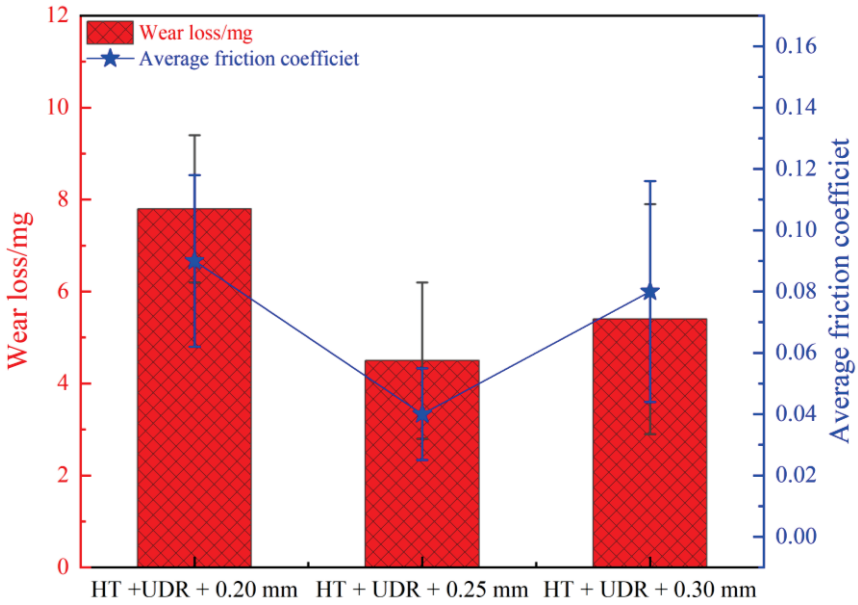


Figure 11. Average friction coefficient and wear of the coating under different preloading depths.

3.3.2. Wear Type and Mechanism Analysis

Figure 12 shows the surface wear morphologies of the dry sliding friction under different preloading depths. The wear surface of HT + UDR + 0.20 mm showed flake peeling, with spalling pits and adhesion points. The furrows were wide and deep, accompanied by the accumulation of debris. There were many pits and rough peaks on the surface, and the rough peaks were cut during dry sliding wear, resulting in adhesion on the worn surface. Further wear generated more friction heat and aggravated adhesion, eventually forming larger adhesion points. The main forms of friction wear were adhesive wear and fatigue wear. There were many furrows on the wear surface under the 0.25 mm preloading depth in Figure 12b, and the furrows were narrow and shallow. The furrows were parallel to each other and moved in the same direction as the friction pair, without obvious cracks and spalling pits. There were no obvious defects on the surface of the coating before wear, and the friction curve showed that the sample entered the stable wear stage from the point contact transition surface. The width and depth of scratches and furrows in the silver–white area were smaller than those in the black area, which was attributed to the higher hardness and strength of hard phases (such as WC), as well as strong wear resistance and deformation. The friction and wear of the hard phase in the coating was a "skeleton" effect, and the soft phase exhibited good capability of plastic deformation. The embedded WC hard phases in Ni and Fe underwent plastic deformation, absorbed energy, and prevented the hard phase from peeling, thus achieving the effect of the "strong and tough bonding". The main wear form was abrasive wear. In Figure 12c, there were deep furrows and fatigue cracks, as well as spalling pits at the crack edges. On the surface of high hardness, the pin plate with the sample in the process of wear and tear led to the extrusion edge grinding crack area of the bulge and increased some parts that were prone to large stress concentration. The area of the bulge was separated from the surface under the repeated friction of the pin plate to form a high hardness abrasive grain and then fell into the furrow area to form three-body abrasive wear of the pin plate, high hardness abrasive grain, and coating, thus generating deeper furrows during the wear process. As the yield stress of the material is certain, cyclic stress was formed in the contact area with continuous wear. When the cyclic stress was greater than the yield stress of the material, the coating surface underwent irreparable plastic deformation, and microcracks occurred

and expanded to a certain extent on the surface, resulting in material fracture and spalling. The main wear forms were fatigue wear and abrasive wear.

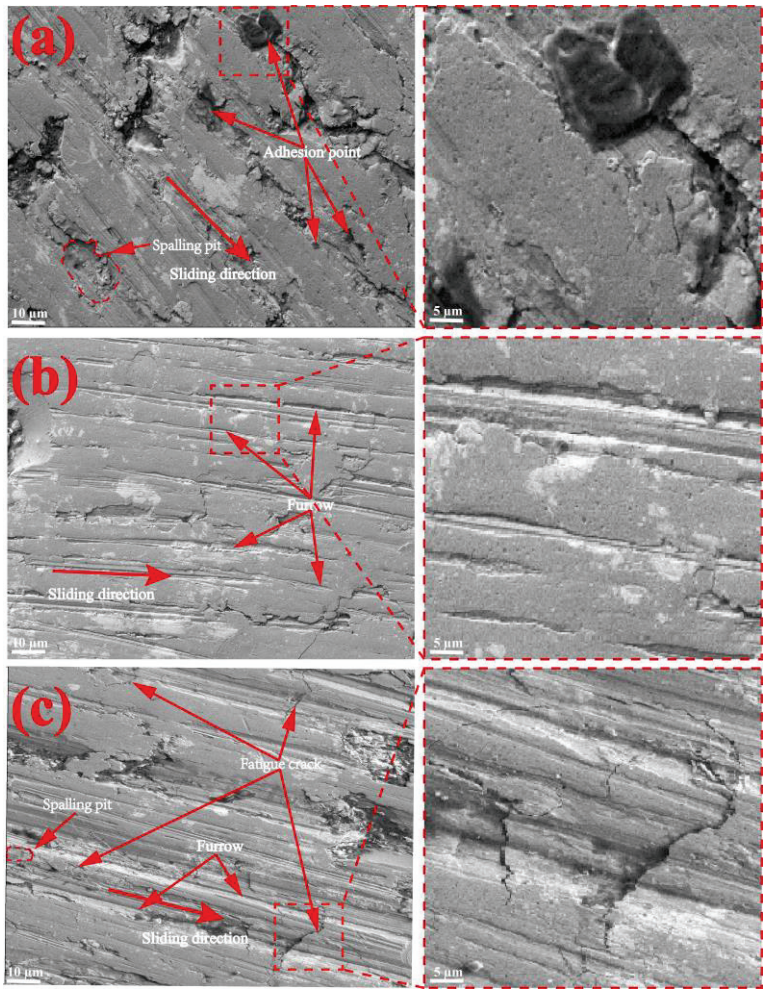


Figure 12. Wear morphology of coatings with different preloading depths: (**a**) HT + UDR + 0.20 mm; (**b**) HT + UDR + 0.25 mm; (**c**) HT + UDR + 0.30 mm.

The mechanism analysis pre and post wear resistance strengthening is shown in Figure 13. The surface defects of the coating were eliminated by high-temperature ultrasonic deep rolling, and WC particles were dispersed in the coating structure. At the same time, the surface hardness of the coating was improved and the residual compressive stress was introduced to further improve the wear resistance of the coating [32]. In the early stage of wear, the pin plate was continuously squeezed and rotated along the surface of the Ni-WC coating to cause friction and wear. The hardness of the nickel-based alloy is smaller than that of the WC particles, and it is quickly removed by the asperities on the surface of the pin plate, exposing the skeleton of the WC particles, which can effectively block the ploughing of the abrasive particles on the nickel-based alloy area. The convex WC particles and the concave nickel-based alloy structure continuously flow into the concave nickel-based alloy area during the wear process, avoiding the sliding of the wear debris between the pin plate and the coating and reducing the probability of plastic deformation and spalling on the coating surface. With the increase of wear time, the height of WC particles reaches the concave area, and the next cycle is carried out until the wear fails. The preloading depth mainly affects the degree of plastic deformation of the coating. With the increase in preloading depth, the surface roughness and microhardness of the coating increased first and then decreased, and the tribological properties increased first and then decreased.

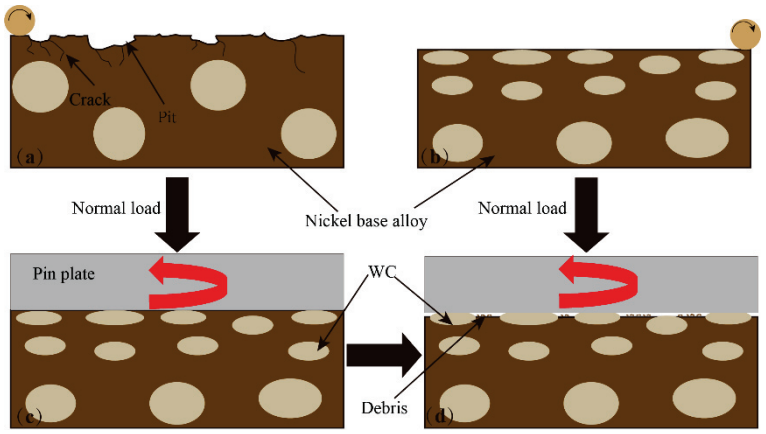


Figure 13. Wear resistance mechanism diagram pre and post coating strengthening: (**a**,**b**) pre and post HT + UDR; (**c**,**d**) pre and post coating wear.

4. Conclusions

The Ni-WC coatings were posttreated by HT + UDR to investigate the effect of preloading depth on the microstructure and tribological properties of the coatings. The main conclusions of this study are as follows:

(1) After HT + UDR treatment, plastic rheology occurred on the surface of the coating, achieving the effect of "peak cutting and valley filling". The surface defects were eliminated and the coating becomes denser. The large WC particles were elongated and fractured along the deep rolling direction, and then flowed and dispersed between the coatings with the coating structure.

(2) After HT + UDR treatment, the coating underwent grain refinement and work hardening to improve the hardness of the coating. The microhardness of HT + UDR + 0.25 mm was the highest. The residual tensile stress was transformed into residual compressive stress.

(3) After Ni-WC coating HT + UDR, more hard phases, such as WC, were exposed on the surface, which played the role of "skeleton" in the wear process. When the preloading depth was 0.25 mm, the tribological properties of the coating after HT + UDR treatment were the best.

Author Contributions: Conceptualization, Y.Z. and J.Z.; methodology, Y.H.; software, C.M., X.Z. and S.Z.; validation, Y.Z., J.Z. and Y.H.; formal analysis, C.M., X.Z. and S.Z.; investigation, Y.Z.; resources, J.Z.; data curation, J.Z.; writing—original draft preparation, C.M., X.Z. and S.Z.; writing—review and editing, Y.Z.; visualization, J.Z.; supervision, Y.H.; project administration, C.M. and X.Z.; funding acquisition, Y.Z. All authors have read and agreed to the published version of the manuscript.

Funding: This research was funded by National Natural Science Foundation of China (No. 51965023).

Institutional Review Board Statement: Not applicable.

Informed Consent Statement: Not applicable.

Data Availability Statement: The authors confirm that the data supporting the findings of this study are available within the article.

Acknowledgments: Thanks to Engineering Research Institute of Jianxi University of Science and Technology for supporting the experiment.

Conflicts of Interest: The authors declare no conflict of interest.

References

1. Wang, J.; Wang, H.; Wang, H.; Zeng, Z. Preparation of Ni60-WC coating by plasma spraying, plasma re-melting and plasma spray welding on surface of hot forging die. *J. Wuhan Univ. Technol. Mater. Sci. Ed.* **2012**, *27*, 640–643. [CrossRef]
2. Yang, S.; Meng, Q.; Geng, L.; Guo, L.; Wu, L. Ni–TiC coating deposited on Ti–6Al–4V substrate by thermal spraying and laser remelting of Ni-clad graphite powder. *Mater. Lett.* **2007**, *61*, 2356–2358. [CrossRef]

3. Liu, Y.; Xu, T.; Liu, Y.; Gao, Y.; Di, C. Wear and heat shock resistance of Ni-WC coating on mould copper plate fabricated by laser. *J. Mater. Res. Technol.* **2020**, *9*, 8283–8288. [CrossRef]
4. Thi, H.P.; Van, T.N.; Nguyen, T.A.; Le Thu, Q.; Thi, L.P.; Bich, T.D.; Van, T.T.; Quoc, C.L. Cr_3C_2-25NiCr cermet coating: Preparation, PTFE sealant, wear and corrosion resistances. *J. Therm. Spray Technol.* **2021**, *30*, 716–724. [CrossRef]
5. Thakare, J.G.; Pandey, C.; Mahapatra, M.M.; Mulik, R.S. Thermal barrier coatings—A state of the art review. *Met. Mater. Int.* **2021**, *27*, 1947–1968. [CrossRef]
6. Hu, Y.; Ning, F.; Cong, W.; Li, Y.; Wang, X.; Wang, H. Ultrasonic vibration-assisted laser engineering net shaping of ZrO_2-Al_2O_3 bulk parts: Effects on crack suppression, microstructure, and mechanical properties. *Ceram. Int.* **2018**, *44*, 2752–2760. [CrossRef]
7. Zhao, Y.; Wu, X.; Du, H.; Shangguan, X.; He, W. Influence of different laser re-melting paths on the microstructure of a spray coating: Defect prevention and tribological properties. *Surf. Coat. Technol.* **2019**, *367*, 11–18. [CrossRef]
8. Konyashin, I.Y. Wear-resistant coatings for cermet cutting tools. *Surf. Coat. Technol.* **1995**, *71*, 284–291. [CrossRef]
9. Zhao, X.Q.; Zhou, H.D.; Chen, J.M. Comparative study of the friction and wear behavior of plasma sprayed conventional and nanostructured WC–12% Co coatings on stainless steel. *Mater. Sci. Eng.* **2006**, *431*, 290–297. [CrossRef]
10. Ojha, S.; Thakare, J.G.; Giri, A.; Pandey, C.; Mahapatra, M.M.; Mulik, R.S. Experimental and numerical investigation of residual stress in coatings on steel. *J. Test. Eval.* **2020**, *48*, 4370–4386. [CrossRef]
11. Xu, G.; Wang, C.; Li, Q.; Zhang, X.; Zhu, Z.; Liang, T.; Yang, B. Effects of ultrasonic rolling on surface performance of 7B85-T6 alloy. *Mater. Manuf. Process.* **2020**, *35*, 250–257. [CrossRef]
12. Luo, X.; Ren, X.; Jin, Q.; Qu, H.; Hou, H. Microstructural evolution and surface integrity of ultrasonic surface rolling in Ti6Al4V alloy. *J. Mater. Res. Technol.* **2021**, *13*, 1586–1598. [CrossRef]
13. Liu, C.; Liu, D.; Zhang, X.; He, G.; Xu, X.; Ao, N.; Ma, A.; Liu, D. On the influence of ultrasonic surface rolling process on surface integrity and fatigue performance of Ti-6Al-4V alloy. *Surf. Coat. Technol.* **2019**, *370*, 24–34. [CrossRef]
14. Sweeney, C.A.; O'Brien, B.; Dunne, F.P.E.; McHugh, P.E.; Leen, S.B. Strain-gradient modelling of grain size effects on fatigue of CoCr alloy. *Acta Mater.* **2014**, *78*, 341–353. [CrossRef]
15. Valiev, R. Nanostructuring of metals by severe plastic deformation for advanced properties. *Nat. Mater.* **2004**, *3*, 511–516. [CrossRef] [PubMed]
16. Lu, L.X.; Sun, J.; Li, L.; Xiong, Q.C. Study on surface characteristics of 7050-T7451 aluminum alloy by ultrasonic surface rolling process. *Int. J. Adv. Manuf. Technol.* **2016**, *87*, 2533–2539. [CrossRef]
17. Lu, K.; Lu, J. Nanostructured surface layer on metallic materials induced by surface mechanical attrition treatment. *Mater. Sci. Eng.* **2004**, *375*, 38–45. [CrossRef]
18. Bagheri, S.; Guagliano, M. Review of shot peening processes to obtain nanocrystalline surfaces in metal alloys. *Surf. Eng.* **2009**, *25*, 3–14. [CrossRef]
19. Meyer, D.; Brinksmeier, E.; Hoffmann, F. Surface hardening by cryogenic deep rolling. *Procedia Eng.* **2011**, *19*, 258–263. [CrossRef]
20. Prevéy, P.S.; Cammett, J.T. The influence of surface enhancement by low plasticity burnishing on the corrosion fatigue performance of AA7075-T6. *Int. J. Fatigue* **2004**, *26*, 975–982. [CrossRef]
21. Yang, J.; Liu, D.; Zhang, X.; Liu, M.; Zhao, W.; Liu, C. The effect of ultrasonic surface rolling process on the fretting fatigue property of GH4169 superalloy. *Int. J. Fatigue* **2020**, *133*, 105373. [CrossRef]
22. Li, G.; Qu, S.; Xie, M.; Li, X. Effect of ultrasonic surface rolling at low temperatures on surface layer microstructure and properties of HIP Ti-6Al-4V alloy. *Surf. Coat. Technol.* **2017**, *316*, 75–84. [CrossRef]
23. Shen, X.; Gong, X.; Wang, B.; He, J.; Xu, C.; Su, G. Surface properties enhancement of Inconel 718 alloy by ultrasonic roller burnishing coupled with heat treatment. *Arch. Civ. Mech. Eng.* **2021**, *21*, 122. [CrossRef]
24. Amanov, A.; Pyun, Y.S. Local heat treatment with and without ultrasonic nanocrystal surface modification of Ti-6Al-4V alloy: Mechanical and tribological properties. *Surf. Coat. Technol.* **2017**, *326*, 343–354. [CrossRef]
25. MacLeod, S.G.; Errandonea, D.; Cox, G.A.; Cynn, H.; Daisenberger, D.; Finnegan, S.E.; McMahon, M.I.; Munro, K.A.; Popescu, C.; Storm, C.V. The phase diagram of Ti-6Al-4V at high-pressures and high-temperatures. *J. Phys. Condens. Matter* **2021**, *33*, 154001. [CrossRef] [PubMed]
26. Wang, X.; Zhu, L.; Zhou, Z.; Liu, G.; Liu, E.; Zeng, Z.; Wu, X. Tribological properties of WC-reinforced Ni-based coatings under different lubricating conditions. *J. Therm. Spray Technol.* **2015**, *24*, 1323–1332. [CrossRef]
27. Ren, Z.; Lai, F.; Qu, S.; Zhang, Y.; Li, X.; Yang, C. Effect of ultrasonic surface rolling on surface layer properties and fretting wear properties of titanium alloy Ti5Al4Mo6V2Nb1Fe. *Surf. Coat. Technol.* **2020**, *389*, 125612. [CrossRef]
28. Angkurarach, L.; Juijerm, P. Effects of high-temperature deep rolling on fatigue, work hardening, and residual stress relaxation of martensitic stainless steel AISI 420. *J. Mater. Eng. Perform.* **2020**, *29*, 1416–1423. [CrossRef]
29. Amanov, A.; Umarov, R. The effects of ultrasonic nanocrystal surface modification temperature on the mechanical properties and fretting wear resistance of Inconel 690 alloy. *Appl. Surf. Sci.* **2018**, *441*, 515–529. [CrossRef]
30. Zhao, Y.; He, W.; Du, H.; Luo, P. The effect of laser power on the interface microstructure of a laser remelting nano-SiC modified Fe-based Ni/WC composite coating. *Coatings* **2018**, *8*, 297. [CrossRef]
31. Dang, J.; Zhang, H.; An, Q.; Lian, G.; Li, Y.; Wang, H.; Chen, M. Surface integrity and wear behavior of 300M steel subjected to ultrasonic surface rolling process. *Surf. Coat. Technol.* **2021**, *421*, 127380. [CrossRef]
32. Zhang, Y.; Li, L.; Wang, X.; Zhao, Y.; Chang, Q.; Wang, W.; Xu, A. Experimental study on aluminum bronze coating fabricated by electro-spark deposition with subsequent ultrasonic surface rolling. *Surf. Coat. Technol.* **2021**, *426*, 127772. [CrossRef]

33. Ye, C.; Telang, A.; Gill, A.S.; Suslov, S.; Idell, Y.; Zweiacker, K.; Wiezorek, J.M.; Zhou, Z.; Qian, D.; Mannava, S.R. Gradient nanostructure and residual stresses induced by Ultrasonic Nano-crystal Surface Modification in 304 austenitic stainless steel for high strength and high ductility. *Mater. Sci. Eng.* **2014**, *613*, 274–288. [CrossRef]
34. Suh, C.M.; Song, G.H.; Suh, M.S.; Pyoun, Y.S. Fatigue and mechanical characteristics of nano-structured tool steel by ultrasonic cold forging technology. *Mater. Sci. Eng.* **2007**, *443*, 101–106. [CrossRef]

Disclaimer/Publisher's Note: The statements, opinions and data contained in all publications are solely those of the individual author(s) and contributor(s) and not of MDPI and/or the editor(s). MDPI and/or the editor(s) disclaim responsibility for any injury to people or property resulting from any ideas, methods, instructions or products referred to in the content.

coatings

MDPI

Article

High-Temperature Oxidation Properties of Ti-Hf-Mo-Ta-Nb-B Composite Coating Deposited on Ti60 Alloy with Laser Cladding

Kaijin Huang [1,2,*] and Xianchao Han [1]

[1] State Key Laboratory of Materials Processing and Die and Mould Technology, Huazhong University of Science and Technology, Wuhan 430074, China; m202171092@hust.edu.cn
[2] Key Laboratory of Laser Technology and Optoelectronic Functional Materials of Hainan Province, Hainan Normal University, Haikou 571158, China
* Correspondence: huangkaijin@hust.edu.cn; Tel.: +86-027-87543676

Abstract: In order to improve the high-temperature oxidation resistance of Ti60 alloy, a Ti-Hf-Mo-Ta-Nb-B composite coating was prepared on Ti60 alloy with Ti, Hf, Mo, Ta and Nb powder and B powder as raw materials using laser cladding. The microstructure and oxidation behavior of the coating before and after oxidation at 1100 °C × 120 h in static air were studied with XRD, SEM, EDS and isothermal oxidation techniques. The results show that the coating was mainly composed of six phases, $(Ti_{0.2}Hf_{0.2}Mo_{0.2}Ta_{0.2}\ Nb_{0.2})B_2$, TiB, HfB_2, $Mo_{4.00}\ B_{3.40}$, TiHf and $Hf_{1.86}Mo_{0.14}$. The high-temperature oxidation of the coating and Ti60 alloy followed parabolic law, and the oxidation weight gain rate of the coating after 110 °C × 120 h was only 1/4.8 of that of the Ti60 alloy. The improvement of the high-temperature oxidation resistance of the coating may benefit from high-temperature oxidation resistance $(Ti_{0.2}Hf_{0.2}\ Mo_{0.2}Ta_{0.2}Nb_{0.2})B_2$, HfB_2 and TiB boride ceramic phases.

Keywords: laser cladding; Ti60 alloy; high-entropy borides; high-temperature oxidation

1. Introduction

Ti60 alloy is a kind of near α type high-temperature titanium alloy designed for a long-term service temperature of 600 °C. The alloy is based on Ti-Al-Sn-Zr and adds a certain amount of Ta-Nb-Mo and other elements. The alloy is made into a heat-strength titanium alloy with multiple composite strengthening, which integrates fine crystal strengthening, solid solution strengthening and second phase (α_2 and silicide) dispersion strengthening. It has a good match of high oxidation resistance, thermal strength and thermal stability at working temperature [1]. However, at a long-term oxidation temperature of more than 700 °C, not only does the alloy form a thick oxide layer on the surface, the peeling of oxidation products also leads to poor long-term oxidation resistance of the Ti60 alloy. At the same time, the surface layer of the alloy also has a microstructure transformation due to the entry of oxygen, forming an embrittlement layer [2]. In order to improve the application of Ti60 alloy at higher temperatures, as early as 1998, Liu et al. [2] used vacuum cathode ion plating equipment to deposit the NiCrAlY coating on the Ti60 alloy and observed its oxidation behavior at 700 °C × 1000 h, as well as the protective effect of the NiCrAlY coating at different thicknesses. The results show that the NiCrAlY coating can inhibit the oxidation of Ti60 alloy caused by titanium diffusion from inside to outside, and the oxidation resistance of the NiCrAlY coating can meet the requirements of long-term use at 700 °C. In the same year, Tang et al. [3] studied the effects of sputtering Al, NiCrAl, TiAl, TiAlCr and reactive sputtering Al_2O_3 coatings on the oxidation resistance of Ti60 alloy, and the results show that sputtering pure Al, Ti-36Al, Ni-16Cr-2.5Al and reactive sputtering Al_2O_3 coatings can improve the oxidation performance of Ti60 alloy by 2–4 times at 700 °C × 100 h and 800 °C × 100 h. In 2004, Xiong et al. [4] studied the effect of an ultra-fine special enamel coating on the oxidation performance of Ti60 alloy at 800 °C × 100 h. The results show that the oxidation rate of the coating is about 0.8 mg /cm^2, which is 10 times higher than

that of the substrate. In 2010, Li et al. [5] studied the high-temperature oxidation behavior of Ni-Co-Cr-Al-Y-Si coating deposited on Ti60 alloy with cathodic multi-arc ion plating at 600 °C, 650 °C and 750 °C × 120 h, and the results show that the Ni-Co-Cr-Al-Y-Si coating improves the oxidation resistance of Ti60 alloy at 600 °C, 650 °C and 750 °C by 13 times, 8 times and 1.5 times, respectively. In the same year, Yan et al. [6] used arc ion plating technology to deposit Ti-48Al-12Cr coating on Ti60 alloy and carried out isothermal oxidation of the coating at 900 °C, but no experimental results for isothermal oxidation of Ti60 alloy at the same temperature were reported. The results show that a continuous and dense Al_2O_3 protective oxide film was formed on the surface of the coating; no cracks appeared under the oxide film and the coating remained intact. In 2017, Chen [7] prepared NiCrAlYSi coating on Ti60 alloy using cathodic multi-arc ion plating technology and confirmed that after oxidation at 600 °C and 650 °C × 120 h, it had a good antioxidant protection effect, and the oxidation performance was increased by 13 times and 6 times, respectively. However, a titanium element was found in the oxide skin at 800 °C. This indicates that the oxygen in the environment can pass through the coating and oxidize with the substrate, and the oxidation resistance of the coating at this temperature was only 1.5 times higher than that of the substrate.

It can be seen from the above that the highest temperature of the high-temperature anti-oxidation coating prepared on Ti60 alloy reported in the literature does not exceed 900 °C, and although there are many literature reports [8–12] on the preparation of high-temperature oxidation-resistant coatings on the surface of different titanium alloys, such as TA2 [8], TA15 [9] and TC4 [10–12], using laser cladding, there is no literature report on the preparation of high-temperature anti-oxidation coating resistant to 1100 °C on Ti60 alloy. The melting point of titanium is 1668 °C, the boiling point is 3260 °C, and the density is 4.5 g/cm^3, which has a wide range of uses in the aerospace field. With the increase in the thrust-to-weight ratio, the pursuit of titanium alloys with higher temperature resistance has become the research goal of scientists. Although scientists are studying TiAl-based alloys at 900 °C and Nb-TiAl-based alloys above 1000 °C, both of them have the disadvantages of low room temperature plasticity and difficult processing [13]. These cannot be solved in the short term, and we still need to greatly improve their oxidation resistance temperature via coating modification technology.

On the other hand, high-entropy borides are formed with a solid solution of five or more single-component diborides, usually forming an AlB_2 hexagonal structure with an alternating two-dimensional boron network and a high-entropy cation layer. Due to their excellent high-temperature oxidation resistance and mechanical properties [14], they have been a subject of wide concern throughout the world, and their structure schematic diagram is shown in Figure 1.

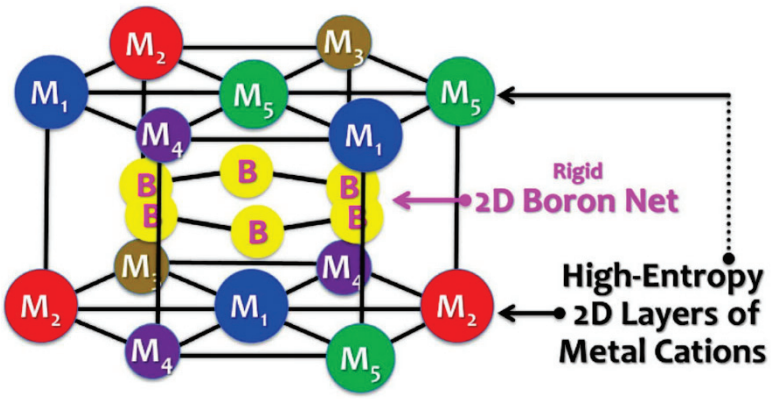


Figure 1. Structure schematic diagram of the high-entropy borides.

The two-dimensional high-entropy metal layers are separated by a rigid two-dimensional boron network without any significant stratified segregation between the metal atomic layers

perpendicular to the C-axis, and M-B bonds have mixed ionic and covalent bond properties. In the two-dimensional metal layer, M-M bonds are significantly affected by the stronger B-B bonds formed by the rigid boron network. This unique structure makes the hardness and oxidation resistance of high-entropy borides better than the average performance of five single metal diborides prepared via the same process. Mayrhofer et al. [15] reported that $(Zr_{0.23}V_{0.14}Ti_{0.20}Ta_{0.24}Hf_{0.19})B_2$ high-entropy boride coating at 1500 °C still has thermal stability, not breaking down into two-boride, and the coating hardness at 1500 °C is for at least 36 GPa after annealing. However, when the temperature is greater than 1100 °C, the affinity of the coating for oxygen is also high, showing significant boron loss and oxygen absorption, thus limiting its thermal stability, which is also the reason why 1100 °C was used as the isothermal oxidation temperature in this paper. Kirnbauer et al. [16] reported that $(HfTaVWZr)B_2$ coating still maintains a single-phase structure at 1200 °C, and the high-entropy borides decompose into a very small amount of $(HfTaZr)B_2$ and $(VW)B_2$ at 1400 °C, most of which are still single-phase solid solutions, with the mechanical properties almost unchanged. Zhang et al. [17] reported that $(Hf_{0.25}Zr_{0.25}Ti_{0.25}Cr_{0.25})B_2$-SiC-Si coating can protect the C/C matrix from oxidation for more than 205 h at 1700 °C, which is mainly due to the formation of a dense and stable Hf-Zr-Ti-Cr-Si-O oxide layer. Up to now, there have been limited reports on high-entropy boride coating, especially the study of the oxidation properties of high-entropy boride composite coating prepared with laser cladding at high temperature. In this paper, Ti, Mo, Hf, Ta and Nb pure metal powder was mixed with amorphous B powder, and an in situ reaction occurred under the action of a laser heat source so as to synthesize a high-entropy boride composite coating containing high-temperature oxidation resistance, aiming to improve the oxidation resistance of Ti60 alloy at higher temperatures. The oxidation behavior of the composite coating at 1100 °C in static air was studied.

2. Materials and Methods

The base material was Ti60 alloy with a size of 100 mm × 50 mm × 5 mm, and its composition is shown in Table 1. First, equal molar Ti, Mo, Hf, Ta and Nb metal powder with a purity of 99.9 wt.% and amorphous B powder with a purity of 99.99 wt.% were mixed evenly using a grinding machine. Then, 4 wt.% PVA solution was used as a binder to preset the mixed powder on the surface of the Ti60 alloy. The thickness of the preset powder layer was about 1.5 mm. The ratio of mixed powder is shown in Table 2.

Table 1. Main chemical compositions of Ti60 alloy.

Element	Al	Sn	Zr	Mo	Nb	Ta	Si	C	Ti
Wt.%	5.0–6.3	3.0–5.0	2.5–7.0	0.2–1.5	0.2–1.0	0.2–3.0	0.2–0.55	0.01–0.09	Bal.

Table 2. Ratio of preset powder layer.

Element	Ti	Hf	Mo	Ta	Nb	B
Wt.%	6.80	25.36	13.57	25.71	13.20	15.36

The Raycus RFL-C6000 fiber laser (Wuhan Raycus Fiber Laser Technology Co., LTD, Wuhan, China) was used for laser cladding, and argon was used to protect the cladding process. The laser cladding process parameters were as follows: the laser power was 2600 W, the spot diameter was 4.5 mm, the laser scanning speed was 8 mm/s, the laser spot overlap rate was 30%, the argon purity was 99.99% and the pressure gas flow rate was 15 L/min. After laser cladding, the coating and Ti60 alloy were wire-cut to 9 mm × 9 mm × 5 mm for XRD and SEM and 9 mm × 9 mm × 1.2 mm for high-temperature oxidation. The phases of the coating and Ti60 alloy before and after oxidation were analyzed using an X 'Pert PRO X-ray meter (XRD) produced by the PANalytical Company in Almelo, Newtherlands. The morphologies and compositions of the coating and Ti60 alloy before and after oxidation

were observed using a JSM-7600F scanning electron microscope (SEM) produced by JEOL Company in Tokyo, Japan, equipped with energy disperse spectroscopy. The corrosion reagent used was HF:HNO_3:H_2O = 1:1:3. Using the static air oxidation weighing method, the coating and Ti60 alloy were put into different crucibles, and the isothermal oxidation experiment was carried out for 120 h in the Muffle furnace at 1100 °C. Among them, each high-temperature oxidation weight gain experiment was carried out three times, and the average value of the three times was taken as the oxidation weight gain value under each oxidation time. The M1210 1200 °C box furnace produced by Henan Chengyi Equipment Technology Co., Ltd (Zhengzhou, China). and the Swiss Mettler Toledo XS105 Dual Range (Mettler Toledo, Zurich, Switzerland) analytical balance with an accuracy of 0.1 mg were used in the oxidation experiment.

3. Results and Discussion

3.1. Microstructure

Figure 2 shows the XRD pattern of the laser cladding coating. As can be seen from the figure, the coating was mainly composed of seven phases, $(Ti_{0.2}Hf_{0.2}Mo_{0.2}Ta_{0.2}Nb_{0.2})B_2$, HfB_2 (JCPDS 96-151-0712), TiB (JCPDS 96-900-8947), $Mo_{4.00}$ $B_{3.40}$ (JCPDS 96-434-3334), TiHf (JCPDS 96-152-3026), $Hf_{1.86}Mo_{0.14}$(JCPDS 96-152-2717) and TiO_2 (JCPDS 96-900-4145). The existence of the TiO_2 phase was mainly due to the involvement of oxygen in the air during the laser cladding process. The diffraction peak positions of the $(Ti_{0.2}Hf_{0.2}Mo_{0.2}$ $Ta_{0.2}Nb_{0.2})B_2$ phase are consistent with what was reported in the literature [18]. Under the action of the laser, the melted mixed powders were mixed with the partially melted Ti60 matrix to form a laser melt pool, and various borides and intermetallic compounds were generated via in situ reaction. The following reactions may occur in the laser melt pool:

$$0.2Ti + 0.2Mo + 0.2Hf + 0.2Nb + 0.2Ta + 2B = (Ti_{0.2}Mo_{0.2}Hf_{0.2}Ta_{0.2}Nb_{0.2})B_2 \quad (1)$$

$$Hf + 2B = HfB_2 \quad (2)$$

$$Ti + Hf = TiHf \quad (3)$$

$$1.86Hf + 0.14Mo = Hf_{1.86}Mo_{0.14} \quad (4)$$

$$Ti + B = TiB \quad (5)$$

$$4.00Mo + 3.40B = Mo_{4.00}B_{3.40} \quad (6)$$

$$Ti + O_2 = TiO_2 \quad (7)$$

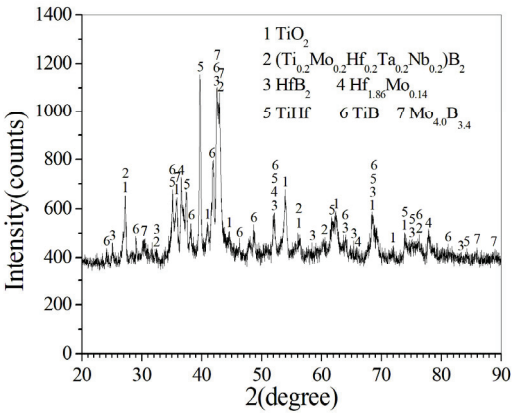


Figure 2. XRD pattern of laser cladding coating.

In addition, Figure 2 shows that in addition to the designed ($Ti_{0.2}Hf_{0.2}Mo_{0.2}Ta_{0.2}Nb_{0.2}$)$B_2$ phase, the coating also generated HfB_2, $Hf_{1.86}Mo_{0.14}$, TiHf, TiB, $Mo_{4.00}B_{3.40}$ and TiO_2. According to the different intensity of the strongest diffraction peak of each phase, the semi-quantitative content of each phase in the coating can be calculated by using the XRD-K value method reported by Zheng et al. [19]. That is, the ratio of the mass fraction of phase i and phase j in the coating is calculated according to Formula (8):

$$\frac{W_i}{W_j} = \frac{W_i'/(1-W_c)}{W_j'/(1-W_c)} = \frac{I_i/K_c^i}{I_j/K_c^j} \tag{8}$$

where W_i' and W_j' represent the mass fraction of phase i and phase j, respectively; W_c represents the mass fraction of the added standard material, such as Al_2O_3; I_i and I_j represent the 2θ diffraction intensity corresponding to the strongest diffraction peak of the i and j phases, respectively; and K_c^i and K_c^j represent the reference intensity values (RIR values) of the i and j phases, respectively.

The strongest diffraction peaks of the TiO_2, ($Ti_{0.2}Hf_{0.2}Mo_{0.2}Ta_{0.2}Nb_{0.2}$)$B_2$, HfB_2, $Hf_{1.86}Mo_{0.14}$, TiHf, TiB and $Mo_{4.00}B_{3.40}$ phases were (110), (101), (101), (011), (101), (111) and (101), respectively. The corresponding RIR values were 3.5, 9.56, 15.36, 32.23, 14.93, 1.85 and 5.94, respectively. According to Formula (8), the mass fractions of each phase in the coating are 5.91%, 29.27%, 6.10%, 2.65%, 9.07%, 34.23% and 12.77%, respectively. That is to say, TiB and ($Ti_{0.2}Hf_{0.2}$ $Mo_{0.2}Ta_{0.2}Nb_{0.2}$)B_2 are the two main generation phases.

Figure 3 shows the overall morphology of the laser cladding cross-section coating. It can be seen from the figure that there are no obvious defects, such as pores and cracks, in the laser cladding coating. The interface of the coating and the Ti60 matrix are well combined. The thickness of the coating is about 1.6~2.4 mm.

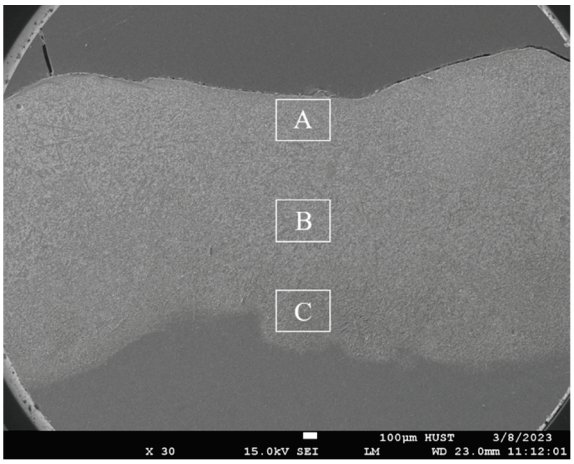


Figure 3. Overall morphology of laser cladding cross-section coating.

Figure 4 shows the SEM amplified morphology at different zones in Figure 3. It can be seen from Figure 4 that the laser cladding coating is mainly composed of a whisker or prismatic microstructure. Due to the effect of convection mass transfer during laser cladding, there is no significant difference in the morphology of different parts of the molten pool. From the combination of the EDS results in Table 3 and the XRD calibration results in Figure 2, it can be roughly speculated that the phase formation process is as follows: in the process of solidification, first of all, the HfB_2 (melting point 3380 °C) and ($Ti_{0.2}Hf_{0.2}Mo_{0.2}Ta_{0.2}Nb_{0.2}$)$B_2$ (melting point 3006 °C) phases with high melting points are solidified from the liquid phase; as the temperature of the molten pool decreases, TiB (melting point 2227 °C), TiHf, $Mo_{4.00}B_{3.40}$ and $Hf_{1.86}Mo_{0.14}$ with low melting points are solidified successively from the remaining liquid phase. The specific formation mechanism

needs to be further studied in the future. One of the more interesting facts is the formation process of whisker or prismatic structure TiB: as TiB has a B27 structure, it grows faster in the direction (010) than in other directions, and it is easy to form a whisker or prismatic structure [20], which plays a role in the strengthening phase in the coating [21]. The structure morphology of TiB in Figure 4 is consistent with reports in the literature [22,23]. Moreover, as the (001) plane grows at the fastest rate, it cannot form a crystal plane, and the remaining (100), (101) and $(10\bar{1})$ crystal faces are the sides of TiB, so the cross sections of whisker-like or prismatic structures are mostly hexagonal [21].

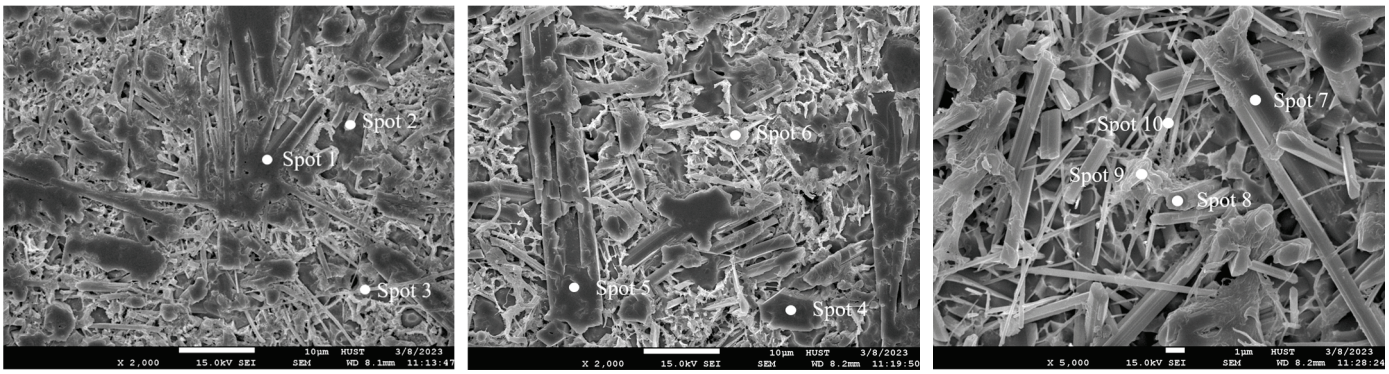


Figure 4. SEM-amplified morphology of different zones in Figure 3: (**a**) surface zone A. (**b**) Middle zone B. (**c**) Interface zone C.

Table 3. EDS results of different points in Figure 4 (at.%).

Element	Spot 1	Spot 2	Spot 3	Spot 4	Spot 5	Spot 6	Spot 7	Spot 8	Spot 9	Spot 10
Ti	12.45	11.43	11.20	12.54	12.09	18.51	15.65	20.09	21.17	19.51
Hf	0.20	0.13	0.13	0.73	0.62	0.27	0.10	0.44	0.26	0.29
Mo	0.90	1.26	0.77	0.61	0.96	0.50	0.74	1.20	1.57	1.41
Ta	1.72	1.54	2.13	1.24	1.21	1.27	1.01	0.94	2.08	0.83
Nb	1.03	1.06	1.04	1.02	1.07	0.95	1.19	1.23	1.08	1.06
B	83.70	84.58	84.73	83.86	84.05	78.50	81.31	76.10	73.84	76.90
Possible phases	TiB + $(Ti_{0.2}Hf_{0.2}Mo_{0.2}Ta_{0.2}Nb_{0.2})B_2$	TiB + $(Ti_{0.2}Hf_{0.2}Mo_{0.2}Ta_{0.2}Nb_{0.2})B_2$	TiB + $(Ti_{0.2}Hf_{0.2}Mo_{0.2}Ta_{0.2}Nb_{0.2})B_2$	TiB + $(Ti_{0.2}Hf_{0.2}Mo_{0.2}Ta_{0.2}Nb_{0.2})B_2$	TiB + $(Ti_{0.2}Hf_{0.2}Mo_{0.2}Ta_{0.2}Nb_{0.2})B_2$	TiB + $(Ti_{0.2}Hf_{0.2}Mo_{0.2}Ta_{0.2}Nb_{0.2})B_2$	TiB + $(Ti_{0.2}Hf_{0.2}Mo_{0.2}Ta_{0.2}Nb_{0.2})B_2$	TiB + $(Ti_{0.2}Hf_{0.2}Mo_{0.2}Ta_{0.2}Nb_{0.2})B_2$	TiB + $(Ti_{0.2}Hf_{0.2}Mo_{0.2}Ta_{0.2}Nb_{0.2})B_2$	TiB + $(Ti_{0.2}Hf_{0.2}Mo_{0.2}Ta_{0.2}Nb_{0.2})B_2$

In addition, the size of the TiB formed at the bottom of the molten pool is small, which is due to the large temperature gradient near the bottom of the molten pool [24]. When the temperature drops to room temperature, the coating finally forms the TiB mixed structure with a whisker or prismatic structure as the main body.

3.2. High-Temperature Oxidation Properties

Figure 5 shows the oxidation weight gain curve of the laser cladding coating and Ti60 matrix after different oxidation times in the air at 1100 °C. The figure shows that the oxidation resistance of the laser cladding coating is superior to the Ti60 matrix. The reason may be related to the fact that the coating contained high-temperature oxidation resistance $(Ti_{0.2}Hf_{0.2}Mo_{0.2}Ta_{0.2}\ Nb_{0.2})B_2$, HfB_2 and TiB phases (Figure 2); the maximum oxidation gain rates of the laser cladding coating and the Ti60 matrix were 54.79 mg/cm^2 and 262.92 mg/cm^2, respectively. That is, the high-temperature oxidation resistance of the laser cladding coating was about 4.8 times that of the Ti60 matrix. It should be noted that, although the literature [25] reported that the oxidation weight gain rate of single-phase $(Ti_{0.2}Hf_{0.2}Mo_{0.2}Ta_{0.2}\ Nb_{0.2})B_2$ prepared with SHS-SPS technology was about 2 mg/cm^2 at 1200 °C × 5 h in air, and the oxidation weight gain rate was lower than that

of the laser cladding coating (8.7 mg/cm^2 at 1100 °C × 5 h in air, Figure 5) in this paper, the possible reason is that the content of $(Ti_{0.2}Hf_{0.2}Mo_{0.2}Ta_{0.2}\ Nb_{0.2})B_2$ in the laser cladding coating was only 29.27%, and the content of the oxidation resistance test samples used in the literature [25] was 100%.

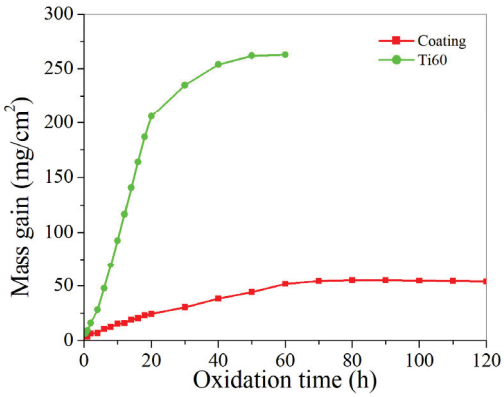


Figure 5. Oxidation weight gain curves of laser cladding coating and Ti60 matrix after oxidation at 1200 °C at different times.

In addition, it can be seen from Figure 5 that the oxidation weight gain of the Ti60 matrix at 1100 °C mainly occurred in the first 50 h. At a high temperature of 1100 °C, Ti in the Ti60 matrix was rapidly oxidized to form loose TiO_2 so that oxygen in the air could continue to diffuse into the internal matrix, resulting in continuous oxidation and weight gain of the Ti60 matrix. However, after more than 50 h, the oxidation and weight gain of the Ti60 matrix had stopped, indicating that the Ti60 matrix had been basically completely oxidized. This is evidenced by the fact that there were only thin yellowish sheets in the crucible (Figure 6). The oxidation weight gain of the laser cladding coating at 1100 °C reached the highest value after 80 h, and after more than 80 h, the oxidation weight gain of the laser cladding coating basically stopped, indicating that the oxidation of the laser cladding coating entered a stable equilibrium state but was not completely oxidized, which could be demonstrated by the large pieces of unoxidized coating in the crucible (Figure 7a). Figure 7b is a macroscopic photo of the laser cladding coating oxidized for 120 h. It can be seen that there are still large pieces of unoxidized coating, that is, the laser cladding coating can withstand oxidation at least at 1100 °C × 120 h.



Figure 6. Photo of Ti60 matrix oxidized at 1100 °C × 60 h.



(**a**) 80 h (**b**) 120 h

Figure 7. Photo of laser cladding coating oxidized at 1100 °C for different times: (**a**) 80 h; (**b**) 120 h.

Table 4 shows the oxidation rate constant k and oxidation weight gain index n of the laser cladding coating and Ti60 matrix, respectively, calculated by fitting the modified Wagner Formula (9). As can be seen from Table 4, the oxidation weight gain indexes n of the laser cladding coating and the Ti60 matrix after oxidation at 1100 °C for different times are 0.5833 and 0.8921, respectively, both of which are less than 1 and are power functions of the transverse parabola; that is, the oxidation kinetics curves of both of them follow parabolic law. Among them, the oxidation law of the Ti60 matrix is consistent with the result of the oxidation kinetics curve of Ti60 alloy at 650~750 °C reported by Jia et al. [26]. The oxidation rate constant k (3.9907) of the laser cladding coating is significantly lower than that of the Ti60 matrix (10.585); that is, the laser cladding coating always maintains a low oxidation rate during the whole high-temperature oxidation process.

$$\Delta m_t/S = kt^n \quad (9)$$

where Δmt/S is the oxidation gain per unit area, k is the oxidation rate constant, n is the oxidation gain index and t is the oxidation time.

Table 4. Kinetics curve fitting of laser cladding coating and Ti60 matrix at 1100 °C for different oxidation times.

Samples	Oxidation Rate Constant (k)	Oxidation Mass Gain Index (n)	Oxidation Time (h)
Ti60 matrix	10.585	0.8921	0–60
Coating	3.9907	0.5833	0–120

Since the oxide film of the Ti60 matrix is characterized by layer-by-layer peeling during the oxidation process (Figure 6), we tested the XRD pattern of the outer surface and the inner surface of the Ti60 matrix after oxidation at 1100 °C × 60 h (Figure 8). As can be seen from Figure 8, the outer surface of the spalling oxide film layer consists of two phases, TiO_2 (PDF 96-153-4782) and srilankite $ZrTiO_4$ (PDF 96-901-0851). The inner surface is three phases of rutile TiO_2 (PDF 96-900-9084), $ZrTiO_4$ (PDF 96-901-0851) and Al_2O_3 (PDF 96-900-9682). According to Formula (8), the mass fractions of the TiO_2 and $ZrTiO_4$ phases on the outer surface are 91% and 9%, respectively. The strongest diffraction peaks of TiO_2 and $ZrTiO_4$ are (110) and (111), respectively, and the corresponding RIR values are 3.74 and 6.43, respectively. The mass fractions of TiO_2, $ZrTiO_4$ and Al_2O_3 on the inner surface are 61.07%, 4.06% and 34.87%, respectively. During the calculation, the strongest diffraction peaks of TiO_2, $ZrTiO_4$ and Al_2O_3 were (110), (111) and (116), respectively, and the corresponding RIR values were 3.74, 6.43 and 1.05, respectively.

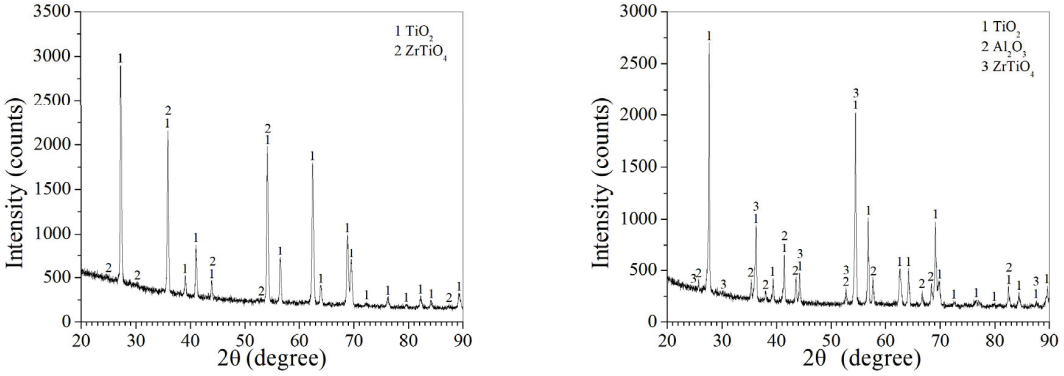


Figure 8. XRD patterns of the inner and outer surfaces of Ti60 matrix at 1100 °C × 60 h: (**a**) outer surface, (**b**) inner surface.

Figure 9 shows the SEM morphology of the outer surface and inner surface of the Ti60 matrix shedding oxide film. As can be seen from Figure 9a, the outer surface of the oxide film is composed of massive large particles + dispersed white small particles. Combined with the results of EDS (Table 5) and XRD (Figure 8a), it can be seen that the massive particles are TiO_2, which come from the oxidation of Ti (Table 1) in the Ti60 matrix, that is, $Ti + O_2 = TiO_2$. The small white particles are srilankite $ZrTiO_4$, which may be due to the reaction of Zr and Ti in the Ti60 matrix with O_2 in the air at 1100 °C, that is, $Ti + Zr + 2O_2 = ZrTiO_4$, but the content is less (9%). Instead, Ti and Zr in the Ti60 matrix first react with O_2 in the air to produce TiO_2 and ZrO_2, respectively, and then TiO_2 reacts with ZrO_2 to produce $ZrTiO_4$ ($TiO_2 + ZrO_2 = ZrTiO_4$) because the free energy of $Ti + Zr + 2O_2 = ZrTiO_4$ is the lowest according to the reaction formula (Figure 10). It is easiest for this reaction to proceed.

Table 5. EDS results of different points on the inner and outer surfaces of Ti60 oxide film (at.%).

Element	Spot 1	Spot 2	Spot 3	Spot 4	Spot 5	Spot 6
Ti	28.59	16.30	32.23	1.24	8.04	24.20
Zr	12.70	11.44	13.40	8.81	13.70	12.52
Mo	0.54	1.04	2.00	0.99	0.78	0.92
Sn	0.12	0.29	0.13	-	0.43	-
Nb	-	-	-	-	0.16	-
Al	-	-	2.96	21.40	16.26	-
O	58.05	70.93	49.28	67.56	60.63	62.36
Possible phases	TiO_2 + $ZrTiO_4$	$ZrTiO_4$	TiO_2 + $ZrTiO_4$	Al_2O_3 + $ZrTiO_4$	$ZrTiO_4$ + Al_2O_3	TiO_2 + $ZrTiO_4$

It can be seen from Figure 9b–d that the inner surface of the oxide film is massive particles + rock sugar-like particles. Combined with the results of EDS (Table 5) and XRD (Figure 8b), it can be seen that the massive particles are mainly TiO_2, which comes from the oxidation of Ti (Table 1) in the Ti60 matrix, that is, $Ti + O_2 = TiO_2$. The bulk particles of rock sugar are mainly Al_2O_3, which comes from the oxidation of Al in the Ti60 matrix (Table 1), that is, $4Al + 3O_2 = 2Al_2O_3$. In addition, a small amount of srilankite $ZrTiO_4$ is also produced (4.06%, Table 1).

Figure 11 shows the cross-section SEM morphology of the oxide film layer of the Ti60 matrix after oxidation at 1100 °C × 60 h. As can be seen from Figure 11, Table 6 and XRD (Figure 8), the thickness of the shed oxide film is about 320~380 μm. The content of the Al element near the upper (outer) surface of the oxide film is less, while the content of the Al element near the lower (inner) surface of the oxide film is relatively more. There are two phases of $TiO_2 + ZrTiO_4$ in the oxide film layer near the upper (outer) surface and three phases of $TiO_2 + ZrTiO_4 + Al_2O_3$ in the oxide film layer near the lower (inner) surface.

This oxidation product indicates that the Ti60 matrix follows the selective oxidation theory at 1100 °C; that is, under the condition of high-temperature oxidation, Ti and Zr elements diffuse outward and preferentially form $ZrTiO_4$ and TiO_2 (in excess of Ti) on the surface layer. Because their Pilling–Bedworth volume ratios γ are 3.16 and 1.95, respectively, both of which are greater than 1, the oxide films of $ZrTiO_4$ and TiO_2 have integrity. However, because the γ value of $ZrTiO_4$ is too large, the internal stress of the films is large, and the films are prone to rupture and lose protection or have poor protection, which can be demonstrated by the numerous cracks in Figure 11. However, the Al element diffused slowly and was enriched at the interface between the $ZrTiO_4$ + TiO_2 oxide film and the Ti60 matrix, oxidizing to form Al_2O_3. As the Pilling–Bedworth volume ratio γ of Al_2O_3 was 1.28, the Al_2O_3 film had integrity.

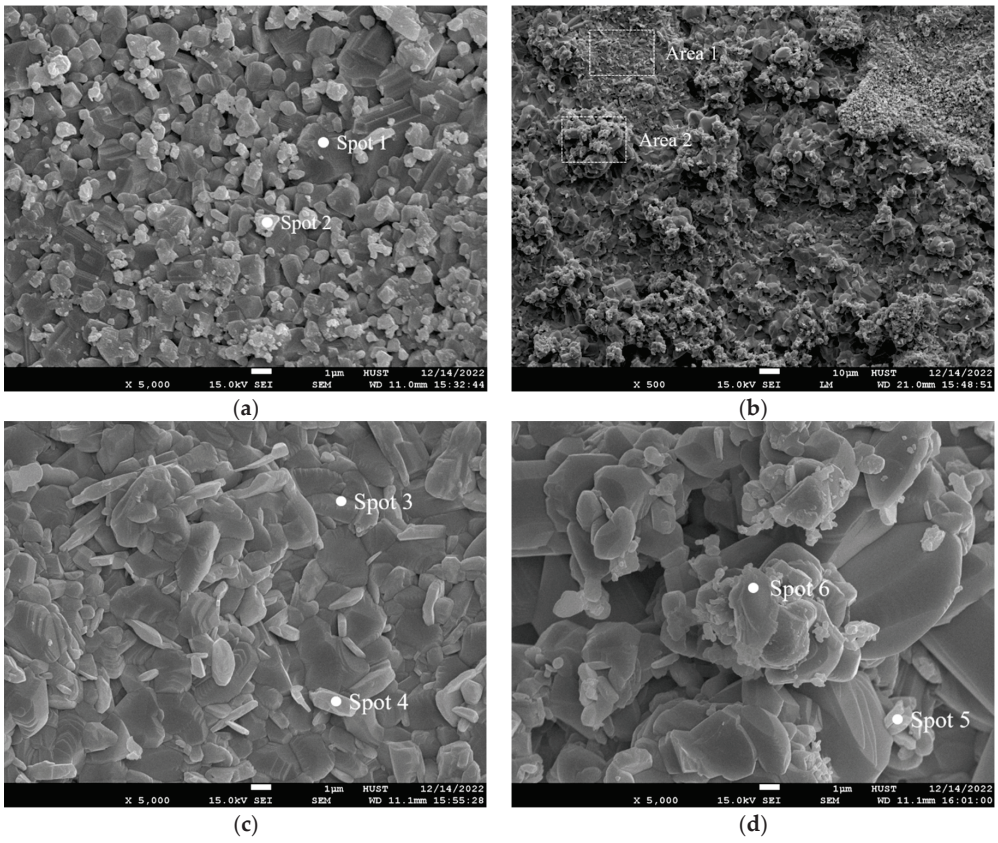


Figure 9. SEM morphology of the inner and outer surfaces of Ti60 matrix after oxidation at 1100 °C × 60 h: (**a**) outer surface, (**b**) inner surface, (**c**) local magnification of Area 1 in Figure 9b, (**d**) local magnification of Area 2 in Figure 9b.

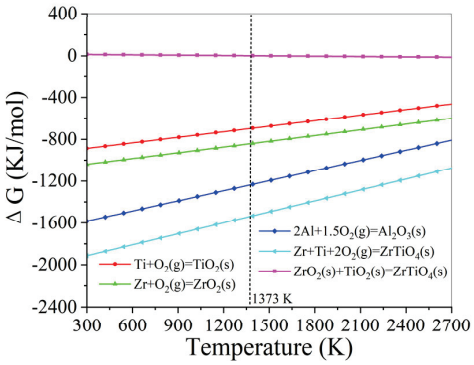
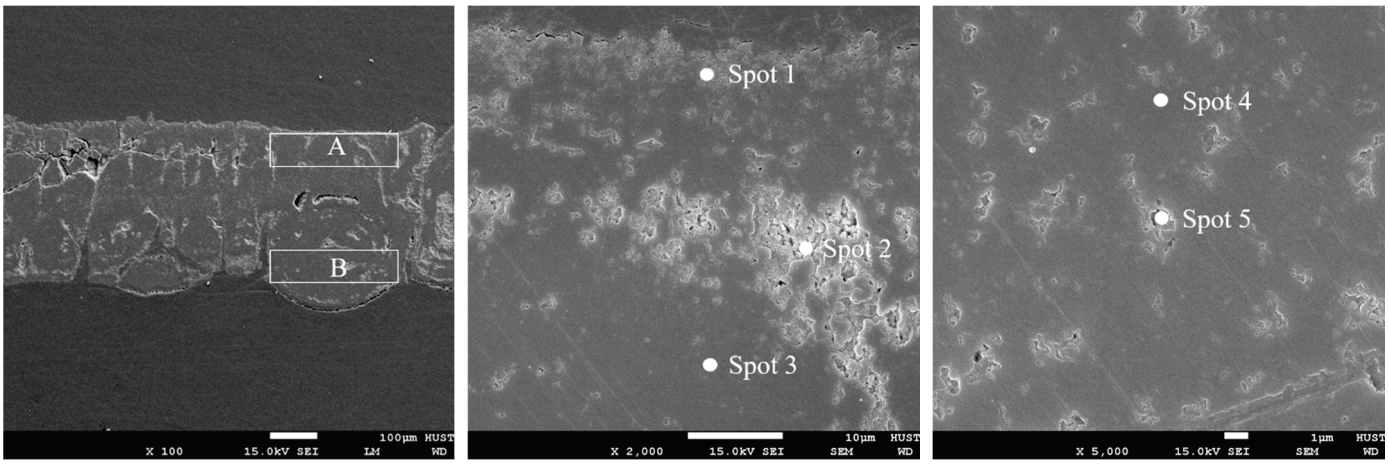


Figure 10. Free energy–temperature curves of different reactions.



(**a**) (**b**) (**c**)

Figure 11. SEM images of the oxide film cross-section layer of Ti60 matrix after oxidation at 1100 °C × 60 h: (**a**) whole, (**b**) local amplification of zone A, (**c**) local amplification of zone B.

Table 6. EDS results of Ti60 oxide film at different points (at.%).

Element	Spot 1	Spot 2	Spot 3	Spot 4	Spot 5
Ti	25.25	21.53	40.6	33.15	25.51
Zr	20.1	15.75	16.47	18.36	16.27
Mo	1.13	1.27	0.92	2.17	1.47
Sn	0.19	-	0.66	0.92	0.49
Nb	-	-	-	-	0.69
Al	-	1.08	1.76	2.63	1.86
O	53.33	60.37	39.59	42.77	53.71
Possible phases	TiO_2 + $ZrTiO_4$	TiO_2 + Al_2O_3 + $ZrTiO_4$	TiO_2 + Al_2O_3 + $ZrTiO_4$	TiO_2 + Al_2O_3 + $ZrTiO_4$	TiO_2 + Al_2O_3 + $ZrTiO_4$

It should be pointed out that the protection of the oxide film depends not only on the integrity of the oxide film, but also on the melting point of the oxide film, the density of the oxide film, the thermodynamic stability of the oxide film, the adhesion of the oxide film, the thermal expansion coefficient of the oxide film, the stress in the oxide film and other factors. Therefore, with the increase in the oxide film thickness, the internal stress of the oxide film increases, and the thermal expansion coefficient of the oxide film is different from that of the matrix, which easily cracks and falls off. Once this happens, the external oxygen can contact the internal unoxidized matrix and selective oxidation occurs again, repeating the above process. Figure 12 shows the schematic diagram of the oxidation process of the Ti60 matrix.

Figure 13 is the XRD pattern of the laser cladding coating after air oxidation at 1100 °C × 120 h. It can be seen from the figure that the laser coating after oxidation is mainly composed of four phases, TiO_2 (PDF 96-900-4143), HfO_2 (PDF 96-154-5065), Ta_2O_5 (PDF 96-210-2125) and Nb_2O_5 (PDF 96-152-8679). This is consistent with what has been reported in the literature [17,27,28]. However, no diffraction peaks of MoO_3 and B_2O_3 were found, which may be due to the evaporation of MoO_3 and B_2O_3 generated during the oxidation process of the laser cladding coating surface because the melting points of MoO_3 and B_2O_3 are 795 °C and 450 °C, respectively, and the boiling points are 2065 °C and 1155 °C, respectively. It can be seen that MoO_3 and B_2O_3 generated during the oxidation process were liquid at the oxidation temperature of 1100 °C but did not reach the boiling point, so there was evaporation. On the other hand, the melting points of TiO_2, HfO_2, Ta_2O_5 and Nb_2O_5 are 1843 °C, 2774 °C, 1785 °C and 1512 °C, respectively, which are all higher than the oxidation temperature of 1100 °C, so they could be retained after oxidation.

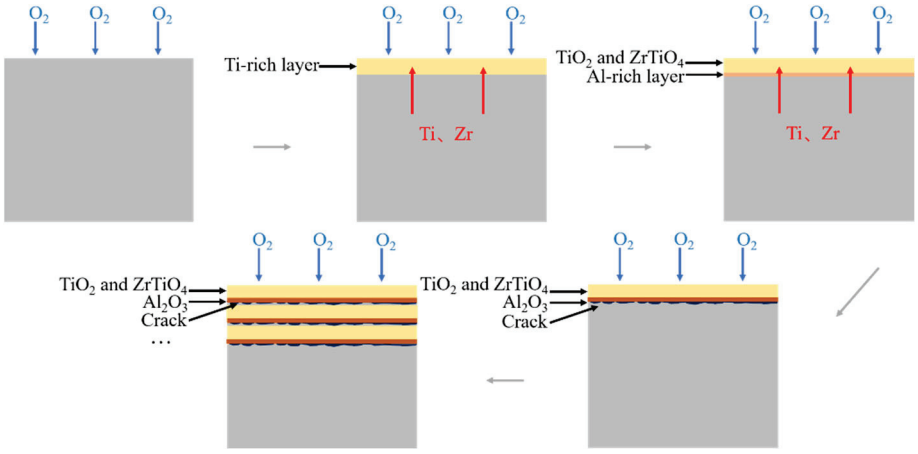


Figure 12. Schematic diagram of oxidation process of Ti60 matrix.

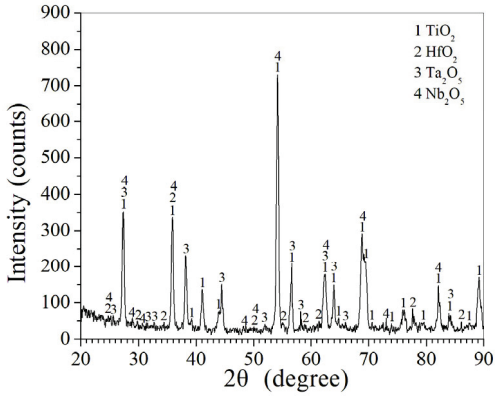


Figure 13. XRD pattern of laser cladding coating after air oxidation at 1100 °C × 120 h.

The laser cladding coating is mainly composed of seven phases, TiO_2, $(Ti_{0.2}Hf_{0.2}Mo_{0.2}Ta_{0.2}Nb_{0.2})B_2$, HfB_2, $Hf_{1.86}Mo_{0.14}$, TiHf, TiB and $Mo_{4.00}B_{3.40}$ (Figure 2); therefore, the coating may react as follows during the air oxidation process:

$$(Ti_{0.2}Mo_{0.2}Hf_{0.2}Ta_{0.2}Nb_{0.2})B_2(s) + 2.7O_2(g) = 0.2TiO_2(s) + 0.2MoO_3(l) + 0.2HfO_2(s) + 0.1Nb_2O_5(s) + 0.1Ta_2O_5(s) + B_2O_3(l) \quad (10)$$

$$HfB_2(s) + 2.5O_2(g) = HfO_2(s) + B_2O_3(l) \quad (11)$$

$$TiHf(s) + 2O_2(g) = TiO_2(s) + HfO_2(s) \quad (12)$$

$$Hf_{1.86}Mo_{0.14}(s) + 2.07O_2(g) = 1.86HfO_2(s) + 0.14MoO_3(l) \quad (13)$$

$$TiB(s) + 1.75O_2(g) = TiO_2(s) + 0.5B_2O_3(l) \quad (14)$$

$$Mo_{4.0}B_{3.4}(s) + 8.55O_2(g) = 4MoO_3(l) + 1.7B_2O_3(l) \quad (15)$$

Figure 14 shows the relationship between the free energy and temperature of the partial reaction equations with thermodynamic data. It can be seen from the figure that the free energies of Equations (10), (11) and (14) are all negative at 1100 °C, that is, these reactions can occur.

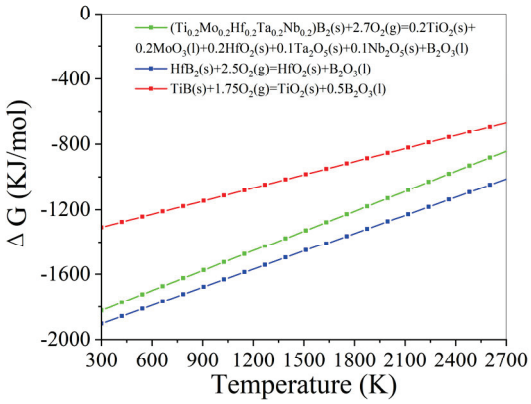
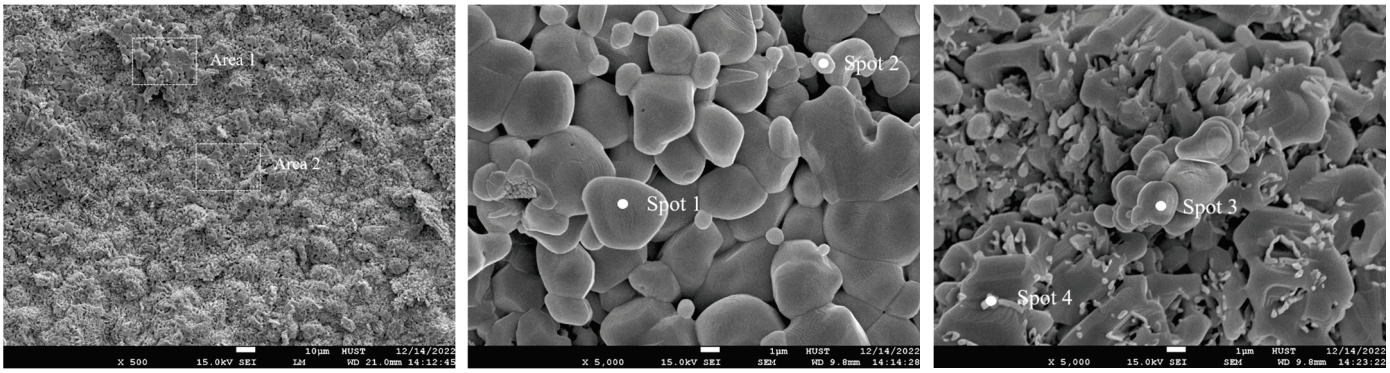


Figure 14. Relationship between the free energy of different reactions and temperature.

In addition, the mass fractions of TiO_2, HfO_2, Ta_2O_5 and Nb_2O_5 calculated according to Formula (8) are 55.72%, 1.81%, 32.12% and 10.35%, respectively. The strongest diffraction peaks of TiO_2, HfO_2, Ta_2O_5 and Nb_2O_5 are (110), (111), ($\bar{1}$11) and ($\bar{1}$11), and the corresponding RIR values are 3.62, 15.89, 6.28 and 3.43, respectively.

Figure 15 shows the SEM morphology of the surface of the laser cladding coating after air oxidation at 1100 °C × 120 h. It can be seen from the figure that the oxidized surface of the laser cladding coating is formed via the aggregation of dense fine particles (Figure 15a), which is the same as the oxidized surface morphology of high-entropy ceramics reported by Ye [29]. Combined with the results of EDS (Table 7) and XRD (Figure 13), it can be seen that these fine particles are mainly composed of Ti-Hf-Ta-Nb-O polyphase mixed oxides, which have a low oxygen diffusion rate and excellent high-temperature stability. The porosity on the surface of the oxide layer may be due to the low melting point of MoO_3 and B_2O_3 generated through oxidation at 1100 °C.



(**a**) (**b**) (**c**)

Figure 15. SEM morphology of the surface of laser cladding coating after oxidation at 1100 °C × 120 h: (**a**) whole, (**b**) local magnification at Area 1, (**c**) local magnification at Area 2.

Table 7. EDS results of oxidized surface of laser cladding coating at different points (at.%).

Element	Spot 1	Spot 2	Spot 3	Spot 4
Ti	38.89	17.43	26.84	18.60
Hf	2.07	0.62	1.34	0.22
Mo	-	-	-	-
Ta	2.53	1.01	1.57	-
Nb	2.01	1.04	1.05	-
O	54.50	79.90	69.20	81.18
Possible phases	TiO_2 + Ta_2O_5 + HfO_2	TiO_2 + Ta_2O_5 + HfO_2	TiO_2 + Ta_2O_5 + HfO_2	TiO_2 + HfO_2

Figure 16 shows the SEM morphology of the laser cladding cross-section coating after air oxidation at 1100 °C × 120 h. It can be seen from Figure 16 and Table 8 that the laser cladding cross-section coating presents an alternating situation of dense oxide layer and loose inner oxide layer, and the loose inner oxide layer has fine particles and no B and Mo elements. Among them, the dense oxide layer may be the reaction between the metal elements in the laser cladding coating and the oxygen diffused inside the coating to produce a dense Ti-Hf-Ta-Nb-Mo-B-O oxide layer, which has an excellent high-temperature protection effect and can effectively reduce the rate of oxygen diffusion to the inside of the coating. However, with the extension of oxidation time, oxygen ions will eventually spread through the dense oxide layer to the interior of the coating. Once the liquid B_2O_3 and MoO_3 phases generated by the oxidation of the internal coating cannot escape, a porous loose oxide layer is formed at the subsurface layer.

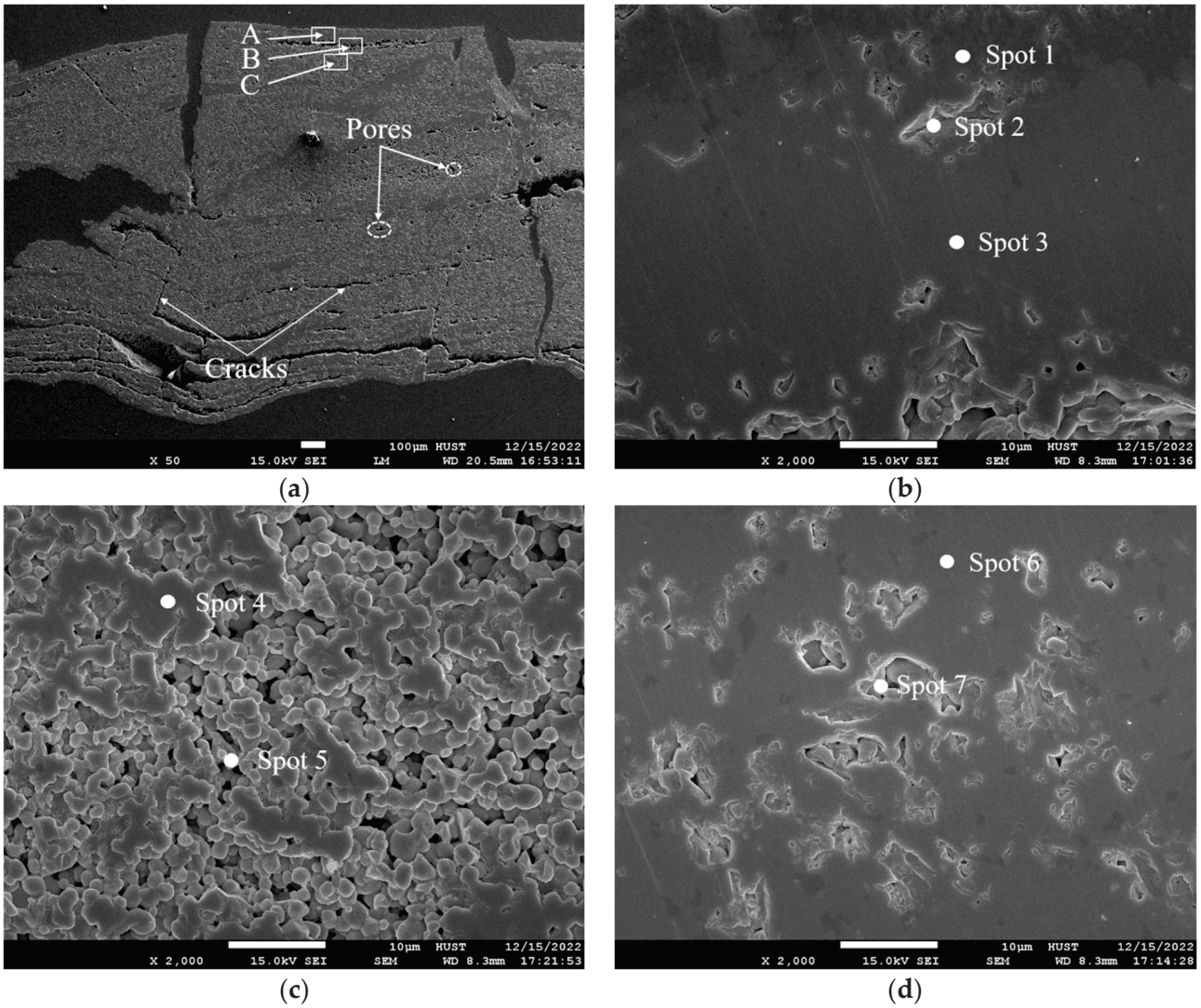


Figure 16. SEM morphology of laser cladding cross-section coating after air oxidation at 1100 °C × 120 h: (**a**) whole, (**b**) local magnification at zone A, (**c**) local magnification at zone B, (**d**) local magnification at zone C.

As we all know, the oxidation of laser cladding coating is essentially the oxidation of various phases in the coating, and the different elements of phases have a significant impact on the oxidation resistance of the coating [30]. In order to investigate the oxidation possibility of each element in the laser cladding coating at 1100 °C, the free energy of each element in the laser cladding coating reacting with O_2 was calculated as ΔG. Figure 17 shows

the standard free energy ΔG–temperature T curve of the reaction of each element with O_2 in the laser cladding coating. It can be seen from the figure that the ΔG values of Ti, Hf, Mo, Ta, Nb and B in the laser cladding coating are all negative when reacting with O_2 at 1100 °C, indicating that they can be oxidized to their respective oxides. Liquid B_2O_3 and MoO_3 cannot become gaseous B_2O_3 and MoO_3 at 1100 °C, indicating that liquid B_2O_3 and MoO_3 run away via evaporation rather than vaporization.

Table 8. EDS results of laser cladding cross-section coating at different points after oxidation (at.%).

Element	Spot 1	Spot 2	Spot 3	Spot 4	Spot 5	Spot 6	Spot 7
Ti	5.37	8.63	9.94	37.21	29.78	5.81	5.18
Hf	0.33	0.08	0.27	0.97	0.83	0.18	0.12
Mo	0.62	0.43	0.60	-	-	0.58	0.36
Ta	0.18	0.20	0.20	1.08	0.82	0.06	0.15
Nb	0.17	0.21	0.27	1.24	0.87	0.08	0.12
B	80.30	74.47	76.50	-	-	82.80	88.19
O	13.03	15.98	12.22	59.50	67.70	10.49	5.88
Possible phases	TiO_2 + Ta_2O_5 + HfO_2 + Nb_2O_5 + MoO_3 + B_2O_3	TiO_2 + Ta_2O_5 + HfO_2 + Nb_2O_5 + MoO_3 + B_2O_3	TiO_2 + Ta_2O_5 + HfO_2 + Nb_2O_5 + MoO_3 + B_2O_3	TiO_2 + Nb_2O_5 + Ta_2O_5 + HfO_2	TiO_2 + Ta_2O_5 + HfO_2 + Nb_2O_5	TiO_2 + Ta_2O_5 + HfO_2 + Nb_2O_5 + MoO_3 + B_2O_3	TiO_2 + Ta_2O_5 + HfO_2 + Nb_2O_5 + MoO_3 + B_2O_3

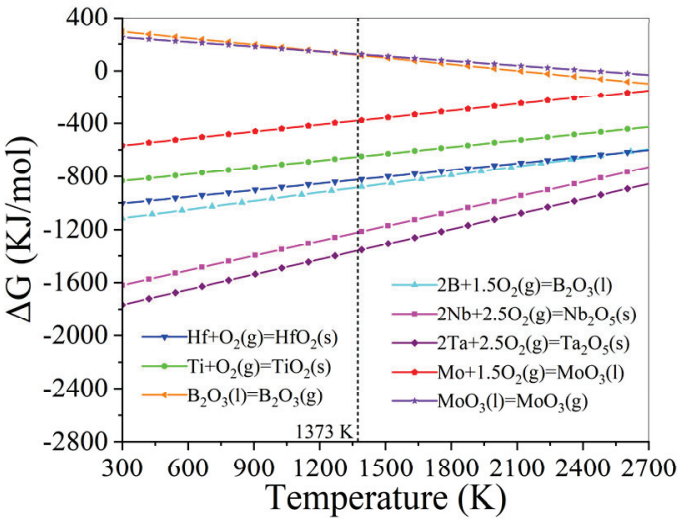


Figure 17. Standard free energy ΔG–temperature T curve of the reaction of each element with O_2 in the laser cladding coating.

Figure 18 shows the schematic diagram of the oxidation process of the laser cladding coating. In the initial oxidation stage of the laser cladding coating at 1100 °C, O_2 adsorbed on the surface of the coating, and the elements of Ti, Hf, Ta, Mo, Nb and B in the coating diffused outward and reacted with the O_2 diffused inside the coating to form high thermal stability for TiO_2, HfO_2, Ta_2O_5, MoO_3, Nb_2O_5 and B_2O_3 oxides. It formed a dense Ti-Hf-Ta-Nb-Mo-B-O oxide layer with MoO_3 and B_2O_3 in the coating. With the extension of oxidation time, O^{2-} ions will still spread through the dense oxide layer on the surface to the interior of the coating and form the inner oxide layer. However, the thermal expansion coefficient of different oxides is different from that of the unoxidized phase in the coating, resulting in local cracking. Once this happens, the external oxygen can come into contact with the internal unoxidized coating and the selective oxidation occurs again, repeating the process.

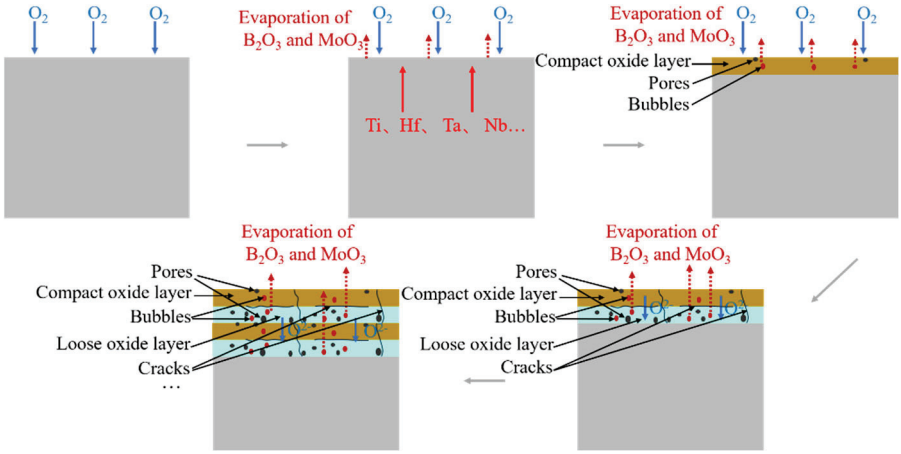


Figure 18. Schematic diagram of oxidation process of laser cladding coating.

In short, with the continuous increase in the thrust-to-weight ratio of aero engines, the temperature of the compressor outlet continues to rise, and the urgent need for new high-temperature titanium alloys with higher temperature resistance is put forward. For as long as the problem of low ductility and toughness of Ti_3Al, Ti_2AlNb and TiAl-based alloys resistant to more than 600 °C has not been completely solved, the use of coating technology to improve the service life of existing 600 °C high-temperature titanium alloys such as Ti60 alloy is a solution. In addition, high-entropy borides are a new class of high-temperature and high-entropy materials that can withstand 1500 °C, discovered since 2016 [14]. If this new high-temperature and high-entropy material can be applied to the surface of high-temperature titanium alloy, it will certainly improve its high-temperature oxidation resistance. Based on this idea, a composite coating containing $(Ti_{0.2}Hf_{0.2}Mo_{0.2}Ta_{0.2}Nb_{0.2})B_2$ high-entropy borides was prepared on the surface of Ti60 alloy by using advanced laser cladding technology. The experimental results also preliminarily confirmed the feasibility of this technical scheme, but the question of how to prepare high-entropy boride coating with a high content of $(Ti_{0.2}Hf_{0.2}Mo_{0.2}Ta_{0.2}Nb_{0.2})B_2$ needs further research in the future.

4. Conclusions

(1) With Ti, Hf, Mo, Ta and Nb metal powder and B powder as raw materials, a composite coating with 29.27% $(Ti_{0.2}Hf_{0.2}Mo_{0.2}\ Ta_{0.2}Nb_{0.2})B_2$ high-entropy boride was prepared on Ti60 alloys using laser cladding based on 2600 W laser power, 4.5 mm spot diameter, 8 mm/s laser scanning speed, 30% laser spot overlap rate, 99.99% argon purity and 15 L/min pressure gas flow rate. The coating was well combined with the substrate.

(2) The oxidation kinetics curves of both the laser cladding coating and the Ti60 matrix followed parabolic law, but the oxidation resistance of the laser cladding coating at 1100 °C was obviously better than that of the Ti60 matrix, and its oxidation rate was 1/4.8 of that of Ti60 matrix; specifically, the maximum oxidation gain rates of the laser cladding coating and the Ti60 matrix were 54.79 mg/cm^2 and 262.92 mg/cm^2, respectively.

(3) The surface products of the Ti60 matrix after oxidation at 1100 °C and 60 h were mainly TiO_2 and $ZrTiO_4$ phases, whose mass fractions were 91% and 9%, respectively, while the surface products of the laser cladding coating after oxidation at 1100 °C and 120 h were mainly TiO_2, HfO_2, Ta_2O_5 and Nb_2O_5 phases, whose mass fractions were 55.72%, 1.81%, 32.12% and 10.35%, respectively.

(4) The successful preparation of Ti-Hf-Mo-Ta-Nb-B composite coating resistant to 1100 °C will greatly improve the application ratio of Ti60 high-temperature titanium alloy in new advanced aero engines for the purpose of weight reduction and increase in thrust–weight ratio.

Author Contributions: Investigation—K.H. and X.H.; writing—original draft preparation, X.H.; writing—review and editing, K.H. All authors have read and agreed to the published version of the manuscript.

Funding: This work was supported by the Open Project Program of the Key Laboratory of Laser Technology and Optoelectronic Functional Materials of Hainan Province, Hainan Normal University.

Institutional Review Board Statement: Not applicable.

Informed Consent Statement: Not applicable.

Data Availability Statement: The data of this study are available from the corresponding author upon reasonable request.

Acknowledgments: The authors are also grateful to the Analytical and Testing Center of Huazhong University of Science and Technology.

Conflicts of Interest: The authors declare no conflict of interest.

References

1. Wei, S.Y.; Shi, W.M.; Wang, D.C.; Wang, Q.J.; Chen, Z.Y.; Liu, J.R. Microstructure and mechanical properties of high temperature titanium alloy Ti60 at 600 °C. *Chin. J. Nonferrous Met.* **2010**, *20*, 801–806.
2. Liu, H.P.; Wang, X.H.; Hao, S.S.; Feng, Z.X.; Hao, M.Y. Oxidation of Ti60 alloy and its protection by NiCrAlY coating. *J. Mater. Eng.* **1998**, *7*, 18–20.
3. Tang, Z.L.; Wang, F.H.; Wang, Q.J.; Wu, W.T.; Li, D. Effect of coatings on oxidation resistance and mechanical properties of Ti60 alloy. *Acta Metall. Sin.* **1998**, *34*, 325–331.
4. Xiong, Y.M.; Zhu, S.L.; Wang, F.H. Effect of ultrafine enamel coating on the oxidation and mechanical property of Ti60 alloy. *Acta Metall. Sin.* **2004**, *40*, 768–772.
5. Li, J.F.; Liao, Y.J.; Li, X.H.; Wang, Z.S.; Li, G.Q. Oxidation resistance enhancement of Ti60 alloy coated with Ni-Co-Cr-Al-Y-Si layer. *Chin. J. Vac. Sci. Technol.* **2010**, *30*, 520–523.
6. Yan, W.; Sun, F.J.; Liu, J.R.; Liu, J. Cycling thermal shock resistance of Ti-Al-Cr coating deposited on Ti60 alloy by arc ion plating. *J. Northeast. Univ.* **2010**, *31*, 411–414.
7. Chen, C. Study on Antioxidative Coating of Titanium Alloy. Master's Thesis, Dalian Maritime University, Dalian, China, September 2017.
8. Zhang, Z.; Li, J.N.; Sun, X.G.; Ma, F.K.; Zhang, Z.Z.; Shi, C.W.; Li, Y.J.; Li, C.J.; Zhao, B.; Liu, Z.Y.; et al. Microstructure performance enhancement of Si_3N_4 reinforced laser clad KF110 base composite coatings. *Int. J. Appl. Ceram. Tec.* **2022**, *19*, 409–414. [CrossRef]
9. Zhang, Z.; Li, J.N.; Ye, Z.Y.; Jing, C.N.; Wang, M.; Li, T.T.; Sun, X.G. Enhancing high-temperature oxidation resistance of titanium alloy with KF110-B_4C-Ag through laser technology. *Surf. Rev. Lett.* **2022**, *29*, 2250003. [CrossRef]
10. Hong, S.C.; Li, J.; Zhao, P.; Xu, Y.S.; Li, W.G. Evolution in wear and high-temperature oxidation resistance of laser-clad $Al_xMoNbTa$ refractory high-entropy alloys coatings with Al addition content. *Coatings* **2022**, *12*, 121. [CrossRef]
11. Zhang, S.; Qi, W.J.; Zhang, R. Effect of Ti content on wear and high-temperature oxidation resistances of laser-clad $CoCrMoNbTi_x$ high-entropy alloy coatings. *Mater. Lett.* **2023**, *345*, 134490. [CrossRef]
12. Zhao, H.; Zhao, C.C.; Xie, W.X.; Wu, D.; Du, B.N.; Zhang, X.R.; Wen, M.; Ma, R.; Li, R.; Jiao, J.K.; et al. Research progress of laser cladding on the surface of titanium and its alloys. *Materials* **2023**, *16*, 3250. [CrossRef] [PubMed]
13. Zhao, Y.Q. Study on high temperature titanium alloy. *Titan. Ind. Prog.* **2001**, *1*, 33–39.
14. Gild, J.; Zhang, Y.Y.; Harrington, T.; Jiang, S.C.; Hu, T.; Quinn, M.C.; Mellor, W.M.; Zhou, N.X.; Vecchio, K.; Luo, J. High-entropy metal diborides: A new class of high-entropy materials and a new type of ultrahigh temperature ceramics. *Sci. Rep.* **2016**, *6*, 37946. [CrossRef] [PubMed]
15. Mayrhofer, P.H.; Kirnbauer, A.; Ertelthaler, P.; Koller, C.M. High-entropy ceramic thin films; a case study on transition metal diborides. *Scr. Mater.* **2018**, *149*, 93–97. [CrossRef]
16. Kirnbauer, A.; Wagner, A.; Moraes, V.; Primetzhofer, D.; Hans, M.; Schneider, J.M.; Polcik, P.; Mayrhofer, P.H. Thermal stability and mechanical properties of sputtered (Hf, Ta, V, W, Zr)-diborides. *Acta Mater.* **2020**, *200*, 559–569. [CrossRef]
17. Zhang, P.; Cheng, C.Y.; Liu, B.; Xie, W.; Zhu, X.F.; Zhang, J.P.; Fu, Q.Q. Multicomponent $(Hf_{0.25}Zr_{0.25}Ti_{0.25}Cr_{0.25})B_2$ ceramic modified SiC-Si composite coatings: In-situ synthesis and high temperature oxidation behavior. *Ceram. Int.* **2022**, *48*, 12608–12624. [CrossRef]
18. Tallarita, G.; Licheri, R.; Garroni, S.; Orrù, R.; Cao, G. Novel processing route for the fabrication of bulk high-entropy metal diborides. *Scr. Mater.* **2019**, *158*, 100–104. [CrossRef]
19. Zheng, Q.; Wang, X.H.; Xing, J.J.; Gu, H.; Zhang, G.J. Quantitative analysis for phase compositions of ZrB_2-SiC-ZrC ultra-high temperature ceramic composites. *J. Inorg. Mater.* **2013**, *28*, 358–362. [CrossRef]
20. Li, J.; Yu, Z.S.; Wang, H.P.; Li, M.P. Microstructural evolution of titanium matrix composite coatings reinforced by in situ synthesized TiB and TiC by laser cladding. *Int. J. Min. Met. Mater.* **2010**, *17*, 481–488. [CrossRef]
21. He, B.; Lan, J.J.; Yang, G.; Wei, H. Microstructure and wear-resistant properties of in situ TiB-TiC reinforced titanium matrix composites by laser deposition manufacturing. *Rare Metal Mat. Eng.* **2017**, *46*, 3805–3810.

22. Lu, W.J.; Wu, R.J.; Zhang, D.; Zhang, X.N.; Sakata, T.; Mori, H. Interfacial microstructure of TiB/Ti in a Ti-TiB-TiC in situ composite. *Compos. Interface* **2002**, *9*, 41–50. [CrossRef]
23. Feng, H.B.; Zhou, Y.; Jia, D.C.; Meng, Q.C.; Rao, J.C. Growth mechanism of in situ TiB whiskers in spark plasma sintered TiB/Ti metal matrix composites. *Cryst. Growth Des.* **2006**, *6*, 1626–1630. [CrossRef]
24. Yang, S.; Huang, W.D.; Liu, W.J.; Su, Y.P.; Zhou, Y.H. Research on laser rapid directional solidification with ultra-high temperature gradient. *Chin. J. Lasers* **2002**, *29*, 475–479.
25. Tallarita, G.; Licheri, R.; Garroni, S.; Barbarossa, S.; Orru, R.; Cao, G. High-entropy transition metal diborides by reactive and non-reactive spark plasma sintering: A comparative investigation. *J. Eur. Ceram. Soc.* **2020**, *40*, 942–952. [CrossRef]
26. Jia, X.Y.; Liu, P.Y.; Tao, Y. Oxidation behavior of Ti60 alloy at 650~750 °C. *J. Mater. Eng.* **2003**, *6*, 18–22.
27. Zhang, H.Z.; Akhtar, F. Refractory multicomponent boron-carbide high entropy oxidation-protective coating for carbon-carbon composites. *Surf. Coat. Technol.* **2021**, *425*, 127697. [CrossRef]
28. Wang, Y.C.; Zhang, R.Z.; Zhang, B.H.; Skurikhina, O.; Balaz, P.; Araullo-Peters, V.; Reece, M.J. The role of multi-elements and interlayer on the oxidation behaviour of (Hf-Ta-Zr-Nb)C high entropy ceramics. *Corros. Sci.* **2020**, *176*, 109019. [CrossRef]
29. Ye, B.L. Study of High-Entropy Transition Metal Carbide Ceramics. Master's Thesis, South China University of Technology, Guangzhou, China, May 2020.
30. Backman, L.; Opila, E.J. Thermodynamic assessment of the group IV, V and VI oxides for the design of oxidation resistant multi-principal component materials. *J. Eur. Ceram. Soc.* **2019**, *39*, 1796–1802. [CrossRef]

Disclaimer/Publisher's Note: The statements, opinions and data contained in all publications are solely those of the individual author(s) and contributor(s) and not of MDPI and/or the editor(s). MDPI and/or the editor(s) disclaim responsibility for any injury to people or property resulting from any ideas, methods, instructions or products referred to in the content.

coatings

MDPI

Article

Flexible Finely and Directly Patternable Liquid Metal Electrodes via Selective Surface Wetting Technique

Seong Ju Park and Chanwoo Yang *

Advanced Nano-Surface & Wearable Electronics Research Laboratory, Heat and Surface Technology R&D Department, Korea Institute of Industrial Technology, Incheon 21999, Republic of Korea
* Correspondence: chanu@kitech.re.kr

Abstract: Eutectic gallium–indium (EGaIn) is an ideal material for preparing flexible electrodes, but its high surface tension poses a challenge during deposition and patterning. Herein, we propose a laser-induced selective surface wetting technique (SSWT) to enable the facile and straightforward fabrication of flexible finely and directly patternable EGaIn liquid metal electrodes. Our proposed technique selectively controls the wettability of EGaIn by establishing a perfluorinated self-assembled monolayer on a zinc oxide nanorod array to impart superhydrophobicity and then inducing specific sites on the hydrophilized surface by ultraviolet (UV) pulsed laser ablation, thereby enabling fine patterning (linewidth, ~50 μm). Surface analysis of the effect of laser ablation was also performed to elucidate the mechanism of SSWT. The patterned EGaIn liquid metal electrode fabricated by SSWT exhibited superior flexibility, with a resistance change ($\Delta R/R_0$) of only 18.6% compared with a Ag thin film electrode, which showed a dramatic increase in $\Delta R/R_0$ to nearly 500% after 50,000 folding cycles at a peak strain of 2.5%. The simple and easily implementable liquid metal patterning technique proposed in this study may potentially be applied in the field of wearable and stretchable electronics, which requires extreme flexibility.

Keywords: liquid metals; eutectic indium gallium; pulsed laser ablation; patterning; ZnO nanorods; self-assembled monolayer; flexible electrodes; cyclic bending fatigue

1. Introduction

Flexible electronics is an expanding research area that focuses on the creation of electronic devices capable of being bent, twisted, or stretched without impeding their functionality [1]. These unique capabilities enable new form factors, such as carrying in a folded or rolled state or attachment to the body. Recently, the field of flexible electronics has advanced to the point of mimicking human skin with bio-inspired robotic skin for sliding tactile perception [2]. Maintaining device performance under stress from deformation is a critical aspect of flexible device design. All device components must possess flexibility and the ability to distribute the stress caused by deformation to ensure device durability after mechanical deformation. The application of brittle materials to flexible device components can result in damage and breakdown owing to stress during deformation [3]. Liquid metals offer an attractive alternative to rigid materials for flexible electrodes. These metals can remain in a liquid state at room temperature because their melting points are below or near room temperature. This state provides liquid metals with unique advantages over other metals, such as the ability to flow, bend, and reform at room temperature [4]. However, their use is limited to specific applications owing to the inherent radioactivity of cesium, the high instability of francium and rubidium, and the toxicity of mercury [5].

Fortunately, unlike other liquid metals, eutectic gallium–indium (EGaIn) alloy does not have such limitations. The conductivity of EGaIn ($\sigma = 3.4 \times 10^6$ S m^{-1}) is comparable with that of other metals [6]. Thus, EGaIn not only exhibits high electrical conductivity but also withstands folding and stretching stress, rendering it ideal for use as a flexible electrode

material on account of its outstanding features. Chen et al. reported self-healing, robustly conductive, and stretchable conductors by embedding EGaIn liquid-metal patterns within an imprintable self-healing elastomer [7]. EGaIn is an ideal material for flexible electrodes, but its high surface tension poses a challenge during deposition and patterning. Several methods, such as direct inkjet printing, photolithography, injection molding, and stamp lithography, have been proposed to control the patterning of EGaIn liquid metals [8–13]. However, these methods have limitations when applied to actual production owing to factors such as time consumption, low resolution, and complexity. Jiang et al. reported the direct patterning of EGaIn liquid metal by inducing selective wettability differences via a laser ablation process; however, the authors did not perform a surface analysis of the effects of the laser ablation process and did not show the realization of fine linewidths below 50 μm [14].

Herein, we present a cost-effective, easily customizable, and direct patterning approach for liquid EGaIn via a selective surface wetting technique (SSWT). A superhydrophobic surface was created by establishing a fluorine-containing self-assembled monolayer (SAM) on a zinc oxide (ZnO) nanorod array using a straightforward hydrothermal synthesis method under atmospheric conditions. Because the ZnO nanorods react favorably to ultraviolet (UV) light, a UV pulsed laser can selectively hydrophilize the surface. Thereafter, EGaIn was brushed onto and effectively coated on the selectively hydrophilized surface. We demonstrate that EGaIn liquid metal can form micropatterns with fine linewidths of as low as 50 μm. Furthermore, the EGaIn liquid metal patterned electrode displayed superb flexibility after 50,000 cycles of folding fatigue.

2. Materials and Methods

2.1. Materials

A 1-mm-thick soda–lime glass slide (Paul Marienfeld, 1000412, Berlin, Germany) and a 50-μm-thick polyethersulfone film (PES, SU30-FM-000150, GoodFellow, Huntingdon, UK) were used as substrates. Zinc acetate dihydrate (99.999%, Sigma-Aldrich, St. Louis, MO, USA) and 1-propanol (99.5%, Sigma-Aldrich) were used as the solute and solvent, respectively, for the ZnO seed coating solution. Zinc nitrate hexahydrate (98%, Sigma-Aldrich) and hexamethylenetetramine (99.5%, Sigma-Aldrich) were used for ZnO growth. For superhydrophobic surface treatment, 1H,1H,2H,2H-perfluorooctyltriethoxysilane (PFOTES, 98%, Sigma-Aldrich), butylamine (99.5%, Sigma-Aldrich), and toluene were used as the self-assembling molecules, catalyst, and SAM solution solvent, respectively. Diiodomethane (DIM, 99%, Sigma-Aldrich) was used to calculate the surface energy (γ_s) from the droplet contact angles of the hydrophilized surfaces. EGaIn electrodes were purchased from MIDAS (Seoul, Korea) and used as conductive electrodes (Ga:In = 75.5:24.5 wt%).

2.2. Fabrication of Patterned EGaIn Electrodes

A schematic diagram of the fabrication process of the patterned EGaIn electrode is shown in Figure 1. The process for fabricating a selectively wettable substrate includes seed-layer coating (Figure 1b), ZnO-nanorod growth (Figure 1c), superhydrophobic treatment with the PFOTES SAM (Figure 1d), UV pulsed laser ablation (Figure 1e), and EGaIn brush deposition (Figure 1f). The substrates were cleaned by sonication with isopropyl alcohol, acetone, and deionized (DI) water and treated with UV ozone for 10 min. A 10 mM solution of zinc acetate dihydrate (99.999%, Sigma-Aldrich) in 1-propanol was spin-coated on the cleaned substrates at 2000 rpm for 30 s. The samples were then baked at 130 °C for 1 min. The above coating and baking process was repeated five times to ensure the uniform coverage of the zinc acetate crystallites on the substrate. All samples were pre-annealed in an air atmosphere at 200 °C for 1 h to obtain ZnO seeds. For ZnO nanorod growth, the samples were soaked in 25 mM zinc nitrate hexahydrate and 25 mM hexamethylenetetramine in DI water and heated in a microwave oven (2.45 GHz) at 1000 W for 3 min. The residual solvent in the samples was removed by rinsing with DI water [15]. Next, the samples were immersed in 1 mM PFOTES and a solution of 0.01 vol% butylamine

in toluene at 45 °C for 90 min to form a SAM composed of PFOTES molecules on the ZnO nanorods. The treated samples were rinsed with toluene to remove excess PFOTES molecules [16]. The superhydrophobic samples were selectively ablated by a nanosecond UV pulsed laser (LSU5DS 3D Laser Marking System, HGTECH, Wuhan, China), as shown in Figure 1e, to expose the hydrophilic surfaces of channels with different widths. The widths of the laser-ablated channels were 50, 100, 200, 500, and 1000 μm. The wavelength of the laser was 355 nm, the pulse frequency was 100,000 Hz, the off time was 6500 ns, and the scan rate was 1000 mm/s. Finally, EGaIn liquid metal patterns were formed on the selectively wettable substrate using a brush, as shown in Figure 1f.

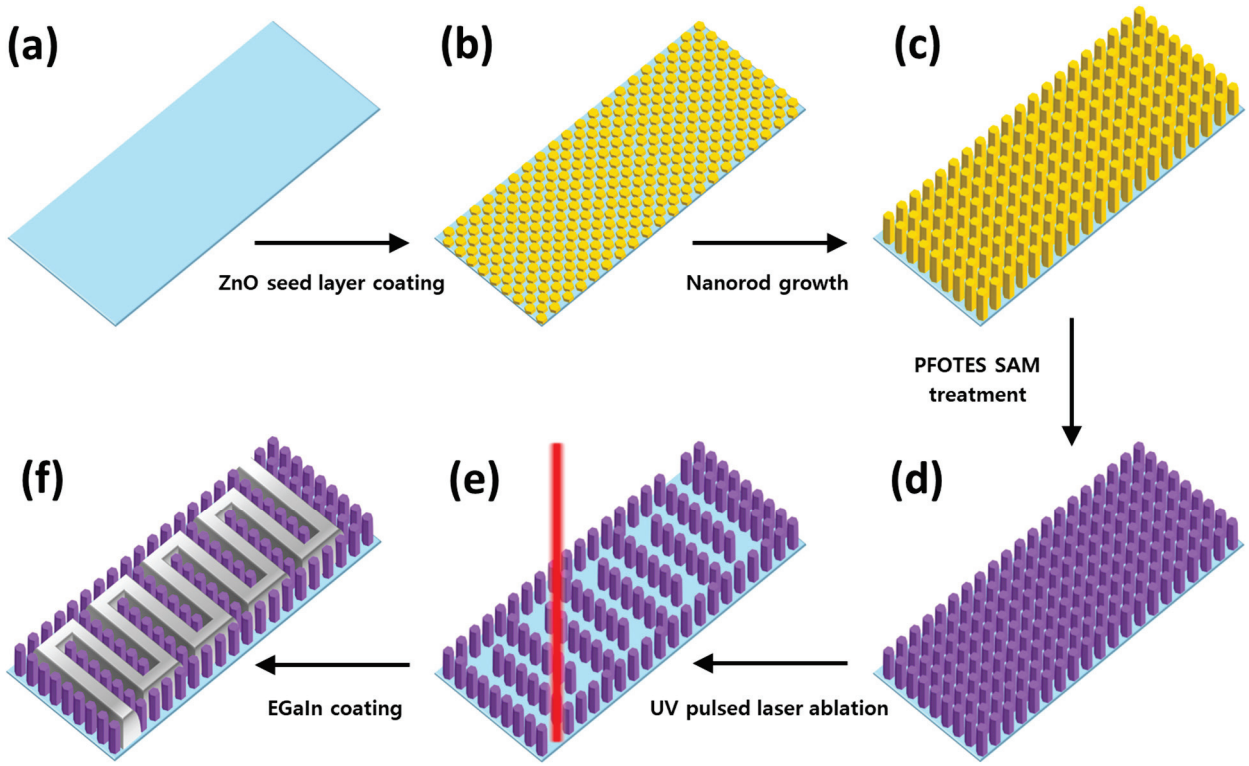


Figure 1. Schematic of the fabrication process of patterned EGaIn electrodes via SSWT: (**a**) substrate cleaning, (**b**) ZnO seed layer coating on the substrate and pre-annealing, (**c**) ZnO nanorod growth fabricated by microwave heating, (**d**) PFOTES SAM treatment on the ZnO nanorods, (**e**) UV pulsed laser ablation, (**f**) EGaIn patterns on the selectively wettable substrate using a brush.

2.3. Characterization

The surface top-view and cross-section of the samples were characterized using a field emission scanning electron microscope (FE-SEM, NOVA-600, FEI, Hillsboro, OR, USA) equipped with an energy-dispersive X-ray spectrometer (EDS). X-ray diffraction (XRD, X'Pert-Pro MPD, Malvern Panalytical, Malvern, UK) analysis was performed to investigate the crystal structure of the ZnO nanorods. The absorbance of the samples was analyzed using a UV-Vis spectrophotometer (UV-2550, Shimadzu, Kyoto, Japan) to characterize their optical absorption at 355 nm. A drop shape analyzer (DSA100, KRÜSS, Hamburg, Germany) was used to measure the contact angles of DI water and DIM droplets on the hydrophilized samples. Here, 3 μL of the liquids was applied to the surface of each sample. Images of the obtained EGaIn conductive patterns and the ablation linewidths were captured by optical microscopy (OM, BX51M, OLYMPUS, Tokyo, Japan). Folding tests were performed for 50,000 cycles using CFT-070i equipment (COVOTECH, Hwaseong-si, Korea) to demonstrate the flexibility of the EGaIn conductive layer, and electrical resistances were measured and averaged every 10,000 cycles using a two-point probe multimeter (Fluke 289, Fluke, Everett, WA, USA). The resistance change ($\Delta R/R_0$) was calculated as $\Delta R/R_0 = (R - R_0)/R_0$, where R is the resistance after folding and R_0 is the initial resistance.

3. Results and Discussion

Figure 2 shows top-view images of the laser-ablated interface region of the PFOTES SAM-processed ZnO nanorod array layer (hereafter referred to as ZnO-PFOTES) at different magnifications. The ZnO nanorods were grown on the substrate and then subjected to selective laser irradiation to enable the analysis of the laser-irradiated and pristine surfaces using FE-SEM and EDS. The ZnO nanorods grew uniformly and densely, as shown in Figure 2a. The surface images of the non-irradiated area on the left and the laser-irradiated area on the right were compared, as demonstrated in Figure 2b. The noticeable difference in morphology between these areas subjected to laser irradiation and those without it was apparent. Redeposited ZnO nanorod fragments from laser ablation were detected. One-dimensional EDS analysis (distance, ~2220 μm) was performed on the boundary region to investigate whether the ZnO nanorods were well-ablated by the UV pulsed laser, as shown in Figure 2c,d. The laser-ablated region exhibited a significantly lower Zn-Kα intensity than the non-ablated area, which was consistent with the results obtained from the FE-SEM top-view image shown in Figure 2b. Hence, based on the FE-SEM and EDS analysis, the use of the UV pulsed laser was confirmed to lead to the removal of the ZnO-PFOTES layer.

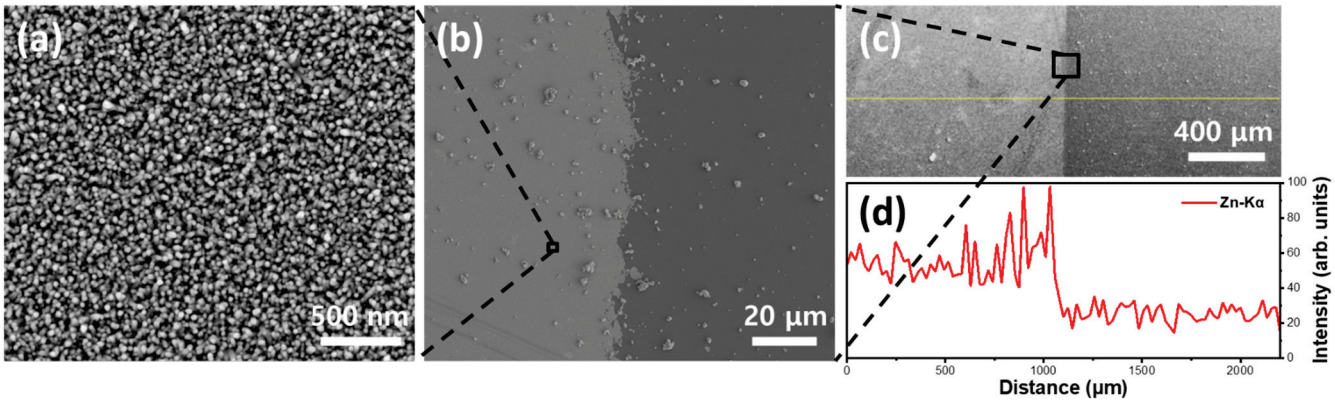


Figure 2. FE-SEM top-view images of (**a**) pristine ZnO-PFOTES and (**b**,**c**) laser-ablated interface area. (**d**) EDS line scan Zn-Kα spectrum of the laser-ablated interface area (yellow line in (**c**)).

The crystallinity and optical characteristics of the pristine and laser-ablated ZnO-PFOTES were investigated by XRD and UV-Vis, respectively, to further confirm successful ablation by the UV pulsed laser, as shown in Figure 3. In the case of the pristine ZnO-PFOTES, ZnO crystal growth was more dominant along the z-axis than along the x-axis, which was confirmed by the stronger intensity of the (002) plane at 34.4° than that of the (100) plane at 31.8°, as shown in Figure 3a. This result aligns well with the FE-SEM image in Figure 2c and previous studies on hydrothermally synthesized ZnO nanorods, which showed a dominant tendency for z-axis growth [17]. The presence of ZnO was also confirmed by the absorbance peak at 369 nm, which is an inherent absorption characteristic of ZnO, as shown in Figure 3b [18]. In contrast, the XRD peaks and absorption peak of ZnO at 369 nm were considerably diminished in the laser-ablated ZnO-PFOTES. ZnO-PFOTES exhibited a broad absorption peak at 355 nm and a central wavelength of 369 nm, as shown in Figure 3b. Thus, ZnO-PFOTES was effectively eliminated by the UV-pulsed laser with a central wavelength of 355 nm.

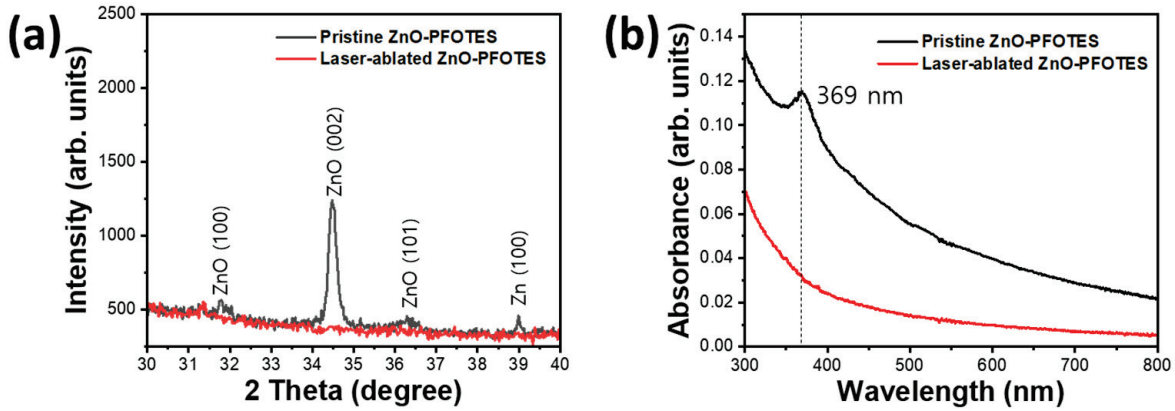


Figure 3. (**a**) Out-of-plane XRD patterns and (**b**) UV-Vis optical absorption spectra of the pristine (black line) and laser-ablated (red line) ZnO-PFOTES samples.

The general mechanism of laser ablation involves the absorption of light energy, where excited electrons transfer heat to the lattice due to photon absorption, causing the heating effect to melt or vaporize the material, resulting in macroscopic removal of material from the substrate [19]. This phenomenon occurs when the peak fluence (F_0) of the laser is above the ablation threshold fluence (F_{th}) and is calculated as follows [20]:

$$D^2 = 2w^2 \ln\left(\frac{F_0}{F_{th}}\right), \tag{1}$$

where D and w are the ablation linewidth and $1/e^2$ beam radius of the Gaussian beam profile, respectively. The peak fluence of the Gaussian laser beam is calculated from the pulse energy (E) of the UV pulsed laser with the following equation:

$$F_0 = \frac{2E}{\pi w^2} \tag{2}$$

Figure 4 shows the correlation of the ablation linewidth with the peak fluence of the UV pulse laser. Figure 4a shows the OM images of the laser scanning ablation trace lines of the ZnO-PFOTES layer at different laser pulse energies. The higher the pulse energy of the laser, the more the ablation linewidth of the ZnO-PFOTES layer tended to increase. This phenomenon is a natural consequence of the Gaussian profile of the laser beam, which increases the portion of the laser beam with higher fluence as the pulse energy increases [20]. In general, the higher the irradiation fluence, the higher the absorbed energy density, which induces higher temperatures. As a result, a larger portion of the irradiated area is ablated, and the ablation linewidth increases (Figure 4b). From these results, the calculated ablation threshold fluence for the ZnO-PFOTES was 5.01 J/cm^2 from the x-intercept obtained by extrapolation from Equation (1) and Figure 4c.

The Droplet contact angle analysis was adopted to quantitatively calculate the change in γ_s induced by laser ablation. Table 1 shows the γ_s characteristics and droplet shapes of liquids on the pristine and laser-ablated ZnO-PFOTES.

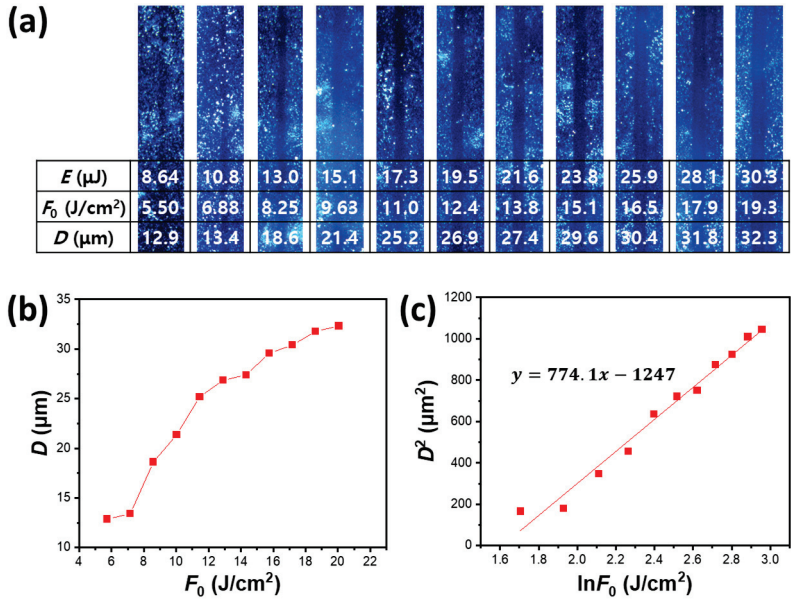
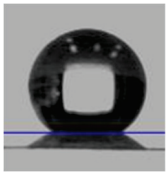
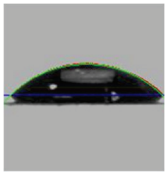
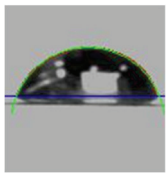
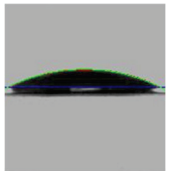


Figure 4. (**a**) OM images and ablation linewidths of laser scanning ablation trace lines of the ZnO-PFOTES layer as a function of peak fluence calculated with different laser pulse energies, (**b**) ablation linewidth as a function of laser peak fluence, and (**c**) plot of the square of the ablation linewidth versus the natural logarithm of peak fluence.

Table 1. Surface energy (γ_s) characteristics and droplet shapes of liquids on the pristine and laser-ablated ZnO-PFOTES samples.

Sample	Contact Angle (°)		γ_s^p (mJ m^{-2})	γ_s^d (mJ m^{-2})	γ_s (mJ m^{-2})	$X_p\left(=\gamma_s^p/\gamma_s\right)$
	DI Water	DIM				
Pristine ZnO-PFOTES	 141.0	 70.63	5.906	29.01	34.92	0.1691
Laser-ablated ZnO-PFOTES	 42.87	 26.50	24.71	33.97	58.68	0.4210

The contact angles of the DI water and DIM droplets on pristine ZnO-PFOTES were 141° and 70.63°, respectively, while those on the laser-ablated ZnO-PFOTES were 42.87° and 26.5°, respectively. The DI water contact angle of 141° on the pristine ZnO-PFOTES sample is much larger than 90°, which means the sample exhibits superhydrophobicity owing to the lotus effect induced by the nanostructure of ZnO-PFOTES [21]. Surface energy γ_s, which is an indicator of the strength of intermolecular forces in a sample and is related to its wettability, can be calculated using the following equations [22,23]:

$$1+\cos\theta = \frac{2\left(\gamma_s^d\right)^{1/2}\left(\gamma_{lv}^d\right)^{1/2}}{\gamma_{lv}} + \frac{2\left(\gamma_s^p\right)^{1/2}\left(\gamma_{lv}^p\right)^{1/2}}{\gamma_{lv}}, \quad (3)$$

$$\gamma_s = \gamma_s^p + \gamma_s^d, \tag{4}$$

$$X_p = \frac{\gamma_s^p}{\gamma_s}, \tag{5}$$

where γ_s^p and γ_s^d refer to the surface energies of the polar and dispersive components of the sample, respectively, and γ_{lv} is the surface tension of the test liquid. The quantitative γ_s values of the samples were obtained by inserting the known values of γ_{lv}, γ_{lv}^d, and γ_{lv}^p of the test liquids [22] and the measured contact angle θ into the above equation. The γ_s, γ_s^d, and γ_s^p calculated for the pristine ZnO-PFOTES were 34.92, 29.01, and 5.906 mJ/m^2, respectively, while those calculated for the laser-ablated ZnO-PFOTES were 58.68, 33.97, and 24.71 mJ/m^2, respectively. Because γ_s increased from 34.92 to 58.68 mJ/m^2 and the polar component ratio X_p increased from 0.1691 to 0.4210 following laser ablation, the selective wetting of EGaIn was clearly facilitated by this process.

Figure 5 displays the different EGaIn patterns created using SSWT. In Figure 5a, the line patterns of EGaIn formed on the PES substrate had varying linewidths of 50, 100, 200, 500, and 1000 μm. Electrical resistance was successfully measured in all patterned EGaIn lines. The resistance increased considerably as the linewidth decreased. However, even at the narrowest linewidth of 50 μm, an accurate measurement of resistance was still obtained, indicating a seamless patterning process. Magnified OM images of the 50, 100, and 200 μm fine-line patterns are shown in Figure 5b–d, respectively. The advantage of laser for designing patterns is demonstrated in Figure 5e, which shows the text pattern formed using SSWT as a digitalized process. Although some dewetting areas are evident in the enlarged OM images shown in Figure 5f,g, the overall patterns demonstrated good resolution with clear boundary definitions.

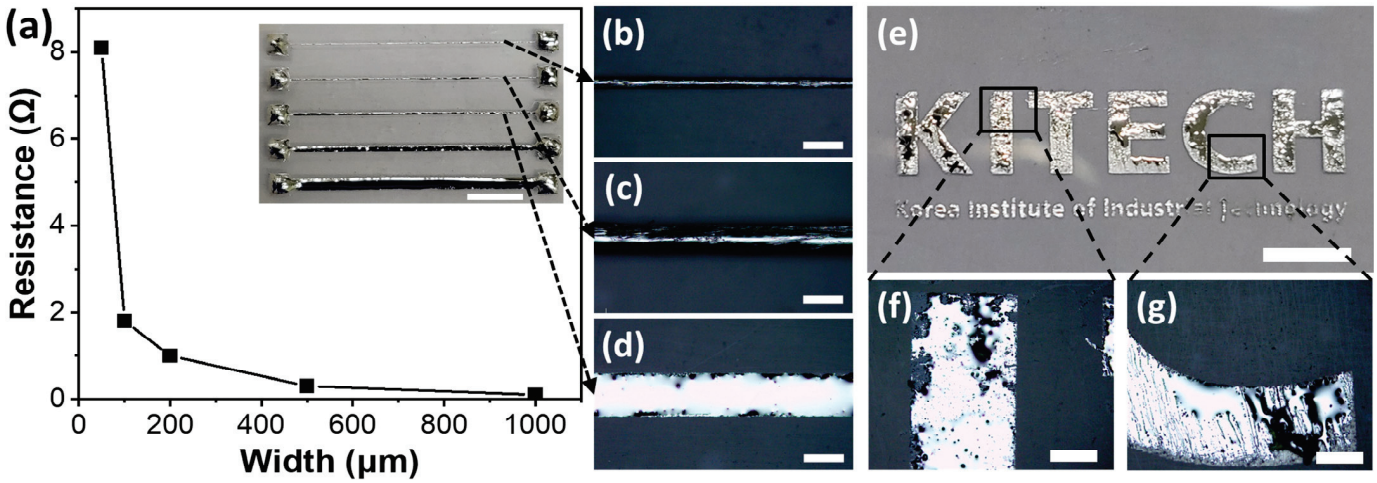


Figure 5. (**a**) Electrical resistance and OM image (inset) of flexible EGaIn electrodes with different patterned linewidths of 50, 100, 200, 500, and 1000 μm. Scale bar = 5 mm. (**b**–**d**) OM images of the fine-line patterns with linewidths of 50, 100, and 200 μm, respectively. Scale bar = 200 μm. (**e**) Text logo pattern and (**f**,**g**) enlarged OM images of the areas marked in (**e**). Scale bars = (**e**) 5 mm and (**f**,**g**) 500 μm.

Figure 6 shows the inward-folding cyclic fatigue-deformation characteristics of patterned EGaIn liquid metal and Ag thin film electrodes. The stability of the electrodes under cyclic folding was estimated by assessing $\Delta R/R_0$. The EGaIn and Ag electrodes on the flexible PES film substrate were fabricated by SSWT and sputtering, respectively. When electrodes on a film substrate are folded at 180°, the peak strain (ε) on the sample surface could be determined using the following equation:

$$\varepsilon = \frac{t}{2r}, \tag{6}$$

where t is the thickness of the substrate and r is the bending radius [24,25]. In the cyclic folding test, t and r were 50 μm and 1 mm, respectively, corresponding to a peak strain of 2.5%. The cyclic folding test was performed in five sets of 10,000 cycles to achieve a total of 50,000 cycles, and resistance measurements were taken every 10,000 cycles. The $\Delta R/R_0$ the Ag electrode increased dramatically to over 150% after 10,000 cycles and increased linearly to almost 500% after 50,000 cycles. Most electrodes composed of thin film metals, including those made of Ag, have been reported to fracture at strains below 2% when used on polymer substrates [24,25]. Therefore, in this study, the cyclic folding test was performed at a peak strain of 2.5%, which is greater than the fracture strain, resulting in a sharp change in resistance. In contrast, the $\Delta R/R_0$ of the EGaIn electrode increased moderately to ~15% and then remained stable over subsequent measurements, increasing to only 18.6% after 50,000 cycles. This result is attributed to EGaIn's higher flexibility resulting from its much lower Young's modulus (2.1×10^5 Pa) compared to Ag metal ($\sim 5 \times 10^9$ Pa) [26–28]. Thus, compared with the Ag thin film electrode, the EGaIn liquid metal electrode fabricated with SSWT was much more stable against cyclic folding fatigue owing to the flexibility of the intrinsic liquid state of EGaIn. To compare with previously reported findings on flexible electrodes, we defined an εN value (in this work, $\varepsilon N = 2.5\% \times 50{,}000 = 1250$) to represent the degree of cyclic folding fatigue, where N is the number of folding cycles, as shown in Figure 6b. Most previous studies on flexible electrodes have validated their flexibility under mild conditions with εN values below 1000. Our study showed that the patterned EGaIn electrode fabricated with SSWT under harsher conditions with an εN value of 1250 exhibited comparable or superior flexibility when compared to previously reported flexible electrodes made of materials such as metal nanowires, metal nanomeshes, graphene, carbon nanotube (CNT), indium tin oxide (ITO), ITO/Ag/ITO (IAI), and poly(3,4-ethylenedioxythiophene):poly(styrenesulfonate) (PEDOT:PSS) films [25,29–40].

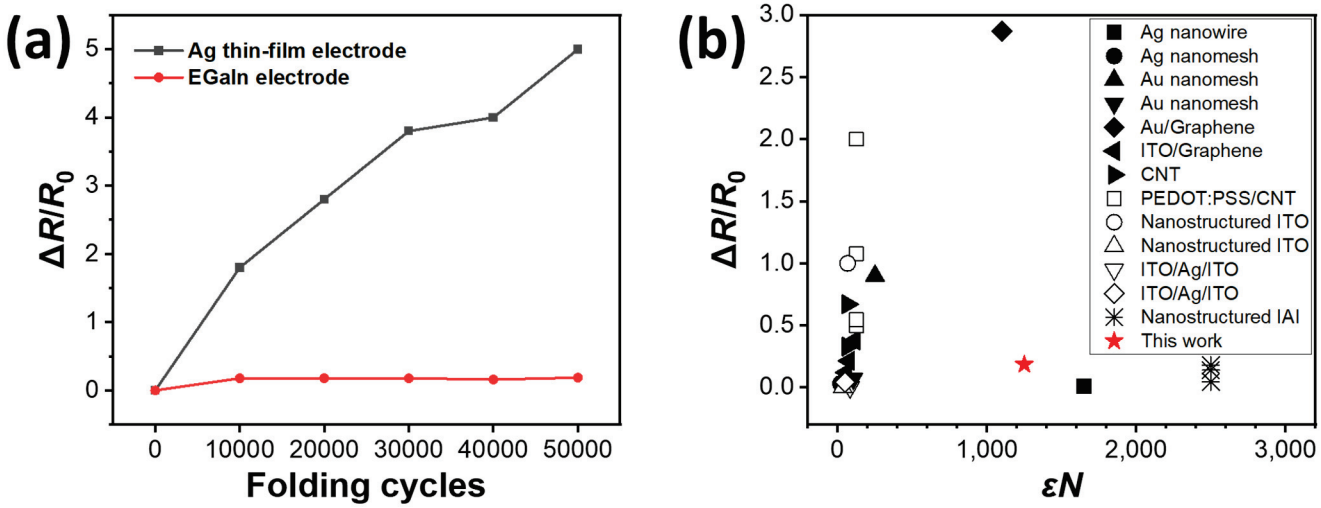


Figure 6. Inward-folding cyclic fatigue-deformation characteristics of electrodes: (**a**) change in resistance behaviors of patterned EGaIn liquid metal and Ag thin film electrodes under cyclic folding condition (ε = 2.5%, N = 50,000, εN = 1250) and (**b**) change in resistance with respect to degree of cyclic folding fatigue of patterned EGaIn electrode fabricated with SSWT compared to those of previously reported flexible electrodes: Ag nanowire [29], Ag nanomesh [30], Au nanomesh [31,32], Au/Graphene [33], ITO/Graphene [34], CNT [35], PEDOT:PSS/CNT [36], Nanostructured ITO [37,38], ITO/Ag/ITO [39,40], Nanostructured IAI [25].

4. Conclusions

In this work, we presented a simple method to easily fabricate flexible finely and directly patterned EGaIn electrodes using SSWT based on γ_s differences. All fabrication steps utilized a solution process that can be carried out under atmospheric conditions, and direct patterning was made possible by UV pulsed laser ablation, which is inexpensive

and applicable to large areas. We also investigated the mechanism by which UV-pulsed laser ablation effectively removed the SAM-treated ZnO nanorod array, rendering the liquid metal superhydrophobic, and induced an increase in γ_s, resulting in improved liquid metal wettability and patterning, using surface analysis. The linewidths of the EGaIn liquid metal patterns fabricated with SSWT could be freely adjusted to realize linewidths as fine as 50 μm. The EGaIn liquid metal patterned electrode fabricated on a flexible substrate exhibited significantly better flexibility than the Ag thin film electrode under severe conditions with an εN value of 1250, corresponding to 50,000 cycles of folding fatigue at a peak strain of 2.5%. The simple and easily implementable liquid metal patterning technique proposed in this study, when combined with a passivation layer to protect the liquid metal electrodes, may potentially be applied in the promising field of wearable and stretchable electronics, which requires extreme flexibility.

Author Contributions: Conceptualization, C.Y.; data curation, S.J.P.; formal analysis, S.J.P.; funding acquisition, C.Y.; methodology, C.Y.; investigation, C.Y.; project administration, C.Y.; resources, C.Y.; supervision, C.Y.; validation, S.J.P. and C.Y.; visualization, S.J.P. and C.Y.; writing—original draft preparation, S.J.P. and C.Y.; writing—review and editing, C.Y. All authors have read and agreed to the published version of the manuscript.

Funding: This work was supported by Enterprise Demand-based Production Technology Commercialization Project of the Korea Institute of Industrial Technology (KITECH), and granted financial resources from the Ministry of Economy and Finance, Republic of Korea (No. JD230008).

Institutional Review Board Statement: Not applicable.

Informed Consent Statement: Not applicable.

Data Availability Statement: Data are contained within the article.

Conflicts of Interest: The authors declare no conflict of interest.

References

1. Chen, G.; Wang, H.; Guo, R.; Duan, M.; Zhang, Y.; Liu, J. Superelastic EGaIn composite fibers sustaining 500% tensile strain with superior electrical conductivity for wearable electronics. *ACS Appl. Mater. Interfaces* **2020**, *12*, 6112–6118. [CrossRef] [PubMed]
2. Li, S.; Chen, X.; Li, X.; Tian, H.; Wang, C.; Nie, B.; He, J.; Shao, J. Bioinspired robot skin with mechanically gated electron channels for sliding tactile perception. *Sci. Adv.* **2022**, *8*, eade0720. [CrossRef] [PubMed]
3. Kim, B.-J.; Shin, H.-A.S.; Jung, S.-Y.; Cho, Y.; Kraft, O.; Choi, I.-S.; Joo, Y.-C. Crack nucleation during mechanical fatigue in thin metal films on flexible substrates. *Acta Mater.* **2013**, *61*, 3473–3481. [CrossRef]
4. Bo, G.; Ren, L.; Xu, X.; Du, Y.; Dou, S. Recent progress on liquid metals and their applications. *Adv. Phys. X* **2018**, *3*, 1446359. [CrossRef]
5. Clarkson, T.W.; Magos, L. The toxicology of mercury and its chemical compounds. *Crit. Rev. Toxicol.* **2006**, *36*, 609–662. [CrossRef] [PubMed]
6. French, S.J.; Saunders, D.J.; Ingle, G.W. The system gallium-indium. *J. Phys. Chem.* **2002**, *42*, 265–274. [CrossRef]
7. Chen, X.; Sun, P.; Tian, H.; Li, X.; Wang, C.; Duan, J.; Luo, Y.; Li, S.; Chen, X.; Shao, J. Self-healing and stretchable conductor based on embedded liquid metal patterns within imprintable dynamic covalent elastomer. *J. Mater. Chem. C* **2022**, *10*, 1039–1047. [CrossRef]
8. Hao, X.P.; Li, C.Y.; Zhang, C.W.; Du, M.; Ying, Z.; Zheng, Q.; Wu, Z.L. Self-shaping soft electronics based on patterned hydrogel with stencil-printed liquid metal. *Adv. Funct. Mater.* **2021**, *31*, 2105481. [CrossRef]
9. Yan, J.; Lu, Y.; Chen, G.; Yang, M.; Gu, Z. Advances in liquid metals for biomedical applications. *Chem. Soc. Rev.* **2018**, *47*, 2518–2533. [CrossRef]
10. Boley, J.W.; White, E.L.; Chiu, G.T.C.; Kramer, R.K. Direct writing of gallium-indium alloy for stretchable electronics. *Adv. Funct. Mater.* **2014**, *24*, 3501–3507. [CrossRef]
11. Park, C.W.; Moon, Y.G.; Seong, H.; Jung, S.W.; Oh, J.-Y.; Na, B.S.; Park, N.-M.; Lee, S.S.; Im, S.G.; Koo, J.B. Photolithography-based patterning of liquid metal interconnects for monolithically integrated stretchable circuits. *ACS Appl. Mater. Interfaces* **2016**, *8*, 15459–15465. [CrossRef] [PubMed]
12. Yang, J.; Zhou, T.; Zhang, L.; Zhu, D.; Handschuh-Wang, S.; Liu, Z.; Kong, T.; Liu, Y.; Zhang, J.; Zhou, X. Defect-free, high resolution patterning of liquid metals using reversibly sealed, reusable polydimethylsiloxane microchannels for flexible electronic applications. *J. Mater. Chem. C* **2017**, *5*, 6790–6797. [CrossRef]
13. Zhang, S.; Wang, B.; Jiang, J.; Wu, K.; Guo, C.F.; Wu, Z. High-fidelity conformal printing of 3D liquid alloy circuits for soft electronics. *ACS Appl. Mater. Interfaces* **2019**, *11*, 7148–7156. [CrossRef] [PubMed]

14. Jiang, Y.; Su, S.; Peng, H.; Kwok, H.S.; Zhou, X.; Chen, S. Selective wetting/dewetting for controllable patterning of liquid metal electrodes for all-printed device application. *J. Mater. Chem. C* **2017**, *5*, 12378–12383. [CrossRef]
15. Yang, C.; Hong, K.; Jang, J.; Chung, D.S.; An, T.K.; Choi, W.S.; Park, C.E. Solution-processed flexible ZnO transparent thin-film transistors with a polymer gate dielectric fabricated by microwave heating. *Nanotechnology* **2009**, *20*, 465201. [CrossRef] [PubMed]
16. Yang, C.; Kwack, Y.; Kim, S.H.; An, T.K.; Hong, K.; Nam, S.; Park, M.; Choi, W.-S.; Park, C.E. Ambipolar thin-film transistors and an inverter based on pentacene/self-assembled monolayer modified ZnO hybrid structures for balanced hole and electron mobilities. *Org. Electron.* **2011**, *12*, 411–418. [CrossRef]
17. Çolak, H.; Karaköse, E.; Kartopu, G. Effect of consumption of the sol–gel deposited ZnO seed layer on the growth and properties of high quality ZnO nanorods. *J. Mater. Sci. Mater. Electron.* **2018**, *29*, 11964–11971. [CrossRef]
18. Usha, A.; Christy, J. Characterization, thermal effect on optical band gap energy and photoluminescence in wurtzite ZnO: Er nanocrystallites. *Mater. Today Proc.* **2016**, *3*, 145–151. [CrossRef]
19. Ravi-Kumar, S.; Lies, B.; Zhang, X.; Lyu, H.; Qin, H. Laser ablation of polymers: A review. *Polym. Int.* **2019**, *68*, 1391–1401. [CrossRef]
20. Lee, H.-L.; Hussain, A.; Moon, Y.-J.; Hwang, J.Y.; Moon, S.J. Influence of pre-sintering on the nanosecond pulsed laser ablation patterns of spin-coated silver nanoparticles. *Appl. Phys. A* **2023**, *129*, 705. [CrossRef]
21. Lee, J.; Yong, K. Combining the lotus leaf effect with artificial photosynthesis: Regeneration of underwater superhydrophobicity of hierarchical ZnO/Si surfaces by solar water splitting. *NPG Asia Mater.* **2015**, *7*, e201. [CrossRef]
22. Kinloch, A.J. *Adhesion and Adhesives: Science and Technology*; Springer: Berlin, Germany, 1987; ISBN 978-0-412-27440-4.
23. Sim, I.; Park, S.; Shin, K.Y.; Yang, C.; Kang, H.; Hwang, J.Y.; Moon, S.J. Inkjet printing of high aspect ratio silver lines via laser-induced selective surface wetting technique. *Coatings* **2023**, *13*, 683. [CrossRef]
24. Mao, L.; Meng, Q.; Ahmad, A.; Wei, Z. Mechanical analyses and structural design requirements for flexible energy storage devices. *Adv. Energy Mater.* **2017**, *7*, 1700535. [CrossRef]
25. Han, S.; Ju, B.K.; Yang, C. Ultra-flexible and transparent electrodes with controllable crack length via metal–polymer hybrid nanostructure. *Thin Solid Film.* **2022**, *757*, 139388. [CrossRef]
26. Zhao, Z.; Soni, S.; Lee, T.; Nijhuis, C.A.; Xiang, D. Smart eutectic gallium–indium: From properties to applications. *Adv. Mater.* **2023**, *35*, 2203391. [CrossRef] [PubMed]
27. Park, Y.-G.; Lee, G.-Y.; Jang, J.; Yun, S.M.; Kim, E.; Park, J.-U. Liquid metal-based soft electronics for wearable healthcare. *Adv. Healthc. Mater.* **2021**, *10*, 2002280. [CrossRef] [PubMed]
28. Chen, S.; Wang, H.-Z.; Zhao, R.-Q.; Rao, W.; Liu, J. Liquid metal composites. *Matter* **2020**, *2*, 1446. [CrossRef]
29. Kim, S.; Lee, H.; Kim, D.; Ha, H.; Qaiser, N.; Yi, H.; Hwang, B. Ethylcellulose/Ag nanowire composites as multifunctional patchable transparent electrodes. *Surf. Coat. Technol.* **2020**, *394*, 125898. [CrossRef]
30. Song, M.; Kim, H.-J.; Kim, C.S.; Jeong, J.-H.; Cho, C.; Lee, J.-Y.; Jin, S.-H.; Choi, D.-G.; Kim, D.-H. ITO-free highly bendable and efficient organic solar cells with Ag nanomesh/ZnO hybrid electrodes. *J. Mater. Chem. A* **2015**, *3*, 65–70. [CrossRef]
31. Guo, C.F.; Sun, T.; Liu, Q.; Suo, Z.; Ren, Z. Highly stretchable and transparent nanomesh electrodes made by grain boundary lithography. *Nat. Commun.* **2014**, *5*, 3121. [CrossRef]
32. Chauvin, A.; Txia Cha Heu, W.; Buh, J.; Tessier, P.-Y.; El Mel, A.-A. Vapor dealloying of ultra-thin films: A promising concept for the fabrication of highly flexible transparent conductive metal nanomesh electrodes. *NPJ Flex. Electron.* **2019**, *3*, 5. [CrossRef]
33. Cho, C.; Kang, P.; Taqieddin, A.; Jing, Y.; Yong, K.; Kim, J.M.; Haque, M.F.; Aluru, N.R.; Nam, S.W. Strain-resilient electrical functionality in thin-film metal electrodes using two-dimensional interlayers. *Nat. Electron.* **2021**, *4*, 126–133. [CrossRef]
34. Lee, S.J.; Kim, Y.; Hwang, J.-Y.; Lee, J.-H.; Jung, S.; Park, H.; Cho, S.; Nahm, S.; Yang, W.S.; Kim, H.; et al. Flexible indium-tin oxide crystal on plastic substrates supported by graphene monolayer. *Sci. Rep.* **2017**, *7*, 3131. [CrossRef] [PubMed]
35. Han, S.-H.; Kim, B.-J.; Park, J.-S. Surface modification of plastic substrates via corona-pretreatment and its effects on the properties of carbon nanotubes for use of flexible transparent electrodes. *Surf. Coat. Technol.* **2015**, *271*, 100–105. [CrossRef]
36. Kim, B.-J.; Han, S.-H.; Park, J.-S. Properties of CNTs coated by PEDOT:PSS films via spin-coating and electrophoretic deposition methods for flexible transparent electrodes. *Surf. Coat. Technol.* **2015**, *271*, 22–26. [CrossRef]
37. Königer, T.; Münstedt, H. Coatings of indium tin oxide nanoparticles on various flexible polymer substrates: Influence of surface topography and oscillatory bending on electrical properties. *J. Soc. Inf. Disp.* **2008**, *16*, 559–568. [CrossRef]
38. Yun, J.; Park, Y.H.; Bae, T.-S.; Lee, S.; Lee, G.-H. Fabrication of a completely transparent and highly flexible ITO nanoparticle electrode at room temperature. *ACS Appl. Mater. Interfaces* **2013**, *5*, 164–172. [CrossRef] [PubMed]

39. Kim, T.-H.; Park, S.-H.; Kim, D.-H.; Nah, Y.-C.; Kim, H.-K. Roll-to-roll sputtered ITO/Ag/ITO multilayers for highly transparent and flexible electrochromic applications. *Sol. Energy Mater. Sol. Cells* **2017**, *160*, 203–210. [CrossRef]
40. Wu, C.-C. Highly flexible touch screen panel fabricated with silver-inserted transparent ITO triple-layer structures. *RSC Adv.* **2018**, *8*, 11862–11870. [CrossRef]

Disclaimer/Publisher's Note: The statements, opinions and data contained in all publications are solely those of the individual author(s) and contributor(s) and not of MDPI and/or the editor(s). MDPI and/or the editor(s) disclaim responsibility for any injury to people or property resulting from any ideas, methods, instructions or products referred to in the content.

coatings

MDPI

Article

Effect of Spherical WC Content on the Microstructure and Properties of SiCp Aluminium Composite Material

Xinyi Feng, Xiao Li *, Fei Wang, Zengzhi Liu and Wenping Wang

School of Mechanical Engineering, Xinjiang University, Urumqi 830047, China; 107552101393@stu.xju.edu.cn (X.F.); 107552001095@stu.xju.edu.cn (F.W.); 107552101392@stu.xju.edu.cn (Z.L.); 107552204287@stu.xju.edu.cn (W.W.)
* Correspondence: likebaijia@126.com

Abstract: In this paper, SiCp aluminium matrix composites were used as the matrix, and AlSi10Mg powder, which has a relatively similar coefficient of thermal expansion to that of the matrix, was used to prepare laser cladding Al-based coatings. The results show that the optimal process parameters are P = 4400 W, V_f = 11.3 g·min^{-1}, and V_S = 1800 mm·min^{-1}, and, although the hardness of the coatings is lower than the hardness of the substrate, it reduces the generation of defects such as cracks and porosity. With the increase in WC reinforced phase and the hardness of the coatings, wear resistance increases, the granular cytocrysts are transformed into rod-like cytocrysts, and at the same time generate the dendritic crystals, and the undergo grain refining and generate the new phases such as Al_4C_3, Al_4SiC_4. There is no obvious defect in AlSi10Mg + 40%WC coatings, the macro morphology of the coatings is good, there is no spalling in the friction wear morphology, and the wear resistance is excellent, but there are obvious cracks and obvious spalling in the coatings of AlSi10Mg + 60%WC. Compared to the matrix hardness of 171.61 HV, the hardness of the 20%WC cladding layer increased by a factor of 1.06, while the hardness of the 40%WC cladding layer increased by a factor of 1.65 and that of the 60%WC cladding layer increased by a factor of 1.8. In terms of wear, compared to a substrate wear amount of 9.36 mg, the wear for the 20%WC cladding layer was reduced to 6.13 mg (34.5% less than the substrate), for the 40%WC cladding layer it was reduced to 4.58 mg (51.06% less than the substrate), and for the 60%WC cladding layer it was reduced to 7.35 mg (21.47% less than the substrate). The quality of the coatings decreases although the hardness is higher than that of AlSi10Mg + 40%WC. The comprehensive performance of AlSi10Mg + 40%WC coatings is optimal.

Keywords: laser cladding; pulsed electric field; preheating; wear performance

1. Introduction

Aluminium content is the most abundant metallic substance in the world, and aluminium alloys have become the most widely used metallic materials worldwide, with their excellent fracture toughness, high specific strength, and good forming and metallurgical properties attracting the attention of industries in various countries. However, its inherent drawbacks, such as low hardness, low wear resistance, and low modulus of elasticity, make aluminium alloys increasingly unable to meet the needs of emerging fields of industry [1,2]. For this reason, researchers and scholars have thought of adding certain substances that can enhance the properties of traditional aluminium alloys to prepare composites with excellent properties, in which various reinforcing particles, including SiC particles, have the advantages of low density (3.21 g/cm^3), high modulus of elasticity and hardness, good chemical stability, wear resistance, and low cost of preparation, and at the same time, have good chemical compatibility with aluminium alloys. The comprehensive performance of SiC particles makes them the most commonly used in aluminium matrix composites [3,4]. SiC particles reinforced aluminium matrix composites have stronger properties of elastic modulus, wear resistance, specific strength, and dimensional stability compared to traditional aluminium alloys, and the addition of different volume fractions of SiC particles

has different effects on their properties, which are widely used in the fields of electronic packaging and aerospace and automotive manufacturing.

AlSi10Mg [5–8] as an aluminium–silicon alloy is used in the field of material forming because of its good castability and corrosion resistance. In recent years, researchers in the field of civil aviation widely used SLM technology [9–11] for its complex shape, and relevant research shows that the mechanical properties of SLM-forming alloys [12–15] are better than those of the traditional casting products [16]. At the same time, in terms of wear resistance, the most commonly used surface texture technology is laser surface texture, which can greatly improve friction performance [17,18]. However, many factors limit the development of laser additive manufacturing; AlSi10Mg alloys, such as aluminium alloys are prone to oxidation at high temperatures [19], high thermal conductivity, and laser reflectivity [20], and defects are prone to porosity, cracks, and other defects. How to effectively reduce coating cracks is a hot topic in the field of laser cladding, Li [21] In the laser cladding process, pulse current is applied to effectively mitigate coating cracks and enhance coating hardness and wear resistance. At the same time, because of the low heat input of laser cladding and a high degree of automation, it is suitable for metal repair technology. Al-based alloy cladding materials are mainly used in the laser cladding repair of aluminium alloy products, in order to adapt to the economy of saving, research on the laser cladding repair technology of aluminium alloy is particularly necessary. Scholars have studied the laser repair technology; Meinert and Bergan [22] first reported on the laser cladding repair of aluminium alloys, in 6061 and 7075 aluminium alloy surface cladding 4000 series aluminium alloys, the tensile strength of the repaired specimens for the original 6061-T6 and 7075-T651 specimens were 61% and 64%, respectively. Corbin et al. [23] carried out laser cladding of 6061-T6-aluminium alloy powder on the surface of 6061 aluminium alloy powder laser cladding on the surface of 6061T6-aluminium alloy; they found that the hardness of the coating is lower than the substrate, and there are defects such as porosity, but the substrate and the coating powder properties are similar to reduce the generation of cracks, but did not continue to carry out the coating performance enhancement of the relevant research.

Wear calculations are very important in order to predict the life cycle of a certain component, and thus schedule the forehand replacement or prevent the failure [24]. WC [25–27] is a kind of ceramic particle, with high hardness and wear resistance, and has good electrical and thermal conductivity, WC has good chemical properties [28,29], and its powder is often used for cemented carbide reinforcing materials. With the development of laser additive manufacturing, more and more scholars will also be WC ceramic particles added to its coating powder as a reinforcing phase, C element, and W element in the laser high temperature will occur with other elements [30,31]. C and W elements will react with other elements under the high temperature of the laser to strengthen the coating with a solid solution, and then improve the hardness, wear resistance, and corrosion performance of the coating surface [32–34]. In Yu [35], AlSi5Cu1Mg aluminium alloy surface laser cladding Ni60 + WC powder, the cladding layer microhardness of the substrate is about 9~11 times. Qing et al. [36] studied the microstructure, microhardness, and wear resistance of 60% WC-reinforced FeCoNiCr composite coatings prepared by laser cladding. The study showed that the composite coatings have good forming quality, better microhardness, and wear resistance.

Although the desired properties can be achieved through laser cladding of metal powders with varying characteristics on the substrate, the coating may develop cracks due to its high coefficient of thermal expansion. This issue significantly impacts the binding properties of the coating itself. In this study, we aim to address these concerns by following previous scholars' theories on repairing cracks and defects in original aluminum alloy substrates through laser cladding different types of Al-based powders onto an Al substrate. By selecting AlSi10Mg powder with a similar thermal expansion coefficient as the substrate and incorporating the WC reinforcing phase to enhance surface wear resistance and hardness properties, we can effectively minimise crack formation.

This approach has potential cost-saving implications for commercial applications while expanding the utilisation of aluminum alloys. The key distinction between our research and others lies in our focus on improving aluminum alloy laser cladding properties to reduce crack occurrence, thereby providing a valuable reference for preparation processes and theoretical foundations.

2. Experimental

2.1. Experimental Materials

Experiments selected by the AVIC Xi'an Aircraft Manufacturing Company Limited Materials Research Institute, Xi'an, China provided by the 15% SiCp/2009Al composition (see Table 1) and size 150 mm × 60 mm× 10 mm, before using, 400 #, 800 #, and 1000 # of sandpaper will be used to sand the surface to a bright, remove the surface of the oil and oxidation, and then put into the ultrasonic vibration instrument filled with anhydrous ethanol. Cleaned 30 min, and then placed in a drying box for 120 min standby, the powder material selection of 100–250 mesh AlSi10Mg; for powder composition see Table 2. Then, mix 20%, 40%, and 60% WC spherical ceramic powder; powder composition is shown in Table 3. The mixing process is conducted using a KQM-Z/B-type planetary ball mill for a duration of 2 h to ensure thorough and uniform blending. The ratio of balls to material is maintained at 3:1, while the milling speed is set at 500 r/min. Subsequently, the mixed powder is transferred into a drying oven for a period of 60 min in order to eliminate any moisture content present. Once dried, it is then placed onto a tray and allowed to cool down naturally until reaching room temperature before being carefully stored in an air-tight bag.The SEM images of AlSi10Mg powder and WC powder are depicted in Figure 1.

Table 1. Chemical composition of 15% SiCp/2009Al substrate (wt.%).

Cu	Mg	Fe	Si	Al
4.2	1.6	0.05	0.25	Bal.

Table 2. Chemical composition of AlSi10Mg coated powder (wt.%).

Si	Fe	Cu	Mg	Mn	Ni	Al
9.880	0.051	0.005	0.400	0.009	0.180	Bal.

Table 3. Chemical composition of WC ceramic reinforced phase powders (wt.%).

Fe	Si	Mg	Al	k	Na	Ca	S	Mo	W	C
0.02	0.003	0.002	0.002	0.0015	0.0015	0.002	0.002	0.01	Bal.	Bal.

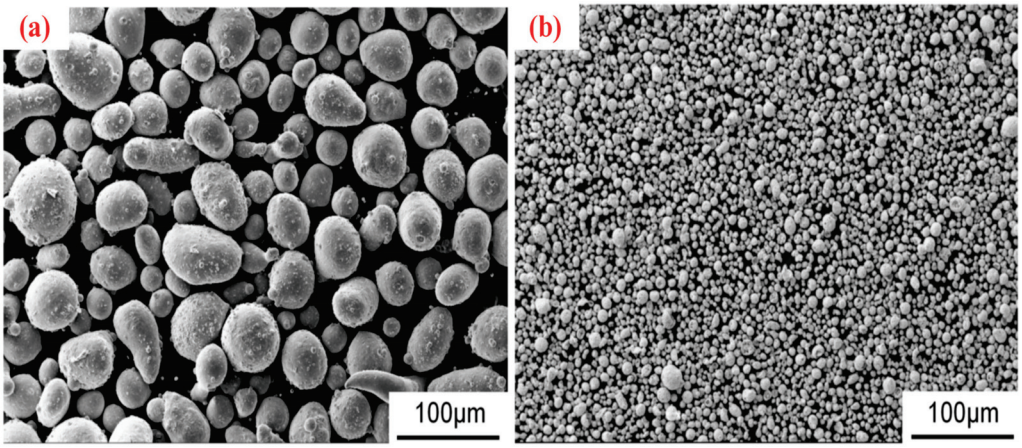


Figure 1. (**a**) SEM (Scanning Electron Microscope) morphology of spherical AlSi10Mg. (**b**) SEM (Scanning Electron Microscope) morphology of spherical WC.

2.2. Experimental Methods

The cladding layer was prepared by an 8 kW JPT-6000 IPG continuous wave fiber laser from Shaanxi Yunding Optoelectronic Technology Co, Ltd., Xi'an, China with a 1080 nm wavelength. The spot diameter is 2 mm and was used to process the AlSi10Mg coated single-pass specimen; with coaxial powder feeding processing, the protective gas was argon, and the gas flow rate was set at 13 L/min. The laser schematic is shown in Figure 2.

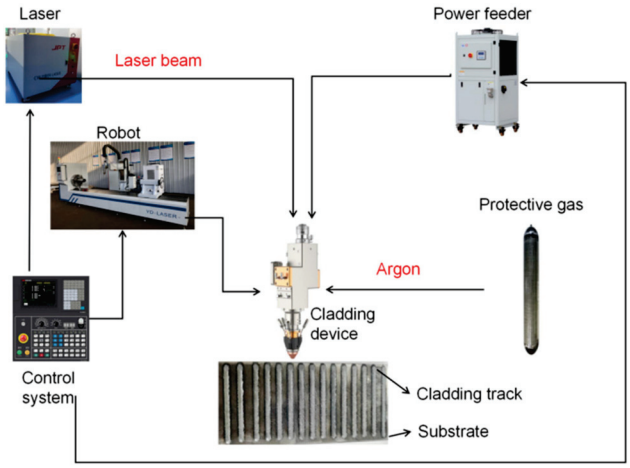


Figure 2. Component modules of the fusion cladding system.

Firstly, a one-factor orthogonal test of AlSi10Mg coating was carried out, and the effects of different laser power, powder feeding rate, and scanning rate on the coating quality could be analysed through the one-factor experiment, and the orthogonal test method is an experimental method to study the combination of multi-factors and multi-levels, whose main function is that it can be substituted for the full-scale test by a small number of tests, which saves time and cost. We selected the better process parameters as the intermediate level value and establish three factors and three levels of orthogonal test; the value of each factor is shown in Table 4.

Table 4. Orthogonal test factor level table.

Factors	(A) Laser Power/(w)	(B) Powder Feeding Rate/(g·min^{-1})	(C) Scanning Speed/(mm·min^{-1})
Level 1	4200	6.78	1800
Level 2	4400	9.04	2000
Level 3	4600	11.3	2200

According to the number of levels of each factor to choose a single level of orthogonal table L_9 (3*3), the level of each factor based on the table arrangement to obtain the orthogonal test parameter table, each line of the factors to take the value of the combination of a group of test parameters [37], for a total of 9 groups of tests, as shown in Table 5.

Figure 3 shows the macroscopic morphology of the single-pass coating cross-sections obtained under the orthogonal test parameters described above, and it can be seen that the cross-sectional morphology of the different groups varies relatively widely, and the dilution rates of all specimens are generally high. Different scanning rates change the laser scanning dwell time, which also changes the amount of powder obtained from the substrate in disguise. As can be seen from Figure 3, under the variation of the current parameter gradient, when the power is certain, the scanning rate has a greater influence on the melt height and depth than the scanning speed, and the difference in this influence is gradually obvious when accompanied by the power increase. This is because the change of 200 mm·min^{-1} powder feeding rate on the coating of the same position of the scanning rate of the substrate to obtain a greater amount of powder; when the power gradually

increases, the heat in the melt pool rises, the unmelted powder decreases, and the powder utilisation increases; compared to the lower power, the increase in the amount of powder permitted by the higher power will also be more, thus producing a significant difference. When P = 4200 W and 4600 W, the coatings are produced with more porosity as seen in Figure 3 1–3,7,9, while when P = 4400 W, Figure 3 5,6 have no obvious porosity defects, indicating that the appropriate power parameters have a greater impact on the generation of defects.

Table 5. Parameter list of orthogonal test.

No.	A	B	C
1	1 (4200)	1 (6.78)	1 (1800)
2	1	2 (9.04)	2 (2000)
3	1	3 (11.3)	3 (2200)
4	2 (4400)	1	2
5	2	2	3
6	2	3	1
7	3 (4600)	1	3
8	3	2	1
9	3	3	2

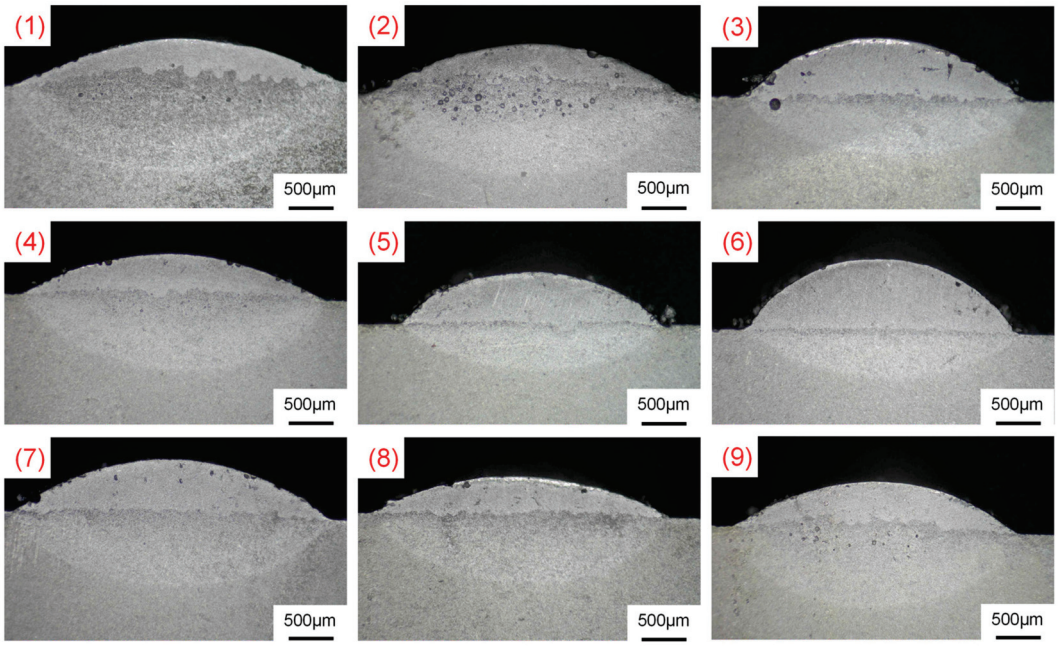


Figure 3. Macroscopic morphology of single-pass coating cross-section with orthogonal test parameters. (1) P = 4200 W, V_f = 6.78 g·min^{-1}, V_S = 1800 mm·min^{-1}. (2) P = 4200 W, V_f = 9.04 g·min^{-1}, V_S = 2000 mm·min^{-1}. (3) P = 4200 W, V_f = 11.3 g·min^{-1}, V_S = 2200 mm·min^{-1}. (4) P = 4400 W, V_f = 6.78 g·min^{-1}, V_S = 2000 mm·min^{-1}. (5) P = 4400 W, V_f = 9.04 g·min^{-1}, V_S = 2200 mm·min^{-1}. (6) P = 4400 W, V_f = 11.3 g·min^{-1}, V_S = 1800 mm·min^{-1}. (7) P = 4600 W, V_f = 6.78 g·min^{-1}, V_S = 2200 mm·min^{-1}. (8) P = 4600 W, V_f = 9.04 g·min^{-1}, V_S = 1800 mm·min^{-1}. (9) P = 4600W, V_f = 11.3 g·min^{-1}, V_S = 2000 mm·min^{-1}.

The melt width and dilution rate of each group of tests are shown in Table 6. The variation rule of melt width and dilution rate with the level of individual factors is not clear, and in order to further explore the influence of each factor on the melt width and dilution rate, the extreme difference analysis is used to further illustrate.

The extreme difference analysis table shown in Table 7, R_j table on the extreme difference of factor j, reflecting the magnitude of changes in the test indicators with the level of the factor, is a measure of the degree of influence of the factor. According to the size of

the extreme difference R_j, you can judge the influence of the factors of the primary and secondary. The formula for calculating the extreme difference R_j is shown in Equation (1), where K_{jm} represents the factor j to take the level m, the sum of the test indicators.

$$R_j = \max\left(\overline{K_{J1}}, \overline{K_{J2}}, \ldots \overline{K_{Jm}}\right) - \min\left(\overline{K_{J1}}, \overline{K_{J2}}, \ldots \overline{K_{Jm}}\right) \quad (1)$$

Table 6. Melt width and dilution rate of orthogonal test coatings.

No.	Dilution Rate/%	Melt Wide
1	68.2	5.04
2	59.5	4.97
3	49.7	4.37
4	63.5	4.71
5	46.3	4.04
6	38.3	4.18
7	57.0	4.96
8	65.0	4.55
9	64.6	5.41

Table 7. Orthogonal test extreme variance analysis table.

		A	B	C
Melt wide	K1	14.38	14.71	13.77
	K2	12.93	13.56	15.09
	K3	14.92	13.96	13.37
	$\overline{K_1}$	4.79	4.90	4.59
	$\overline{K_2}$	4.31	4.52	5.03
	$\overline{K_3}$	4.97	4.65	4.46
	Kmax	4.97	4.90	5.03
	Kmin	4.31	4.52	4.46
	R	0.66	0.38	0.57
Dilution rate/%	K1	177.40	188.70	174.40
	K2	151.00	170.80	187.60
	K3	186.60	155.50	153.00
	$\overline{K_1}$	59.13	62.90	58.13
	$\overline{K_2}$	50.33	56.93	62.53
	$\overline{K_3}$	62.20	51.83	51.00
	Kmax	62.20	62.90	62.53
	Kmin	50.33	51.83	51.00
	R	11.87	11.07	11.53

As can be seen from Table 8, for the coating melt width RA > RC > RB and the dilution rate RA > RC > RB, with reference to the method of polar deviation can be seen, the different process parameters for the coating melt width of the influence of the size of laser power is the largest, followed by the scanning rate, the smallest rate of powder delivery; on the dilution rate of the influence the size of the laser power is the largest, the scanning rate of the second, the smallest rate of powder delivery, it can be seen clearly that, in the test, the laser power of the largest influence on the coating is the influence of the coating melt width and the dilution rate of the primary factors.

Table 8. Process parameters after orthogonal optimisation.

Laser Power/(w)	Powder Feeding Rate/(g·min^{-1})	Scanning Speed/(mm·min^{-1})
4400	11.3	1800

For the evaluation index of the coating, the moderate melt width and the lowest dilution rate are used as the selection principle of the parameters. For factor A, the influence of melt width and dilution rate of the coating is in the first place, the comprehensive

consideration of the coating morphology and dilution rate selection of A_2; for factor B, the melt width of the coating and the dilution of the rate of influence of the coating are in the last place, the comprehensive consideration of the selection of B_3; for factor C, the melt width of the coating and the dilution rate of the influence of the coating are in the middle place, the comprehensive consideration of the selection of C_1, and optimal combination of the analysis of the polarity of the difference for $A_2B_3C_1$.

After the end of laser cladding, the sample is cut into an 8 × 8 × 8 mm size, polished with 800#, 1000#, and 1200# sandpaper, and then configured with aluminium-based electrolytic polishing solution (volume ratio of $HClO_4$:CH_3CH_2OH = 1:9) and electrolytic polishing with the electrolytic polishing machine model KXN-305D, set the voltage at 25 v, the electrolysis time is 20 s. During the electrolysis period, the electrolyte was stirred with a magnetic stirrer, and liquid nitrogen was added to cool down the temperature to prevent the electrolysis from increasing with time; the temperature increased, the resistance increased, and the specimen was blackened by over-electrolysis, which affected the amount of electrolytic quality.

An industrial microscope was used to analyse the macroscopic morphology and dilution rate of the coating cross-section; a Bruker D8 Advance X-ray diffractometer (XRD) was used to scan the coating for physical analysis; and JSM-7610F plus Scanning Electron Microscope (SEM) and energy spectrometry (EDS) were used to observe the microscopic morphology and elemental distribution. The microhardness was measured by Huayin HV-1000A digital microhardness tester with an applied force of 200 N and a dwell time of 15 s; the friction factor was tested by MFT-5000 friction and wear tester, and the dry friction experiment was carried out by using Si_3N_4 ceramic ball as the friction partner under a load of 60 N, with a loading time of 20 min, a frequency of 2 Hz, and a scratch distance of 10 mm.

3. Results and Discussion

3.1. Macroscopic Morphology Analysis

Through the above single-channel orthogonal experiment and range analysis, it is concluded that sample No. 6 ($A_2B_3C_1$) is the best process parameter, and the data are shown in Table 8.

Figure 4 shows the macroscopic morphology cross-section of AlSi10Mg coated powder and WC ceramic powder added with different proportions under an industrial microscope.

As can be seen from the figure, under the optimal orthogonal process parameters, the surface morphology of the AlSi10Mg coatings without added WC ceramic powder is good, the surface is flat and smooth, and there are no defects such as cracks and porosity, while the coatings with 60% WC addition has obvious cracks and porosity defects, and the moulding quality is poor. Is due to the thermal stress easily generated during the laser cladding process, and the difference between the thermal expansion coefficient of WC ceramic powder and the thermal expansion coefficient of the substrate, along with the continuous improvement of the WC content, the difference between the thermal expansion coefficient of WC ceramic powder and the substrate is also increasing. In the case of the same laser power, there is a large amount of unmelted powder in the 60% WC cladding group, and these particles are prone to produce a source of cracks, and, ultimately, cracks are generated. In addition, the changes in the composition of the alloy also caused a phase transition that increased the phase transition stress in the cladding material.

In the process of rapid cooling of laser cladding, the thermal stress of the cladding layer exceeds the yield strength of the material itself, and the gas that cannot be discharged by the rapid cooling of laser cladding will turn into porosity. So, the combined effect of the escape velocity of the gas and the speed of the laser condensation is one of the main reasons for the generation of porosity, and the WC makes the viscosity of the molten pool rise, which in turn restricts the escape of the gas, and a large number of WC particles into the molten pool. Burnout decomposition will occur to form W_2C and C, and C atoms and O atoms, in the air reaction precipitation of CO and CO_2, the chemical formula seen in

Formulas (2) and (3) [36], making 60% of WC additions to the coatings produced defects such as pores and cracks, from the coatings colour, with the increase in WC powder content, the coatings metal gloss is reduced, which is due to the WC ceramic powder itself was black. This is due to the WC ceramic powder itself being black, with the increase in the content of WC powder, AlSi10Mg powder addition decreased, which led to a reduction in the gloss of the cladding layer, and the colour became darker.

$$2WC \rightarrow W_2C + C \quad (2)$$

$$3C + 2O_2 \rightarrow 2CO + CO_2 \quad (3)$$

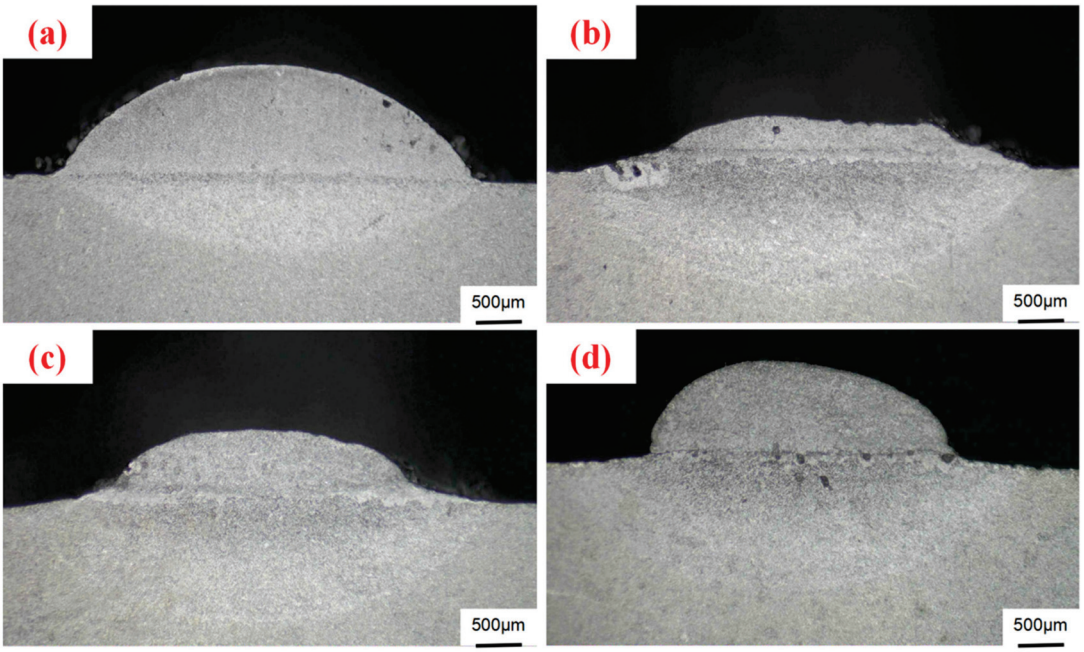


Figure 4. Macroscopic morphology of the cross-section of different powder coatings: (**a**) AlSi10Mg coating; (**b**) AlSi10Mg + 20% WC coating; (**c**) AlSi10Mg + 40% WC coating; (**d**) AlSi10Mg + 60% WC coating.

This also contains a small amount of metal gas evaporated at high temperatures, these gases in the molten pool solidification process cannot come up to overflow and remain in the coating to form pores.

The dilution rate is a key parameter to judge the quality of the cladding layer. If the dilution rate is small, it will lead to poor metallurgical bonding between the cladding layer and the substrate, and it is easy to peel off; if the dilution rate is too large, it will lead to a large number of elements in the substrate precipitation into the cladding layer, which will weaken the performance of the cladding layer. The cross-section of the cladding layer is shown in Figure 5, and the dilution rate is calculated as shown in Equation (4).

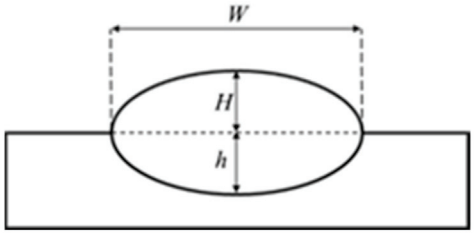


Figure 5. Schematic cross-section of the coatings.

Where W is the melt width of the melt pool, H is the height of the cladding layer, h is the height of the melt pool, and μ is the dilution rate of the cladding layer.

$$\mu = \frac{H}{H + h} \times 100\% \quad (4)$$

Figure 6 shows the parameters such as melt width, melt height, melt depth, and dilution rate for four different powder ratios. It can be seen that, in the case of four different powders coated with the optimal process parameters under orthogonal optimisation, the melting height tends to increase with the increase in WC content, and the melting depth and dilution rate also increase, which is due to the high metallic gloss of aluminium, laser cladding, laser, and aluminium substrate contact with a large number of light sources' refraction occurs in the process of laser coefficient utilisation is poorer, and WC joining makes the reduction of the metallic gloss, the laser coefficient of utilisation rate increases, the temperature in the cladding layer rises, the depth of fusion becomes deeper, and the dilution rate increases.

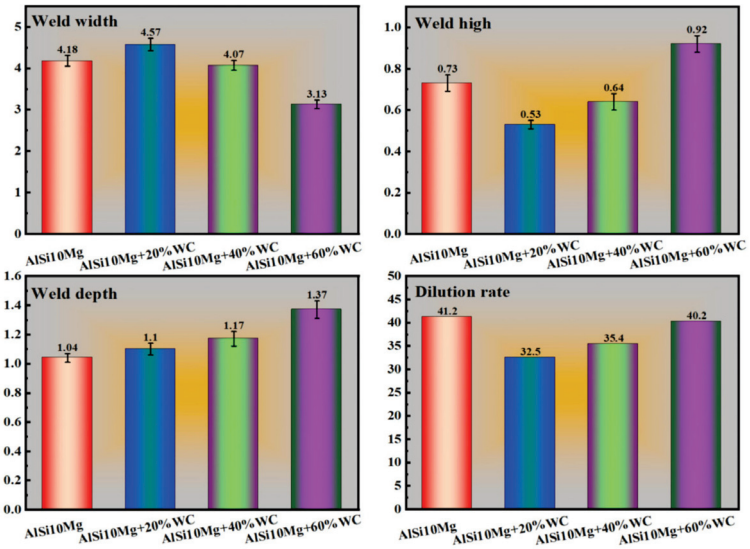


Figure 6. Melt width (mm), melt height (mm), melt depth (mm), and dilution rate (%) parameters for four different powder ratios.

3.2. Phase Analysis

A German Bruker D8 Advance type X-ray diffraction (XRD) was used to scan the coating for physical analysis with a voltage of 40 kV, a current of 40 mA, a step size of 0.02, and a step rate of 0.2 s/step. the XRD results were then physically analysed using the Jade 6.5 software, and the resultant XRD diffraction pattern is shown in Figure 7.

As can be seen from the figure, there are obvious Al and Al_2O_3 diffraction peaks, as well as a small number of SiC diffraction peaks in the coating tissue without the addition of WC ceramic powder; this is due to the fact that a small number of SiC particles in the substrate floats upward in the process of laser fusion cladding, appearing in the substrate and the combination of coatings, Al is very easy to oxidate, generating Al_2O_3, the reaction formula is shown in Formula (5). When AlSi10Mg powder is added, the physical phase in the coating changes, and a new diffraction peak appears. WC powder is added, the coating phase changes, new diffraction peaks, and WC firing production of W_2C and C, C and Al and Al's oxide Al_2O_3 reaction to generate Al_4C_3. The reaction formula is shown in Formula (6), with the WC content continuing increase to 40% WC additions, the coatings appeared in the new phase of Al_4SiC_4, which is because with the increase in the WC content of the coatings absorbs more heat, and when the melt pool temperature is higher than 1670 K, SiC in the substrate reacts in situ with Al and Al_4C_3 as shown in Formulas (7) and (8), and produces Al_4SiC_4 [38]. The increasing W and C

elements decomposed in the melt pool react with the Al and Si atoms to produce more carbides, which have higher hardness, and therefore the microhardness of the coatings is significantly improved compared to the coatings of the no WC addition group, increasing the wear resistance of the coatings. At the same time, the solid solution may produce lattice distortion will also hinder the occurrence of dislocation movement, further enhancing the wear resistance of the cladding layer.

$$2Al + 3O_2 \rightarrow Al_2O_3 \quad (5)$$

$$4Al + 3C \rightarrow Al_4C_3 \quad (6)$$

$$4Al + 4SiC \rightarrow Al_4SiC_4 \quad (7)$$

$$SiC + Al_4C_3 \rightarrow Al_4SiC_4 \quad (8)$$

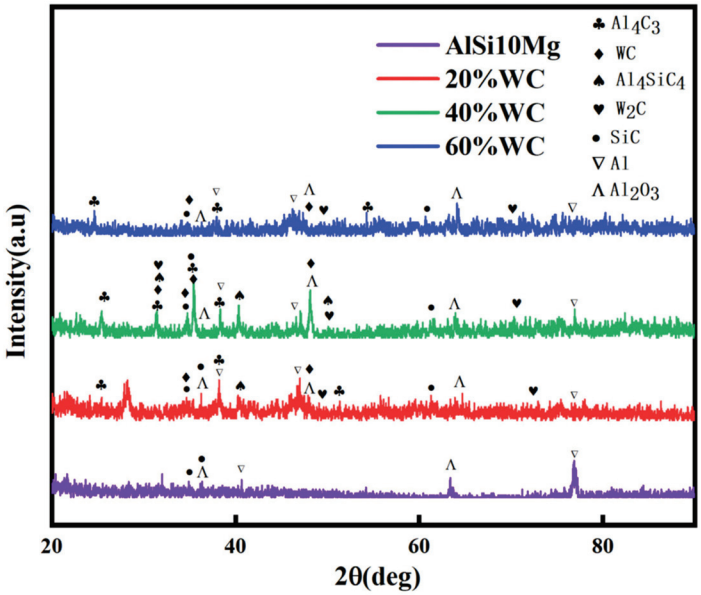


Figure 7. XRD patterns of coating with different WC additions.

3.3. Microstructure Analysis

JSM-7610F plus Scanning Electron Microscope (SEM) and energy spectrometer (EDS) were used to observe the micro-morphology and elemental distribution. The different areas of the three coatings were scanned for micro-morphology using SEM and Figure 8 shows the micro-morphological microstructure of the four fused coatings.

From Figure 8a–c, it can be seen that the microstructure of the top of the AlSi10Mg cladding layer mainly consists of a large number of granular cellular grains; the microstructure of the middle of the cladding layer shows dendritic grains with an upward growth direction, and the bottom of the cladding layer consists of rod-like cytosine crystals, which contain SiC particles in the substrate, which is mainly due to the fact that the laser cladding is a fast warming and cooling process, and the top of the cladding layer dissipates heat to all sides after laser cladding, and there is no restriction on the direction of grain growth so that granular cytosine is formed. In the solidification process of laser cladding, the microscopic grain structure is related not only to the temperature gradient (G) between the solid–liquid interface but also to the rapid solidification rate (S) during the melting process, where the value of S gradually increases from the bottom to the top of the coating. The larger the G/S value is, the coarser the grain structure is, while the smaller the G/S value, the finer the grain structure [39].

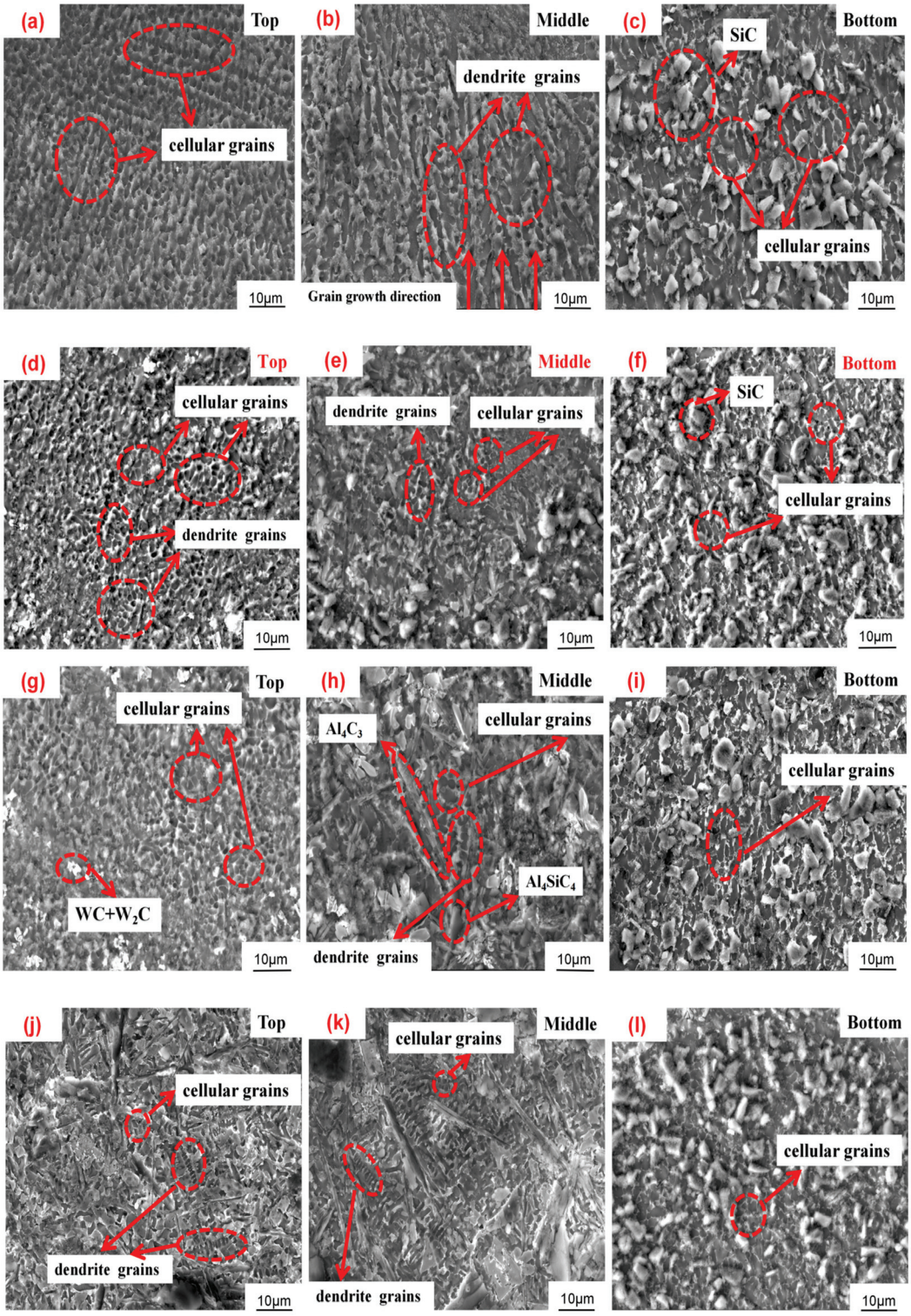


Figure 8. Micro-morphological images of four coatings: (**a**–**c**) AlSi10Mg; (**d**–**f**) AlSi10Mg + 20% WC; (**g**–**i**) AlSi10Mg + 40% WC; (**j**–**l**) AlSi10Mg + 60% WC.

As can be seen from Figure 8d–i, when WC was added into AlSi10Mg powder as a reinforcing phase, the morphology of the grains changed due to the change of the physical phase, and the production of the secondary crystal axes started, which was due to the fact that after the addition of WC, a lot of metal compounds and carbides were produced, such as W_2C, Al_4C_3, and Al_4SiC_4, which altered the original microstructure of the AlSi10Mg coating. Comparing Figure 8a,d,g, the morphology of the cellular grain at the top of

the coating changed after the addition of WC, the cellular grain was no longer regular granular but appeared honeycomb, and the carbides such as WC and W_2C appeared in the coating, and the cellular grain appeared in the middle of the layer, which can be seen in Figure 8b,e,h, which indicated that the intermetallic compounds and carbides formed by the addition of WC particles and their decomposition. These compounds provide more efficient and effective solutions to the problems of the AlSi10Mg coatings, and they are not only the most important for the fusion of the AlSi10Mg and Al_4SiC_4 layers, but carbide, these compounds provide more nucleation sites, which leads to non-uniform nucleation during solidification, hinders the growth of dendrites and obtains smaller grains, refines the grains of AlSi10Mg coating, generates the needle-like substance Al_4C_3 [38], and generates the flaky new phase of Al_4SiC_4 when the content of WC reaches 40%; however, the WC also leads to the emergence of a large thermal expansion coefficient, reducing the mobility of the melt pool and generating a small number of porosities. Comparing the bottom Figure 8c,f,i, it can be clearly seen that the grains are refined, on the one hand, due to the addition of WC to refine the grains, and on the other hand, due to the addition of WC to reduce the metal lustre of the molten pool absorbed more heat inside the molten pool, and this heat provides energy for the new nuclei.

As can be seen from Figure 8j–l, When the WC content reaches 60%, significant changes occur in the grain morphology of the cladding layer. A considerable amount of WC forms W_2C compounds, leading to the formation of numerous new nucleation points around W_2C and Al_4C_3. In addition to vertically growing cell crystals and dendrites along the growth direction, transverse dendrites also develop at the top of the cladding layer due to newly generated nucleation points that impede vertical grain growth. The presence of solid solutions containing aluminum (such as W, Mg, and Cu atoms) in the cladding layer contributes to solution strengthening, resulting in a shift in grain growth direction within the middle region of the cladding layer and inducing grain dislocation. Consequently, grains grow in multiple directions while interactions between phase interfaces and grains exert a pinning effect, thereby refining and fining down microstructure.

3.4. Distribution of Element

The energy spectrum analysis and scanned elemental distribution of the two types of coatings, AlSi10Mg and AlSi10Mg + WC, were carried out by using an energy spectrometer EDS, and the results of energy spectrum analysis and their elemental distributions of the regional surface scans of the AlSi10Mg and AlSi10Mg+WC coatings are shown in Figures 9 and 10, respectively.

From Figure 9 EDS surface scan of AlSi10Mg coating, we can see the distribution of each element, the main distribution of the coatings has Al, Si, C, Mg, and Cu elements, as well as some oxides, in which Mg, Cu elements are diffusely distributed in the whole area, and Mg, Cu elements originally belong to the matrix, which indicates that under laser conduction, the convection in the molten pool makes the elements in the matrix metallurgical bonding with the cladding layer. Therefore, Mg and Cu elements can be detected in the whole cladding layer. Combined with the EDS spectroscopy detection, the results are shown in Table 9, EDS spectroscopy scanning A1 is rich in Si and C elements, and the atomic ratio is close to 1:1, it can be deduced that it is SiC particles, the at.% ratio of Al and O is also close to 2:3.

It can be deduced that it is oxides such as Al_2O_3, A2 cellular grains are mainly dominated by the elements of Al and C, and the grain boundaries of A3 are rich in the element of Si, The A3 grain boundary is rich in Si elements. It can be inferred that grains are Al-solid solution, and solid solution particles are Si, C, Cu, Mg, and other elements, due to the high temperature of laser cladding and convection in the molten pool, the SiC particles in the matrix floated upward, and the unmelted SiC particles appeared in the middle of the cladding layer, which improved the hardness and wear resistance of the coating.

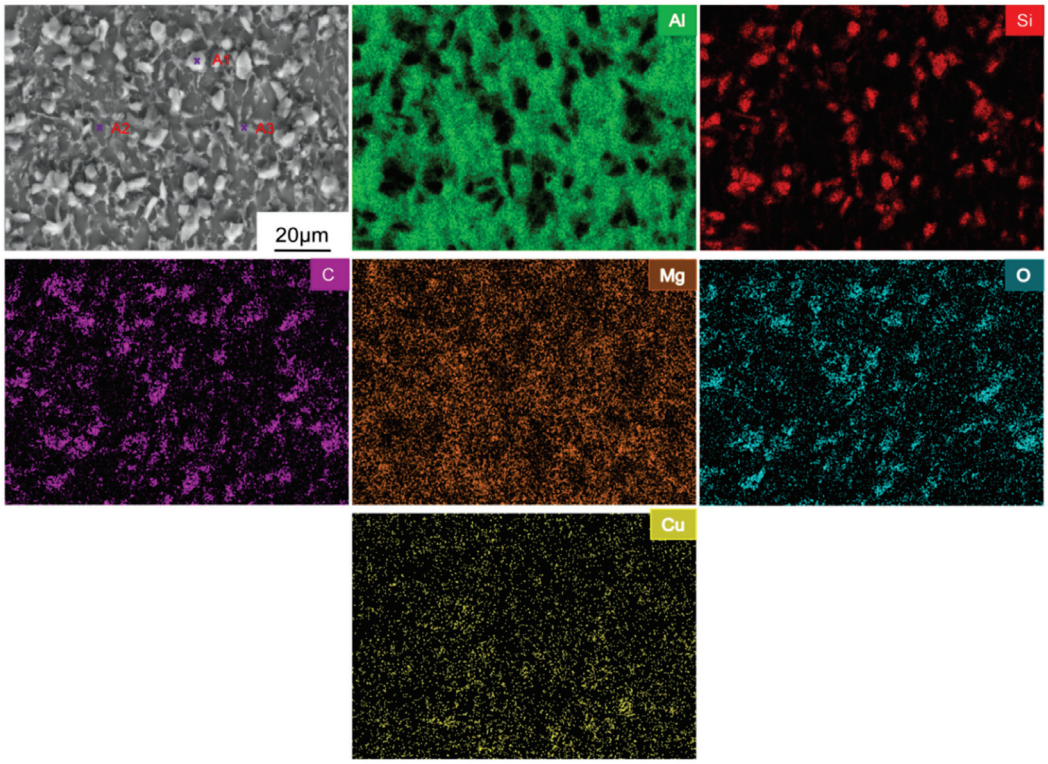


Figure 9. EDS map analysis of each element of AlSi10Mg coatings; (**A1**) SiC point scan; (**A2**) Cellular crystal point scan; (**A3**) Grain boundary point scan.

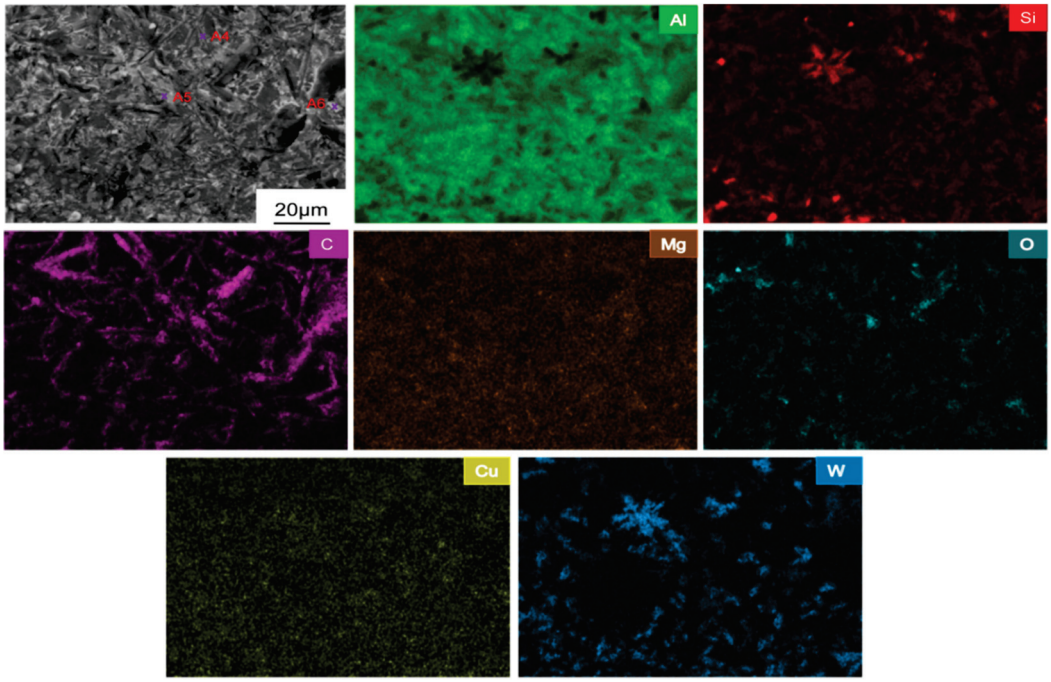


Figure 10. EDS map analysis of each element of AlSi10Mg+WC coating: (**A4**) Al_4C_3 point scan; (**A5**) Carbide such as WC and W_2C point scan; (**A6**) Al_4SiC_4 point scan.

As can be seen from Figure 10 EDS surface scan of AlSi10Mg+WC coatings. After the addition of WC, WC decomposed under the thermal effect of the laser beam and the liquid molten pool, and new substances were generated. It can be seen that the Mg and Cu elements are still diffusely and uniformly distributed in the coatings, the C element is enriched on the needle-like precipitates, and the W element and the Si element are also

distributed in the coatings, but they appear to be enriched in some areas. The results are shown in Table 10 in combination with the EDS energy spectrum.

Table 9. Energy spectrum detection of AlSi10Mg coatings.

		Al	Si	C	O	Cu	Mg
A1	wt.%	14.44	50.25	28.75	6.56	-	-
	at.%	9.34	37.25	38.32	15.09	-	-
A2	wt.%	74.87	3.68	7.90	1.32	10.58	1.64
	at.%	71.51	3.38	16.95	2.13	4.29	1.74
A3	wt.%	61.63	18.45	9.13	6.94	2.36	1.48
	at.%	52.49	17.09	17.89	10.22	0.87	1.44

Table 10. Energy spectrum detection of AlSi10Mg + WC coatings.

		Al	Si	C	O	Cu	Mg	W
A4	wt.%	49.18	5.51	23.49	5.46	7.37	2.35	6.64
	at.%	43.25	3.68	37.75	6.20	2.33	1.38	5.41
A5	wt.%	18.96	14.28	12.22	7.31	-	-	47.23
	at.%	23.88	17.28	34.59	15.52	-	-	8.73
A6	wt.%	51.34	7.24	20.41	12.35	2.43	3.43	2.80
	at.%	41.25	8.68	46.75	1.13	0.40	0.38	1.41

From the EDS spectrum, A4 area elements can be seen, Al elements and C elements are heavily enriched, and the atomic ratio is approximated to 4:3. By combining with the XRD spectrum, we can see that the needle-like material is Al_4C_3, A5 area atoms of W content of 8.73 at.%, and C elements of the atomic content of 34.59 at.%;The reason may be that the melting pool temperature exceeds the melting point of WC particles, which makes part of the WC particles dissolve, and some of the W elements are burned, generating unfused WC and carbides such as W_2C. The A6 area can be seen through the spectral analysis of the atomic mass ratio of the Al, Si, and C elements, about 4:1:4, which can be roughly judged to be Al_4SiC_4, the morphology is a lamellar structure, and the hardness and abrasion resistance of coatings are both significantly improved by Al_4C_3 and Al_4SiC_4.

3.5. Microhardness Analysis

Huayin HV-1000A digital microhardness tester was used to measure the microhardness of the substrate and the three coatings, with an applied force of 200 N and a dwell time of 15 s. Figure 11 shows the Vickers microhardness distribution of the coatings of AlSi10Mg powder and different proportions of the WC ceramic powder additions in a line graph, and the microhardness values were measured from the top of the coatings to the direction of the substrate depth at intervals of 0.2 mm. The average hardness value of the three points is taken as the final hardness value of the point, and two more points are taken above and below the same point for three measurements. The hardness map can be divided into two parts from left to right: the cladding zone (CZ) and the substrate (SZ). Overall, the distribution of hardness curves for different WC additions to the coatings has a similar trend of increasing and then decreasing, while the AlSi10Mg powder hardness line graph is gradually increasing. The hardness of the added WC ceramic powder is greater in the coatings zone, followed by the heat-affected zone, and the substrate is the lowest, while the AlSi10Mg coating is the coatings zone where the hardness is lower than the substrate hardness.

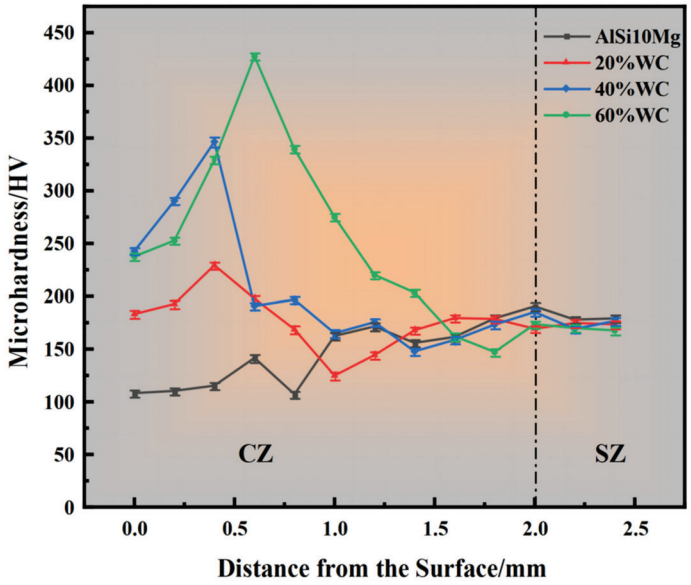


Figure 11. Microhardness distribution curve.

It can be seen from the figure that the highest hardness point did not occur in the surface layer. This is because, in the cladding process, the surface layer of the powder has been absorbing laser energy, generating a large amount of heat, in which the alloying elements Al, W, etc., at high temperatures sintering occurs, and the surface hardness is reduced. The hardness of the upper part of the cladding layer is higher than the lower part because the upper part of the cladding layer is in contact with the atmosphere, the cooling crystallisation rate is fast, the grain size is small, and the formation of fine crystalline reinforcement and increase hardness; add WC ceramic powder, the cladding layer microhardness are higher than the substrate, this is because of the addition of the WC powder and the substrate in the high-temperature melting of the SiC. The WC decomposition out of the W atoms and C atoms solidly dissolved in the formation of the Al substrate solid solution.

Strengthening enhances the hardness of the cladding layer, the decomposition of C, Si to form Al_4C_3, Al_4SiC_4, and other hard phases, the formation of the second strengthening, uniformly distributed in the cladding layer, and the formation of diffuse strengthening to further enhance the cladding layer microhardness. The hardness of the cladding layer in the figure has a large gap in which the average hardness of the matrix, AlSi10Mg powder, 20% WC, 40% WC, and 60% WC powder cladding layer is 171.61 HV, 124.20 HV, 182.74 HV, 283.77 HV, and 310.37 HV, respectively, compared to the hardness of the matrix of 171.61 HV, 20% WC cladding layer. The hardness of 20% WC coatings increased 1.06 times, 40% WC coatings increased 1.65 times, and 40% WC coatings increased 1.8 times, while the hardness of AlSi10Mg powder coatings was lower than that of the substrate, which is because the substrate contains SiC hard particles. The coefficient of thermal expansion of SiC particles is lower than the coefficient of thermal expansion of aluminium, and in the solidification process, the accumulation of SiC particles around the particles will generate a large number of thermal. During solidification, the SiC particles will accumulate around the SiC particles to produce a large number of heat-altering dislocations, and at the same time, the SiC particles will inhibit the grain growth of aluminium crystals and reduce the grain size of the aluminium alloy.

3.6. Wear Performance Analysis

The friction factor of the coating was tested by MFT-5000 friction and wear tester, the friction and wear curves obtained are shown in Figure 12.

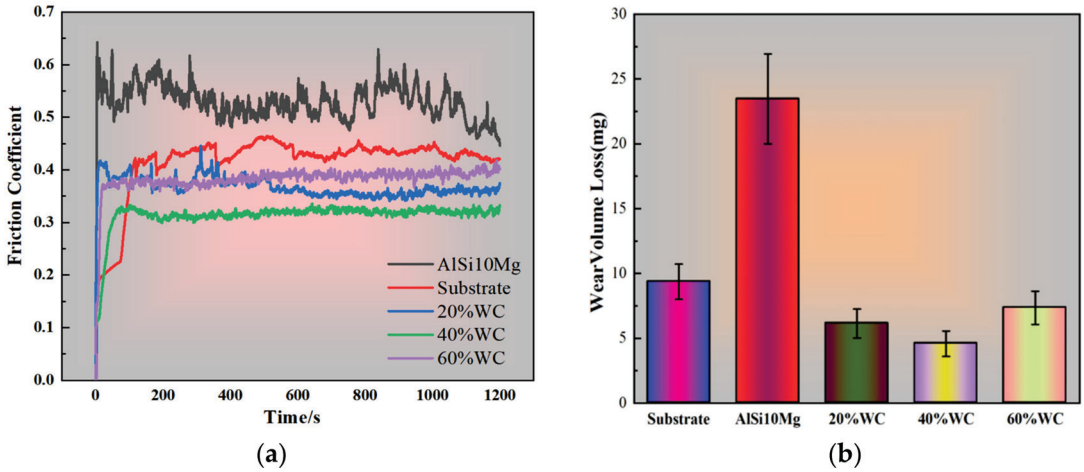


Figure 12. (**a**) Friction wear curves for different coatings; (**b**) wear weight loss diagram for different coatings.

Figure 12a,b show the friction and wear curves of several different coatings and substrates over time and the wear loss graphs before and after the specimen tests, respectively. It can be seen that there are two stages of initial run-in and steady wear for several coatings. Among them, the friction wear curve of AlSi10Mg coating has been in a large fluctuation state, and the wear curve of the substrate tends to stabilise after about 400 s, the wear curve of the coating with 20% WC added tends to stabilise after about 500 s, the wear curve of 40% WC tends to stabilise around 200 s, and the wear curve of 60% WC goes to the steady stage around 20 s. This is due to the fact that AlSi10Mg coating hardness is low, from the initial stage of frictional wear coating which has a large amount of wear, Si_3N_4 ceramic ball friction vice, and the sample surface of the micro-convex body of the collision between friction, the contact stress caused by the friction coefficient fluctuations. The convex body was worn flat, the ceramic ball and the coating of the contact area increased, the pit deepened, the friction between the contact surface also increased, and the coefficient of friction is the largest of the groups of data and the least resistant.

The largest, but also the least wear-resistant group due to the substrate is 15% SiCp/2009Al. The substrate contains SiC ceramic particles, the hardness is enhanced, and the surface roughness increases; the friction factor cannot tend to a stable stage in a short time, and occasionally there are fluctuations, it may be the friction side of the ceramic ball in contact with the SiC ceramic particles, the coating will play a role in the addition of 20% WC-40% WC solid solution strengthening and diffusion strengthening role, the generation of hard phase carbide improves the hardness and wear resistance of the coating and the friction factor is also reduced.With the increase in WC content, the hardness continues to improve and the coating surface will be a flaking phenomenon, increasing the friction between the friction sub and the coating, but instead of the friction factor appearing in the 60% WC additions to the coating is higher than the 40% WC content of the coating. In turn, it can be shown that the hardness is not the higher the better.

From the tests, it can be seen that under the same load, the average coefficient of friction of 15% SiCp/2009Al substrate, AlSi10Mg coating, AlSi10Mg + 20% WC coating, AlSi10Mg + 40% WC coating, and AlSi10Mg + 60% WC coating are 0.54, 0.43, 0.39, 0.31, and 0.36 specimens, respectively. The observation was consistent with the friction coefficient results that specimens with a lower friction coefficient also exhibited a lower wear loss [40]. The wear was 9.36 mg, 23.47 mg, 6.13 mg (34.5% reduction compared to the substrate), 4.58 mg (51.06% reduction compared to the substrate), and 7.35 mg (21.47% reduction compared to the substrate), respectively.

The SEM microscopic morphology of 15% SiCp/2009Al substrate, AlSi10Mg coating, AlSi10Mg + 20%WC coating, AlSi10Mg + 40%WC coating, and AlSi10Mg + 60%WC coating at different magnifications after surface friction are shown in Figure 13a–j, respectively, and

the main wear in the coatings is the abrasive wear and the adherent wear, as can be seen in Figure 13a,b.The wear characteristics of the substrate are mainly flaking and friction grooves there are some irregular pits and a small number of plough grooves with attached abrasive debris on the abrasive marks on the surface of the substrate. This is because the matrix and the friction pair contact adhesion and plastic deformation.

In Figure 13c,d, it can be seen that the surface of the coating has a large number of flaking and plough grooves, and there is a slight depression, the coating is very soft in texture, and the abrasion resistance is Very poor, Si_3N_4 ceramic ball friction vice adhesion with the coating, adhesion point tearing, plastic deformation of the coating; from Figure 13e,f, it can be clearly seen that the coating grooves become shallower, accompanied by a small amount of spalling; this is because of the addition of WC in the coating to make the hardness of the coating increased, compared with the substrate and AlSi10Mg coating wear resistance increased.

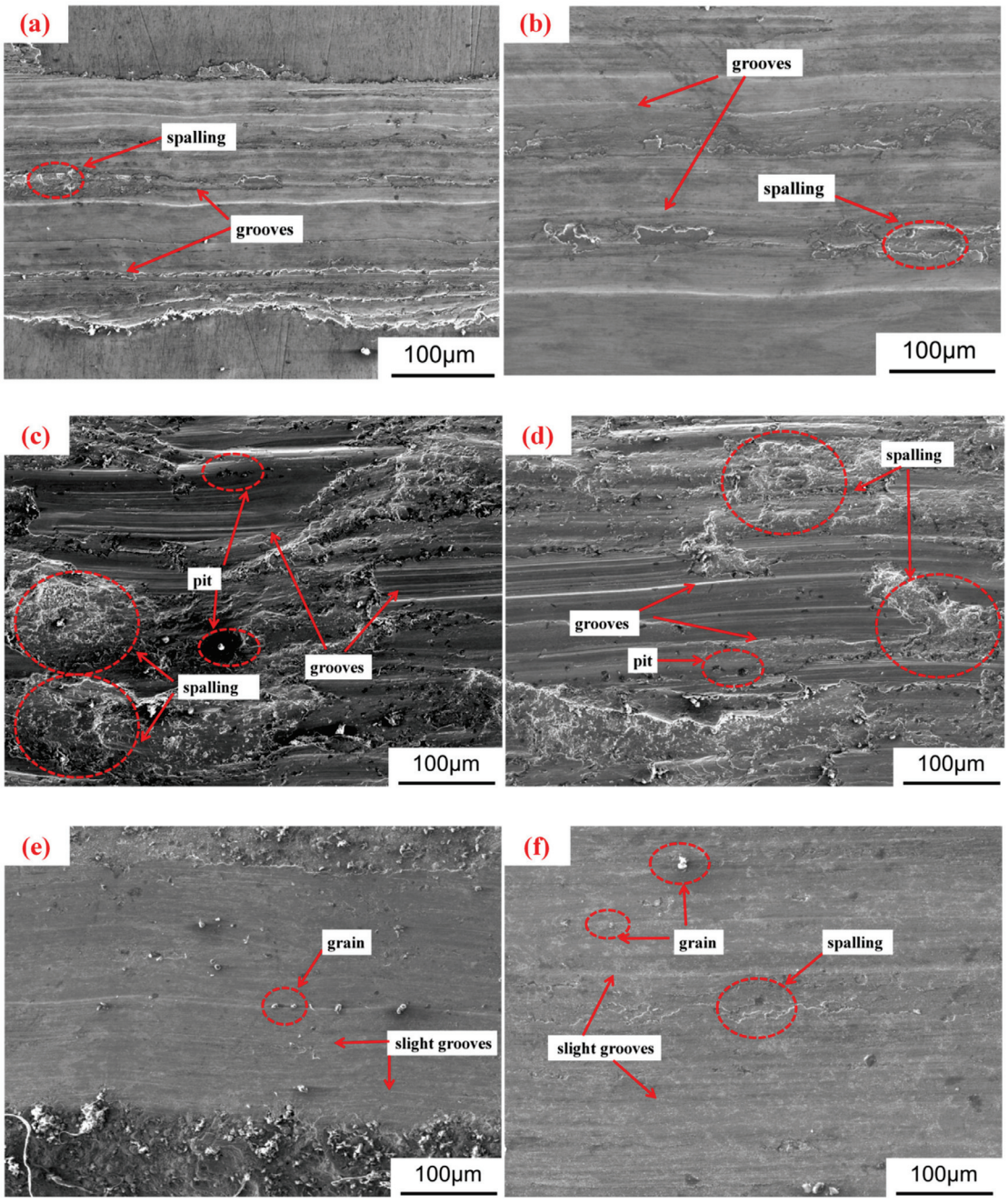


Figure 13. *Cont.*

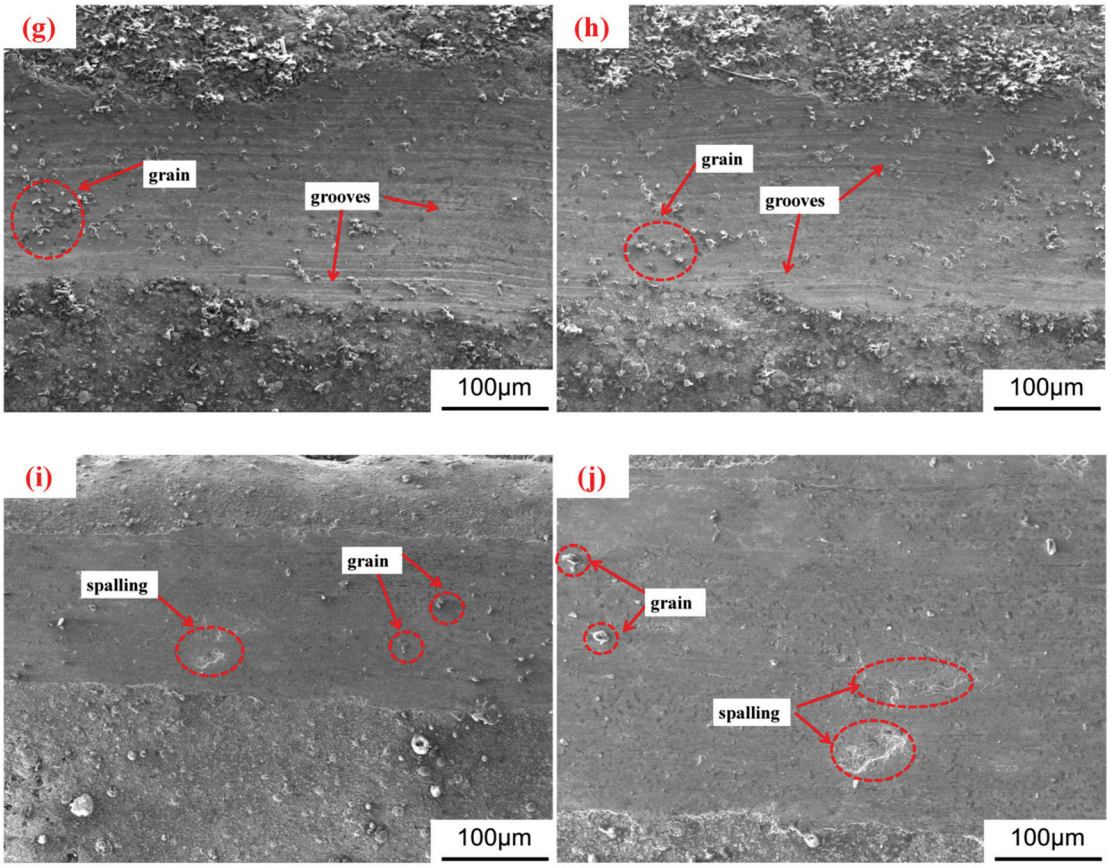


Figure 13. Wear morphology and microstructure of four coatings: (**a**,**b**) substrate; (**c**,**d**) AlSi10Mg; (**e**,**f**) AlSi10Mg + 20% WC; (**g**,**h**) AlSi10Mg + 40% WC; (**i**,**j**) AlSi10Mg + 60% WC.

Figure 13g,h show that the content of WC continues to increase and the hardness continues to increase; due to the high hardness, there is no spalling, only slight scratches and some particles, which is due to the production of hard compounds in the coating, so that the wear mechanism becomes abrasive wear and the abrasive marks become narrower, with better abrasion resistance. Figure 13i,j show in the 60% WC additions, although it makes the coating hardness higher and there are no obvious grooves, there is a flaking and the coating toughness decreases, increasing the possibility of coating cracking, and the performance is rather reduced [40].

Roughness is also an important parameter to reflect the quality of coating fusion. The higher the roughness [41], the softer the coating texture, the increased contact area between the friction vice and the coating surface, the wear resistance is reduced, and the quality of the coating decreases. The 3D contour of the friction wear was obtained by using the super depth of field microscope, and the ends of the friction wear grooves of the coated coating were marked with two points and analysed, respectively, for 15% SiCp/2009Al substrate, AlSi10Mg coating, AlSi10Mg + 20% WC coating, AlSi10Mg + 40% WC coating, and AlSi10Mg + 60% WC coating. WC coating, AlSi10Mg + 40%WC coating, and AlSi10Mg + 60%WC coating. The analysed morphology diagram is shown in the Figure 14a–e.

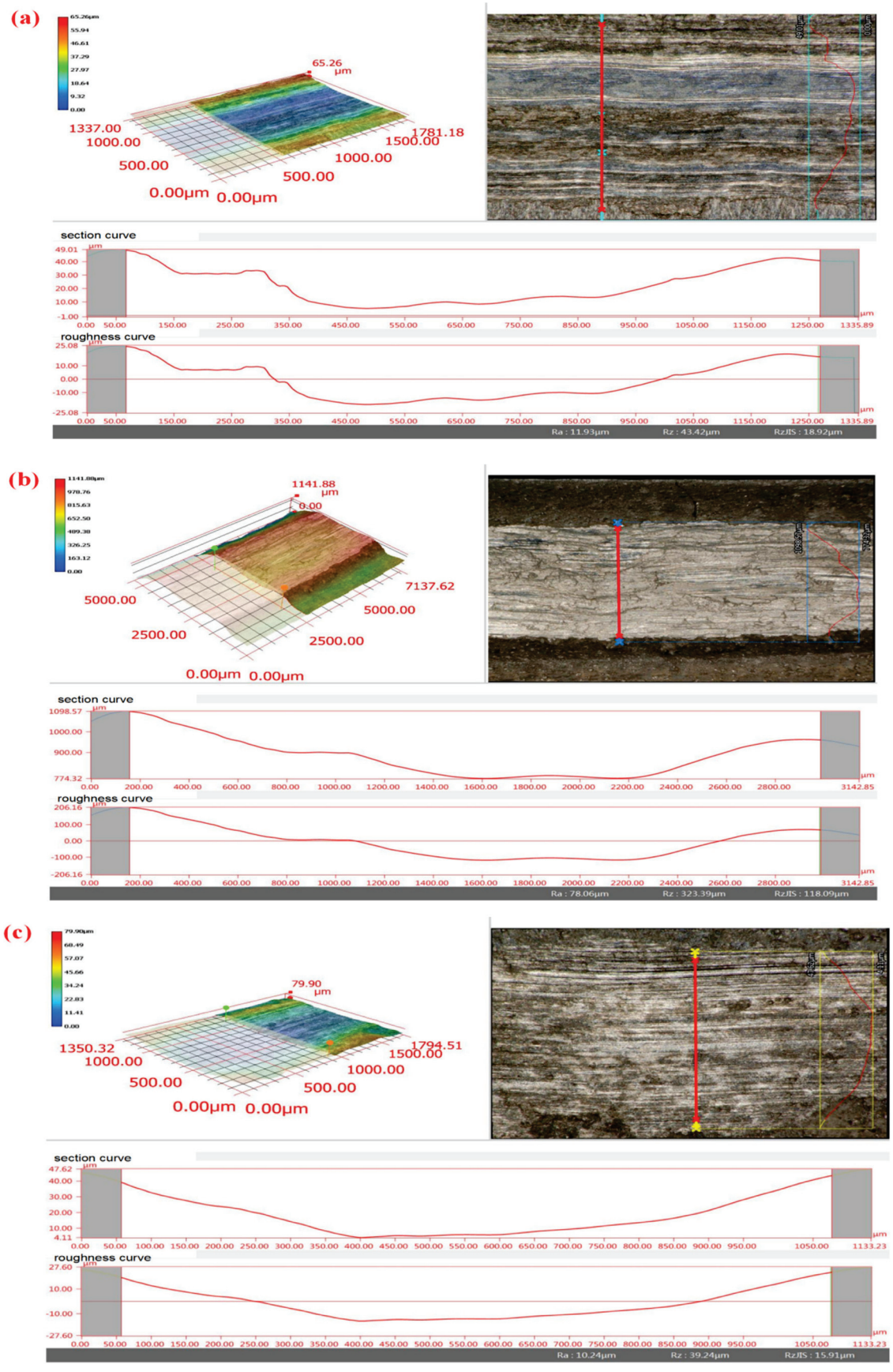


Figure 14. *Cont.*

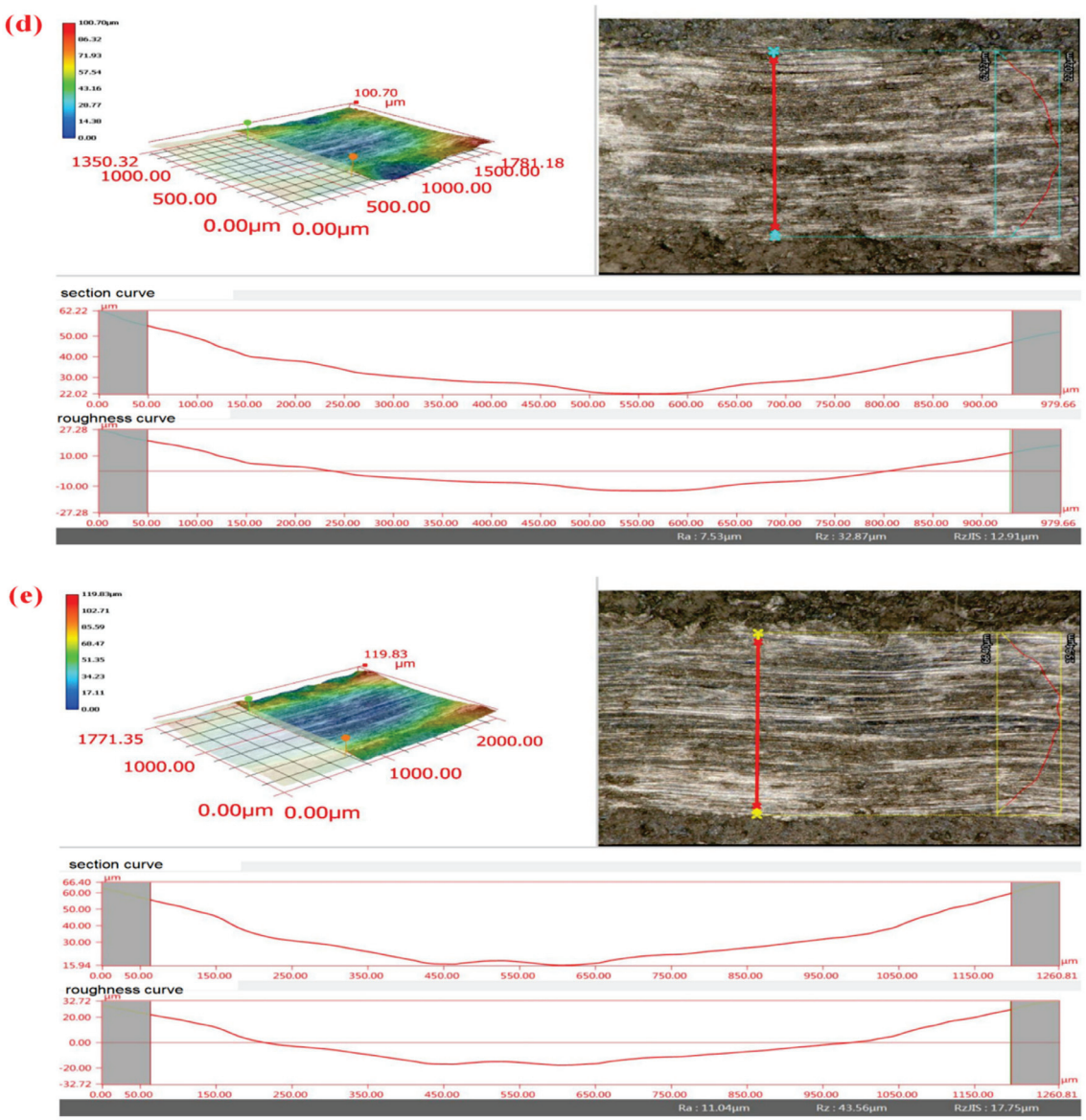


Figure 14. Friction and wear morphology and microstructure of the four coatings. (**a**) Substrate; (**b**) AlSi10Mg; (**c**) AlSi10Mg + 20%WC; (**d**) AlSi10Mg + 40%WC; (**e**) AlSi10Mg + 60%WC.

From the above Figure 14, it can be seen that the coating cross-section curves are all low in the middle and high on both sides, showing a concave tendency; the concave tendency is Rz(b) > Rz(e) > Rz(a) > Rz(c) > Rz(d) in descending order, the highest degree of concavity is 323.39 μm for the AlSi10Mg coating Rz(b), and the lowest degree of concavity is 32.87 μm for the AlSi10Mg + 40% WC coating Rz(d) 32.87 μm; and the roughness size from high to low is Ra(b) > Rz(a) > Ra(e) > Ra(c) > Ra(d), the largest coating roughness is 78.06 μm for AlSi10Mg coating Ra(b), and the smallest one is 7.53 μm for AlSi10Mg + 40%WC coating Ra(d). The analysis of the two data sets and the coating weight loss Figure 14b reveals that the AlSi10Mg coating exhibits low hardness, with a significant accumulation of coating powder in the friction pair resulting in high weight loss. Consequently, the coating demonstrates poor hardness and limited wear resistance. However, upon incorporating 40% WC ceramic powder into the coating, there is a substantial increase in its hardness while minimising powder adhesion in the friction pair and reducing weight loss to a minimum. This optimised performance can be attributed to WC powder's higher melting point compared to AlSi10Mg powder coating.

4. Conclusions

(1) The exploration of laser cladding process parameters and the optimisation of orthogonal tests through the selection of the lowest dilution rate and suitable melt width, as well as a comprehensive analysis of the macro-morphology, the optimal process parameters were finally determined to be P = 4400 W, V_f = 11.3 g·min^{-1}, and V_S = 1800 mm·min^{-1}.

(2) By incorporating WC enhanced phase, the cladding layer facilitates the reaction between metal elements and WC, resulting in an abundance of hard compounds within the coating. This leads to the emergence of new phases such as W_2C, Al_4C_3, and Al_4SiC_4 in the cladding layer. Additionally, there is an increased presence of nucleation particles and a distribution of WC at grain boundaries. Consequently, this delays grain growth and refines the microstructure of the coating, ultimately improving its overall quality. Simultaneously, by introducing solid solution strengthening through aluminum's incorporation with atoms like W, Mg, and Cu in the cladding layer; it causes a shift in grain growth direction within the middle region of the said layer while inducing dislocation among grains. The interaction between phase interfaces and grains exhibits a pinning effect that further enhances microstructural refinement by promoting multi-directional grain growth.

(3) The average hardness and abrasion resistance of the coatings increased with the increase in WC additive amount, and when the additive amount was 40%, the macroscopic morphology was good, and no spalling was found in the friction and wear morphology, and the lowest friction factor, which indicated that the abrasion resistance was the best; however, when the additive amount was 60%, there were obvious macroscopic cracks in the coatings and obvious spalling in the friction and wear morphology, and the quality of the coatings was reduced. The result is consistent with experimental predictions.

Author Contributions: Conceptualization, X.F.; formal analysis, X.F. and X.L.; methodology, X.F.; investigation, X.F. and F.W.; data curation, X.F. and Z.L.; writing—original draft, X.F.; writing—review and editing, X.F. and F.W; visualization, Z.L. and W.W. All authors have read and agreed to the published version of the manuscript.

Funding: This research was funded by the Tianchi Doctor of Philosophy Program of Xinjiang Uygur Autonomous Regions (No. 610221023).

Institutional Review Board Statement: Not applicable.

Informed Consent Statement: Informed consent was obtained from all subjects involved in this study.

Data Availability Statement: Data are contained within the article.

Conflicts of Interest: The authors declare no conflict of interest.

References

1. Fan, J.; Sang, J.; Shi, L. Research, Development and Application of Particulate Reinforced Aluminum Matrix Composites. *Mater. Her.* **2001**, *10*, 55–57.
2. Adebisi, A.A.; Maleque, M.A.; Rahman, M.M. Metal Matrix Composite Brake Rotor: Historical Development and Product Life Cycle Analysis. *Int. J. Automot. Mech. Eng.* **2011**, *4*, 471–480. [CrossRef]
3. Read, N.; Wang, W.; Essa, K. Selective laser melting of AlSi10Mg alloy: Process optimisation and mechanical properties development. *Mater. Des.* **2014**, *65*, 417–424. [CrossRef]
4. Yu, K.B.; Liu, Y.Z.; Yang, C.Y. Effects of heat treatment on microstructures and mechanical properties of AlSi10Mg alloy produced by selective laser melting. *Powder Metall. Mater. Sci. Eng.* **2018**, *23*, 298–305.
5. Kempenk, K.; Thijs, L.; Yasa, E. Process optimization and microstructural analysis for selective laser melting of AlSi10Mg. *Solid Free Fabr. Symp.* **2011**, *22*, 484–495.
6. Brand, E.; Heckenberger, U.; Holzinger, V. Additive manufactured AlSi10Mg samples using selective laser melting (SLM): Microstructure, high cycle fatigue, and fracture behavior. *Mater. Des.* **2012**, *34*, 159–169. [CrossRef]
7. Kempen, K.; Thijs, L.; Van, H.J. Mechanical properties of AlSi10Mg produced by selective laser melting. *Phys. Procedia* **2012**, *39*, 439–446. [CrossRef]
8. Buchbinder, D.; Schleifenbaum, H.; Heidrich, S. High power selective laser melting (HP SLM) of aluminum parts. *Phys. Procedia* **2011**, *12*, 271–278. [CrossRef]
9. Manfredi, D.; Calignano, F.; Krishnan, M. From powders to dense metal parts: Characterization of a commercial AlSi10Mg alloy processed through direct metal laser sintering. *Materials* **2013**, *6*, 856–869. [CrossRef]

10. Thijs, L.; Kempen, K.; Kruth, J.P. Fine-structured aluminum products with controllable texture by selective laser melting of pre-alloyed AlSi10Mg powder. *Acta Mater.* **2013**, *61*, 1809–1819. [CrossRef]
11. Godino Martinez, M. AlSi10Mg Parts Produced by Selective Laser Melting (SLM). Ph.D. Thesis, Universidad Carlos III de Madrid, Getafe, Spain, 2013.
12. Ashwath, P.M.; Xavior, A.; Batako, A.; Jeyapandiarajan, P.; Joel, J. Selective laser melting of Al–Si–10 Mg alloy: Microstructural studies and mechanical properties assessment. *J. Mater. Res. Technol.* **2022**, *17*, 2249–2258. [CrossRef]
13. Aboulkhair, N.T.; Everitt, N.M.; Ashcroft, I.; Tuck, C. Reducing porosity in AlSi10Mg part processed by selective laser melting. *Addit. Manuf.* **2014**, *1*, 77–86. [CrossRef]
14. Bartkowiak, K.; Ullrich, S.; Frick, T. New developments of laser processing aluminum alloys via additive manufacturing technique. *Phys. Procedia* **2011**, *12*, 393–401. [CrossRef]
15. Buchbinder, D.; Meiners, W.; Wissenbach, K. Selective laser melting of aluminum die-cast alloy correlations between process parameters, solidification conditions, and resulting mechanical properties. *J. Laser Appl.* **2015**, *27*, S29205. [CrossRef]
16. Dong, P.; Li, Z.H.; Yan, Z.Y. Research Status of Selective Laser Melting of Aluminum Alloys. *Appl. Laser* **2015**, *35*, 607–611.
17. Vencl, A.; Ivanović, L.; Stojanović, B.; Zadorozhnaya, E.; Miladinović, S.; Svoboda, P. Surface texturing for tribological applications: A review. *Proc. Eng. Sci.* **2019**, *1*, 227–239. [CrossRef]
18. Stanković, M.; Marinković, A.; Grbović, A.; Mišković, Ž.; Rosić, B.; Mitrović, R. Determination of Archard's wear coefficient and wear simulation of sliding bearings. *Ind. Lubr. Tribol.* **2019**, *71*, 119–125. [CrossRef]
19. Zhang, K.; He, C.; Lin, Y. Microstructures and mechanical properties of laser cladding repaired 5A06 alloys. *Laser Optoelectron. Prog.* **2020**, *57*, 231409. [CrossRef]
20. Grohol, C.M.; Shin, Y.C.; Frank, A. Laser cladding of aluminum alloy 6061 via off-axis powder injection. *Surf. Coat. Technol.* **2021**, *2*, 127099. [CrossRef]
21. Li, X.; Peng, J.H. Effect of Electrically Assisted Preheating on Microstructure and Properties of Laser-Cladded Co-Based Coating on CP-Ti Alloy Substrate. *Coatings* **2023**, *13*, 1379. [CrossRef]
22. Meinert, J.; Kenneth, C.; Patric, B. Refurbishment of aluminum alloys by laser cladding. In *International Congress on Applications of Lasers & Electro-Optics*; AIP Publishing: Woodbury, NJ, USA, 1999; pp. F49–F57.
23. Grohol, C.M.; Shin, Y.C.; Frank, A. Laser cladding of aluminum alloys with concurrent cryogenic quenching for improved microstructure and hardness. *Surf. Coat. Technol.* **2022**, *439*, 128460. [CrossRef]
24. Stanković, M.; Marinković, A.; Kolarević, N. Wear simulation of the polymer based composite sliding bearings by means of ansys. In Proceedings of the 16th International Conference on Tribology, Kragujevac, Serbia, 15–17 May 2019.
25. Picas, J.A.; Punset, M.; Baile, M.T. Properties of WC-CoCr Based Coatings Deposited by Different HVOF Thermal Spray Processes. *Plasma Process. Polym.* **2010**, *6*, S948–S953. [CrossRef]
26. He, B.F.; Ma, F.; Ma, D.Y. Study of microstructure and properties of laser cladding Ni60-WC+TiC composte coating. *Sci. Adv. Mater.* **2020**, *12*, 659–664. [CrossRef]
27. Bartkowski, D.; Mynarczak, A.; Piasecki, A. Microstructure, microhardness and corrosion resistance of Stellite-6 coatings reinforced with WC particles using laser cladding. *Opt. Laser Technol.* **2015**, *68*, 191–201. [CrossRef]
28. Enrici, T.M.; Dedry, O.; Boschini, F. Microstructural and Thermal Characterization of 316L+WC Composite Coatings Obtained by Laser Cladding. *Adv. Eng. Mater.* **2020**, *22*, 2000291. [CrossRef]
29. Wang, J.D.; Li, L.Q.; Tao, W. Crack initiation and propagati on behavior of WC particles reinforced Fe-based metal matrix composite produced by laser meltingdeposition. *Opt. Laser Technol.* **2016**, *82*, 170–182. [CrossRef]
30. Mostajeran, A.; Shoja-Razavi, R.; Hadi, M. Evaluation of the mechanical properties of WC-FeAl composite coating fabricated by laser cladding method. *Int. J. Refract. Met. Hard Mater.* **2020**, *88*, 105199. [CrossRef]
31. Ortiz, A.; Garía, A.; Cadenas, M. WC particles distribution model in the cross-section of laser cladded NiCrBSi+WC coatings for different wt% WC. *Surf. Coat. Technol.* **2017**, *324*, 298–306. [CrossRef]
32. Man, H.C.; Yang, Y.Q.; Lee, W.B. Laser induced reaction synthesis of TiC+WC reinforced metal matrix composites coating on Al 6061. *Surf. Coat. Technol.* **2004**, *185*, 74–80. [CrossRef]
33. Ma, Q.; Lu, B.; Zhang, Y.; Wang, Y.; Yan, X.; Liu, M.; Zhao, G. Crack-free 60 wt% WC reinforced FeCoNiCr high-entropy alloy composite coating fabricated by laser cladding. *Mater. Lett.* **2022**, *324*, 132667. [CrossRef]
34. Ji, S.; Li, J.; Yang, H.; Wang, S.; Qiao, J.; Wen, Q. Deposition Behavior of HVOF Sprayed WC-12Co Particles on AA7075. *Rare Met. Mater. Eng.* **2023**, *52*, 3345–3354.
35. Yu, B.B. Microstructure and Properties of AlSi5Cu1Mg Alloy with Rare Earth and Laser Cladding. Master's Thesis, Nanchang University, Nanchang, China, 2019.
36. Chen, L.; Chen, W.; Li, D.; Jing, P.; Yin, H.; Wu, H.; Xie, Y.; Wang, X. Effect of nano-La_2O_3 doping on the tribological behavior of laser cladded WC-12Co coating on 65Mn steel under water lubrication condition. *Tribol. Int.* **2022**, *169*, 107428. [CrossRef]
37. Zhang, S.M.; Sun, W.L.; Wang, K.D. Optimum Selection of Laser Cladding Process Parameters Based on Orthogonal Test. *Mod. Manuf. Technol. Equip.* **2019**, *6*, 190–191+193.
38. Anandkumar, R.; Almeida, A.; Colaco, R. Microstructure and wear studies of laser clad Al-Si/SiC(p) composite. *Surf. Coat. Technol.* **2007**, *201*, 9494–9505. [CrossRef]
39. Hu, D.; Liu, Y.; Chen, H.; Liu, J.; Wang, M.; Deng, L. Microstructure and properties of Ta-reinforced NiCuBSi + WC composite coating deposited on 5Cr5MoSiV1 steel substrate by laser cladding. *Opt. Laser Technol.* **2021**, *142*, 107210. [CrossRef]

40. Chen, Y.; Gong, W.; Kang, R. Coupling Behavior between Adhesive and Abrasive Wear Mechanism of Aero-Hydraulic Spool Valves. *Chin. J. Aeronaut.* **2016**, *29*, 1119–1131.
41. Sousa, J.M.S.D.; Ratusznei, F.; Pereira, M.; Castro, R.D.M.; Curi, E.I.M. Abrasion Resistance of Ni-Cr-B-Si Coating Deposited by Laser Cladding Process. *Tribol. Int.* **2020**, *143*, 106002. [CrossRef]

Disclaimer/Publisher's Note: The statements, opinions and data contained in all publications are solely those of the individual author(s) and contributor(s) and not of MDPI and/or the editor(s). MDPI and/or the editor(s) disclaim responsibility for any injury to people or property resulting from any ideas, methods, instructions or products referred to in the content.

coatings

Article

Study on the Microstructure and Properties of FeCoNiCrAl High-Entropy Alloy Coating Prepared by Laser Cladding-Remelting

Tianyi Lv, Wenkai Zou, Jiaqi He, Xiang Ju and Chuanbo Zheng *

School of Metallurgy and Materials Engineering, Jiangsu University of Science and Technology, Zhenjiang 212100, China; ltyyyasmy@gmail.com (T.L.); z984731733@gmail.com (W.Z.); 17348673267@163.com (J.H.); 18232560007@163.com (X.J.)
* Correspondence: 15952802516@139.com

Abstract: Laser remelting technology effectively repairs defects such as pores and cracks in the coating. To investigate the impact of laser remelting on high-entropy alloy coatings, this study used Q235 steel as the substrate and employed laser cladding technology to prepare FeCoNiCrAl high-entropy alloy coatings, followed by laser remelting treatment. The phase composition and microstructure of the coatings were extensively characterized using equipment such as optical microscopy, X-ray diffraction (XRD), and scanning electron microscopy (SEM). Additionally, the wear resistance and corrosion resistance of the coatings were tested using a multifunctional material surface performance tester, an electrochemical workstation, and SVET (Scanning Vibrating Electrode Technique). The results indicate that following laser remelting treatment, the atomic proportion of Fe elements on the coating surface decreased from 33.21% to 26.03%, while the atomic proportion of Al elements increased from 12.56% to 20.31%. The phase composition of the coating underwent a marked transformation, shifting from a structure composed of FCC, A2, and B2 phases to a singular BCC structure characterized by the presence of A2 and B2 phases. Concurrently, the grain morphology on the coating surface transitioned from elongated plate-like grains to equiaxed grains. Laser remelting enhanced the wear resistance of the coating. Laser remelting had no significant impact on the corrosion resistance of the non-cracked regions of the coating.

Keywords: high-entropy alloys coatings; laser cladding; laser remelting; corrosion; microstructure

1. Introduction

As the industrial sector advances, the demand for metal materials in industrial settings has become increasingly rigorous. Merely altering the composition and structure of the material is insufficient to fully enhance numerous properties of the material. By preparing a protective coating on the surface of the matrix material, the properties of the matrix material are maintained and the abrasion and corrosion resistance of the material in the service environment is improved [1]. The combination of high entropy, slow diffusion, lattice distortion, and cocktail effects such as excellent corrosion resistance [2], high microhardness [3], good abrasion resistance [4], and excellent high-temperature antioxidant properties [5] makes high-entropy alloys a promising option for protective coating additive manufacturing. Different techniques can be employed to create high-entropy alloy coatings, such as magnetron sputtering [6], cold spraying [7], plasma spraying [8], high-speed oxygen fuel spraying [9], electrochemical deposition [10], and laser cladding [11]. Laser cladding has a strong bond with the substrate, making it a popular choice for the fabrication and exploration of high-entropy alloy coatings [11].

Rapid heating and cooling during laser cladding causes thermal stress to the coating material. Various components of the material may enlarge and shrink at varying speeds, resulting in fissures appearing on the surface [12]. Undoubtedly, repreparing the coating

increases costs, so there is an urgent need to find a cost-effective solution. In order to repair surface defects and enhance material properties, laser modification technology is widely applied in the field of materials [13]. Laser remelting is a commonly used technique in laser modification. By combining laser rapid solidification and chemical (Sr) modification, Ghosh et al. [14] synthesized a fully eutectic Al-Si microstructure with heavily twinned silicon nanofibers, which has high hardness up to 2.9 GPa and high compressive flow strength (~840 MPa) with a plastic flow that stabilizes to approximately 26% plastic strain. Wu et al. [15] combined the advantages of laser remelting and micro-arc oxidation to prepare a graded structure wear-resistant coating on the surface of titanium alloy, enhancing the wear resistance of the titanium alloy surface. Wang et al. [16] used laser cladding and laser remelting to fabricate iron-based amorphous coating on H13 steel. The results showed that the cracks and stomata defects on the coating decreased significantly. Jin et al. [17] prepared iron-based amorphous and nanocrystalline coatings by plasma spraying and performed laser remelting. Chen et al. [18] improved the density and surface quality of $FeCrCoNiAl_{0.6}$ high-entropy alloy coatings; in order to do this, the coating was prepared and laser remelted using high velocity oxygen fuel (HVOF). The results showed that the friction coefficient of the remelting coating was significantly lower than that of the HVOF coating and no sputtering stratification or cracks were observed in the remelted coating. Some studies indicate that laser remelting technology also enhances the corrosion resistance of the material surface. Al-Sayed et al. [19] conducted laser surface treatment on Ti-6Al-4V alloy. Laser treatment produced a transformed layer with acicular martensite α'-Ti as a result of the recrystallization of the fully lamellar α + β microstructure of the substrate. The results indicated that ultra-short pulses (in nanosecond scale) from a Nd:YAG laser effectively enhanced the corrosion resistance of this alloy in acidic media (Ringer's solution). Liu et al. [20] conducted laser remelting treatment on the surface of TA15 alloy. The results indicate that as energy density increases, the corrosion rate decreases first and then increases. With an energy density of 8.75 $J{\cdot}cm^{-2}$, the surface corrosion rate was 20.43 times slower than that of the untreated sample.

Currently, there is a lack of research into laser remelting to improve the coating of high-entropy alloy. Further investigation is necessary to determine the alterations in the element distribution, microstructure, and properties of the coating following remelting. AlCoCrFeNi HEA systems have attracted increasing attention due to their light weight and low cost [21]. Coaxial powder feeding laser cladding was used to create a high-entropy alloy coating of FeCoNiCrAl on Q235 steel in this study. In this study, the Scanning Vibrating Electrode Technique (SVET) was employed in addition to the kinetic potential and electrochemical impedance techniques typically utilized in prior research to gauge and analyze the corrosion potential produced by the microregion of the remelted coating. The influence of remelting on the corrosion resistance of the coating was further explored due to SVET's capability to display local cathode and anode reactions [22].

2. Experimental Procedures

2.1. Materials

Laser cladding was employed to create a coating of FeCoNiCrAl high-entropy alloy. Using a Q235 plate of 130 mm × 130 mm × 10 mm as a substrate, the cladding material was FeCoNiCrAl High-Entropy Alloy Powder with 53–105 μm diameter produced by vacuum atomization of cladding. (See Figure 1).

2.2. Laser Cladding and Laser Remelting Process

Before the thermal spraying process, the oxide film on the substrate surface was polished using a grinding wheel, and any grease was removed by cleaning with anhydrous ethanol. The substrate was preheated to 200 °C, with a laser power of 1200 W, a scanning speed of 300 mm/min, a spot diameter of 4 mm, and the use of coaxial powder feeding at a rate of 20 g/min. The entire process was carried out under an argon gas shield with a flow rate of 2 L/min. The laser remelting was performed at a power of 800 W, a scanning

speed of 500 mm/min, and a spot diameter of 4 mm. To reduce surface roughness and ensure uniformity, the scanning direction was perpendicular to the direction of the thermal spraying [23], as shown in Figure 2:

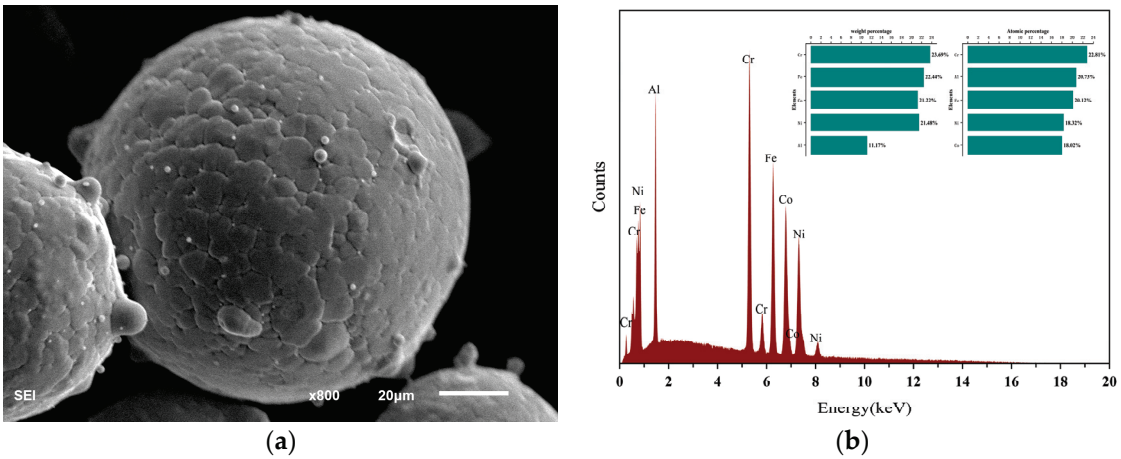


Figure 1. FeCoNiCrAl high-entropy alloy powder: (**a**) micromorphology; (**b**) element content.

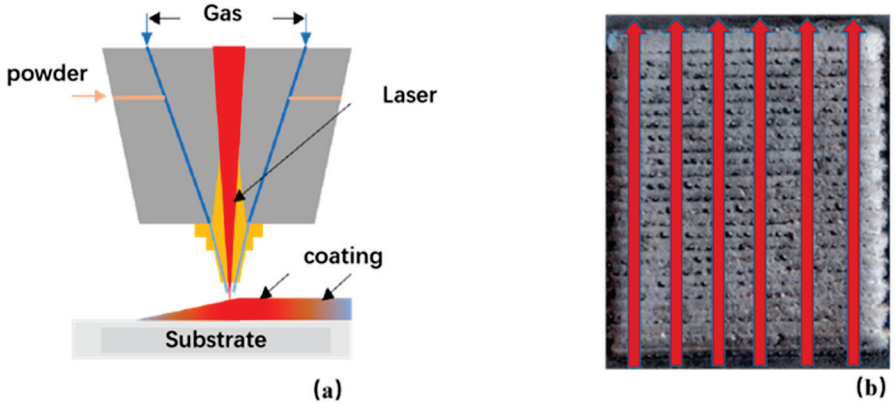


Figure 2. Schematic representation of laser cladding and remelting: (**a**) laser cladding with coaxial powder feeding; (**b**) laser remelting direction.

2.3. Characterization

Following the process of cutting the laser cladding and remelting the coating to a thickness of 10 mm × 10 mm × 10 mm, sanding and polishing the coating's cross-section using wire cutters, and corroding it with king water (hydrochloric acid: nitric acid = 3:1), the microstructure and phase composition of the coated samples were subsequently examined using optical microscopy (Axio Scope A1), scanning electron microscopy (JSM-6510LA), and an Ultima IV X-ray diffractometer (XRD). The X-ray diffraction analysis focused on the Cu target, which had a scanning rate of 0.02°/s and a scanning angle from 20° to 80°.

An HVS-1000A Micro Vickers scale hardness meter was used to measure the hardness of the coating cross-section, which was then measured at a distance of 0.1 mm from the substrate to the top of the coating. The coating had a payload of 200 g and a retention time of 15 s. The friction performance of the coating was assessed using the MFT-4000 multifunctional material surface performance tester.

ZenniumE4 electrochemical workstations were used to conduct electrochemical corrosion experiments on the samples, with the saturated glycerine electrode as the reference electrode and the platinum electrode as the three-electrode measurement system. A Princeton VersaSCAN Microscan Electrochemical Workstation (AMETEK, Inc., Berwyn, PA, USA) was utilized for microelectrochemical testing, with potentiometric scanning ranging from −1 to 1.5 V, frequency ranging from 0.01 to 10^5 HZ, and scanning speed of 0.001 V/s. An

investigation was conducted on the microcorrosion of coatings in SVET technology. The frequency selection was set at 5 KHz, the scanning area spanned 1 mm × 1 mm, and the step length measured 40 μm.

3. Results

3.1. Pahse

The XRD spectra of FeCoNiCrAl HEA powders and coatings are shown in Figure 3. The powders exhibit a single BCC structure, including an Al-Ni-rich BCC(B2) phase, and a Fe-Cr rich disordered BCC(A2) phase. The HEA coating prepared by laser melting contains FCC, A2, and B2 phases. After the coatings were treated by laser remelting, the diffraction peaks of the phase representing FCC disappeared, and only the peaks of the A2 and B2 phases were detected in the XRD tests. Based on the Bragg equation, the lattice parameters of the FCC, A2, and B2 phases were calculated as shown in Table 1.

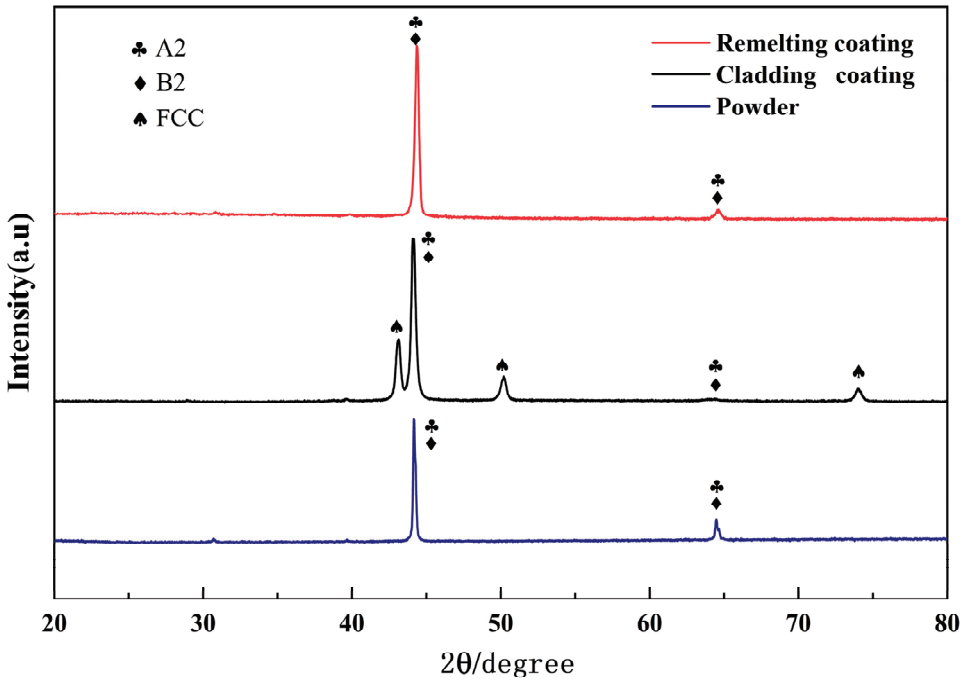


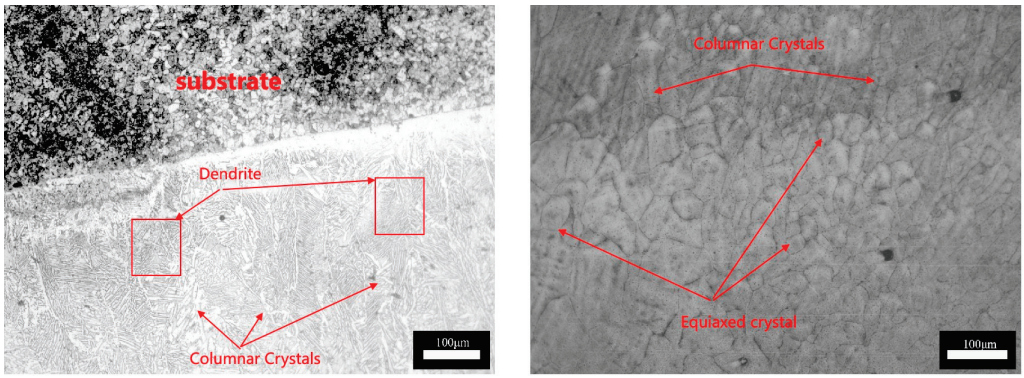
Figure 3. XRD diffraction pattern.

Table 1. Lattice parameter (Å).

Sample	FCC	A2	B2
Cladding coating	3.581	2.872	2.871
Remelting coating		2.875	2.873

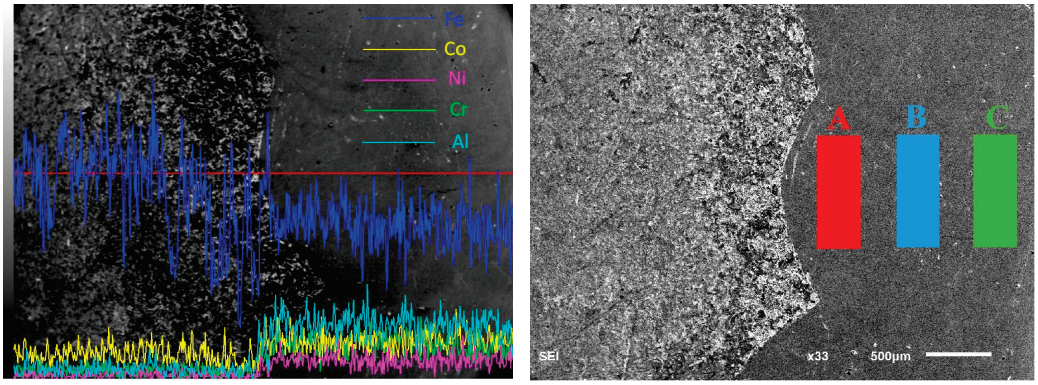
3.2. Microstructure Characterization

Figure 4 shows the cross-sectional morphology of laser cladding under an optical microscope, and there are apparent bonding lines between the coating and substrate. The bottom and middle parts of the coating are mainly dominated by dendritic crystal distribution, containing a small number of columnar crystals. As the distance from the substrate increases, columnar crystals and equiaxed crystals begin to appear in the upper and middle parts of the coating. Figure 5 shows the EDS scan of the elemental content of the coating cross-section. From the line scan results, it can be seen that during the laser cladding process, due to the dilution effect, the Fe in the coating diffuses into the coating, and with the increase in the distance from the substrate, the Fe elemental content decreases gradually, and the content of the Al element in the coating increases, thus promoting the transformation from dendritic crystals to equiaxed grains. (See Table 2).



(**a**) (**b**)

Figure 4. Cross-sectional microstructure of the coating: (**a**) midsection of the coating; (**b**) top section of the coating.



(**a**) (**b**)

Figure 5. Elemental distribution in the cross-section of the coating: (**a**) linear scanning (**b**) selected area scanning.

Table 2. EDS results of FeCoNiCrAl high-entropy alloy coatings (At%).

	Fe	Co	Ni	Cr	Al
A	39.77	14.96	13.55	14.69	17.03
B	32.50	18.13	12.74	16.31	20.31
C	31.65	17.46	17.39	14.65	18.85

Figure 6a shows the micromorphology of the surface of the FeCoNiCrAl high-entropy alloy coating prepared by laser melting cladding, which is mainly distributed with elongated plate-like grains and some fine grains. After the coating was laser remelted as shown in Figure 6b, the grain structure of the coating surface was transformed into equiaxed grains. To determine whether there is any elemental segregation on the coating surface, the coating before and after remelting was analyzed by surface scanning, and the results are shown in Figures 7 and 8. It can be seen that there is no obvious elemental segregation in the coating before and after remelting, and the five elements of Fe, Co, Ni Cr, and Al are uniformly distributed in the grain boundaries. However, the proportion of each element in the coating changed significantly after remelting. After remelting, the atomic ratio of Fe decreased from 33.21% to 26.03% and the atomic ratio of Al increased from 12.56% to 20.31%, which may be the reason for the transformation of the grain structure of the coating surface.

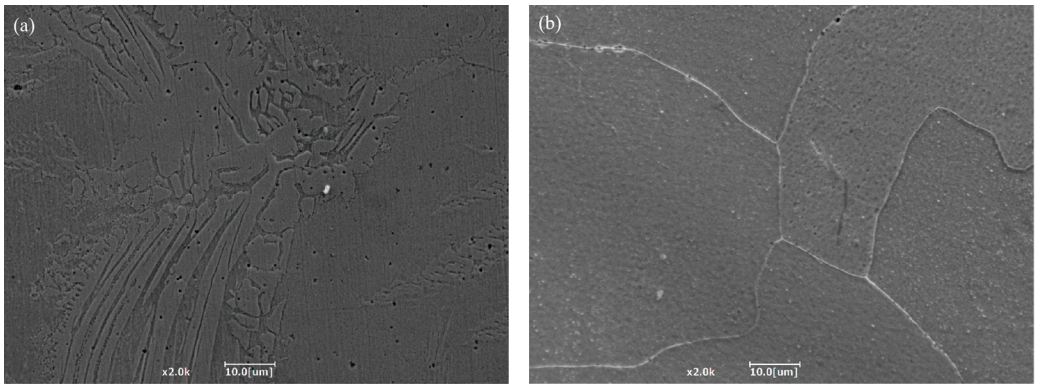


Figure 6. SEM images of the coating surfaces: (**a**) cladding coating; (**b**) remelting coating.

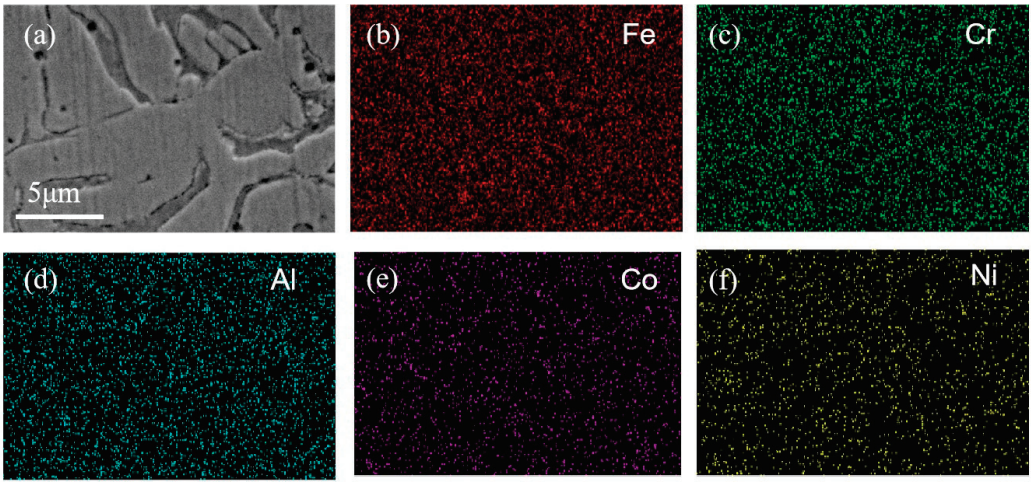


Figure 7. EDS mapping of FeCoNiCrAl high-entropy alloy coatings: (**a**) cladding coating; (**b**) Fe; (**c**) Cr; (**d**) Al; (**e**) Co; (**f**) Ni.

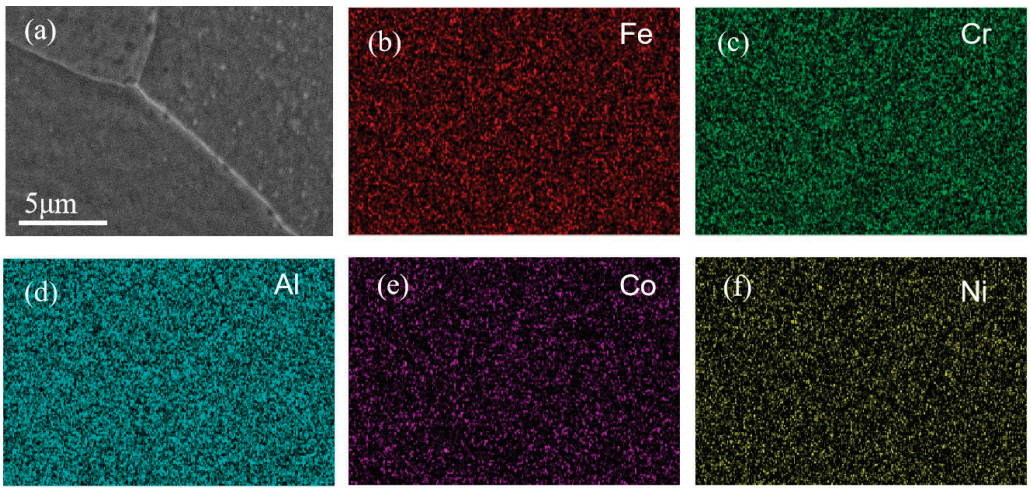


Figure 8. EDS mapping of FeCoNiCrAl high-entropy alloy coatings: (**a**) remelting coating; (**b**) Fe; (**c**) Cr; (**d**) Al; (**e**) Co; (**f**) Ni.

3.3. Microhardness and Wear Resistance of Coatings

Figure 9 shows the microhardness distribution of the laser cladding coating and laser remelting coating. The hardness test is conducted at 12 point intervals, with each interval measuring 0.1 mm from the junction of the coating and substrate, perpendicular to the

direction of the cross-section to the coating's surface. The diagram indicates that the coating and substrates have a hardness of approximately 250 to 300 $Hv_{0.2}$ at the junction and 500 to 600 $Hv_{0.2}$ at a distance of 0.4 mm to 0.6 mm from the coating's surface. The remelting area experiences a gradual increase in microhardness, specifically within the range of 0 to 0.4 mm from the coating's surface. The coating exhibited a microhardness of 613 $Hv_{0.2}$ and 754 $Hv_{0.2}$, correspondingly, until it underwent fusion and subsequent remelting. The laser-remelted coating exhibited a 23% increase in hardness in comparison to the non-remelted coating.

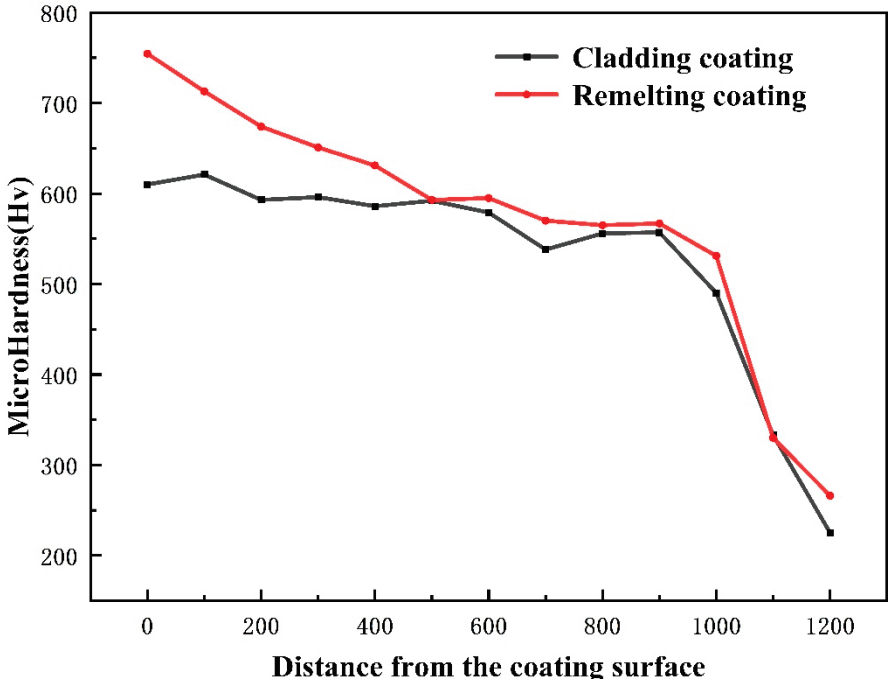


Figure 9. Hardness distribution across the coating cross-section.

Figure 10 shows the friction coefficients of the coating surface after 15 min of reciprocating friction experiments. The laser-remelted coating exhibits a lower friction coefficient of 0.345, whereas the non-remelted coating has an average friction coefficient of 0.431. To provide a more intuitive representation of the wear resistance of the coating, measurement of the wear volume of the coating was conducted. A profilometer was utilized to measure the cross-sectional area (s) of the wear track along a direction perpendicular to the direction of the frictional wear, as illustrated in Figure 11. The measurement was performed three times, and the average value was calculated. The formula for calculating the wear volume (V) is as follows:

$$V = s \times h$$

where h is the wear scar length and s is the wear scar cross-sectional area.

Following the remelting treatment of the coating, there was a reduction in wear volume. The coating that underwent remelting exhibited a smaller wear volume of 2.55×10^{-4} cm^3, whereas the unmelted coating displayed a larger wear volume of 7.45×10^{-4} cm^3. It was observed that the wear resistance of the coating is directly proportional to its hardness. The laser remelting process can significantly enhance the wear resistance of the FeCoNiCrAl high-entropy alloy coating, possibly attributable to the enrichment of Al and Ni within the grain interiors after remelting, leading to the formation of hard phases.

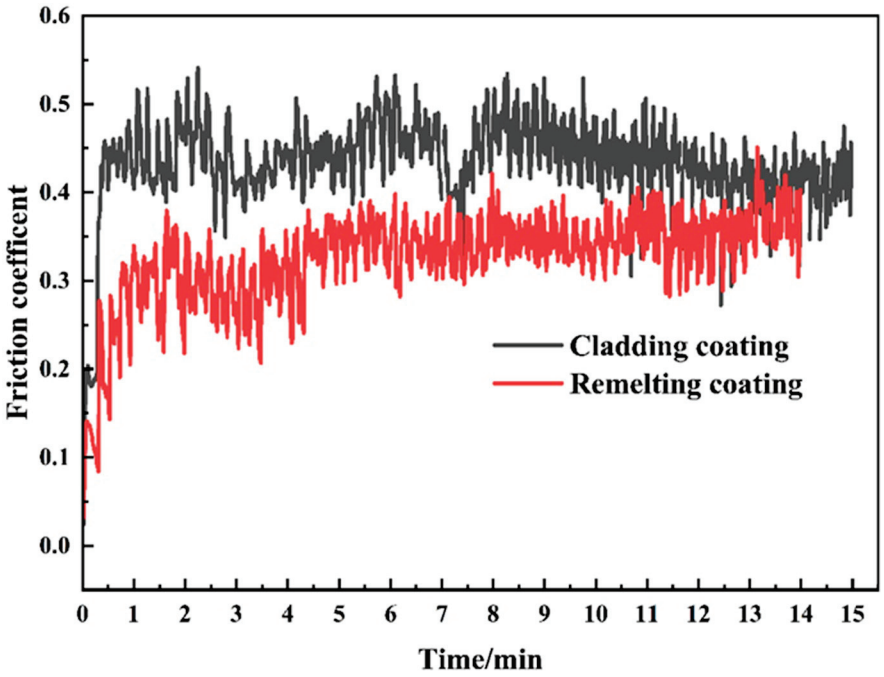


Figure 10. Friction coefficient.

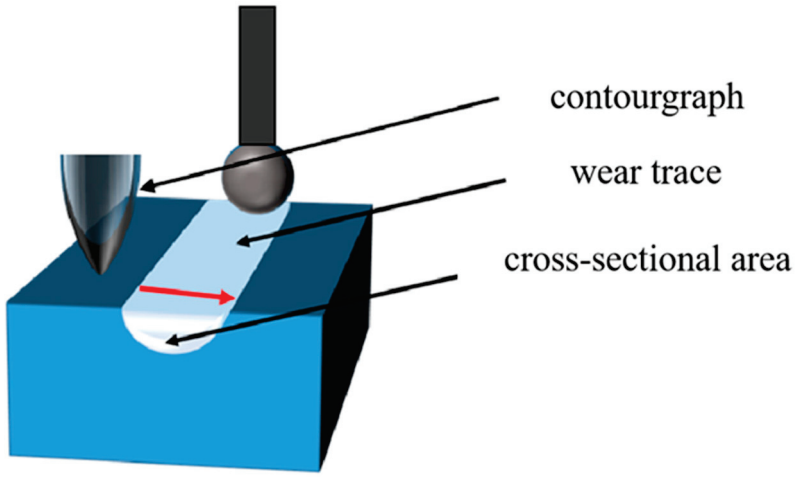


Figure 11. Schematic representation of wear experiment.

3.4. Corrosion Test

In order to investigate the impact of remelting on the corrosion resistance of the coating, electrochemical corrosion tests were conducted on both the substrate and the coating in a 3.5% wt NaCl solution. Figure 12 shows the potentiodynamic polarization curves for the coating and the Q235 substrate, and Tafel extrapolation was employed to determine the relevant parameters.

Figure 12 shows that the FeCoNiCrAl high-entropy alloy coating prepared by laser cladding exhibits the lowest corrosion current density, which is two orders of magnitude lower than the substrate. After remelting, the coating shows an increase in the corrosion potential, indicating a lower susceptibility to corrosion, but there is a slight increase in the corrosion current density. From the specific results of potentiodynamic polarization, as indicated in Table 3, it can be observed that the corrosion resistance of the coating is not significantly affected by laser remelting.

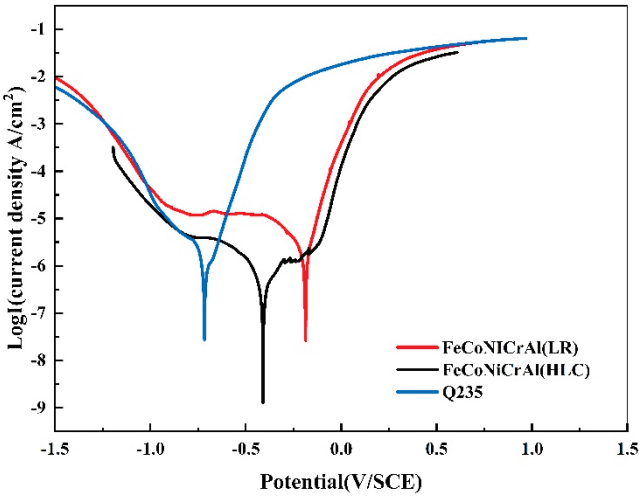


Figure 12. Potentiodynamic polarization curve.

Table 3. EDS results of FeCoNiCrAl high-entropy alloy coatings (At%).

	Fe	Co	Ni	Cr	Al
Cladding coating	33.21	19.12	18.1	17.01	12.56
Remelting coating	26.02	18.03	19.63	16.01	20.31

To further validate the corrosion resistance of the remelted coating, electrochemical impedance testing was conducted. The alternating current impedance curve of the samples is depicted in the graph in Figure 13, which shows the Nyquist plot of the coating in a 3.5% wt NaCl solution. In the plot, Z' represents the real part of impedance, and Z'' represents the imaginary part. The impedance modulus Z is defined as:

$$|Z| = \sqrt{Z\prime^2 + Z''^2}$$

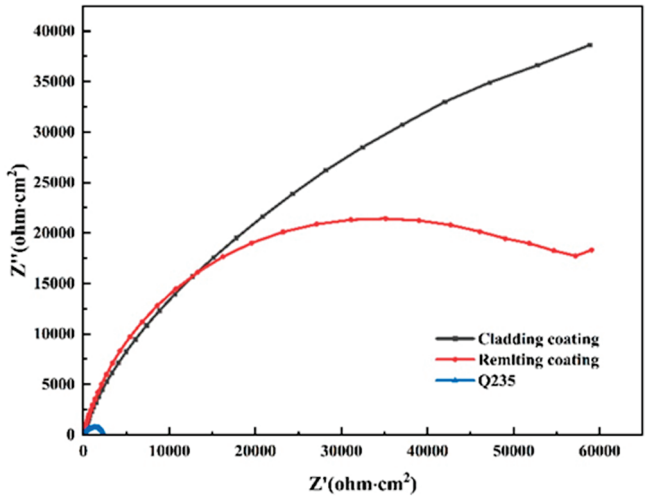


Figure 13. Nyquist plot.

The results, as shown in Figure 13, reveal that the HEA coating exhibits a larger capacitive arc in the high-frequency region, while the Q235 substrate's capacitive arc takes a semi-circular shape, albeit smaller in radius when compared to the coating. The remelting coating displays a significantly smaller capacitive arc radius than the cladding coating, approximately half of the cladding coating's radius. A larger capacitive arc radius indicates

a higher coating resistance, which can effectively protect the substrate from corrosion damage [24]. The corrosion resistance is ranked as follows: cladding coating > remelting coating > substrate.

Figure 14 represents a Bode plot showing the relationship between frequency and |Z|. In an electrochemical system, the system's resistance values change when alternating current is applied at various frequencies. Based on the above analysis, an equivalent circuit was constructed to describe the electrochemical reaction process. Figure 15 represents the equivalent circuit for the three samples in a 3.5% wt NaCl solution. In this circuit, Rs represents the electrolyte resistance and R_{corr} stands for charge transfer resistance, depicting the transfer process between the clad layer and the substrate. To account for the non-uniformity of the electrode surface, Constant Phase Element (CPE) is often used in place of the Q element.

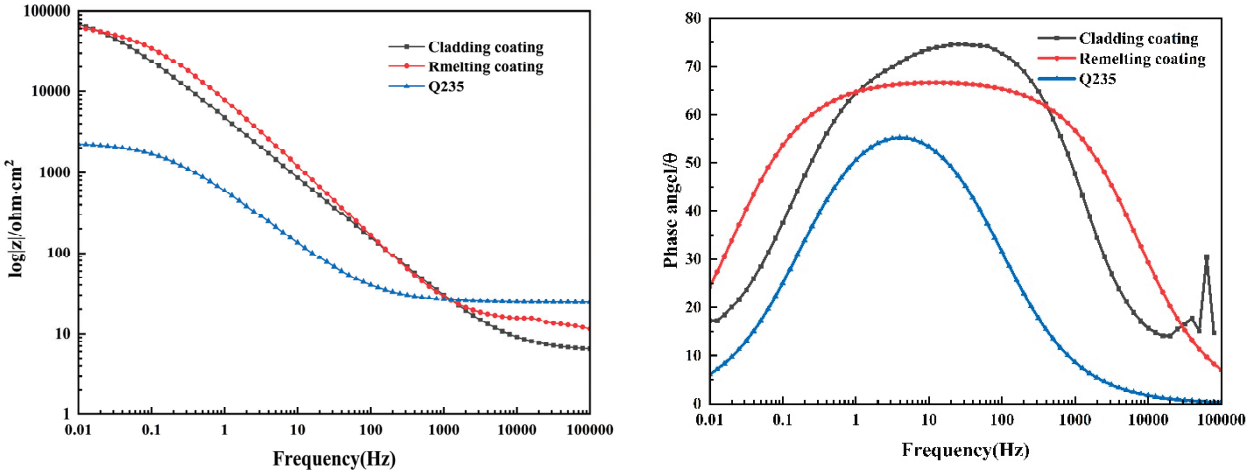


Figure 14. Bode plot.



Figure 15. Equivalent circuit.

The resistance values can be calculated using the following equation:

$$Z = RS + \frac{1}{Y_0(j,\omega)^n}$$

where ω represents the angular frequency, j is the imaginary unit, Y_0 is a frequency-independent constant, and n is the fitting exponent for the CPE (n = 1 represents ideal capacitive behavior and n = 0 represents pure resistance). The fitted data, as shown in Table 4, reveal that the charge transfer resistances for the Q235 substrate, the cladding coating, and the remelting coating are 2343 Ω·cm^2, 91,840 Ω·cm^2, and 59,540 Ω·cm^2, respectively. The charge transfer resistance is a parameter related to the corrosion rate, and the larger the R_{corr} value, the lower the corrosion rate [25]. Therefore, this further confirms that the HEA coating exhibits excellent corrosion resistance compared to the substrate, and laser remelting did not significantly impact the coating's corrosion resistance.

Table 4. EIS fitting data.

	Q235	Cladding Coating	Remelting Coating
R_s	24.37	6.105	15.17
Y_0	4.01×10^{-4}	9.199×10^{-5}	2.65
n	0.72	0.7498	0.8424
R_{corr}	2343	91,840	59,540

3.5. SVET Test

SVET employs microelectrodes, signal converters, and amplifiers to reduce the disruption caused by microscans, thereby enhancing sensitivity and precision in measurements. The low destructiveness, high precision, and high sensitivity of SVET enable it to precisely gauge the electrochemical activity of samples in limited areas [26]. The SVET assay results, depicted in Figure 16, demonstrate the impact of immersing the laser-coated FeCoNiCrAl high-entropy alloy coating in a 3.5 wt% NaCl solution for 48 h, followed by the combination of 3D and 2D flat images. The 3D stereogram can be used to calculate the overall current density, and the SVET scan line can be used to determine the corrosion activity of the defect position, with the microanode and microcathode currents indicated by the peaks and troughs, respectively. The two-dimensional plane diagram illustrates the dispersion of the microanode and microcathode, indicating the diverse electrochemical reactions occurring on the coating's surface when chlorine ions are present. The degree of erosion of the coating by chlorine ions can be determined by analyzing SVET 3D and 2D floor plans. In situ observation of the FeCoNiCrAl high-entropy alloy coating in a 3.5% wt NaCl solution was conducted using SVET, revealing its local current density.

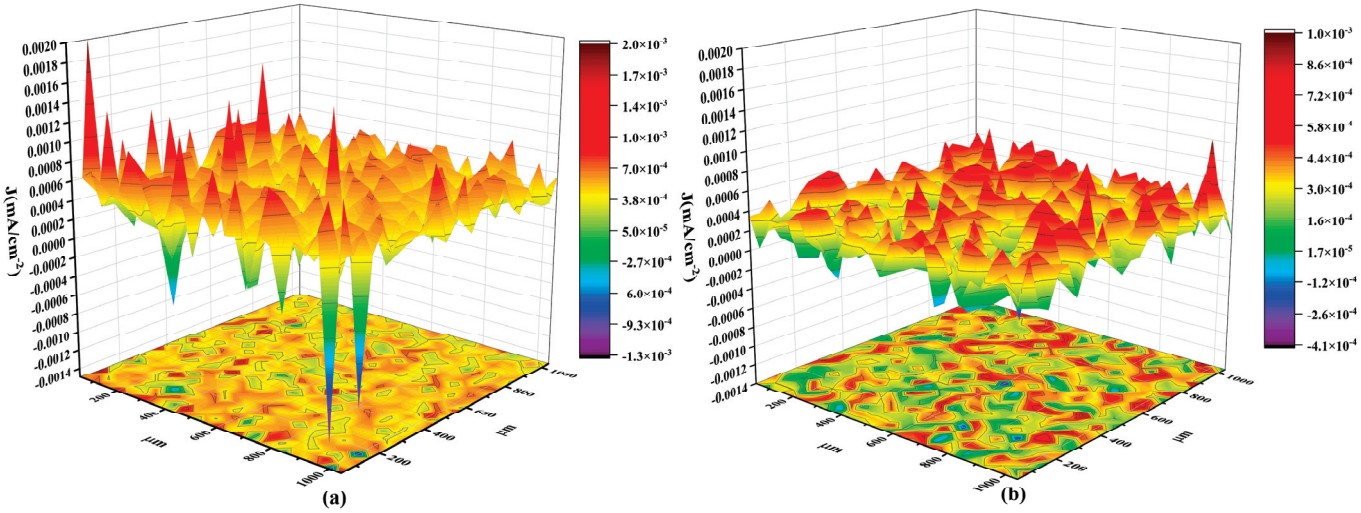


Figure 16. Scanning Vibrating Electrode Technique (SVET) testing: (**a**) cladding coating; (**b**) remelting coating.

The current density of the anode and cathode can be determined using the following equations to evaluate the corrosion behavior of the coating.

$$I_c = \int_0^{X\ max} \int_0^{Y\ max} [j_Z(x,y) < 0]dxdy$$

$$I_a = \int_0^{X\ max} \int_0^{Y\ max} [j_Z(x,y) > 0]dxdy$$

where I_c is the cathode current density and I_a is the anode current density.

The coating was immersed in a 3.5% wt NaCl solution for a continuous 48 h period. Upon analyzing the selected microregions, a significant elevation in the anodic peak was

observed in the edge region, accompanied by substantial fluctuations in current around the anodic peak. This is attributed to the presence of crack distribution in the edge region. In contrast, another coating subjected to laser remelting exhibited a uniform distribution of anodic current. SVET utilizes a microprobe to examine the material's surface and determine the dispersion of surface currents. The size of the surface current is related to the corrosion reaction and state of the FeCoNiCrAl high-entropy alloys coatings. The negative current is related to the cathode reaction and the positive current is related to the anode reaction. The results of applying the conversion formula are displayed in Table 5.

Table 5. Anodic current density.

	I_a/(μA·cm^{-2})
Cladding coating	0.52
Remelting coating	0.63

4. Discussion

4.1. Phase Formation and Evolution

The thermodynamic parameters ΔH_{mix} (enthalpy of mixing), δ (atomic radius difference), ΔS_{mix} (mixed entropy), and Ω can be used to forecast the formation and structural stability of HEAs [27]. The formation of the solid solute phase [28] was contingent upon the fulfillment of -15 kJ mol$^{-1} \leq \Delta H_{mix} \leq 5$ kJ mol^{-1} and $\delta \leq 6.5\%$) as well as the $\delta \leq 6.6\%$ criteria $\Omega \geq 1.1$. Furthermore, Guo et al. [29] determined that a greater abundance of valence electrons (*VEC*) (≥8) was advantageous for the formation of FCC solid solutions, whereas a smaller *VEC* (<6.87) was advantageous for the formation of BCC solid solutions. This is the equation for the calculation:

$$\Delta H_{mix} = 4 \sum_{i=1, i \neq j} \Delta H_{ij} c_i c_j$$

$$\Delta S_{mix} = -R \sum_{i=1}^{n} c_i ln c_i$$

$$\Omega = \frac{T_m \Delta S_{mix}}{|\Delta H_{mix}|}$$

$$\delta_r = 100 \sqrt{\sum_{i=1}^{n} c_i \left(1 - \frac{r_i}{\bar{r}}\right)^2}$$

$$\bar{r} = \sum_{i=1}^{n} c_i r_i$$

$$T_m = \sum_{i=1}^{n} C_i (T_m)_i$$

$$VEC = \sum_{i=1}^{n} c_i (VEC)_i$$

where c_i and c_j are the atomic fraction of elements i and j in the alloy, R is the gas constant, $(T_m)_i$ is the melting point of element i, r_i represents the radius of the element i, and $\bar{r}$ is the average atomic radius.

The parameters of FeCoNiCrAl high-entropy alloys coatings were calculated as shown in Table 6. After laser remelting treatment, the VEC value of the FeCoNiCrAl high-entropy alloy coating decreased from 7.81 to 7.12, and the δ value increased from 3.92 to 4.81. A small VEC was more conducive to the formation of a BCC structure. The BCC structure could adapt to large d values with a lower strain energy penalty. The solidification rate in laser remelting (typically 105 K/s [30]) is much slower than that in laser cladding (~106 K/s [31]). As a result, the elements in the coatings migrated significantly, with an

increase in the percentage of Al elements in the coatings and a decrease in the percentage of Fe elements, leading to the transformation of the coatings from a mixture of FCC, A2, and B2 to a mixture of A2 and B2.

Table 6. Thermodynamic parameters.

Alloy	ΔH_{mix} (kJ·mol^{-1})	$\Delta Smix$ (J·K^{-1} mol^{-1})	T_m (K)	Ω	δ (%)	*VEC*
Cladding coating	−7.61	12.45	1745.26	2.86	3.92	7.81
Remelting coating	−9.92	12.82	1715.32	2.216	4.81	7.12

4.2. Effect of Laser Remelting on the Wear Resistance of Coatings

The process of preparing FeCoNiCrAl high-entropy alloy coatings using laser cladding on the surface of Q235 base material is prone to defects such as porosity cracks, which tend to promote the emergence and expansion of cracks, thus seriously affecting the wear-resistant properties of the coatings. After remelting treatment, these defects in FeCoNiCrAl coatings basically disappeared, and the wear resistance of the coatings was improved.

The surface analysis indicated a higher proportion of Fe elements and a lower proportion of Al elements on the coating surface. After undergoing laser remelting treatment, there was an increase in the proportion of Al elements on the coating surface. Research has demonstrated that the elevated proportion of Al elements contributes to an improvement in the coating's hardness [32], consequently enhancing its wear resistance.

4.3. Effect of Laser Remelting on the Corrosion Resistance of Coatings

Laser remelting proved effective in eliminating surface defects, such as cracks and pores, thereby reducing the inherent corrosion susceptibility of the coating. Nevertheless, despite the positive impact on surface integrity, laser remelting did not yield a substantial enhancement in the corrosion resistance of the coatings when subjected to NaCl solution, as evidenced by both macroscopic electrochemical tests involving kinetic potential polarization and electrochemical impedance.

Analysis of the Scanning Vibrating Electrode Technique (SVET) plots revealed a pronounced anodic current peak in the cracked region of the coating (Figure 17a), contrasting with the low anodic current observed in the non-cracked region (Figure 17b). The uniform distribution of anodic current on the coating's surface following remelting played a pivotal role in mitigating the higher anodic current peaks associated with cracks. The average current density in cracked and non-cracked areas, presented in Table 7, indicated a significantly higher anodic current density in the cracked region.

Table 7. Anodic current density.

	I_a/(μA·cm^{-2})
Cladding coating (crack area)	1.257
Cladding coating	0.424
Remelting coating	0.63

The corrosion morphology of the cracked area of the fusion cladding, as depicted in the Figure 18, illustrated crack expansion along the vertical plane. The confined space within the crack hindered oxygen diffusion, resulting in oxygen deficiency inside the crack. This led to the formation of a concentration battery, with the higher oxygen concentration acting as the cathode and the lower oxygen concentration as the anode, facilitating anodic dissolution within the crack.

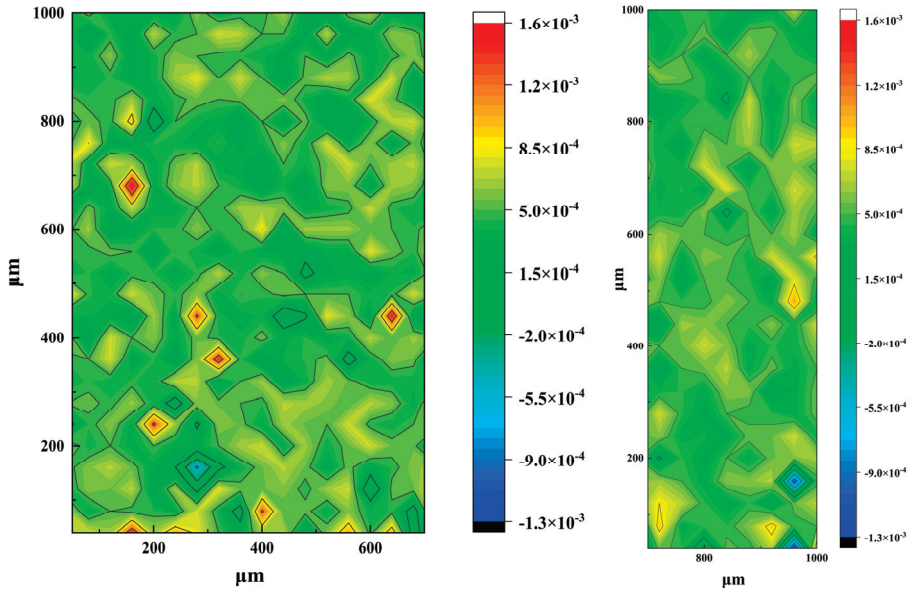


Figure 17. Scanning Vibrating Electrode Technique (SVET) Testing: (**a**) cracked region; (**b**) non-cracked region.

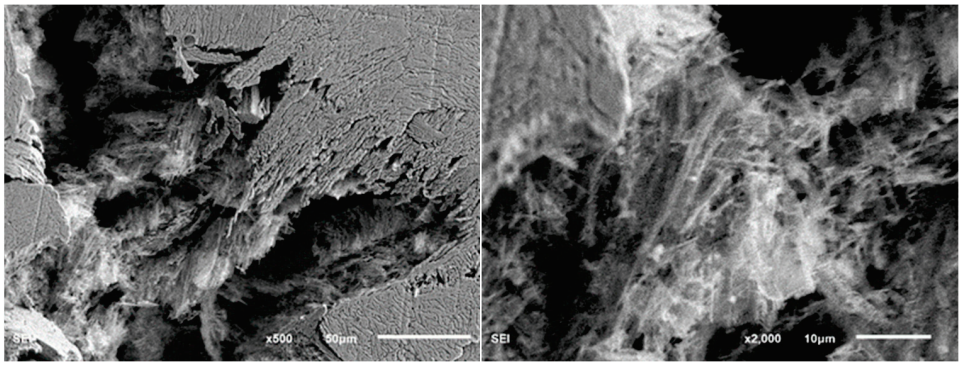


Figure 18. Corrosion morphology of the crack region: (**a**) outside of the crack; (**b**) inside of the crack.

Conversely, Figure 19 illustrates that the coating surface post laser remelting exhibited a lack of crack defects, an absence of evident corrosion pits, and only a few isolated pitting holes. Thus, while laser remelting significantly improved the corrosion resistance of the cracked areas, its impact on crack-free regions was not significant.

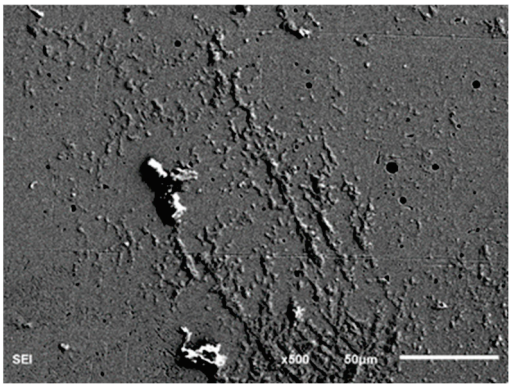


Figure 19. Corrosion morphology of remelting coating.

5. Conclusions

In this study, laser cladding was used to prepare FeCoNiCrAl high-entropy alloy coatings, and laser remelting was performed. The study examined the influence of laser remelting on the phase composition, microstructure, and coating properties, including wear resistance and corrosion resistance.

Following laser remelting treatment, the atomic proportion of Fe elements on the coating surface decreased from 33.21% to 26.03%, while the atomic proportion of Al elements increased from 12.56% to 20.31%. The phase composition of the coating underwent a marked transformation, shifting from a structure composed of FCC, A2, and B2 phases to a singular BCC structure characterized by the presence of A2 and B2 phases. Concurrently, the grain morphology on the coating surface transitioned from elongated plate-like grains to equiaxed grains.

After remelting, the hardness of the AlCoCrFeNi coating changed from 613 to 754 $HV_{0.2}$, an increase of 23%. The coefficient of friction on the coating surface decreased from 0.431 to 0.345, resulting in a 65% reduction in wear volume.

The FeCoNiCrAl coating exhibits excellent corrosion resistance, and laser remelting repairs defects such as cracks, further enhancing the corrosion resistance of the coating. However, it has no significant impact on the corrosion resistance of non-cracked regions.

Further investigation is necessary to determine the structure and characteristics of coating when using a single laser power to remelt the surface under various remelt powers, as certain restrictions exist.

Author Contributions: The experiment was designed by T.L. and W.Z. Methodology, X.J. The result analysis was performed by T.L. J.H., W.Z. and C.Z. were responsible for writing the paper. All authors have read and agreed to the published version of the manuscript.

Funding: This research received no external funding

Data Availability Statement: Data are contained within the article.

Conflicts of Interest: The authors declare no conflict of interest.

References

1. Yeh, J.W.; Chen, S.K.; Lin, S.J.; Gan, J.Y.; Chin, T.S.; Shun, T.T.; Tsau, C.H.; Chang, S.Y. Nanostructured High-Entropy Alloys with Multiple Principal Elements: Novel Alloy Design Concepts and Outcomes. *Adv. Eng. Mater.* **2004**, *6*, 299–303. [CrossRef]
2. Shang, X.; Wang, Z.; He, F.; Wang, J.; Li, J.; Yu, J. The intrinsic mechanism of corrosion resistance for FCC high entropy alloys. *Sci. China Technol. Sci.* **2018**, *61*, 189–196. [CrossRef]
3. Tian, L.-H.; Xiong, W.; Liu, C.; Lu, S.; Fu, M. Microstructure and wear behavior of atmospheric plasma-sprayed AlCoCrFeNiTi high-entropy alloy coating. *J. Mater. Eng. Perform.* **2016**, *25*, 5513–5521. [CrossRef]
4. Mu, Y.; Jia, Y.; Xu, L.; Jia, Y.; Tan, X.; Yi, J.; Wang, G.; Liaw, P. Nano oxides reinforced high-entropy alloy coatings synthesized by atmospheric plasma spraying. *Mater. Res. Lett.* **2019**, *7*, 312–319. [CrossRef]
5. Li, L.-C.; Li, M.-X.; Liu, M.; Sun, B.-Y.; Wang, C.; Huo, J.-T.; Wang, W.-H.; Liu, Y.-H. Enhanced oxidation resistance of MoTaTiCrAl high entropy alloys by removal of Al. *Sci. China Mater.* **2021**, *64*, 223–231. [CrossRef]
6. Chunhai, L.; Guo, P.; Wei, Z.; Chengjie, Y.; Xuejun, C.; Chang, C.; Yongzhong, J. Preparation of FeCrNiMoCu High-entropy Alloy Coating by Magnetron Co-sputtering and Its Microstructure. *Rare Met. Mater. Eng.* **2018**, *47*, 1578–1582.
7. Lehtonen, J.; Koivuluoto, H.; Ge, Y.; Juselius, A.; Hannula, S.-P. Cold gas spraying of a high-entropy CrFeNiMn equiatomic alloy. *Coatings* **2020**, *10*, 53. [CrossRef]
8. Zhu, S.; Zhang, Z.; Zhang, B.; Yu, Y.; Wang, Z.; Zhang, X.; Lu, B. Microstructure and Properties of Al_2O_3-13wt.% TiO_2-Reinforced CoCrFeMnNi High-Entropy Alloy Composite Coatings Prepared by Plasma Spraying. *J. Therm. Spray Technol.* **2021**, *30*, 772–786. [CrossRef]
9. Wei, Z.; Wu, Y.; Hong, S.; Cheng, J.; Qiao, L.; Cheng, J.; Zhu, S. Ultrasonic cavitation erosion behaviors of high-velocity oxygen-fuel (HVOF) sprayed AlCoCrFeNi high-entropy alloy coating in different solutions. *Surf. Coat. Technol.* **2021**, *409*, 126899. [CrossRef]
10. Aliyu, A.; Rekha, M.; Srivastava, C. Microstructure-electrochemical property correlation in electrodeposited CuFeNiCoCr high-entropy alloy-graphene oxide composite coatings. *Philos. Mag.* **2019**, *99*, 718–735. [CrossRef]
11. Zhang, P.; Li, Z.; Liu, H.; Zhang, Y.; Li, H.; Shi, C.; Liu, P.; Yan, D. Recent progress on the microstructure and properties of high entropy alloy coatings prepared by laser processing technology: A review. *J. Manuf. Process.* **2022**, *76*, 397–411. [CrossRef]
12. Gao, Z.; Wang, L.; Wang, Y.; Lyu, F.; Zhan, X. Crack defects and formation mechanism of FeCoCrNi high entropy alloy coating on TC4 titanium alloy prepared by laser cladding. *J. Alloys Compd.* **2022**, *903*, 163905. [CrossRef]

13. Sypniewska, J.; Szkodo, M. Influence of Laser Modification on the Surface Character of Biomaterials: Titanium and Its Alloys—A Review. *Coatings* **2022**, *12*, 1371. [CrossRef]
14. Ghosh, A.; Wu, W.; Sahu, B.P.; Wang, J.; Misra, A. Enabling plastic co-deformation of disparate phases in a laser rapid solidified Sr-modified Al–Si eutectic through partial-dislocation-mediated-plasticity in Si. *Mater. Sci. Eng. A* **2023**, *885*, 145648. [CrossRef]
15. Wu, G.; Yin, Y.; Zhang, S.; Wang, Y.; Xiang, Y.; Li, L.; Yao, J. Effect of laser texturing on the antiwear properties of micro-arc oxidation coating formed on Ti-6Al-4V. *Surf. Coat. Technol.* **2023**, *453*, 129114. [CrossRef]
16. Wang, H.; Zhang, W.; Peng, Y.; Zhang, M.; Liu, S.; Liu, Y. Microstructures and wear resistance of FeCoCrNi-Mo high entropy alloy/diamond composite coatings by high speed laser cladding. *Coatings* **2020**, *10*, 300. [CrossRef]
17. Jin, B.; Zhang, N.; Yin, S. Strengthening behavior of AlCoCrFeNi $(TiN)_x$ high-entropy alloy coatings fabricated by plasma spraying and laser remelting. *J. Mater. Sci. Technol.* **2022**, *121*, 163–173. [CrossRef]
18. Chen, L.; He, D.; Han, B.; Guo, Z.; Zhang, L.; Lu, L.; Wang, X.; Tan, Z.; Zhou, Z. Effect of laser remelting on wear behavior of HVOF-sprayed FeCrCoNiTiAl0. 6 high entropy alloy coating. *Appl. Sci.* **2020**, *10*, 7211. [CrossRef]
19. Al-Sayed, S.R.; Abdelfatah, A. Corrosion behavior of a laser surface-treated alpha–beta 6/4 titanium alloy. *Met. Lography Microstruct. Anal.* **2020**, *9*, 553–560. [CrossRef]
20. Liu, B.-W.; Mi, G.-Y.; Wang, C.-M. Reoxidation process and corrosion behavior of TA15 alloy by laser ablation. *Rare Met.* **2021**, *40*, 865–876. [CrossRef]
21. Fu, X.; Schuh, C.A.; Olivetti, E.A. Materials selection considerations for high entropy alloys. *Scr. Mater.* **2017**, *138*, 145–150. [CrossRef]
22. Jadhav, N.; Gelling, V.J. The use of localized electrochemical techniques for corrosion studies. *J. Electrochem. Soc.* **2019**, *166*, C3461. [CrossRef]
23. Chong, Z.; Sun, Y.; Cheng, W.; Huang, L.; Han, C.; Ma, X.; Meng, A. Laser remelting induces grain refinement and properties enhancement in high-speed laser cladding AlCoCrFeNi high-entropy alloy coatings. *Intermetallics* **2022**, *150*, 107686. [CrossRef]
24. Wei, J.; Dong, J.; Zhou, Y.; He, X.; Wang, C.; Ke, W. Influence of the secondary phase on micro galvanic corrosion of low carbon bainitic steel in NaCl solution. *Mater. Charact.* **2018**, *139*, 401–410. [CrossRef]
25. He, X.; Song, R.; Kong, D. Microstructure and corrosion behaviours of composite coatings on S355 offshore steel prepared by laser cladding combined with micro-arc oxidation. *Appl. Surf. Sci.* **2019**, *497*, 143703. [CrossRef]
26. Mi, C.; Tian, Z.; Cao, C.; Wang, Z.; Mao, C.; Xu, S. Novel microwave-assisted solvothermal synthesis of NaYF4: Yb, Er upcon version nanoparticles and their application in cancer cell imaging. *Langmuir* **2011**, *27*, 14632–14637. [CrossRef]
27. Yang, X.; Zhang, Y. Prediction of high-entropy stabilized solid-solution in multi-component alloys. *Mater. Chem. Phys.* **2012**, *132*, 233–238. [CrossRef]
28. Zhang, Y.; Zhou, Y.J.; Lin, J.P.; Chen, G.L.; Liaw, P.K. Solid-solution phase formation rules for multi-component alloys. *Adv. Eng. Mater.* **2008**, *10*, 534–538. [CrossRef]
29. Sheng, G.; Liu, C.T. Phase stability in high entropy alloys: Formation of solid-solution phase or amorphous phase. *Prog. Nat. Sci. Mater. Int.* **2011**, *21*, 433–446.
30. Yuan, W.; Li, R.; Chen, Z.; Gu, J.; Tian, Y. A comparative study on microstructure and properties of traditional laser cladding and high-speed laser cladding of Ni45 alloy coatings. *Surf. Coat. Technol.* **2021**, *405*, 126582. [CrossRef]
31. Pawlowski, L.; Smurov, I. Modeling of high power laser interaction with APS deposited FeCrTiC. *Surf. Coat. Technol.* **2002**, *151*, 308–315. [CrossRef]
32. Jin, B.; Zhang, N.; Yu, H.; Hao, D.; Ma, Y. AlxCoCrFeNiSi high entropy alloy coatings with high microhardness and improved wear resistance. *Surf. Coat. Technol.* **2020**, *402*, 126328. [CrossRef]

Disclaimer/Publisher's Note: The statements, opinions and data contained in all publications are solely those of the individual author(s) and contributor(s) and not of MDPI and/or the editor(s). MDPI and/or the editor(s) disclaim responsibility for any injury to people or property resulting from any ideas, methods, instructions or products referred to in the content.

coatings

MDPI

Article

Comparison of the Erosive Wear Resistance of Ductile Cast Iron Following Laser Surface Melting and Alloying

Jacek Górka, Aleksandra Lont *, Damian Janicki, Tomasz Poloczek and Agnieszka Rzeźnikiewicz

Welding Department, Faculty of Mechanical Engineering, Silesian University of Technology, Konarskiego Street 18A, 44-100 Gliwice, Poland; jacek.gorka@polsl.pl (J.G.); damian.janicki@polsl.pl (D.J.); tomasz.poloczek@polsl.pl (T.P.); agnieszka.rzeznikiewicz@polsl.pl (A.R.)
* Correspondence: aleksandra.lont@polsl.pl

Abstract: This article presents research results on the influence of the laser surface melting and alloying processes on the erosive wear resistance of ductile cast iron. For the research, an EN-GJS 350-22 ductile cast iron surface was laser-melted and laser-alloyed with titanium powder in an argon and nitrogen atmosphere. Solid-particle erosion tests were carried out on the laser-melted and -alloyed surface layers and the base material according to the ASTM G76-04 standard with 30° and 90° impingement angles. The erosive wear resistance results were correlated with Vickers hardness and microstructural test results with the use of SEM (scanning electron microscopy), TEM (transmission electron microscopy), EDS (energy dispersive spectroscopy), and XRD (X-ray diffraction). The mechanisms of erosive wear were also analyzed for the laser-treated surface layers and the base material. The research showed that the laser melting and alloying processes with titanium powder had a positive effect on the hardness and erosive wear resistance of the ductile cast iron surface due to microstructure modification. Moreover, despite the lower hardness of the laser-alloyed surface layers, their composite microstructure had a positive impact on the erosive wear resistance in comparison to the laser-melted surface layers.

Keywords: laser melting; laser alloying; ductile cast iron; solid-particle erosion

1. Introduction

The ductile cast irons (DCIs) are alloys commonly used for machine parts due to their high mechanical and fatigue strengths and plastic properties. DCIs also show a low stress concentration tendency, vibration-damping abilities, and good casting properties and machinability, which makes them relatively cheap and easy to form, even into complex shapes. The disadvantage that limits the use of DCIs in some applications is their insufficient hardness and wear resistance [1]. The degradation of materials due to wear mechanisms is a serious problem for many applications in industry. In response to this problem, and the need for wear-resistant materials with high strength, plastic, and fatigue properties, the various surface treatment technologies are constantly improved to meet the demands of industry [2–5]. Among the many surface treatment technologies, laser surface treatment provides many possibilities and potential applications for a wide range of materials. The high power density of the laser beam results in a low heat impact on the processed material, and low deformation and stress level, and enables precise treatment of small areas. High heating and cooling rates result in the formation of fine-grained structures with unique properties [6,7]. In the case of DCIs, in order to improve their surface hardness and wear resistance while maintaining the beneficial properties of the core, surface treatment technologies can be used, including laser surface treatment. For DCIs, the main laser surface treatments used are laser transformation hardening (LTH) [8,9], laser surface melting (LSM) [10,11], laser surface alloying (LSA) [12–14], and laser cladding (LC) [15–18].

It was previously reported that during the LSM process of DCI, a thin surface layer of the material is melted and the graphite precipitate dissolves in the liquid metal causing its enrichment with carbon. After passing the laser beam, dynamic cooling and crystallization of the metal occurs, resulting in the formation of a fine-grained, dendritic structure of the surface layer. In the melted zone, as a result of the high cooling rate, carbon precipitates as cementite, causing an increase in the hardness in comparison to the base material [19]. The structural modification obtained in the laser-melted surface layer of DCIs results in wear resistance improvement in comparison to the base material [20–22].

LSA provides much wider possibilities of shaping the structure and properties of the DCI surface layer in comparison to LSM by the addition of alloying elements or reinforcing particles [23–25]. The LSA process also enables the formation of metal–matrix composite (MMC) surface layers, which are commonly used in industry for machine parts exposed to wear in order to extend their service life, and therefore, reduce operating costs [26]. It was previously proven that due to the high carbon content in the liquid metal and the low Gibbs free energy for the formation of the TiC phase, with the addition of titanium powder in the LSA process of DCI, an in situ MMC structure can be formed in the surface layer. Selecting the proper process parameters enables the formation of the homogeneous MMC structure and enables control of the fraction, size, and morphology of titanium carbides. As shown by research conducted on this topic, such structural modifications result in increased hardness and wear resistance in comparison to the substrate material [27,28].

In previous work [29], an analysis of the influence of nitrogen in the LSA process of DCI with titanium powder was carried out. Due to the strong affinity of titanium to both carbon and nitrogen, the process led to titanium carbonitride precipitation in the surface layers. The current work aims to compare the influence of the LSM and LSA processes with titanium powder on the erosive wear resistance of the DCI surface. The influence of the process atmosphere (argon and nitrogen), structure (TiC/TiCN fraction, cementite fraction), and hardness on the erosive wear resistance are analyzed, as well as the erosion mechanisms.

2. Materials and Methods

For the research, ductile cast iron of grade EN-GJS-350-22 was selected as the substrate material. The chemical composition of the used DCI is presented in Table 1. The microstructure of the selected DCI is composed of about 20 vol.% spheroidal graphite precipitate in a ferritic matrix (Figure 1). Prior to the laser processing, the substrate surface was ground to an Ra of 0.5 μm and degreased with ethyl alcohol. For the LSA processes, 99.0% pure titanium powder (H.C. Starck Amperit 154) with 45–70 μm gradation was used, which was dried directly before the process in an oven at 50 °C for 30 min. As shielding and powder-transporting gases for the LSM and LSA processes, 99.999% pure nitrogen and argon were used.

Table 1. Chemical composition of EN-GJS-350-22 ductile cast iron.

Chemical Composition, wt.%								
C	**Si**	**Mn**	**P**	**S**	**Cu**	**Ti**	**Mg**	**Cr**
3.66	2.71	0.527	0.042	0.001	0.068	0.032	0.012	0.124

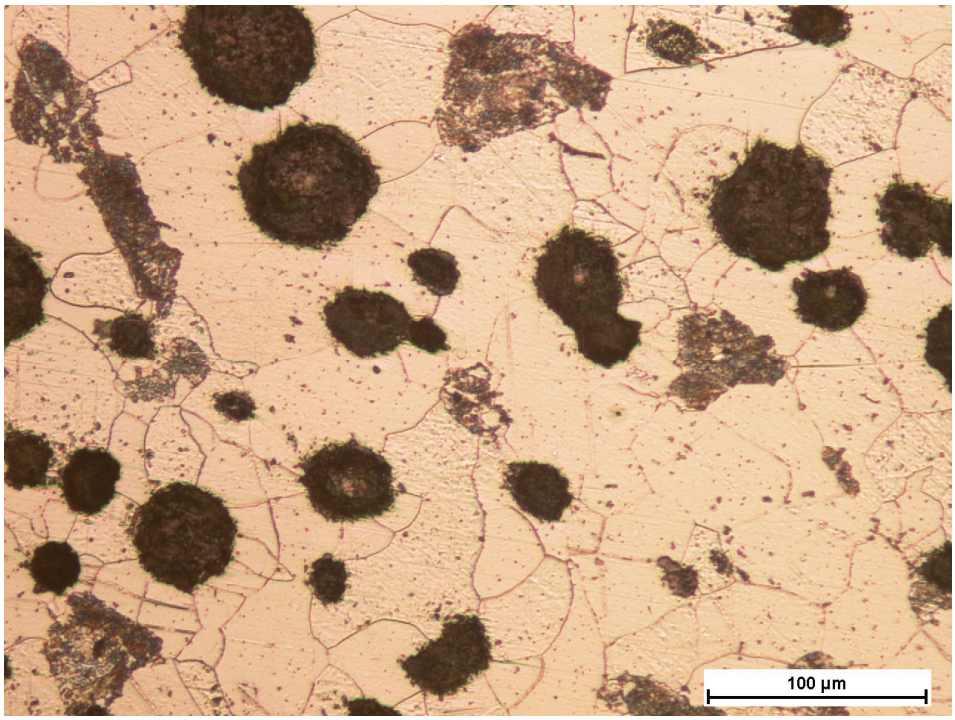


Figure 1. The EN-GJS-350-22 ductile cast iron's microstructure (optical microscope).

The laser processing was carried out using a stand equipped with the high-power direct diode laser (HPDDL) Rofin Sinar DL020. The technical specifications of the laser are presented in Table 2. The stand was also equipped with a numerically controlled positioning system for the laser head and substrate material. The movement of the traverse was parallel to the short axis of the laser beam focus. For the powder feeding for the LSA process, a disk powder-feeding system with a vibrator was used. The titanium powder was fed directly into the area of laser beam impact at an angle of 45° to the substrate surface. The powder nozzle's shape and size were adapted to the laser beam focus's shape and size in order to ensure uniform powder injection (Figure 2). The rectangular laser beam spot, of size 1.5 × 6.6 mm and uniform density distribution along the focus axis, was focused on the substrate surface. Single-scan LSM and LSA processes were carried out without preheating. The flow rates and powder feed rates of the powder-transporting gases and shielding gases, and the laser beam power and speed were selected on the basis of preliminary tests. A list of the samples made for the research and the process parameters is presented in Table 3. The shielding gas flow rate for the LSM process was 20 L/min and for the LSA process 15 L/min. The powder-transporting gas flow rate for the LSA process was 3 L/min.

Table 2. Technical specifications of the Rofin Sinar DL020 HPDDL.

Wavelength of the Laser Radiation, nm	808–940 ± 5
Range of Laser Power, W	100–2000
Focal Length, mm	82
Laser Beam Spot Size, mm	1.5 × 6.6
Range of Laser Power Intensity, W/mm^2	10.1–202.0

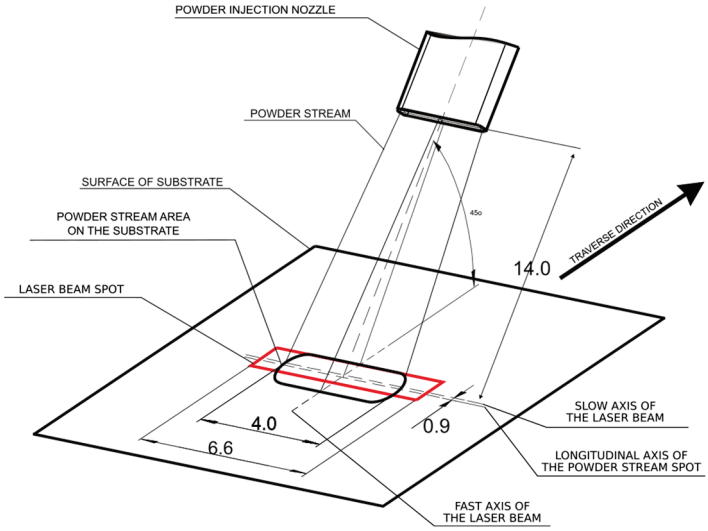


Figure 2. Diagram showing the alignment of the powder injection nozzle relative to the laser beam spot [28].

Table 3. The laser surface treatment process parameters.

Designation	Process	Laser Beam Power, W	Traverse Speed, m/min	Shielding Gas	Powder-Transporting Gas	Powder Feed Rate, mg/mm
A1	LSM	2000	0.2	argon	-	-
A2	LSM	2000	0.4	argon	-	-
A3	LSM	1500	0.075	argon	-	-
N1	LSM	2000	0.2	nitrogen	-	-
N2	LSM	2000	0.4	nitrogen	-	-
N3	LSM	1500	0.075	nitrogen	-	-
TA1	LSA	2000	0.075	argon	argon	4
TA2	LSA	2000	0.075	argon	argon	8
TA3	LSA	2000	0.075	argon	argon	12
TA4	LSA	2000	0.075	argon	argon	16
TN1	LSA	1750	0.075	nitrogen	nitrogen	5.33
TN2	LSA	2000	0.075	nitrogen	nitrogen	4
TN3	LSA	2000	0.075	nitrogen	nitrogen	5.33

The macroscopic observations were carried out using an Olympus SZX9 optical microscope (Olympus, Tokyo, Japan) manufacturer, city, state (only for USA and Canada), country). Microstructural characterization was performed using a Phenom-World PRO scanning electron microscope (SEM, Thermo Fisher Scientific, Waltham, MA, USA) and FEI TITAN 80/300 transmission electron microscope (TEM, Scientific and Technical Instruments, Hillsboro, OR, USA) with energy dispersive spectroscopy analysis (EDS). The thin foil for TEM investigations was prepared using Xe-PFIB technology. Samples for the macro- and microscopic observations were etched in 4% Nital solution. The phase compositions of the processed surface layers were determined using X-ray diffraction (XRD) analysis with a PANalytical X'Pert PRO MPD diffractometer (Malvern Panalitycal, Malvern, UK) equipped with a PIXcel3D 1 × 1 detector using filtered radiation from a lamp with a cobalt anode. The average TiC(N) precipitate and cementite fractions were measured using the Image-Pro Plus software (version 4.5.0.29) on a total of 8 SEM images of nonetched LSA surface-layer cross-sections (4 near the surface and 4 near the fusion line).

The Vickers hardness was measured using a Wilson Wolpert 401 MVD tester (Wilson Instruments, Instron Company, Norwood, MA, USA) for each surface-layer cross-section with a load of 200 g and dwell time of 10 s. The hardness tests were performed in three measuring lines from the surface to the substrate with a 0.1 mm step (Figure 3).

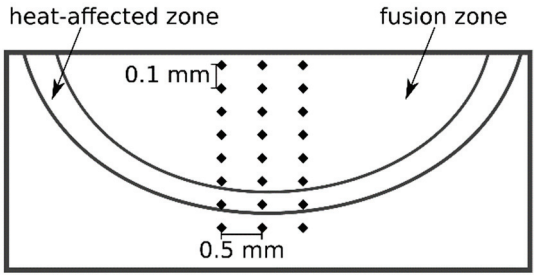


Figure 3. The Vickers hardness measurement point distribution on the cross-sections of laser-treated surface layers [29].

The solid-particle erosion tests of the laser-processed layers and substrate material were performed on a test stand that met the requirements of the ASTM G76-04 standard [30]. Angular 50 μm Al_2O_3 was used as the erodent material in a stream of dry compressed air with a velocity of 70 m/s and a feed rate of 2 g/min. The erodent was injected onto the tested surface for 10 min through a 1.5 mm diameter and 50 mm long nozzle. The distance between the nozzle and the material's surface was 10 mm. The solid-particle erosion tests were carried out using impingement angles of 30° and 90°. To determine average results (steady-state erosion rate and erosion value according to ASTM G76-04 [30]) for each surface layer and impingement angle, 3 tests were performed. The mass loss was obtained using a laboratory scale with 0.001 g accuracy. The tested surface layers and the substrate densities were determined using the Archimedes method. In order to determine the erosive wear mechanism, SEM microscopic observations of the crater surfaces were carried out.

3. Results and Discussion

The macrographs of the representative surface layers are shown in Figure 4. The SEM microstructures of the laser-treated surface layers are shown in Figure 5 and the microstructural parameters are presented in Table 4. The representative EDS maps of the laser-alloyed surface layers are shown in Figure 6. Figure 7 presents the EDS line-scan profile of the composition of the TiCN precipitate from the TEM. The XRD results are presented in Figure 8. In general, the mechanism of fluid flow during laser surface processing is a surface tension gradient (Marangoni convection) [31]. The shapes of the fusion zones of the laser-melted and -alloyed surface layers indicate that during those processes the surface tension was highest at the center of the molten pool and produced fluid flow inward along the molten pool surface. The laser surface melting processes in the argon and nitrogen atmospheres caused the graphite precipitate's dissolution in the liquid metal pool, which resulted in carbon enrichment of the liquid metal. As a result of the fast cooling of the metal pool, during crystallization graphite did not precipitate. After the laser beam passing, due to the cooling by heat conduction to the base metal, the primary austenite dendrites grew from the fusion line, then the eutectic austenite and cementite precipitated in the interdendritic spaces. Then, due to the high cooling rate, the martensitic transformation occurred. The microscopic analysis did not show any influence of nitrogen compared to argon shielding on the microstructure or chemical and phase compositions of the LSM surface layers. The XRD analysis for both of the atmospheres used indicated the presence of α-Fe (martensite), γ-Fe (retained austenite), and Fe_3C (cementite) in the structures. No significant differences in the fractions of these components were noted for the same LSM process parameters. For both atmospheres used, for samples laser-melted with a 2000 W laser beam power and speeds of 0.2 and 0.4 cm/min, the increased speed caused the cementite fraction to decrease (by 10.7 vol.% and 6.8 vol.% for the argon and nitrogen shields, respectively) and the retained austenite fraction to increase (by 19.3 wt.% and 22.0 wt.% for the argon and nitrogen shields, respectively), due to the cooling rates resulting from the process parameters.

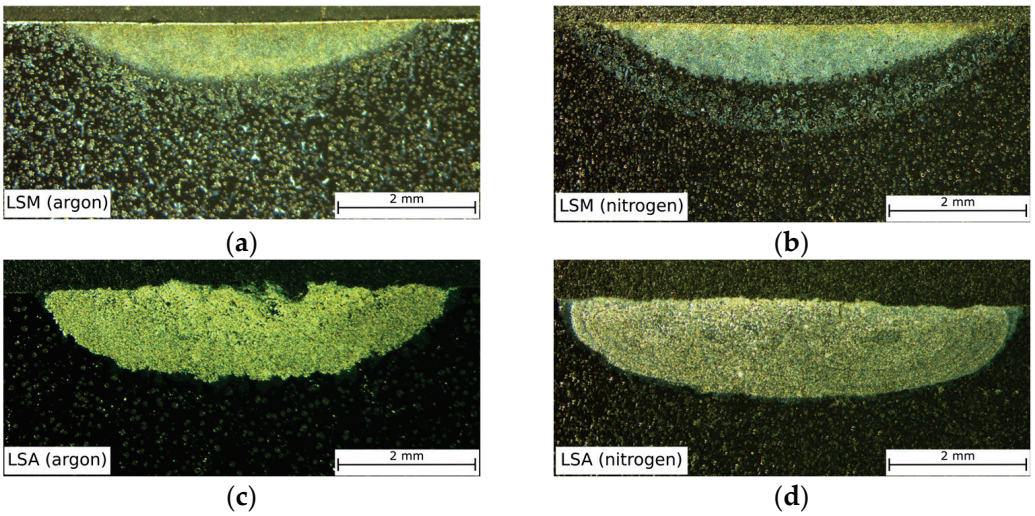


Figure 4. The macrographs of representative surface layers: (**a**) A1, (**b**) N1, (**c**) TA3, and (**d**) TN2 [29]. Designations according to Table 3.

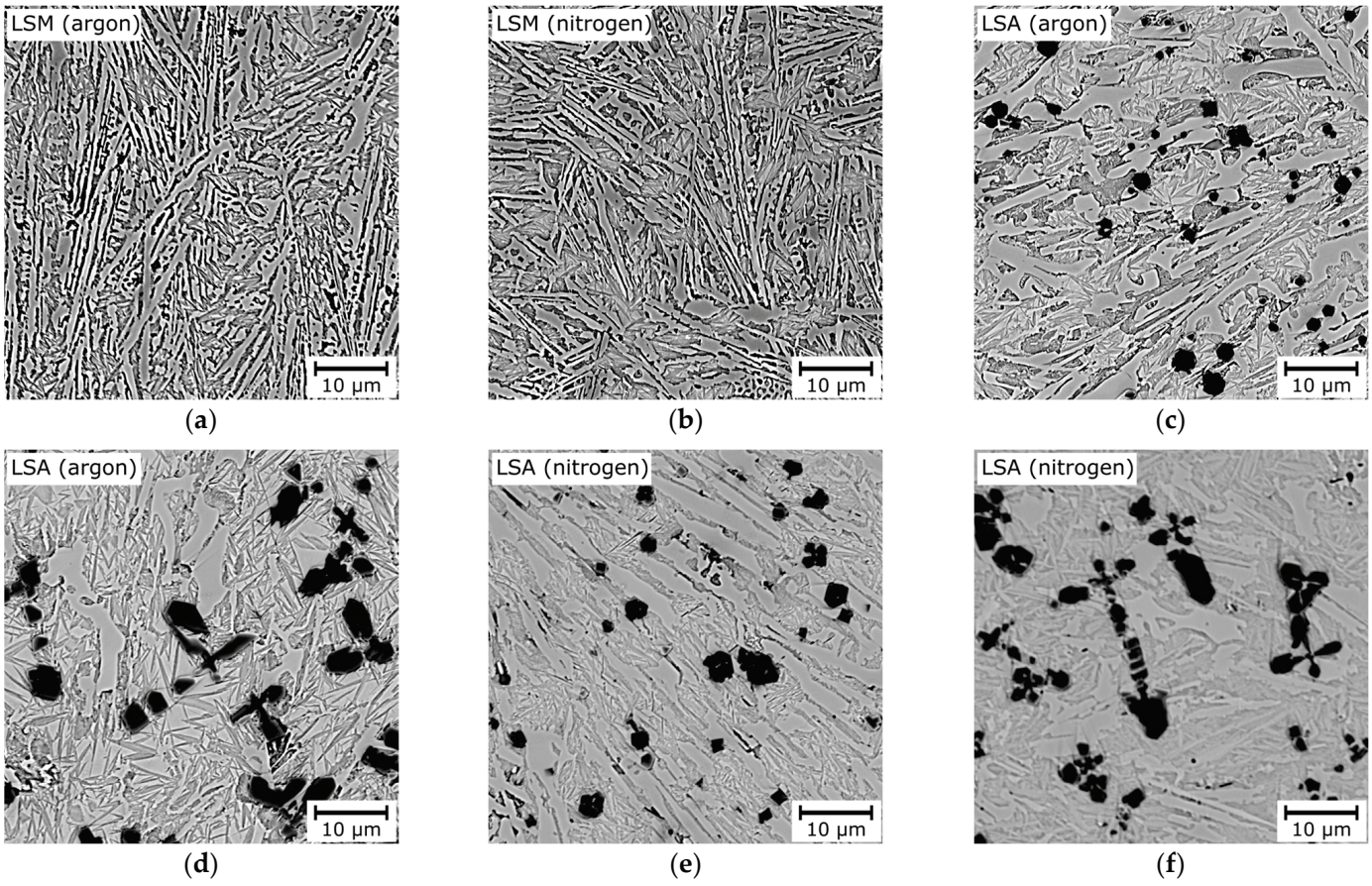


Figure 5. The SEM microstructures of representative surface layers: (**a**) A1, (**b**) N1, (**c**) TA1, (**d**) TA3, (**e**) TN1, (**f**) and TN3. Designations according to Table 3.

Table 4. The microstructural parameters of laser surface melted and alloyed ductile cast iron surface layers.

Designation (According to Table 3)	Average Titanium Content, wt.%	Average TiC(N) Fraction, vol.%	Average Fe_3C Fraction, vol.%	Average Retained Austenite Fraction, wt.%	Average Fe-α (Martensite) Fraction, wt.%
A1	-	-	55.7 ± 2.86	10.9 ± 1.23	33.6 ± 1.71
A2	-	-	45.0 ± 4.24	30.2 ± 1.41	19.7 ± 1.83
A3	-	-	53.8 ± 1.66	6.9 ± 0.91	39.3 ± 1.75
N1	-	-	48.9 ± 1.17	10.4 ± 0.97	40.9 ± 1.62
N2	-	-	42.1 ± 1.88	32.4 ± 1.34	26.0 ± 0.94
N3	-	-	50.9 ± 1.19	8.2 ± 1.15	41.1 ±1.14
TA1	3.2 ± 0.33	5.5 ± 1.13	32.7 ± 4.33	11.3 ± 0.89	50.9 ± 2.05
TA2	5.5 ± 1.7	9.6 ± 2.29	26.6 ± 2.08	11.6 ± 1.17	53.1 ± 1.62
TA3	9.1 ± 2.78	14.1 ± 3.91	13.9 ± 1.52	10.1 ± 1.21	62.0 ± 1.15
TA4	12.9 ± 1.71	20.1 ± 2.29	4.7 ± 2.34	9.5 ± 1.18	66.1 ± 1.39
TN1	3.6 ± 0.88	6.5 ± 1.71	33.4 ± 2.25	11.8 ± 1.31	48.6 ± 1.81
TN2	3.2 ± 1.26	4.8 ± 1.57	34.4 ± 5.76	12.4 ± 1.05	48.7 ± 1.37
TN3	5.8 ± 1.35	10.1 ± 2.23	27.1 ± 3.93	13.3 ± 0.88	49.5 ± 1.42

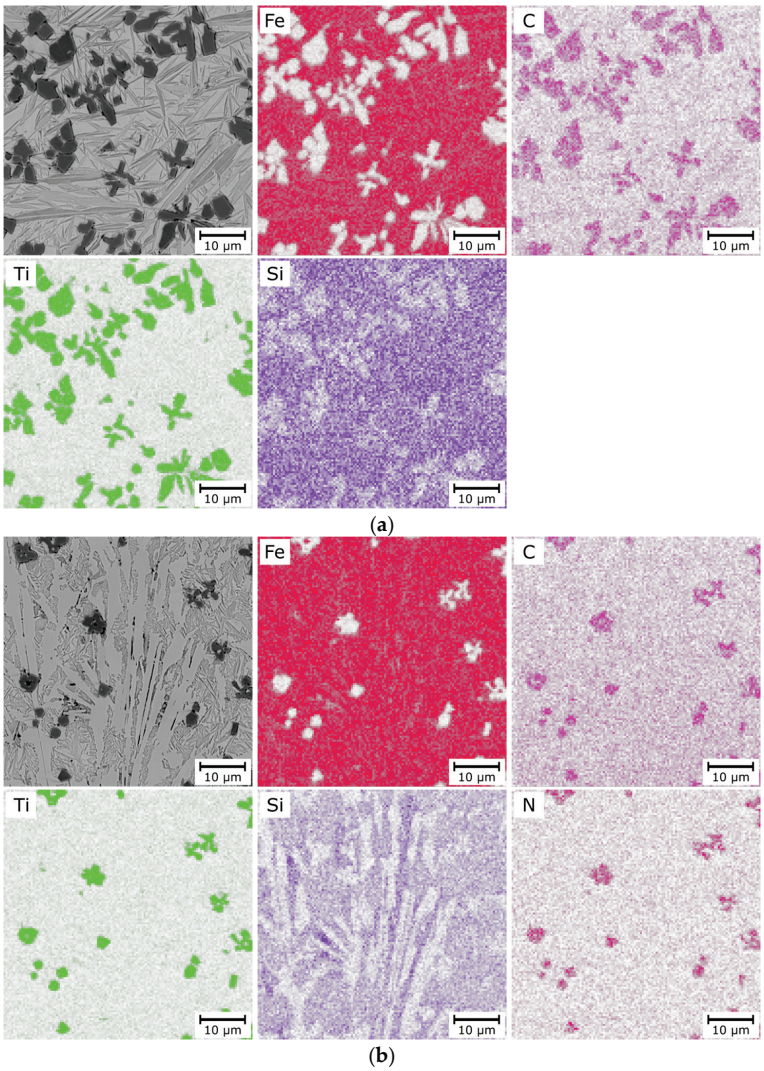
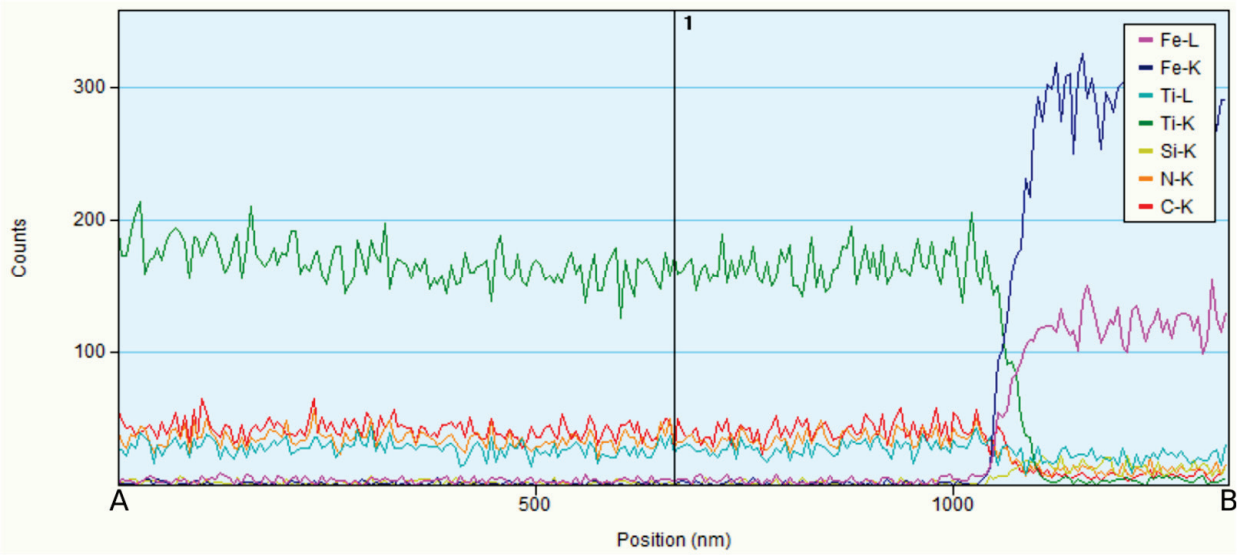
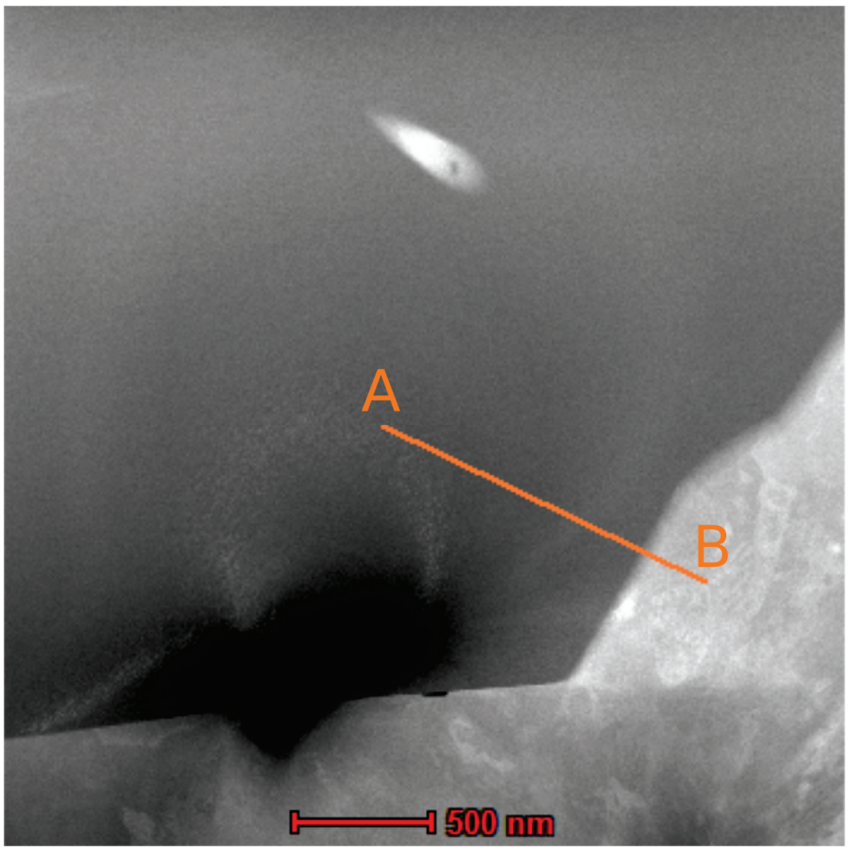


Figure 6. The EDS mapping of the composition of representative laser-alloyed surface layers: (**a**) TA2 and (**b**) TN2 [29]. Designations according to Table 3.

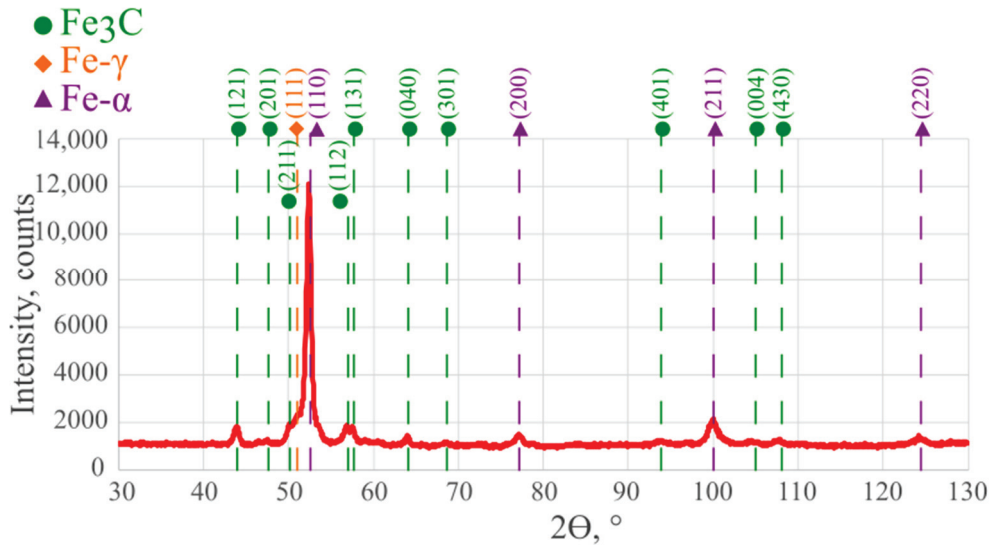


(**a**)

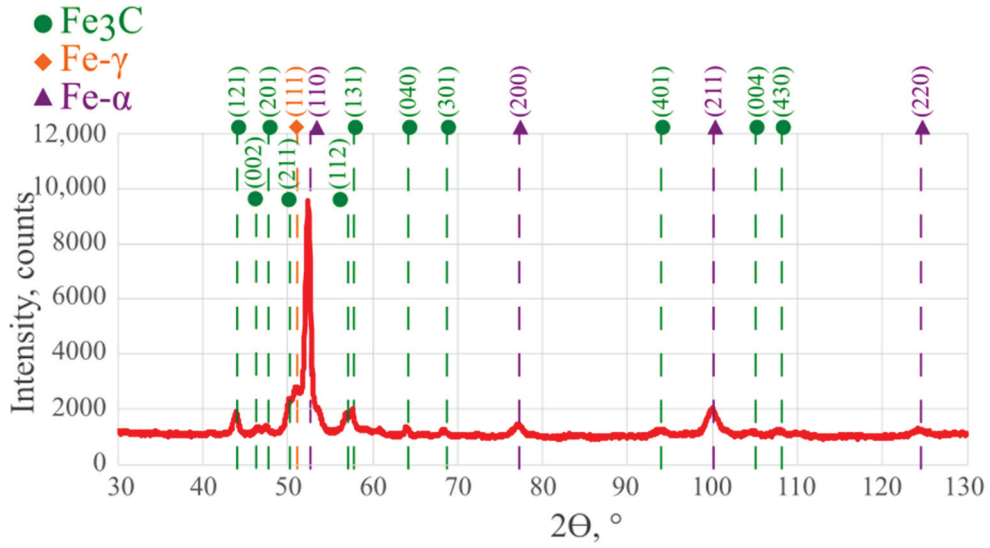


(**b**)

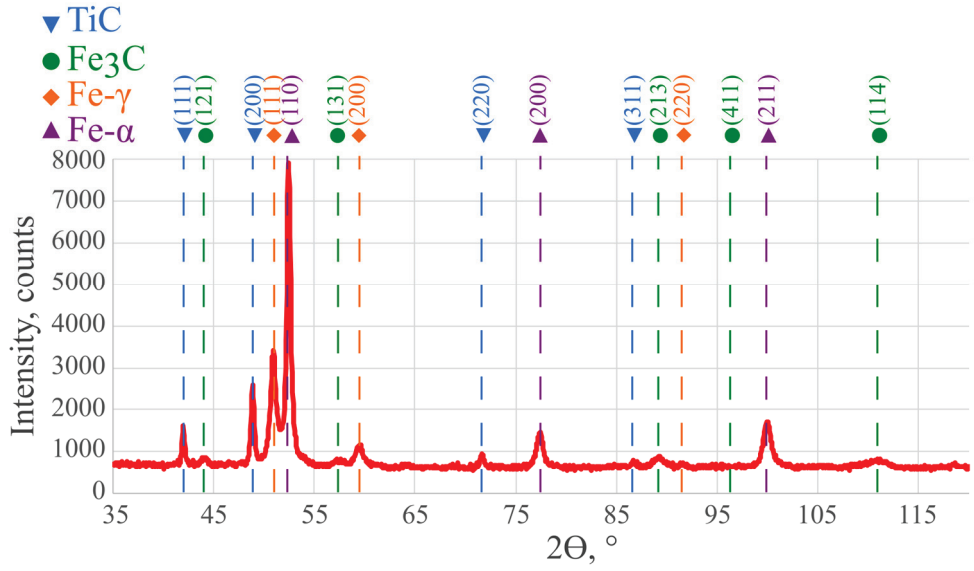
Figure 7. (**a**) The TEM EDS line-scan profile of the composition of TiCN precipitate from the laser-alloyed surface layer in nitrogen shield; (**b**) the measuring line from A to B [29].



(**a**)

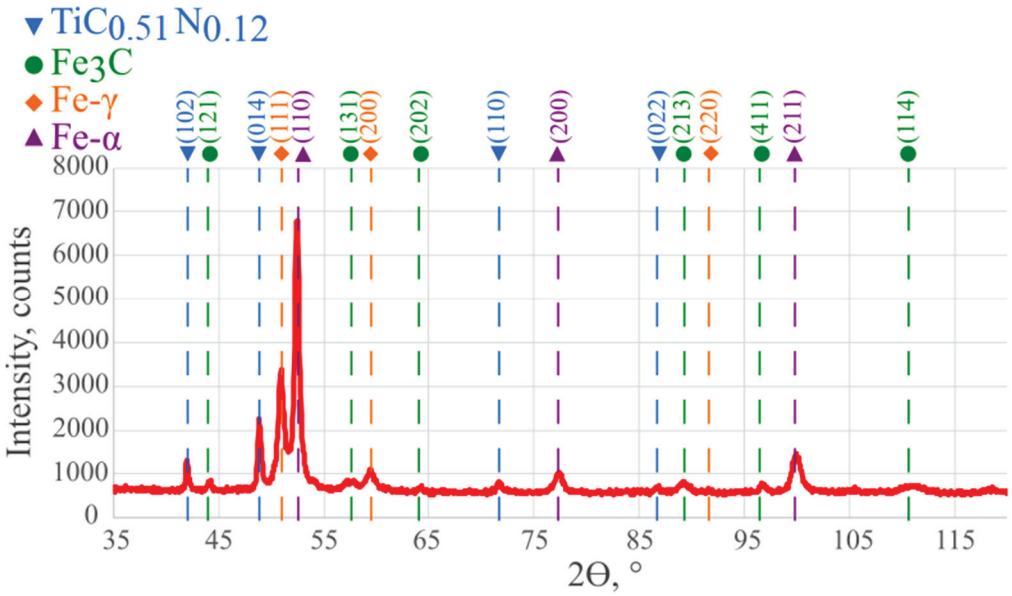


(**b**)



(**c**)

Figure 8. *Cont.*



(**d**)

Figure 8. The XRD results of representative surface layers: (**a**) A1, (**b**) N1, (**c**) TA2, and (**d**) TN2. Designations according to Table 3.

The LSA process on the DCI's surface caused in situ metal–matrix composite microstructure formation in the surface layers, in which the matrix was composed of primary austenite dendrites transformed to martensite and ledeburite in the interdendritic regions, which is similar to the LSM surface layers' microstructure. Depending on the process parameters (mainly titanium powder feed rate) the cubic or dendritic phases precipitated from the liquid metal during crystallization. The EDS and XRD analyses proved that those precipitates were titanium carbides or titanium carbonitrides for the process being carried out in an argon or nitrogen shield, respectively. In general, the analyzed process parameters produced homogeneous in situ metal–matrix composite surface layers reinforced by 5.5–20.1 vol.% of TiC precipitate and 4.8–10.1 vol.% of TiCN precipitate for the argon and nitrogen shields, respectively. With a titanium content increase in the liquid metal pool, the TiC(N) precipitate fraction increased. In comparison to LSM processes, the cementite fractions are lower for LSA surface layers. The cementite fraction also decreased with titanium content increases. This is due to the order of phase formation during cooling of liquid metal in the Fe-Ti-C and Fe-Ti-C-N systems [32–36]. The lower Gibbs free energy for TiC and TiCN resulted in the formation of those phases from the liquid metal first during cooling. With the increase in the titanium content and simultaneous increase in the TiC(N) precipitate fraction, the carbon content in the remaining liquid decreased, which resulted in a lower cementite fraction in the matrix. The titanium content did not affect the retained austenite fraction.

The average Vickers hardness and solid-particle erosion test results are presented in Table 5. For all analyzed samples, the laser surface treatment process caused the average hardness to increase. In the case of the LSM process, the hardness increased by 524–639 HV0.2 and 587–618 HV0.2 for the argon and nitrogen shields, respectively, in comparison to the base metal. The LSA process resulted in hardness increases of 458–591 HV0.2 and 391–460 HV0.2 for the argon and nitrogen shields, respectively, in comparison to the base metal. The higher hardness results of the LSM surface layers in comparison to the LSA surface layers are affected by the higher fraction of cementite in the microstructure. In general, the cementite fraction influenced the hardness results the most for the laser-melted and -alloyed surfaces, regardless of the shielding gas used. The hardness measurements distribution profiles are presented in Figure 9. The LSM surface layers show highly consistent hardness in the melted zone, due to the high homogeneity of the microstructure. In

the case of the LSA surface layers, due to the composite microstructure, a slightly wider range of hardness results was obtained in the alloyed zone. For all laser-treated surface layers, the hardness gradually decreased in the heat-affected zone, reaching values typical for the substrate material.

Table 5. The hardness and solid-particle erosion test results.

Designation (According to Table 3)	Average Vickers Hardness, HV0.2	Average Erosion Value, mm^3/g		Average Steady-State Erosion Rate, mg/min	
		30°	90°	30°	90°
A1	875 ± 19.6	0.047 ± 0.004	0.038 ± 0.006	0.69 ± 0.05	0.57 ± 0.1
A2	843 ± 17.2	0.047 ± 0.002	0.043 ± 0.007	0.7 ± 0.03	0.64 ± 0.1
A3	792 ± 21.7	0.050 ± 0.003	0.039 ± 0.002	0.73 ± 0.05	0.58 ± 0.04
N1	854 ± 19.0	0.046 ± 0.008	0.041 ± 0.002	0.69 ± 0.11	0.61 ± 0.03
N2	833 ± 57.3	0.043 ± 0.009	0.048 ± 0.004	0.63 ± 0.14	0.71 ± 0.06
N3	832 ± 33.3	0.048 ± 0.005	0.039 ± 0.004	0.72 ± 0.07	0.57 ± 0.06
TA1	695 ± 39.5	0.036 ± 0.001	0.025 ± 0.003	0.52 ± 0.02	0.37 ± 0.04
TA2	702 ± 33.0	0.032 ± 0.001	0.025 ± 0.004	0.45 ± 0.02	0.36 ± 0.04
TA3	694 ± 62.7	0.039 ± 0.001	0.028 ± 0.002	0.56 ± 0.02	0.39 ± 0.02
TA4	701 ± 43.7	0.039 ± 0.001	0.031 ± 0.005	0.54 ± 0.01	0.43 ± 0.06
TN1	663 ± 54.1	0.041 ± 0.003	0.027 ± 0.002	0.6 ± 0.05	0.39 ± 0.03
TN2	696 ± 30.5	0.037 ± 0.004	0.029 ± 0.004	0.55 ± 0.04	0.43 ± 0.04
TN3	627 ± 40.8	0.041 ± 0.002	0.026 ± 0.003	0.6 ± 0.03	0.38 ± 0.04
Substrate	236 ± 36.4	0.0617 ± 0.0004	0.034 ± 0.0032	0.88 ± 0.01	0.48 ± 0.05

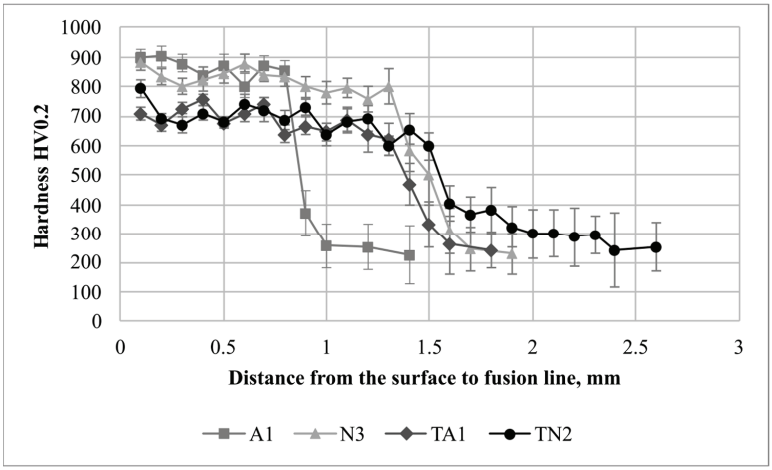


Figure 9. The hardness distribution in the representative surface layers from the surface towards the fusion line; designations according to Table 3.

The solid-particle erosion test results show that the laser surface melting and alloying processes carried out to modify the ductile cast iron surface had a positive effect on improving its erosion wear resistance. The average erosion values of all the tested surface layers and the substrate material are higher for the impingement angle of 30° than for 90°. Such results are typical for plastic materials [37]. In the case of the LSM surface layers, the average erosion values and rates for all samples are similar, so the shielding gas did not influence the erosion wear resistance of the layers. Generally, the laser surface melting process caused the average erosion values to decrease for the impingement angle of 30° in comparison to the base material, by up to 24% and 30% for the argon and nitrogen shields, respectively. For the 90° angle, the erosion rates and values are similar for LSM surface layers and the substrate. In the case of the LSA process, for both the tested impingement angles, the average erosion value decreased in comparison to the substrate material. In the case of the 30° impingement angle, the erosion values decreased by up to 48% and 40% for the argon and nitrogen shields, respectively. For the 90° impingement angle, the

average erosion values decreased by up to 26% and 23% for the argon and nitrogen shields, respectively. The results show that the shielding gas and, consequently, the precipitate's chemical composition did not significantly influence the erosion wear resistance. Despite the lower average hardness of the LSA surface layers in comparison to LSM, the erosion test results showed better resistance of the alloyed layers. This result is related to the composite microstructure of the LSA surface layers—the presence of an evenly dispersed TiC(N) precipitate in the structure.

The SEM images of the surfaces after the solid-particle erosion tests are presented in Figure 10. The observations allow us to specify the erosion mechanisms of the tested surface layers and the substrate material. In the case of the ductile cast iron surface, during erosion, plastic deformation occurred and scars, grooves, and craters can be observed on the surface for both the tested impingement angles. Additionally, embedded erodent particles can be observed on the surface due to the low hardness of the material. The erosion mechanism of the used ductile cast iron is therefore ductile. On the LSM surface layers, plastic deformation can be observed as a result of erosion, therefore, the erosion mechanism is also ductile for these layers. In this case, no embedded erodent particles were observed, which is due to the higher hardness of the surface. For the LSA surface layers, the erosion behavior is more complex due to the composite microstructure. In the matrix, plastic deformation occurred during erosion similar to in the LSM layers. However, for the in situ-formed TiC(N) precipitate, cracks were observed, indicating a brittle erosion mechanism. Additionally, on the composite layer's surfaces, voids were also observed on the surfaces, from which the precipitate was torn out during erosion.

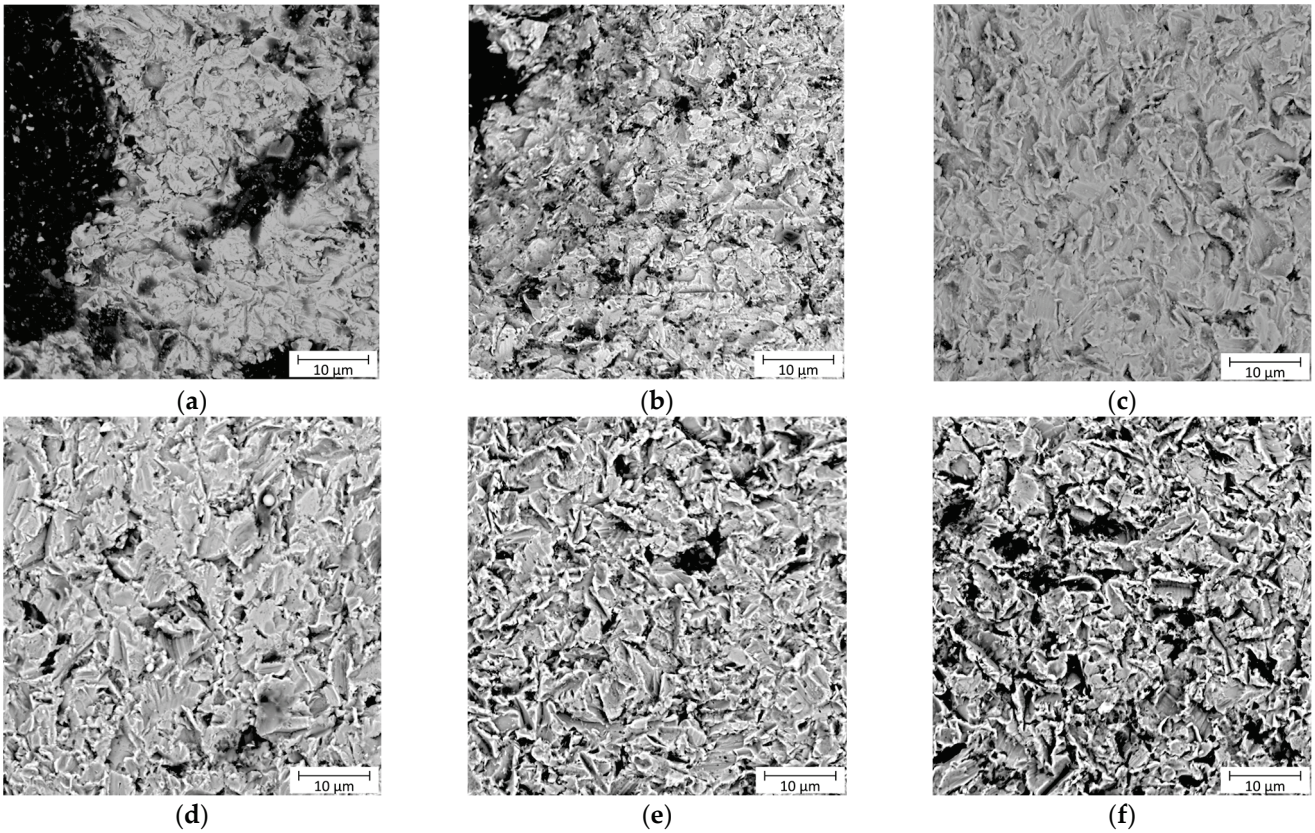


Figure 10. The SEM images of representative surface layers after solid-particle erosion tests: (**a**) impingement angle 30° [29], EN-GJS-350-22; (**b**) impingement angle 90°, EN-GJS-350-22; (**c**) impingement angle 30°, A3; (**d**) impingement angle 90°, N1; (**e**) impingement angle 30°, TA2; (**f**) impingement angle 90°, TN2; designations according to Table 3.

4. Conclusions

Based on the analysis of the achieved research results, the following conclusions have been reached:

1. The laser surface melting processes of the EN-GJS-350-22 ductile cast iron in argon and nitrogen shields caused modification of the microstructure of the surface layers that consist of primary austenite dendrites, partly after martensitic transformation, and eutectic austenite and ledeburite in the interdendritic spaces. The use of the nitrogen shield did not affect the microstructure or nitrogen's presence in the surface layer's chemical composition.
2. The laser surface alloying process of the EN-GJS-350-22 ductile cast iron with titanium allowed the formation of homogeneous in situ metal–matrix composite surface layers. Depending on the shielding gas (argon or nitrogen), cubic or dendritic TiC/TiCN particles precipitated from the liquid metal. The matrix microstructure consisted of primary austenite dendrites, partly after martensitic transformation, and ledeburite in the interdendritic spaces.
3. By the selection of the LSA process parameters it is possible to shape the structure of the surface layers, in particular the titanium concentration, precipitate's morphology, fraction, and chemical composition. The parameters selected for the research allowed surface layers reinforced with 5.5–20.2 vol.% of TiC and 4.8–10.1 vol.% of TiCN to be produced.
4. The modification of the microstructure by the laser surface melting of ductile cast iron resulted in the average Vickers hardness increasing by a maximum of 370% and 362% for the argon and nitrogen shields, respectively. The laser-alloyed surface layers showed average Vickers hardness increases of a maximum of 297% and 295% for the argon and nitrogen shields, respectively.
5. The laser surface melting and alloying processes caused an erosion resistance increase in the ductile cast iron. The erosion values of the LSM and LSA surface layers for a 30° impingement angle decreased by a maximum of 30% and 48%, respectively. In the case of the 90° impingement angle, the LSM layers showed similar erosion values, and for LSA layers, the erosion values decreased by up to 26% in comparison to the substrate material. The composite microstructure of the LSA surface layers caused a higher increase in the erosion resistance in comparison to LSM layers in addition to the lower hardness.
6. The erosion mechanism of the substrate material and laser-melted surface layers is ductile. For the laser-alloyed surface layers, the erosion mechanism is more complex, being ductile for the matrix material and brittle for the TiC(N) precipitate.

Author Contributions: Conceptualization, J.G., A.L. and D.J.; methodology, D.J., A.L. and T.P.; software, A.L. and A.R.; validation, J.G., A.L., D.J., T.P. and A.R.; formal analysis J.G., A.L., D.J., T.P. and A.R.; investigation, A.L. and D.J.; resources, J.G. and T.P.; data curation, A.L. and A.R.; writing—original draft preparation, A.L.; writing—review and editing, J.G. and D.J. All authors have read and agreed to the published version of the manuscript.

Funding: This research received no external funding.

Institutional Review Board Statement: Not applicable.

Informed Consent Statement: Not applicable.

Data Availability Statement: The original contributions presented in the study are included in the article, further inquiries can be directed to the corresponding author.

Conflicts of Interest: The authors declare no conflicts of interest.

References

1. Elliot, R. *Cast Iron Technology*, 1st ed.; Butterworth & Co.: London, UK, 1988; pp. 13–20.
2. Czupryński, A.; Żuk, M. Matrix Composite Coatings Deposited on AISI 4715 Steel by Powder Plasma-Transferred Arc Welding. Part 3. Comparison of the Brittle Fracture Resistance of Wear-Resistant Composite Layers Surfaced Using the PPTAW Method. *Materials* **2021**, *14*, 6066. [CrossRef] [PubMed]
3. Poloczek, T.; Lont, A.; Górka, J. The Structure and Properties of Laser-Cladded Inconel 625/TiC Composite Coatings. *Materials* **2023**, *16*, 1265. [CrossRef] [PubMed]
4. Krella, A. Resistance of PVD Coatings to Erosive and Wear Processes: A Review. *Coatings* **2020**, *10*, 921. [CrossRef]
5. Jonda, E.; Szala, M.; Sroka, M.; Łatka, L.; Walczak, M. Investigations of cavitation erosion and wear resistance of cermet coatings manufactured by HVOF spraying. *Appl. Surf. Sci.* **2023**, *608*, 155071. [CrossRef]
6. Cui, C.; Wu, M.; Miao, X.; Gong, Y.; Zhao, Z. The effect of laser energy density on the geometric characteristics, microstructure and corrosion resistance of Co-based coatings by laser cladding. *JMR&T* **2021**, *15*, 2405–2418.
7. Anas, A.S.; Avanish, K.D. Recent trends in laser cladding and surface alloying. *Opt. Laser Technol.* **2021**, *134*, 106619.
8. Malek Ghaini, F.; Ameri, M.H.; Torkamany, M.J. Surface transformation hardening of ductile cast iron by a 600w fiber laser. *Optik* **2020**, *203*, 163758. [CrossRef]
9. Ion, J.C. Laser Transformation Hardening. *Mater. Surf. Eng.* **2002**, *18*, 14–31. [CrossRef]
10. Kotarska, A.; Janicki, D.; Górka, J.; Poloczek, T. Solid particle erosion of laser surface melted ductile cast iron. *Arch. Foundry Eng.* **2020**, *20*, 105–111. [CrossRef]
11. Murakami, R.; Narita, I.; Miyahara, H. Surface microstructure and properties of nodular cast iron rapidly solidified by laser surface melting. *Mater. Trans.* **2018**, *59*, 1465–1470. [CrossRef]
12. Jeyaprakash, N.; Yang, C.H.; Duraiselvam, M.; Prabu, G. Microstructure and tribological evolution during laser alloying WC-12%Co and Cr_3C_2-25%NiCr powders on nodular iron surface. *Results Phys.* **2019**, *12*, 1610–1620. [CrossRef]
13. Yan, H.; Wang, A.; Xiong, Z.; Xu, K.; Huang, Z. Microstructure and wear resistance of composite layers on a ductile iron with multicarbide by laser surface alloying. *Appl. Surf. Sci.* **2010**, *256*, 7001–7009. [CrossRef]
14. Paczkowska, M. The Comparison of the Effects of Nodular Cast Iron Laser Alloying with Selected Substances. *Materials* **2022**, *15*, 7561. [CrossRef] [PubMed]
15. Sun, F.; Cai, K.; Li, X.; Pang, M. Research on Laser Cladding Co-Based Alloy on the Surface of Vermicular Graphite Cast Iron. *Coatings* **2021**, *11*, 1241. [CrossRef]
16. Li, Y.; Dong, S.; Yan, S.; Liu, X.; He, P.; Xu, B. Microstructure evolution during laser cladding Fe-Cr alloy coatings on ductile cast iron. *Opt. Laser Technol.* **2018**, *108*, 255–264. [CrossRef]
17. Arias-Gonzalez, F.; del Val, J.; Comesana, R.; Penide, J.; Lusquinos, F.; Quintero, F.; Riveiro, A.; Boutinguiza, M.; Pou, J. Fiber laser cladding of nickel-based alloy on cast iron. *Appl. Surf. Sci.* **2016**, *374*, 197–205. [CrossRef]
18. Li, Y.; Dong, S.; He, P.; Yan, S.; Li, E.; Liu, X.; Xu, B. Microstructure characteristics and mechanical properties of new-type FeNiCr laser cladding alloy coating on nodular cast iron. *J. Mater. Process. Technol.* **2019**, *269*, 163–171. [CrossRef]
19. Grum, J.; Sturm, R. Microstructure analysis of nodular iron 400-12 after laser surface melt hardening. *Mater. Charact.* **1996**, *37*, 81–88. [CrossRef]
20. Yang, H.; Zhou, T.; Wang, Q.; Zhou, H. Effects of Laser Melting Distribution on Wear Resistance and Fatigue Resistance of Gray Cast Iron. *Metals* **2020**, *10*, 1257. [CrossRef]
21. Pagano, N.; Angelini, V.; Ceschini, L.; Campana, G. Laser remelting for enhancing tribological performances of a ductile iron. *Proc. CIRP* **2016**, *41*, 987–991. [CrossRef]
22. Alabeedi, K.F.; Abboud, J.H.; Benyounis, K.Y. Microstructure and erosion resistance enhancement of nodular cast iron by laser melting. *Wear* **2009**, *266*, 925–933. [CrossRef]
23. Paczkowska, M.; Makuch, N.; Kulka, M. The influence of various cooling rates during laser alloying on nodular iron surface layer. *Opt. Laser Technol.* **2018**, *102*, 60–67. [CrossRef]
24. Chen, Z.; Meng, C.; Dong, J.; Zhou, T.; Tong, X.; Zhou, H. The comparative study of W/Cr addition in Fe-base by laser surface alloying on fatigue wear resistance of GCI. *Surf. Coat. Technol.* **2016**, *286*, 25–35. [CrossRef]
25. Yilbas, B.S.; Akhtar, S.S.; Karatas, C.; Boran, K. Laser treatment of dual matrix cast iron with presence of WC particles at the surface: Influence of self-annealing on stress fields. *Opt. Laser Technol.* **2016**, *76*, 6–18. [CrossRef]
26. Janicki, D. The friction and wear behaviour of in-situ titanium carbide reinforced composite layers manufactured on ductile cast iron by laser surface alloying. *Surf. Coat. Technol.* **2021**, *406*, 126634. [CrossRef]
27. Kotarska, A. The Laser Alloying Process of Ductile Cast Iron Surface with Titanium. *Metals* **2021**, *11*, 282. [CrossRef]
28. Janicki, D. *Shaping the Structure and Properties of Surface Layers of Ductile Cast Iron by Laser Alloying*, 1st ed.; Wydawnictwo Politechniki Śląskiej: Gliwice, Poland, 2018; p. 29.
29. Lont, A.; Górka, J.; Janicki, D.; Matus, K. The Laser Alloying Process of Ductile Cast Iron Surface with Titanium Powder in Nitrogen Atmosphere. *Coatings* **2022**, *12*, 227. [CrossRef]
30. *ASTM G76-04*; Standard Test Method for Conducting Erosion Tests by Solid Particle Impingement Using Gas Jets. ASTM International: West Conshohocken, PA, USA, 2004.
31. Kundakcıoğlu, E.; Lazoglu, I.; Poyraz, Ö.; Yasa, E.; Cizicioğlu, N. Thermal and molten pool model on selective laser melting process of Inconel 625. *Int. J. Adv. Manuf. Technol.* **2018**, *95*, 3977–3984. [CrossRef]

32. Frisk, K. A revised thermodynamic description of the Ti-C system. *Calphad* **2003**, *27*, 367–373. [CrossRef]
33. Zhu, H.; Dong, K.; Wang, H.; Huang, J.; Li, J.; Xie, Z. Reaction mechanisms of the TiC/Fe composite fabricated by exothermic dispersion from Fe-Ti-C element system. *Powder Technol.* **2013**, *246*, 456–461. [CrossRef]
34. Jonsson, S. Calculation of the Ti-C-N system. *Z. Metallkde* **1996**, *87*, 713–720. [CrossRef]
35. Dumitrescu, L.F.S.; Hillert, M.; Sundman, B. A reassessment of Ti-C-N based on a critical review of available assessments of Ti-N and Ti-C. *Z. Metallkde* **1999**, *90*, 534–541. [CrossRef]
36. Gorbachev, I.I.; Popov, V.V. Analysis of the solubility of carbides, nitrides and carbonitrides in steels using methods of computer thermodynamics: III. Solubility of carbides, nitrides and carbonitrides in the Fe-Ti-C, Fe-Ti-N and Fe-Ti-C-N systems. *Phys. Met. Metallogr.* **2009**, *108*, 484–495. [CrossRef]
37. Stachowiak, G.W.; Batchelor, A.W. *Engineering Tribology*, 4th ed.; Butterworth-Heinemann: Oxford, UK, 2014; pp. 551–556.

Disclaimer/Publisher's Note: The statements, opinions and data contained in all publications are solely those of the individual author(s) and contributor(s) and not of MDPI and/or the editor(s). MDPI and/or the editor(s) disclaim responsibility for any injury to people or property resulting from any ideas, methods, instructions or products referred to in the content.

coatings

MDPI

Article

Laser Surface Hardening of Austempered Ductile Iron (ADI)

Ladislav Záhon *, Jiří Kuchař, Jakub Horník, Jan Krčil and Jan Kudláček

Department of Manufacturing Technology, Faculty of Mechanical Engineering, Czech Technical University in Prague, Technická 4, 16000 Prague, Czech Republic; jiri.kuchar@fs.cvut.cz (J.K.); jakub.hornik@fs.cvut.cz (J.H.)
* Correspondence: ladislav.zahon@fs.cvut.cz

Abstract: The subject of the research is the possibility of using laser surface hardening to modify the tribological properties of ADI castings. ADI cast irons are a very progressive material; these cast irons find their application (due to their characteristic properties) in demanding applications. In these applications, the tribology of their surface is an essential parameter. This research focused on the change in tribological properties due to laser hardening of the surface layers. ADI cast iron samples processed at different isothermal holding temperatures were selected for the experiment. This is because these temperatures have a major influence on the initial structure (before laser exposure), which also affects the laser hardening process. To analyze the structural changes, metallographic examinations were performed. The microhardness was also measured on each sample in relation to the distance from the surface. The samples were also subjected to a tribological test (linear reciprocating tribometer) during which the coefficient of friction was recorded. The surface conditions after the tribological experiment were evaluated using an electron microscope. Tribological experiments revealed very different behavior of laser-hardened ADI cast iron surfaces depending on their isothermal holding temperature. At the same time, a homogeneous martensitic layer on the surface (a consequence of the relatively uniform distribution of carbon in the initial ausferritic structure) was achieved by laser, which contributed to a significant increase in hardness and wear resistance. A trend of decreasing friction coefficient as a function of isothermal holding temperature was observed for non-laser-hardened surfaces. This phenomenon supports the theory of a possible martensitic transformation of the high-carbon austenite contained in the structure of ADI castings.

Keywords: ADI; cast irons; austempering; laser surface hardening; tribology

1. Introduction

Graphitic cast irons have exceptional foundry properties that enable high-quality castings to be achieved. The mechanical properties of the casting, including tribological properties, are crucial parameters for many applications [1,2]. The tribology of the surface of graphitic cast irons is influenced by the graphite contained in the cast iron structure (graphite has certain lubricating effects due to its bonds in the crystal lattice). The shape of the graphitic formations is essential. Some studies [3] point out the different behavior of cast iron with graphite in the form of spheres and flakes. At the same time, however, graphite formations can act as surface heterogeneities that can initiate the formation of cracks in their surroundings [4–7]. The problem with the structure of graphitic cast irons was (and to some extent still is) relatively low mechanical properties. With the development of the process of modifying cast iron with magnesium to produce cast iron with graphite in the form of spheres, the mechanical properties have been significantly improved (cast irons with spherical graphite approach the mechanical properties of steels) [8,9]. With further efforts to improve the mechanical properties of graphitic cast irons (especially cast iron with spherical graphite), the austempering process was developed. The result of this heat treatment is ADI (Austempered Ductile Iron) or AGI (Austempered Gray Iron) [10,11].

Austempering is a very progressive heat treatment method, which can achieve several times the yield strength compared to the cast structure of the casting, while at the same time the cast iron processed in this way has relatively good tribological properties and excellent toughness [12]. Due to the combination of these mechanical properties, ADI cast irons find applications in the automotive, aerospace, and military industries [13]. Typical applications are gears, crankshafts, and camshafts. Very often these are applications where surface tribology is a major factor [14]. For this reason, it is important to focus on this issue and to consider various options for increasing the abrasion resistance of the ADI surface. One of the options may be the use of laser for surface hardening of ADI castings. This is the focus of this research. Specifically, this research focuses on the influence of the initial ausferritic structure (which is determined by the isothermal holding temperature, the influence of this temperature on the structural changes is still a matter of debate) on the surface laser hardening process. The aim is to map the structural changes after laser hardening and the change in tribological properties of the surface due to the laser treatment. Surface laser hardening has its specificities that made this method selected as a possible option to increase the wear resistance of ADI castings. A description of laser hardening (including the specific reasons for its selection) is given below. First, the process of austempering needs to be clarified.

The austempering process consists of several stages. The first phase is the austenitization of the casting; the cast iron is heated to 850–950 °C. At this temperature, the initial structure changes to austenitic. After austenitization, the casting is transferred to a salt bath at a temperature of 250–450 °C. At these temperatures, nucleation of acicular ferrite on graphite and its subsequent growth occurs. Carbon diffuses into the ferrite surroundings and the austenite is stabilized in this way. This results in a typical ausferritic structure consisting of acicular ferrite and high-carbon austenite [15–19]. The effect of isothermal tempering temperature is not fully understood even at present. Lower isothermal temperatures lead to higher nucleation of finer ferrite. Conversely, higher temperatures contribute to more intense diffusion, resulting in coarser ferrite and larger austenite blocks between the plates of acicular ferrite. According to the authors of [14,20–23], austenite (in the ausferritic structure of ADI) can be transformed to martensite at sufficiently high contact pressure. The authors of the studies agree that this phenomenon occurs mainly in ADI cast irons processed at higher temperatures; these cast irons contain block austenite, which is more susceptible to transformation. The transformation of austenite to martensite in the surface layers can significantly improve the surface tribology. However, this is a complicated issue on which there is no clear consensus even at present.

In this research, (due to its characteristic properties) laser surface hardening of ADI castings is tested. The laser is a powerful source of energy. When a laser is applied to the surface of a component, the heat entering the surface layers is significantly greater than the heat dissipated into the cold core. This creates a large thermal gradient. The laser action increases the surface temperature and transforms the initial structure into austenite. Subsequent movement of the laser to another location allows heat to be dissipated from its previous focusing location, thereby rapidly cooling the surface and transforming it to martensite. With induction hardening and flame hardening, the thermal gradient is not as large; additional cooling is required to harden the surface, and most commonly various water showers are used. In these methods, the shape of the burner or inductor must also follow the shape of the surface. The laser can be programmed to harden a variety of surface shapes and is also suitable for piece production. By very fast cooling of the surface during laser hardening, very fine structures with other possible specific elements can be achieved. In the case of the initial ausferritic structure, it would be possible to achieve very fine martensite (with better mechanical properties), but the question remains, for example, about the influence of carbon distribution in this initial structure [24–27].

2. Materials and Methods

The experimental part is focused on the analysis of the surface hardening of ADI (Austempered Ductile Iron) by laser and its influence on the tribological characteristics of the tested samples. The experiment thus includes the evaluation of the microstructure of the laser-hardened samples, the measurement of the hardness of the hardened layer (for each sample, the microhardness of the hardened layer was measured in relation to the distance from the surface), and the tribological analysis itself. The latter consists of testing the samples on a tribometer with linear reciprocating motion, during which the friction coefficient was recorded. This test was followed by an evaluation of the worn surfaces using scanning electron microscopy.

2.1. Tested Samples

For the experimental part, samples of ductile cast iron with nodular graphite were used; the chemical composition is shown in Table 1 (the chemical composition was analyzed by the OES method). These are samples that have an identical chemical composition but differ in isothermal holding temperature. This difference is also indicated by the marking of the samples, i.e., 'k'-nodular graphite; the number after 'k' indicates the isothermal cure temperature ('6'–60 min). The last three digits indicate the value of the isothermal cure temperature. The samples had dimensions of 40 × 30 mm^2, and their thickness was 15 mm.

Table 1. Chemical composition of the samples used (the remainder of the chemical composition consists of Fe).

Samples	Chemical Composition [wt.%]						
	C	**Si**	**Mn**	**P**	**S**	**Mg**	**Cu**
ADI 9k6 240 ADI 9k6 310 ADI 9k6 400	ADI 9k6 240	2.45	0.25	0.02	0.02	0.04	0.01

2.2. Tribological Analysis

In the experimental part, laser-hardened and non-hardened surfaces of the samples were tested. It was thus possible to compare the change in their tribological properties. First, the tribological test itself was carried out on the MFT-5000 (Rtec Instruments, San Jose, CA, USA) tribometer. It is a multifunctional tribometer, so it is possible to test samples with both PIN-ON-DISC and PIN-ON-PLATE methods. The tribometer can also be equipped with high-temperature modules to allow tribological experiments to be performed at elevated temperatures. For this experiment, the PIN-ON-PLATE method without a temperature module was chosen. A hardened, chromium-alloyed steel (material-100Cr6, San Jose, CA, USA) ball with a diameter of 6.35 mm was used as PIN.

Each sample was clamped to a table that was movable relative to the PIN before testing. Subsequently, the PIN (steel ball) was clamped in a special fixture; the fixture with the clamp prevented any unwanted movement (rotation) of the PIN. For a correct measurement, it was necessary to set the fixture in a perpendicular position to the sample. Before running the test, it was necessary to clean the sample and the PIN to eliminate the influence of various contaminants that may have been present on the contact surfaces. For cleaning, isopropyl alcohol was used; cleanliness was checked visually. This was followed by setting the fixture to the initial position (using a special controller). After this step, the tribological test was started. During the experiment, the PIN was loaded with a predefined force (30 N). The PIN moved along a predefined path relative to the specimen; the distance between the movements was set to 5 mm, and the speed of movement was 5 mm/s. The baseline tribological test time was set to 30 min. However, a control measurement of 11 min was carried out at the same time. The different test lengths made it possible to observe the evolution of the surface wear as a function of time (the surface was analyzed by

scanning electron microscopy). At the same time, it was possible to observe the measured values of the friction coefficient at the 10th min of the test for both types of measurements.

The friction coefficient was recorded throughout the measurement period. Since the linear reciprocating method was used, it would be possible to evaluate the static and dynamic friction coefficients. However, this option was not offered by the software of the tribometer used. Thus, the tables presented here show the average values of the friction coefficient measured during the test.

The surface condition of the samples after the tribological test was evaluated by scanning electron microscopy. To evaluate the effect of surface hardening on the tribology of cast irons, both hardened and non-hardened surfaces of the samples were analyzed, thus allowing their comparison with each other. For hardened surfaces, traces of both the 30 min and 11 min tests were imaged.

In scanning electron microscopy, imaging based on secondary electrons (specifically SEI and LEI) was used. An EDS analysis was also performed. The samples were previously cleaned of coarse impurities using compressed air.

2.3. Parameters of Laser Hardening

For the experimental part, the individual samples used were laser surface hardened. The laser hardening parameters used are shown in Table 2. The diode laser YAG laserline LDF 10,000–100 (made in Mülheim-Kärlich, Germany) was used for the experimental part; the wavelength of this laser is 940–1020 $\pm$ 10 nm. It is a laser commonly used for surface hardening of iron alloys. It has a suitable wavelength that guarantees sufficient absorption of radiation. Another factor for choosing this laser was its availability. The laser spot had the shape of a rectangle. One track (laser pass) was created on each sample. The laser power during surface hardening was 10 kW; thus, the laser power density was 62.5 W/mm^2. The laser hardening parameters were chosen based on the experience of the authors of this article, the laser operator, and the literature (e.g., [28]).

Table 2. Parameters of laser hardening.

Laser Used	Laserline LDF 10,000–100
Focusing distance [mm]	348
Clouding optics	Laserline zoom optics
Laser spot size [mm]	8 × 20
Temperature [°C]	1120
Speed [cm/min]	45
Power [kW]	10

3. Results

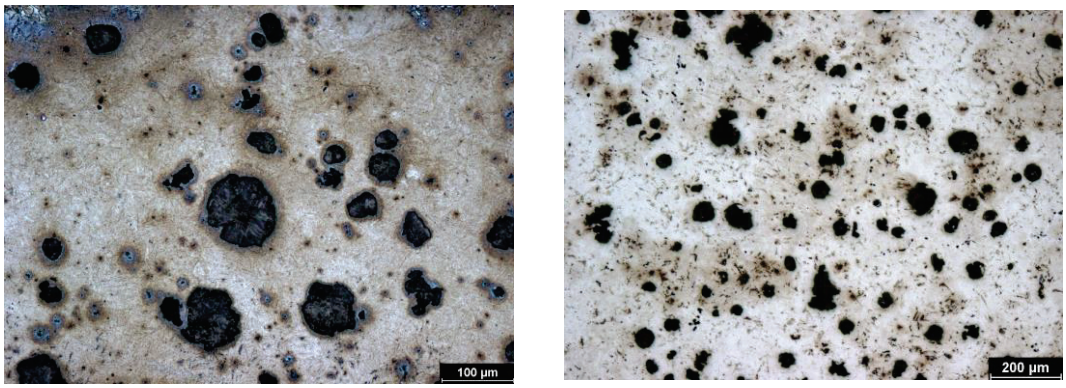
3.1. Microstructure of the Tested Samples

In this section, the microstructures of individual samples without laser hardening are shown. Furthermore, structural changes after surface hardening by laser are shown here. The section also includes graphical hardness dependences for a laser-hardened surface. All microstructures of the samples were obtained in the same way. First, the samples were cut on a special saw designed for the preparation of metallographic samples (this allows the samples to be separated without thermal influence on their structure). Subsequently, the samples were fixed in a special material (Bakelite). Then the samples were sanded with sandpaper of different grits; after sanding, the samples were polished and etched.

3.1.1. ADI 9k6 240

This is a sample of cast iron with spherical graphite that has been subjected to austempering, which is why it is referred to as ADI (Austempered Ductile Iron). This sample was heat treated at the lowest isothermal holding temperature (240 °C) of all the samples tested. Therefore, the initial structure of the sample is the finest. The structure consists of bainite, fine plates of acicular ferrite, and high-carbon austenite. However, this austenite does not

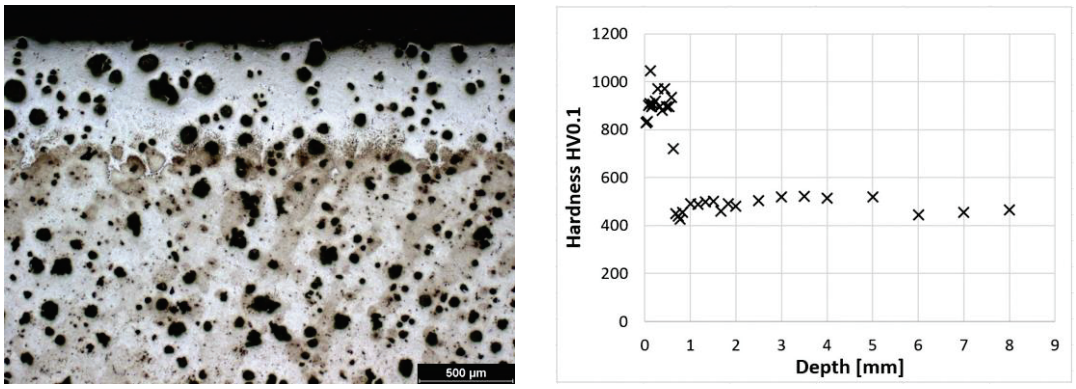
form blocks but rather is in the form of a thin film. Figure 1b represents the initial (non-hardened) structure. Images were taken with a metallographic microscope.



(**a**) (**b**)

Figure 1. Microstructure of ADI 9k6 240; (**a**) Detail of the structure of the laser-hardened surface of ADI 9k6 240; (**b**) Structure of the laser non-hardened core of the ADI 9K6 240 cast iron sample.

Figure 2a shows the microstructure of a laser-hardened surface. A detail of this laser-hardened structure is shown in Figure 1a. It can be seen from these photographs that the structure is predominantly composed of fine martensite and residual austenite (to a depth of approximately 0.5 mm). Figure 2b shows the dependence of hardness on distance from the surface. From these values, it can be seen that at the surface, the sample reaches a hardness of 900–1000 HV0.1. The microstructure of the hardened surface shows that the proportion of coarser martensite increases with increasing distance from the surface. The hardness of the cast iron decreases gradually to a depth of about 0.8 mm, where it stabilizes at the hardness values of the austempered cast iron itself.

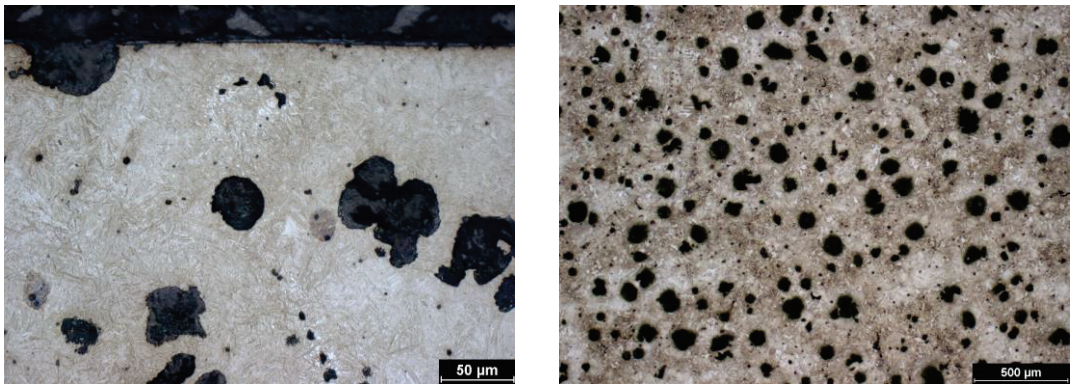


(**a**) (**b**)

Figure 2. ADI 9k6 240; (**a**) Structure of the laser-hardened surface of ADI 9k6 240; (**b**) Dependence of hardness on the distance from the ADI 9k6 240 surface.

3.1.2. ADI 9k6 310

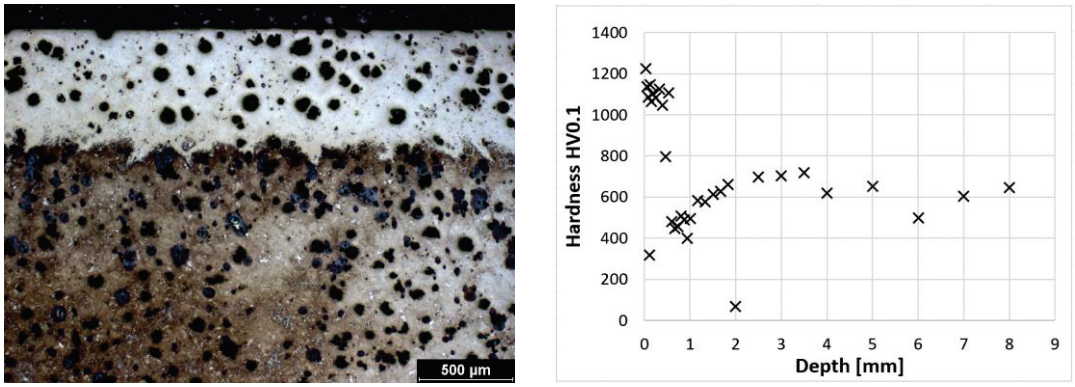
Similar to the previous sample, the starting material is austempered cast iron with spheroidal graphite. The isothermal holding temperature for this sample was 310 °C, which is an intermediate value compared to the other two samples. This is consistent with the structure. Due to the heat treatment, it is again composed of bainite, acicular ferrite, and high-carbon austenite. Due to the higher isothermal holding temperature (than in the previous case), the ferrite is coarser and the high-carbon austenite forms more bulky blocks. The initial structure is shown in the image of the unhardened core (Figure 3b).



(**a**) (**b**)

Figure 3. Microstructure of ADI 9k6 310; (**a**) Detail of the structure of the laser-hardened surface of ADI 9k6 310; (**b**) Structure of the laser non-hardened core of the ADI 9K6 310 cast iron sample.

Figure 4a shows the laser-hardened surface of the cast iron; a detail of the structure of the hardened layer is shown in Figure 3a. This laser-hardened layer is again composed of martensite and some residual austenite. However, when compared with the previous sample, it is noticeable that in this case, the martensite is coarser. Figure 4b shows a graphical dependence of the hardness versus distance from the surface. The coarser martensite contributes to the gradual decrease in hardness, and its proportion increases with distance from the surface. The hardness values are steady at the hardness of the initial cast iron structure. The course of hardness is very similar to the previous sample. Some of the significantly different hardness values are due to indentation in the graphite.

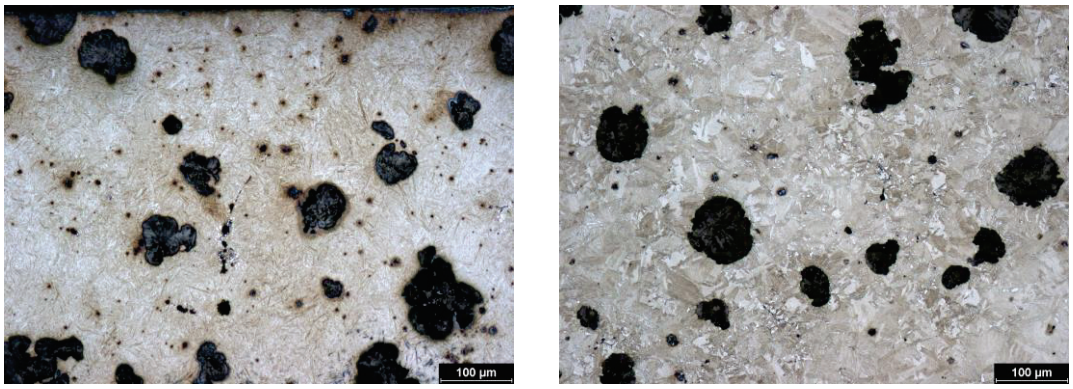


(**a**) (**b**)

Figure 4. ADI 9k6 310; (**a**) Structure of the laser-hardened surface of ADI 9k6 310; (**b**) Dependence of hardness on the distance from the ADI 9k6 310 surface.

3.1.3. ADI 9k6 400

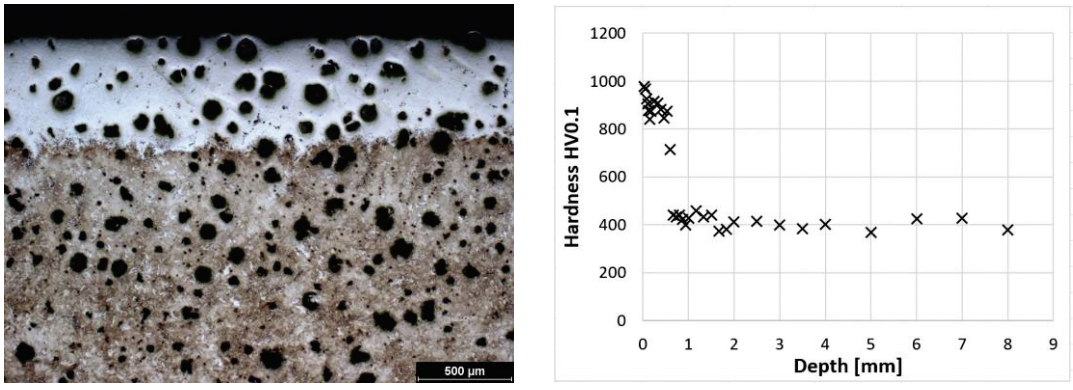
The starting material is identical to the previous samples (austempered cast iron with spheroidal graphite). This sample was subjected to the highest isothermal heat treatment temperature of all the tested samples (400 °C). The relatively high temperature contributed to the creation of a coarser structure (compared to the previous samples); the initial microstructure (before the laser treatment) is shown in Figure 5b. The structure of the cast iron prior to laser surface hardening is again composed of bainite, acicular ferrite, and high-carbon austenite. The higher isothermal holding temperature contributed to the formation of block austenite; such austenite can transform to martensite under certain conditions. This phenomenon may affect the results of the tribological laser test of the non-hardened surface (as described earlier in this article).



(**a**) (**b**)

Figure 5. Microstructure of ADI 9k6 400; (**a**) Detail of the structure of the laser-hardened surface of ADI 9k6 400; (**b**) Structure of the laser non-hardened core of the ADI 9K6 400 cast iron sample.

Figure 6a shows the laser-hardened surface of a sample of ADI 9k6 400 cast iron. The detail of this hardened structure is then shown by metallographic etching (Figure 5a). This hardened layer is composed of martensite and residual austenite, similar to the previous samples. The depth of the hardened layer is also very similar to the previous samples. At the surface, the layer is composed of relatively fine martensite (mainly to a depth of about 0.5 mm); then there is again a transition zone with coarser martensite, which leads to a decrease in hardness. The dependence of hardness on distance from the surface is shown in Figure 6b. The actual pattern is again very similar to the previously mentioned samples.



(**a**) (**b**)

Figure 6. ADI 9k6 400; (**a**) Structure of the laser-hardened surface of ADI 9k6 400; (**b**) Dependence of hardness on the distance from the ADI 9k6 400 surface.

3.2. Results of Tribological Analysis

This section records the values of the friction coefficient for each specimen tested. At the same time, tables with the resulting average values of the friction coefficient for the respective samples are given. This section also includes the evaluation of the wear test surfaces. These surfaces were analyzed by electron microscopy.

3.2.1. Progress of the ADI 9k6 240 Tribological Test

Figure 7 shows a record of the friction coefficient produced during a 30 min tribological test of a non-hardened surface. It can be seen from this record that there was a definite decrease and then an increase in the recorded values during the running-in of the tribological pair (non-hardened surface and pin). This phenomenon was also observed during the control 11 min measurement. The record of this measurement is shown in Figure 8. The periodic alternation of higher and lower values of the friction coefficient is caused by

linear reciprocating motion. This is because there is an alternation of static (coefficient at rest) and dynamic (during movement) friction coefficients.

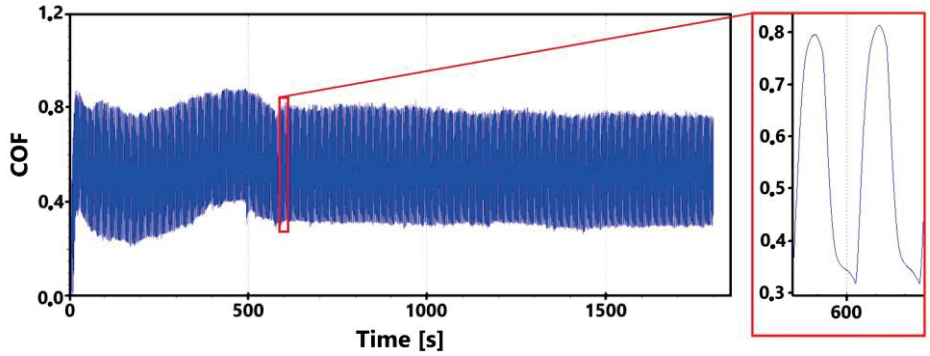


Figure 7. Record of the friction coefficient of the laser non-hardened surface of the sample ADI 9k6 240 (30 min).

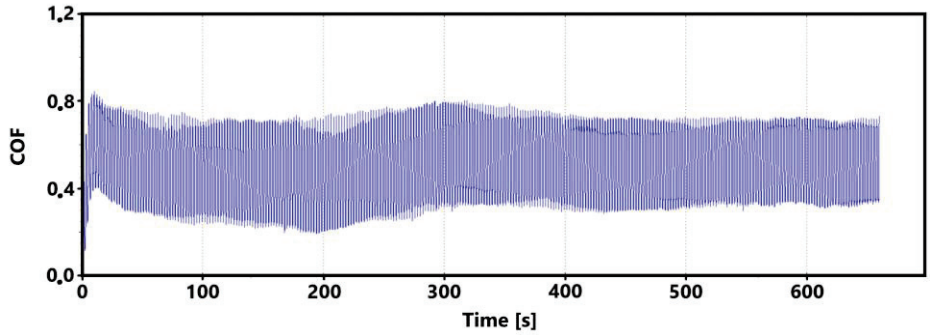


Figure 8. Record of the friction coefficient of the laser non-hardened surface of the sample ADI 9k6 240 (control measurement, 11 min).

There may be a number of reasons for the fluctuations in the values at the beginning of the test. For example, it may be due to the release of large amounts of graphite, which can have a significant effect on friction. Another and more likely reason may be the formation of an oxide layer on the surface of the cast iron. The movement of the pin across the surface may erode this layer, thus creating separate parts of the oxide layer. The movement of these parts can then also have a significant effect on the value of the friction coefficient. It is evident from both recordings that the steady-state values occurred around the 10th min of the test. The range of values over which the friction coefficient varies in the 10th min of the test is very similar for both measurements.

Figure 9 shows the graphical dependence of the friction coefficient values recorded during the 30 min tribological test of the laser-hardened surface. This figure shows a similar trend to that of the non-hardened surface. That is, the initial fluctuation in values that is associated with the running-in of the tribological pair.

The initial increase with a later decrease in values can be associated with a number of factors. However, the most likely effect appears to be the formation of the oxide layer and its subsequent breaking during the test. Electron microscope analysis of the sample surface after the 11 min test (see Figure 10 for a record of the friction coefficient) shows that the oxide layer is relatively compact at the 11 min mark. Its subsequent disintegration and movement of parts of this layer (together with parts of the separated cast iron matrix) may be associated with an increase in the values of the friction coefficient.

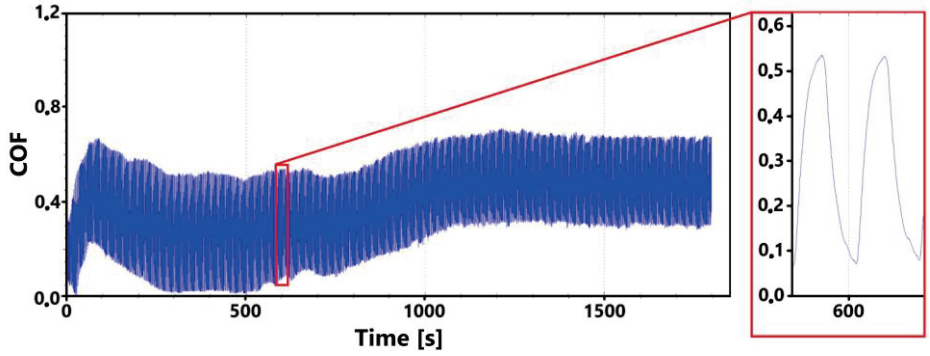


Figure 9. Record of the friction coefficient of the laser-hardened surface of the sample ADI 9k6 240 (30 min).

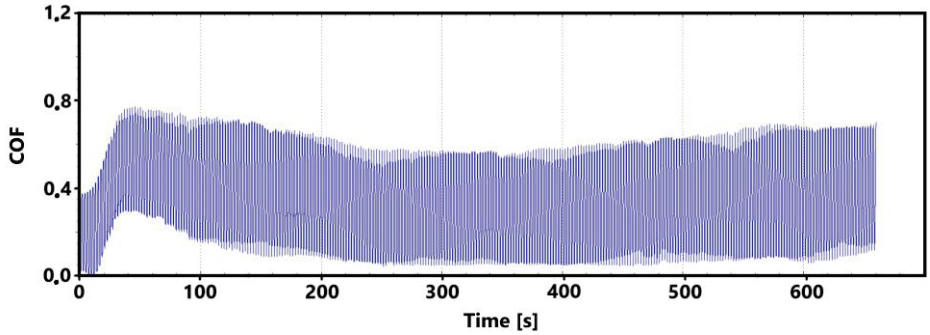
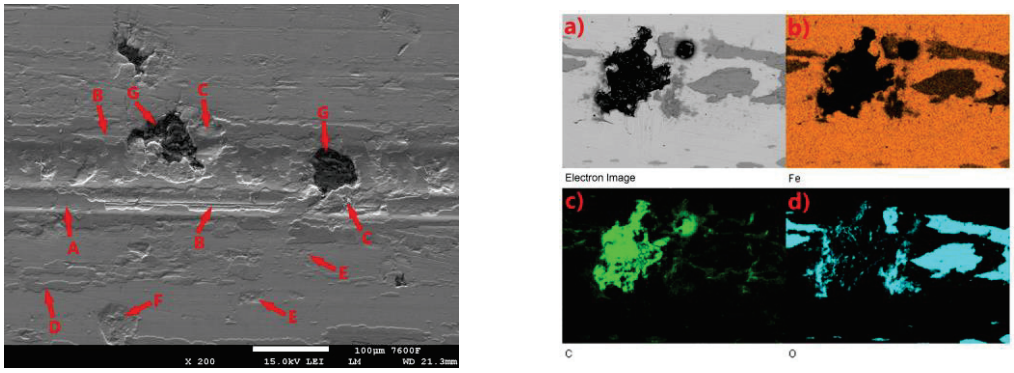


Figure 10. Record of the friction coefficient of the laser hardened surface of the sample ADI 9k6 240 (control measurement, 11 min).

The records show that the behavior of hardened and non-hardened surfaces in the run-in phase is similar. However, the hardened surface shows a stabilization of values after a longer period of time. The fluctuation interval is larger for the hardened surface. This may be due to the harder and stronger surface of the quenched sample, which may have contributed to the stability of the emerging oxide layer.

3.2.2. Surface Analysis of ADI 9k6 240 Sample after Tribological Test

All tested samples showed significant oxidation of the base material during the tribological test. The oxidation layer can be observed, for example, in Figure 11i-A. EDS analysis of the worn surface was performed to confirm the oxidation. The analyzed area is shown in Figure 11ii(a). Figure 11ii(b) shows the iron distribution in the analyzed area, Figure 11ii(c) shows the carbon distribution, and Figure 11ii(d) shows the oxygen distribution. Thus, Figure 11ii(b) shows that the analyzed layer is darker relative to its surroundings and thus contains less iron relative to its surroundings. In the oxygen analysis 11ii(d), the analyzed layer contains a significantly higher amount of oxygen relative to its surroundings (the oxygen distribution is shown in blue in the figure). Thus, the EDS analysis confirmed the assumption that an oxide layer was formed during the tribological test, which could have had a major influence on the resulting surface tribology. Figure 11i shows the worn surface of the non-hardened ADI 9k6 240 specimen after the 30 min tribological test. The aforementioned oxide layer in this case is highly non-compact, showing a rather significant violation of integrity. One of the causes may be the deformation of the cast iron matrix that occurs due to the movement of the PIN on the surface. This in turn may contribute to the formation and propagation of cracks in this oxide layer. Further movement of the PIN may then lead to separation of parts of the layer (together with the cast iron matrix). These separated parts may then move during the test and move outside the main tribological test track (Figure 11i-D).



(i) **(ii)**

Figure 11. ADI 9k6 240; (**i**) The surface of a non-laser-hardened ADI 9k6 240 sample; (**ii**) EDS analysis of the surface after the tribological test.

Another major factor that can contribute to the breaking of the oxide layer is the graphitic formations that the cast iron contains. If they are located just below the surface, they may be progressively exposed during the test (Figure 11i-G). Graphite is a stress concentrator. The thin layer of matrix that overlies it at the beginning of the test is deformed during the test, which can lead to subsequent fatigue and failure of integrity, and the graphite is gradually exposed. This mechanism is likely to result in significant separation of the matrix parts around the graphitic formations, as seen in Figure 11i-C. Traces of abrasive damage are also evident on the surface after tribological testing (Figure 11i-B). The movement of detached parts of the hard oxide layer, or the hardened part of the base material, could probably have contributed to the abrasion.

Figure 11i-E shows traces of adhesive damage. This was probably caused by close contact between the PIN (steel ball) and the cast iron matrix. Given the chemical composition, this is not surprising. The surface was probably protected from significant adhesive damage by an emerging oxide layer. The worn surface shows where there has been a significant separation of the base material of the cast iron (Figure 11i-F). There may be a number of causes. The separation may be due to fatigue of the cast iron surface layers, or adhesive wear, or the presence of graphite (which was not detected during the test) may have contributed.

Figure 12 shows the condition of the laser-hardened surface after the 11 min tribological test. The resulting trace is relatively compact, with the oxide layer (Figure 12-A) showing no significant distortion. Nevertheless, some distortion did occur during testing. The detached portions of the oxide layer then moved from the breach location to the edge of the footprint during the test. Such separated and relocated portions can be seen in Figure 12-H. The surface of the specimen also shows signs of abrasion (Figure 12-C), likely due to the aforementioned movement of hard oxide particles or movement of the hardened and separated portion of the cast matrix (Figure 12-D).

The surface image (Figure 12) also shows the influence of graphite formations. These formations, as already mentioned, are the heterogeneities of the structure around which the stress concentration increases. The thin matrix layer that overlies the graphite is intensely stressed. The result is fatigue and separation of that part of the matrix. The initial state can be seen clearly in Figure 12-F, while a more advanced stage with exposed graphite (Figure 12-G) can be seen in Figure 12-B. The cracks that form and gradually propagate around the graphitic formations are clearly visible in the figure. By stressing the graphite and surrounding matrix, it may also be released (Figure 12-E); in this way, some lubrication effect may occur, which may affect the resulting tribological behavior of the cast iron.

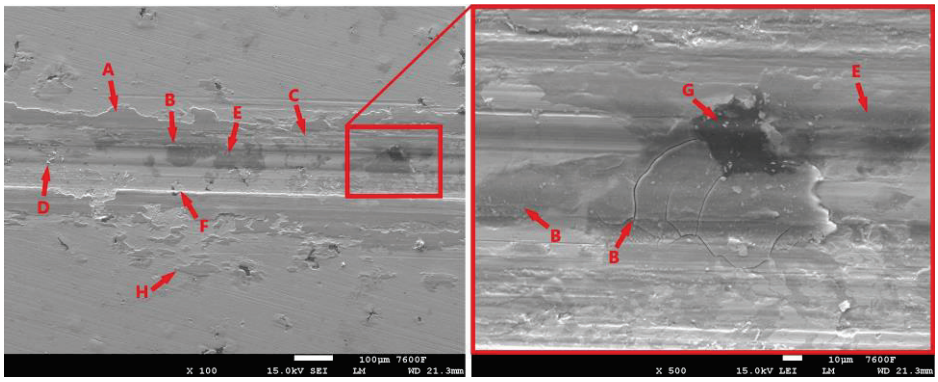
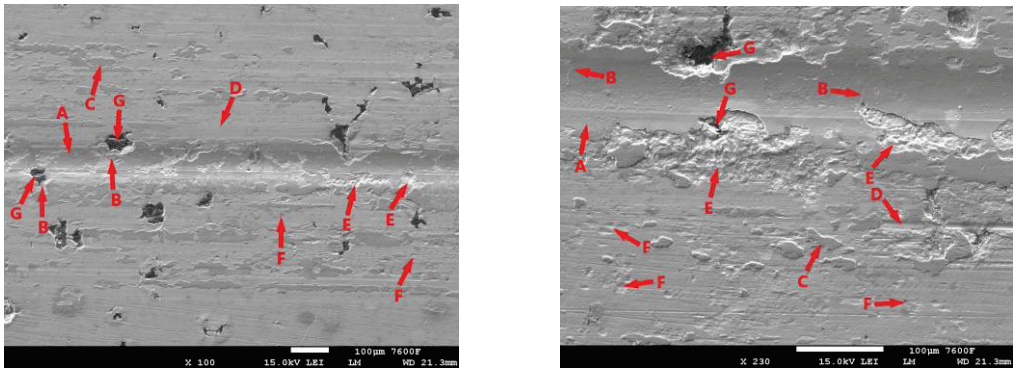


Figure 12. The surface of the laser-hardened sample after an 11 min tribological test.

The surface of the laser-hardened specimen after the 30 min tribological test is shown in Figure 13. The trace produced by the PIN movement during the test is largely covered by an oxide layer (Figure 13a,b-A), but this layer is not very continuous. It shows considerable distortion, and cracks are visible (Figure 13b-B), which may propagate gradually with PIN movement and cause delamination. One of the causes of the disruption of the oxide layer may be the aforementioned presence of graphite (Figure 13a,b-G). The figure shows that there was also considerable disruption of the surrounding matrix around these graphitic formations (Figure 13a,b-B). During the test, hard parts of the oxide layer were separated and displaced (Figure 13a,b-C), which probably contributed significantly to the abrasive damage of the surface (Figure 13a,b-D). The figure also shows areas where significant separation of parts of the base material has occurred (Figure 13a,b-E); the presence of graphite is not evident in the surrounding area (it may be hidden beneath the surface), but this is probably the result of fatigue damage to the cast iron matrix. The surface also shows signs of adhesive damage (Figure 13a,b-F).



(**a**) (**b**)

Figure 13. ADI 9k6 240; (**a**) Surface of the laser-hardened sample after a 30 min tribological test; (**b**) Detail of the laser-hardened surface after a 30 min tribological test.

3.2.3. Progress of the ADI 9k6 310 Tribological Test

Figure 14 shows a record of the friction coefficient for the laser non-hardened surface of the ADI 9k6 310 specimen during the main 30 min test. This record shows an initial slight fluctuation in values. However, this fluctuation stabilized fairly quickly. At the same time, this phenomenon is also evident in the 11 min measurement (Figure 15).

This initial variation in friction coefficient values may again (as with the previous sample 9k6 240) be due to a number of factors. One cause may be the flattening of surface micro-irregularities, or for example, the formation and subsequent failure of an oxide layer. The presence of this oxide layer on the test worn surface was already confirmed in the previous sample.

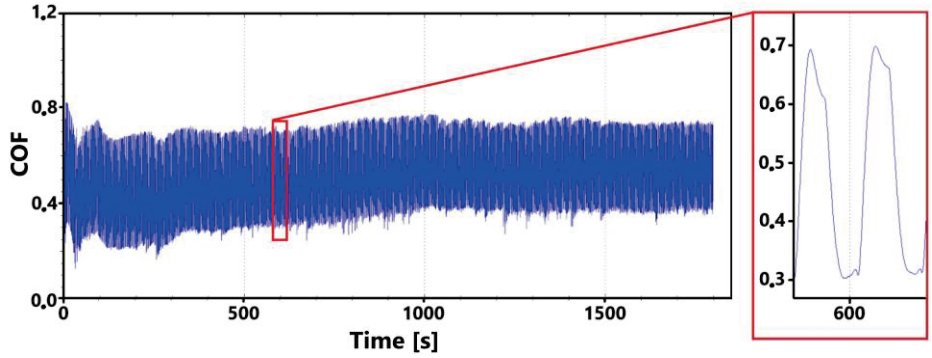


Figure 14. Record of the friction coefficient of the laser non-hardened surface of the sample ADI 9k6 310 (30 min).

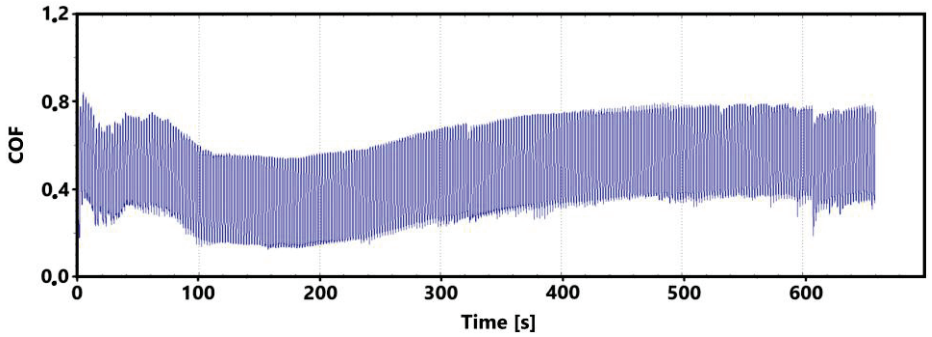


Figure 15. Record of the friction coefficient of the laser non-hardened surface of the sample ADI 9k6 310 (control measurement, 11 min).

Figure 16 shows a record of the friction coefficient for the laser-hardened surface of specimen ADI 9k6 310 taken during a 30 min tribological test. In this case (similar to the non-hardened surface), a slight fluctuation in the values can be observed as the tribological pair is run in; however, these values stabilized fairly quickly. The variation in the friction coefficient values during tribological pair run-in is probably related to the formation and subsequent behavior of the oxide layer (together with the interaction of surface micro-irregularities).

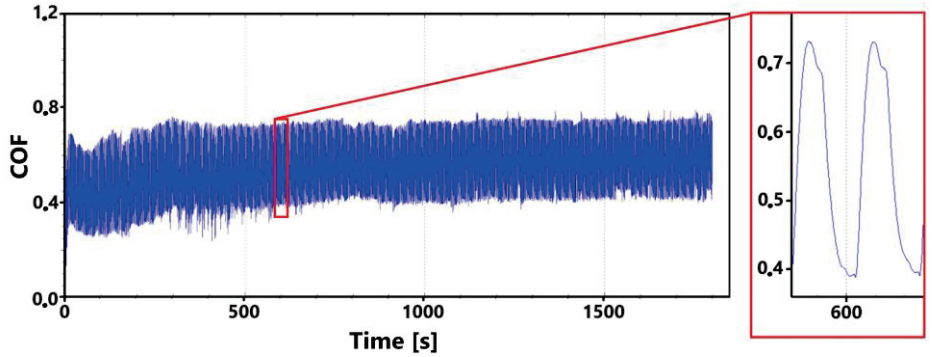


Figure 16. Record of the friction coefficient of the laser-hardened surface of the sample ADI 9k6 310 (30 min).

A similar initial fluctuation of the friction coefficient values, including a relatively rapid settling, is also evident in the record of the control (11 min) measurement (Figure 17). The range of values over which the friction coefficient varies in the 10th min of both tests is again very similar.

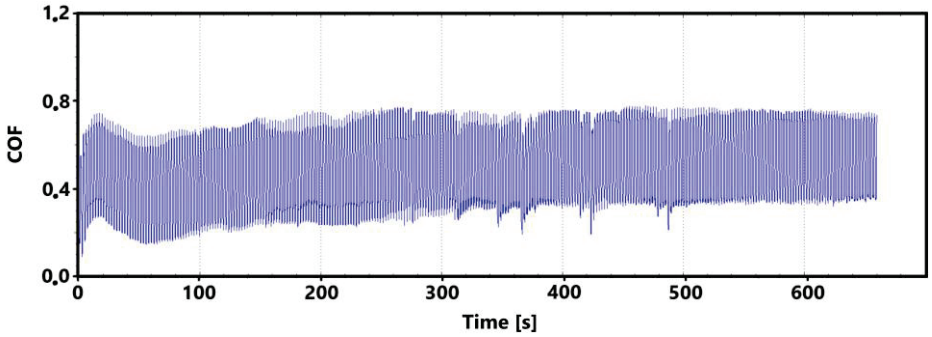
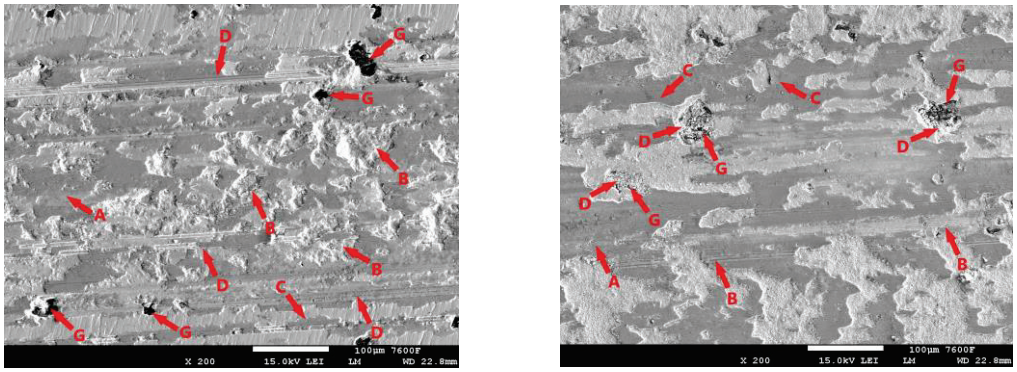


Figure 17. Record of the friction coefficient of the laser hardened surface of the ADI 9k6 310 sample (control measurement, 11 min).

3.2.4. Surface Analysis of the ADI 9k6 310 Sample after the Tribological Test

Figure 18a shows the surface condition of a non-hardened ADI 9k6 310 cast iron specimen after a 30 min tribological test. The surface of this sample shows significant damage after the test. The surface is again (as in the previous cases) partially covered by an oxide layer (Figure 18a-A), but this layer is considerably damaged. Together with the oxide layer, the surface layers of the base material have been significantly delaminated during the test (Figure 18a-B). Thus, the surface of the sample shows quite deep damage to the surface layers, essentially craters.



(**a**) (**b**)

Figure 18. ADI 9k6 310: (**a**) The surface of a non-laser-hardened ADI 9k6 310 sample after a 30 min tribological test; (**b**) The surface of the laser-hardened sample after an 11 min tribological test.

The delamination may have been contributed to by the graphite formations, which (as already mentioned in the previous sample) are essentially surface heterogeneities, and there is an increase in stress concentration in their vicinity. Thus, significant matrix loading and pumping of plasticity may be occurring in the vicinity of the graphite, which may subsequently cause delamination of the surface layers of the cast iron around the graphite (Figure 18a-G). However, this is probably not the primary cause of delamination in this case. The separation of the cast iron matrix occurred over essentially the entire footprint area created by the movement of the PIN during the tribological test. The likely cause of the significant delamination is fatigue damage to the cast iron matrix (adhesive wear may have contributed). The movement of the separated portions of the matrix or portions of the oxide layer (portions of which are visible in Figure 18a-C) is then likely to have also caused significant abrasive wear, traces of which are visible on the surface of the specimen (Figure 18a-D).

Figure 18b shows the condition of the laser-hardened surface after the 11 min tribological test. At first glance, the completely different behavior of the hardened and non-hardened surfaces is evident (Figure 18a). The test-damaged surface is again partially cov-

ered by an oxide layer (Figure 18b-A). By loading this layer during PIN movement, cracks can form, which can be seen in Figure 18b-C. The gradual propagation and interlocking of these cracks leads to the separation of the oxide layer from the base material. Compared to the non-hardened surface, no significant delamination of the cast iron matrix is evident on the laser-hardened surface. The matrix is not fundamentally damaged even around the graphite formations (Figure 18b-G). The matrix shows only minor signs of damage. Accumulated matrix fragments, together with parts of the oxide layer, are trapped on the exposed graphite (Figure 18b-D). The movement of these hardened fragments and hard parts of the oxide layer probably contributed strongly to the abrasive wear, traces of which are visible in Figure 18b-B.

Figure 19 shows the laser-hardened surface of ADI 9k6 310 after a 30 min tribological test. When comparing the hardened surface (Figure 19) and the non-hardened surface (Figure 18a) after an identical test length, a completely different behavior is visible at first glance. The hardened surface does not show areas (the aforementioned craters) where significant separation of the cast iron matrix has occurred. The trace of the tribological test is again partially covered by the oxide layer (Figure 19-A). The movement of the PIN during the test caused cracks to form, propagate, and interlock in this layer; the cracks are visible in Figure 19-F. The moving separated hard parts then probably contributed again to the abrasive damage, traces of which are visible in Figure 19-C.

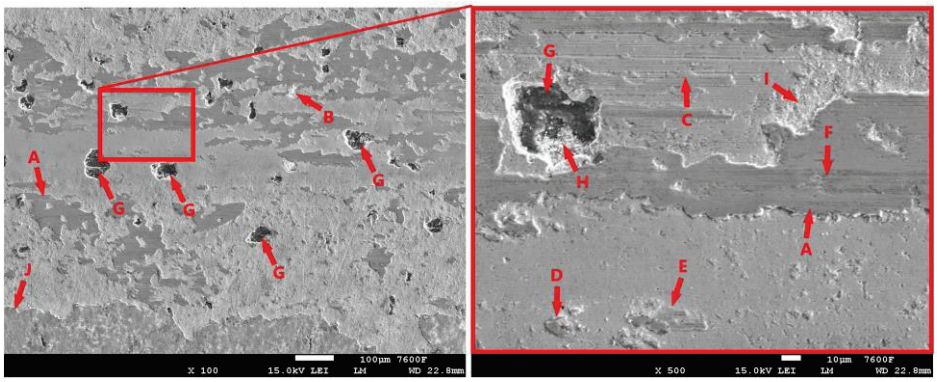


Figure 19. Surface of the laser-hardened ADI 9k6 310 sample after a 30 min tribological test.

In general, the cast iron matrix did not show signs of significant delamination, with only minor traces of delamination visible on the surface (Figure 19-B). A portion of the matrix was separated with the oxide layer during the test (Figure 19-I). The laser-hardened matrix did not show significant distortion even around the aforementioned graphite heterogeneities (Figure 19-G). The amount of particles that accumulated on the graphite surface during the 11 min control test (Figure 18b-D) was greatly reduced during this main measurement (Figure 19-H). The surface of the cast iron also shows minor signs of adhesive wear (Figure 19-E). More fundamental damage could have been prevented by the oxide layer, which limited the contact between the PIN and the cast iron matrix. An oxide layer was present on the laser-blinded surface (Figure 19-J), but this was broken fairly quickly during the test.

3.2.5. Progress of the ADI 9k6 400 Tribological Test

Figure 20 is a record of the friction coefficient for the non-laser-hardened surface of the ADI 9k6 400 specimen, which was subjected to a 30 min tribological test. It can be seen from this record that the values of the friction coefficient exhibit considerable scatter when the tribological pair is being run in.

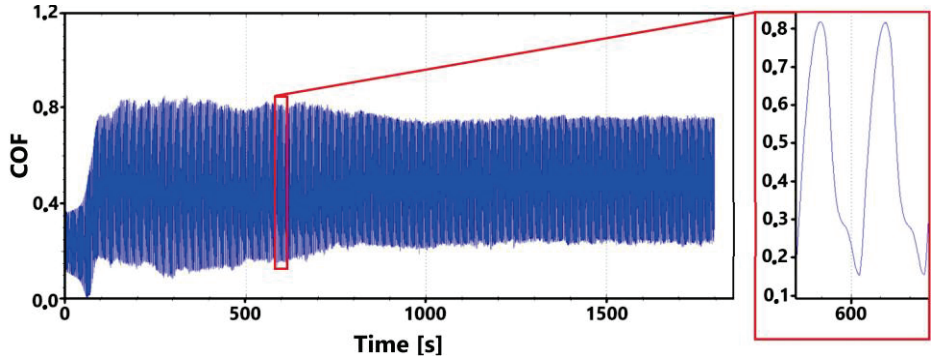


Figure 20. Record of the friction coefficient of the non-laser-hardened surface of the ADI 9k6 400 sample (30 min).

As mentioned several times, such dispersion of values can be caused by a number of factors. An example is the formation and subsequent breaking of the oxide layer; a larger graphite formation, which is gradually revealed, can also play a crucial role. In the 11 min control measurement (Figure 21), such significant dispersion of the value is not visible. The values of the friction coefficient stabilized only during the 16th minute of the test.

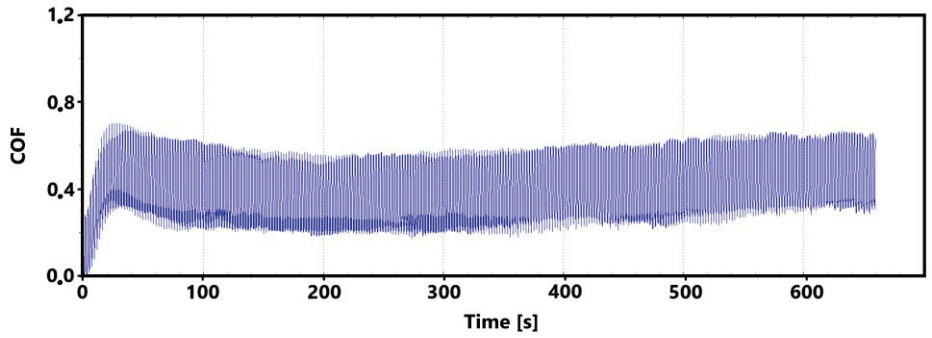


Figure 21. Record of the friction coefficient of the non-laser-hardened surface of the ADI 9k6 400 sample (control measurement, 11 min).

A record of the friction coefficient for the surface of the laser-hardened ADI 9k6 400 specimen is shown in Figure 22 for the main (30 min) test. It can be observed from this record that despite a slight initial fluctuation in the friction coefficient values as the tribological pair is being run in, the measured values are relatively stable until the 9th minute of the test. This initial stability was confirmed by the control (11th minute) measurement (Figure 23). However, a gradual increase in friction coefficient values can be observed thereafter in the recording (Figure 22). This increase may be due to a number of factors.

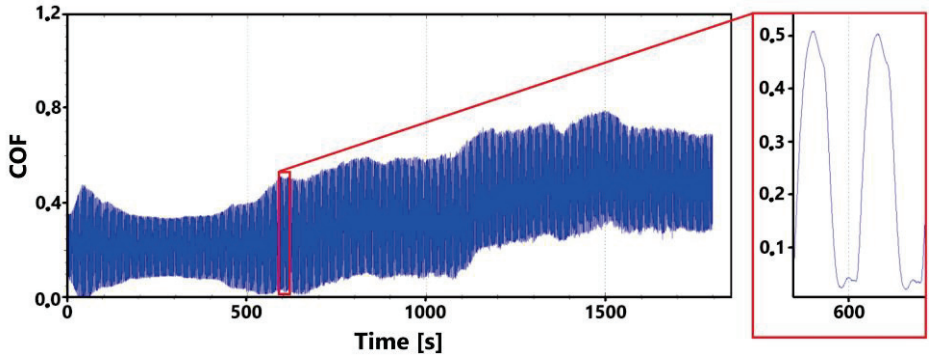


Figure 22. Record of the friction coefficient of the laser-hardened surface of the ADI 9k6 400 sample (30 min).

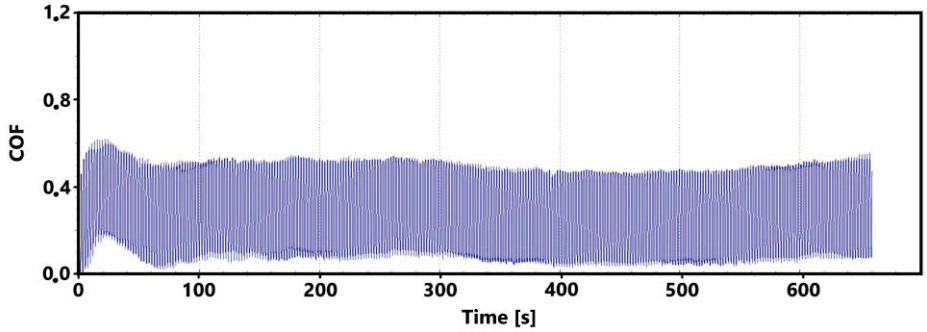


Figure 23. Record of the friction coefficient of the laser-hardened surface of the ADI 9k6 400 sample (control measurement, 11 min).

The movement of the PIN leads to the displacement of separated parts, which is probably one of the main causes of the abrasive wear whose traces are visible on the sample surface. In this way, the values of the friction coefficient may have gradually increased.

Analysis of the hardened surfaces after the tribological test shows that the surface subjected to the 11 min tribological test is covered with a relatively compact oxide layer. On the other hand, the surface of the sample subjected to the longer 30 min test shows significant distortion of the oxide layer and the cast iron matrix.

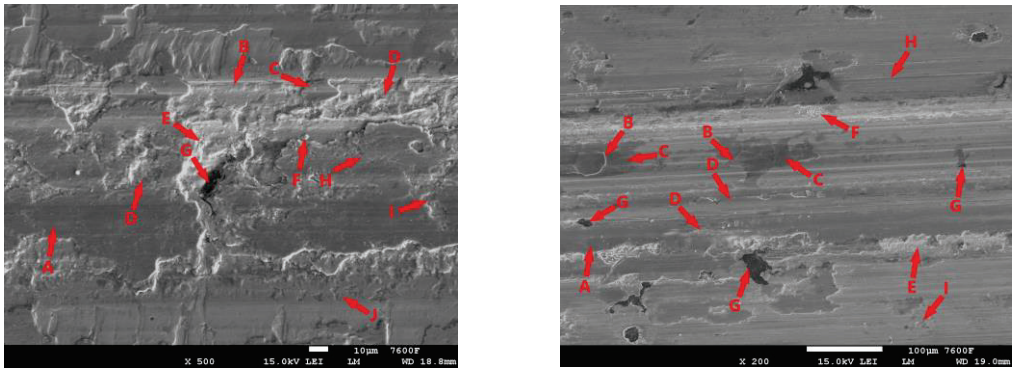
3.2.6. Surface Analysis of the ADI 9k6 400 Sample after the Tribological Test

Figure 24a shows the surface of a non-hardened specimen that was subjected to a 30 min tribological test. The test-worn surface is largely covered again with an oxide layer (Figure 24a-A). However, this layer is not very continuous. Throughout the footprint (which was created by the movement of the PIN), particularly at its edge, there are visible areas where there has been a significant separation of the base material (Figure 24a-D). As this delamination occurs throughout the surface, it is unlikely to be due to the presence of graphite. In that case, there would be a local separation of the matrix. In this case, however, it is more likely to be fatigue damage to the surface layers of the cast iron. Adhesive wear may also have contributed to the delamination, traces of which are also visible on the surface of the sample (Figure 24a-J). Figure 24a also shows a place where a more pronounced separation of the matrix occurred around the graphite (Figure 24a-E,G). Graphite, as a surface heterogeneity and stress concentrator, contributes to the formation of cracks, which can gradually (under further loading) spread through the surface layers (Figure 24a-H). Areas are also visible on the surface where the oxide layer (Figure 24a-I) and the cast iron matrix (Figure 24a-D) have been broken, probably due to loading and deformation of the brittle oxide layer. The surface bears signs of the displacement of the oxide layers (Figure 24a-C); the main track mainly contains smaller fragments (Figure 24a-F). The movement of these separated parts of the surface then probably contributed to the abrasive damage to the surface; traces of abrasion are visible in Figure 24a-B.

The laser-hardened surface of the ADI 9k6 400 sample after the 11 min tribological test is shown in Figure 24b. Again, an oxide layer is present on the surface (Figure 24b-A); in this case, it is quite compact. However, there are signs of its breakage. One reason for this breach may be graphite. The figure shows where heterogeneities in the form of graphite have affected the surrounding matrix, causing more intense stresses on the matrix. The consequence is the formation, propagation, and interconnection of cracks around these graphite formations (Figure 24b-B). These cracks likely released some graphite (Figure 24b-C), which was subsequently spread by the movement of the PIN. The exposed graphite is visible in Figure 24b-G.

The surface also contains cracks that are oriented in the longitudinal direction of the PIN trace (Figure 24b-D). Given the distribution of these cracks, they are probably not the result of the presence of graphite but of fatigue damage to the surface layers. Significant delamination is also evident at the edges of the trace (Figure 24b-E). Adhesive wear, traces

of which are evident on the surface of the sample, may have contributed to the surface delamination (Figure 24b-I). Traces of abrasion are also evident on the surface (Figure 24b-H), the likely cause being the movement of detached parts of the surface (Figure 24b-F).



(**a**) (**b**)

Figure 24. ADI 9k6 400: (**a**) The surface of a non-laser-hardened ADI 9k6 400 sample after a 30 min tribological test; (**b**) The surface of the laser-hardened sample after an 11 min tribological test.

Figure 25 shows the surface of the laser-hardened sample after a 30 min tribological test. The surface is again covered with an oxide layer (Figure 25-A). Compared to the surface of the sample subjected to the shorter 11 min test (Figure 24-B), the oxide layer is significantly less compact in this case. The longitudinal cracks that were present on the sample surface after the shorter test apparently contributed to the delamination of the surface layers (Figure 25-B). The tribological test progressively revealed graphite formations that may have contributed to the delamination of the surface. However, the surrounding matrix around the exposed graphite formations did not appear to be fundamentally disturbed in any way. The movement of detached parts of the hard oxide layer (Figure 25-D) and parts of the base material was probably one of the main causes of the abrasive damage, traces of which are visible on the surface (Figure 25-C). Contact between the PIN and the exposed base material may have led to adhesive damage, traces of which are visible in Figure 25-E. More intense adhesive wear was probably prevented by the presence of the oxide layer.

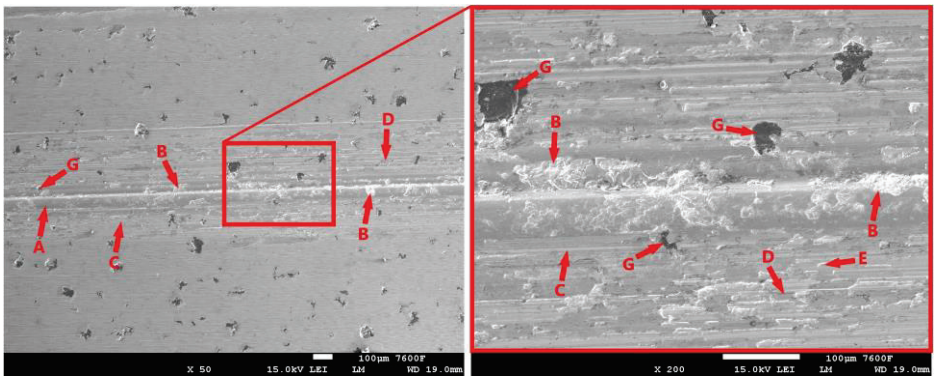


Figure 25. Surface of the laser-hardened ADI 9k6 400 sample after a 30 min tribological test.

3.3. Discussion

From the metallographic analysis of the tested cast iron samples, it is evident that the changes in structure associated with laser exposure are very similar for all tested samples. In the laser-hardened samples, the initial ausferritic structure has been transformed, while the surface layers of the hardened samples are mainly composed of martensite and residual

austenite. At the same time, there are transition regions between the hardened surface and the non-hardened core, which are formed by coarser martensite.

The resulting values of the friction coefficient for each specimen are given in Table 3. Given the type of motion (linear reciprocating) that the PIN performed during the test, it would theoretically be possible to evaluate both the static and dynamic friction coefficients. However, the software of the tribometer used does not offer this possibility. For this reason, the average values of the (static and dynamic) friction coefficient are given in Table 3 below.

Table 3. Average COF values for individual samples.

Sample	Test Length [min]	Non-Hardened Surface		Hardened Surface	
		COF	SD	COF	SD
ADI 9k6 240	30	0.539	0.222	0.392	0.207
	11	0.504	0.198	0.347	0.224
ADI 9k6 310	30	0.512	0.190	0.548	0.169
	11	0.471	0.214	0.489	0.205
ADI 9k6 400	30	0.469	0.250	0.341	0.228
	11	0.423	0.175	0.285	0.200

For the sample whose isothermal refinement temperature was the lowest of the tested samples (240 °C), ADI 9k6 240, the trend of the friction coefficient is quite clear. The laser-hardened surface shows significantly lower values than the non-hardened surface. It can also be seen from Table 3 that for the main and control measurements, the values are slightly different; the main reason for this is the run-in phase of the tribological pair, which, for the shorter (11 min) test, makes up a significantly larger proportion.

The same is true for the sample which, on the other hand, was isothermally cured at the highest temperature tested (400 °C). The ADI 9k6 400 sample also shows lower friction coefficient values for the laser-hardened surface. For this sample, there is a relatively high difference between the average friction coefficient values for the main and control measurements. This difference is probably related to the evolution of the values (seen in the record, Figure 22) during the test. This is because initially the tribological pair shows relatively stable values. This stability was confirmed by the control measurement, which largely consists of just this phase. The main measurement then showed a gradual increase in values, which could not be seen in the shorter control measurement. For this reason, the values for the two types of testing differ significantly. In the case of sample ADI 9k6 310, which was isothermally hardened at 310 °C, there is no significant difference between the values of the laser-hardened and non-hardened surfaces. The hardened surface even shows slightly higher friction coefficient values. Here, the different properties of the laser-hardened surface may play a role, which may be due to the different distribution of carbon in the starting material. As already mentioned, the distribution of carbon in isothermally hardened cast irons as a function of isothermal residence temperature is still a subject of research and discussion. Thus, it is not possible to clearly assess the influence of this factor. After the tamping phase, all three samples show very similar values of the friction coefficient.

Figure 26 shows the average friction coefficient values for the individual measurements graphically for better clarity. It is quite clear from this figure that the friction coefficient of the non-hardened surface decreased as the temperature of the tested samples increased with increasing isothermal hardening temperature. This dependence confirms some publications [29,30].

According to the authors of these publications, austenite can be transformed into martensite under certain circumstances. The most important factor is a sufficiently high contact pressure. According to the authors, cast irons hardened at higher temperatures should be more susceptible to martensitic transformation. These cast irons contain the block austenite mentioned in the introduction. Thin-film austenite, which is contained in cast irons with lower isothermal holding temperatures, is not nearly as susceptible to martensitic transformation. The change in carbon concentration in the stabilized high-

carbon austenite plays a crucial role here. Austenite with a higher carbon concentration is significantly more stable, and its martensitic transformation is strongly limited. Another factor may be the different nature of the loading of the larger block austenite. However, as already mentioned, this issue is still a subject of research and discussion. This issue is discussed in more detail in the introduction to this paper.

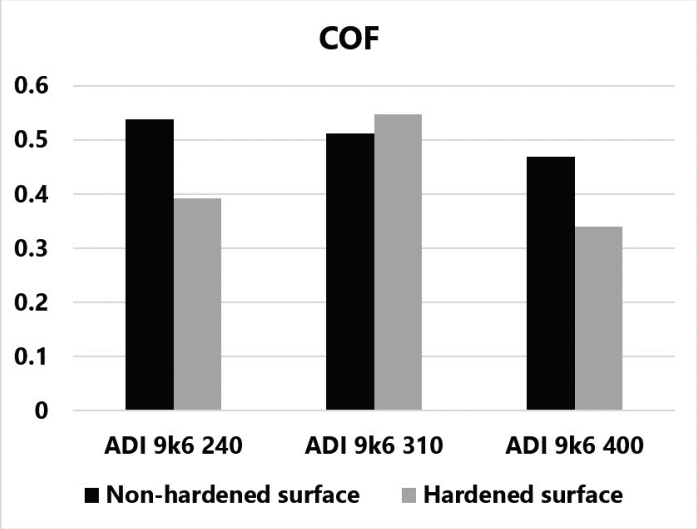


Figure 26. Graphically displayed average COF values for individual samples.

When analyzing the behavior of the tested samples by scanning electron microscopy, the most significant difference in behavior is seen in the ADI 9k6 310 sample. The surface of this non-hardened sample showed the worst behavior after the tribological test. After the 30 min test, the surface was covered with traces of deep matrix separation of the cast iron. These traces are evident across the full width of the footprint created by the movement of the pin. The separation and subsequent movement of the strengthened parts also resulted in significant abrasion of the sample surface. The laser-hardened surface, on the other hand, exhibited completely different behavior, the surface showed no signs of such fundamental disruption of the surface layers as in the case of the non-hardened surface. The oxide layer formed during the test is relatively non-compact. The surface also shows signs of abrasive wear. There was no significant surface disturbance even around the graphite, which has significant heterogeneity of structure and a significant stress concentration around it.

3.4. Conclusions

During surface laser hardening, all samples were transformed from the initial ausferritic structure to a homogeneous martensitic structure (the carbon distribution in the initial ausferritic structure is thus sufficiently uniform to obtain a homogeneous martensite layer). The metallography then shows that this martensite layer also contains a small proportion of residual austenite. The samples also show transition regions between the fine martensite in the hardened surface and the ausferritic core. This transition zone is made up of coarser martensite. The laser treatment increased the surface hardness up to 1100 HV0.1. This hardness gradually decreased to a depth of 0.8–1 mm, where it reached the level of the initial ausferritic structure.

During the tribological test, strong oxidation of the surface due to loading was observed for all samples. The oxide layer thus formed limited the development of adhesive wear. The change in the coefficient of friction due to surface laser hardening is not entirely clear. In the case of ADI 9k6 240 and ADI 9k6 400, the coefficient of friction decreased due to the laser treatment. For sample ADI 9k6 310, there was a slight increase in COF after laser hardening. This sample has the highest hardness after laser hardening and at the

same time the greatest change in tribological properties. On the surface of the non-laser-hardened sample of this cast iron, areas of large damage were observed after tribological testing, essentially crater formation with separated base material. For the same cast iron after laser hardening, no major surface damage was observed after the tribological test (the surface was very compact even after the tribological test). All these phenomena may be related to the different carbon distribution in ADI castings depending on their isothermal retention temperature (the carbon distribution then also affects the properties of the martensitic structure formed).

Interesting is the trend (for unhardened specimens) of decreasing friction coefficient with increasing temperature of ADI isothermal holding of cast iron. Higher temperatures lead to a coarser structure that contains high-carbon austenite retained in relatively large blocks. Such austenite may be susceptible to martensitic transformation at sufficiently high contact pressures, which will essentially increase the strength and hardness of the surface layers. This may result in a reduction in the coefficient of friction.

Author Contributions: Conceptualization, L.Z.; methodology, L.Z., J.H. and J.K. (Jiří Kuchař); sample preparation, L.Z. and J.K. (Jan Krčil); investigation, L.Z., J.H. and J.K. (Jiří Kuchař); writing—original draft preparation, L.Z., J.H. and J.K. (Jiří Kuchař); writing—review and editing, L.Z. and J.K. (Jan Kudláček); supervision, J.K. (Jan Kudláček). All authors have read and agreed to the published version of the manuscript.

Funding: The research was funded by the Technology Agency of the Czech Republic, research project—Research center for surface treatments No. TE02000011.

Institutional Review Board Statement: Not applicable.

Informed Consent Statement: Not applicable.

Data Availability Statement: Data is contained within the article.

Acknowledgments: The research was supported with students by project SGS22/156/OHK2/3T/12—Influence of surface treatments on the quality of production technologies.

Conflicts of Interest: The authors declare no conflict of interest.

References

1. Huai, W.; Zhang, C.; Wen, S. Graphite-based solid lubricant for high-temperature lubrication. *Friction* **2020**, *9*, 1660–1672. [CrossRef]
2. Scharf, T.W.; Prasad, S. Solid lubricants: A review. *J. Mater. Sci.* **2013**, *48*, 511–531. [CrossRef]
3. Hase, A. Visualization of the tribological behavior of graphite in cast iron by in situ observations of sliding interfaces. *Tribol. Int.* **2019**, *138*, 40–46. [CrossRef]
4. Sugishita, J.; Fujiyoshi, S. The effect of cast iron graphites on friction and wear performance I: Graphite film formation on grey cast iron surfaces. *Wear* **1981**, *66*, 209–221. [CrossRef]
5. Meier, L.; Hofmann, M.; Saal, P.; Volk, W.; Hofmann, H. In-situ measurement of phase transformation kinetics in austempered ductile iron. *Mater. Charact.* **2013**, *85*, 124–133. [CrossRef]
6. Catalán, N.; Esteban, R.; Adrian, B.; Diego, C. Surface Laser Treatment of Cast Irons: A Review. *Metals* **2022**, *12*, 562. [CrossRef]
7. Frocisz, L.; Matusiewicz, P.; Krawczyk, J. Effect of Varying the Volume Fractions of Ledeburitic Cementite and Graphite on the Tribological Properties of Commercially Used Cast Irons. *Lubricants* **2023**, *11*, 498. [CrossRef]
8. Tewary, U.; Paul, D.; Mehtani, H.K.; Bhagavath, S.; Alankar, A.; Mohapatra, G.; Sahay, S.S.; Panwar, A.S.; Karagadde, K.; Samajdar, I. The origin of graphite morphology in cast iron. *Acta Mater.* **2022**, *226*, 117660. [CrossRef]
9. Zhang, N.; Zhang, J.; Lu, L.; Zhang, M.; Zeng, D.; Song, Q. Wear and friction behavior of austempered ductile iron as railway wheel material. *Mater. Des.* **2016**, *89*, 815–822. [CrossRef]
10. Wang, X.; Du, Y.; Liu, C. Tribological behaviour and wear mechanism of ADI with different hardness values. *Mater. Sci. Technol.* **2023**, *39*, 2409–2416. [CrossRef]
11. Liu, C.; Du, Y.; Wang, X.; Zheng, Q.; Zhu, X.; Zhang, D.; Liu, D.; Yang, C.; Jiang, B. Comparison of the tribological behavior of quench-tempered ductile iron and austempered ductile iron with similar hardness. *Wear* **2023**, *520–521*, 204668. [CrossRef]
12. Hu, Z.; Du, Y. Mechanical and Tribological Behavior of Austempered Ductile Iron (ADI) under Dry Sliding Conditions. *Lubricants* **2023**, *11*, 182. [CrossRef]
13. Bai, J.; Xu, H.; Chen, X.; Cao, W.; Zhang, X.; Xu, Y. Effect of tempering temperature on the wear behaviour of martensitic ductile iron. *Mater. Sci. Technol.* **2023**, *39*, 744–755. [CrossRef]

14. Wang, B.; Barber, G.; Qui, F.; Zou, Q.; Yang, H. A Review: Phase Transformation and Wear Mechanisms of Single-Step and Dual-Step Austempered Ductile Irons. *J. Mater. Res. Technol.* **2020**, *9*, 1054–1069. [CrossRef]
15. Alaalam, M.; Grech, M. Effect of Austenitizing Conditions on the Impact Properties of an Alloyed Austempered Ductile Iron of Initially Ferritic Matrix Structure. *J. Mater. Eng. Perform.* **1998**, *7*, 265–272. [CrossRef]
16. Tissi, G.; Fonseca, G. Influence of austempering time and austempering temperature in microstructure and mechanical properties in austempered ductile iron. *Int. J. Res.-GRANTHAALAYAH* **2020**, *8*, 51–62. [CrossRef]
17. Hegde, A.; Gurumurthy, B.M.; Hindi, J.; Sharma, S.; Gowrishankar, M.C. Effect of austempering temperature and manganese content on the impact energy of austempered ductile iron. *Cogent Eng.* **2021**, *8*, 1939928. [CrossRef]
18. Hsu, C.-H.; Lin, K.-T. A study on microstructure and toughness of copper alloyed and austempered ductile irons. *Mater. Sci. Eng. A* **2011**, *528*, 5706–5712. [CrossRef]
19. Yang, J.; Putatunda, S.K. Improvement in strength and toughness of austempered ductile cast iron by a novel two-step austempering process. *Mater. Des.* **2004**, *25*, 219–230. [CrossRef]
20. Balos, S.; Rajnovic, D.; Dramicanin, M.; Labus, D.; Eric, O.; Grbovic-Novakovic, J.; Sidjamin, L. Abrasive wear behaviour of ADI material with various retained austenite content. *Int. J. Cast Met. Res.* **2016**, *29*, 187–193. [CrossRef]
21. Wang, B.; Qiu, F.; Barber, G.; Pan, Y.; Cui, W.; Wang, R. Microstructure, Wear Behavior and Surface Hardening of Austempered Ductile Iron. *J. Mater. Res. Technol.* **2020**, *9*, 9838–9855. [CrossRef]
22. Mussa, A.; Krakhmalev, P.; Bergstrom, J. Wear mechanisms and wear resistance of austempered ductile iron in reciprocal sliding contact. *Wear* **2022**, *498–499*, 204305. [CrossRef]
23. Batra, U.; Sharma, J.D. Wear Performance of Cu-Alloyed Austempered Ductile Iron. *J. Mater. Eng. Perform.* **2012**, *22*, 1136–1142. [CrossRef]
24. Sandven, O.A. Laser surface hardening. In *ASM Handbook Heat Treating*; ASM International: Materials Park, OH, USA, 1991; Volume 4, pp. 665–689.
25. Rajan, T.V.; Sharma, C.P.; Sharma, A. Laser Hardening. In *Heat Treatment: Principles and Techniques*, 2nd ed.; PHI Learning: New Delhi, India, 2011; pp. 148–151.
26. Steen, W.M.; Mazumder, J. Laser heat treatment. In *Laser Material Processing*, 4th ed.; Springer: London, UK, 2010; pp. 297–309.
27. Giorleo, L.; Semeraro, Q. Modelling of back tempering in laser hardening. *Int. J. Adv. Manuf. Technol.* **2011**, *54*, 969–977. [CrossRef]
28. García Navas, V.; Lambarri, J.; Leunda, J.; Sanz, C.; Soriano, C. Effect of laser surface hardening on the microstructure, hardness and residual stresses of austempered ductile iron grades. *Appl. Surf. Sci.* **2011**, *257*, 7101–7106. [CrossRef]
29. Du, Y.; Gao, X.; Wang, X.; Wang, X.; Ge, Y.; Jiang, B. Tribological behavior of austempered ductile iron (ADI) obtained at different austempering temperatures. *Wear* **2020**, *456–457*, 203396. [CrossRef]
30. Zhang, J.; Zhang, N.; Zhang, M.; Zeng, D.; Song, Q.; Lu, L. Rolling-sliding wear of austempered ductile iron with different strength grades. *Wear* **2014**, *318*, 62–67. [CrossRef]

Disclaimer/Publisher's Note: The statements, opinions and data contained in all publications are solely those of the individual author(s) and contributor(s) and not of MDPI and/or the editor(s). MDPI and/or the editor(s) disclaim responsibility for any injury to people or property resulting from any ideas, methods, instructions or products referred to in the content.

coatings

MDPI

Article

Study of PVD-Coated Inserts' Lifetime in High-Pressure Die Casting Regarding the Requirements for Surface Quality of Castings

Andrea Sütőová [1,*], Róbert Kočiško [1,*], Patrik Petroušek [1], Martin Kotus [2], Ivan Petryshynets [3] and Andrii Pylypenko [4]

[1] Faculty of Materials, Metallurgy and Recycling, Institute of Materials and Quality Engineering, Technical University of Kosice, 040 01 Kosice, Slovakia; patrik.petrousek@tuke.sk
[2] Faculty of Engineering, Institute of Design and Engineering Technologies, Slovak University of Agriculture in Nitra, 949 76 Nitra, Slovakia; martin.kotus@uniag.sk
[3] Institute of Materials Research of Slovak Academy of Sciences, 040 01 Kosice, Slovakia; ipetryshynets@saske.sk
[4] Faculty of Materials, Metallurgy and Recycling, Institute of Metallurgy, Technical University of Kosice, 040 01 Kosice, Slovakia; andrii.pylypenko@tuke.sk
* Correspondence: andrea.sutoova@tuke.sk (A.S.); robert.kocisko@tuke.sk (R.K.); Tel.: +55-602-2646 (A.S.); +55-602-4124 (R.K.)

Abstract: The wear and degradation of tools applied in the high-pressure die casting of Al alloys induce significant financial losses. The formation of failures on the surface of mold parts caused by erosion, thermal fatigue, corrosion, and soldering negatively affects the surface quality of castings. In this study, the lifetime of inserts protected by physical-vapor-deposited coatings (TiN, TiAlN, and CrAlSiN) is examined under real manufacturing conditions while considering requirements for the castings' surface quality (maximum average roughness Ra) defined by the customer. The goal was to identify the most suitable solution for HPDC in the foundry organization. After the deposition of PVD coatings on the inserts, the hardness (HRC) values increased from two to five depending on the coating used, and also the surface roughness was higher in the case of all inserts (Ra values increased from 0.24 to 0.36 μm). The lifetime of all PVD-coated inserts was higher compared to the uncoated insert. The highest lifetime was achieved by the application of a TiN coating, when 15,000 shots were achieved until the inserts' wear negatively affected (increased) the surface roughness of castings, considering the customer requirements for the maximum Ra value. SEM analysis was used to identify examples of wear and degradation on the surface of the TiN coated insert.

Keywords: high-pressure die casting; Al alloys; insert's lifetime; PVD coatings; wear; casting surface quality; roughness (Ra); SEM

1. Introduction

High-pressure die casting (HPDC) is one of the most important manufacturing processes in the automotive industry, as it enables obtaining automotive components with complex shapes cost-effectively [1]. Molds are exposed to severe conditions during HPDC, such as high pressure and temperature, and rapid temperature fluctuations. The usual casting speed moves between 20 and 60 m/s and the temperature ranges around 700° depending on the aluminum alloy type [2]. Although die lubricants are applied on the mold surface, these severe conditions trigger failure mechanisms due to the complex chemical, metallurgical, and mechanical processes such as erosion, thermal fatigue, corrosion, and soldering [3]. Erosion is characterized by the loss of mold material from the surface as a result of mechanical processes. Thermal fatigue cracks can be divided by their appearance into heat checks and stress cracks. The studies have revealed that crack initiation and propagation are increased by higher heating temperatures and higher heating/cooling rates [4].

According to [5], erosion and soldering are regarded as the primary causes of HPDC production downtime. In HPDC, molten aluminum tends to react with tool steel and forms Fe–Al intermetallic layers because the solidus temperature of the Al–Fe diagram phase is lower than molten aluminum [6]. This condition is referred to as metallurgical/chemical soldering (or die sticking). Die soldering can be classified as metallurgical/chemical and mechanical [4]. Metallurgical soldering occurs at high surface temperatures and takes time to develop. Mechanical soldering happens almost promptly under high pressure, after one shot or a few shots, when there is not enough time for the formation of an intermetallic layer [7]. It does not require too high surface temperatures. Mechanical and chemical soldering can appear simultaneously [8]. The formation of soldering often requires rectifying the tool surface by mechanical processes (machining, grinding, polishing, etc.) after stopping production [9]. The above-mentioned surface failure modes lead to damage of the mold surface and a reduction in casting surface quality. They can also change the dimensions of castings. Tools and maintenance costs constitute a remarkable part of the production costs of HPDC, and different approaches have been sought to maximize the lifetime of tools. This can involve the optimization of process conditions, the consideration of tool material, tool surface treatments, and coatings deposition.

Surface roughness is one of the most important metrics determining the surface quality of produced castings. Besides surface quality characteristics, other quality characteristics can determine the quality of castings, e.g., dimensional, mechanical (hardness, strength, etc.), and chemical characteristics [10]. Organizations supplying parts in the automotive industry are certified according to the International Automotive Task Force (IATF) 16949:2016 automotive quality management system standard and must meet quality requirements specified by customer organizations [11]. The technological service life of mold is often limited by the quality requirements specified for the casting and tolerance intervals for HPDC process parameters [12]. The maintenance or replacement of mold parts due to erosion, cracks, corrosion, and soldering that negatively affect the castings' quality induces costs. Therefore, producers need to find the best solution to increase the lifetime of tools as well as reduce maintenance costs.

Heat treatment, nitriding, and PVD coatings have been employed to withstand the degradation mechanisms of molds. Erosion and soldering can be reduced by maintaining the hardness of the mold at 44–48 HRC, nitriding of the mold surface, and the deposition of PVD coatings [13]. Several studies have confirmed the positive effect of nitride-based PVD coatings in the HPDC of aluminum alloys, e.g., [1,2,14–22]. Multicomponent coatings and multilayer structures have been designed to improve the performance of PVD coatings (mechanical, chemical, and tribological properties). According to [23] (p. 258), multilayer coatings offer the means to tailor the surface properties in demand.

In the study conducted by [14] (pp. 200–205), the positive effect of TiN, CrN, and TiCN coatings deposited on core pins in terms of soldering was confirmed in HPDC (semi-industrial trials). The study also concluded that the increased build-up of aluminum alloy is connected with the increased surface roughness of PVD-coated pins (blasted). TiN and TiAlN have high wear resistance and high hardness [24]. According to [25] (p. 123866), despite the many advantages of TiN, it becomes oxidized at a temperature of 550 °C. The oxidation resistance of TiAlN and TiAlSiN can be enhanced to around 850 to 950 °C [26]. This is much higher than in the case of TiN-coated films. On the other hand, the comparative study [27] (pp. 260–265) examining TiN and TiAlN coating layers showed that TiN coating has higher abrasive resistance than TiAlN. The friction coefficient of TiAlN is higher than TiN [28]. Besides Ti-based coatings, Cr-based coatings have been also widely applied in the industry. A CrN coating has higher oxidation resistance than a TiN coating, however, exposure to higher temperatures, up to 800 °C, causes a deterioration in mechanical properties due to the loss of N. Several studies confirmed that multilayer TiN/CrN coatings have superior properties compared to monolayer TiN and CrN [29]. Authors of the study [30] (pp. 74–81) tested the tribological properties of selected coatings and concluded that CrN outperforms TiN and TiAlN, while TiAlN

performed the worst. Chromium-based hard coatings such as CrN or CrAlN have been proven to have excellent tribological properties [31]. In the case of CrAlSiN, the friction coefficient is lower than for TiAlN and higher than for TiN [32]. The study [33] (p. 17–20) comparing textured and non-textured surfaces of PVD-coated (AlXN3 and nACRo4) tools in HPDC concluded lower values of the coefficient of friction in the case of textured surfaces. CrAlSiN has excellent thermal stability. Within the study [16] (p. 358), CrAlSiN coating systems with different chemical composition modulations were tested regarding washout in HPDC. Washout damage is attributed to corrosion and soldering, where molten aluminum comes into contact with the surface of the steel mold. The correlation between the erosion and soldering of molten aluminum was confirmed by the study [18]. Except for washout, the cracks in PVD coatings can also be the primary reason for molten aluminum penetration, which dissolves the steel substrate, causing the cracked coating to flake off, as was concluded in the study [17].

The selection of the optimal PVD surface treatment of molds in foundry organizations has to be taken into account in terms of effectiveness and costs [34]. Several factors influence the formation of failure mechanisms on mold parts, like the chemical composition of casting alloy, casting temperature, casting speed, tool shape, mold material, surface treatment of a mold, and other process conditions [13,35]. Despite several studies on PVD coatings (primarily in laboratory conditions) in terms of their mechanical wear and chemical resistance, we have not encountered a study comparing the selected nitride-based PVD coatings (TiN, TiAlN, and CrAlSiN) in the HPDC process. Our research focuses on the study of the mold inserts' lifetime—uncoated and coated with selected nitride-based PVD coatings—TiN, TiAlN, and CrAlSiN under real production conditions. The study also aims to identify failure modes resulting in the decommissioning of inserts. The lifetime of the inserts is limited by the requirements on the surface quality (surface roughness) of produced casting that is supplied to the car manufacturer, who determines the maximum tolerance limit of surface roughness (Ra). There have been several studies determining tools' lifetime. The study conducted in [36] examined cores' lifetime with different surface treatments and PACVD coatings in industrial applications, while maximum lifetime (maximum shots achieved) was defined when coating failures appeared on the surface of cores. The study focusing on the effect of additively manufactured inserts in terms of their lifetime in laboratory conditions determined the maximum lifetime of the insert up to the presence of macroscopic cracks on the inserts' surface [37]. It was the same in the research conducted in [38]. In our study, the inserts' lifetime is limited by the customer requirement for the maximum average surface roughness (Ra) of castings. After the formation of failures on the inserts that cause an increase in casting surface roughness (over the maximum specified Ra value), they must be decommissioned and their lifetime ends.

2. Materials and Methods

2.1. Material of Inserts and Surface Treatment

AISI H11 steel (DIN X38CrMoV5-1) was used to manufacture the mold inserts, with high toughness and good strength properties at higher temperatures. It is used for manufacturing tools like pressing tools, high-pressure die casting tools, and tools to produce screws, nuts, pins, etc. The chemical composition of the steel is shown in Table 1. The tool steel went under heat treatment and was hardened and tempered.

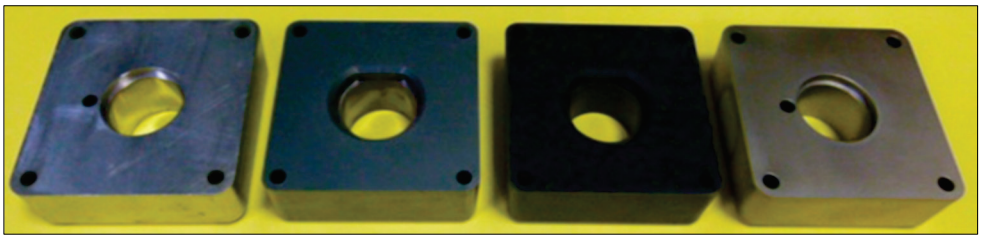
Table 1. AISI H 11 (DIN × 38 CrMoV5-1) chemical composition (wt. %).

C	Si	Mn	Cr	Mo	V	Fe
0.38	0.90	0.40	5.20	1.30	0.45	balance

The following coatings were deposited by the PVD technique on the H11 steel mold inserts: TiN (commercial name—Balint A), TiAlN (commercial name—Balint Futura Nano), and CrAlSiN (commercial name—Alwin), to study their lifetime considering the require-

ments for the surface quality of the castings. The arc vapor deposition technique (low voltage) was used in all cases. The coatings were deposited at 450 °C by the supplier.

Figure 1 shows the inserts used in the study. One insert was uncoated and three were coated with CrAlSiN, TiAlN, and TiN film to examine and compare their wear resistance in real manufacturing conditions that delivered the same product. The thickness of the deposited coatings was around 2 µm. Calo testing was performed to measure the thickness of the coatings. The thickness was declared by the supplier (according to ISO 26423 [39]).



(**a**) (**b**) (**c**) (**d**)

Figure 1. Mold inserts: (**a**) uncoated; (**b**) coated with CrAlSiN; (**c**) coated with TiAlN; and (**d**) coated with TiN.

2.2. Casting and Casting Process Conditions

Figure 2 shows the 3D model of the produced casting. It is the throttle valve for a turbocharger in a car. The functional part of the casting consists, among other things, of the bearing surface for the gasket, where the original equipment manufacturer (OEM) mounts the flange. The roughness of the bearing surface is a special characteristic, and it is required by the OEM to achieve the value Ra = max 2.5 µm. According to IATF 16949:2016, special characteristics are product characteristics or manufacturing process parameters that can affect safety or compliance with regulations, fit, function, and performance. In this case, the bearing surface can affect the fit and function of the product [40]. The standard requires compliance with customer-specified definitions and symbols. Therefore, a product with the bearing surface roughness Ra > 2.5 µm is considered to be a nonconformity and can't be supplied to the OEM.

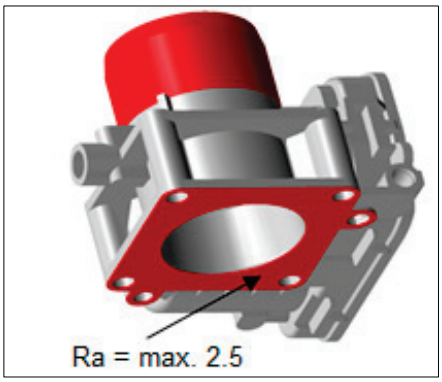


Figure 2. Throttle body with the marked value of the bearing surface roughness specified by the customer (Ra = max. 2.5 µm).

The product was produced within serial production; therefore, it was possible to perform the required number of shots for the study using different PVD coatings. The casting temperature in the process ranged from 708 to 712 °C and the casting speed was from 21 to 21.3 m/s. The lubricant was applied in the process after each shot (Chem-Trend® SL-61014B). The chemical composition of the aluminum alloy AlSi11Cu2(Fe) used in the casting process is shown in Table 2.

Table 2. AlSi11Cu2(Fe) chemical composition (wt. %).

Fe	Si	Mn	Ni	Cr	Ti	Cu	Pb	Mg	Zn	Sn	Al
max 1.1	10–12	max 0.55	max 0.45	max 0.15	max 0.25	1.5–2.5	max 0.25	max 0.3	max 1.7	max 0.15	balance

2.3. Estimation of Hardness of Inserts and Roughness of Bearing Surface of Castings

The hardness (HRC) of the mold inserts (uncoated and with PVD coatings—TiN, TiAlN, and CrAlSiN) that were subsequently used in the HPDC process was measured with the hardness tester TIME 5100 TH-170 (Beijing TIME High Technology Ltd., Beijing, China). The measurement was performed by a certified final inspection according to ASTM A 956 and DIN 50156 [41,42]. The average roughness (Ra) of the bearing surface of inserts was estimated using the surface tester Mitutoyo SJ-210 (Mitutoyo Corporation, Japan) before initiating the casting process. The measurement was performed in accordance with the JIS-B-0601-2001 and ISO 21920-2:2021 standards [43,44]. The average roughness (Ra) of the cast products' surface was subsequently estimated after every 500 shots using different inserts in the HPDC process (uncoated insert and inserts protected with TiN, TiAlN, and CrAlSiN coatings). Mechanical polishing of inserts was done manually in the case of the uncoated insert and inserts with TiN and TiAlN coatings.

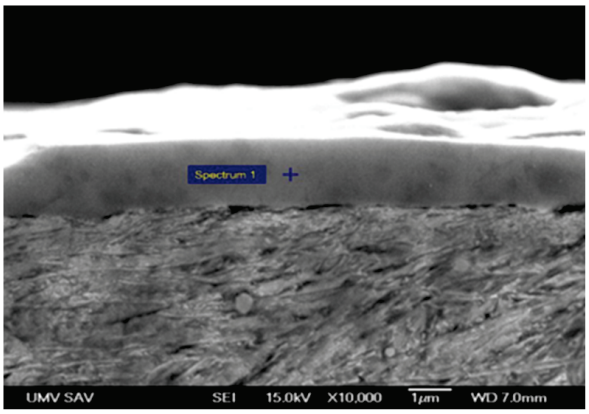
2.4. Specimen Preparation and Optical Microscopy and SEM

The metallographic analysis was performed on the surface of the specimen and in a cross-section. A metallographic cut in the cross-section was prepared by standard procedures: grinding, polishing, and etching in a Nital 4% solution. The microstructure observations of prepared specimens were carried out using a light optical microscope (LOM) OLYMPUS GX71 (Olympus Corporation, Tokyo, Japan) equipped with a digital camera. The local microstructures were observed using a scanning electron microscope (SEM) JEOL JSM-7000F (JEOL Ltd., Tokyo, Japan) equipped with backscatter electron (BSE) detectors and an energy-dispersive X-ray analysis (EDX).

3. Results and Discussion

3.1. Optical Microscopy and SEM Analysis

Figure 3 shows the SEM image of the cross-sections of the TiN-coated insert (with a coating thickness of around 2 μm) and the results of the EDX determining the elemental composition of the TiN.

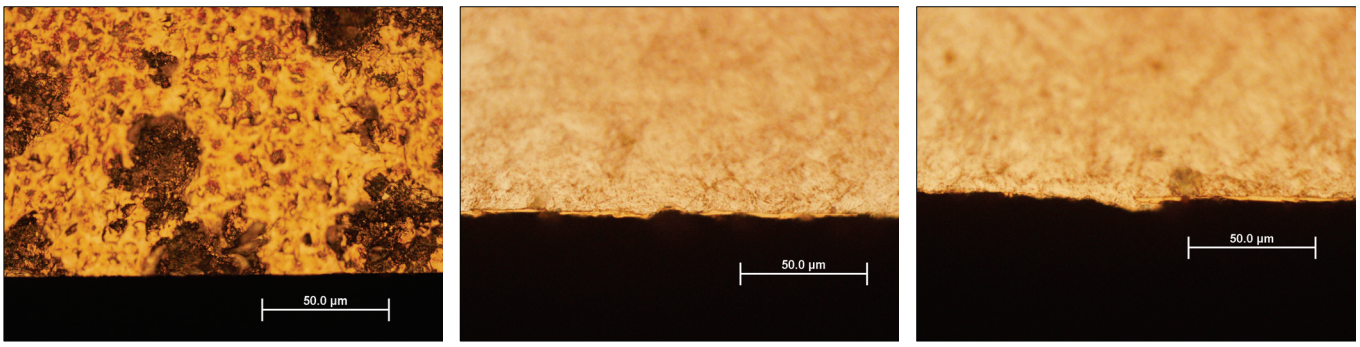


Element	Weight %	Atomic %
Spectrum 1		
N K	14.39	36.5
Ti K	85.61	63.5
Total	100	100

Figure 3. SEM image of cross-section of TiN-coated insert before use and results of EDX analysis.

Optical and SEM analyses were performed to identify possible failures on the surface of the insert. The TiN-coated insert served as an example for the illustration of emerging failures on the surface. The examined insert was after 15,000 shots. Figure 4 shows the

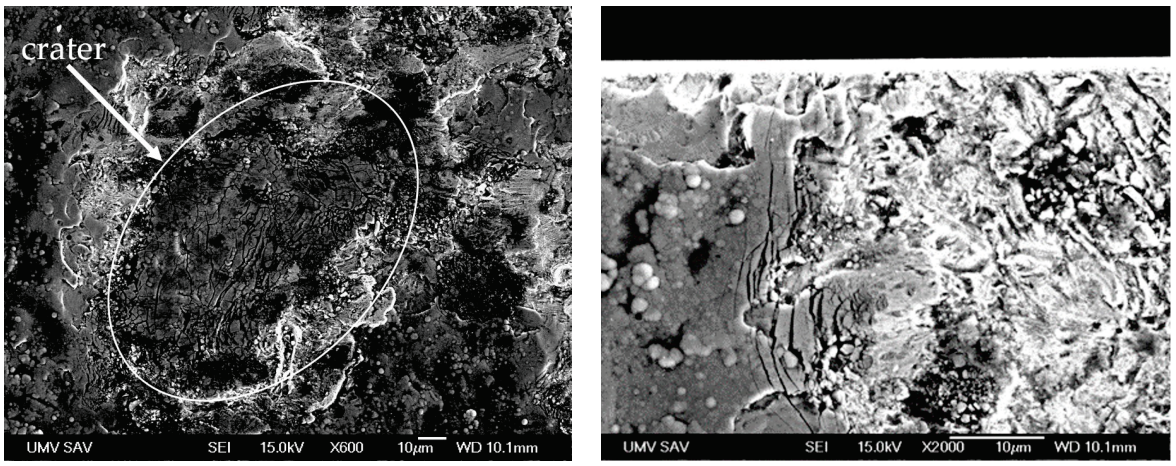
surface morphology and cross-sections of the specimen of the TiN-coated insert. The image of the surface morphology illustrated in Figure 4a shows the erosion of the coating presented by multiple craters, which were concentrated in a ring around the inner hole of the insert. Figure 4b shows the wear and degradation of the coating. There are areas of missing coating and indentation. Figure 4c illustrates that in addition to wear and uncoated areas, there is a visible rise of material above the coating. These failures have significant importance in terms of the surface quality of the produced casting (there is a low maximum tolerance limit of average surface roughness). The failure negatively impacts the insert's lifetime.



(**a**) (**b**) (**c**)

Figure 4. Optical microscopy images of the specimen of the insert coated with TiN after shots: (**a**) surface morphology of specimen; (**b**) cross-section of the specimen; and (**c**) cross-section of the specimen.

Figure 5 shows the SEM images of the specimen with the TiN-coated insert. Figure 5a illustrates the details of the crater, whose center is formed by island-like formations of the coating. In Figure 5b, a more detailed coating failure is visible, which is accompanied by the gradual breaking off of small sharp parts of the coating. This cracking is probably caused by the cyclic thermomechanical effect of the HPDC process.

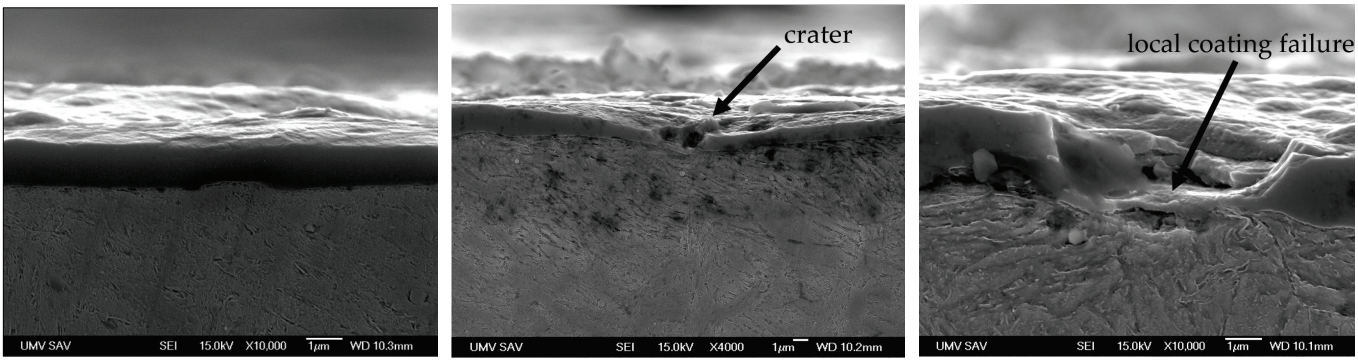


(**a**) (**b**)

Figure 5. SEM backscattered electron images of surface morphology of the insert's specimen coated with TiN after shots: (**a**) crater and (**b**) surface failure.

Figure 6 shows cross-sections of the specimen of the insert coated with TiN after shots. The first, Figure 6a, shows the thinned thickness of the coating, which is around 1.25 µm. Figure 6b shows local erosion of the surface under 0.8 µm in the form of a regular crater. Under the coating, local plastic deformation of the basic material is visible. It is probably

caused by high temperatures and high stress. Cavities were visible in several places in the cross-section. Figure 6c shows local coating failure at the bottom, which is the basic metal of the mold insert. The failures and cracks (Figure 5b) can be a prerequisite for the formation of intermetallic layers of Fe–Al as was mentioned by several studies, but within our analysis, the intermetallic layers were not identified.



(**a**) (**b**) (**c**)

Figure 6. SEM of cross-sections of insert's specimen coated with TiN after shots: (**a**) thinned coating; (**b**) local erosion; and (**c**) local coating failure.

3.2. Hardness and Surface Roughness

Table 3 shows the values of parameters that were measured on the surface of the inserts before the initiation of the casting process. As can be seen in Table 3, the uncoated insert achieved the optimal value of hardness—48 HRC after the heat treatment, as it was mentioned as the value within the desired range according to [13] (p. 120) and [3] (p. 235). The roughness of the uncoated insert was the lowest, achieving Ra = 0.10 μm. PVD coatings increased the hardness of the inserts. The highest hardness of the PVD-coated inserts was measured for the TiAlN and the lowest for the TiN-coated surface. TiAlN and CrAlSiN have more complex crystal structures compared to TiN. The incorporation of aluminum and silicon causes lattice distortions, increasing hardness. The TiN-coated insert had the highest roughness of Ra = 0.46. The lowest roughness was measured for the surface with the deposited CrAlSiN coating with Ra = 0.34. The arc vapor deposition can introduce macroparticles or droplets, affecting the surface roughness. The smoother surface of CrAlSiN could be affected by the refining effect of silicon on the grain structure.

Table 3. Values of parameters of uncoated insert and inserts coated with CrAlSiN, TiAlN, and TiN.

Measured Parameters	Uncoated	CrAlSiN-Coated	TiAlN-Coated	TiN-Coated
Hardness (HRC)				
Mean	48	52	53	50
SD	0.4	0.9	1.1	0.6
Roughness (μm)				
Ra	0.10	0.34	0.39	0.46
Rz	0.6	1.1	1.6	1.4

The following Figure 7 shows the measured Ra values of the casting surface after every 500 shots using the uncoated insert and inserts protected with CrAlSiN, TiAlN, and TiN. The wear of the inserts' surface negatively affects the surface of the castings produced. It increases the roughness of the casting surface. As we take into account the customer requirement, of which the maximum allowed value of the produced casting's surface is Ra = 2.5 μm, the possible inserts' lifetime is limited. Castings with higher values of Ra

cannot be delivered to the customer and are considered as a non-conformity, and inserts are decommissioned.

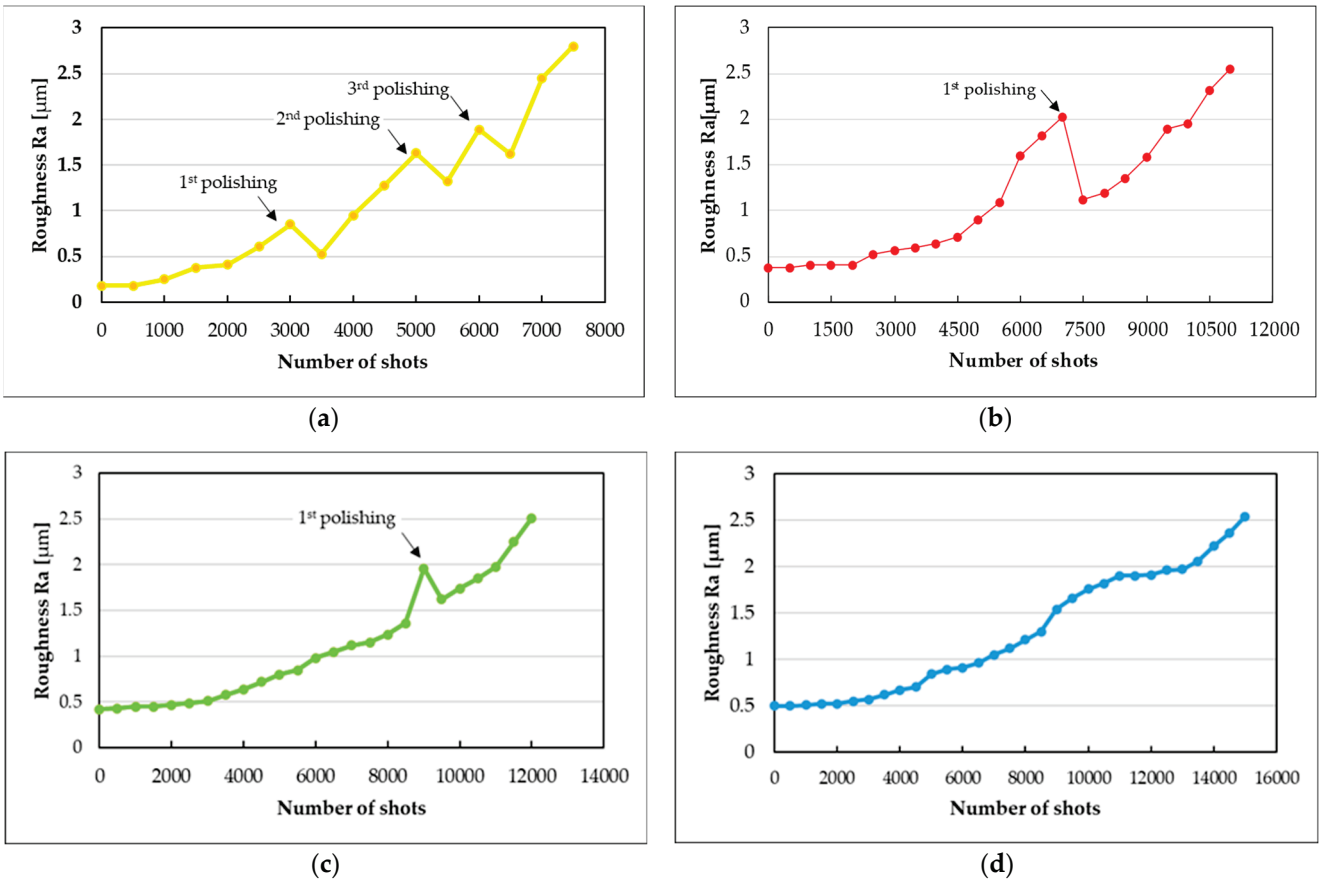


Figure 7. Average roughness values (Ra) of the bearing surfaces of castings after the shots using: (**a**) uncoated insert; (**b**) insert with CrAlSiN-coated film; (**c**) insert with TiAlN-coated film; and (**d**) insert with TiN-coated film.

The uncoated insert during the examination was polished thrice, as the roughness value was rapidly increasing. The goal was to prolong the lifetime of the inserts used in the production, taking into account the maximum prescribed Ra value for castings. However, it had a minimal effect on lowering the roughness value and lifetime prolongation of the insert. The first polishing helped to slightly decrease the roughness—ΔRa 0.32. A similar effect of lowering of the roughness was also observed after the second and third polishing. The lifetime of the insert ended after 7000 shots as the Ra value reached the tolerance limit of Ra = 2.5 µm. If the production had been continued, non-conforming castings would have been produced.

In the case of the inserts protected by CrAlSiN and TiAlN coatings, the polishing was performed one time, when the value of Ra was approaching 2 µm. The TiN-coated insert was not polished. The roughness of the CrAlSiN-coated insert started to grow significantly after 4500 shots (linear growth). Polishing was performed after 7000 shots. The polishing brought a more significant decrease in roughness in comparison with the uncoated insert. However, it started to increase at the same pace, and after 3000 shots, the roughness achieved the value before polishing. The Ra value of the TiAlN-coated insert started to rise more significantly (linear) after 3500 shots. At 900 shots, as it significantly increased up to the value of Ra = 2, it was polished, and after 11,000 shots, the value reached that before polishing. This insert was used until 12,000 shots. The highest efficiency was achieved using the TiN-coated insert, where the increasing roughness of the produced castings was the lowest and compared to the inserts protected with the previously mentioned coatings,

Ra = 2 was reached until 13,000 shots. Therefore, the polishing of this insert was not realized. It was possible to use this insert until 15,000 shots without polishing.

Figure 8 shows the increase of roughness (Ra) of the castings produced using the uncoated insert and PVD-coated inserts (TiN, TiAlN, and CrAlSiN). There is a significant difference between the uncoated insert and other PVD-protected inserts in terms of the insert lifetime. The deposition of PVD coatings prolonged the inserts' lifetime. Despite the highest initial roughness of the TiN-coated insert, it was able to achieve the highest number of shots until the produced castings achieved the limited value of Ra without polishing. Although TiN has a lower oxidation temperature in comparison with the TiAlN and CrAlSiN coatings, and some studies concluded better wear and corrosion resistance of TiAlN than TiN, in our study, under the given process conditions (described in Material and Methods), the TiN coating achieved the longest lifetime. It is considered to be the best option for the organization in terms of effectiveness and efficiency.

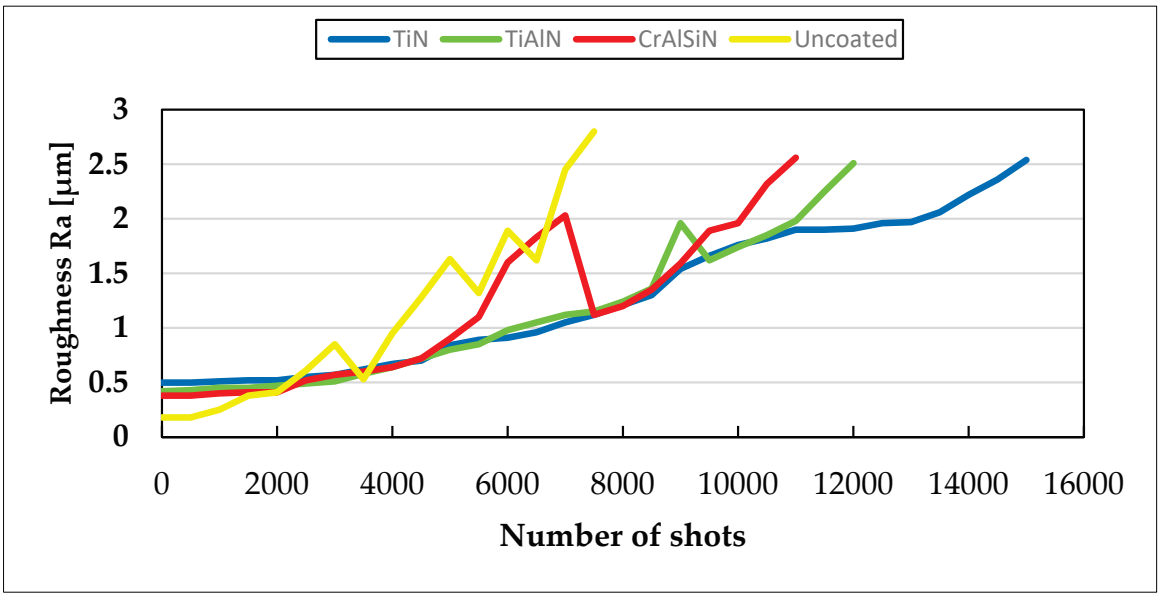


Figure 8. Average roughness values (Ra) of the bearing surfaces of castings using an uncoated insert and coated inserts with TiN, TiAlN, and CrAlSiN.

The TiN-coated surface had the highest roughness, which could cause the capturing of lubricant (applied after shots) that protects the surface. This effect was confirmed in the case of textured PVD coatings in the study according to [33].

4. Conclusions

Based on our study, the main conclusions resulting from the investigations and analysis are as follows:

- The optical and SEM analysis showed wear and the formation of craters at the bottom, of which the uncovered basic material of the insert is visible. The study of surface morphology revealed the presence of cracks probably caused by the cyclic thermomechanical effect. These failures can be prerequisites for the formation of intermetallic Fe–Al layers. They negatively affect the surface quality of castings, manifesting by increasing average roughness (Ra).
- The PVD-coated inserts achieved a significantly longer lifetime than uncoated inserts concerning the requirements of casting surface roughness (Ra), while the TiN-coated insert performed the best in comparison with TiAlN- and CrAlSiN-coated inserts. The difference in lifetime using TiAlN- and CrAlSiN-coated inserts was only 10,000 shots, with an advantage for TiAlN.

- The polishing performed to prolong the inserts' lifetime had a minimal effect on the uncoated insert (prolongation of lifetime by 500 shots). It was also applied in the case of TiAlN- and CrAlSiN-coated inserts when they were approaching the critical value of Ra and the prolongation of lifetime ranged from 2000 to 3000 shots.

Author Contributions: Conceptualization, A.S.; methodology, A.S. and R.K.; formal analysis, I.P. and P.P.; investigation, R.K. and A.S.; resources, M.K.; writing—original draft preparation, A.S.; writing—review and editing, P.P. and A.P.; visualization, A.P. All authors have read and agreed to the published version of the manuscript.

Funding: This research received no external funding.

Institutional Review Board Statement: Not applicable.

Informed Consent Statement: Not applicable.

Data Availability Statement: Data are contained within the article.

Conflicts of Interest: The authors declare no conflicts of interest.

References

1. Mayer, A.R.; de Oliveira, W.R.; Fals, H.D.C.; Lima, M.J.; Gonçalves, C.S.; Munoz, N.; Corso, J.L.; Pukasiewicz, A.G.M.; Mayer, A.R.; de Oliveira, W.R.; et al. Die soldering and corrosion failure of high temperature tool steel for high-pressure die casting Al alloy. *Eng. Fail. Anal.* **2024**, *161*, 108314. [CrossRef]
2. Nunes, V.; Silva, F.J.; Andrade, M.F.; Alexandre, R.; Baptista, A.P. Increasing the lifespan of high-pressure die cast molds subjected to severe wear. *Surf. Coat. Technol.* **2017**, *332*, 319–331. [CrossRef]
3. Terek, P.; Kovačević, L.; Miletić, A.; Panjan, P.; Baloš, S.; Škorić, B.; Kakaš, D. Effects of die core treatments and surface finishes on the sticking and galling tendency of Al–Si alloy casting during ejection. *Wear* **2016**, *356–357*, 122–134. [CrossRef]
4. Markežič, R.; Naglič, I.; Mole, N.; Šturm, R. Experimental and numerical analysis of failures on a die insert for high pressure die casting. *Eng. Fail. Anal.* **2019**, *95*, 171–180. [CrossRef]
5. Chen, Z.W.; Jahedi, M.Z. Die erosion and its effect on soldering formation in high pressure die casting of aluminium alloy. *Mater. Des.* **1999**, *6*, 303–309. [CrossRef]
6. Kohlhepp, M.; Uggowitzer, P.J.; Hummel, M.; Höppel, H.W. Formation of Die Soldering and the Influence of Alloying Elements on the Intermetallic Interface. *Materials* **2021**, *14*, 1580. [CrossRef]
7. Chen, Z.W. Formation and progression of die soldering during high pressure die casting. *Mater. Sci. Eng.* **2005**, *397*, 356–369. [CrossRef]
8. Domkin, K.; Hattel, J.H.; Thorborg, J. Modeling of high temperature- and diffusion-controlled die soldering in aluminum high pressure die casting. *J. Mater. Proc. Technol.* **2008**, *209*, 4051–4061. [CrossRef]
9. Salem, M.; Le Roux, S.; Dour, G.; Lamesle, P.; Choquet, K.; Rézaï-Aria, F. Effect of aluminizing and oxidation on the thermal fatigue damage of hot work tool steels for high pressure die casting applications. *Int. J. Fatigue* **2019**, *119*, 126–138. [CrossRef]
10. Sütőová, A.; Grzinčič, M. Creation of Defects Catalogue for Nonconforming Product Identification in the Foundry Organization. *Qual. Innov. Prosper. J.* **2013**, *17*, 52–58. [CrossRef]
11. Teplická, K. Comparison of Using Managerial Instruments in Industry Companies in Slovakia and the Czech Republic. *TEM J.* **2019**, *8*, 1191–1197. [CrossRef]
12. Brezinová, J.; Viňáš, J.; Džupon, M.; Jakubeczyová, D.; Brezina, J.; Sailer, H.; Hašuľ, J.; Považan, M. Use of Duplex PVD Coatings to Increase the Life of Moulds and Cores for die Casting of Aluminium Alloys in the Automotive Industry. *Acta Mech. Slovaca* **2022**, *26*, 42–51. [CrossRef]
13. Bhaskar, M.; Anand, G.; Nalluswamy, T.; Suresh, P. Die Life in Aluminium High-Pressure Die Casting Industries. *J. Inst. Eng. India Ser. D* **2022**, *103*, 117–123. [CrossRef]
14. Gulizia, S.; Jahedi, M.Z.; Doyle, E.D. Performance evaluation of PVD coatings for high pressure die casting. *Surf. Coat. Technol.* **2001**, *140*, 200–205. [CrossRef]
15. Rosso, M.; Ugues, D.; Torres, E.; Perucca, M.; Kapranos, P. Performance enhancements of die casting tools trough PVD nanocoatings. *Int. J. Mater. Form.* **2008**, *1*, 1259–1262. [CrossRef]
16. Paiva, J.M.; Fox-Rabinovich, G.; Junior, E.L.; Stolf, P.; Ahmed, Y.S.; Martins, M.M.; Bork, C.; Veldhuis, S. Tribological and Wear Performance of Nanocomposite PVD Hard Coatings Deposited on Aluminum Die Casting Tool. *Materials* **2018**, *11*, 358. [CrossRef]
17. Midson, S.P.; De Campos Neto, N.D.; May, W.; Korenyi-Both, A.L.; Kaufman, M.J. Laboratory Testing to Characterize the Use of PVD Coatings and Alternate Die Materials for Reducing Soldering and Erosion for Aluminum Die Casting Applications. *Int. J. Metalcast.* **2024**, *18*, 1–14. [CrossRef]
18. Campos Neto, N.D.; Korenyi-Both, A.L.; Vian, C.; Midson, S.P.; Kaufman, M.J. The development of coating selection criteria to minimize die failure by soldering and erosion during aluminum high pressure die casting. *J. Mater. Proc. Technol.* **2023**, *316*, 117954. [CrossRef]

19. Torres, E.; Ugues, D.; Brytan, Z.; Perucca, M. Development of multilayer coatings for forming dies and tools of aluminium alloy from liquid state. *J. Phys. D Appl. Phys.* **2009**, *42*, 105306. [CrossRef]
20. Vetter, J.; Eriksson, A.O.; Reiter, A.; Derflinger, V.; Kalss, W. Quo Vadis: AlCr-Based Coatings in Industrial Applications. *Coatings* **2021**, *11*, 344. [CrossRef]
21. Ugues, D.; Torres, E.; Perucca, M.; Albertinazzi, M.; Rosso, M. Hard coatings to prevent the washout phenomena in high pressure die casting tools. *BHM Berg- Hüttenmännische Monatshefte* **2006**, *151*, 109–112. [CrossRef]
22. Gurada, C.; Mundotia, R.; Mhatre, R.; Kale, A.; Kothari, D. Thermal Fatigue Resistance Studies of Multilayer CrN and AlTiN Coatings Deposited on Plasma Nitrided H-13 Hot Work Steel. *Lubricants* **2023**, *11*, 19. [CrossRef]
23. Khadem, M.; Penkov, O.V.; Yang, H.K.; Kim, D.E. Tribology of multilayer coatings for wear reduction: A review. *Friction* **2017**, *5*, 248–262. [CrossRef]
24. Matei, A.A.; Turcu, R.N.; Pencea, I.; Herghelegiu, E.; Petrescu, M.I.; Niculescu, F. Comparative Characterization of the TiN and TiAlN Coatings Deposited on a New WC-Co Tool Using a CAE-PVD Technique. *Crystals* **2023**, *13*, 112. [CrossRef]
25. Das, D.; Guha, S.; Ghadai, R.; Swain, B.P. A comparative analysis over different properties of TiN, TiAlN and TiAlSiN thin film coatings grown in nitrogen gas atmosphere. *Mater. Chem. Phys.* **2021**, *258*, 123866. [CrossRef]
26. Obrosov, A.; Gulyaev, R.; Ratzke, M.; Volinsky, A.A.; Bolz, S.; Naveed, M.; Weiß, S. XPS and AFM Investigations of Ti-Al-N Coatings Fabricated Using DC Magnetron Sputtering at Various Nitrogen Flow Rates and Deposition Temperatures. *Metals* **2017**, *7*, 52. [CrossRef]
27. Yoon, S.Y.; Lee, K.O.; Kang, S.S.; Kim, K.H. Comparison for mechanical properties between TiN and TiAlN coating layers by AIP technique. *J. Mater. Proc. Technol.* **2002**, *130–131*, 260–265. [CrossRef]
28. Liew, W.Y.; Jie, J.L.; Yan, L.Y.; Dayou, J.; Sipaut, C.S.; Madlan, M.F. Frictional and Wear Behaviour of AlCrN, TiN, TiAlN Single-layer Coatings, and TiAlN/AlCrN, AlN/TiN Nano-multilayer Coatings in Dry Sliding. *Proc. Eng.* **2013**, *68*, 512–517. [CrossRef]
29. Liu, Y.; Yu, S.; Shi, Q.; Ge, X.; Wang, W. Multilayer Coatings for Tribology: A Mini Review. *Nanomaterials* **2022**, *12*, 1388. [CrossRef]
30. Wang, Q.; Zhou, F.; Wang, C.; Yuen, M.-F.; Wang, M.; Qian, T.; Matsumoto, M.; Yan, J. Comparison of tribological and electrochemical properties of TiN, CrN, TiAlN and a-C:H coatings in simulated body fluid. *Mater. Chem. Phys.* **2015**, *158*, 74–81. [CrossRef]
31. Berger, C.; Scheerer, H.; Ellermeier, J. Modern materials for forming and cutting tools—Overview. *Mater. Werkst.* **2010**, *41*, 5–16. [CrossRef]
32. Valleti, P.C.; Venu Gopal, A.; Joshi, S.V. CrAlSiN nanocomposite thin films for high-speed machining applications. *Mater. Manuf. Process.* **2018**, *33*, 371–377. [CrossRef]
33. Brezinová, J.; Džupon, M.; Puchý, V.; Brezina, J.; Maruschak, P.; Guzanová, A.; Sobotová, L.; Badida, M. Research on the Tribological Properties of a New Generation of Multi-Layer Nanostructured PVD Coatings for Increasing the Technological Lifetime of Moulds. *Metals* **2024**, *14*, 131. [CrossRef]
34. Tošenovský, F.; Tošenovský, J.; Blaštíková, M. Selected Problems in Statistical Modelling of Metallurgical Processes. In Proceedings of the 28th International Conference on Metallurgy and Materials, Brno, Czech Republic, 22–24 May 2019. [CrossRef]
35. Ding, R.; Yang, H.; Li, S.; Hu, G.; Mo, J.; Chu, M.; Paddea, S.; Zhang, S.; Zhang, P.; Liu, Z.; et al. Failure analysis of H13 steel die for high pressure die casting Al alloy. *Eng. Fail. Anal.* **2021**, *124*, 105330. [CrossRef]
36. Mitterer, C.; Holler, F.; Üstel, F.; Heim, F.D. Application of hard coatings in aluminium die casting—Soldering, erosion and thermal fatigue behaviour. *Surf. Coat. Technol.* **2000**, *125*, 233–239. [CrossRef]
37. Wiedenegger, A.; Bruckwilder, J.; Deutsch, C. Ecological and Economic Benefits of Additive Manufacturing in High Pressure Die Casting. *BHM Berg- Hüttenmännische Monatshefte* **2021**, *166*, 237–242. [CrossRef]
38. Kobčar, D.; Kosec, L.; Kosec, B.; Tušek, J. Thermo fatigue cracking of die casting dies. *Ing. Fail. Anal.* **2012**, *20*, 43–53. [CrossRef]
39. *ISO 26423*; Fine Ceramics (Advanced Ceramics, Advanced Technical Ceramics)—Determination of Coating Thickness by Crater-Grinding Method. ISO: Geneva, Switzerland, 2009.
40. *IATF 16949:2015*; Quality Management System. International Automotive Task Force: Torino, Italy, 2016.
41. *ASTM A956:2022*; Standard Test Method for Leeb Hardness Testing of Steel Products. American Society for Testing and Materials: West Conshohocken, PA, USA, 2022.
42. *DIN EN 50156-1:2016*; Electrical Equipment for Furnaces and Ancillary Equipment. VDE: Berlin, Germany, 2016.
43. *JSA-JIS B 0601*; Geometrical Product Specifications (GPS}—Surface Texture: Profile Method—Terms, Definitions and Surface Texture Parameters. JSA: Tokyo, Japan, 2013.
44. *ISO 21920-2:2021*; Geometrical Product Specifications (GPS)—Surface Texture: Profile—Part 2: Terms, Definitions and Surface Texture Parameters. ISO: Geneva, Switzerland, 2021.

Disclaimer/Publisher's Note: The statements, opinions and data contained in all publications are solely those of the individual author(s) and contributor(s) and not of MDPI and/or the editor(s). MDPI and/or the editor(s) disclaim responsibility for any injury to people or property resulting from any ideas, methods, instructions or products referred to in the content.

coatings

MDPI

Article

Study on the Thermal Radiation Characteristics of Tungsten Surface Grating Structures Prepared by Femtosecond Laser Direct Writing

Ruxue Guo [1], Ping Zhou [2], Wanyun Zhang [1], Haiying Song [1,*] and Shibing Liu [1]

[1] Strong-Field and Ultrafast Photonics Lab, School of Physics and Optoelectronic Engineering, Beijing University of Technology, Beijing 100124, China; ruxue_guo@emails.bjut.edu.cn (R.G.); zwy_mail0531@163.com (W.Z.); sbliu@bjut.edu.cn (S.L.)
[2] Beijing Institute of Astronautic System Engineering, Beijing 100076, China; ana0072@163.com
* Correspondence: hysong@bjut.edu.cn

Abstract: In this paper, using laser direct writing technology, a femtosecond laser was used to process a periodic grating structure on a 99.99% tungsten target. The specific parameters of the laser are as follows: a center wavelength of 800 nm, pulse width of 35 fs, repetition rate of 1 kHz, and maximum single pulse energy of 3.5 mJ. The surface morphology of the samples was characterized and analyzed using a scanning electron microscope (SEM, Coxem, Republic of Korea) and atomic force microscope (AFM, Being Nano-Instruments, China). The thermal radiation infrared spectrum of the tungsten target with grating structures was measured using a Fourier transform infrared spectrometer (Vertex 70, Bruker, Germany). The results show that as the laser fluence increases, the depth of the groove, the width of the nanostructure region, and the width of the direct writing etching region all increase. The peak thermal radiation enhancement appears around the wavenumber of 900 cm^{-1} when the laser fluence is sufficient. Additionally, its intensity initially increases and then decreases as the laser fluence increases. If the grating period is too large, the impact on thermal radiation is not clear. The heating temperature significantly affects the intensity of thermal radiation but does not have a noticeable effect on the position of thermal radiation peaks. Moreover, the relative weighting of different wavenumbers changes as the temperature increases.

Keywords: thermal radiation; grating structure; direct writing processing; femtosecond laser

1. Introduction

The emission of thermal radiation is an inherent property of all objects [1–3]. When the temperature is higher than absolute zero, the emitted electromagnetic wave radiation resulting from the changing thermal motion state of microscopic particles is known as thermal radiation [4,5]. All objects emit and absorb radiation energy, and thermal radiation is closely intertwined with human daily life and industrial production [6]. The global energy situation is becoming increasingly tense. The effective use of solar energy has always been a matter of concern. Currently, solar power generation primarily utilizes photovoltaic cells to convert solar radiation energy into electrical energy. However, photovoltaic cells can only absorb and convert a small portion of the frequency of radiation energy into electrical energy. Enhancing the solar cell surface's absorption performance effectively improves its photoelectric conversion efficiency [7–11]. In high-altitude or space environments, traditional heat transfer methods are not effective, so aerospace equipment primarily relies on heat radiation transfer. Currently, most aircraft use nano-coatings to enhance surface emissivity. However, these coatings may introduce safety risks and increase the aircraft's load. Therefore, improving aircraft surface emissivity is extremely important for the aerospace industry. With the continuous advancements in human science and technology, the demand for high-tech equipment across various fields to regulate and control thermal

radiation characteristics is increasing. Existing thermal radiation control technology is inadequate to meet technological development and application needs. Therefore, exploring and researching new thermal radiation control technology is essential.

There are various micro–nano structures in nature, and these structures provide organisms with many unique functional properties [12–14]. When materials have micro- and nano-scale structures on their surface, certain properties can be altered (such as thermal radiation, optics, infiltration, adhesion and desorption, superhydrophobicity, etc.) [15–22]. In recent years, there has been increasing research interest in manipulating the thermal radiation characteristics of materials by altering the micro–nano structures on their surfaces [23–29]. The primary research mechanisms for controlling the thermal radiation characteristics of materials involve changing the micro–nano structures on the material's surface, including the microcavity resonance effect and surface plasmon resonance effect [30–33]. The Japanese scientist Sai used the rigorous coupled wave analysis method to calculate and simulate the impact of microcavity resonance mode on the thermal radiation of the deep metal grating structure. Through experiments, Sai verified that microcavity resonance mode is not dependent on its angle [34,35]. Mason et al. used chemical etching to fabricate a one-dimensional grating on steel, which resulted in a 2.6 increase in the thermal radiation spectrum. Moreover, they explained the thermal radiation enhancement mechanism based on surface plasmon polaritons [36,37]. Jiao et al. demonstrated that through experiments and simulations, a one-step ultrafast laser writing technology based on the phase change material $Ge_2Sb_2Te_5$ (GST) can achieve position-selective regulation of thermal radiation [38]. In recent years, laser technology has rapidly developed, particularly the emergence of ultrafast femtosecond pulse lasers, which have opened up new possibilities for surface micro–nano structure manufacturing. Femtosecond laser processing offers significant advantages such as ultra-short pulse width, ultra-high power density, extremely high processing accuracy, and minimal heat-affected zones. Additionally, femtosecond lasers can achieve high-precision processing on almost all kinds of materials, including metals, non-metals, and semiconductors [39–45]. The femtosecond laser's characteristics make it an effective method for creating micro–nano structures on material surfaces, particularly in surface micro–nano manufacturing. By altering the surface's micro–nano structure, we can control the thermal radiation characteristics of materials, which has significant potential applications in various fields. These applications include improving solar absorbers' absorption efficiency, enhancing electronic device heat dissipation, developing infrared thermal radiators, and advancing aerospace thermal control [46–51].

Tungsten has a high melting point, low vapor pressure, and stable chemical properties, making it extensively utilized in machinery, construction, transportation, electronics, military, and aerospace [52,53]. In this paper, we used femtosecond laser direct writing technology to process a surface periodic grating structure on a 99.99% pure tungsten target. We then experimentally explored the impact of the grating structure on thermal radiation characteristics. We surveyed and recorded the variation rule of the tungsten target's periodic grating structure by changing the laser fluence. At the same time, the infrared spectra of various periodic grating structures were measured to explore their impact on thermal radiation characteristics. Changing the periodic grating structure of the tungsten's surface can help achieve the desired thermal radiation characteristics, which can advance related technologies in different fields. The enhanced peak of thermal radiation is generated due to the emission of thermally excited particles from the heated material's surface, which is coupled with the surface grating structure. The resonance excites the surface plasmon polaritons, which leads to the radiation enhancement at a certain frequency. In previous research, FTIR was used to analyze the thermal radiation spectra of the samples as described in the published paper [36,54,55]. The authors obtained excellent results and made scientific explanations, demonstrating the feasibility of the research approach. Consequently, we modified the measurement method of the Fourier transform infrared (FTIR) spectrometer based on previous research. The specific working mechanism of FTIR is described as follows. Using the FTIR interface, we introduced the heated sample into

the spectrometer as an external light source. An external optical path was set up near the external light source port to collect the thermal radiation generated by the heated sample. The radiation was gathered by the off-axis parabolic mirror and directed to the external light source port of the FTIR. By doing this, we were able to obtain the thermal radiation spectrum of the samples.

2. Materials and Methods

2.1. Preparation and Characterization of Micro–Nano Structure

The femtosecond laser experimental apparatus for processing micro–nano grating structures on a tungsten target includes three main components: an external optical path system, a direct writing processing system, and a sample translation stage. The femtosecond laser source utilizes the Coherent Company's Ti-sapphire femtosecond laser (LEGEND ELITE, Coherent, Saxonburg, PA, USA). The specific parameters are as follows: a center wavelength of 800 nm, a pulse width of 35 fs, a repetition rate of 1 kHz, and a maximum single pulse energy of 3.5 mJ. The laser pulse's fluence could be continuously adjusted using a neutral attenuator. Once the required fluence was set, the femtosecond laser was directed onto the Olympus microscope system (Olympus, Tokyo, Japan). Within the Olympus microscope system, the beam was focused on a 99.99% pure tungsten target surface using an objective lens with a magnification of 10× and a numerical aperture of 0.25. To process surface grating structures with varying periods, the scanning speed and trajectory of the Newport three-dimensional precision translation stage were adjusted (Note: the experiment was conducted in an air environment).

The control script was input into the electronic control translation stage, and the scanning speed was set to 1 mm/s. After the x-axis moved X mm, the y-axis moved P μm. Then the x-axis moved X mm in the opposite direction, and the y-axis moved P μm. This 'S'-shaped path scanning was repeated, and finally, a one-dimensional grating structure with a period of P μm was obtained. Simultaneously, by adjusting the neutral attenuator, the femtosecond laser fluences were set to 0.64 J/cm^2, 1.27 J/cm^2, 1.91 J/cm^2, . . ., 9.55 J/cm^2. Different laser fluences were used to process the tungsten. After direct writing, the samples were placed in ethanol and cleaned using an ultrasonic cleaner. Once dried, their surface morphology was characterized using scanning electron microscopy (SEM, Coxem, Daejeon, Republic of Korea) and atomic force microscopy (AFM, Being Nano-Instruments, Beijing, China). The study established the relationship between different experimental parameters, such as femtosecond laser fluence, scanning speed, and grating structure. Additionally, the surface micro–nano structures were measured using a Bruker Fourier infrared spectrometer (Vertex 70, Bruker, Berlin, Germany) for thermal radiation. We modified the measurement method of the Fourier transform infrared (FTIR) spectrometer (Vertex 70, Bruker, Germany) based on previous research. Using the FTIR interface, we introduced the heated sample into the spectrometer as an external light source. An external optical path was set up near the external light source port to collect the thermal radiation generated by the heated sample. The radiation was gathered by the off-axis parabolic mirror and directed to the external light source port of the FTIR. By doing this, we were able to obtain the thermal radiation spectrum of the samples.

As a result, we analyze how grating structures processed with different laser fluences affect thermal radiation characteristics. Furthermore, we explore the impact of temperature on the thermal radiation characteristics of tungsten targets with specific grating structures. The thermal radiation infrared spectrum measurement device is illustrated in Figure 1.

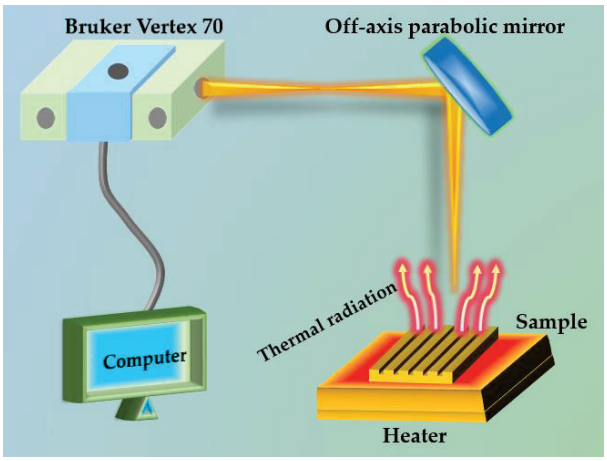


Figure 1. The equipment for measuring the infrared thermal radiation spectrum.

2.2. Simulation Method and Model Design

The simulation utilizes COMSOL Multiphysics software (COMSOL Multiphysics 5.6), which is based on finite element analysis and multi-physics coupling. It can accurately simulate and predict the process of light–matter interaction in optical simulations. In COMSOL, the most commonly used method for electromagnetic field calculation assumes that the electromagnetic field is a first-order time-harmonic field, with the time-independent part being a vector field with complex values. The solution is performed at a certain time-harmonic frequency, known as frequency domain electromagnetic simulation. When working with time-harmonic fields in COMSOL, the frequency domain simulation is used to solve the Helmholtz equation for the electric and magnetic fields. The main modeling steps in COMSOL Multiphysics are as follows: 1. Select the relevant physical fields and research content. 2. Model the geometric structure. 3. Set the material properties. 4. Define the boundary conditions. 5. Create the mesh. 6. Run the operation and perform the calculations.

In this study, we modeled the surface grating structure and simulated the emission spectra of gratings with different periodic structure parameters. We then compared these simulated results with experimental data. Figure 2 displays the schematic diagram illustrating the interaction between electromagnetic waves and micro–nano periodic structures. The structural parameters include the grating period (P), width (W), and depth (d). Meanwhile, the specific parameters were adjusted based on the experimentally prepared grating structure. Because the grating structure was periodic, the simulation was carried out in a two-dimensional plane. The periodic condition was set as the Floquet period, and the appropriate grid accuracy was divided according to the physical field.

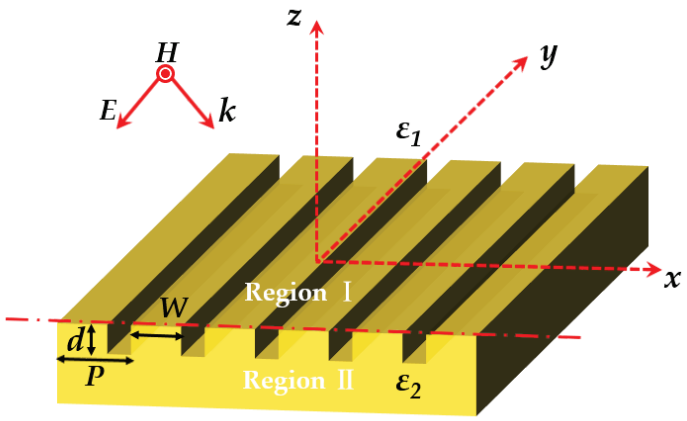


Figure 2. The schematic diagram of an electromagnetic wave incident on the surface of the grating structure.

3. Results and Discussion

3.1. The Influence of Varying Laser Fluence on the Grating Structure

In our experiments, we find that when the laser energy density is 0.64 J/cm^2, an ablation area starts to appear on the surface of the tungsten. The laser ablation threshold depends not only on the material's properties but also on the laser parameters. The pulse width is a crucial parameter that affects the ablation threshold. For long pulse lasers with a pulse width above nanoseconds, the ablation threshold is reflected in statistical characteristics. In the case of ultrashort pulse lasers, the statistical properties of the ablation threshold may not be readily apparent because of the predominant influence of nonlinear effects. The Gaussian distribution of the femtosecond laser beam results in high intermediate energy and low edge energy. The high intermediate energy surpasses the material's ablation threshold, leading to the formation of a direct writing etching region. On the other hand, the relatively weak edge energy fails to reach the ablation threshold, resulting in the formation of a nanostructured region. Figure 3 illustrates the clear definition of the nanostructured region and the direct writing etching region.

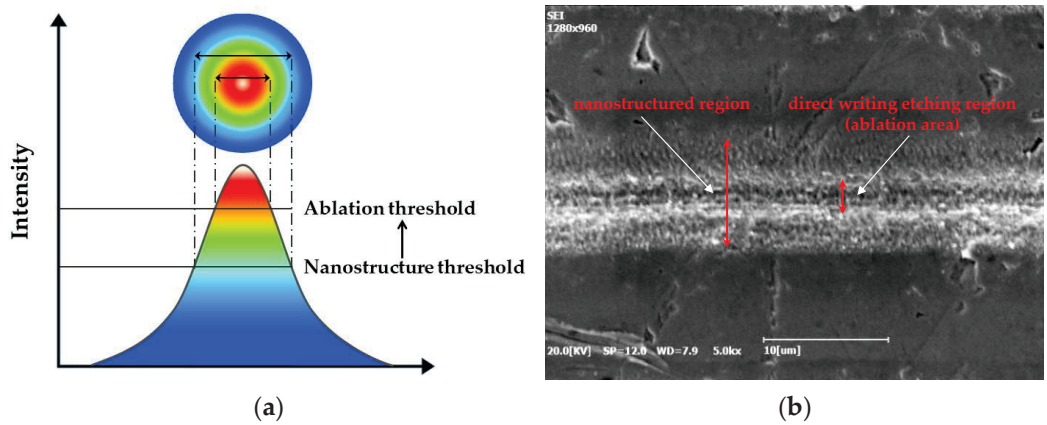
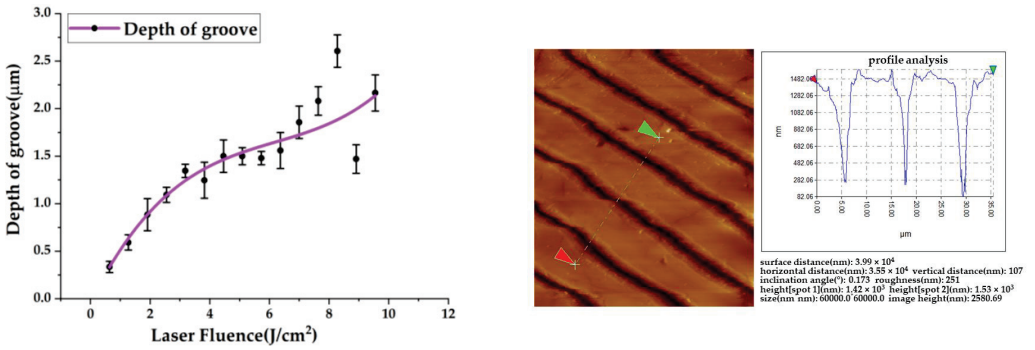


Figure 3. (**a**) Energy distribution of femtosecond laser; (**b**) SEM image with a laser fluence of 5.73 J/cm^2 and scanning speed of 1 mm/s.

In this study, we explore the impact of different laser fluences on the depth of the grating structure's grooves, as illustrated in Figure 4a. We maintained a scanning speed of 1 mm/s while increasing the laser fluence from 0.64 J/cm^2 to 9.55 J/cm^2. To analyze the data, we used polynomial fitting. Polynomial fitting offers high flexibility, better reflects data trends, and involves simple calculations. After optimizing the fitting process, we achieved an R-squared correlation coefficient of over 0.9. This indicates that the fitted curve closely matches the data, demonstrating the feasibility of the fitting process. In Figure 4a, it is evident that the depth of the groove increases as the femtosecond laser fluence increases. At a laser fluence of 0.64 J/cm^2, the depth of the groove is 0.35 μm. However, when the laser fluence is increased to 8.28 J/cm^2, the groove depth also increases to 2.6 μm, and the maximum error is 0.195 μm. As the laser fluence and energy increase, the ablation of the target also increases, resulting in a greater depth of the groove.

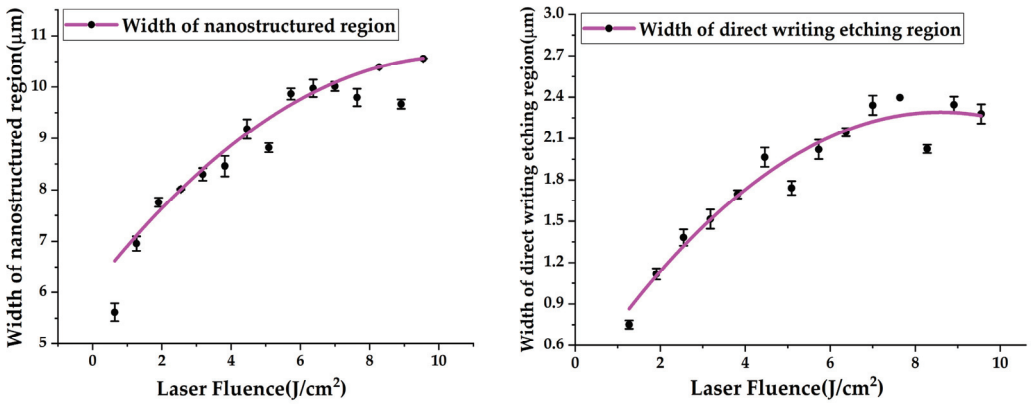
It is crucial to consider several factors when studying the grating structure, such as the period, the depth of the groove, the size of the nanostructure region, and the direct writing etching region. This study specifically focuses on how the femtosecond laser fluence influences the ablation area of the grating structure. The translation stage's scanning speed was 1 mm/s, and the grating period was 20 μm. By adjusting the femtosecond laser fluence using a neutral attenuator, ranging from 0.64 J/cm^2 to 9.55 J/cm^2, we were able to process a tungsten target under varying laser fluence. The grating period measured by SEM was consistent with the procedure's setting. Figure 5 demonstrates how the width of the nanostructured region and the direct writing etching region is influenced by varying laser fluence. In addition, a polynomial fitting was used, and the correlation coefficient

R-squared was over 0.9. Observing Figure 5a,b, it is evident that both the width of the nanostructured region and the width of the direct writing etching region increase as the femtosecond laser fluence increases. At a laser fluence of 0.64 J/cm^2, the width of the nanostructured region is the smallest at 5.62 μm, while at 9.55 J/cm^2, the width of the nanostructured region is the largest at 10.575 μm, and the maximum error of the width of 0.203 μm.



(**a**) (**b**)

Figure 4. (**a**) The variation of the depth of the groove under varying laser fluence; (**b**) AFM image with a laser fluence of 3.18 J/cm^2 and scanning speed of 1 mm/s (the red arrow corresponds to the start of the scanning range and the green arrow to the end).



(**a**) (**b**)

Figure 5. (**a**) The variation of the width of the nanostructured region under varying laser fluence; and (**b**) The variation of the width of the direct writing etching region under varying laser fluence.

The femtosecond laser beam has a Gaussian distribution, resulting in high intermediate and low edge energy. The high intermediate energy reaches the material's ablation threshold, creating a direct writing etching region. The low edge energy does not reach the ablation threshold, resulting in a nanostructured region. Additionally, different laser fluences cause varying light intensity distributions, leading to different widths of the grating nanostructure and the direct writing etching regions.

The surface morphology of the prepared grating structure could be characterized using a scanning electron microscope (SEM, Coxem, Republic of Korea). The grating structure period, the size of the nanostructure region, and the direct writing etching region could be measured. Figure 6 displays the SEM images of the grating structure prepared at the laser fluence of 1.91 J/cm^2, 3.18 J/cm^2, and 4.46 J/cm^2. Meanwhile, the scanning speed during the process was 1 mm/s, and the period was 20 μm. Figure 6 demonstrates that the micro–nano periodic structure, processed by femtosecond laser direct writing technology, is consistent with the period set by the program, and its surface arrangement is regular and orderly. The laser etching processes micron-level deep grooves with many

sub-wavelength nanostructures along the edges. Almost no heat-affected area exists, and microcracks around the groove are not obvious. Significantly, the processing system is simple and does not require harsh conditions. Experiments can be carried out at room temperature in air. This technology can process various structure parameters and large-area micro–nano periodic structures to meet the needs of different fields for periodic grating structures.

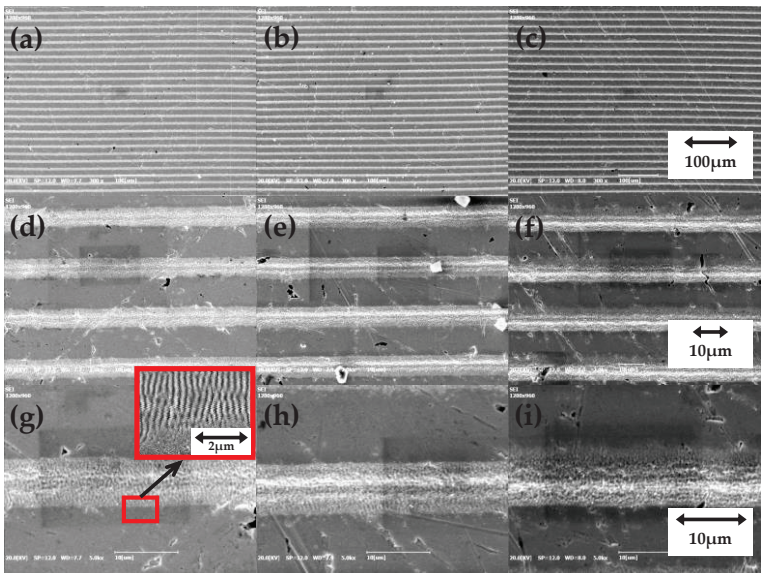


Figure 6. The SEM images of the grating structure prepared under varying laser fluence. (**a**,**d**,**g**) 1.91 J/cm^2; (**b**,**e**,**h**) 3.18 J/cm^2; (**c**,**f**,**i**) 4.46 J/cm^2.

When the pulse energy approaches the material's ablation threshold, a grating structure with a period smaller than the laser wavelength can be directly induced, known as a laser-induced periodical surface structure (LIPSS) [56–62]. Generally, LIPSSs are believed to be generated by the interference between the incident light and the surface plasmon polaritons. LIPSSs usually emerge when the laser fluence is low. Furthermore, LIPSSs gradually decrease as the laser fluence increases [63–66]. Figure 6 illustrates the magnified SEM image of LIPSSs.

3.2. The Influence of Different Grating Structures on the Thermal Radiation Spectrum

The above experiments explored the impact of varying laser fluence on several parameters, including the depth of the groove, the width of the nanostructure region, and the width of the direct writing etching region. In this section, we measured a blank tungsten target sample and a tungsten target with grating structures that were processed using laser fluences of 0.64 J/cm^2, 1.91 J/cm^2, 3.18 J/cm^2, and 4.46 J/cm^2. We conducted the measurements using FTIR. The processing scanning speed was 1 mm/s, the period of the grating structure was 10 μm, and the parameters of the grating structures for each laser fluence are depicted in Figure 7.

The spectrometer detector utilized in the experiment was DTGS, and the beam splitter was KBr. The measured infrared spectrum ranged from 400 cm^{-1} to 4000 cm^{-1}, and the heating temperature was 300 °C. At 300 °C, the thermal radiation energy is primarily concentrated in the infrared region. Additionally, the scanning speed was 1 mm/s, and the grating period was 10 μm. Figure 8 illustrates the thermal radiation spectrum display absorption bands caused by water and carbon dioxide at wavenumbers of 2350 cm^{-1} and 1625 cm^{-1}. As the laser fluence increases, a thermal emission enhancement peak starts to emerge near the wavenumber of 900 cm^{-1} when the laser fluence reaches 1.91 J/cm^2. The enhanced peak of thermal radiation is generated due to the emission of thermally excited particles from the heated material's surface, which is coupled with the surface

grating structure. The resonance excites the surface plasmon polaritons, enhancing the intensity of the resonance excitation on the surface (Appendix A provides the relevant theoretical foundations). Consequently, the electromagnetic wave in the infrared band emitted by the far field has an amplified peak that aligns with the resonance frequency of the surface plasmon polaritons. Even though there are LIPSSs at the edge of the structure when the laser fluence is low, the wavelength of the thermal radiation enhancement peak is consistent with the period of the grating structure. As the laser fluence increases, the LIPSSs gradually decrease. Therefore, we believe that the change in thermal radiation is primarily due to the periodic grating structure.

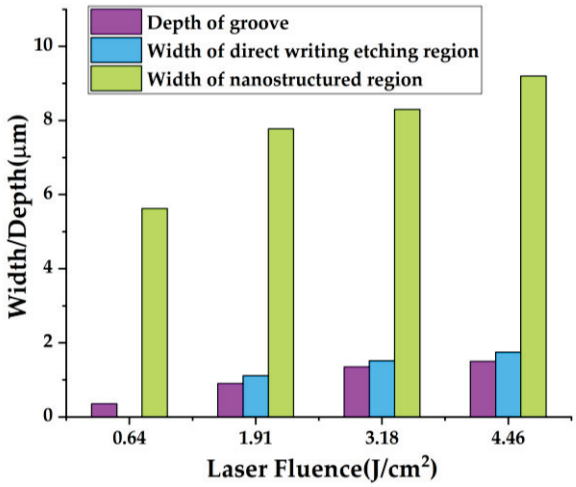


Figure 7. The parameters of the grating structure prepared under varying laser fluence.

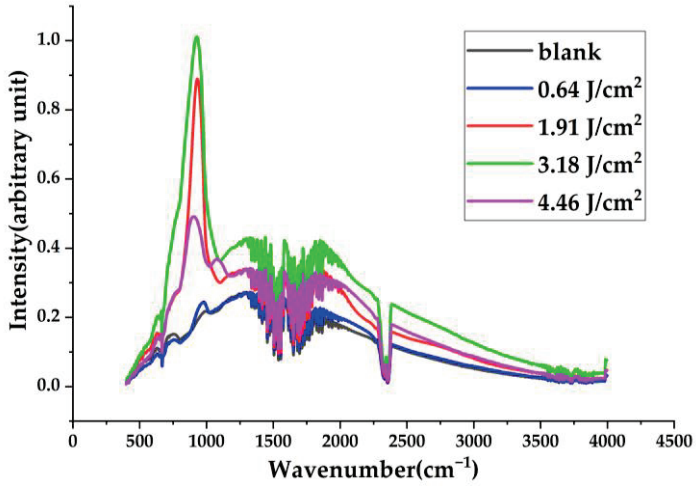


Figure 8. The influence of grating structure processed by varying laser fluence on thermal radiation spectrum.

As the laser fluence increases, the radiation enhancement peak's intensity initially increases and then decreases. This happens because the laser fluence determines the extent of ablation and volatilization during the laser-material interaction process. Higher laser fluence makes the resulting surface structure more noticeable, and the thermal radiation enhancement characteristics become more pronounced. However, when the laser fluence is too large, dense and complex micro–nano structures will form on the material's surface, which absorbs the emitted thermal radiation. As a result, the intensity of the thermal radiation decreases as the fluence increases beyond a certain point.

Furthermore, we notice that the position of the enhancement peak shifts when the laser influence reaches 4.46 J/cm^2. Meanwhile, a new weaker enhancement peak appears.

Following a discussion and a review of the literature, we believe this is attributable to variations in the depth of the grating structure. As shown in Section 3.1, different laser fluences can prepare grating structures with varying depths. We think the enhancement peak of the thermal radiation spectrum exhibits a red shift as the depth increases within a certain range. Consequently, we could observe the peak shifting towards lower wavenumbers, while a second-order enhancement peak appears. Our discussion is consistent with the point presented in the previous literature [21]. While our current work does not systematically explore this result, we consider it an interesting finding and a potential research direction for further work.

Grating structures with periods of 5 μm, 10 μm, 15 μm, and 20 μm were processed using a femtosecond laser with a laser fluence of 3.18 J/cm^2. The processing scanning speed was maintained at 1 mm/s. The thermal radiation spectrum of the grating structure for each period was tested, and the results are presented in Figure 9. For the grating period of 5 μm, a thermal radiation enhancement peak is observed near the wavenumber of 900 cm^{-1}. Subsequently, for the grating period of 10 μm, the intensity of the thermal radiation peak near 900 cm^{-1} shows a significant increase. At a grating period of 15 μm, there is a thermal radiation enhancement peak near the wavenumber of 650 cm^{-1}. However, when the grating period is 20 μm, the thermal radiation enhancement peak basically disappears, and the thermal radiation spectrum is nearly identical to the spectrum of the blank tungsten target. Therefore, when the grating structure period is too large, it has no obvious effect on the thermal radiation characteristics.

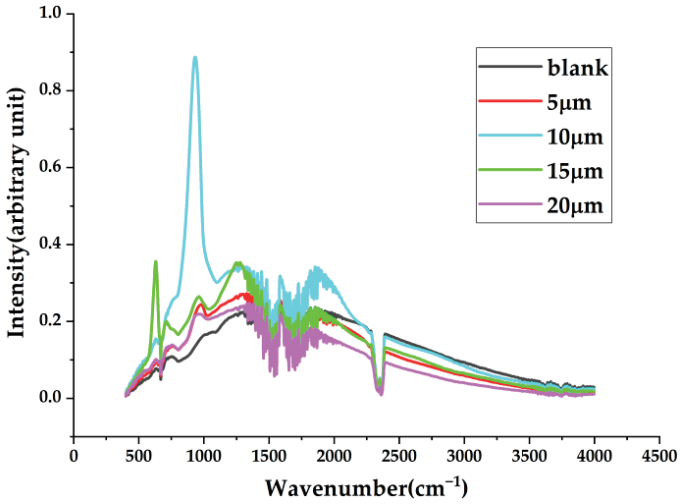


Figure 9. The influence of different periodic grating structures on the thermal radiation spectrum.

In addition, we compared the maximum radiation intensity of a blank sample to samples with different periods. The maximum radiation intensity of the sample with a period of 5 μm is approximately 1.2 times that of the blank sample; for the sample with a period of 10 μm, it is about 3.7 times; for the sample with a period of 15 μm, it is about 1.5 times; and for the sample with a period of 20 μm, it is almost equal to the blank sample.

We subtracted the thermal emission spectra of the blank tungsten sample from the spectra of different periods to perform spectral subtraction. Then, we eliminated the absorption bands caused by carbon dioxide and water vapor in the air. Finally, the thermal radiation spectrum of relative intensity was obtained. In Figure 10, we can see the maximum relative intensity for different periods: at 5 μm, it is approximately 0.09; at 10 μm, it is about 0.74; at 15 μm, it is around 0.26; and at 20 μm, it is roughly 0.08. The enhancement effect on thermal radiation is more significant when the period is 10 μm or 15 μm. In Figure 10, the position of the thermal radiation enhancement peak of the grating structure with different periods is intuitive, and the second-order enhancement peak can be observed in the grating

structure of 10 and 15 μm, which is due to the Floquet–Bloch wave vector of the grating structure $k_g = 2\pi m/\Lambda$ in the order $m = 2$.

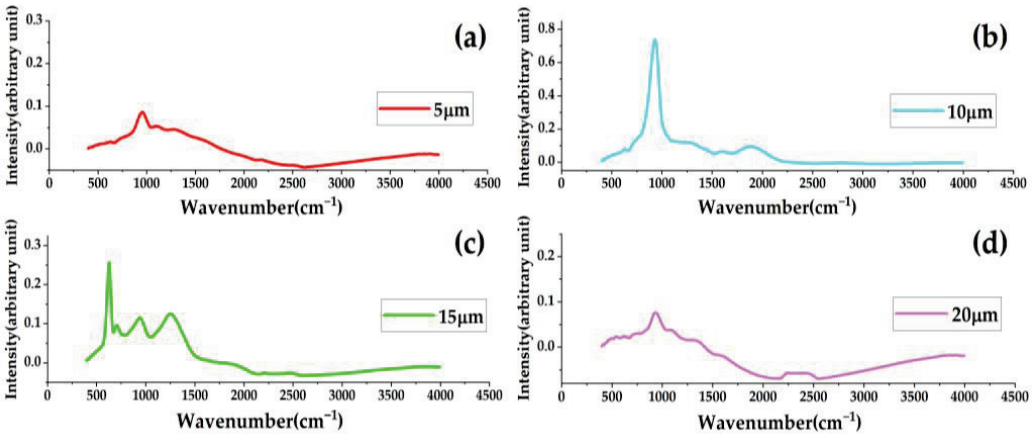


Figure 10. The relative intensity of the thermal radiation spectrum of grating structures with varying periods. (**a**) 5 μm; (**b**) 10 μm; (**c**) 15 μm; and (**d**) 20 μm.

Based on the optical parameters of tungsten found in the literature, we used COMSOL Multiphysics software to calculate the reflectivity of grating structures with periods of 10 μm and 15 μm. We then converted these values to emissivity using Kirchhoff's thermal radiation law. Our simulation results are depicted in Figure 11. It is evident from the results that the calculated enhancement peak of the 10 μm grating structure occurs near the wavenumber of 900 cm^{-1}, while the enhancement peak of the 15 μm grating structure is near the wavenumber of 650 cm^{-1}. The experimental results are consistent with the simulation results, indicating that the position of the peak for enhanced thermal emission can be effectively altered by adjusting the period of the grating structure. This allows for selective spectrum regulation.

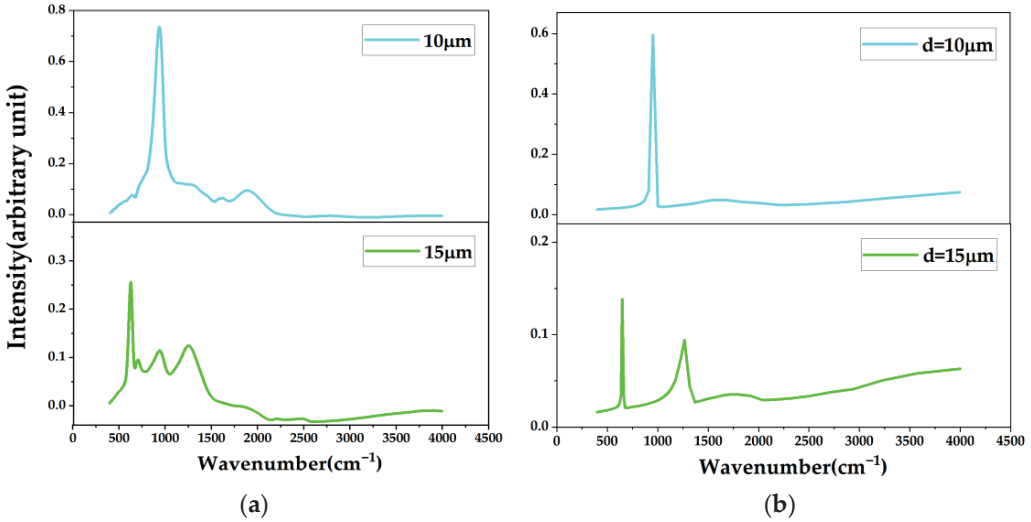


Figure 11. (**a**) The relative intensity thermal radiation spectrum of gratings with periods of 10 μm and 15 μm, and (**b**) the calculation results of COMSOL.

3.3. The Effect of Varying Heating Temperatures on the Thermal Radiation Spectrum

In this part, the grating structure was processed with a period of 10 μm and a laser fluence of 3.18 J/cm^2. At the same time, the scanning speed was 1 mm/s. The spectra obtained at different temperatures were used to analyze how the thermal radiation spectrum characteristics of the tungsten target surface with a grating structure were affected

by temperature variations. Figure 12 displays the thermal radiation spectra measured at heating temperatures ranging from 200 °C to 350 °C with intervals of 25 °C. Figure 12 shows a significant peak in the thermal radiation spectrum at around 900 cm^{-1}, along with absorption bands from water and carbon dioxide at 2350 cm^{-1} and 1625 cm^{-1}, respectively. First, we notice that the positions of the enhancement peaks remain constant as the temperature changes. Additionally, the thermal radiation at all wavenumbers increases with rising temperature. Finally, the relative weighting given to different wavenumbers changes with varying temperatures because the peak of the Planck distribution shifts toward lower wavelengths as temperature increases. In our work, the peaks near 1850 cm^{-1} are insignificant features at 200 °C but became more prominent at 350 °C because the blackbody's spectra shift in such a way that it gives those peaks much more weight than before.

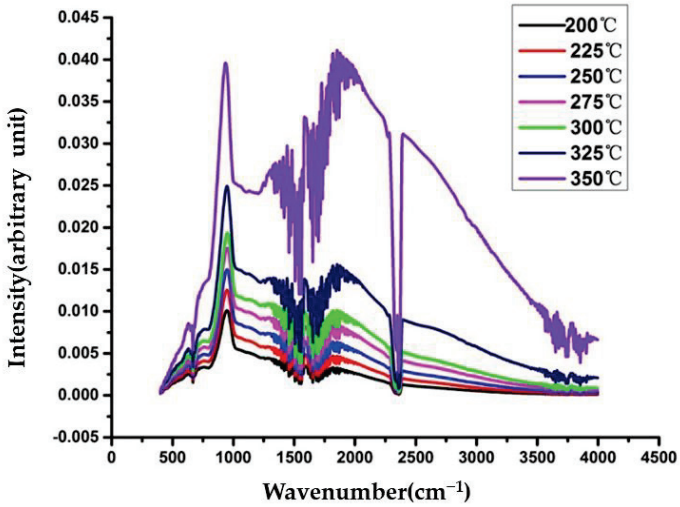


Figure 12. The influence of varying heating temperatures on the thermal radiation spectrum.

4. Conclusions

In this paper, processed grating structures on a tungsten target used femtosecond laser writing to explore their effect on thermal radiation spectral characteristics. Firstly, the effects of varying laser fluence on the grating structure are researched. As the laser fluence increases, the depth of the groove, the width of the nanostructured region, and the width of the direct writing etching region all show an increasing trend. Secondly, the influence of different laser fluences on thermal radiation is studied. When the laser fluence is 1.91 J/cm^2 and the period is 10 um, the peak of thermal radiation enhancement appears near the wavenumber of 900 cm^{-1}. Its intensity increases initially and then decreases with the increase of laser fluence. Additionally, the influence of different periods on thermal radiation is explored. It is observed that the positions of enhanced peaks vary with different periods. When the grating period is too large, the effect is not evident. Finally, the impact of various heating temperatures on thermal radiation is also researched. Heating temperature is a significant factor affecting the intensity of thermal radiation. First, the positions of the enhancement peaks remain constant despite temperature changes. Second, the thermal radiation at all wavenumbers increases with the increasing temperature. Third, the relative weighting given to different wavenumbers changes with temperature increase.

The results demonstrate that controlling thermal radiation can be realized by processing periodic structures on the material. In recent years, with the continuous progress of science and technology, various fields have increasingly demanded specific thermal radiation characteristics. The desired thermal radiation characteristics can be attained by fabricating a grating structure on the material's surface. This approach can find wide applications in the aerospace field, including in infrared remote sensing, infrared detection, and infrared guidance. Moreover, it can be utilized in infrared switches, medical care,

remote controls, infrared interfaces, and anti-theft devices, benefiting different aspects of human production and daily life.

Author Contributions: Conceptualization, H.S.; methodology, R.G.; validation, P.Z.; formal analysis, W.Z., H.S.; investigation, R.G.; resources, R.G. and W.Z.; data curation, R.G. and W.Z.; writing—original draft preparation, R.G. and P.Z.; writing—review and editing, R.G. and P.Z.; supervision, H.S.; funding acquisition, S.L. All authors have read and agreed to the published version of the manuscript.

Funding: Prof. Liu gratefully acknowledges support from the National Natural Science Foundation of China (Grant No. 51875006).

Institutional Review Board Statement: Not applicable.

Informed Consent Statement: Not applicable.

Data Availability Statement: Data can be made available upon request from the authors.

Acknowledgments: Ruxue Guo thanks Yanjie Zhang and Song Liu for the help in the theoretical analysis and experiments discussions.

Conflicts of Interest: The authors declare no conflicts of interest.

Appendix A

When a beam of visible or infrared light is incident on an interface, the free electron density on the metal surface causes a collective oscillation due to the coupling effect of the incident electromagnetic wave. Surface plasmon polaritons (SPPs), generated by this interaction, are excited by electromagnetic waves and display electromagnetic characteristics. Consequently, SPPs obey the basic electromagnetic field equations, i.e., Maxwell's equations. The dispersion properties of surface plasmon polaritons are derived from Maxwell's equations.

The differential form of Maxwell's equations is

$$\begin{cases} \nabla \times \vec{H} = \sigma \vec{E} + \varepsilon_0 \varepsilon \frac{\partial \vec{E}}{\partial t} \\ \nabla \times \vec{E} = -\mu_0 \frac{\partial \vec{H}}{\partial t} \\ \nabla \cdot \vec{H} = 0 \\ \nabla \cdot \vec{E} = \rho \end{cases} \tag{A1}$$

Here, E represents the electric field, H represents the magnetic field, ε is the dielectric constant of the medium, σ is the conductivity of the medium, μ_0 is the permeability of the medium, and ρ is the bulk charge density of the medium. The first two terms of the Equation (A1) are taken curl respectively, and if the infinite homogeneous medium $\sigma = 0$, the equation is simplified as follows:

$$\begin{cases} \nabla^2 \vec{E} - \mu_0 \varepsilon \varepsilon_0 \frac{\partial^2 \vec{E}}{\partial t^2} = 0 \\ \nabla^2 \vec{H} - \mu_0 \varepsilon \varepsilon_0 \frac{\partial^2 \vec{H}}{\partial t^2} = 0 \end{cases} \tag{A2}$$

When the field changes harmonically with time, the Helmholtz equation can be obtained from Equation (A2):

$$\begin{cases} \nabla^2 \vec{E} + k_0^2 \varepsilon_r \vec{E} = 0 \\ \nabla^2 \vec{B} + k_0^2 \varepsilon_r \vec{B} = 0 \end{cases} \tag{A3}$$

where $k_0 = \sqrt{\varepsilon_0 \mu_0}\omega$, $\varepsilon_r = \left(\varepsilon + i\frac{\sigma}{\omega \varepsilon_0}\right)$ is the complex dielectric function of the material. Suppose that the electric field propagating along the x direction is $\vec{E} = E(z)e^{-i\beta x}$, and β is

the wave vector propagating along the x direction. Substituting it into Equation (A3), we can obtain the following:

$$\frac{\partial^2 E(z)}{\partial z^2} + \left(k_0^2\varepsilon - \beta^2\right)\vec{E} = 0 \tag{A4}$$

Suppose the electric field $\vec{E} = \left(E_x + E_y + E_z\right)e^{-i\omega t}$, the magnetic field $\vec{H} = \left(H_x + H_y + H_z\right)e^{-i\omega t}$, and substitute into Equation (A4), after simplification, two sets of solutions of TM mode and TE mode can be obtained, which are represented by the following equations, respectively:

$$\begin{cases} E_x = -i\frac{1}{\omega\varepsilon\varepsilon_0}\frac{\partial H_y}{\partial z} \\ E_z = -i\frac{\beta}{\omega\varepsilon\varepsilon_0}H_y \\ \frac{\partial^2 H_y}{\partial z^2} + \left(k_0^2\varepsilon - \beta^2\right)H_y = 0 \end{cases} \tag{A5}$$

$$\begin{cases} H_x = i\frac{1}{\omega\mu}\frac{\partial E_y}{\partial z} \\ H_z = \frac{\beta}{\omega\mu}E_y \\ \frac{\partial^2 E_y}{\partial z^2} + \left(k_0^2\varepsilon - \beta^2\right)E_y = 0 \end{cases} \tag{A6}$$

When $z > 0$, the electric field wave vector is k_1 and the dielectric constant is ε_1; when $z < 0$, the electric field wave vector is k_2, the dielectric constant is ε_2, and the boundary condition is

$$\frac{k_2}{k_1} = -\frac{\varepsilon_2}{\varepsilon_1} \tag{A7}$$

It can be seen from the above formula that the existence of surface waves requires the real part of the dielectric function at both ends of the interface to be different. Equations can be obtained from (A7):

$$\begin{cases} k_1^2 = \beta^2 - k_0^2\varepsilon_1 \\ k_2^2 = \beta^2 - k_0^2\varepsilon_2 \end{cases} \tag{A8}$$

Substituting the boundary conditions into the equation set (A8), the dispersion relation of SPPs can be obtained as follows:

$$k_{spp} = \beta = k_0\sqrt{\frac{\varepsilon_1\varepsilon_2}{\varepsilon_1 + \varepsilon_2}} \tag{A9}$$

Similarly, for the TE mode, we can obtain

$$E_y(k_{z1} + k_{z2}) = 0 \tag{A10}$$

Since both k_{z1} and k_{z2} are positive, the equation is satisfied only when $E_{y1} = E_{y2} = 0$. Consequently, there are no surface plasmon polaritons associated with TE polarization; that is, SPPs can only exist in the context of TM polarization.

References

1. Modest, M.F.; Mazumder, S. *Radiative Heat Transfer*; Academic Press: Cambridge, MA, USA, 2021.
2. Gray, W.A.; Müller, R. *Engineering Calculations in Radiative Heat Transfer: International Series on Materials Science and Technology*; Elsevier: Amsterdam, The Netherlands, 2013; Volume 13.
3. Li, W.; Fan, S.H. Nanophotonic control of thermal radiation for energy applications [Invited]. *Opt. Express* **2018**, *26*, 15995–16021. [CrossRef] [PubMed]
4. Coutts, T.J. An overview of thermophotovoltaic generation of electricity. *Sol. Energy Mater. Sol. Cells* **2001**, *66*, 443–452. [CrossRef]
5. Inoue, T.; De Zoysa, M.; Asano, T.; Noda, S. Realization of dynamic thermal emission control. *Nat. Mater.* **2014**, *13*, 928–931. [CrossRef] [PubMed]
6. Zhang, X.S.; Chen, Y.J.; Hu, J.L. Recent advances in the development of aerospace materials. *Prog. Aerosp. Sci.* **2018**, *97*, 22–34. [CrossRef]
7. Tian, J.L.; Zhang, W.; Gu, J.J.; Deng, T.; Zhang, D. Bioinspired Au-CuS coupled photothermal materials: Enhanced infrared absorption and photothermal conversion from butterfly wings. *Nano Energy* **2015**, *17*, 52–62. [CrossRef]

8. Lenert, A.; Bierman, D.M.; Nam, Y.; Chan, W.R.; Celanovic, I.; Soljacic, M.; Wang, E.N. A nanophotonic solar thermophotovoltaic device. *Nat. Nanotechnol.* **2014**, *9*, 126–130. [CrossRef]
9. Zhao, B.; Santhanam, P.; Chen, K.F.; Buddhiraju, S.; Fan, S.H. Near-Field Thermophotonic Systems for Low-Grade Waste-Heat Recovery. *Nano Lett.* **2018**, *18*, 5224–5230. [CrossRef] [PubMed]
10. Wang, Z.L.; Zhang, Z.M.; Quan, X.J.; Cheng, P. A perfect absorber design using a natural hyperbolic material for harvesting solar energy. *Sol. Energy* **2018**, *159*, 329–336. [CrossRef]
11. Molesky, S.; Jacob, Z. Ideal near-field thermophotovoltaic cells. *Phys. Rev. B* **2015**, *91*, 205435. [CrossRef]
12. Navarro-Baena, I.; Jacobo-Martín, A.; Hernández, J.J.; Smirnov, J.R.C.; Viela, F.; Monclús, M.A.; Osorio, M.R.; Molina-Aldareguia, J.M.; Rodríguez, I. Single-imprint moth-eye anti-reflective and self-cleaning film with enhanced resistance. *Nanoscale* **2018**, *10*, 15496–15504. [CrossRef] [PubMed]
13. Huang, Z.J.; Shi, X.Y.; Wang, G.; Leukkunen, P.; Huttula, M.; Cao, W. Antireflective design of Si-based photovoltaics via biomimicking structures on black butterfly scales. *Solar Energy* **2020**, *204*, 738–747. [CrossRef]
14. Liu, Y.; Song, Y.Y.; Niu, S.C.; Zhang, Y.L.; Han, Z.W.; Ren, L.Q. Integrated super-hydrophobic and antireflective PDMS bio-templated from nano-conical structures of cicada wings. *RSC Adv.* **2016**, *6*, 108974–108980. [CrossRef]
15. Fan, S.H. Thermal Photonics and Energy Applications. *Joule* **2017**, *1*, 264–273. [CrossRef]
16. Liu, S.; Song, H.Y.; Wang, S.N.; Du, B.R.; Wang, B.; Emara, E.M.; Liu, S.B. Surface micro-nano hydrophobic structuring on silver-coated semiconductor substrate by femtosecond laser irradiation. *J. Laser Appl.* **2022**, *34*, 012019. [CrossRef]
17. Zhang, Z.Y.; Gu, Q.M.; Jiang, W.; Zhu, H.; Xu, K.; Ren, Y.P.; Xu, C. Achieving of bionic super-hydrophobicity by electrodepositing nano-Ni-pyramids on the picosecond laser-ablated micro-Cu-cone surface. *Surf. Coat. Technol.* **2019**, *363*, 170–178. [CrossRef]
18. Yang, G.F.; Zhang, H.; Li, H.W.; Lu, M.K.; Zhai, W.; Cui, J. Experimental study on the ice suppression characteristics of TC4 microstructure surface induced by femtosecond pulsed laser. *Surf. Coat. Technol.* **2021**, *405*, 126558. [CrossRef]
19. Langevin, D.; Verlhac, C.; Jaeck, J.; Abou-Hamdan, L.; Taupeau, E.; Fix, B.; Bardou, N.; Dupuis, C.; De Wilde, Y.; Haidar, R.; et al. Experimental Investigation of the Thermal Emission Cross Section of Nanoresonators Using Hierarchical Poisson-Disk Distributions. *Phys. Rev. Lett.* **2024**, *132*, 043801. [CrossRef] [PubMed]
20. De Zoysa, M.; Asano, T.; Mochizuki, K.; Oskooi, A.; Inoue, T.; Noda, S. Conversion of broadband to narrowband thermal emission through energy recycling. *Nat. Photonics* **2012**, *6*, 535–539. [CrossRef]
21. Ma, X.R.; Du, B.R.; Tan, S.W.; Song, H.Y.; Liu, S.B. Spectral Characteristics Simulation of Topological Micro-Nano Structures Based on Finite Difference Time Domain Method. *Nanomaterials* **2021**, *11*, 2622. [CrossRef] [PubMed]
22. Guo, X.J.; Song, H.Y.; Du, B.R.; Tan, S.W.; Liu, S.B. Study on Spectral Selective Manipulation Characteristics of Surface Multilevel Micro-Nano Structures by FDTD Simulation. *Int. J. Mol. Sci.* **2022**, *23*, 2774. [CrossRef] [PubMed]
23. Arpin, K.A.; Losego, M.D.; Cloud, A.N.; Ning, H.L.; Mallek, J.; Sergeant, N.P.; Zhu, L.X.; Yu, Z.F.; Kalanyan, B.; Parsons, G.N.; et al. Three-dimensional self-assembled photonic crystals with high temperature stability for thermal emission modification. *Nat. Commun.* **2013**, *4*, 2630. [CrossRef]
24. Chan, D.L.C.; Soljacic, M.; Joannopoulos, J.D. Thermal emission and design in 2D-periodic metallic photonic crystal slabs. *Opt. Express* **2006**, *14*, 8785–8796. [CrossRef] [PubMed]
25. Yokoyama, T.; Dao, T.D.; Chen, K.; Ishii, S.; Sugavaneshwar, R.P.; Kitajima, M.; Nagao, T. Spectrally Selective Mid-Infrared Thermal Emission from Molybdenum Plasmonic Metamaterial Operated up to 1000 °C. *Adv. Opt. Mater.* **2016**, *4*, 1987–1992. [CrossRef]
26. Coppens, Z.J.; Valentine, J.G. Spatial and Temporal Modulation of Thermal Emission. *Adv. Mater.* **2017**, *29*, 1701275. [CrossRef] [PubMed]
27. Jin, W.L.; Polimeridis, A.G.; Rodriguez, A.W. Temperature control of thermal radiation from composite bodies. *Phys. Rev. B* **2016**, *93*, 121403. [CrossRef]
28. Liu, B.A.; Gong, W.; Yu, B.W.; Li, P.F.; Shen, S. Perfect Thermal Emission by Nanoscale Transmission Line Resonators. *Nano Lett.* **2017**, *17*, 666–672. [CrossRef]
29. Li, J. Thermal Radiation from Nanophotonic Structures: Theory, Numerical Simulation and Applications. Ph.D. Thesis, Carnegie Mellon University, Pittsburgh, PA, USA, 2020. Available online: https://www.proquest.com/dissertations-theses/thermal-radiation-nanophotonic-structures-theory/docview/2457933729/se-2 (accessed on 15 August 2024).
30. Yu, H.Y.; Zhang, H.C.; Wang, H.M.; Zhang, D. The Equivalent Thermal Conductivity of the Micro/Nano Scaled Periodic Cubic Frame Silver and Its Thermal Radiation Mechanism Analysis. *Energies* **2021**, *14*, 4158. [CrossRef]
31. Bikbaev, R.G.; Vetrov, S.Y.; Timofeev, I.V. Hybrid Tamm and surface plasmon polaritons in resonant photonic structure. *J. Quant. Spectrosc. Radiat. Transf.* **2020**, *253*, 107156. [CrossRef]
32. Ge, C.X.; Wu, Z.S.; Bai, J.; Gong, L. Effect of nanoscale roughness on optical trapping properties of surface plasmon polaritons exerted on nanoparticle. *J. Quant. Spectrosc. Radiat. Transf.* **2018**, *219*, 339–349. [CrossRef]
33. Wang, Q.; Yuan, G.H.; Kiang, K.S.; Sun, K.; Gholipour, B.; Rogers, E.T.F.; Huang, K.; Ang, S.S.; Zheludev, N.I.; Teng, J.H. Reconfigurable phase-change photomask for grayscale photolithography. *Appl. Phys. Lett.* **2017**, *110*, 201110. [CrossRef]
34. Sai, H.; Yugami, H. Thermophotovoltaic generation with selective radiators based on tungsten surface gratings. *Appl. Phys. Lett.* **2004**, *85*, 3399–3401. [CrossRef]
35. Sai, H.; Yugami, H.; Kanamori, Y.; Hane, K. Spectrally selective thermal radiators and absorbers with periodic microstructured surface for high-temperature applications. *Microscale Thermophys. Eng.* **2003**, *7*, 101–115. [CrossRef]

36. Mason, J.A.; Adams, D.C.; Johnson, Z.; Smith, S.; Davis, A.W.; Wasserman, D. Selective thermal emission from patterned steel. *Opt. Express* **2010**, *18*, 25192–25198. [CrossRef] [PubMed]
37. Mason, J.A. Selective Thermal Emission and Absorption from Mid-IR Resonators and Metamaterials. Ph.D. Thesis, University of Massachusetts Lowell, Lowell, MA, USA, 2012. Available online: https://www.proquest.com/dissertations-theses/selective-thermal-emission-absorption-mid-ir/docview/1020571465/se-2 (accessed on 15 August 2024).
38. Jiao, S.H.; Zhao, K.; Jiang, J.H.; Zhao, K.L.; Guo, Q.; Wang, J.B.; Zhang, Y.S.; Chen, G.; Cheng, Q.; Zuo, P.; et al. Metasurface with all-optical tunability for spatially-resolved and multilevel thermal radiation. *Nanophotonics* **2024**, *13*, 1645–1655. [CrossRef]
39. Shirk, M.D.; Molian, P.A. A review of ultrashort pulsed laser ablation of materials. *J. Laser Appl.* **1998**, *10*, 18–28. [CrossRef]
40. Bragheri, F.; Paiè, P.; Vázquez, R.M. Editorial for the Special Issue on New Trends and Applications in Femtosecond Laser Micromachining. *Micromachines* **2022**, *13*, 150. [CrossRef] [PubMed]
41. Butkute, A.; Jonusauskas, L. 3D Manufacturing of Glass Microstructures Using Femtosecond Laser. *Micromachines* **2021**, *12*, 499. [CrossRef]
42. He, J.; Xu, B.J.; Xu, X.Z.; Liao, C.R.; Wang, Y.P. Review of Femtosecond-Laser-Inscribed Fiber Bragg Gratings: Fabrication Technologies and Sensing Applications. *Photonic Sens.* **2021**, *11*, 203–226. [CrossRef]
43. Yan, M.F.; Li, R.; Li, M.; Liu, S.J.; Zhou, G.; Lin, C.G.; Dai, S.X.; Song, B.N.; Zhang, W.; Xu, T.F.; et al. Fabrication of multi-focal chalcogenide glass microlens arrays based on femtosecond laser-assisted chemical etching method. *Opt. Laser Technol.* **2024**, *174*, 110601. [CrossRef]
44. Yao, H.; Pugliese, D.; Lancry, M.; Dai, Y. Ultrafast Laser Direct Writing Nanogratings and their Engineering in Transparent Materials. *Laser Photon. Rev.* **2024**, 2300891. [CrossRef]
45. Li, Q.S.; Shi, H.S.; Xi, S.M.; Xu, Z.H.; Zhang, L.; Liu, Y. Femtosecond-Laser Direct-Writing Hydrogel-Based Microlens Arrays Customized with Multi-Dimensional Optical Configurations for Information Encryption. *Adv. Mater. Technol.* **2024**, *9*, 2301923. [CrossRef]
46. Gupta, M.S.; Ameen, E.; Veeraragavan, A.; Pesala, B. Design and fabrication of grating-based filters for micro-thermophotovoltaic systems. In Proceedings of the 7th International Conference on Advances in Energy Research, Mumbai, India, 10–12 December 2019; Springer: Singapore, 2021; pp. 1113–1119. [CrossRef]
47. Kang, Q.; Guo, K.; Zhang, X.; Wang, W.; Guo, Z. Dynamically manipulating long-wave infrared polarized thermal radiation by a vanadium dioxide metasurface. *Opt. Lett.* **2024**, *49*, 2485–2488. [CrossRef] [PubMed]
48. Chu, Q.Q.; Zhong, F.; Shang, X.H.; Zhang, Y.; Zhu, S.N.; Liu, H. Controlling thermal emission with metasurfaces and its applications. *Nanophotonics* **2024**, *13*, 1279–1301. [CrossRef]
49. Lin, C.J.; Li, Y.; Chi, C.; Kwon, Y.S.; Huang, J.Y.; Wu, Z.X.; Zheng, J.Z.; Liu, G.Z.; Tso, C.Y.; Chao, C.Y.H.; et al. A Solution-Processed Inorganic Emitter with High Spectral Selectivity for Efficient Subambient Radiative Cooling in Hot Humid Climates. *Adv. Mater.* **2022**, *34*, 2109350. [CrossRef] [PubMed]
50. Abbas, M.A.; Kim, J.; Rana, A.S.; Kim, I.; Rehman, B.; Ahmad, Z.; Massoud, Y.; Seong, J.; Badloe, T.; Park, K.; et al. Nanostructured chromium-based broadband absorbers and emitters to realize thermally stable solar thermophotovoltaic systems. *Nanoscale* **2022**, *14*, 6425–6436. [CrossRef] [PubMed]
51. Zhang, J.G.; Wen, Z.J.; Zhou, Z.J.; Zhou, D.J.; Qiu, Q.L.; Ge, J.; Zeng, Y.X.; Sun, Y.; Zhou, L.; Dai, N.; et al. Long-wavelength infrared selective emitter for thermal infrared camouflage under a hot environment. *Opt. Express* **2022**, *30*, 24132–24144. [CrossRef] [PubMed]
52. Seo, M.; Wang, K.; Echols, J.R.; Winfrey, A.L. Microstructure deformation and near-pore environment of resolidified tungsten in high heat flux conditions. *J. Nucl. Mater.* **2022**, *565*, 153725. [CrossRef]
53. Morcos, P.; Elwany, A.; Karaman, I.; Arróyave, R. Review: Additive manufacturing of pure tungsten and tungsten-based alloys. *J. Mater. Sci.* **2022**, *57*, 9769–9806. [CrossRef]
54. Liu, X.L.; Tyler, T.; Starr, T.; Starr, A.F.; Jokerst, N.M.; Padilla, W.J. Taming the Blackbody with Infrared Metamaterials as Selective Thermal Emitters. *Phys. Rev. Lett.* **2011**, *107*, 045901. [CrossRef] [PubMed]
55. Zhong, F.; Ding, K.; Zhang, Y.; Zhu, S.; Chan, C.T.; Liu, H. Angle-Resolved Thermal Emission Spectroscopy Characterization of Non-Hermitian Metacrystals. *Phys. Rev. Appl.* **2020**, *13*, 014071. [CrossRef]
56. Yang, Y.; Yang, J.; Liang, C.; Wang, H.; Zhu, X.; Kuang, D.; Yang, Y. Sub-wavelength surface structuring of NiTi alloy by femtosecond laser pulses. *Appl. Phys. A* **2008**, *92*, 635–642. [CrossRef]
57. Yao, J.; Zhang, C.; Liu, H.; Dai, Q.; Wu, L.; Lan, S.; Gopal, A.V.; Trofimov, V.A.; Lysak, T.M. Selective appearance of several laser-induced periodic surface structure patterns on a metal surface using structural colors produced by femtosecond laser pulses. *Appl. Surf. Sci.* **2012**, *258*, 7625–7632. [CrossRef]
58. Vorobyev, A.; Guo, C. Spectral and polarization responses of femtosecond laser-induced periodic surface structures on metals. *J. Appl. Phys.* **2008**, *103*, 043513. [CrossRef]
59. Gu, H.; Dai, Y.; Wang, H.; Yan, X.; Ma, G. Effect of scanning velocity on femtosecond laser-induced periodic surface structures on HgCdTe crystal. *Appl. Surf. Sci.* **2017**, *425*, 307–313. [CrossRef]
60. Robledo-Taboada, L.H.; Jiménez-Jarquín, J.F.; Flores-Castañeda, M.; Méndez-Blas, A.; Barranco-Cisneros, J.; Camacho-López, S. Single-step femtosecond laser-induced formation of coexisting microstructures in silicon. *Bull. Mater. Sci.* **2023**, *46*, 92. [CrossRef]
61. Dmytruk, A.; Dmitruk, I.; Berezovska, N.; Karlash, A.; Kadan, V.; Blonskyi, I. Emission from silicon as a real-time figure of merit for laser-induced periodic surface structure formation. *J. Phys. D Appl. Phys.* **2021**, *54*, 265102. [CrossRef]

62. Wang, Y.; Segawa, S.; Shimizu, T.; Ota, M.; Agulto, V.C.; Mag-Usara, V.K.; Miyamoto, K.; Omatsu, T.; Makino, K.; Tominaga, J. Laser-Induced Periodic Surface Structures on $Ge_2Sb_2Te_5$ Irradiated by Terahertz Free-Electron Laser Vortex Beam. In Proceedings of the 2022 47th International Conference on Infrared, Millimeter and Terahertz Waves (IRMMW-THz), Delft, The Netherlands, 28 August–2 September 2022; pp. 1–2. [CrossRef]
63. Vorobyev, A.; Guo, C. Femtosecond laser-induced periodic surface structure formation on tungsten. *J. Appl. Phys.* **2008**, *104*, 063523. [CrossRef]
64. Huang, M.; Zhao, F.; Cheng, Y.; Xu, N.; Xu, Z. Origin of laser-induced near-subwavelength ripples: Interference between surface plasmons and incident laser. *ACS Nano* **2009**, *3*, 4062–4070. [CrossRef] [PubMed]
65. Borowiec, A.; Haugen, H. Subwavelength ripple formation on the surfaces of compound semiconductors irradiated with femtosecond laser pulses. *Appl. Phys. Lett.* **2003**, *82*, 4462–4464. [CrossRef]
66. Wang, B.; Wang, Y.; Song, H.; Lam, Y.C.; Shaymaa, E.M.; Liu, S. Threshold effect on the femtosecond laser-induced periodic subwavelength structure: An analytical approach. *Opt. Laser Technol.* **2023**, *158*, 108804. [CrossRef]

Disclaimer/Publisher's Note: The statements, opinions and data contained in all publications are solely those of the individual author(s) and contributor(s) and not of MDPI and/or the editor(s). MDPI and/or the editor(s) disclaim responsibility for any injury to people or property resulting from any ideas, methods, instructions or products referred to in the content.

coatings

MDPI

Article

Laser Cladding of a Ti–Zr–Mo–Ta–Nb–B Composite Coating on Ti60 Alloy to Improve Wear Resistance

Kaijin Huang [1,2,*] and Xianchao Han [1]

[1] State Key Laboratory of Materials Processing and Die & Mould Technology, Huazhong University of Science and Technology, Wuhan 430074, China; m202171092@hust.edu.cn
[2] Key Laboratory of Laser Technology and Optoelectronic Functional Materials of Hainan Province, Hainan Normal University, Haikou 571158, China
* Correspondence: huangkaijin@hust.edu.cn; Tel.: +86-027-87543676

Abstract: To improve the wear resistance of the Ti60 alloy, laser cladding was used to obtain a composite coating containing a high-entropy $(Ti_{0.2}Zr_{0.2}Mo_{0.2}Ta_{0.2}Nb_{0.2})B_2$ boride phase, with Ti, Zr, Mo, Ta, Nb, and B powders as the raw materials. The microstructure and wear characteristics of the coating were studied using XRD, SEM, EDS, and the pin-on-disc friction wear technique. The results show that the coating mainly consists of six phases: $(Ti_{0.2}Zr_{0.2}Mo_{0.2}Ta_{0.2}Nb_{0.2})B_2$, ZrB_2, TiB, TiZr, $Ti_{1.83}$ $Zr_{0.17}$, and $Ti_{0.67}Zr_{0.67}Nb_{0.67}$. The average microhardness of the coating was 1062.9 $HV_{0.1}$ due to the occurrence of the high-entropy, high-hardness $(Ti_{0.2}Zr_{0.2}Mo_{0.2}Ta_{0.2}Nb_{0.2})B_2$ boride phase, which was about 2.9 times that of the Ti60 alloy substrate. The coating significantly improved the wear resistance of the Ti60 alloy substrate, and the mass wear rate was about 1/11 that of the Ti60 alloy substrate. The main types of wear affecting the coating were abrasive, adhesive, and oxidation wear, while the main wear affecting the Ti60 alloy matrix was abrasive wear, accompanied by a small amount of adhesive and oxidation wear.

Keywords: laser cladding; Ti60 alloy; high-entropy boride; wear resistance

1. Introduction

Ti60 titanium alloy is a nearly α-type high-temperature titanium alloy that can be employed for long-term service even at a temperature of 600 °C. As an important material used in aero-engine blades and compressors, it needs to withstand complex loads and high-friction and -wear conditions. For example, fretting wear will occur between the root of the rotor blade and the disc mortise due to the centrifugal force caused by the rotor blade rotating at high speeds or when the engine becomes overexcited. Due to vibrations, thermal expansion, and other factors during high-speed rotations, the blade tip will accidentally scrape the sealing coating on the inner wall of the casing, resulting in adhesive and abrasive wear. When the engine is used in an environment with desert dust or volcanic ash suspended at high altitudes, the hard particles in the air will impact the high-speed rotating blades, resulting in erosion wear. This highlights that the Ti60 titanium alloy also has some shortcomings, such as a low hardness (340 HV) [1] and insufficient friction and wear resistance; however, currently, no relevant studies have attempted to improve the wear resistance of Ti60 alloy.

However, many studies have reported the use of laser cladding technology to improve the wear resistance of other types of titanium alloys. For instance, Di et al. [2] prepared a high-entropy alloy coating of AlCoCrFeMoVTi on the surface of a TC4 titanium alloy via laser cladding technology. The experimental results show that the highest microhardness of the coating $HV_{0.2}$ was 10,990 MPa, which was 3.29 times that of the substrate, and the wear volume of the coating was only 12.01% that of the substrate. Qin et al. [3] used laser cladding technology to prepare a NiCrCoAlY-Cr_3C_2 composite coating on the surface of a TC4 titanium alloy. The results show that the highest microhardness of the composite

coating was 1344 HV, which was about 3.8 times that of the substrate (350 HV), and the wear loss of the coating was 24% that of the substrate. Jiang et al. [4] prepared a WC-Co composite coating using laser cladding to significantly improve the wear resistance of a TC4 substrate, making the maximum microhardness of the coating as high as 1536 $HV_{0.5}$ and the wear rate as high as 1.5 g/h. Huang et al. [5] used laser cladding technology to prepare a Ti_5Si_3/Ti_3Al composite coating on a TA2 titanium alloy. The average microhardness of the coating was about 668 $HV_{0.1}$, which was 3.34 times that of the matrix, and the mass wear rate of the coating was 1/5.79 that of the matrix. Yu et al. [6] used a semiconductor laser to laser clad a Ti-Ni-Si_3N_4-ZrO_2 mixed powder onto the surface of a TA15 alloy to prepare a $ZrO_2/Ti_5Si_3/TiN/Ti_2N$ composite coating. The results show that the microhardness of the composite coating was 835–1050 HV, which was about three times that of the substrate. Under dry sliding friction and wear, the wear of the coating was about 1/6 that of the substrate. Feng et al. [7] used laser cladding technology to prepare a TiB-TiC co-reinforced TiNi-Ti_2Ni intermetallic compound composite coating on the surface of a TA15 titanium alloy, with a Ti-Ni-B_4C powder mixture as the raw material. The highest microhardness value of the coating was about 700 HV, which was about 2.07 times that of the matrix (340 HV), and the wear quality of the coating was only 0.47% of the matrix. Chen et al. [8] used laser cladding technology to clad TiN powder onto the surface of a TC9 titanium alloy to prepare a TiN coating. The results showed that the wear of the TiN coating under 10 kg and 30 kg loads was about 1/100 and 1/30 of the matrix, respectively, which indicates that the wear resistance of the coating greatly improved. Hu et al. [9] used a YAG laser to laser clad a Ti-based Cr_2C_3 alloy powder onto the surface of a Ti600 alloy to prepare a functional gradient coating, with TiC as the enhanced phase, making the average friction coefficient and wear rate of the coating only 0.3–0.5 times that of the Ti600 matrix, indicating that the wear resistance of the coating significantly improved. Cheng et al. [10] used laser cladding technology to prepare a NiCr/TiAl coating on the surface of a Ti600 titanium alloy. Their experimental results showed that the average microhardness of the coating was 832 HV, and the wear rate of the coating at room temperature was 27% that of the substrate.

In short, the current research on improving the wear resistance of titanium alloys mainly focuses on the preparation of metal–alloy composite coatings and ceramic coatings using laser cladding technology, while few studies have been conducted on the preparation of high-entropy boride coatings using laser cladding technology [11]. However, high-entropy borides have attracted much attention due to their comprehensive properties, such as their high melting point, excellent mechanical properties, and high thermal stability. For example, high-entropy diborides are considered candidate materials for components such as the leading edge of supersonic aircraft and metal-melting crucibles [12,13]. Since 2015, high-entropy boride ceramics dominated by high-entropy diborides have been widely studied [14–17]. According to the mixing rule, the theoretical hardness of high-entropy ceramic materials should be the sum of that of the single-phase materials of each component, but the actual values are often higher, particularly in high-entropy boride ceramics [18]. For example, Gild et al. [14] reported that the hardnesses of the ceramic blocks for six high-entropy borides—$(Ti_{0.2}Zr_{0.2}Nb_{0.2}Ta_{0.2}Hf_{0.2})B_2$, $(Ti_{0.2}Zr_{0.2}Hf_{0.2}Ta_{0.2}Mo_{0.2})B_2$, $(Ti_{0.2}Zr_{0.2}Nb_{0.2}Hf_{0.2}Mo_{0.2})B_2$, $(Ti_{0.2}Zr_{0.2}Nb_{0.2}Ta_{0.2}Cr_{0.2})B_2$, $(Ti_{0.2}Zr_{0.2}Nb_{0.2}Ta_{0.2}Mo_{0.2})B_2$, and $(Ti_{0.2}Hf_{0.2}Nb_{0.2}Ta_{0.2}Mo_{0.2})B_2$—were higher than those obtained using the mixing rule at 17.5 GPa, 19.1 GPa, 21.9 GPa, 19.9 GPa/23.7 GPa, and 22.5 GPa, respectively.

In view of the abovementioned excellent hardness properties of high-entropy borides, laser cladding was used in this study to obtain a composite coating containing the high-entropy $(Ti_{0.2}Zr_{0.2}Mo_{0.2}Ta_{0.2}Nb_{0.2})B_2$ boride phase on a Ti60 alloy with the Ti, Zr, Mo, Ta, Nb, and B powders as the raw materials. The microstructure and dry sliding friction and wear behavior of the coating were studied to provide a basis for the application of Ti60 alloy in wear-resistant environments.

2. Materials and Methods

Ti60 alloy, with a size of 100 mm × 50 mm × 5 mm, was used, and its composition is shown in Table 1. The base material samples were ultrasonically cleaned using acetone, ethanol, and deionized water, in that order, and then dried in an electric temperature air-drying oven at 60 °C for 8 h. Ti, Zr, Mo, Ta, and Nb metal powders with purities of 99.9 wt.% and B metal powder with a purity of 99.99 wt.% were evenly mixed in a grinding machine, and then the mixed powder was pre-coated onto the surface of the Ti60 alloy with a 4 wt.% PVA solution as the binder. The powder layer thickness was preset to about 1.5 mm. The proportions of the different elements in the mixed powder are shown in Table 2.

Table 1. Chemical composition of the main components in the Ti60 alloy.

Element	Al	Sn	Zr	Mo	Nb	Ta	Si	C	Ti
Wt.%	5.0–6.3	3.0–5.0	2.5–7.0	0.2–1.5	0.2–1.0	0.2–3.0	0.2–0.55	0.01–0.09	Bal.

Table 2. The proportion of different elements in the mixed powder.

Element	Ti	Zr	Mo	Ta	Nb	B
Wt.%	7.76	14.80	15.49	29.35	15.07	17.53

Laser cladding was carried out on a Rayco RFL-C6000 fiber laser cladding system (Wuhan Rayco Fiber Laser Technology Co., LTD., Wuhan, China), and the cladding process was protected using argon gas. The laser power, spot diameter, scanning speed, laser spot overlap rate, argon purity, and argon flow rate were 2600 W, 4.5 mm, 8 mm/s, 30%, 99.99%, and 15 L/min, respectively. The laser cladding samples were cut into 9 mm × 9 mm × 5 mm pieces using the wire cutting method in preparation for XRD, SEM, and the wear test. The phase composition of the coating was analyzed using an X'Pert PRO X-ray meter (XRD) produced by PANalytical in Almelo, The Netherlands. The target material of the XRD test, starting position 2θ, ending position 2θ, step size 2θ, scanning type, and divergence slit size were Cu, 19.9999°, 89.9975°, 0.0131303°, continuous, and 0.76 mm, respectively. The morphology and composition of the coating before and after the wear test were observed using a JSM-7600F high resolution scanning electron microscope (SEM) produced by JEOL Corporation, Akishima, Japan, which was equipped with an energy spectrometer.

Before the microhardness test of the coating and matrix, the sample was polished first, and then the microhardness at the cross-section of the coating was tested using a DHV-1000 digital display Vickers microhardness tester produced by Dongguan Zhongte Precision Instrument Technology Co., LTD, Dongguan, China. The loading load and loading time of the microhardness test were 100 g and 15 s, respectively. The microhardness test was carried out from the top of the coating to the substrate, and the interval of microhardness test points was 0.15 mm. The volume ratio of the corrosion reagent used in the experiment was $HF:HNO_3:H_2O$ = 1:1:3.

Dry friction and wear tests were carried out on Ecomet300/Automet300 equipment (Buehler Company, Lake Bluff, IL, USA). A specific schematic diagram of the dry friction and wear is shown in [5]. The rotary speed, applied load, dry sliding speed, dry sliding wear time, total wear distance, and abrasive material were 200 r/min, 45 N, 0.921 m/s, 5 min, 276.3 m, and 200# SiC sandpaper, respectively. A Swiss Mettler Toledo XS105 (Mettler Toledo Company, Zurich, Switzerland) Dual Range analytical balance with an accuracy of 0.1 mg was used to weigh the wear samples before and after wear.

3. Results

3.1. Microstructure

The XRD pattern of the laser cladding coating is shown in Figure 1. Figure 1 shows that the coating mainly consisted of seven phases: $(Ti_{0.2}Zr_{0.2}Mo_{0.2}Ta_{0.2}Nb_{0.2})B_2$, ZrB_2 (JCPDS

96-151-0857), TiB (JCPDS 96-900-8947), TiZr (JCPDS 96-153-9806), $Ti_{1.83}Zr_{0.17}$ (JCPDS 96-154-1223), $Ti_{0.67}Zr_{0.67}Nb_{0.67}$ (JCPDS 96-153-7634), and TiO_2 (JCPDS 96-900-4145). The appearance of the TiO_2 phase may have been caused by oxygen being present in the air during the laser cladding process. The position of the diffraction peak in the $(Ti_{0.2}Zr_{0.2}Mo_{0.2}Ta_{0.2}Nb_{0.2})B_2$ phase was the same as that reported in [19]. During the laser cladding process, the mixed powder layer and part of the Ti60 matrix melted due to the absorption of the laser energy. Then, in the laser melt pool, the surface tension and buoyancy generated by the uneven temperature distribution promoted the formation of laser melt pool convection, so that various chemical elements in the mixed powder layer and the chemical elements of the partially melted Ti60 matrix were fully mixed. Finally, various borides and intermetallic compounds were generated following an in situ reaction. The following reactions may occur in the laser melt pool:

$$0.2Ti + 0.2Zr + 0.2Mo + 0.2Ta + 0.2Nb + 2B = (Ti_{0.2}Zr_{0.2}Mo_{0.2}Ta_{0.2}Nb_{0.2})B_2 \quad (1)$$

$$Zr + 2B = ZrB_2 \quad (2)$$

$$Ti + Zr = TiZr \quad (3)$$

$$1.83Ti + 0.17Zr = Ti_{1.83}Zr_{0.17} \quad (4)$$

$$Ti + 2B = TiB_2 \quad (5)$$

$$TiB_2 + Ti = 2TiB \quad (6)$$

$$0.67Ti + 0.67Zr + 0.67Nb = Ti_{0.67}Zr_{0.67}Nb_{0.67} \quad (7)$$

$$Ti + O_2 = TiO_2 \quad (8)$$

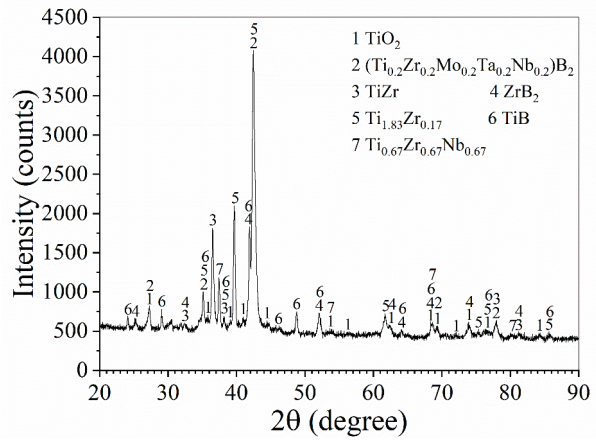


Figure 1. XRD pattern of the laser cladding coating.

Based on the strongest diffraction peak intensity of each phase, the XRD-K value method reported by Zheng et al. [20] was used in this study to calculate the semi-quantitative content of each phase in the coating. Detailed calculation formulas and methods can be found in [11]. In this study, the strongest diffraction peaks of TiO_2, $(Ti_{0.2}Zr_{0.2}Mo_{0.2}Ta_{0.2}Nb_{0.2})B_2$, ZrB_2, $Ti_{0.67}Zr_{0.67}Nb_{0.67}$, TiB, TiZr, and $Ti_{1.83}Zr_{0.17}$ were (110), (101), (101), (011), (111), (101), and (101), respectively. The corresponding reference strength values (RIR values) were 3.5, 9.6, 9.32, 17.91, 1.85, 3.5, and 7.9, respectively. According to Formula (8) in [11], the mass fraction of each phase in the coating can be calculated as 3.4%, 34.17%, 6.18%, 3.75%, 36.19%, 6.20%, and 10.11%, respectively. That is to say, TiB and $(Ti_{0.2}Zr_{0.2}\ Mo_{0.2}Ta_{0.2}Nb_{0.2})B_2$ are the two main generation phases.

The morphology of the whole laser cladding coating is shown in Figure 2, which demonstrates that the laser cladding coating was of good quality, and no obvious defects

such as pores and cracks were present in the coating. The interface between the coating and substrate was clear and well combined. The thickness of the coating was about 1.4–1.7 mm.

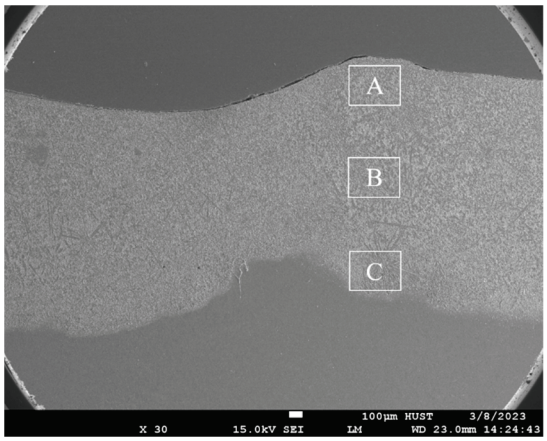


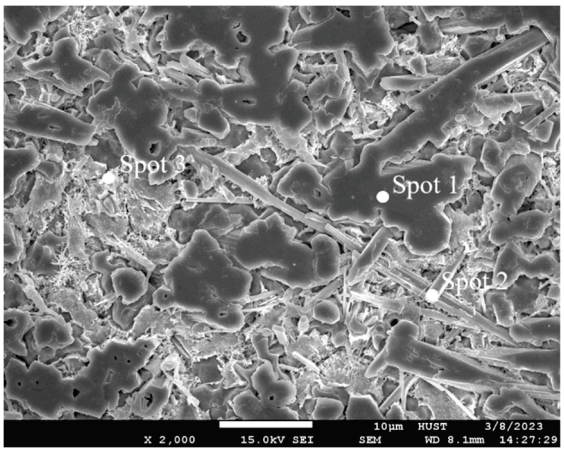
Figure 2. Morphology of a cross-section of the whole laser cladding coating. Where A represents the surface region of the coating, B represents the middle region of the coating, and C represents the interface region between the coating and substrate.

Enlarged images of the morphology of different regions in Figure 2 are shown in Figure 3, where Figure 3a–c show enlarged images of the morphology of surface region A, middle region B, and interface region C, respectively. Figure 3 shows that the morphology of the laser cladding coating mainly consists of whiskers or prisms. The reason why no significant differences were found in the morphology of different parts of the laser melt pool may be related to the homogenization of the convection mass transfer during the laser cladding process.

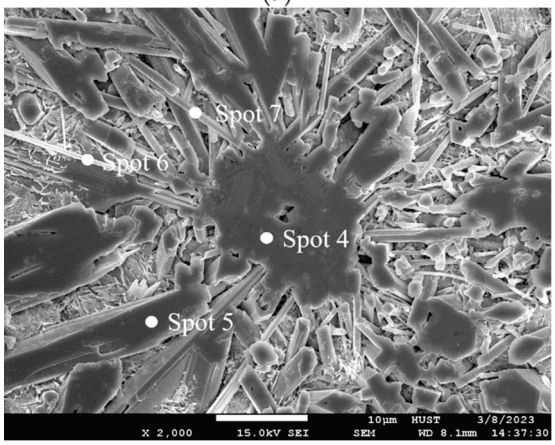
According to the EDS results in Table 3 and the XRD results in Figure 1, different phases in the laser cladding coating were roughly inferred to have formed via the following processes: firstly, via liquid solidification of the high-melting-point ZrB_2 (melting point: 3250 °C) and $(Ti_{0.2}Zr_{0.2}Mo_{0.2}Ta_{0.2}Nb_{0.2})B_2$ (melting point: 2966 °C) boride phases, and secondly, via solidification of the low-melting-point TiB (melting point: 2227 °C), TiZr, $Ti_{1.83}Zr_{0.17}$, and $Ti_{0.67}Zr_{0.67}Nb_{0.67}$ phases after a decrease in the laser pool temperature following the residual liquid phase. The specific formation mechanism was studied in detail in the next step.

Table 3. EDS results at different positions in the laser cladding coating (at.%).

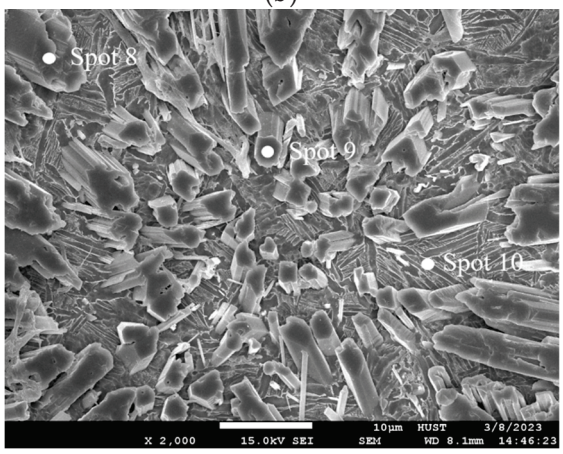
Position	Ti	Zr	Mo	Ta	Nb	B	Main Possible Phase
Spot 1	6.37	2.07	1.63	1.00	1.56	87.37	TiB + $(Ti_{0.2}Zr_{0.2}Mo_{0.2}Ta_{0.2}Nb_{0.2})B_2$
Spot 2	9.01	3.23	1.04	1.13	1.63	83.96	TiB + $(Ti_{0.2}Zr_{0.2}Mo_{0.2}Ta_{0.2}Nb_{0.2})B_2$
Spot 3	10.01	3.10	1.35	1.23	1.42	82.89	TiB + $(Ti_{0.2}Zr_{0.2}Mo_{0.2}Ta_{0.2}Nb_{0.2})B_2$
Spot 4	2.28	1.48	1.22	1.50	1.13	92.39	TiB + $(Ti_{0.2}Zr_{0.2}Mo_{0.2}Ta_{0.2}Nb_{0.2})B_2$
Spot 5	3.89	1.24	1.22	1.57	1.10	90.98	TiB + $(Ti_{0.2}Zr_{0.2}Mo_{0.2}Ta_{0.2}Nb_{0.2})B_2$
Spot 6	6.35	1.73	1.62	1.27	1.37	87.66	TiB + $(Ti_{0.2}Zr_{0.2}Mo_{0.2}Ta_{0.2}Nb_{0.2})B_2$
Spot 7	5.56	1.66	1.29	1.52	1.15	88.82	TiB + $(Ti_{0.2}Zr_{0.2}Mo_{0.2}Ta_{0.2}Nb_{0.2})B_2$
Spot 8	4.87	1.47	1.27	1.59	1.24	89.56	TiB + $(Ti_{0.2}Zr_{0.2}Mo_{0.2}Ta_{0.2}Nb_{0.2})B_2$
Spot 9	13.46	1.23	1.33	1.70	1.68	80.60	TiB + $(Ti_{0.2}Zr_{0.2}Mo_{0.2}Ta_{0.2}Nb_{0.2})B_2$
Spot 10	4.79	0.97	1.09	1.07	1.03	91.05	TiB + $(Ti_{0.2}Zr_{0.2}Mo_{0.2}Ta_{0.2}Nb_{0.2})B_2$



(**a**)



(**b**)



(**c**)

Figure 3. Enlarged images of the morphologies at different positions in Figure 2 for a cross-section of the laser cladding coating: (**a**) surface region A, (**b**) middle region B, and (**c**) interface region C.

The formation of the whisker or prismatic structure TiB in a laser cladding coating followed the following process: the B27 structure of TiB increased the growth rate in the [010] direction to be significantly faster than that in other directions, so whiskers or prismatic structures easily form [21], which can play roles in strengthening the substrate in the coating [22]. The structural morphology of TiB in Figure 3 is consistent with that reported in the literature [23,24]. In addition, because plane (001) of TiB grows the fastest and the remaining crystal faces, (100), (101), and $(10\bar{1})$, make up the sides of TiB, the sectional whiskers or prismatic structures are mostly hexagonal [22]. When the temperature drops

to room temperature, the coating will eventually form a TiB mixed structure with whiskers or prismatic structures as the main body.

3.2. Wear Resistance Properties

The microhardness change curve for a cross-section of the laser cladding coating is shown in Figure 4, which shows that the microhardness of the laser cladding coating has a gradient trend, and the microhardness can be divided into a typical three-interval step distribution. The uneven distribution of the microhardness value of the coating was caused by the uneven distribution of the phases in the coating. The microhardness value of the coating surface was the highest (1287.8 $HV_{0.1}$), with the microhardness value fluctuating slightly between 1287.8 and 1129.6 $HV_{0.1}$. At 0.64 mm, a large decrease occurs, forming the second step, with a microhardness value between 905.3 and 824.2 $HV_{0.1}$. Then, at 1.24 mm, a sharp drop characterizes the third step, with a microhardness value ranging from 420.5 to 356.6 $HV_{0.1}$. We believe that the reasons for the variation in the hardness gradient of the coating are mainly correlated with the distribution and volume fraction of the phases with different proportions and hardnesses in the coating. This problem needs to be further studied in the future. Understanding the phase composition and volume fraction of different parts of the coating requires study of the temperature, flow, and mass fields of the coating via numerical simulations, and phase diagrams and rapid solidification theory should be used in combination with these results for further clarity. At present, we can only make a rough interpretation: the surface of the coating has a higher hardness, which decreases in the middle part and even further decreases near the interface. This is because only this distribution of high hardness phases may cause a gradient change in the studied coating. The minimum microhardness of the Ti60 matrix in this study was higher than that of the Ti60 matrix (340 HV) reported in [1]. That is, the microhardness of the coating fluctuated between 824.2 and 1287.8 $HV_{0.1}$, and the average microhardness of the coating was about 1062.9 $HV_{0.1}$, while the average microhardness of the Ti60 matrix was about 366.7 $HV_{0.1}$. Thus, the average microhardness of the coating was about 2.9 times that of the Ti60 matrix. Three possible reasons can be proposed for the increase in microhardness of the laser cladding coating: First, the high-entropy boride phase and intermetallic compound phase in the coating are high-hardness phases (the hardness of $(Ti_{0.2}Zr_{0.2}Mo_{0.2}Ta_{0.2}Nb_{0.2})B_2$ is 23.7 GPa [14], the hardness of TiB is 35 GPa [25], and the hardness of ZrB_2 is 15.3 GPa [26]), and they are distributed in the coating to strengthen dispersion. Second, the coating contains a TiB phase with a nano-indentation hardness up to 35 GPa [25], and its whisker-like or prismatic structures play roles in strengthening the coating phase. Third, the laser cladding process is characterized by rapid heating and cooling, and the microstructure of the coating after laser cladding is fine, which thus results in fine crystal strengthening. In short, the increase in microhardness of the laser cladding coating will help to improve the wear resistance of the coating.

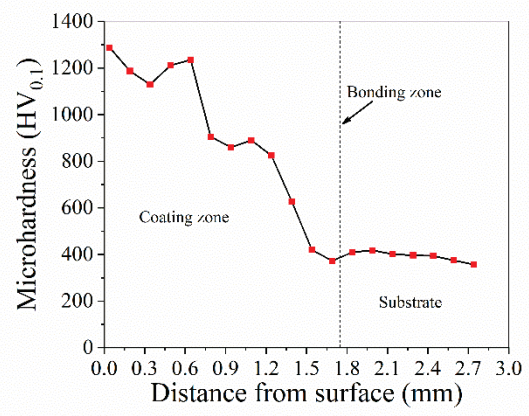


Figure 4. Microhardness curve for a cross-section of the laser coating.

A columnar comparison of the mass wear rates of the coating and Ti60 substrate under dry friction and wear conditions at room temperature is shown in Figure 5. Figure 5 shows that under the same wear conditions, the mass wear rate of the coating was 5.14 mg/min, while that of the Ti60 substrate was 56.32 mg/min; that is, the wear resistance of the coating is significantly higher than that of the Ti60 alloy substrate, and the former was about 1/11 of the latter, which could be related to the high microhardness of the coating. In general, the greater the hardness of a material, the better its wear resistance [27]. Figure 4 shows that the average microhardness of the coating was 1062.9 $HV_{0.1}$, which was about 2.9 times that of the Ti60 substrate, so the wear resistance of the coating significantly improved compared with that of the Ti60 substrate.

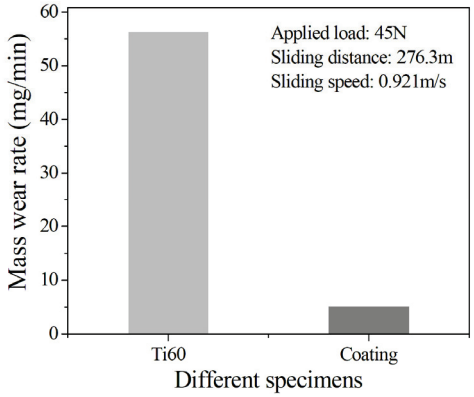
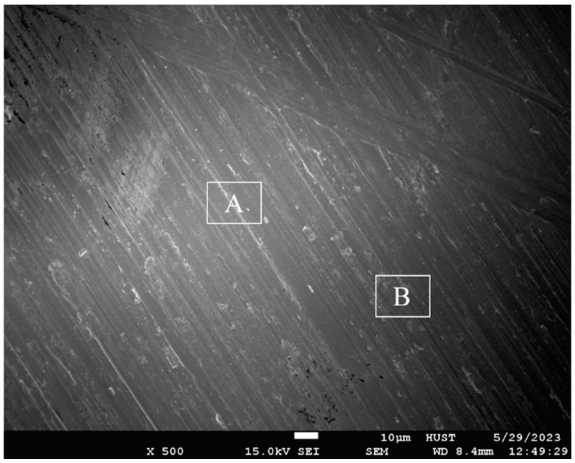
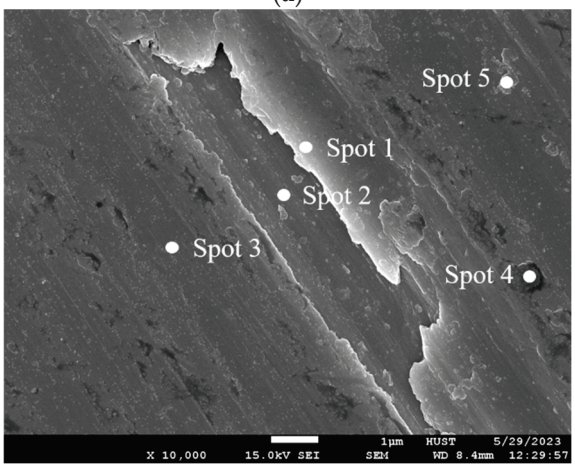


Figure 5. Columnar comparison of mass wear rates between the coating and Ti60 matrix.

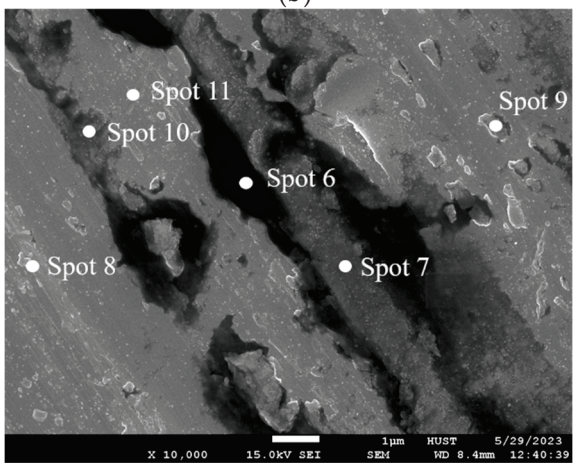
Figure 6 shows the surface wear morphology of the Ti60 matrix after dry friction and wear. Figure 6 shows that the worn surface of the Ti60 substrate was severely scratched and presented many parallel furrows, which was a typical abrasive wear characteristic. The friction pair was pressed into the friction surface under normal load, and the sliding friction force caused the friction surface to shear, plow, and cut through the furrow action of the grinding pair, resulting in grooving wear marks. The number of furrows on the surface of the Ti60 matrix was large, the depth and width were large, metal debris accumulated at the edges of the wear marks, and serious plastic deformation occurred on the surface of the wear marks. This was due to the low hardness of the Ti60 matrix, at about 366.7 $HV_{0.1}$ (Figure 4), while the hardness value of the SiC particles in the grinding pair was as high as 3200 HV [28]. Therefore, during dry friction and wear, hard SiC particles have a strong ploughing effect on the surface of the Ti60 matrix, resulting in a large amount of wear. At the same time, under the repeated action of friction pairs, the materials cut off from the surface of the Ti60 matrix were compressed and adhered to the surface, leading to adhesive wear (Figure 6b,c). In addition, the EDS results in Table 4 show that the Ti60 matrix was oxidized due to heat generation during dry friction and wear. Therefore, the type of wear affecting the Ti60 matrix was a combination of abrasive, adhesive, and oxidation wear, but the proportion of abrasive wear was the largest.



(**a**)



(**b**)



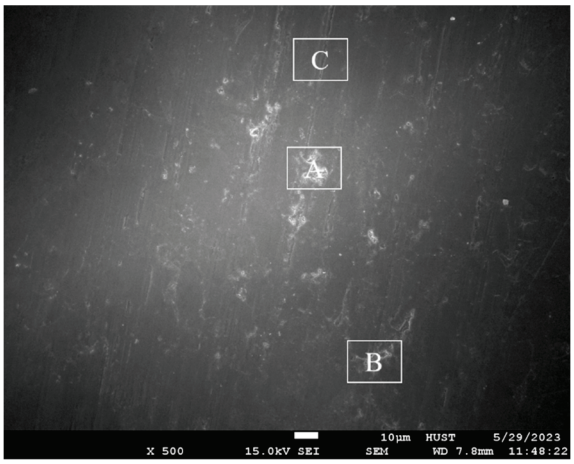
(**c**)

Figure 6. SEM image of the Ti60 matrix after wear: (**a**) whole worn surface, (**b**) enlarged SEM image at zone A in (**a**), and (**c**) enlarged SEM image at zone B in (**a**).

Table 4. EDS results of the Ti60 matrix's worn surface at different positions (at.%).

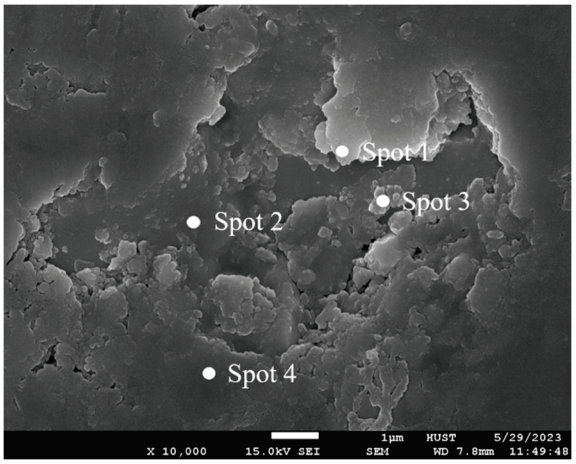
Element	Spot 1	Spot 2	Spot 3	Spot 4	Spot 5	Spot 6	Spot 7	Spot 8	Spot 9	Spot 10	Spot 11
Ti	68.99	69.83	68.78	58.93	70.01	58.00	65.09	65.07	54.94	65.71	61.82
Al	8.73	7.84	8.67	8.11	8.27	6.70	9.55	7.86	7.57	8.41	8.43
Zr	7.40	6.32	6.61	6.24	6.46	5.56	6.57	7.08	6.03	6.56	6.15
Mo	0.39	0.39	0.13	0.73	0.60	0.18	0.47	0.58	0.35	0.37	0.34
Ta	0.06	0.11	0.15	-	-	-	0.16	-	-	-	-
Nb	0.25	-	-	-	0.33	0.04	0.07	0.38	-	-	0.23
Si	0.53	0.80	0.74	0.90	0.64	0.40	0.69	0.54	0.52	0.91	0.74
Sn	1.38	1.16	1.35	1.22	1.33	1.18	1.20	1.24	0.94	1.28	1.18
O	12.27	13.55	13.57	23.87	12.36	27.94	16.20	17.25	29.65	16.76	21.11

The morphology of the worn surface of the coating after dry friction and wear is shown in Figure 7, which shows that the worn surface of the coating was relatively smooth, with shallow furrows and partial adhesion to the crushed area on the surface. This shows that the types of wear affecting the coating were abrasive and adhesive wear. At the same time, the material debris at the edge of the furrow accumulated in the furrow after repeated rolling, which hindered smooth formation of the furrow and improved the wear resistance of the coating. The size of the furrow on the coating surface was closely related to the microhardness of the coating. The abrasive dust accumulated on and adhered to the surface of the coating during repeated grinding of the friction pair, and the harder abrasive dust hindered complete formation of the furrow. The different sizes of the particles in the coating were related to the volume fraction of the different kinds of boride ceramic phases and intermetallic compound phases. In addition, the EDS results in Table 5 show that during dry friction and wear, the coating was oxidized due to the generation of friction heat. Therefore, the type of wear affecting the coating was actually a combination of abrasive, adhesive, and oxidation wear.

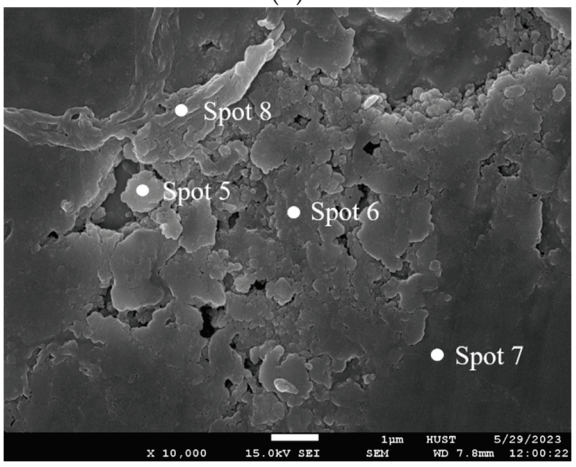


(**a**)

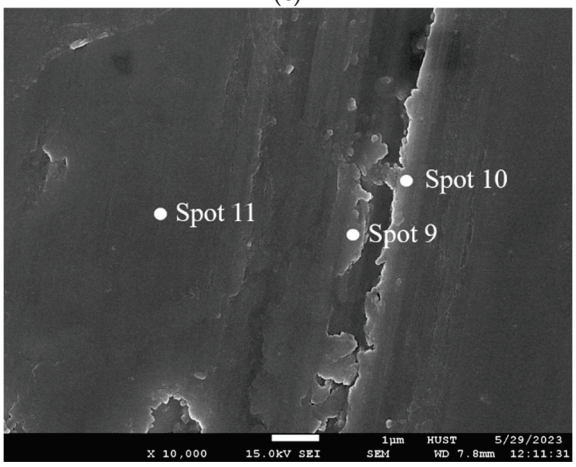
Figure 7. *Cont.*



(**b**)



(**c**)



(**d**)

Figure 7. SEM image of coating after wear: (**a**) whole worn surface, (**b**) enlarged SEM image at zone A in (**a**), (**c**) enlarged SEM image at zone B in (**a**), and (**d**) enlarged SEM image at zone C in (**a**).

Table 5. EDS results of the coating's worn surface at different positions (at.%).

Element	Spot 1	Spot 2	Spot 3	Spot 4	Spot 5	Spot 6	Spot 7	Spot 8	Spot 9	Spot 10	Spot 11
Ti	11.97	12.41	21.75	10.92	7.73	8.7	8.07	8.89	13.46	10.26	15.86
Zr	3.18	2.36	4.52	2.15	2.14	2.82	2.33	2.2	2.86	2.47	2.52
Mo	1.24	0.89	1.83	0.72	1.13	0.87	1.11	0.98	1.77	1.93	1.78
Ta	0.79	2.03	1.87	1.58	0.64	0.99	0.66	1.23	0.38	0.27	1.23
Nb	0.57	1.08	1.59	0.96	0.66	0.66	0.4	0.68	0.85	0.72	0.87
B	68.29	71.82	53.58	75.16	74.6	69.7	75.89	76.59	69.34	71.73	67.99
O	13.96	9.41	14.86	8.51	13.1	16.26	11.54	9.43	11.34	12.62	9.75

In summary, the type of wear affecting the Ti60 matrix was mainly abrasive wear, accompanied by a small amount of adhesive and oxidative wear, while a combination of abrasive, adhesive, and oxidative wear affected the coating.

4. Discussion

4.1. Microstructure Formation Mechanism of the Coating

During the laser cladding process, a large temperature gradient forms inside and on the surface of the general laser melt pool. The surface tension and buoyancy generated by the uneven temperature distribution promote the formation of convection in the laser melt pool, so that various chemical elements in the mixed powder layer become fully mixed with those in the partially melted Ti60 matrix. The composition distribution of the cladding layer was macroscopically uniform, and an in situ reaction occurred to form high-entropy borides, diborides, TiB, and the intermetallic compound phases. In accordance with the in situ reaction formation mechanism of the laser cladding coating reported in [29], Figure 8 shows the formation process of different phases in the laser cladding pool of the coating. The formation process of each phase in the coating can be seen in Table 6 and Figure 8: under the action of a laser heat source, the Ti, Zr, Mo, Ta, Nb, and B powders of the preset powder layer melt to form a laser cladding pool, and TiB_2 and ZrB_2 single-component diborides were preferentially formed, which can be seen in Figures 1 and 9. At the same time, the transition metals Ti, Zr, Mo, Ta, and Nb react in situ with B elements to form the high-entropy $(Ti_{0.2}Zr_{0.2}Mo_{0.2}Ta_{0.2}Nb_{0.2})B_2$ boride phase. The TiB, TiZr, $Ti_{1.83}Zr_{0.17}$, and $Ti_{0.67}Zr_{0.67}Nb_{0.67}$ intermetallic compound phases were then subsequently formed. In addition, it should be pointed out that Reactions (9)–(12) in Figure 9 are as follows:

$$Mo + 2B = MoB_2 \quad (9)$$

$$Ta + 2B = TaB_2 \quad (10)$$

$$Nb + 2B = NbB_2 \quad (11)$$

$$0.2TiB_2 + 0.2MoB_2 + 0.2ZrB_2 + 0.2TaB_2 + 0.2NbB_2 = (Ti_{0.2}Zr_{0.2}Mo_{0.2}Ta_{0.2}Nb_{0.2})B_2 \quad (12)$$

Table 6. Melting points and boiling points of different elements (K).

Element	Ti	Zr	Hf	Ta	Nb	Cr	Mo	B
Melting point	1941	2125	2506	3287	2750	2180	2896	2348
Boiling point	3560	4682	4876	5726	5017	2952	4912	4273

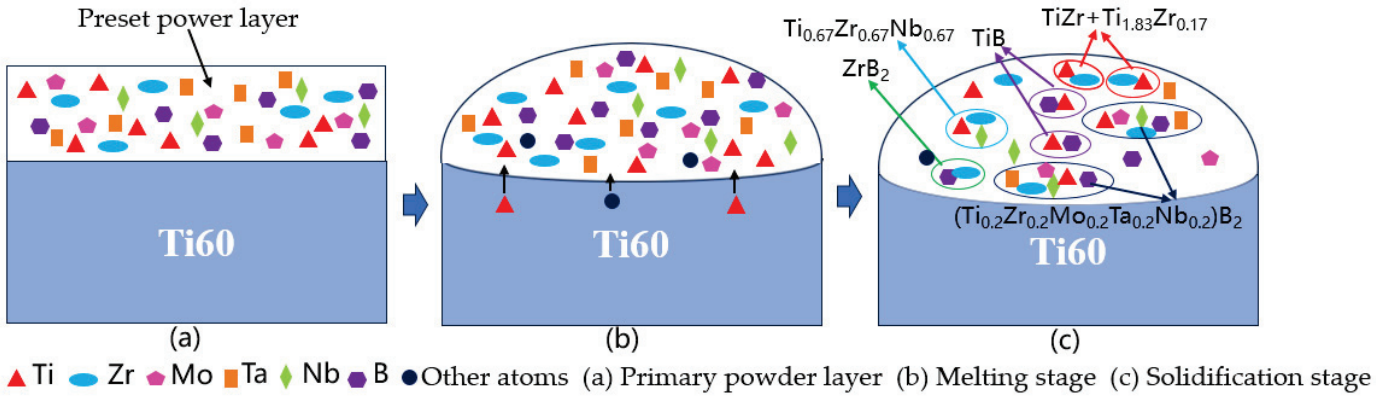


Figure 8. Schematic diagram of the different phase formation processes in the laser cladding pool of the coating.

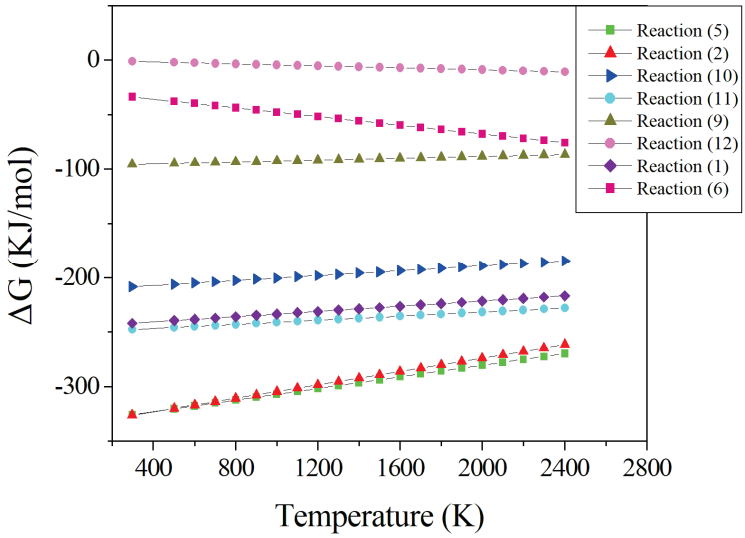


Figure 9. Gibbs free energy, ΔG, curves of different reactions with temperature T.

4.2. Wear Mechanism of the Coating and Ti60 Matrix

In the material friction and wear test, the amount of wear in the material is usually used to evaluate the wear resistance of the material. That is to say, the smaller the amount of wear loss per unit time or per unit friction distance, the better the wear resistance of the material. The wear mechanism of the material, under dry friction and wear conditions, generally involves three kinds of wear: adhesive wear, abrasive wear, and oxidation wear.

(1) *Adhesive wear*

According to the adhesive wear theoretical model proposed by world-renowned tribology expert Professor Archard in 1953 [30], hemispherical micro-convex bodies with multiple smooth surfaces are assumed to exist between the friction pair materials. When the micro-convex bodies come into contact, due to the action of local concentrated stress, plastic deformation occurs at the area of contact, which is relative to the amount of motion. The formula for calculating adhesive wear V is derived as follows:

$$V = K_1(NL/H) \quad (13)$$

where K_1, V, N, L, and H are the wear coefficient, adhesive wear amount, normal load, relative sliding distance, and material hardness, respectively.

From Formula (13), adhesive wear V can be seen to be proportional to friction sliding distance L and normal load N and is inversely proportional to the surface hardness H of the softer material. Therefore, under the same wear conditions, the amount of wear in the high-hardness materials is low and the wear resistance is good.

In the friction pairs presented in this study, the hardness of the abrasive SiC sandpaper (3200 HV [28]) is significantly higher than that of the coating and Ti60 matrix (Figure 4), indicating that both the coating and Ti60 matrix are suitable for the Archard model and consistent with the SEM morphology of the wear surface (Figures 6 and 7). Therefore, adhesive wear affects the coating and Ti60 matrix.

(2) *Abrasive wear*

In the model proposed by Rabinowicz [31] for wear with abrasive particles, assuming that a conical rigid micro-convex body with radius r slides on the surface of the grinding material to form a furrow with depth x, the amount of wear V of the material per unit distance can be expressed as follows:

$$V = K_2(N/H) \quad (14)$$

where K_2, N, and H are the wear coefficient, normal load, and hardness of the pressed material, respectively. From Formula (14), we can conclude that the higher the hardness of the material, the lower the wear amount.

In the friction pair composed of abrasive SiC sandpaper, the coating and Ti60 matrix in this study also conform to the Rabinowicz model and the SEM morphology of the wear surface (Figures 6 and 7); that is, the wear surface of the coating and Ti60 matrix have typical furrow characteristics. Therefore, abrasive wear also affects the coating and Ti60 matrix.

(3) *Oxidative wear*

Under dry friction and wear conditions, the surface temperature increases due to heating, which leads to oxidation of the surface material. Since both the coating and Ti60 matrix experience dry friction wear, the generation of friction heat will become increasingly serious with an increase in wear over time, resulting in oxidation on the surface of the coating and Ti60 matrix, evidenced by the detection of O at each position in Tables 4 and 5.

In summary, the types of wear affecting the laser cladding coating and Ti60 substrate in this study were abrasive, adhesive, and oxidation wear in the friction pair composed of abrasive SiC sandpaper. However, the proportions of these three types of wear are different with different hardnesses of the coating or Ti60 matrix.

5. Conclusions

(1) Laser cladding was successfully used to obtain a composite containing the high-entropy $(Ti_{0.2}Zr_{0.2}Mo_{0.2}Ta_{0.2}\ Nb_{0.2})B_2$ boride phase at 34.17 wt.% to coat the Ti60 alloy. Ti, Zr, Mo, Ta, Nb, and B powders were used as the raw materials, and the bond between the coating and the substrate was strong.

(2) The wear resistance of the laser cladding composite coating was greatly improved due to the occurrence of the high-hardness $(Ti_{0.2}Zr_{0.2}Mo_{0.2}Ta_{0.2}Nb_{0.2})B_2$ phase, and the mass wear rate of the coating was about 1/11 that of the Ti60 substrate.

(3) The main types of wear in the laser cladding composite coating were abrasive, adhesive, and oxidative wear, while that of the Ti60 matrix was mainly abrasive wear, accompanied by a small amount of adhesive and oxidative wear.

Author Contributions: Investigation, K.H. and X.H.; writing—original draft preparation, X.H.; writing—review and editing, K.H. All authors have read and agreed to the published version of the manuscript.

Funding: This work was supported by the Open Project Program (No. 23-1) of the Key Laboratory of Laser Technology and Optoelectronic Functional Materials of Hainan Province, Hainan Normal University.

Institutional Review Board Statement: Not applicable.

Informed Consent Statement: Not applicable.

Data Availability Statement: The data used in this study are available from the corresponding author upon reasonable request.

Acknowledgments: The authors are also grateful to the Analytical and Testing Center of Huazhong University of Science and Technology.

Conflicts of Interest: The authors declare no conflicts of interest.

References

1. Wang, S.H.; Xin, B.; Zhao, Q.Z.; Jiao, Y.X.; Qiang, W. Effect of heat treatment on microstructure and tensile properties of electron beam welded TC4/Ti60 joint. *Electr. Weld. Mach.* **2020**, *50*, 16–20.
2. Di, Y.N.; Liu, H.X.; Zhang, X.W.; Chen, L.; Liu, J.Z.; Lin, J.Q.; Hao, X.H.; Wang, Y.Y. Friction and wear behavior and high-temperature oxidation resistance of laser cladding AlCoCrFeMoVTi high-entropy alloy coating on titanium alloy surface. *Rare Met. Mat. Eng.* **2021**, *50*, 2883–2891.
3. Qin, X.; Qi, W.J.; Zuo, X.G. Friction and high temperature oxidation resistance of laser cladding NiCrCoAlY-Cr_3C_2 composite coating on TC4 titanium alloy. *J. Mater. Eng.* **2021**, *49*, 107–114.
4. Jiang, C.P.; Zhang, J.; Chen, Y.N.; Hou, Z.M.; Zhao, Q.Y.; Li, Y.; Zhu, L.X.; Zhang, F.Y.; Zhao, Y.Q. On enhancing wear resistance of titanium alloys by laser cladded WC-Co composite coatings. *Int. J. Refract. Met. Hard Mater.* **2022**, *107*, 105902. [CrossRef]
5. Huang, K.J.; Huang, W.X. Microstructure and wear resistance of Ti_5Si_3/Ti_3Al composite coatings prepared by laser cladding on TA2 titanium alloy. *Lubricants* **2023**, *11*, 213. [CrossRef]
6. Yu, J.J.; Zhang, X.Y.; Ma, L.L.; Li, H.; Zou, L.J.; Zhang, W.P. Microstructures and properties of laser cladding Ti/Ni+Si_3N_4/ZrO_2 composite coatings on TA15 titanium alloys. *Surf. Technol.* **2016**, *45*, 105–109.
7. Feng, S.R.; Tang, H.B.; Zhang, S.Q.; Wang, H.M. Microstructure and wear resistance of laser clad TiB-TiC/TiNi-Ti_2Ni intermetallic coating on titanium alloy. *Trans. Nonferrous Met. Soc. China* **2012**, *22*, 1667–1673. [CrossRef]
8. Chen, C.N.; Su, M. Study on microstructure and abrasive resistance of laser cladding TiN surface alloyed TC9. *Beijing Univ. Aeronaut. Astronaut. J.* **1998**, *24*, 253–255.
9. Hu, F.Y.; Cui, A.Y.; Hui, L.; Peng, X. Wear and corrosion behavior of Ti-matrix functional gradient layer. *J. Funct. Mater.* **2012**, *43*, 36–38.
10. Cheng, C.X.; Li, Y.F.; Liu, S.D. Surface modification of Ti600 Ti-alloy with laser cladded NiCr/TiAl coating. *Chin. J. Vac. Sci. Technol.* **2020**, *40*, 1166–1170.
11. Huang, K.J.; Han, X.C. High-temperature oxidation properties of Ti-Hf-Mo-Ta-Nb-B composite coating deposited on Ti60 alloy with laser cladding. *Coatings* **2023**, *13*, 1646. [CrossRef]
12. Fahrenholtz, W.G.; Hilmas, G.E. Ultra-high temperature ceramics: Materials for extreme environments. *Scr. Mater.* **2017**, *129*, 94–99. [CrossRef]
13. Weinberger, C.R.; Thompson, G.B. Review of phase stability in the group IVB and VB transition-metal carbides. *J. Am. Ceram. Soc.* **2018**, *101*, 4401–4424. [CrossRef]
14. Gild, J.; Zhang, Y.Y.; Harrington, T.; Jiang, S.C.; Hu, T.; Quinn, M.C.; Mellor, W.M.; Zhou, N.X.; Vecchio, K.; Luo, J. High-entropy metal diborides: A new class of high-entropy materials and a new type of ultrahigh temperature ceramics. *Sci. Rep.* **2016**, *6*, 37946. [CrossRef] [PubMed]
15. Gu, J.F.; Zou, J.; Sun, S.K.; Wang, H.; Yu, S.Y.; Zhang, J.Y.; Wang, W.M.; Fu, Z.Y. Dense and pure high-entropy metal diboride ceramics sintered from self-synthesized powders via boro/carbothermal reduction approach. *Sci. China Mater.* **2019**, *62*, 1898–1909. [CrossRef]
16. Gild, J.; Wright, A.; Quiambao-Tomko, K.; Qin, M.D.; Tomko, J.A.; Shafkat bin Hoque, M. Thermal conductivity and hardness of three single-phase high-entropy metal diborides fabricated by borocarbothermal reduction and spark plasma sintering. *Ceram. Int.* **2020**, *46*, 6906–6913. [CrossRef]
17. Zhang, Y.; Jiang, Z.B.; Sun, S.K.; Guo, W.M.; Chen, Q.S.; Qiu, J.X.; Plucknett, K.; Lin, H.T. Microstructure and mechanical properties of high-entropy borides derived from boro/carbothermal reduction. *J. Eur. Ceram. Soc.* **2019**, *39*, 3920–3924. [CrossRef]
18. Zhao, P.B.; Zhang, Y.; Zhu, J.P.; Xu, L.; Zhou, Y.Z.; Guo, W.M.; Zhang, G.J.; Wang, H.L.; Lin, H.T. Research progress on high-entropy boride ceramics. *J. Chin. Ceram. Soc.* **2022**, *50*, 1512–1526.
19. Barbarossa, S.; Orrù, R.; Cannillo, V.; Iacomini, A.; Garroni, S.; Murgia, M.; Cao, G. Fabrication and characterization of quinary high entropy-ultra-high temperature diborides. *Ceramics* **2021**, *4*, 108–120. [CrossRef]
20. Zheng, Q.; Wang, X.H.; Xing, J.J.; Gu, H.; Zhang, G.J. Quantitative analysis for phase compositions of ZrB_2-SiC-ZrC ultra-high temperature ceramic composites. *J. Inorg. Mater.* **2013**, *28*, 358–362. [CrossRef]
21. Li, L.; Yu, Z.S.; Wang, H.P.; Li, M.P. Microstructural evolution of titanium substrate composite coatings reinforced by in situ synthesized TiB and TiC by laser cladding. *Int. J. Miner. Metall. Mater.* **2010**, *17*, 481–488. [CrossRef]
22. He, B.; Lan, J.J.; Yang, G.; Wei, H. Microstructure and wear-resistant properties of in situ TiB-TiC reinforced titanium matrix composites by laser deposition manufacturing. *Rare Met. Mat. Eng.* **2017**, *46*, 3805–3810.

23. Lu, W.J.; Wu, R.J.; Zhang, D.; Zhang, X.N.; Sakata, T.; Mori, H. Interfacial microstructure of TiB/Ti in a Ti-TiB-TiC in situ composite. *Compos. Interface* **2002**, *9*, 41–50. [CrossRef]
24. Feng, H.B.; Zhou, Y.D.; Jia, C.; Meng, Q.C.; Rao, J.C. Growth mechanism of in situ TiB whiskers in spark plasma sintered TiB/Ti metal substrate composites. *Cryst. Growth Des.* **2006**, *6*, 1626–1630. [CrossRef]
25. Zhang, M.Q.; Yu, H.L.; Wang, H.M.; Yin, Y.L.; Wei, M.; Qiao, Y.L.; Zhang, W.; Xu, B.S. Microstructure and mechanical properties of in-situ TiB reinforced Ti-based composite coating by induction cladding. *J. Mater. Eng.* **2020**, *48*, 111–118.
26. Chamberlain, A.L.; Fahrenholtz, W.G.; Hilmas, G.E.; Ellerby, D.T. High-strength zirconium diboride-based ceramics. *J. Am. Ceram. Soc.* **2004**, *87*, 1170–1172. [CrossRef]
27. Li, X.Y.; Shao, H.H.; Zhang, B.S.; Dong, Q.S.; Li, C.L. High-temperature tribological properties of plasma sprayed Al_2O_3-13% TiO_2 coatings with microstructured and nanostructured feedstocks. *Mater. Prot.* **2019**, *52*, 1–7.
28. Zhang, H.X. Investigation on Microstructure and Wear Resistance of Ti-Al-Si Ceramic Composite Coatings on Titanium Alloys by Laser Cladding. Doctoral Thesis, Shandong University, Jinan, China, 23 May 2016.
29. Yang, L.Q.; Li, Z.Y.; Zhang, Y.Q.; Wei, S.Z.; Wang, Y.J.; Kang, Y. In-situ TiC-Al_3Ti reinforced Al-Mg composites with Y_2O_3 addition formed by laser cladding on AZ91D. *Surf. Coat. Technol.* **2020**, *383*, 125249. [CrossRef]
30. Archard, J.F. Contact and rubbing of flat surfaces. *J. Appl. Phys.* **1953**, *24*, 981–988. [CrossRef]
31. Rabinowicz, E.; Mutis, A. Effect of abrasive particle size on wear. *Wear* **1965**, *8*, 381–390. [CrossRef]

Disclaimer/Publisher's Note: The statements, opinions and data contained in all publications are solely those of the individual author(s) and contributor(s) and not of MDPI and/or the editor(s). MDPI and/or the editor(s) disclaim responsibility for any injury to people or property resulting from any ideas, methods, instructions or products referred to in the content.

coatings

MDPI

Article

Microsurface Defect Recognition via Microlaser Line Projection and Affine Moment Invariants

J. Apolinar Muñoz Rodríguez

Centro de Investigaciones en Óptica, A. C., Lomas del Bosque 115, Col. Comas del Campestre, León 37000, GTO, Mexico; munoza@cio.mx

Abstract: Advanced non-destructive techniques play an important role in detecting surface defects in the context of additive manufacturing, with non-destructive technologies providing surface data for the recognition of surface defects. In this line, it is necessary to implement microscope vision technology for the inspection of surface defects. This study proposes an approach for microsurface defect recognition using affine moment invariants based on microlaser line contouring, allowing for the detection of microscopic holes and scratches. For this purpose, the surface is represented by a Bezier surface to characterize microsurface defects through patterns of affine moment invariants after the surface is contoured via microlaser line projection. In this way, microholes and scratches can be recognized by computing a pattern of affine moment invariants for each region of the target surface. This technique is performed using a microscope vision system, which retrieves the surface topography via microlaser line scanning. The proposed technique allows for the recognition of holes and scratches with a surface depth greater than 20 microns, with a minor relative error of less than 2%. The proposed surface defect recognition approach enhances the literature on recognition techniques performed using visual technologies based on optical microscope systems. This contribution is corroborated through a discussion focused on the recognition of holes and scratches by means of various optical-microscope-based systems.

Keywords: surface defect recognition; affine moment invariants; microsurface contouring; microlaser line projection

1. Introduction

At present, non-destructive testing methods allow for the utilization of technologies to inspect surface defects in the context of additive manufacturing [1], where surface pattern recognition serves as a powerful tool to detect surface defects [2]. In this way, non-destructive testing methods have been implemented for the monitoring of microsurface holes and scratches [3]. Non-destructive testing methods include techniques such as visual testing, ultrasonic testing, acoustic emission, radiographic testing, magnetic particle inspection, and penetration testing [4]. Ultrasonic testing is performed based on the behavior of sound waves, where a pulse travels through uniform regions but changes in the presence of a discontinuity [5]. Similarly, acoustic emission testing is carried out by assessing wave disturbances generated by discontinuities on a surface [6]. Radiographic testing is based on the variation in radiation associated with the thickness of the material [7]. Magnetic particle testing is performed based on the continuous lines of force, which are distorted by discontinuities in ferromagnetic materials [8]. Penetration testing is carried out by applying a penetrant liquid to the surface in order to fill any discontinuity, which is

then observed by means of fluorescent dyes [9]. Of the non-destructive testing methods, the simplest and cheapest method is non-destructive visual testing, where surface defect inspection is typically performed in the range between 30 microns and 400 microns [10]. Therefore, non-destructive visual testing is the most useful method for the inspection of holes and scratches in additively manufactured materials [11]. The hardware used for visual testing typically includes only a camera and computational algorithms for the inspection of holes and scratches. Thus, non-destructive visual testing has been employed as the standard method to detect surface defects with a minimum depth of 30 microns [12]. In this way, the present study on surface defect detection was carried out based on visual testing methods. Surface defect recognition is generally applied to inspect surface holes and scratches with a minimum depth of 20 microns, and microsurface defect detection is typically carried out via visual testing by means of computer vision systems based on image processing [13], where surface defect detection is performed by means of methods such as statistics-, frequency-, and model-based approaches, including machine learning and deep learning models. Statistical methods allow for the detection of surface defects according to the pixel intensity distribution; for instance, a surface defect detection approach has been implemented using statistics [14], where the surface features are determined via a local binary pattern. Furthermore, surface defect recognition has been performed using a Gauss function modulated in the spatial domain [15], where the defect features are characterized using a core based on a complete dictionary. Additionally, surface defect detection has been carried out based on texture analysis [16], where the texture features were obtained by an iterative framework based on the absolute intensity deviation and local aggregation.

In a similar way, frequency-based methods are used to detect surface defects using pixel intensity distributions; for instance, surface defect detection has been performed using the Fourier transform [17], where the Fourier spectrum of the image under testing is compared with the spectrum of the real sample. Surface defect detection has also been carried out by means of the Fourier transform and the Hough transform [18], where the presence of surface defects is determined by comparing the difference between the tested image and the original sample. Additionally, surface defect defection has been implemented according to the Fourier transform amplitude [19], where the amplitude variation in the Fourier spectrum is used to determine surface defects based on a homogeneous image region.

Furthermore, model-based methods allow for surface defect inspection according to the image intensity distribution; for instance, surface defect detection has been performed by means of a hidden Markov model [20], where the recognition is computed through the hidden Markov model using a library of defects. Additionally, surface defect detection has been performed using a regularized robust principal component model [21], where a matrix separates the data into a low-rank component and a sparse component to characterize the surface pattern. Additionally, surface defect inspection has been carried out through a model-based approach using the intensity distribution [22], where a saliency map is determined by a continuous curve that represents the surface edge.

Moreover, machine learning methods can be used to detect surface defects using the pixel intensity distribution; for instance, surface defect detection has been performed via machine learning [23], where a gray-level image model was generated by training a neural network to determine surface defects. Additionally, surface defect inspection has been implemented via machine learning based on nearby points [24], where surface defect detection is carried out through a random forest method using a point cloud. Furthermore, surface defect detection has been carried out using neural networks [25], where potential defect images are compared with original images through the use of a database of defect images.

More recently, surface defect recognition has been implemented via deep learning [26]; for example, deep features can be determined using residual or convolutional neural networks. For instance, surface defect detection has been performed using a convolutional neural network [27], where a convolutional matrix was used to extract the features from an image without defects. In a similar way, surface defect detection has been carried out using convolutional neural networks [28], where a data set of defects was employed to determine surface features by means of a deep convolutional neural network.

The above computer vision techniques allow for the recognition of surface defects through computing the surface features from the pixel intensity distribution. However, the intensity distribution profile does not necessarily depict the topography accurately. This is because the intensity profile varies based on the surface reflectance, light source position, and viewer's position. Therefore, it has been established that traditional computer vision techniques do not employ the three-dimensional coordinates to perform surface defect detection, leading to some inaccuracies in microsurface defect recognition. Moreover, deep learning approaches employ large models with a great quantity of parameters and thus potentially low accuracy and slow speed [29]. This is because several hundred images are generally necessary to train neural network models, which leads to the need to perform complex optimization processes to accurately determine the surface defect features. From these statements, it can be deduced that the microsurface recognition of holes and scratches still represents a complicated task. Therefore, it is necessary to implement defect recognition through the use of three-dimensional coordinates to enhance the recognition of microsurface defects.

The proposed microsurface defect recognition approach is performed using three-dimensional coordinates, which are retrieved via microlaser line projection. Furthermore, the microsurface defect recognition approach is implemented via affine moment invariants [30]. Thus, the affine moment invariants can characterize patterns of holes and scratches through the three-dimensional coordinates, which are contoured via microlaser line scanning. To accomplish this, the affine moment invariants are computed from the surface, which is represented as a Bezier surface. In this way, the Bezier surface is determined using surface coordinates by means of a genetic algorithm. Thus, a pattern of affine moment invariants is computed from the Bezier surface to obtain the pattern of holes and scratches. In this way, a surface defect can be recognized when the pattern of affine moment invariants corresponds to holes or scratches. This procedure is performed to recognize holes and scratches on flat, cylindrical, and free-form surfaces. The microsurface defect recognition approach is carried out using an optical microscope vision system, which includes a CCD camera and a 39 μm laser line. The microlaser line scans the surface and the camera captures the laser line images, thus providing the surface contour. The microsurface coordinates are then computed according to the laser line position and the microscope's geometry. In this way, the surface defects can be computationally determined from the surface topography coordinates, which are not computed in traditional surface defect detection methods. The proposed surface defect recognition approach can recognize holes and scratches with a minimum depth surface of 30 microns, which is the most common surface defect depth inspected in the context of additive manufacturing. The microscope vision system can inspect a surface area of 3×60 cm in one scan as the slider can move the microscope vision system a distance of 60 cm in the x-axis, while the microscope observes a distance of 3 cm in the y-axis. The proposed defect recognition technique improves the accuracy of recognizing surface holes and scratches to the microscale. The proposed technique reduces the error of the optical microscope systems to a level smaller than 2%. This enhancement is achieved through the use of a surface contour recovered via the microlaser line projection. Furthermore, the surface defect characterization approach improves the

recognition accuracy; this is because the affine moment invariants are computed based on the three-dimensional surface data. In particular, the accuracy is computed according to the relative error provided by the affine moment pattern. The contribution of the proposed microsurface defect recognition approach is established through a discussion based on the accuracy of the techniques performed using optical microscope systems. The remainder of this paper is organized as follows: the surface characterization via affine moment invariants is described in Section 2.1, the Bezier surface representation is described in Section 2.2, the contouring of the surface topography via microlaser line projection is described in Section 2.3, the microsurface defect recognition results are presented in Section 3, and the key contributions associated with the proposed microsurface defect recognition approach are discussed in Section 4.

2. Materials and Methods

2.1. Microsurface Defect Characterization via Affine Moment Invariants

Microsurface defect recognition is carried out by computing a pattern of affine moment invariants from the surface topography. In this way, the affine moment invariants are computed to characterize the determined surface features. Thus, the pattern of affine moment invariants is computed from the holes and scratches to recognize surface defects on a surface region. The affine moment invariants are described by means of the following expressions:

$$I_1 = (\mu_{2,0}\mu_{0,2} - \mu_{1,1}^2)/\mu_{00}^4. \tag{1}$$

$$I_2 = (-\mu_{3,0}^2\mu_{0,3}^2 + 6\mu_{3,0}\mu_{2,1}\mu_{1,2}\mu_{0,3} - 4\mu_{3,0}\mu_{1,2}^3 - 4\mu_{2,1}^3\mu_{0,3} + 3\mu_{2,1}^2\mu_{1,2}^2)/\mu_{00}^{10}. \tag{2}$$

$$I_3 = (\mu_{2,0}\mu_{2,1}\mu_{0,3} - \mu_{2,0}\mu_{1,2}^2 - \mu_{1,1}\mu_{3,0}\mu_{0,3} + \mu_{1,1}\mu_{2,1}\mu_{1,2} + \mu_{0,2}\mu_{3,0}\mu_{1,2} - \mu_{0,2}\mu_{2,1}^2)/\mu_{00}^7. \tag{3}$$

$$\begin{aligned} I_4 = (&-\mu_{2,0}^3\mu_{0,3}^2 + 6\mu_{2,0}^2\mu_{1,1}\mu_{1,2}\mu_{0,3} - 3\mu_{2,0}^2\mu_{0,2}\mu_{1,2}^2 - 6\mu_{2,0}\mu_{1,1}^2\mu_{2,1}\mu_{0,3} - 6\mu_{2,0}\mu_{1,1}^2\mu_{1,2}^2 \\ &+ 12\mu_{2,0}\mu_{1,1}\mu_{0,2}\mu_{2,1}\mu_{1,2} - 3\mu_{2,0}\mu_{0,2}^2\mu_{2,1}^2 + 2\mu_{1,1}^3\mu_{3,0}\mu_{0,3} + 6\mu_{1,1}^3\mu_{2,1}\mu_{1,2} \\ &- 6\mu_{1,1}^2\mu_{0,2}\mu_{3,0}\mu_{1,2} - 6\mu_{1,1}^2\mu_{0,2}\mu_{2,1}^2 + 6\mu_{1,1}\mu_{0,2}^2\mu_{3,0}\mu_{2,1} - \mu_{0,2}^3\mu_{3,0}^2)/\mu_{00}^{11} \end{aligned}. \tag{4}$$

$$I_5 = (\mu_{4,0}\mu_{0,4} - 4\mu_{3,1}\mu_{1,3} + 3\mu_{2,2}^2)/\mu_{00}^6. \tag{5}$$

$$I_6 = (\mu_{4,0}\mu_{2,2}\mu_{0,4} - \mu_{4,0}\mu_{1,3}^2 - \mu_{3,1}^2\mu_{0,4} + 2\mu_{3,1}\mu_{2,2}\mu_{1,3} - \mu_{2,2}^3)/\mu_{00}^9. \tag{6}$$

$$I_7 = (\mu_{2,0}^2\mu_{2,4} - 4\mu_{2,0}\mu_{1,1}\mu_{1,3} + 2\mu_{2,0}\mu_{0,2}\mu_{2,2} + 4\mu_{1,1}^2\mu_{2,2} - 4\mu_{1,1}\mu_{0,2}\mu_{3,1} + \mu_{0,2}^2\mu_{4,0})/\mu_{00}^7. \tag{7}$$

$$\begin{aligned} I_8 = (&\mu_{2,0}^2\mu_{2,2}\mu_{0,4} - \mu_{2,0}^2\mu_{1,3}^2 - 2\mu_{2,0}\mu_{1,1}\mu_{3,1}\mu_{0,4} + 2\mu_{2,0}\mu_{1,1}\mu_{2,2}\mu_{1,3} + \mu_{2,0}\mu_{0,2}\mu_{4,0}\mu_{0,4} \\ &- 2\mu_{2,0}\mu_{0,2}\mu_{3,1}\mu_{1,3} + \mu_{2,0}\mu_{0,2}\mu_{2,2}^2 + 4\mu_{1,1}^2\mu_{3,1}\mu_{1,3} - 4\mu_{1,1}^2\mu_{2,2}^2 - 2\mu_{1,1}\mu_{0,2}\mu_{4,0}\mu_{1,3} \\ &+ 2\mu_{1,1}\mu_{0,2}\mu_{3,1}\mu_{2,2} + \mu_{0,2}^2\mu_{4,0}\mu_{2,2} - \mu_{0,2}^2\mu_{3,1}^2)/\mu_{00}^{10} \end{aligned}. \tag{8}$$

$$\begin{aligned} I_9 = (&\mu_{3,0}^2\mu_{1,2}^2\mu_{0,4} - 2\mu_{3,0}^2\mu_{1,2}\mu_{0,3}\mu_{1,3} + \mu_{3,0}^2\mu_{0,3}^2\mu_{2,2} - 2\mu_{3,0}\mu_{2,1}^2\mu_{1,2}\mu_{0,4} + 2\mu_{3,0}\mu_{2,1}^2\mu_{0,3}\mu_{1,3} \\ &+ 2\mu_{3,0}\mu_{2,1}\mu_{1,2}^2\mu_{1,3} - 2\mu_{3,0}\mu_{2,1}\mu_{0,3}^2\mu_{3,1} - 2\mu_{3,0}\mu_{1,2}^3\mu_{2,2} + 2\mu_{3,0}\mu_{1,2}^2\mu_{0,3}\mu_{3,1} + \mu_{2,1}^4\mu_{0,4} \\ &- 2\mu_{2,1}^3\mu_{1,2}\mu_{1,3} - 2\mu_{2,1}^3\mu_{0,2}\mu_{2,2} + 3\mu_{2,1}^2\mu_{1,2}^2\mu_{2,2} + 2\mu_{2,1}^2\mu_{1,2}\mu_{0,3}\mu_{3,1} + \mu_{2,1}^2\mu_{0,3}\mu_{4,0} \\ &- 2\mu_{2,1}\mu_{1,2}^3\mu_{3,1} - 2\mu_{2,1}\mu_{1,2}^2\mu_{0,3}\mu_{4,0} - \mu_{1,2}^4\mu_{4,0})/\mu_{00}^{13} \end{aligned}. \tag{9}$$

$$\begin{aligned} I_{10} = (&-\mu_{5,0}^2\mu_{5,0}^2\mu_{0,4} + 10\mu_{5,0}\mu_{4,1}\mu_{1,4}\mu_{0,5} - 4\mu_{5,0}\mu_{3,2}\mu_{2,3}\mu_{0,5} - 16\mu_{5,0}\mu_{3,2}\mu_{1,4}^2 \\ &+ 12\mu_{5,0}\mu_{2,3}^2\mu_{1,4} - 16\mu_{4,1}^2\mu_{2,3}\mu_{0,5} - 9\mu_{4,1}^2\mu_{1,4}^2 + 12\mu_{4,1}\mu_{3,2}^2\mu_{0,5} \\ &+ 76\mu_{4,1}\mu_{3,2}\mu_{3,3}\mu_{1,4} - 48\mu_{4,1}\mu_{2.3}^3 - 48\mu_{3,2}^3\mu_{1,4} + 32\mu_{3,2}^2\mu_{2,3}^2)/\mu_{00}^{14} \end{aligned} \tag{10}$$

where the central moments $\mu_{p,q}$ are computed using the coordinates (x_c, y_c) by means of the expression

$$\mu_{p,q} = \sum_{i=0}^{m-1} \sum_{j=0}^{n-1} (x_{i,j} - x_c)^p (y_{i,j} - y_c)^q f(x_{i,j}, y_{i,j}),\ x_c = \frac{\mathcal{M}_{10}}{\mathcal{M}_{00}},\ y_c = \frac{\mathcal{M}_{01}}{\mathcal{M}_{00}}. \tag{11}$$

In this equation, $f(x_{i,j}, y_{i,j})$ represents the surface depth in the position $(x_{i,j}, y_{i,j})$, and the statistical moments $\mathcal{M}_{p,q}$ are determined according to the expression

$$\mathcal{M}_{p,q} = \sum_{i=0}^{M-1} \sum_{j=0}^{N-1} x_{i,j}^p y_{i,j}^q f(x_{i,j}, y_{i,j}). \tag{12}$$

where the sub-indices (i, j) represent the numbers of surface points in the x- and y-directions, respectively. Thus, the affine moment invariants represented by Equations (1)–(10) are invariant to scale, translation, and orientation [31]. These affine moment invariants generate a pattern $(I_1, I_2, I_3, I_4, I_5, I_6, I_7, I_8, I_9, I_{10})$, which represents the surface features of a region. In this way, a microsurface defect is characterized through a pattern of affine moment invariants to perform surface defect recognition on a target surface. For this purpose, microsurface defect characterization is performed through the computation of a pattern of affine moment invariants from data provided by a sixth-order Bezier surface. Thus, the affine moment invariants in Equations (1)–(10) are computed by means of the microsurface $z_{i,j}$, as shown in Figure 1. To compute the affine moment invariants, the surface depth $f(x_{i,j}, y_{i,j}) = z_{i,j}$ is replaced in Equations (11) and (12) to calculate $\mu_{p,q}$ and $\mathcal{M}_{p,q}$, respectively. Then, Equations (1)–(10) are computed to determine the pattern of affine moment invariants for a tested region. For instance, the affine moment invariant Equations (1)–(10) were computed to characterize the pattern of the surface hole shown in Figure 2a; in this case, the affine moment invariants are $I_1 = 1.2482 \times 10^{-5}$, $I_2 = 0$, $I_3 = 0$, $I_4 = 0$, $I_5 = 7.8118 \times 10^{-10}$, $I_6 = 4.4077 \times 10^{-15}$, $I_7 = 3.4851 \times 10^{-9}$, $I_8 = 1.2060 \times 10^{-14}$, $I_9 = 0$, and $I_{10} = 0$. This pattern describes a decreasing function from I_1 to I_4, and then the function increases until I_7 and decreases from I_8 to I_{10}. These affine moment invariants represent a surface hole, whose pattern is defined as a surface defect. Additionally, the holes provide a surface depth that is greater at the borders of x- and y-axes than in the center.

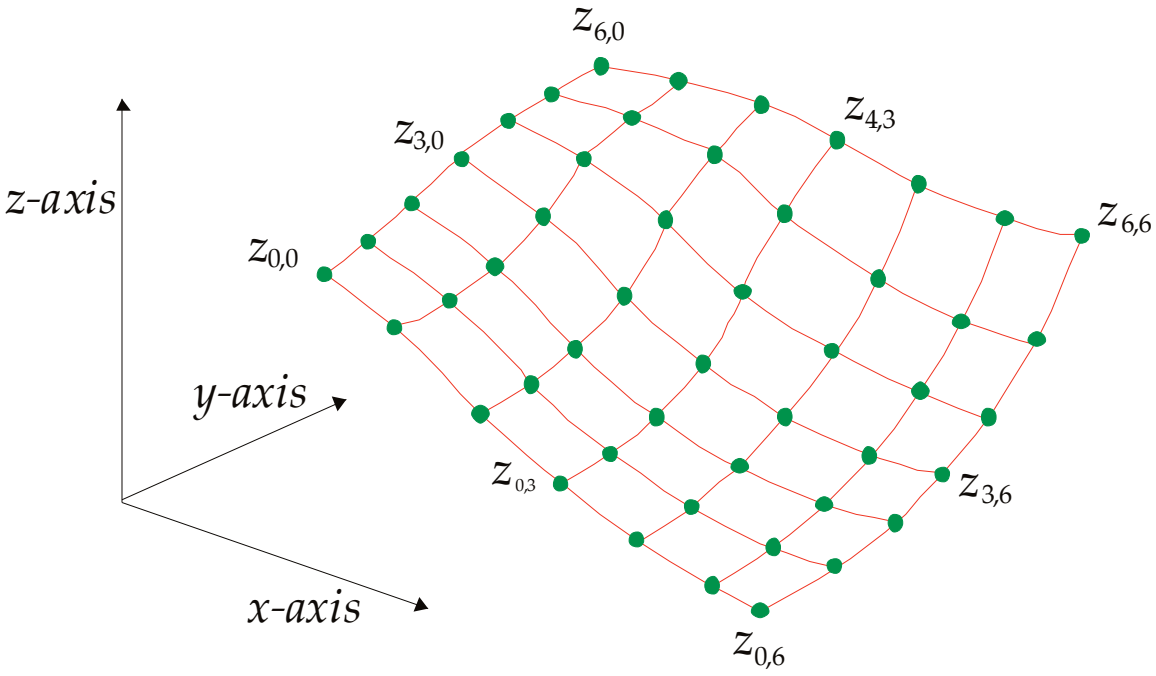
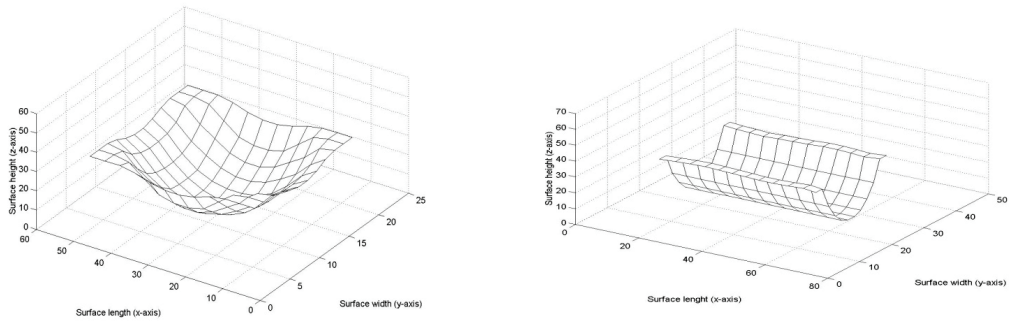


Figure 1. Surface points to compute affine moment invariants.



(**a**) (**b**)

Figure 2. (**a**) Surface hole to compute the pattern of affine moment invariants. (**b**) Surface scratch to compute the pattern of affine moment invariants.

In the same way, the affine moment invariants were computed for the surface scratches shown in Figure 2b to establish the surface pattern. To accomplish this, Equations (1)–(10) are computed and the results are $I_1 = 1.4751 \times 10^{-5}$, $I_2 = 0$, $I_3 = 0$, $I_4 = 0$, $I_5 = 1.1972 \times 10^{-9}$, $I_6 = 8.0305 \times 10^{-15}$, $I_7 = 6.8277 \times 10^{-9}$, $I_8 = 2.1468 \times 10^{-14}$, $I_9 = 0$, and $I_{10} = 0$. This pattern describes a decreasing function from I_1 to I_4, after which the function increases until I_7 and then decreases from I_8 to I_{10}. Here, the peaks I_1 and I_7 are larger than I_1 and I_7 of the surface hole. Additionally, the scratches do not provide a surface depth that is greater at the borders of x-axis than in the center. Thus, the scratches are characterized to represent a surface defect.

Furthermore, the affine moment invariant patterns were computed for holes and scratches of minor surface depth in order to deduce the minimum criteria for holes and scratches. In this way, the pattern was computed from a hole with a surface depth of 10 microns, as shown in Figure 3a.

In this case, the results of the affine moment invariants are $I_1 = 5.8014 \times 10^{-5}$, $I_2 = -3.0539 \times 10^{-71}$, $I_3 = 2.9462 \times 10^{-38}$, $I_4 = -5.4140 \times 10^{-42}$, $I_5 = 3.0515 \times 10^{-8}$, $I_6 = 7.0167 \times 10^{-13}$, $I_7 = 1.4557 \times 10^{-7}$, $I_8 = 2.9442 \times 10^{-12}$, $I_9 = 7.4184 \times 10^{-63}$, and $I_{10} = -2.5673 \times 10^{-77}$. This pattern is similar to that for the 30-micron hole shown in Figure 2a. Notably, both holes provide a surface depth that is greater at the borders of x- and y-axes than in the center. In the same way, the pattern of affine moment invariants was computed for an irregular hole with surface depth of 12 microns, as shown in Figure 3b. In this case, the result was $I_1 = 8.9835 \times 10^{-6}$, $I_2 = -3.8241 \times 10^{-28}$, $I_3 = 1.2369 \times 10^{-15}$, $I_4 = -3.9449 \times 10^{-20}$, $I_5 = 9.3422 \times 10^{-11}$, $I_6 = 1.2848 \times 10^{-16}$, $I_7 = 4.1607 \times 10^{-9}$, $I_8 = 4.6672 \times 10^{-16}$, $I_9 = 2.5581 \times 10^{-29}$, and $I_{10} = -6.4044 \times 10^{-29}$. This pattern is similar to that for the 12-micron hole shown in Figure 3a. Notably, the holes provide a surface depth that is greater at the borders of x- and y-axes than in the center. Furthermore, the pattern of affine moment invariants was computed for an irregular scratch with surface depth of 10 microns, as shown in Figure 3c.

In this case, the result was $I_1 = 4.3172 \times 10^{-5}$, $I_2 = -2.5260 \times 10^{-24}$, $I_3 = -7.2989 \times 10^{-15}$, $I_4 = -4.2398 \times 10^{-18}$, $I_5 = 1.0328 \times 10^{-8}$, $I_6 = 1.2525 \times 10^{-13}$, $I_7 = 5.8863 \times 10^{-8}$, $I_8 = 5.4378 \times 10^{-13}$, $I_9 = 3.2650 \times 10^{-26}$, and $I_{10} = -1.2082 \times 10^{-29}$. This pattern is similar to that for the 30-micron scratch shown in Figure 2b. Notably, the scratches do not provide a surface depth that is greater at the borders of the x-axis than in the center. Thus, the scratches are characterized as representing a surface defect. Based on these patterns, it is established that the pattern of affine moment invariants provides similarity for holes and scratches of surface depth over 10 microns. Furthermore, the irregularities of the holes and scratches reduce the peak I_1 in the pattern of affine moment invariants. In this way, it is established that the holes and scratches can be defined for a peak I_1 greater than 4.70×10^{-6}. Additionally,

a flat surface was characterized by computing the pattern of affine moment invariants to perform surface monitoring. In this case, the peak I_1 of the flat surface was smaller than those for the holes and scratches but was larger than I_1 for a cylindrical surface. Furthermore, the peak I_7 was smaller than those for the holes and scratches but, again, was larger than I_7 for the cylindrical surface. Thus, the pattern of affine moment invariants can determine whether the target surface presents holes or scratches. In the same way, the pattern of affine moment invariants can help to deduce whether the target surface corresponds to a flat or cylindrical surface. Notably, the peaks I_1 and I_7 for a cylindrical surface are smaller than those for a flat surface. Therefore, surface defect recognition is performed when a discontinuity appears in the surface profile provided by the microlaser line projection. This criterion is described based on surface profile discontinuity, as shown in Figure 3d. Here, the surface profile width is represented in the y-axis and the surface profile depth is indicated in the z-axis, and a surface defect can be detected when a surface discontinuity appears in the surface profile. In particular, the surface discontinuity is defined when the derivative $\partial f(y,x)/\partial y$ changes in the y-axis. This criterion can be observed with respect to points A, B, and C of the surface profile shown in Figure 3d. Furthermore, the presence of a hole is established when the surface discontinuity depth is greater at the borders than in the center in both the x- and y-axes. Meanwhile, scratches are determined when the surface discontinuity does not provide a greater surface at the borders than in the center with respect to the x-axis. Additionally, the surface defect depth is determined by computing the difference between the surface profile point (A), (B) and the minimum of the surface discontinuity point (B).

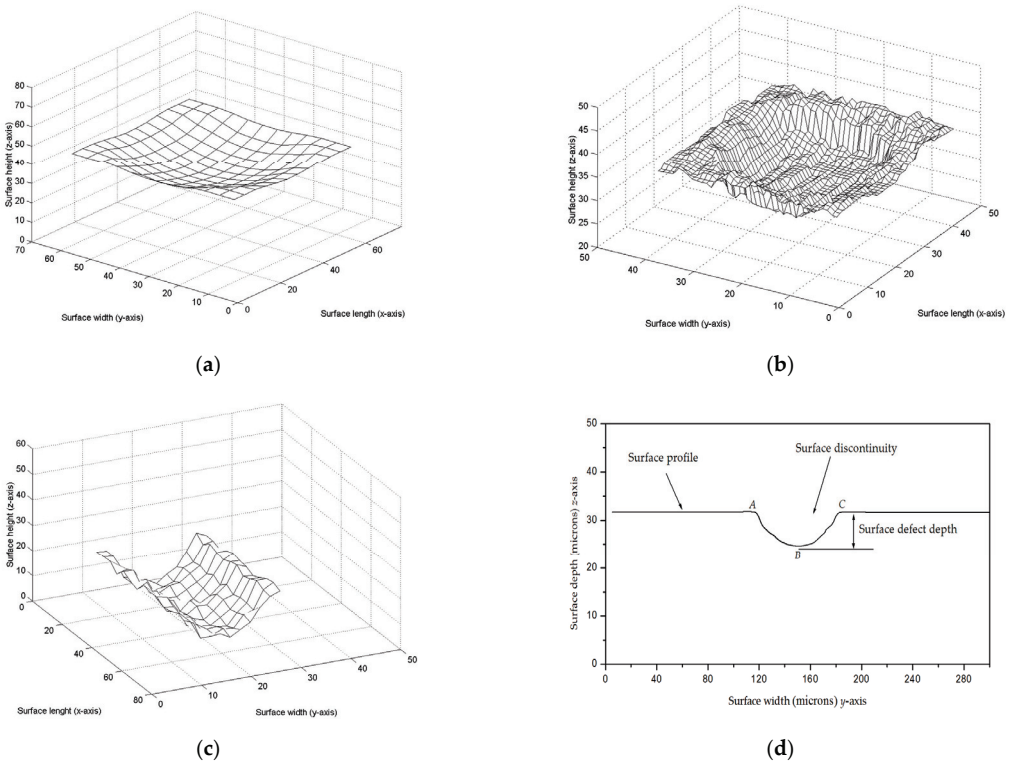


Figure 3. (**a**) Surface hole with surface depth of 10 microns to compute the pattern of affine moment invariants. (**b**) Irregular surface hole to compute the pattern of affine moment invariants. (**c**) Irregular surface scratch with surface depth of 12 microns to compute the pattern of affine moment invariants. (**d**) Surface profile showing discontinuity used to determine surface defects.

2.2. Surface Representation via Sixth-Order Bezier Surface

Microsurface defect recognition is carried out by computing the affine moment invariants from a surface region, which is represented as a Bezier surface. In particular, the

Bezier surface is computed from the surface points $z_{i,j}$, as depicted in Figure 1. Here, the coordinates ($x_{i,j}$, $y_{i,j}$) depict the surface position in the *x*- and *y*-axes, while the sub-indices (*i,j*) represent the number of surface points in the *x*- and *y*-directions, respectively. Thus, a sixth-order Bezier surface is built through the surface points ($z_{0,0}$, $z_{1,0}$, …, $z_{5,0}$, …, $z_{6,6}$). From these data, the Bezier surface is generated based on the control points $P_{i,j}$ by means of the following expressions:

$$S_{R,T}(u,v) = \sum_{i=0}^{i=6}\sum_{j=0}^{j=6} \frac{6!\,6!}{(6-i)!i!(6-j)!j!}(1-u)^{6-i}(1-v)^{6-j}u^i v^j P_{5R+i,5T+j},\ u,v \in [0,1], \quad (13)$$

$$u_{i,j} = \frac{(x_{6R+i,j} - x_{6R,j})}{(x_{6(R+1)_{,j}} - x_{6R,j})},\ v_{i,j} = \frac{(y_{i,6T+j} - y_{i,6T})}{(y_{i,6(T+1)} - y_{i,6T})}.$$

In this equation, the sub-indices (*R,T*) represent the surface region under test, $P_{i,j}$ denote control points that move the Bezier surface $S_{R,T}(u,v)$ toward the surface points $z_{i,j}$, and the values (*u*, *v*) are defined in the *x*- and *y*-axes, respectively. Based on these statements, the target surface is represented by the Bezier surfaces $S_{0,0}(u,v)$, $S_{1,0}(u,v)$, $S_{1,0}(u,v)$, and $S_{1,1}(u,v)$, ……, $S_{M,N}(u,v)$. To determine each of the Bezier surfaces, the control points $P_{6R+i,6T+j}$ must be computed. In this way, the values ($u_{i,j}$, $v_{i,j}$) and the surface points z_i are substituted into Equation (13) to obtain the following system of equations:

$$\begin{bmatrix} S_{R,T}(u_{0,0}, v_{0,0}) \\ S_{R,T}(u_{0,0}, v_{0,1}) \\ S_{R,T}(u_{0,0}, v_{0,2}) \\ \\ S_{R,T}(u_{5,5}, v_{5,5}) \end{bmatrix} = \begin{bmatrix} B_{0,0}(u_{0,0}, v_{0,0}) + B_{0,1}(u_{0,0}, v_{0,0}) + B_{0,2}(u_{0,0}, v_{0,0}) + \ldots + B_{6,6}(u_{0,0}, v_{0,0}) \\ B_{0,0}(u_{0,0}, v_{0,1}) + B_{0,1}(u_{0,0}, v_{0,1}) + B_{0,2}(u_{0,0}, v_{0,1}) + \ldots + B_{6,6}(u_{0,0}, v_{0,1}) \\ B_{0,0}(u_{0,0}, v_{0,2}) + B_{0,1}(u_{0,2}, v_{0,0}) + B_{0,2}(u_{0,2}, v_{0,0}) + \ldots + B_{6,6}(u_{0,0}, v_{0,2}) \\ \vdots \qquad\qquad \vdots \qquad\qquad\qquad \vdots \\ wB_{0,0}(u_{6,6}, v_{6,6}) + B_{0,1}(u_{6,6}, v_{6,6}) + B_{0,2}(u_{6,6}, v_{6,6}) + \ldots + B_{5,5}(u_{6,6}, v_{6,6}) \end{bmatrix} \begin{bmatrix} w_{0,0}z_{0,0} \\ w_{0,1}z_{0,1} \\ w_{0,2}z_{0,2} \\ \vdots \\ w_{6,6}z_{6,6} \end{bmatrix}. \quad (14)$$

In this system, $B_{i,j}(u,v) = 6!6!(1-u)^{6-i}(1-v)^{6-j}u^i v^j/(6-i)!i!(6-j)!j!$, and the control points are defined based on the weights $w_{6R+i,6T+j}$ according to the expression $P_{6R+i,6T+j} = w_{6R+i,6T+j}\, z_{6R+i,6T+j.}$ To solve Equation (14), $S_{R,T}(u_{i,j},v_{i,j})$ are replaced by the surface data $z_{6R+i,6T+j}$, and ($u_{i,j}$, $v_{i,j}$) are computed using the expressions given in Equation (13). Thus, the weights $w_{6R+i,6T+j}$ are calculated through a genetic algorithm by means of the following steps. The first step involves computing the initial population from the maximum and minimum of each weight. In this way, the maximum and minimum are determined by computing the initial Bezier surface $S_{R,T}(u_{i,j},v_{i,j})$. Then, $w_{6R+i,6T+j} = 1$ and $P_{6R+i,6T+j} = (w_{6R+i,6T+j})\,(z_{6R+i,6T+j})$ are substituted into Equation (13). Thus, if the Bezier surface $S_{R,T}(u_{i,j}, v_{i,j})$ is over the surface $z_{6R+i,6T+j}$, the maximum is equal to 1, while the minimum is given by the expression $(z_{6R+i,6T+j} - 3[S_{R,T}(u_{i,j}, v_{i,j}) - z_{6R+i,6Tm+j}])/z_{6R+i,6T+j}$. However, if the Bezier surface $S_{R,T}(u_{i,j}, v_{i,j})$ is under $z_{6R+i,6T+j}$, the minimum is equal to 1 and the maximum is given by the expression $(z_{6R+i,6T+j} - 3[S_{R,T}(u_{i,j}, v_{i,j}) - z_{6R+i,6T+j}])/z_{6R+i,6T+j}$. Thus, the search space is obtained for each weight. From the search space, four values are randomly taken to determine the initial population for each weight. These values are defined as the parents ($P_{1,k}$, $P_{2,k}$, $P_{3,k}$, $P_{4,k}$), which represent the initial population. In this case, the sub-index *k* indicates the generation number. The second step computes the children in generation *k* via crossover based on exploration and exploitation [32]. This procedure computes two children inside parents and one child outside parents. In this way, the children ($C_{1,k}$, $C_{2,k}$) and ($C_{4,k}$, $C_{5,k}$) are calculated via exploration from the parents ($P_{1,k}$, $P_{2,k}$) and ($P_{3,k}$, $P_{4,k}$), respectively. Meanwhile, the children ($C_{3,k}$, $C_{6,k}$) are computed via exploitation. Thus, the current children are calculated using the following expressions:

$$C_{1,k} = 0.5[(P_{1,k} + P_{2,k}) + \beta\,|\,P_{1,k} - P_{2,k}\,|\,], \quad (15)$$

$$C_{2,k} = 0.5[(P_{1,k} + P_{2,k}) - \beta\,|\,P_{1,k} - P_{2,k}\,|\,], \tag{16}$$

$$C_{4,k} = 0.5[(P_{4,k} + P_{3,k}) + \beta\,|\,P_{4,k} - P_{3,k}\,|\,], \tag{17}$$

$$C_{5,k} = 0.5[(P_{4,k} + P_{3,k}) - \beta\,|\,P_{4,k} - P_{3,k}\,|\,], \tag{18}$$

$$C_{3,k} = P_{0,k} + \beta\,|\,P_{min,k} - P_{0,k}\,|\,, \tag{19}$$

$$C_{6,k} = P_{\max,k} + \beta\,|\,P_{5,k} - P_{\max,k}\,|\,. \tag{20}$$

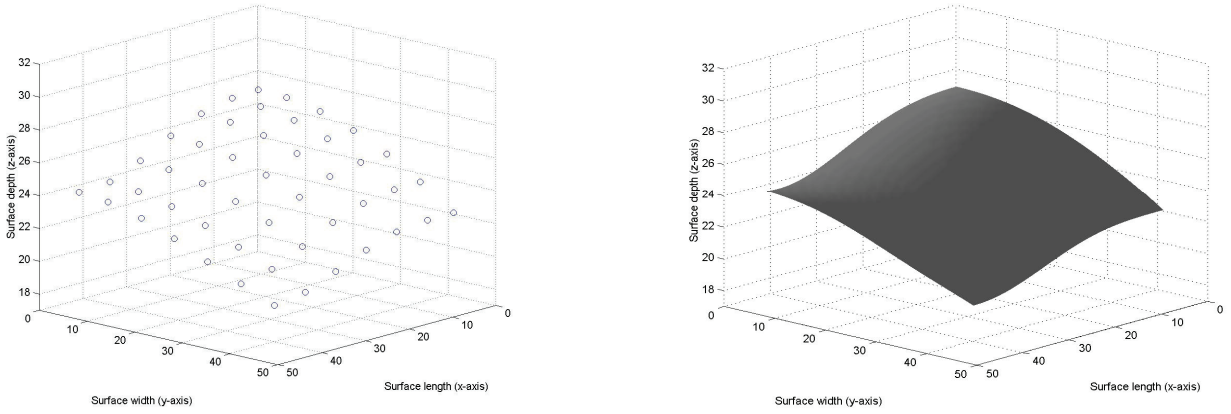
In these equations, $P_{0,k}$ and $P_{5,k}$ denote the minimum and maximum of each weight, and $P_{\min,k}$, and $P_{\max,k}$, are the maximum and minimum values of the parents ($P_{1,k}$, $P_{2,k}$, $P_{3,k}$, $P_{4,k}$). Additionally, the parameter β is calculated by means of the factor α, which is a random value in the interval between 0 and 1. In this way, $\beta = (2\alpha)^{1/2}$ if $\alpha > 0.5$; otherwise, $\beta = [2(1 - \alpha)]^{1/2}$. Thus, Equations (15)–(18) produce children inside parents, while Equations (19) and (20) produce children outside parents. From this procedure, the generation k children are generated. Additionally, the boundary control points are determined by means of the expressions $P_{6*R+6,j} = (P_{6Rn+5,j} + P_{6*R+7,j})/2$ and $P_{i,6*T} = (P_{i,6*T+5} + P_{i,6*T+7})/2$ in order to preserve continuity G^1. The third step involves calculating the population fitness throughout the Bezier surface $S_{R,T}$ ($u_{i,j}$,$v_{\,i,j}$) by means of an objective function, which is presented in the following expression

$$O_{R,T} = \min\left\{\sqrt{\frac{1}{49}\sum_{i=0}^{i=6}\sum_{j=0}^{j=6}\left[S_{R,T}(u_{i,j}, v_{i,j}) - z_{i,j}\right]^2}\right\}. \tag{21}$$

This equation allows for computation of the fitness utilizing the surface points $z_{i,j}$ and the Bezier surface $S_{R,T}$ ($u_{i,j}$,$v_{\,i,j}$). In the fourth step, the best current parents and children are determined according to the fitness values to obtain the parents of the (k + 1)th generation. In this way, the parent $P_{1,k+1}$ is taken from the parents ($P_{1,k}$, $P_{2,k}$), the parent $P_{3,k+1}$ is collected from the parents ($P_{3,k}$, $P_{4,k}$), the parent $P_{2,k+1}$ is taken from children ($C_{1,k}$, $C_{2,k}$, $C_{3,k}$), and the parent $P_{4,k+1}$ is chosen from the children ($C_{4,k}$, $C_{5,k}$, $C_{6,k}$). The fifth step involves mutating one parent and one weight to avoid a local minimum. For this purpose, a new parent replaces the worst parent to calculate the fitness using Equation (21). If the new parent enhances the fitness, the worst parent is changed by the new parent. Otherwise, the mutation is not carried out. Additionally, a new weight is substituted for an existing weight of a parent, which is selected in random form, and the fitness is calculated via Equation (21). If the new weight enhances the fitness, the selected weight is replaced by the new weight; otherwise, the selected weight is not mutated. In this way, the parents in the (k + 1)th generation are obtained. Then, Equations (15)–(20) are computed to obtain the (k + 1)th generation children. Thus, the (k + 1)th generation population is generated. Then, steps 2–5 are iteratively computed until weights that minimize the objective function Equation (21) are obtained.

To describe the procedure to generate the Bezier surface, the surface $S_{0,0}(u, v)$ was obtained using the genetic algorithm from the surface points shown in Figure 4a. In this way, the weights ($w_{0,0}$, $w_{0,1}$, $w_{0,2}$, …., $w_{6,6}$) were computed through the genetic algorithm. In this case, the Bezier surface weights were established as $w_{0,0}$ = 1, $w_{6,0}$ = 1, $w_{0,6}$ = 1, and $w_{6,6}$ = 1. Meanwhile, the control points ($P_{6,1}$, $P_{6,2}$, $P_{6,3}$, $P_{6,4}$, $P_{6,5}$) and ($P_{1,6}$, $P_{2,6}$, $P_{3,6}$, $P_{4,6}$, $P_{5,6}$) were computed according to the expressions $P_{6*R+6,j} = (P_{6*R+5,j}+P_{6*R+7,j})/2$ and $P_{i,6*T} = (P_{i,6*T+5} + P_{i,6*T+7})/2$ in order to ensure continuity G^1. Based on these statements, the first step determines the maximum and minimum for the initial Bezier surface through Equation (13). Thus, the search space for each weight was obtained. From this search space, four parents were randomly chosen to generate the initial population for each weight. These first parents are presented in Table 1, where the first column depicts the weights to be

computed and the parents ($P_{1,1}$, $P_{2,1}$, $P_{3,1}$, $P_{4,1}$) are listed in the second to fifth column. Then, the second step involved computing the current children via crossover. Here, the children ($C_{1,k}$, $C_{2,k}$, $C_{4,k}$, $C_{5,k}$) were calculated via Equations (15)–(18), while the children ($C_{3,k}$, $C_{6,k}$) were calculated via Equations (20) and (21). These children are listed in columns 6–11 of Table 1. Then, the third step involved calculating the fitness by computing Equation (21), substituting $S_{R,T}(u_{i,j}, v_{i,j})$ and $z_{6R+i,6T+j}$. These fitness values are indicated in row 25. The fitness results indicate that the initial population produced a low error. Next, in the fourth step, the (k + 1)th generation's parents were selected from the best parents and children in generated k. For this purpose, parent $P_{1,k+1}$ was taken from ($P_{1,k}$, $P_{2,k}$), $P_{3,k+1}$ was chosen from the parents ($P_{3,k}$, $P_{4,k}$), parent $P_{2,k+1}$ was taken from the children ($C_{1,k}$, $C_{2,k}$, $C_{3,k}$), and e parent $P_{4,k+1}$ was chosen from the children ($C_{4,k}$, $C_{5,k}$, $C_{6,k}$), where $P_{1,2} = P_{2,1}$, $P_{3,2} = P_{4,1}$, $P_{2,2} = C_{1,1}$, and $P_{4,2} = C_{5,1}$. Then, the fifth step involved taking the worst parent ($P_{4,2}$) to perform a mutation. Thus, a new mutated parent replaced the parent $P_{4,2}$ to compute the fitness using Equation (21). In this case, the new parent enhanced the fitness, so this new parent replaced $P_{4,2}$. Then, parent $P_{3,2}$ was randomly designated to mutate the weight $w_{2,0}$. A new weight was generated to replace the weight $w_{2,0}$, and the fitness was calculated by computing Equation (21). In this case, the new weight enhanced the fitness, and, therefore, the new weight was used to replace $w_{2,0}$. Next, Equations (15)–(20) were computed to obtain the children in generation k+1, and their fitness was computed using Equation (21). The population of the (k + 1)th generation is provided in Table 2.



(**a**) (**b**)

Figure 4. (**a**) Surface points to generate a Bezier surface. (**b**) Sixth-order Bezier surface obtained through the control points computed via genetic algorithm.

Table 1. Surface control points generated via genetic algorithm for the first generation.

$P_{i,j}$	$P_{1,1}$	$P_{2,1}$	$P_{3,1}$	$P_{4,1}$	$C_{1,1}$	$C_{2,1}$	$C_{3,1}$	$C_{4,1}$	$C_{5,1}$	$C_{6,1}$
$P_{1,1}$	28.9056	28.6469	28.1968	28.2735	28.7853	28.7672	27.7224	28.2378	28.2325	28.8730
$P_{1,2}$	27.3941	27.3509	28.0884	27.3139	27.3740	27.3710	27.2886	27.7284	27.6739	29.6848
$P_{1,3}$	28.3126	28.3822	27.7694	27.9575	28.3498	28.3449	26.7137	27.8701	27.8569	28.9754
$P_{1,4}$	26.8157	26.7326	26.8962	26.9868	26.7770	26.7712	25.7988	26.9446	26.9383	28.8012
$P_{1,5}$	24.9463	24.8807	24.8769	24.8898	24.9158	24.9112	24.8290	24.8838	24.8829	25.1638
$P_{2,1}$	28.8557	28.0752	29.6197	29.0564	28.4929	28.4381	27.4121	29.3578	29.3183	29.6697
$P_{2,2}$	29.4513	27.3254	27.1183	29.1966	28.4630	28.3136	27.1639	28.2305	28.0844	30.4944
$P_{2,3}$	27.7453	28.5685	29.1180	27.1936	28.1858	28.1280	26.4440	28.2234	28.0882	29.2922
$P_{2,4}$	25.9628	25.6473	27.2727	28.8625	25.8161	25.7940	25.5324	28.1234	28.0117	29.3302
$P_{2,5}$	25.8177	25.2971	25.7607	25.2551	25.5757	25.5391	24.6848	25.5257	25.4901	25.9688

Table 1. *Cont.*

$P_{i,j}$	$P_{1,1}$	$P_{2,1}$	$P_{3,1}$	$P_{4,1}$	$C_{1,1}$	$C_{2,1}$	$C_{3,1}$	$C_{4,1}$	$C_{5,1}$	$C_{6,1}$
$P_{3,1}$	28.3144	27.2626	27.6421	28.7311	27.8255	27.7516	26.7868	28.2249	28.1483	28.8677
$P_{3,2}$	26.4725	26.4747	27.0929	28.5052	26.4737	26.4735	26.4204	27.8486	27.7494	29.8719
$P_{3,3}$	29.5190	26.8259	29.2607	29.7010	28.2671	28.0778	26.0964	29.4963	29.4654	30.0632
$P_{3,4}$	26.3625	25.8400	29.4144	26.2292	26.1196	26.0829	25.1292	27.9337	27.7099	29.7836
$P_{3,5}$	25.3259	25.2249	26.5099	24.1571	25.2789	25.2718	24.2256	25.4162	25.2508	26.5848
$P_{4,1}$	26.4720	28.3858	27.7431	26.2314	27.4962	27.3617	25.8685	27.0404	26.9341	28.6909
$P_{4,2}$	27.0939	28.1520	28.4976	28.3975	27.6601	27.5858	25.7236	28.4510	28.4440	29.5432
$P_{4,3}$	26.2671	25.3507	25.4891	28.2084	25.8411	25.7767	25.1914	26.9443	26.7532	29.8229
$P_{4,4}$	30.3870	28.5053	29.7856	24.4233	29.5123	29.3800	24.7849	27.2929	26.9161	30.1598
$P_{4,5}$	23.6267	25.4344	25.3135	26.2478	24.5941	24.4670	23.4984	25.8135	25.7478	26.2922
$P_{5,1}$	26.6206	26.6891	25.9057	26.5238	26.6573	26.6525	24.9156	26.2364	26.1930	27.7168
$P_{5,2}$	26.4087	26.3596	26.0120	25.2285	26.3859	26.3824	24.7510	25.6477	25.5927	28.3167
$P_{5,3}$	27.9725	24.9619	24.9479	28.6485	26.5730	26.3614	24.4469	26.9282	26.6682	28.6723
$P_{5,4}$	28.2968	26.0172	28.7166	27.8049	27.2371	27.0769	23.8313	28.2928	28.2287	29.2507
$P_{5,5}$	24.0497	23.3524	24.8296	25.2043	23.7256	23.6766	22.7612	25.0301	25.0038	26.0630
fitness	1.4608	1.2323	1.5853	1.4859	1.3596	1.3289	0.7742	1.5572	1.5102	2.2006

Table 2. Surface control points generated via genetic algorithm for the second generation.

$P_{i,j}$	$P_{1,1}$	$P_{2,1}$	$P_{3,1}$	$P_{4,1}$	$C_{1,1}$	$C_{2,1}$	$C_{3,1}$	$C_{4,1}$	$C_{5,1}$	$C_{6,1}$	**Last Iteration**
$P_{1,1}$	28.6469	27.7224	28.2735	27.9080	28.2172	28.1522	27.7043	28.1036	28.0779	28.8473	27.6033
$P_{1,2}$	27.3509	27.2886	27.3139	28.2726	27.3219	27.3176	27.2856	27.8269	27.7596	29.7522	26.5566
$P_{1,3}$	28.3822	26.7137	27.9575	26.8905	27.6065	27.4893	26.7186	27.4615	27.3865	28.9005	25.9509
$P_{1,4}$	26.7326	25.7988	26.9868	27.6245	26.2985	26.2329	25.7929	27.3281	27.2832	28.8461	24.0033
$P_{1,5}$	24.8807	24.8290	24.8898	24.9741	24.8567	24.8530	24.8244	24.9349	24.9290	25.1697	23.2542
$P_{2,1}$	28.0752	27.4121	29.0564	28.2970	27.7669	27.7203	27.3572	28.7034	28.6500	29.6163	26.8506
$P_{2,2}$	27.3254	27.1639	29.1966	29.1827	27.2503	27.2390	27.0145	29.1901	29.1891	30.4934	26.4636
$P_{2,3}$	28.5685	26.4440	27.1936	27.1367	27.5809	27.4316	26.5018	27.1672	27.1632	29.2882	25.8039
$P_{2,4}$	25.6473	25.5324	28.8625	29.1113	25.5939	25.5858	25.5103	28.9956	28.9782	29.3477	23.8593
$P_{2,5}$	25.2971	24.6848	25.2551	25.2502	25.0125	24.9694	24.6482	25.2528	25.2525	25.9684	22.9206
$P_{3,1}$	27.2626	26.7868	28.7311	28.1793	27.0414	27.0080	26.7129	28.4746	28.4358	28.8290	26.1063
$P_{3,2}$	26.4747	26.4204	28.5052	26.6214	26.4494	26.4456	26.4205	27.6295	27.4971	29.7395	25.8393
$P_{3,3}$	26.8259	26.0964	29.7010	26.8240	26.4868	26.4355	25.9072	28.3636	28.1614	29.8610	25.5426
$P_{3,4}$	25.8400	25.1292	26.2292	28.2756	25.5096	25.4596	25.0924	27.3243	27.1805	29.9274	23.1096
$P_{3,5}$	25.2249	24.2256	24.1571	24.9234	24.7603	24.6901	24.2185	24.5672	24.5133	26.6386	21.9303
$P_{4,1}$	28.3858	25.8685	26.2314	26.4554	27.2156	27.0387	26.0030	26.3513	26.3355	28.7066	24.9330
$P_{4,2}$	28.1520	25.7236	28.3975	25.9571	27.0231	26.8525	25.7979	27.2631	27.0916	29.3717	24.6096
$P_{4,3}$	25.3507	25.1914	28.2084	26.0330	25.2766	25.2654	25.1270	27.1971	27.0443	29.6701	24.3633
$P_{4,4}$	28.5053	24.7849	24.4233	25.2153	26.7758	26.5144	24.6527	24.8471	24.7915	30.2155	22.5072
$P_{4,5}$	25.4344	23.4984	26.2478	25.0400	24.5344	24.3984	23.6255	25.6863	25.6014	26.2073	21.0366
$P_{5,1}$	26.6891	24.9156	26.5238	26.1501	25.8647	25.7401	24.9204	26.3501	26.3238	27.6905	23.7936
$P_{5,2}$	26.3596	24.7510	25.2285	27.2772	25.6118	25.4988	24.7475	26.3248	26.1808	28.4606	23.4075
$P_{5,3}$	24.9619	24.4469	28.6485	26.1567	24.7225	24.6863	24.2354	27.4901	27.3150	28.4972	23.1939
$P_{5,4}$	26.0172	23.8313	27.8049	27.5258	25.0011	24.8474	23.6711	27.6752	27.6555	29.2311	21.3660
$P_{5,5}$	23.3524	22.7612	25.2043	23.9659	23.0776	23.0360	22.7122	24.6286	24.5416	25.9760	20.5068
fitness	1.2323	0.7742	1.4859	1.3105	1.1611	1.1418	1.0142	1.3748	1.3529	1.9422	0.0001

The procedure to compute the $(k + 1)$th generation population was repeated until the objective function (Equation (21)) was minimized. Through this procedure, the optimal weights were obtained, as shown in column 15 of Table 2. These weights were employed to compute the control points $P_{i,j} = w_{i,j}z_{i,j}$, which generate the Bezier surface $S_{0,0}(u, v)$. Meanwhile, the control points ($P_{6,1}$, $P_{6,2}$, $P_{6,3}$, $P_{6,4}$, $P_{6,5}$) and ($P_{1,6}$, $P_{2,6}$, $P_{3,6}$,

$P_{4,6}$, $P_{5,6}$) were computed according to the expressions $P_{6*R+6,j} = (P_{5*R+5-1,j} + P_{6*R+7,j})/2$ and $P_{i,6*T} = (P_{i,6*T+5} + P_{i,6*T+7})/2$ in order to ensure continuity G^1. The Bezier surface $S_{0,0}(u, v)$ generated via the genetic algorithm is shown in Figure 4b. In the same way, the Bezier surfaces $S_{0,1}(u,v)$, $S_{1,0}(u,v)$, and $S_{1,1}(u,v)$ were computed to obtain the complete Bezier surface. Thus, the generation of the Bezier surface was accomplished through the use of the genetic algorithm.

2.3. Microsurface Contouring via Microlaser Line Scanning

In the proposed approach, microsurface contouring is performed via microlaser line projection using the microscope vision system shown in Figure 5a. This vision system consists of an optical microscope, on which a microlaser line and a CCD array are attached. The microscope system is mounted on a slider platform, which moves the setup using Matlab to perform microlaser line scanning. In this optical setup, the x-axis represents the horizontal axis, the y-axis depicts the depth, and the z-axis represents the vertical axis. In this way, the surface is generally located on the x-y plane, and the surface height is parallel to the z-axis. The optical geometry of the microscope system is outlined in Figure 5b. In particular, a 39 μm laser line is projected perpendicularly to the surface, and the microscope is aligned at an angle θ, which represents the angle generated between the optical axis and the microlaser line. The distance between the surface and the objective lens is represented by A_0, the distance between the objective lens and the intermediate image plane is indicated by A_1, and the distance between the intermediate image plane and the ocular lens is represented by A_2. The objective lens focus is denoted by F_1, while the ocular lens focus is given by F_2. The laser's position in the image plane is represented by the coordinates ($x_{i,j}$, $y_{i,j}$). The image center is given by the coordinates (x_c, y_c) and the pixel size is denoted by η. For the geometry shown in Figure 5b, the surface depth $z_{i,j}$ and surface width $y_{i,j}$ are defined according to the following equations:

$$z_{i,j} = \frac{\eta(\boldsymbol{x}_c - \boldsymbol{x}_{i,j})F_1F_2}{(A_1A_2 - A_1F_2 - A_2F_1 + F_1F_2)sin\theta} + O, \tag{22}$$

$$y_{i,j} = \eta y_c - \frac{\eta(y_c - y_{i,j})F_1F_2}{(A_1A_2 - A_1F_2 - A_2F_1 + F_1F_2)}. \tag{23}$$

The surface length $x_{i,j}$ is acquired from the laser line position, which is provided by the slider platform. Meanwhile, the surface depth $z_{i,j}$ and the surface width $y_{i,j}$ are calculated by means of the parameters (x_c, y_c, η, θ, A_1, A_1, F_1, F_2), computed using a genetic algorithm that allows for computation of the objective function via Equations (22) and (23). The genetic algorithm is implemented through the following five steps. The first step involves collecting the initial population from the search space of each parameter. In this way, the maximum and minimum values of the parameters x_c, y_c, and η are obtained from the image size data. Meanwhile, the maximum and minimum values of the parameters A_1, F_1, A_2, F_2, and θ are deduced from the geometry of the optical microscope. In particular, the minimum F_2 is established as the ocular lens ratio multiplied by 1.2 and the maximum F_2 is defined as the ocular lens ratio multiplied by 2.4. Furthermore, the minimum A_2 is defined as the ocular lens ratio multiplied by 1.4 and the maximum A_2 is established as the ocular lens ratio multiplied by 2.8.

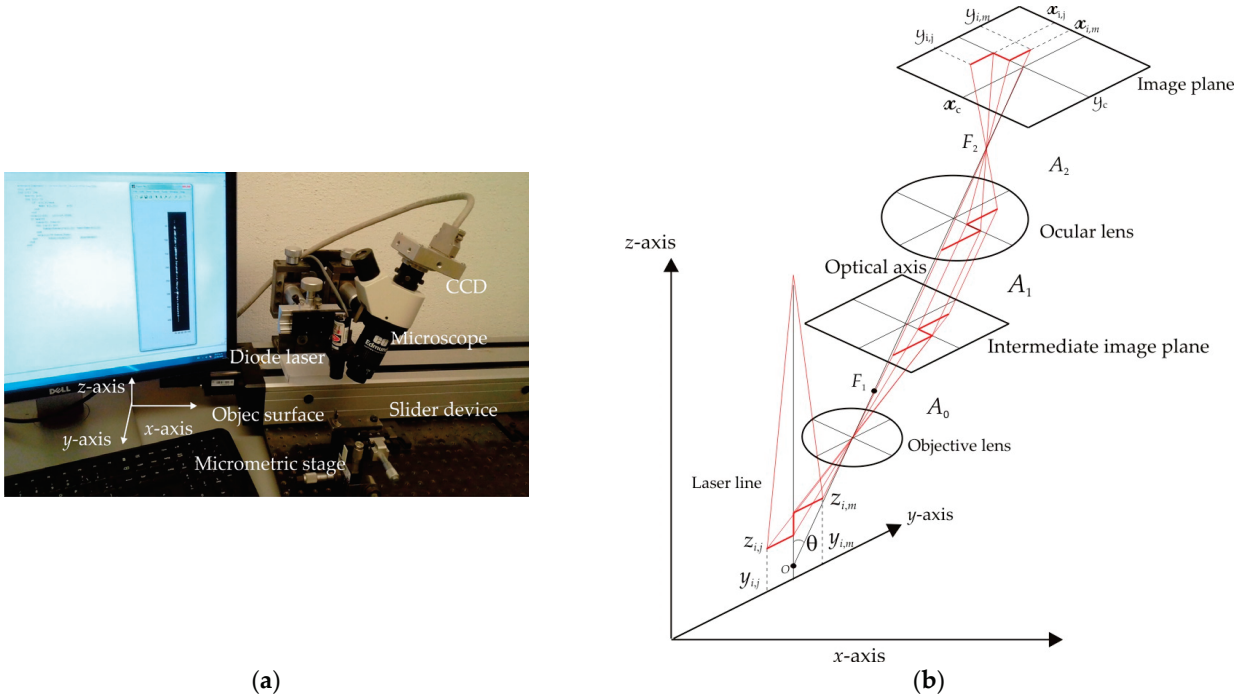


Figure 5. (**a**) Microscope vision system used to perform microsurface defect recognition. (**b**) Optical geometry of the microscope vision system.

Additionally, the minimum and maximum F_1 values are defined as the objective lens ratio multiplied by 1.2 and 2.4, respectively. Moreover, the minimum and maximum A_1 values are defined as the objective lens ratio multiplied by 1.4 and 3.2, respectively. The minimum and maximum θ values are defined as 20° and 50°, respectively. Collectively, these ranges define the search space. Then, four parents ($P_{1,k}$, $P_{2,k}$, $P_{3,k}$, $P_{4,k}$) are chosen randomly from the intervals between the maximum and minimum values for each parameter. In this way, all the parameters (x_c, y_c, η, θ, A_1, F_1, A_2, F_2) are collected into four parents, which represent the initial population. The second step involves generating four children ($C_{1,k}$, $C_{2,k}$, $C_{4,k}$, $C_{5,k}$) by computing Equations (15)–(18) and an additional two children ($C_{3,k}$, $C_{6,k}$) by computing Equations (20) and (21). Then, in the third step, the fitness is calculated via an objective function, represented as follows:

$$FO_1 = \min\left\{\frac{1}{mxn}\sum_{i=}^{n}\sum_{j=0}^{m}\left[(z_{i,j}-z_{i,m}) - \frac{\eta(\boldsymbol{x}_c-\boldsymbol{x}_{i,j})F_1F_2}{(A_1A_2-A_1F_2-A_2F_1+F_1F_2)sin\theta} + \frac{\eta(\boldsymbol{x}_c-\boldsymbol{x}_{i,m})F_1F_2}{(A_1A_2-A_1F_2-A_2F_1+F_1F_2)sin\theta}\right]^2\right\}, \quad (24)$$

$$FO_2 = \min\left\{\frac{1}{mxn}\sum_{i=}^{n}\sum_{j=0}^{m}\left[(y_{i,j}-y_{i,m}) + \frac{\eta(y_c-y_{i,j})F_1F_2}{(A_1A_2-A_1F_2-A_2F_1+F_1F_2)} - \frac{\eta(y_c-y_{i,m})F_1F_2}{(A_1A_2-A_1F_2-A_2F_1+F_1F_2)}\right]^2\right\}. \quad (25)$$

From these equations, the fitness is calculated by computing the equation $FO = (FO_1 + FO_2)/2$, where $(z_{i,j} - z_{i,m})$ and $(y_{i,j} - y_{i,m})$ are known. In the fourth step, the parents of the $(k + 1)$th generation are obtained according to the fitness values. Here, the parents $P_{1,k+1}$ and $P_{3,k+1}$ are collected from the parents ($P_{1,k}$, $P_{2,k}$) and ($P_{3,k}$, $P_{4,k}$), respectively, while the parents $P_{2,k+1}$ and $P_{4,k+1}$ are collected from the children ($C_{1,k}$, $C_{2,k}$, $C_{3,k}$) and ($C_{4,k}$, $C_{5,k}$, $C_{6,k}$), respectively. Next, in the fifth step, the worst parent is replaced by a new parent from the search space and the fitness is calculated. If the new parent has improved the fitness, the new parent is substituted for the worst parent; otherwise, the worst parent is not mutated. Furthermore, a new parameter value replaces a randomly chosen parameter in the obtained parents. If the new parameter improves the fitness,

this parameter is mutated; otherwise, it is not mutated. Thus, the parents in the (k + 1)th generation are determined. From these parents, the (k + 1)th generation children are computed using Equations (15)–(20), and their fitness is computed via Equations (24) and (25). In this way, the (k + 1)th generation population has been determined. The procedure to calculate the (k + 1) generation population is iteratively performed until a parameter combination (x_c, y_c, η, θ, A_1, F_1, A_2, F_2) that minimizes Equations (25) and (26) is obtained. Furthermore, the length between zero and O is obtained by computing the term $z_{0,j} = \eta(\mathrm{x}_{0,j} - \mathrm{x}_c)\, F_1F_2/(A_1 - F_1)\,(A_2 - F_2)sin\theta$.

The laser line coordinates are determined by computing the maximum intensity in the x-axis of the microscopic image [33]. For this purpose, a Bezier curve is fitted from the laser line pixels in the x-axis by means of the following equations:

$$\boldsymbol{x}(u) = \sum_{i=0}^{N} \mathcal{C}_i (1-u)^{N-i} u^i \mathrm{x}_{i,j},\ \mathcal{C}_i = \mathcal{C}_{i-1}(N+1-i)/i,\ \mathcal{C}_0 = 1, 0 \le u \le 1 \tag{26}$$

$$\boldsymbol{\mathcal{I}}(u) = \sum_{i=0}^{N} \mathcal{C}_i (1-u)^{N-i} u^i \boldsymbol{\mathcal{I}}_{i,j},\ \mathcal{C}_i = \mathcal{C}_{i-1}(N+1-i)/i,\ \mathcal{C}_0 = 1, 0 \le u \le 1 \tag{27}$$

In Equation (26), $\mathrm{x}_{i,j}$ indicates the laser line pixel position in the x-axis and N represents the laser line width (in pixels). Meanwhile, $\mathrm{I}_{i,j}$ depicts the pixel intensity in Equation (27). Here, the sub-indices (i, j) denote the number of laser line pixels in the x- and y-axes, respectively. To fit the Bezier curve, $\mathrm{I}_{i,j}$ is substituted in Equation (27) to obtain a concave curve I(u), whose second derivative I$''$(u) is positive in the interval $0 \le u \le 1$. In this way, the maximum intensity is computed using the first derivative I$'$(u) = 0. Here, the bisection method is used to compute the value u satisfying this condition. Thus, u is replaced in Equation (26) to compute $\mathrm{x}_{i,j}$ = x(u), which depicts the line position in the x-axis. The position $y_{i,j}$ is obtained from the row number of the laser line image. The laser line edges $y_{i,0}$ and $y_{i,m}$ are then determined by computing the first derivative in the y-axis. To determine the laser line coordinates ($\mathrm{x}_{i,j}$, $y_{i,j}$), the microscope vision system scans the surface. The CCD camera captures the microlaser line to compute the coordinates ($\mathrm{x}_{i,j}$, $y_{i,j}$) by means of Equations (26) and (27), respectively. Then, the surface depth $z_{i,j}$ is computed by replacing $\mathrm{x}_{i,j}$ in Equation (22) and the surface width $y_{i,j}$ is computed by substituting $y_{i,j}$ in Equation (24). The surface length coordinate in the x-axis is provided by the slider device. Thus, the three-dimensional microsurface topography is recovered.

For this microscope vision system, the laser line provides the reference position to determine the radial distortion. In this way, the laser line coordinates ($\mathrm{x}_{i,j}$, $y_{i,j}$,) are computed via Equations (26) and (27). Based on the distorted coordinates ($\mathrm{x}_{i,j}$, $\mathrm{y}_{i,j}$), the undistorted coordinates are defined $\mathrm{x}_{i,j} = \mathrm{x}_{i,j} + \delta\mathrm{x}_i$and $y_{i,j} = \mathrm{y}_{i,j} + \delta\mathrm{y}_j$, where ($\delta\mathrm{x}_i$, $\delta\mathrm{y}_j$) denotes the distortion. Therefore, the expression $S_{i,j} = \mathrm{x}_{1,j} - \mathrm{x}_{i,j}$ represents distorted line shifting and $s_{i,j} = (\mathrm{x}_{1,j} + \delta\mathrm{x}_1) - (\mathrm{x}_{i,j} + \delta\mathrm{x}_i)$ provides undistorted line shifting. In this way, $\delta\mathrm{x}_i = (\mathrm{x}_{1,j} - \mathrm{x}_{i,j}) - s_{i,j} + \delta\mathrm{x}_1 = S_{i,j}$–$s_{i,j} + \delta\mathrm{x}_1$ is used to compute the distortion in the x-axis. To obtain the first line shifting without distortion, the laser line is placed near to the image center to achieve $\delta\mathrm{x}_1 = 0$ and $s_{1,j} = S_{1,j}$. Thus, the expression $s_{i,j} = i{*}S_{1,j}$ provides undistorted shifting, where the distortion in the x-axis is computed using the expression $\delta\mathrm{x}_i = (\mathrm{x}_{1,j} - \mathrm{x}_{i,j}) - i{*}\mathrm{S}_{1,j}$. Similarly, the distortion in the y-axis is deduced from the expressions $(y_{i,1} - y_{i,j}) = (\mathrm{y}_{i,1} + \delta\mathrm{y}_1) - (\mathrm{y}_{i,j} + \delta\mathrm{y}_j)$ and $T_{i,j} = (\mathrm{y}_{i,1} - \mathrm{y}_{i,j})$. From these terms, the expression $\delta\mathrm{y}_j = (\mathrm{y}_{i,1} - \mathrm{y}_{i,j}) - j{*}T_{i,1}$ is obtained to compute the distortion in the y-axis.

3. Results of Microsurface Defect Recognition

Microsurface defect recognition was performed using the microscope vision system shown in Figure 5a. In particular, the recognition of holes and scratches was carried out on flat, cylindrical, and free-form surfaces. First, microsurface defect recognition was performed for the metallic flat surface shown in Figure 6a, where the scale is indicated in *mm* in the *x*-axis. The laser line projected on the flat surface is also shown in Figure 6b. Thus, the flat surface was scanned in the *x*-direction by the microscope vision system to retrieve the surface contour. During scanning, the camera captured the laser line to determine the laser line position ($x_{i,j}$, $y_{i,j}$) by computing Equations (26) and (27). Then, the surface depth $z_{i,j}$ and the surface width $y_{i,j}$ were calculated by computing Equations (22) and (23), using the position ($x_{i,j}$, $y_{i,j}$), where the surface coordinate $x_{i,j}$ is given by the slider platform. Thus, 268 laser lines were processed to retrieve the flat surface topography. The surface contouring accuracy was determined according to the relative error [34], where a contact method was used for reference measurement. Thus, the relative error of surface contouring was calculated as follows:

$$Er\% = \frac{100}{n \cdot m} \sum_{i=0}^{n} \sum_{j=0}^{m} \frac{\left| z_{i,j} - h_{i,j} \right|}{h_{i,j}} \tag{28}$$

In this equation, $h_{i,j}$ is the surface measurement via contact method, $z_{i,j}$ is the surface measurement computed via Equation (22), and $n \cdot m$ denotes the number of data. Thus, Equation (28) was computed and the result indicated a relative error of $Er\% = 0.727\%$. Then, a Bezier surface was computed from the surface retrieved via microlaser line scanning using the genetic algorithm. For this purpose, the surface was divided into regions of 7×7 points in order to compute each Bezier surface $S_{R,T}(u,v)$. Furthermore, the weights $w_{6R+0,\,6T+0} = 1$, $w_{6R+6,6T+0} = 1$, $w_{6R+0,6T+6} = 1$, and $w_{6R+6,6T+6} = 1$ were established for each Bezier surface. Additionally, the control points ($P_{6*R,1}$, $P_{6*R,2}$, $P_{6*R,3}$, $P_{6*R,4}$, $P_{6*R,5}$) and ($P_{1,6*T}$, $P_{2,6*T}$, $P_{3,6*T}$, $P_{4,6*T}$, $P_{5,6*T}$) were computed according to the expressions $P_{6*R+6,j} = (P_{6*R+5,j} + P_{6*R+7,j})/2$ and $P_{i,6*T} = (P_{i,6*T+5} + P_{i,6*T+7})/2$ in order to ensure continuity G^1. Then, the genetic algorithm determined the maximum and minimum of each weight $w_{6R+i,6T+j}$ for the initial Bezier surface via Equation (13). In this context, if $S_{R,T}(u_{i,j}, v_{i,j})$ was greater than $z_{6R+i,6T+j}$, the maximum was equal to 1 and the minimum was provided by the expression $(z_{6R+i,6T+j} - 3[S_{R,T}(u_{i,j}, v_{i,j}) - z_{6R+i,6Tm+j}])/z_{6R+i,6T+j}$. Meanwhile, if $z_{6R+i,6T+j}$ was greater than $S_{R,T}(u_{i,j}, v_{i,j})$, the minimum was equal to 1 and the maximum was provided by the expression $(z_{6R+i,6T+j} - 3[S_{R,T}(u_{i,j}, v_{i,j}) - z_{6R+i,6T+j}])/z_{6R+i,6T+j}$. Thus, the search space was obtained for each weight. Then, four parents were taken randomly from the search space to obtain the initial population for each weight. Next, the current children were generated by computing Equations (15)–(21). Then, the fitness of each $S_{R,T}(u_{i,j}, v_{i,j})$ was determined through computing Equation (21) by means of the surface $z_{6R+i,6T+j}$. Next, $P_{1,\,k+1}$ was selected from ($P_{1,k}$, $P_{2,k}$), $P_{3,k+1}$ from ($P_{3,k}$, $P_{4,k}$), $P_{2,k+1}$ from ($C_{1,k}$, $C_{2,k}$, $C_{3,k}$), and $P_{4,k+1}$ from ($C_{4,k}$, $C_{5,k}$, $C_{6,k}$) to serve as the parents for the $(k + 1)$th generation. Then, the worst parent with respect to each weight was replaced by a new parent to compute the fitness (Equation (21)). If the new parent enhanced the fitness, the worst parent was mutated; otherwise, the mutation was not performed. Additionally, a new weight was used to replace a weight from a random parent to calculate the fitness via Equation (21). If the new weight enhanced the fitness, the selected weight was mutated; otherwise, mutation was not performed. Then, Equations (15)–(20) were computed to obtain the $(k + 1)$th generation children. The procedure to compute the $(k + 1)$th generation population was repeated until the objective function (Equation (21)) was minimized. Then, the control points $P_{6R+i,6T+j} = (w_{6R+i,6T+j})(z_{6R+i,6T+j})$ were computed using the optimal weights and the surface data. Next, the control points $P_{6R+i,6T+j}$ were replaced in the Bezier surfaces $S_{0,0}(u,v)$,

$S_{1,0}(u,v)$, $S_{1,0}(u,v)$, and $S_{1,1}(u,v)$, ..., $S_{M,N}(u,v)$ to obtain the surface topography shown in Figure 6c. Here, the scale is represented in *mm* in the *x*- and *y*-axes and in microns in the *z*-axis. The accuracy of the Bezier surface was determined according to Equation (28). Here, $z_{i,j}$ was replaced by the Bezier surface $S_{R,T}(u_{i,j}, v_{i,j})$ and $h_{i,j}$ was replaced by the surface retrieved through microlaser line scanning. In this case, the accuracy of the surface shown in Figure 6c indicated a relative error of $Er\% = 0.402\%$.

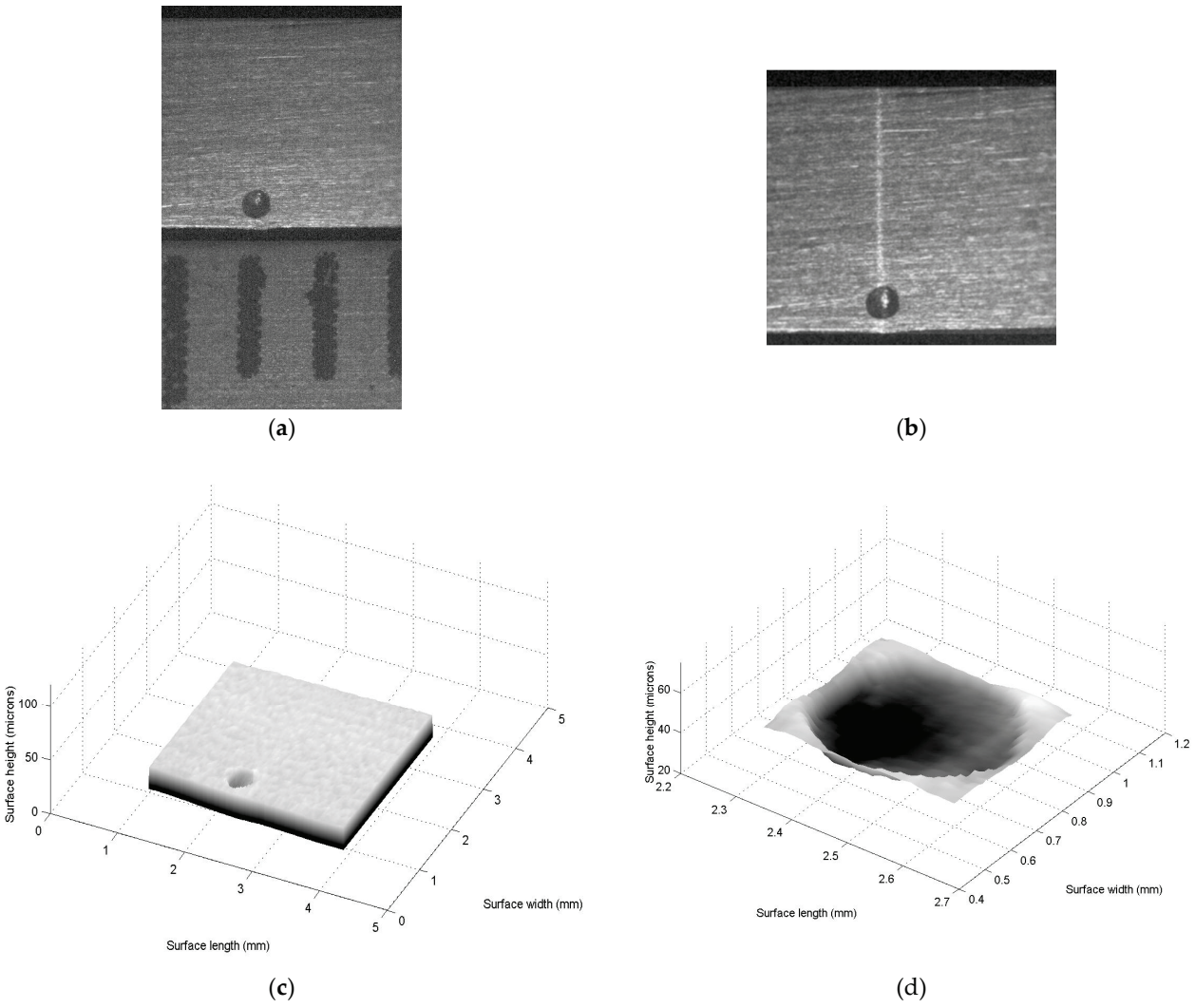


Figure 6. (**a**) Flat surface to perform surface defect recognition (scale in *mm* in *x*-direction). (**b**) Microlaser line projected on the flat surface. (**c**) Microsurface generated using the Bezier surface (Equation (13)). (**d**) Hole surface to compute the pattern of affine moment invariants.

Then, surface defect recognition is performed from the Bezier surface shown in Figure 6c. This procedure was carried out by computing the affine moment invariant Equations (1)–(10), employing regions of 34 × 34 surface points. The central moments $\mu_{p,q}$ of each region were also computed by means of Equations (11) and (12). Here, the surface depth is represented by $f(x_{i,j}, y_{i,j}) = z_{i,j}$, and the sub-indices (i,j) denote the number of surface points in the *x*- and *y*-axes. Equations (1)–(10) were computed to establish the pattern of affine moment invariants for each region. The result of the affine moment invariants for the flat surface was as follows: $I_1 = 4.6776 \times 10^{-6}$, $I_2 = -1.8352 \times 10^{-31}$, $I_3 = -1.4511 \times 10^{-18}$, $I_4 = -3.6474 \times 10^{-23}$, $I_5 = 1.3521 \times 10^{-10}$, $I_6 = 2.2314 \times 10^{-16}$, $I_7 = 5.4774 \times 10^{-10}$, $I_8 = 7.9281 \times 10^{-16}$, $I_9 = 6.7816 \times 10^{-33}$, and $I_{10} = -5.0054 \times 10^{-39}$. This pattern describes a decreasing function from I_1 to I_4, where the function peak I_1 is smaller than 4.6776×10^{-6}

and the moments (I_2, I_3, I_4) are negative. Meanwhile, the function increased from I_5 to I_7, then tended to zero from I_8 to I_{10}. In this way, the pattern of affine moment invariants was established. This is elucidated through the next pattern of affine moment invariants for the flat surface: $I_1 = 4.2802 \times 10^{-6}$, $I_2 = -2.3213 \times 10^{-32}$, $I_3 = -1.8357 \times 10^{-19}$, $I_4 = -2.4127 \times 10^{-23}$, $I_5 = 1.1322 \times 10^{-10}$, $I_6 = 1.7093 \times 10^{-16}$, $I_7 = 4.5861 \times 10^{-10}$, $I_8 = 6.0742 \times 10^{-16}$, $I_9 = 0$, and $I_{10} = 0$. Here, the function peak I_1 is smaller than 4.6776×10^{-6} and the moments (I_2, I_3, I_4) are negative. Then, the window was moved in the x- and y-directions to compute the pattern of affine moment invariants for each surface region. When the window covered the hole, the surface shown in Figure 6d was obtained. In this case, a discontinuity appears in the y-axis surface profile, which is indicated by the microlaser line projection. This surface discontinuity was detected when the derivative $\partial f(y,x)/\partial y$ changes signs in the y-axis. This criterion is described based on the surface profile discontinuity shown in Figure 3d. Additionally, the surface defect depth was determined by computing the difference between the minimum of the surface defect and the maximum of the surface defect. Here, the surface profile $f(y,x) = z_{i,j}$ was computed via Equation (22), and the surface profile width $y_{i,j}$ was computed via Equation (23). In this case, the maximum of the surface defect was obtained at the border of the surface defect in the y-axis. Also, the presence of a hole is established when the surface discontinuity depth is greater at the borders than in the center in both the x- and y-axes. Based on these statements, the hole length is 336 microns in the x-axis, the hole width is 438 microns in the y-axis, and the hole depth is 32 microns in the z-axis. The bottom of the hole is an irregular surface, presenting topographic variation. Thus, the hole surface was represented as a Bezier surface with smoothed topography in order to compute the pattern of affine moment invariants, and the result was $I_1 = 1.0513 \times 10^{-5}$, $I_2 = -1.4891 \times 10^{-22}$, $I_3 = 3.0546 \times 10^{-14}$, $I_4 = -2.4710 \times 10^{-18}$, $I_5 = 6.5353 \times 10^{-10}$, $I_6 = 2.3198 \times 10^{-15}$, $I_7 = 8.5784 \times 10^{-8}$, $I_8 = 6.0742 \times 10^{-16}$, $I_9 = 1.6635 \times 10^{-27}$, and $I_{10} = -1.6881 \times 10^{-29}$. This pattern describes a decreasing function from I_1 to I_4, where I_1 represents the function peak and (I_2, I_4) are negative. Then, the function increases to I_7, which represents a peak, and tends to zero from I_8 to I_{10}. The peaks I_1 and I_7 are larger than those of the flat surface, so it is considered that a hole defect was detected.

This determination occurred as the hole peak was greater than 4.7×10^{-6}, I_4 was negative, and the peak I_7 was greater than that of the flat surface. Additionally, the surface defect was greater at the borders than in the center in both the x- and y-axes. Based on these statements, it was deduced that the pattern of affine moment invariants corresponded to a hole surface defect. Thus, the shown region contoured by the microlaser line was recognized as a microhole surface defect according to the pattern of affine moment invariants.

The second microsurface defect recognition test was performed using the cylindrical metallic surface shown in Figure 7a (where the scale is indicated in millimeters in the x-direction). The microlaser line projected onto the cylindrical surface is shown in Figure 7b. Thus, the cylindrical surface was scanned in the x-direction using the microscope vision system to retrieve the surface contour. From the scanning result, the laser line position ($x_{i,j}$, $y_{i,j}$) was computed using Equations (26) and (27). Then, the surface depth $z_{i,j}$ and the surface width $y_{i,j}$ were obtained by computing Equations (22) and (23). The surface coordinate $x_{i,j}$ is provided by the slider platform. Thus, 242 laser lines were processed to retrieve the microcylindrical surface. The surface contouring accuracy was determined via Equation (28), where $z_{i,j}$ denotes the surface measured via the contact method, $h_{i,j}$ is the surface contour computed via Equation (22), and $n{\cdot}m$ is the number of data. From the computed result, a relative error of $Er\% = 0.818\%$ was determined. Then, a Bezier surface was computed from the surface retrieved via microlaser line scanning using the genetic

algorithm. For this purpose, the cylindrical surface was divided into regions of 7×7 points to compute each Bezier surface $S_{R,T}(u,v)$. Furthermore, for each Bezier surface, the weights $w_{6R+0,\,6T+0} = 1$, $w_{6R+6,6T+0} = 1$, $w_{6R+0,6T+6} = 1$, and $w_{6R+6,6T+6} = 1$ were established. Meanwhile, the control points ($P_{6*R,1}$, $P_{6*R,2}$, $P_{6*R,3}$, $P_{6*R,4}$, $P_{6*R,5}$) and ($P_{1,6*T}$, $P_{2,6*T}$, $P_{3,6*T}$, $P_{4,6*T}$, $P_{5,6*T}$) were computed according to the expressions $P_{6*R+6,j} = (P_{6*R+5,j}+P_{6*R+7,j})/2$ and $P_{i,6*T} = (P_{i,6*T+5} + P_{i,6*T+7})/2$ in order to ensure continuity G^1. Then, the first step of the genetic algorithm was performed to determine the maximum and minimum value of each weight $w_{6R+i,6T+j}$ through the initial Bezier surface Equation (13). If $S_{R,T}(u_{i,j}, v_{i,j})$ was greater than $z_{6R+i,6T+j}$, the maximum was equal to 1, and the minimum was computed using the expression $(z_{6R+i,6T+j} - 3[S_{R,T}(u_{i,j}, v_{i,j}) - z_{6R+i,6Tm+j}])/z_{6R+i,6T+j}$. Meanwhile, if $z_{6R+i,6T+j}$ was greater than $S_{R,T}(u_{i,j}, v_{i,j})$, the minimum was equal to 1 and the maximum was calculated according to the expression $(z_{6R+i,6T+j} - 3[S_{R,T}(u_{i,j}, v_{i,j}) - z_{6R+i,6T+j}])/z_{6R+i,6T+j}$. Then, four parents were collected at random from the search space to obtain the initial population for each weight. Next, the current children were generated by computing Equations (15)–(21). Then, the fitness of each $S_{R,T}(u_{i,j}, v_{i,j})$ was determined by computing Equation (21) according to the surface $z_{6R+i,6T+j}$. Next, $P_{1,\,k+1}$ was selected from ($P_{1,k}$, $P_{2,k}$), $P_{3,k+1}$ from ($P_{3,k}$, $P_{4,k}$), $P_{2,k+1}$ from ($C_{1,k}$, $C_{2,k}$, $C_{3,k}$), and $P_{4,k+1}$ from ($C_{4,k}$, $C_{5,k}$, $C_{6,k}$), serving as the parents of the (k + 1)-generation. Next, the worst parent was replaced by a new parent for each weight and the fitness was calculated according to Equation (21). If the new parent enhanced the fitness, the worst parent was replaced; otherwise, mutation was not performed. Additionally, a new weight replaced a weight from a randomly chosen parent and the fitness was calculated via Equation (21). If the new weight enhanced the fitness, the selected weight was mutated; otherwise, mutation was not performed. Then, Equations (15)–(20) were computed to obtain the (k + 1)th generation children. The procedure to compute the (k + 1)th generation population was repeated until the objective function (Equation (21)) had been minimized. Then, the control points $P_{6R+i,6T+j} = (w_{6R+i,6T+j})(z_{6R+i,6T+j})$ were calculated using the optimal weights. Next, the control points $P_{6R+i,6T+j}$ were replaced in the Bezier surfaces $S_{0,0}(u,v)$, $S_{1,0}(u,v)$, $S_{1,0}(u,v)$, and $S_{1,1}(u,v)$, ……, $S_{\mathrm{M,N}}(u,v)$ to obtain the surface topography shown in Figure 7c, where the scale is presented in *mm* for the x- and y-axes but in microns for the z-axis. The accuracy of the Bezier surface was determined via Equation (28). For this purpose, $z_{i,j}$ was replaced by the Bezier surface $S_{R,T}(u_{i,j}, v_{i,j})$ and $h_{i,j}$ was replaced by the surface retrieved through microlaser line scanning. The results indicated a relative error of $Er\% = 0.5305\%$. Then, surface defect recognition was performed using the Bezier surface shown in Figure 7c. This procedure was carried out by computing the affine moment invariants via Equations (1)–(10), employing regions of 38×38 surface points. Furthermore, the central moments $\mu_{p,q}$ of each region were computed via Equations (11) and (12) by means of the surface depth $f(x_{i,j}, y_{i,j}) = z_{i,j}$, where the sub-indices (i,j) depict the number of surface points in the x- and y-axes. Thus, Equations (1)–(10) were computed to establish the pattern of affine moment invariants for each region. The resulting affine moment invariants on the cylindrical surface were as follows: $I_1 = 3.9808 \times 10^{-6}$, $I_2 = -4.9844 \times 10^{-74}$, $I_3 = 2.6080 \times 10^{-40}$, $I_4 = -4.3482 \times 10^{-45}$, $I_5 = 9.8394 \times 10^{-11}$, $I_6 = 1.3935 \times 10^{-16}$, $I_7 = 3.9194 \times 10^{-10}$, $I_8 = 4.9154 \times 10^{-16}$, $I_9 = -1.9091 \times 10^{-66}$, and $I_{10} = 1.8154 \times 10^{-82}$. This pattern describes a decreasing function from I_1 to I_4, where I_1 represents the peak. Meanwhile, the function increases from I_5 to I_7, then decreases from I_8 to I_{10}. From this pattern, it is deduced that the peak I_1 is smaller than those for the flat surface and the hole surface defect. Furthermore, the peak I_7 is also smaller than those for the flat surface and the hole surface defect. This criterion is elucidated by the pattern of affine moment invariants for another cylindrical surface: $I_1 = 4.0776 \times 10^{-6}$, $I_2 = -1.1929 \times 10^{-48}$, $I_3 = 8.9806 \times 10^{-28}$, $I_4 = -7.8272 \times 10^{-25}$, $I_5 = 1.0294 \times 10^{-10}$, $I_6 = 1.4854 \times 10^{-16}$, $I_7 = 4.1449 \times 10^{-10}$, $I_8 = 5.2635 \times 10^{-16}$, $I_9 = 6.3026 \times 10^{-54}$, and

$I_{10} = -4.2746 \times 10^{-45}$. Then, the window is moved in the x-direction and y-direction to compute the pattern of affine moment invariants in each surface region. When the window covered a hole, an irregular topography was determined. In this case, a discontinuity appears in the y-axis in the surface profile, which is provided by the microlaser line projection. This surface discontinuity was detected due to the derivative $\partial f(y,x)/\partial y$ changing sign in the y-axis. The surface defect depth was determined by computing the difference between the minimum and maximum depth values for the surface defect. The surface profile $f(y,x) = z_{i,j}$ was computed via Equation (22), and the surface profile width $y_{i,j}$ was computed via Equation (23). Meanwhile, the maximum of the surface defect is obtained at the border of the surface defect in the y-axis. Furthermore, the presence of a hole was established as the surface discontinuity depth was greater at the borders than in the center in both the x- and y-axes. In this case, the hole presented an irregular topography, with variations in the x-, y-, and z-axes. The hole length was 620 microns in the x-axis, the hole width was 504 microns in the y-axis, and the hole depth was 32 microns in the z-axis.

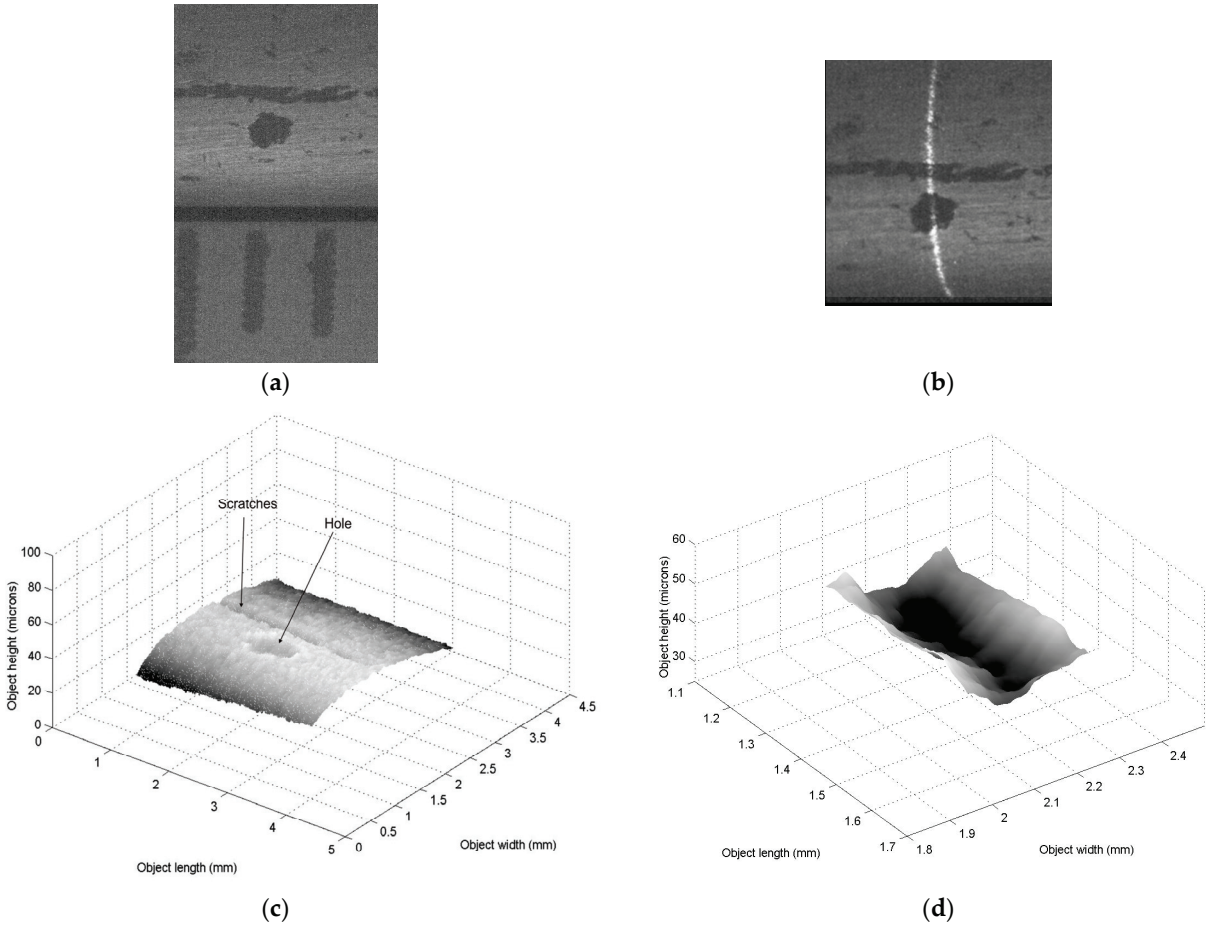


Figure 7. (**a**) Cylindrical metallic surface used to perform surface defect recognition (scale in *mm* in x-direction). (**b**) Microlaser line projected onto the cylindrical surface. (**c**) Microsurface generated using the Bezier surface Equation (13). (**d**) Scratch surface used to compute the pattern of affine moment invariants.

The hole surface was represented by the Bezier surface to compute the pattern of affine moment invariants and the results were as follows: $I_1 = 4.9004 \times 10^{-6}$, $I_2 = -6.1116 \times 10^{-24}$, $I_3 = 2.1951 \times 10^{-15}$, $I_4 = -9.1065 \times 10^{-20}$, $I_5 = 1.4666 \times 10^{-10}$, $I_6 = 2.5385 \times 10^{-16}$, $I_7 = 6.4527 \times 10^{-9}$, $I_8 = 9.0208 \times 10^{-16}$, $I_9 = 5.7381 \times 10^{-29}$, and $I_{10} = -2.2245 \times 10^{-31}$. This pattern describes a decreasing function from I_1 to I_4, where I_1 represents the function's peak. The function then increased until I_7 and tended to zero from

I_8 to I_{10}. In this case, it can be deduced that the peak I_1 was greater than those for the flat and cylindrical surfaces. Furthermore, the peak I_7 was greater than those for the flat and cylindrical surfaces. In this way, the characteristic pattern of the hole surface defect was recognized as the function peak I_1 was greater than 4.7×10^{-6} and (I_2, I_4) were negative. Furthermore, the surface defect was greater at the borders than in the center in both the *x*- and *y*-axes. Based on these statements, it can be deduced that the pattern of affine moment invariants corresponded to a hole surface defect. From this pattern of affine moment invariants, the surface defect was recognized as a hole. Thus, a region contoured by the microlaser line was recognized as a microsurface hole defect on a cylindrical surface. Then, the window size was modified to 38×26 surface points to perform microsurface defect recognition based on the presence of scratches. When the window covered the scratched area indicated by the arrow, the surface shown in Figure 7d was obtained. In this case, a discontinuity appeared in the *y*-axis in the surface profile provided by the microlaser line projection. This surface discontinuity was detected when the derivative $\partial f(y,x)/\partial y$ changed signs in the *y*-axis. The surface defect depth was determined by computing the difference between the minimum and maximum depth values of the surface defect, where the surface profile $f(y,x) = z_{i,j}$ was computed via Equation (22) and the surface profile width $y_{i,j}$ was computed via Equation (23). The maximum of the surface defect was obtained on the border of the surface defect in the *y*-axis, and the presence of a scratch can be established when the surface discontinuity depth is not greater at the borders than in the center in the *x*-axis. The scratch length was 412 microns in the *x*-axis, the scratch width was 298 microns in the *y*-axis, and the scratch depth was 22 microns in the *z*-axis. The bottom of the scratch presents an irregular surface, which contains topographic variations in the *x*-, *y*-, and *z*-axes. The pattern of affine moment invariants was computed from the Bezier surface using Equations (1)–(10), and the result was as follows: $I_1 = 5.4895 \times 10^{-6}$, $I_2 = -1.7040 \times 10^{-24}$, $I_3 = 9.0153 \times 10^{-16}$, $I_4 = -2.5433 \times 10^{-20}$, $I_5 = 1.8663 \times 10^{-10}$, $I_6 = 3.6278 \times 10^{-16}$, $I_7 = 5.1067 \times 10^{-9}$, I_8= 1.284910^{-15}, $I_9 = 9.5397 \times 10^{-30}$, and $I_{10} = -1.3892 \times 10^{-32}$. This pattern indicates a decreasing function from I_1 to I_4, where I_1 represents the function peak and (I_2, I_4) are negative. Then, the function increases to I_7, which represents a peak, following which the function tends to zero from I_8 to I_{10}. Additionally, the peak I_1 is greater than 4.7×10^{-6}. Furthermore, the surface defect is not greater at the borders than in the center in the *x*-axis. From this pattern of affine moment invariants, the surface defect was recognized as a scratch. Thus, a region contoured by the microlaser line was recognized as a scratch-type microdefect on a cylindrical surface. This criterion was elucidated by the pattern of affine moment invariants of another scratch-type surface defect as follows: $I_1 = 5.4084 \times 10^{-6}$, $I_2 = 1.5246 \times 10^{-25}$, $I_3 = -1.2930 \times 10^{-15}$, $I_4 = -4.0845 \times 10^{-21}$, $I_5 = 1.8104 \times 10^{-10}$, $I_6 = 3.4704 \times 10^{-16}$, $I_7 = 4.9610 \times 10^{-9}$, $I_8 = 1.2282 \times 10^{-15}$, $I_9 = 3.0332 \times 10^{-30}$, and $I_{10} = -2.6570 \times 10^{-33}$. Here, the peak I_1 is greater than 4.7×10^{-6}, and the surface defect is not greater at the borders than in the center in the *x*-axis.

Next, microsurface defect recognition was performed on the plastic free-form surface shown in Figure 8a, where the scale is indicated in millimeters in the *x*-direction. The microlaser line projected onto the plastic free-form surface is shown in Figure 8b. The free-form surface was scanned via microlaser line in the *x*-axis to compute the surface depth $z_{i,j}$ and the surface width $y_{i,j}$ via Equations (22) and (23). The coordinate $x_{i,j}$ was obtained from the slider platform. Thus, 232 laser lines were processed to retrieve the free-form surface. The surface accuracy was determined via Equation (28), where $z_{i,j}$ was the surface measured via contact method, $h_{i,j}$ was the surface contour computed via Equation (22), and $n \cdot m$ denotes the number of data. Thus, the result indicated a relative error of $Er\% = 0.883\%$. Then, the Bezier surfaces $S_{0,0}(u,v)$, $S_{1,0}(u,v)$, $S_{1,0}(u,v)$, and $S_{1,1}(u,v)$, ……, $S_{M,N}(u,v)$ were computed using the genetic algorithm to obtain the surface topography shown in Figure 8c.

Here, the scale is represented in *mm* for the *x*- and *y*-axes and in microns for the *z*-axis. The Bezier surface accuracy was calculated via Equation (28). Here, $z_{i,j}$ is given by the Bezier surface $S_{R,T}(u_{i,j}, v_{i,j})$ and $h_{i,j}$ is the surface retrieved through microlaser line scanning. The result indicated a relative error of $Er\% = 0.617\%$. Then, the pattern of affine moment invariants was computed from the Bezier surface shown in Figure 8c to recognize the microsurface holes. For this purpose, the affine moment invariants were computed for each surface region using Equations (1)–(10).

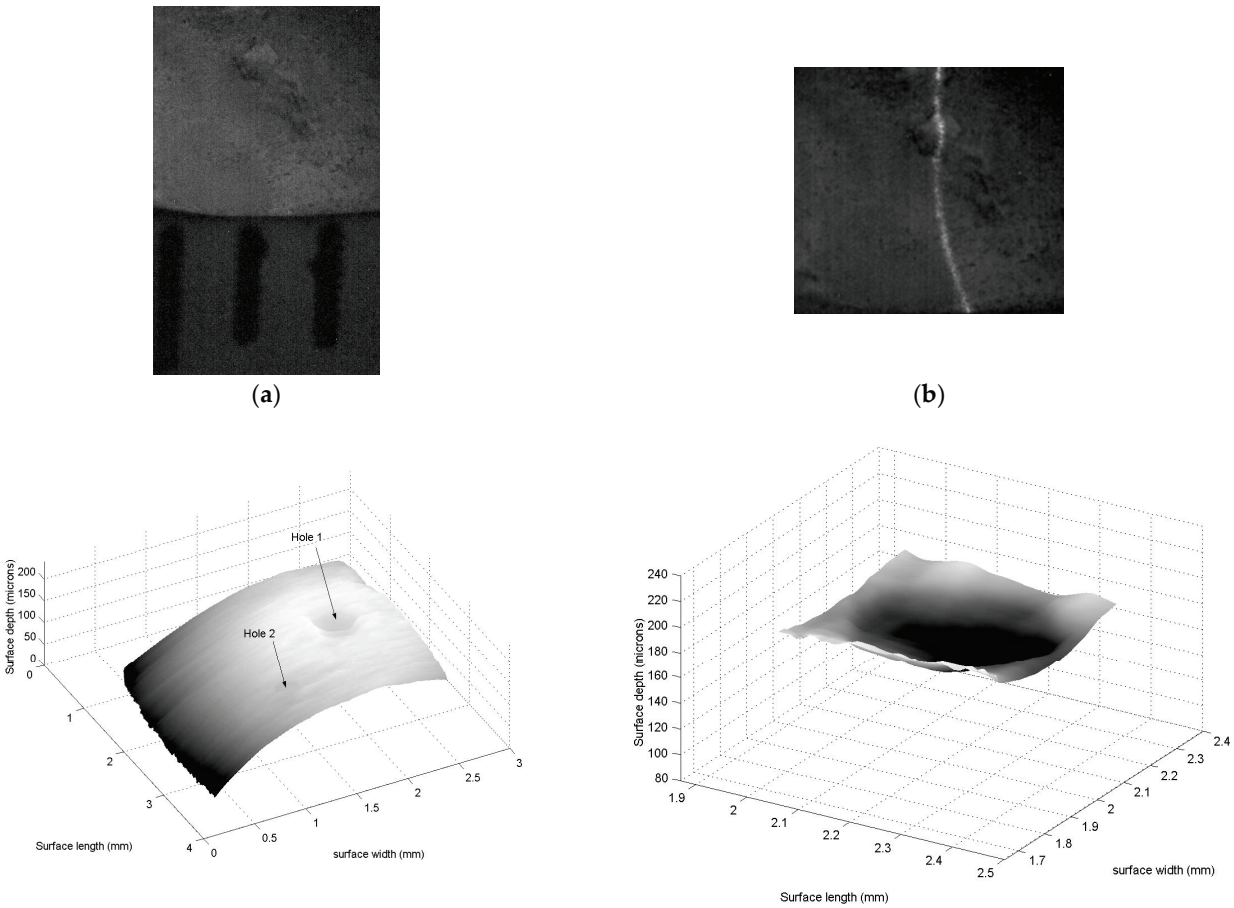


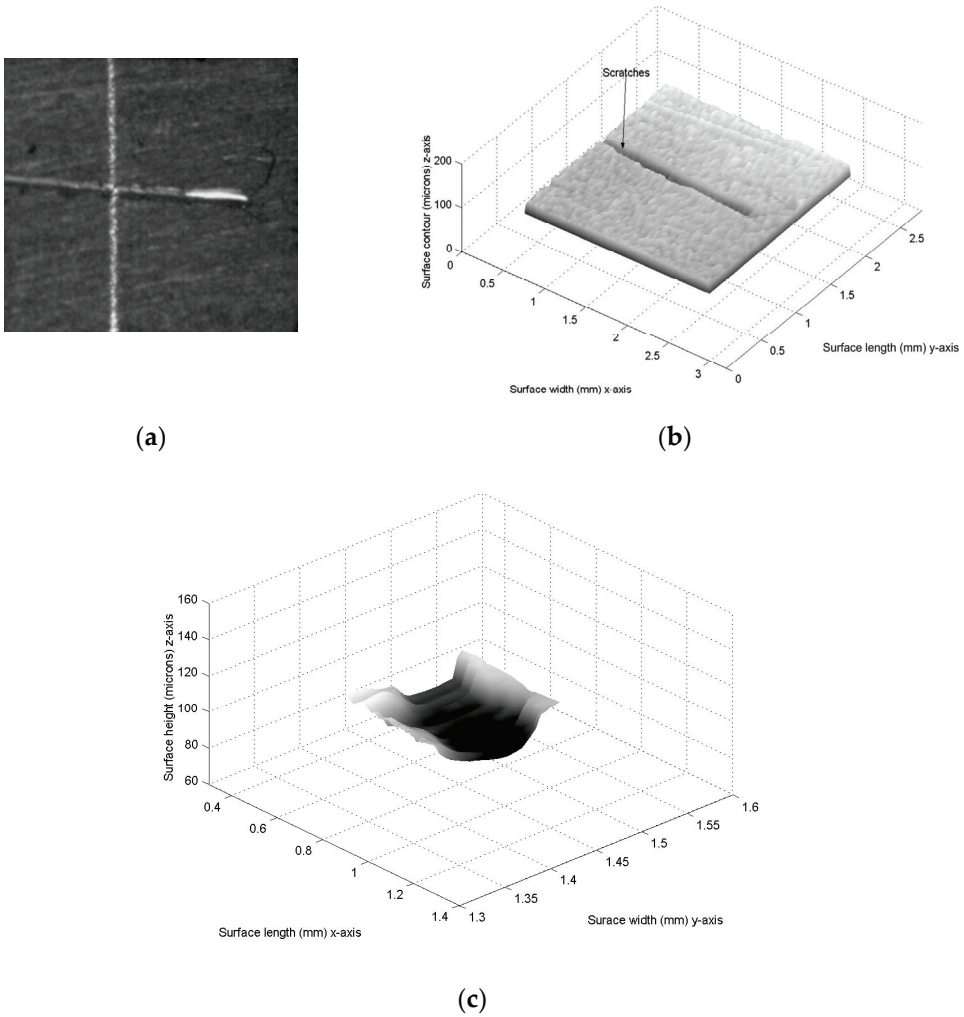
Figure 8. (**a**) Plastic free-form surface to perform surface defect recognition (scale in *mm* in *x*-direction). (**b**) Microlaser line projected onto the free-form surface. (**c**) Microsurface generated by the Bezier surface Equation (13). (**d**) Hole surface used to compute the pattern of affine moment invariants.

In this way, the central moments $\mu_{p,q}$ for each region were computed by means of Equations (11) and (12), where the surface depth is represented by $f(x_{i,j}, y_{i,j}) = z_{i,j}$. Thus, the pattern of affine moment invariants was computed for the free-form surface. When the window covered hole 1, as shown in Figure 8c, a discontinuity appeared in the *y*-axis of the surface profile. This surface discontinuity was detected when the derivative $\partial f(y,x)/\partial y$ changed signs in the *y*-axis. The surface of this hole is shown in Figure 8d, where the hole length was 410 microns in the *x*-axis and the hole width was 480 microns in the *y*-axis. The surface defect depth was determined by computing the difference between the minimum and maximum depths of the surface defect, where the surface profile $f(y,x) = z_{i,j}$ was computed via Equation (22) and the surface profile width $y_{i,j}$ was computed via Equation (23). As expected, the maximum of the surface defect was obtained on the border of the surface defect in the *y*-axis. The hole depth was 34 microns in the *z*-axis, and the bottom of this hole presented surface irregularities. Thus, the pattern of affine moment invariants was

computed, resulting in $I_1 = 5.1340 \times 10^{-6}$, $I_2 = -1.2086 \times 10^{-23}$, $I_3 = 2.3292 \times 10^{-15}$, $I_4 = -9.8397 \times 10^{-20}$, $I_5 = 1.5805 \times 10^{-10}$, $I_6 = 2.8393 \times 10^{-16}$, $I_7 = 7.0254 \times 10^{-9}$, $I_8 = 1.0185 \times 10^{-15}$, $I_9 = 8.9124 \times 10^{-29}$, and $I_{10} = -3.2539 \times 10^{-31}$. This pattern describes a decreasing function from I_1 to I_4, following which the function increases until I_7. Then, the function tends to zero from I_8 to I_{10}. In this case, the peak I_1 was greater than 4.7×10^{-6} and (I_2, I_4) are negative; therefore, the region was recognized as a hole defect, particularly as the surface bottom was greater at the borders than in the center of the *x*- and *y*-axes. In the same way, a surface discontinuity appeared on the surface profile of hole 2, which is marked with an arrow in Figure 8c. The hole length was 260 microns in the *x*-axis, the hole width was 280 microns in the *y*-axis, and the hole bottom was 22 microns in the *z*-axis. Thus, the pattern of affine moment invariants was computed, given as follows: $I_1 = 8.9378 \times 10^{-6}$, $I_2 = -1.3273 \times 10^{-22}$, $I_3 = 1.3318 \times 10^{-14}$, $I_4 = -7.3403 \times 10^{-19}$, $I_5 = 4.7081 \times 10^{-10}$, $I_6 = 1.4533 \times 10^{-15}$, $I_7 = 2.0972 \times 10^{-8}$, $I_8 = 5.2772 \times 10^{-15}$, $I_9 = 1.5830 \times 10^{-27}$, and $I_{10} = -8.9553 \times 10^{-30}$. In this case, the peak I_1 is greater than 4.7×10^{-6} and (I_2, I_4) are negative; therefore, the region is recognized as a hole defect. As the surface bottom was greater at the borders than in the center of both the *x*- and *y*-axes, it was deduced that the pattern of affine moment invariants corresponded to a hole surface defect. Additionally, the pattern of affine invariant moments was computed for all the regions of the free-form surface, but the patterns were different to those for hole and scratch defects.

The fourth microsurface defect recognition test was carried out for the metallic flat surface shown in Figure 9a. The microlaser line was projected to retrieve the surface topography, and the flat surface was scanned in the *x*-axis to allow for computation of the surface depth $z_{i,j}$ and the surface width $y_{i,j}$ via Equations (22) and (23), while the slider platform provided the coordinate $x_{i,j}$. Thus, 228 laser lines were processed to retrieve the flat surface. The accuracy of this surface indicated a relative error of $Er\% = 0.795\%$, as computed via Equation (28). Here, $z_{i,j}$ is the surface measured via contact method, $h_{i,j}$ is the surface contour computed via Equation (22), and $n \cdot m$ is the number of data. Then, Bezier surfaces $S_{0,0}(u,v)$, $S_{1,0}(u,v)$, $S_{1,0}(u,v)$, and $S_{1,1}(u,v)$,. . . . . ., $S_{M,N}(u,v)$ were computed to obtain the surface topography shown in Figure 10b. Here, the scale is indicated in *mm* in the *x*- and *y*-axes, and in microns for the *z*-axis. According to Equation (28), the Bezier surface presented a relative error of $Er\% = 0.601\%$. Then, the recognition of microscratches was performed by computing the pattern of affine moment invariants for each region of the Bezier surface shown in Figure 9b. This procedure was carried out by computing Equations (1)–(10) for each region of the flat surface. For this purpose, Equations (11) and (12) were computed to obtain the central moments of each region. Then, Equations (1)–(10) were computed to obtain the affine moment invariants on the flat surface, yielding $I_1 = 4.0635 \times 10^{-6}$, $I_2 = -2.3280 \times 10^{-29}$, $I_3 = -1.5206 \times 10^{-17}$, $I_4 = -3.3215 \times 10^{-22}$, $I_5 = 1.0203 \times 10^{-10}$, $I_6 = 1.4636 \times 10^{-16}$, $I_7 = 4.1340 \times 10^{-10}$, $I_8 = 5.1978 \times 10^{-16}$, $I_9 = 2.0020 \times 10^{-31}$, and $I_{10} = -4.7761 \times 10^{-39}$. This result is similar to the pattern of affine moment invariants for a flat surface, where the peak I_1 is smaller than 4.7×10^{-6}. Then, the presence of a discontinuity was detected by computing the derivative $\partial f(y,x)/\partial y$ in the *y*-axis, associated with the point at which the derivative changes sign in the *y*-axis. In this way, the window was moved to the location of the scratch marked with an arrow in Figure 9b. In this way, the surface shown in Figure 9c was obtained. The scratch length was 440 microns in the *x*-axis and its width was 202 microns in the *y*-axis. Furthermore, the surface defect depth was determined by computing the difference between the minimum and maximum depth values of the surface defect, where the surface profile $f(y,x) = z_{i,j}$ was computed via Equation (22). The maximum of the surface defect was obtained on the border of the surface defect in the *y*-axis, and the scratch depth was found to be 28 microns in the *z*-axis, with the bottom presenting surface irregularities. Thus, the pattern of affine moment invariants

was computed from the Bezier surface, and the resulting values were $I_1 = 1.5337 \times 10^{-5}$, $I_2 = -2.0332 \times 10^{-24}$, $I_3 = -4.6206 \times 10^{-15}$, $I_4 = -1.3259 \times 10^{-20}$, $I_5 = 1.3140 \times 10^{-9}$, $I_6 = 5.7091 \times 10^{-15}$, $I_7 = 2.8682 \times 10^{-8}$, $I_8 = 2.4603 \times 10^{-14}$, $I_9 = 8.4472 \times 10^{-29}$, and $I_{10} = 2.0184 \times 10^{-30}$. This pattern indicates a decreasing function from I_1 to I_4, after which the function increased until I_7. Then, the function tended to zero from I_8 to I_{10}. In this case, the peak I_1 was greater than 4.7×10^{-6}, and the surface bottom was not greater at the border than in the center of the x-axis. Therefore, the region was recognized as a scratch defect. This criterion was elucidated by moving the window in the x-axis to compute the pattern of the neighboring region. Thus, the pattern of affine moment invariants was computed, yielding $I_1 = 1.6157 \times 10^{-5}$, $I_2 = -1.0939 \times 10^{-24}$, $I_3 = -7.0285 \times 10^{-16}$, $I_4 = -2.1275 \times 10^{-21}$, $I_5 = 1.4549 \times 10^{-10}$, $I_6 = 6.6265 \times 10^{-15}$, $I_7 = 3.1959 \times 10^{-8}$, $I_8 = 2.8683 \times 10^{-14}$, $I_9 = 1.9100 \times 10^{-29}$, and $I_{10} = 3.2143 \times 10^{-31}$. This result is similar to that of the scratch marked by the arrow in Figure 9b. Here, the function decreases from I_1 to I_4, then increases until I_7, and finally tends to zero from I_8 to I_{10}. In this case, the peak I_1 is greater than 4.7×10^{-6} and the surface bottom is not greater at the borders than in the center of the x-axis. Therefore, the region is recognized as a scratch defect.



(**a**) (**b**)

(**c**)

Figure 9. (**a**) Microlaser line projected onto metallic flat surface to perform surface defect recognition. (**b**) Surface generated by the Bezier surface Equation (13). (**c**) Scratch surface used to compute the pattern of affine moment invariants.

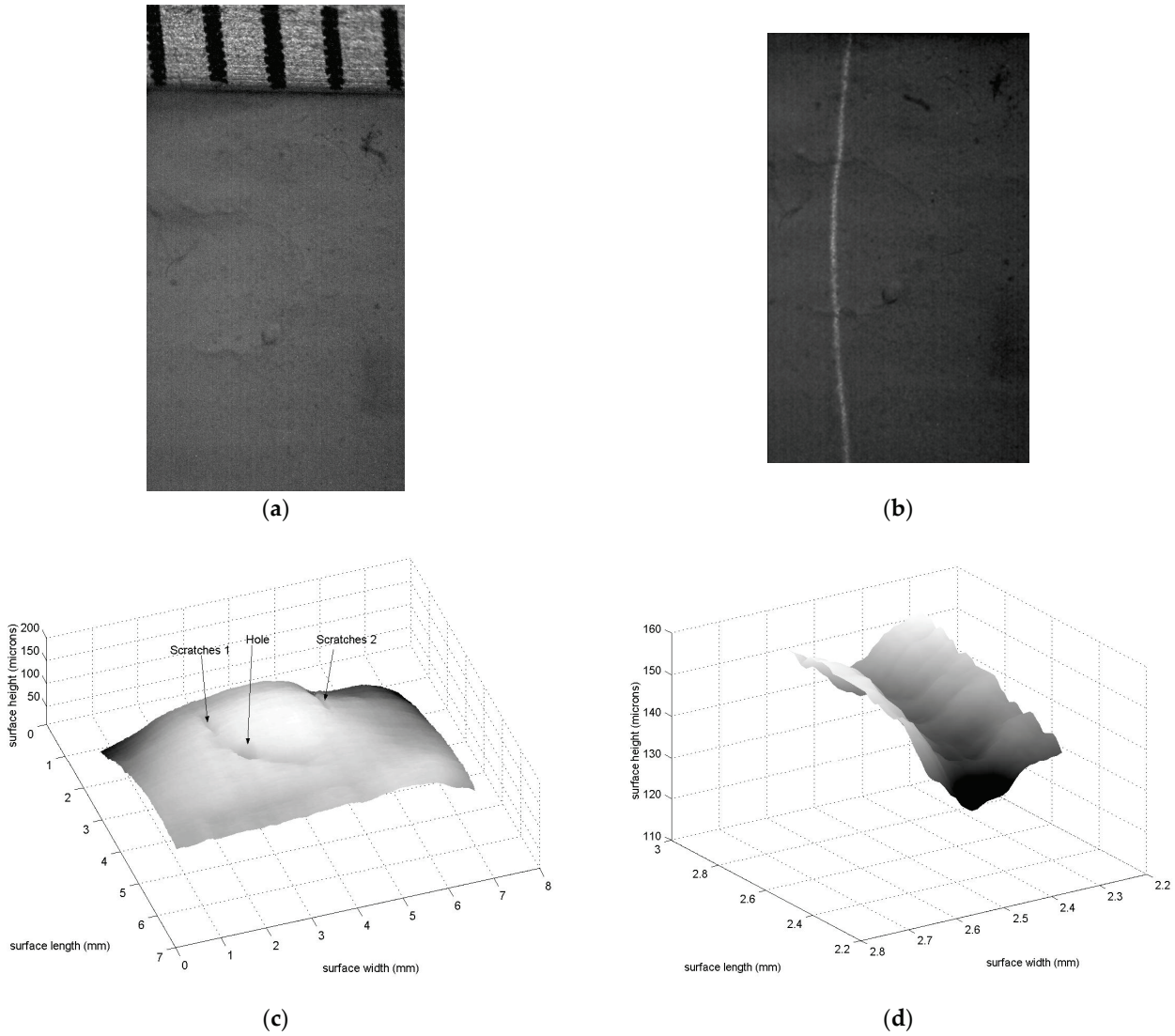


Figure 10. (**a**) Plastic free-form surface used to perform surface defect recognition (scale in *mm* in *x*-direction). (**b**) Microlaser line projected onto the free-form surface. (**c**) Microsurface generated using the Bezier surface Equation (13). (**d**) Scratch surface used to compute the pattern of affine moment invariants.

The fifth microsurface defect recognition test was carried out on the plastic free-form surface shown in Figure 10a. Here, the scale is represented in millimeters in the *x*-direction. Additionally, the microlaser line projected onto the free-form surface is shown in Figure 10b. Thus, the free-form surface was scanned in the *x*-axis to compute the surface depth $z_{i,j}$ and the surface width $y_{i,j}$ via Equations (22) and (23), while the slider platform provided the coordinate $x_{i,j}$. Thus, 310 laser lines were processed to retrieve the free form surface. The contouring accuracy indicated a relative error of $Er\%$ = 0.826%, as computed via Equation (28) in a similar manner as mentioned above. Then, Bezier surfaces $S_{0,0}(u,v)$, $S_{1,0}(u,v)$, $S_{1,0}(u,v)$, and $S_{1,1}(u,v)$, ……, $S_{M,N}(u,v)$ were computed to obtain the surface topography shown in Figure 10c, where the scale is indicated in *mm* for the *x*- and *y*-axes and in microns for the *z*-axis. The Bezier surface accuracy indicated a relative error of $Er\%$ = 0.641%, as computed via Equation (28). Then, microsurface defect recognition was performed by computing the pattern of affine moment invariants from each region of the Bezier surface shown in Figure 10c. For this purpose, Equations (1)–(10) were computed for each region, and Equations (11) and (12) were computed to obtain the central moments for each region.

Then, a discontinuity was detected by computing the derivative $\partial f(y,x)/\partial y$ in the y-axis due to the derivative changing signs in the y-axis. In this way, the window was moved to cover scratch 1 (marked with an arrow in Figure 10c). In this case, the surface shown in Figure 10d was obtained, where the scratch length was 610 microns in the x-axis and the scratch width was 286 microns in the y-axis.

The surface defect depth was also determined by computing the difference between the minimum and maximum depths of the surface defect, where the surface profile $f(y,x) = z_{i,j}$ was computed via Equation (22). The maximum of the surface defect was obtained on the border of the surface defect in the y-axis. Therefore, the depth of scratch 1 was determined as 28 microns in the z-axis. Furthermore, the bottom of the scratch presented surface irregularities. The pattern of affine moment invariants was computed, and the result was as follows: $I_1 = 1.4788 \times 10^{-5}$, $I_2 = -1.6251 \times 10^{-23}$, $I_3 = -8.7892 \times 10^{-17}$, $I_4 = -1.8519 \times 10^{-20}$, $I_5 = 1.2225 \times 10^{-9}$, $I_6 = 5.1200 \times 10^{-15}$, $I_7 = 2.6508 \times 10^{-8}$, $I_8 = 2.2065 \times 10^{-14}$, $I_9 = 2.5372 \times 10^{-28}$, and $I_{10} = 1.1187 \times 10^{-30}$. This pattern describes a decreasing function from I_1 to I_4, after which the function increases until I_7. Then, the function tends to zero from I_8 to I_{10}. In this case, the peak I_1 is greater than 4.7×10^{-6}; therefore, this region was recognized as a scratch, particularly as the surface bottom was not greater at the borders than in the center of the x-axis. This criterion was elucidated by obtaining the pattern of affine moment invariants of the scratch 2 surface defect, resulting in $I_1 = 5.4084 \times 10^{-6}$, $I_2 = 1.5246 \times 10^{-25}$, $I_3 = -1.2930 \times 10^{-15}$, $I_4 = -4.0845 \times 10^{-21}$, $I_5 = 1.8104 \times 10^{-10}$, $I_6 = 3.4704 \times 10^{-16}$, $I_7 = 4.9610 \times 10^{-9}$, $I_8 = 1.2282 \times 10^{-15}$, $I_9 = 3.0332 \times 10^{-30}$, and $I_{10} = -2.6570 \times 10^{-33}$. In this case, the peak I_1 was greater than 4.7×10^{-6}, and the surface bottom was not greater at the borders than in the center of the x-axis. Additionally, the pattern of affine moment invariants was computed for the hole, also marked with an arrow in Figure 10c. Here, the hole length was 460 microns in the x-axis, the hole width was 534 microns in the y-axis, and the hole depth was 46 microns in the z-axis. The hole's bottom presented surface irregularities. The pattern of affine moment invariants is computed, yielding $I_1 = 1.1280 \times 10^{-5}$, $I_2 = -3.0274 \times 10^{-21}$, $I_3 = 1.0087 \times 10^{-13}$, $I_4 = -3.3440 \times 10^{-18}$, $I_5 = 6.5086 \times 10^{-10}$, $I_6 = 2.2408 \times 10^{-15}$, $I_7 = 1.0998 \times 10^{-8}$, $I_8 = 9.1200 \times 10^{-15}$, $I_9 = 4.1001 \times 10^{-26}$, and $I_{10} = -8.2710 \times 10^{-29}$. This pattern describes a decreasing function from I_1 to I_4, while the function increases to I_7 and then tends to zero from I_8 to I_{10}. In this case, the peak I_1 is greater than 4.7×10^{-6}, while I_4 is negative. Therefore, the region was recognized as a hole defect, particularly as the surface bottom was greater at the borders than in the center of both the x- and y-axes. In the same way, the pattern of affine invariant moments was computed for all the regions of the free-form surface, but these differed from the hole and scratch defect patterns.

The sixth microsurface defect recognition test was carried out for the metallic free-form surface shown in Figure 11a, where the scale is indicated in millimeters in the x-axis. The microlaser line projected onto the metallic free form surface is also shown in Figure 11b. Thus, the free-form surface was scanned in the x-axis to compute the surface depth $z_{i,j}$ and the surface width $y_{i,j}$ via Equations (22) and (23), while the slider platform provided the coordinate $x_{i,j}$. Thus, 224 laser lines were processed to retrieve the free-form surface. The contouring accuracy presented a relative error of $Er\% = 0.884\%$, as computed via Equation (28). Then, Bezier surfaces $S_{0,0}(u,v)$, $S_{1,0}(u,v)$, $S_{1,0}(u,v)$,and $S_{1,1}(u,v)$, ……, $S_{M,N}(u,v)$ were computed to obtain the surface topography shown in Figure 11c. Here, the scale is indicated in *mm* for the x- and y-axes and in microns for the z-axis. The Bezier surface accuracy yielded a relative error of $Er\% = 0.664\%$, which was computed via Equation (28). Then, microsurface defect recognition was performed by computing the pattern of affine moment invariants for each region of the Bezier surface shown in Figure 11c. In particular, Equations (1)–(10)

were computed for each region, and Equations (11) and (12) were computed to obtain the central moments for each region. Thus, the affine moment invariants were computed to establish the pattern in each region. Then, a discontinuity was detected by computing the derivative $\partial f(y,x)/\partial y$ in the y-axis, revealing the hole shown in Figure 11c, which corresponded to the location where the derivative changed signs in the y-axis. In this case, the surface shown in Figure 11d was obtained. Here, the hole length was 472 microns in the x-axis, the hole width was 400 microns in the y-axis, and the hole depth was 27 microns in the z-axis, with the hole's bottom presenting surface irregularities. The pattern of affine moment invariants is computed from the Bezier surface, yielding $I_1 = 8.6825 \times 10^{-6}$, $I_2 = -5.7967 \times 10^{-24}$, $I_3 = 3.4759 \times 10^{-16}$, $I_4 = -1.8328 \times 10^{-18}$, $I_5 = 4.4638 \times 10^{-10}$, $I_6 = 1.3420 \times 10^{-15}$, $I_7 = 1.9741 \times 10^{-8}$, $I_8 = 4.8606 \times 10^{-15}$, $I_9 = 5.29607 \times 10^{-27}$, and $I_{10} = -3.9497 \times 10^{-29}$. This pattern describes a decreasing function from I_1 to I_4, after which the function increases to I_7. Then, the function tends to zero from I_8 to I_{10}. In this case, the peak I_1 was greater than 4.7×10^{-6}. Therefore, the region is recognized as a hole defect, particularly as the surface bottom was greater at the borders than in the center of both the x- and y-axes. In the same way, the pattern of affine invariant moments was computed for all the regions of the free-form surface, but these patterns differed from the hole and scratch defect patterns.

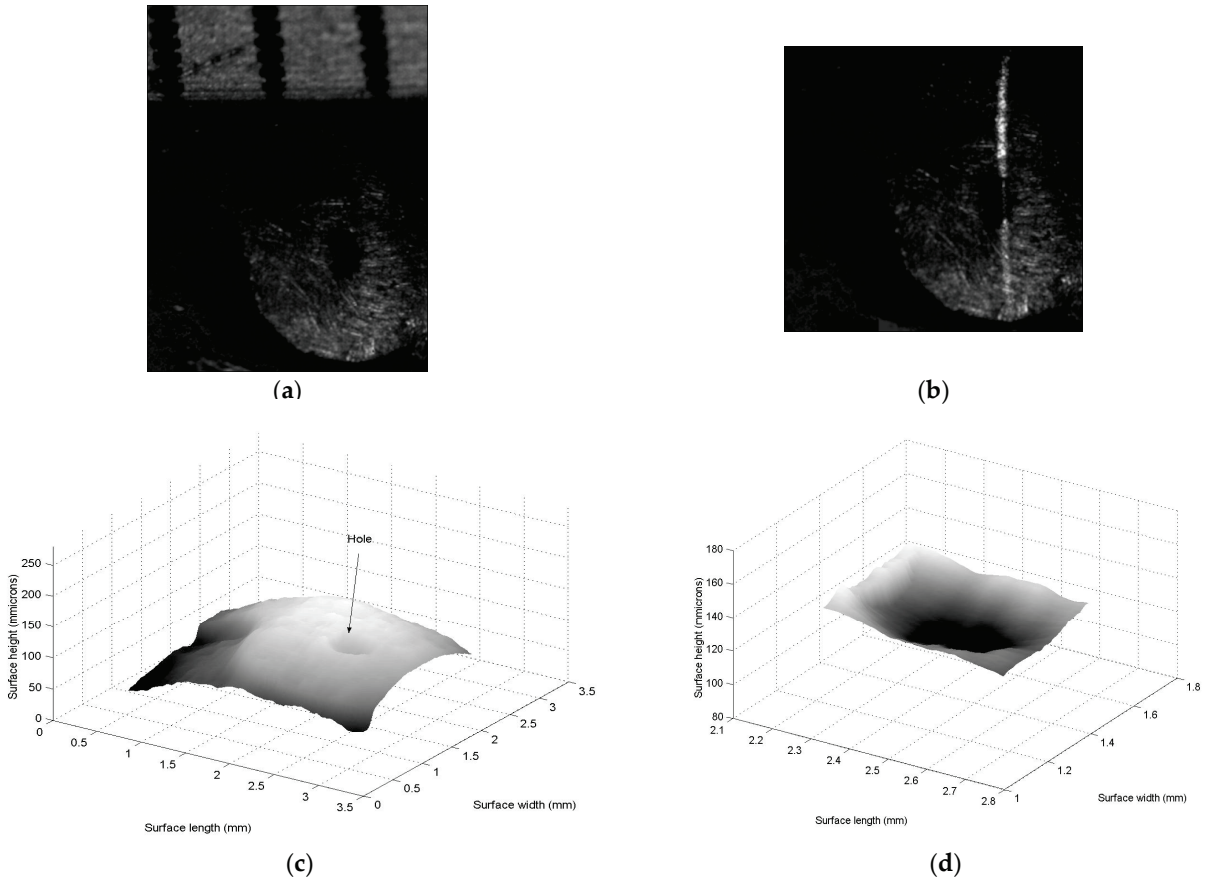


Figure 11. (**a**) Metallic free-form surface used to perform surface defect recognition (scale in *mm* in x-direction). (**b**) Microlaser line projected onto the free-form surface. (**c**) Microsurface generated using the Bezier surface Equation (13). (**d**) Hole surface used to compute the pattern of affine moment invariants.

In the following, the contributions of the proposed microsurface defect recognition are described based on its advantages over the existing hole and scratch detection methods using optical-microscope-based systems. The advantages of the proposed visual testing

method are described as follows. First, the patterns of affine moment invariants and microlaser scanning provide high accuracy (with a maximum relative error of 0.721% in the tests) to recognize microholes and scratches. The validation of this accuracy was performed by computing the pattern of affine moment invariants from the surface profiles measured using the contact method and microlaser line projection. The pattern recognition of holes and scratches using the contact method is considered to be the most accurate procedure to detect surface defects as this method utilizes the real surface profile. Therefore, the pattern of affine moment invariants via microlaser line projection was compared with respect to that obtained via the contact method to obtain the accuracy. In this way, the accuracy of patterns of affine moment invariants was computed as the relative error by means of Equation (28), where $z_{i,j}$ denotes the affine moment invariants computed from the surface measured via contact method, $h_{i,j}$ is the affine moment invariants computed via the microlaser line Equation (22), and $n \cdot m$ is the number of data. In particular, $z_{i,j}$ and $h_{i,j}$ are substituted by (I_1, I_2, I_3, I_4, I_5, I_6, I_7, I_8, I_9, I_{10}) by employing the sub-index $z_{i,j} = I_{\mathrm{i}}$ for $j = 0$. In this way, the accuracy provided by the microscope vision system and the affine moment invariants was found to be less than 2%, which is the level typically provided by traditional defect detection methods. However, it should be noted that, for traditional defect detection methods, the accuracy is computed as (TP + TN)/(TP + FP +TN + FN) by means of the expressions for precision = TP/(TP + FP) and recall = TP/(TN + FN) [35]. Here, TP denotes true positives, FP denotes false positives, TN denotes true negatives, and FN denotes false negatives. Overall, the accuracy obtained when using the pattern of affine moment invariants provided an advantage over traditional optical-microscope-system-based methods due to the obtained relative error being lower than 2%. Second, the use of affine moment invariants and microlaser line contouring provides good robustness in terms of the characterization of microholes and scratches. In this regard, a hole surface defect contoured using a microlaser line provides the same pattern of affine moment invariants. This allowed us to consistently recognize hole surface defects in each test. In the same way, scratch surface defects contoured via microlaser line always provide the same pattern of affine moment invariants. Thus, scratch surface defects can also be consistently recognized. In addition, flat and cylindrical surfaces contoured via microlaser lines produced the same respective patterns of affine moment invariants in each test. Third, microlaser line contouring provides the real topography of microsurfaces as the microlaser line reflects the real surface contour onto the camera's image plane. In contrast, traditional optical microscope systems do not retrieve a surface contour to perform surface defect recognition. Based on these statements, the recognition of microholes and scratches has been achieved in a generally superior manner. A further discussion of the contributions of the proposed microsurface defect recognition approach is provided in Section 4.

4. Discussion

The viability of a microsurface defect recognition approach is determined by means of its recognition accuracy [35], so the capability of the proposed method to effectively recognize microholes and scratches was deduced through calculation of the recognition accuracy [36,37]. In this way, the contribution of the proposed microsurface defect recognition approach was established, indicating the high accuracy of hole and scratch recognition. In particular, the accuracy of the microsurface defect recognition approach was determined through a comparison with defect recognition based on a contact method [38,39]. Furthermore, the effectiveness of recognition indicated the viability of the method. Regarding the proposed microsurface defect recognition approach using patterns of affine moment invariants, the recognition accuracy and the efficiency indicated that it yields good results. For instance, the proposed approach for microsurface defect recognition via affine moment

invariants and microlaser line contouring consistently recognizes hole defects; this is because hole defects always produce the same pattern of affine moment invariants. This pattern is described as a decreasing function from I_1 to I_4, then increasing to I_7 and tending to zero from I_8 to I_{10}. Here, the peak I_1 is greater than 4.7×10^{-6}, and the surface depth is greater at the borders than in the center of both the x- and y-axes. A region satisfying these conditions can be effectively recognized as a hole defect. In the same way, the microsurface defect recognition approach consistently recognizes scratch defects as scratches always produce the same pattern of affine moment invariants. In particular, this pattern presents a decreasing function from I_1 to I_4 and then increases to I_7 and tends to zero from I_8 to I_{10}. Furthermore, the peak I_1 is greater than 4.7×10^{-6}, and the surface bottom is not greater at the borders than in the center in the x-axis. A region satisfying these conditions can be effectively recognized as a scratch defect. To elucidate the viability of the proposed surface defect recognition approach, the accuracies of traditional methods for the detection of hole and scratch defects are mentioned in the following. The accuracy of surface defect recognition is related to the surface contouring, which is not included in traditional surface defect recognition methods. Typically, the recognition of holes and scratches is performed with a relative error exceeding 3.8% when using traditional optical microscope systems [40,41]. In these approaches, the surface data of holes and scratches are deduced through gray-level microscope images. Therefore, surface defect recognition is not performed utilizing the surface contour. This lack of microsurface contouring leads to reduced surface defect recognition accuracy. The traditional optical-microscope-based techniques may also characterize the surface defect patterns through the use of image intensity data [42,43]. However, the image intensity does not reproduce the real surface contours. Therefore, traditional optical microscope imaging systems do not characterize the forms of microsurface defect patterns accurately. In contrast, the microlaser line reflects the accurate form of the surface contour on the image plane through the microscope. This surface contouring leads to consistent patterns of affine moment invariants being provided for holes and scratches. This statement is elucidated by means of the hole and scratch surface defect recognition results provided in Section 3, where the accuracy of surface defect recognition was within a relative error of 0.721%. This indicates a certain degree of enhancement over traditional microscope imaging systems. To elucidate this improvement, the accuracy of the traditional optical microscope imaging systems is discussed in the following. A deep learning approach performing hole surface defect detection via image intensity obtained a relative error over 3%. Furthermore, surface scratch defect detection was carried out through a computer vision approach based on intensity descriptors, with a relative error over 3% [44]. Moreover, surface scratch defect detection was carried out using a deep learning approach, also with a relative error over 3% [45]. In the same way, a deep learning model performing hole and scratch detection yielded a relative error exceeding 3% [46]. Based on these results, it can be established that the proposed surface defect recognition approach utilizing the pattern of affine moment invariants and microlaser contouring presents superior accuracy when compared to traditional surface defect detection systems. To elucidate this statement, the accuracy values of the traditional visual testing methods for detecting holes and scratches were compared with respect to the proposed recognition approach. For this purpose, the accuracy and performance of traditional defect detection methods were computed according to the expression accuracy = (TP + TN)/(TP + FP + TN + FN). In this way, the accuracies of the visual testing methods were obtained, as presented in Table 3. Here, the visual testing methods are listed in the first column, the algorithmic structure of each method is mentioned in the second column, the tested surface is depicted in the third column, the defect shape is mentioned in the fourth column, and the error (in terms of percentage) is provided in the fifth column. In particular, a machine vision approach based on edge

detection to detect holes and scratches on cylindrical surfaces obtained an error of 5% [47]. A machine vision approach based on segmentation detected holes and scratches on flat surfaces with an error of 3% [48]. A machine vision approach based on regularization detected holes and scratches on flat surfaces with an error of 5% [49]. A machine vision approach based on the Fourier transform detected holes and scratches on flat surfaces with an error of 6% [50]. A statistics-based approach using the local binary pattern detected holes and scratches on flat surfaces with an error of 3% [51]. A statistics-based method using a Gaussian function detected holes and scratches on cylindrical surfaces with an error of 2% [52]. A machine learning approach based on neural networks detected holes and scratches on flat surfaces with an error of 9% [53]. A machine learning approach based on convolutional neural networks detected holes and scratches on cylindrical surfaces with an error of 5% [54]. A machine learning approach based on self-supervised learning detected holes and scratches on flat surfaces with an error of 2.1% [55]. A deep learning approach based on multi-scale and channel-compressed mechanisms detected holes and scratches with an error of 5% [56]. A deep learning approach based on convolutional neural networks detected holes and scratches with an error of 2% [57]. A deep learning approach based on residual neural networks detected holes and scratches with an error of 3.3% [57]. A deep learning and machine vision approach based on convolutional neural networks detected holes and scratches with an error of 3.3% [58,59]. Additionally, the time consumption for training the convolutional neural network was over 450 s. Therefore, hole and scratch detection via deep learning takes over 450 s. While the times consumed by the statistics, machine vision, and machine learning approaches are generally much less than 450 s, their error is increased. In comparison, the proposed hole and scratch recognition method consistently obtained an error smaller than 2%, while its time consumption is moderately lower than that of traditional visual testing methods.

Table 3. Accuracy of existing visual testing methods in comparison with the proposed method.

Visual Testing Method	Algorithm Structure	Tested Surface	Defect Shape	Recognition Error (%)
Machine vision	Edge detection	Cylindrical surface	Holes and scratches	5%
Machine vision	Segmentation and template statistics	Flat surface	Holes and scratches	3%
Machine vision	Model-based Regularization	Flat surface	Holes and scratches	5%
Machine vision	Fourier Transform	Flat surface	Holes and scratches	6%
Statistical	Local binary pattern	Flat surface	Holes and scratches	3%
Statistical	Segmentation via Gaussian Function	Cylindrical surface	Holes and scratches	2%
Machine learning	BP neural network	Flat surface	Holes and scratches	9%
Machine learning	Convolutional neural networks	Cylindrical surface	Holes and scratches	5%
Machine learning	Self-supervised learning and image segmentation	Flat surface	Holes and scratches	2.1%
Deep Learning	Multi-scale and channel-compressed features	Flat surface	Holes and scratches	5%
Deep Learning	Convolutional neural networks	Flat surface	Holes and scratches	2%
Deep Learning	Residual neural networks	Flat surface	Holes and scratches	3.3%
Deep Learning and machine vision	Convolutional neural networks	Flat surface	Holes and scratches	3%
Deep Learning and machine vision	Convolutional neural networks	Cylindrical surface	Holes and scratches	4%
Proposed method	Affine moment invariants and microlaser line projection	Flat, cylindrical, and free-form surfaces	Holes and scratches	0.721%

Additionally, the effectiveness of the proposed surface defect recognition was determined via the structured procedure, which allows for the recognition of surface defects. For instance, microlaser line contouring allows the surface topography to be retrieved with great accuracy. Furthermore, the Bezier surface Equation (13) provides all the surface points necessary to compute the pattern of affine moment invariants. Therefore, the pattern of affine moment invariants yields the same characteristic patterns for holes and scratches, respectively. In the same way, the method produces the same characteristic patterns for flat and cylindrical surfaces. Therefore, the pattern-based characterization is computed by means of efficient procedures that facilitate robust surface defect recognition. These statements were validated through the trials focused on microhole and scratch recognition on various surfaces, as presented in Section 3. The improvements provided by the proposed approach were further deduced based on a comparison with deep learning methods, which are commonly used to detect holes and scratches at present. A deep learning model has been implemented using a convolutional neural network and a large data set of images related to surface defects [60]. The deep learning approach involves performing training utilizing several hundred images or more [61] that do not necessarily provide the same pattern. This is because the characteristic patterns are computed from image intensity data, which can vary according to the surface's reflectance, light source, and viewer angle. Therefore, surface defect recognition via patterns of affine moment invariants and microlaser line contouring provides a more suitable, robust, and effective structure when compared to those methods based on characterization via image intensity. This statement was validated by means of the steps of the proposed method, where the capability of the proposed approach to enable microsurface defect recognition using the pattern of affine moment invariants and microlaser line contouring was proven. Furthermore, the simple optical-microscope-based arrangement provides an inexpensive system, making the proposed microsurface defect recognition approach more suitable. Thus, the proposed surface defect recognition approach can be considered as a novel contribution in the field of microhole and scratch surface defect recognition.

The microscope vision system was used to inspect a surface area of 3 cm in the y-axis and 60 cm in the x-axis in a single movement as a slider is used to move the microscope vision system a distance of 60 cm in the x-axis while observing a 3 cm region in the y-axis. To inspect surfaces greater than 3 cm in the y-axis, the slider platform must also move the microscope in the y-axis. In this way, the dimensions of the slider platform should be adjusted according to the surface area to be inspected in the x- and y-axes. Additionally, an important condition of the system is to capture the microlaser line using the microscope system as the microlaser line allows the surface profile to be determined. Therefore, it may be necessary to adjust the microscope parameters to focus on the microlaser line.

The microsurface defect recognition approach was implemented on a computer at 2.4 GHz of velocity. Regarding this computer, 64 images are captured per second through the CCD camera. The computer moves the slider platform by means of a computer program. Thus, the contouring of a transverse section is computed in 0.0049 s through the processing of one laser line image. The overall time for surface defect recognition includes surface contouring via laser line scanning, Bezier surface representation, and the calculation of the pattern of fine moment invariants for each region. In particular, hole surface defect recognition on the flat metallic surface was performed in 102.43 s, hole and scratch surface defect recognition on the cylindrical surface was performed in 176.26 s, hole recognition on the free-form surface was performed in 192.65 s, scratch recognition on the flat surface shown in Figure 9b was performed in 189.88 s, hole and scratch recognition on the free-form surface shown in Figure 10c was performed in 207.12 s, and hole recognition on the free-form surface shown in Figure 11c was performed in 186.53 s.

5. Conclusions

A technique to perform hole and scratch surface defect recognition using the pattern of affine moment invariants and microlaser line contouring was presented. The surface defect recognition results computed using the proposed approach demonstrated improved accuracy when compared to traditional optical microscope imaging systems. The capability of the microsurface defect recognition approach was validated in terms of the recognition accuracy of surface defects and its effectiveness in terms of characterizing hole and scratch surface patterns. Overall, the joint use of the pattern of affine moment invariants and microlaser line contouring improved the accuracy of surface defect recognition, leading to a relative error of 0.721%. This high accuracy was obtained as the computational process for microhole and scratch surface defect recognition involves the real surface contour. Furthermore, the developed structure enables more efficient and robust pattern characterization than traditional microscope imaging systems. Thus, the proposed surface defect recognition approach can be considered a good tool for the recognition of hole and scratch defects on flat and cylindrical surfaces. Moreover, the simple microscope system used increases the capability to perform microsurface defect recognition. Thus, the proposed microhole and scratch surface defect recognition approach based on patterns of affine moment invariants and microlaser line contouring can be considered a highly effective and novel contribution to relevant fields.

Funding: This research received no external funding.

Institutional Review Board Statement: Not applicable.

Informed Consent Statement: Not applicable.

Data Availability Statement: Data is contained within the article.

Conflicts of Interest: The author declares no conflicts of interest.

References

1. Ghate, N.D.; Shrivastava, A. Numerical and experimental investigation of complex surface topography evolution during laser surface modification with raster scan. *J. Manuf. Process.* **2021**, *69*, 368–377. [CrossRef]
2. Wen, X.; Shan, J.; He, Y.; Song, K. Steel surface defect recognition: A survey. *Coatings* **2023**, *13*, 17. [CrossRef]
3. Zhang, J.; Li, Z.; Hao, R.; Wang, X.; Du, X.; Yan, B.; Ni, G.; Liu, J.; Liu, L.; Liu, Y. Classification of microscopic laser engraving surface defect images based on transfer learning method. *Electronics* **2021**, *10*, 1993. [CrossRef]
4. Gupta, M.; Khan, M.A.; Butola, R.; Singari, R.M. Advances in applications of non-destructive testing (NDT): A review. *Adv. Mater. Process. Technol.* **2021**, *8*, 2286–2307. [CrossRef]
5. Ha, J.M.; Seung, H.M.; Choi, W. Autoencoder-based detection of near-surface defects in ultrasonic testing. *Ultrasonics* **2022**, *119*, 106637. [CrossRef]
6. Liu, S.; Wang, X.; Liu, Z.; Wang, Y.; Chen, H. Machined surface defects monitoring through VMD of acoustic emission signals. *J. Manuf. Process.* **2022**, *79*, 587–599. [CrossRef]
7. Xu, H.; Yan, Z.H.; Ji, B.W.; Huang, P.F.; Cheng, J.P.; Wu, X.D. Defect detection in welding radiographic images based on semantic segmentation methods. *Measurement* **2022**, *188*, 110569. [CrossRef]
8. Wu, Q.; Dong, K.; Qin, X.; Hu, Z.; Xiong, X. Magnetic particle inspection: Status, advances, and challenges—Demands for automatic non-destructive testing. *NDT E Int.* **2024**, *143*, 103030. [CrossRef]
9. Kutman, M.K.; Muftuler, F.Z.B.; Harmansah, C.; Kozgus Guldu, O. Use of bacteria as fluorescent penetrant for penetrant testing (PT). *J. Nondestruct. Eval.* **2020**, *39*, 15. [CrossRef]
10. Mondal, A.; Kumar Halder, A.; Nayak, S.; Ranjan Kumar, R.; Chakraborty, A.; Kumar Gudimetla, S.; Ghosh, R.; Dubois, M. Root cause analysis of indentation mark defect on Zn coated steel sheet in continuous galvanizing line. *Eng. Fail. Anal.* **2024**, *157*, 107883. [CrossRef]
11. Zhou, J.; Li, H.; Lu, L.; Cheng, Y. Machine vision-based surface defect detection study for ceramic 3D printing. *Machines* **2024**, *12*, 166. [CrossRef]
12. Zhang, W.; Hu, Y.; Shan, H.; Liu, E. An online automatic carbide insert high-resolution surface defect detection system based on template-guided model. *Expert Syst. Appl.* **2024**, *238*, 122089.

13. Zhang, J.; Kang, X.; Ni, H.; Ren, F. Surface defect detection of steel strips based on classification priority YOLOv3-dense network. *Ironmak. Steelmak.* **2021**, *48*, 547–558.
14. Wang, J.; Li, Q.; Gan, J.; Yu, H.; Yang, X. Surface defect detection via entity sparsity pursuit with intrinsic priors. *IEEE Trans. Ind. Inform.* **2020**, *16*, 141–150.
15. Qu, T.; Zou, L.; Zhang, Q.; Chen, X.; Fan, C. Defect detection on the fabric with complex texture via dual-scale over-complete dictionary. *J. Text. Inst.* **2016**, *107*, 743–756.
16. Yan, Y.; Kaneko, S.; Asano, H. Accumulated and aggregated shifting of intensity for defect detection on micro 3D textured surfaces. *Pattern Recognit.* **2020**, *98*, 107057.
17. Zorić, B.; Matić, T.; Hocenski, Ž. Classification of biscuit tiles for defect detection using Fourier transform features. *ISA Trans.* **2022**, *125*, 400–414.
18. Chen, Y.; Ding, Y.; Zhao, F.; Zhang, E.; Wu, Z.; Shao, L. Surface defect detection methods for industrial products: A review. *Appl. Sci.* **2021**, *11*, 76. [CrossRef]
19. Massaro, A.; Dipierro, G.; Cannella, E.; Galiano, A.M. Comparative analysis among discrete Fourier transform, k-means and artificial neural networks image processing techniques oriented on quality control of assembled tires. *Information* **2020**, *11*, 257. [CrossRef]
20. Zhou, Y. Research on image-based automatic wafer surface defect detection algorithm. *J. Image Graph.* **2019**, *7*, 26–31.
21. Wang, J.; Xu, G.; Li, C.; Wang, Z.; Yan, F. Surface defects detection using non-convex total variation regularized RPCA with kernelization. *IEEE Trans. Instrum. Meas.* **2021**, *70*, 5007013. [CrossRef]
22. Luo, Q.; Fang, X.; Liu, L.; Yang, C.; Sun, Y. Automated visual defect detection for flat steel surface: A Survey. *IEEE Trans. Instrum. Meas.* **2020**, *69*, 626–644. [CrossRef]
23. Mariniuc, A.M.; Cojocaru, D.; Abagiu, M.M. Building surface defect detection using machine learning and 3D scanning techniques in the construction domain. *Buildings* **2024**, *14*, 669. [CrossRef]
24. Li, R.; Jin, M.; Paquit, V.C. Geometrical defect detection for additive manufacturing with machine learning models. *Mater. Des.* **2021**, *206*, 109726. [CrossRef]
25. Wei, B.; Hao, K.; Gao, L.; Tang, X. Detecting textile micro-defects: A novel and efficient method based on visual gain mechanism. *Inf. Sci.* **2020**, *541*, 60–74. [CrossRef]
26. Demir, K.; Ay, M.; Cavas, M. Automated steel surface defect detection and classification using a new deep learning-based approach. *Neural Comput. Applic.* **2023**, *35*, 8389–8406.
27. Shaikh, S.; Hujare, D.; Yadav, S. Surface defect detection using convolutional neural network model architecture. *J. Eng. Res. Sci.* **2022**, *1*, 134–144. [CrossRef]
28. Tao, X.; Zhang, D.; Ma, W.; Liu, X.; Xu, D. Automatic metallic surface defect detection and recognition with convolutional neural networks. *Appl. Sci.* **2018**, *8*, 1575. [CrossRef]
29. Bai, T.; Gao, J.; Yang, J.; Yao, D. A study on railway surface defects detection based on machine vision. *Entropy* **2021**, *23*, 1437. [CrossRef]
30. Liu, J.; Li, D.; Tao, W.; Yan, L. An automatic method for generating affine moment invariants. *Pattern Recognit. Lett.* **2007**, *28*, 2295–2304.
31. Suk, T.; Flusser, J. Affine moment invariants generated by graph method. *Pattern Recognit.* **2011**, *44*, 2047–2056.
32. Tan, K.C.; Chiam, S.C.; Mamun, A.A.; Goh, C.K. Balancing exploration and exploitation with adaptive variation for evolutionary multi–objective optimization. *Eur. J. Oper. Res.* **2009**, *197*, 701–713.
33. Muñoz-Rodríguez, J.A.; Rodríguez-Vera, R. Evaluation of the light line displacement location for object shape detection. *J. Mod. Opt.* **2003**, *50*, 137–154.
34. Yu, H.; Huang, Q.; Zhao, J. Fabrication of an optical fiber micro-sphere with a diameter of several tens of micrometers. *Materials* **2014**, *7*, 4878–4895. [CrossRef] [PubMed]
35. Cui, L.; Jiang, X.; Xu, M.; Li, W.; Lv, P.; Zhou, B. SDDNet: A fast and accurate network for surface defect detection. *IEEE Trans. Instrum. Meas.* **2021**, *70*, 2505713.
36. Usamentiaga, R.; Lema, D.G.; Pedrayes, O.D.; Garcia, D.F. Automated surface defect detection in metals: A comparative review of object detection and semantic segmentation using deep learning. *IEEE Trans. Ind. Appl.* **2022**, *58*, 4203–4213.
37. Lin, H.I.; Wibowo, F.S. Image data assessment approach for deep learning-based metal surface defect-detection systems. *IEEE Access* **2021**, *9*, 47621–47638.
38. Konovalenko, I.; Maruschak, P.; Brezinová, J.; Viňáš, J.; Brezina, J. Steel surface defect classification using deep residual neural network. *Metals* **2020**, *10*, 846. [CrossRef]
39. Choi, E.; Sul, O.; Lee, J.; Seo, H.; Kim, S.; Yeom, S.; Ryu, G.; Yang, H.; Shin, Y.; Lee, S.B. Biomimetic tactile sensors with bilayer fingerprint ridges demonstrating texture recognition. *Micromachines* **2019**, *10*, 642. [CrossRef]
40. Lee, Y.K.; Lee, S.; Kim, S.H. Real-time defect monitoring of laser micro-drilling using reflective light and machine learning models. *Int. J. Precis. Eng. Manuf.* **2024**, *25*, 155–164. [CrossRef]

41. Jiang, Q.; Tan, D.; Li, Y.; Ji, S.; Cai, C.; Zheng, Q. Object detection and classification of metal polishing shaft surface defects based on convolutional neural network deep learning. *Appl. Sci.* **2020**, *10*, 87. [CrossRef]
42. Williams, J.; Dryburgh, P.; Clare, A.; Rao, P.; Samal, A. Defect detection and monitoring in metal additive manufactured parts through deep learning of spatially resolved acoustic spectroscopy signals. *Smart Sustain. Manuf. Syst.* **2018**, *2*, 204–226. [CrossRef]
43. Fu, G.; Sun, P.; Zhu, W.; Yang, J.; Cao, Y.; Yang, Y.M.; Cao, Y. A deep-learning-based approach for fast and robust steel surface defects classification. *Opt. Lasers Eng.* **2019**, *121*, 397–405.
44. Juhler Hansen, A.; Moeslund, T.B.; Knoche, H. Defect or design? leveraging the angle of opportunity for detecting Scratches on brushed aluminium surfaces. *IEEE Access* **2021**, *9*, 99526–99538.
45. Zheng, X.; Zheng, S.; Kong, Y.; Chen, J. Recent advances in surface defect inspection of industrial products using deep learning techniques. *Int. J. Adv. Manuf. Technol.* **2021**, *113*, 35–58.
46. Xia, K.; Lv, Z.; Zhou, C.; Gu, G.; Zhao, Z.; Liu, K.; Li, Z. Mixed receptive fields augmented YOLO with multi-path spatial pyramid pooling for steel surface defect detection. *Sensors* **2023**, *23*, 5114. [CrossRef]
47. Zhou, P.; Zhang, C.; Zhou, G.; He, Z.; Yan, X.; Wang, S.; Sun, M.; Hu, B. Whole surface defect detection method for bearing rings based on machine vision. *Meas. Sci. Technol.* **2023**, *34*, 015017.
48. Jia, L.; Chen, C.; Xu, S.; Shen, J. Fabric defect inspection based on lattice segmentation and template statistics. *Inf. Sci.* **2020**, *512*, 964–984.
49. Tsai, D.M.; Fan, S.K.S.; Chou, Y.H. Auto-annotated deep segmentation for surface defect detection. *IEEE Trans. Instrum. Meas.* **2021**, *70*, 5011410.
50. Si, J.; Kim, S. V-DAFT: Visual technique for texture image defect recognition with denoising auto encoder and Fourier Transform. *Signal Image Video Process.* **2024**, *18*, 7405–7418.
51. Luo, Q.; Fang, X.; Sung, Y.; Liu, L.; Ai, J.; Yang, C.; Simpson, O. Surface defect classification for hot-rolled Steel strips by selectively dominant Local binary patterns. *IEEE Access* **2019**, *7*, 23488–23499. [CrossRef]
52. Yu, D.; Zhang, X.; Zhou, J.; Wu, N. An enhancement algorithm based on adaptive updating template with Gaussian model for Si3N4 ceramic bearing roller surface defects detection. *Ceram. Int.* **2022**, *48*, 6672–6680.
53. Chen, W.; Zou, B.; Yang, J.; Huang, C.; Yao, P.; Liu, J. The machined surface defect detection of improved superpixel segmentation and two-level region aggregation based on machine vision. *J. Manuf. Process.* **2022**, *80*, 287–301. [CrossRef]
54. Huang, Y.C.; Hung, K.C.; Lin, J.-C. Automated machine learning system for defect detection on cylindrical metal surfaces. *Sensors* **2022**, *22*, 9783. [CrossRef] [PubMed]
55. Xu, R.; Hao, R.; Huang, B. Efficient surface defect detection using self-supervised learning strategy and segmentation network. *Adv. Eng. Inform.* **2022**, *52*, 101566. [CrossRef]
56. Lv, X.; Duan, F.; Jiang, J.J.; Fu, X.; Gan, L. Deep metallic surface defect detection: The new benchmark and detection network. *Sensors* **2020**, *20*, 1562. [CrossRef]
57. Konovalenko, I.; Maruschak, P.; Brevus, V. Steel surface defect detection using an ensemble of deep residual neural networks. *J. Comput. Inf. Sci. Eng.* **2022**, *22*, 014501. [CrossRef]
58. Yang, H.; Wang, Y.; Hu, J.; He, J.; Yao, Z.; Bi, Q. Deep learning and machine vision-based inspection of rail surface defects. *IEEE Trans. Instrum. Meas.* **2022**, *71*, 5005714. [CrossRef]
59. Singh, S.A.; Choudhari, S.J.; Desai, K.A. Augmenting human-guided progressive learning with machine vision systems for robust surface defect detection. *Adv. Eng. Inform.* **2024**, *62*, 102906. [CrossRef]
60. Yue, X.; Chen, J.; Zhong, G. Metal surface defect detection based on metal-YOLOX. *Int. J. Netw. Dyn. Intell.* **2023**, *2*, 100020. [CrossRef]
61. Deng, H.; Cheng, Y.; Feng, Y.; Xiang, J. Industrial laser welding defect detection and image defect recognition based on deep learning model developed. *Symmetry* **2021**, *13*, 1731. [CrossRef]

Disclaimer/Publisher's Note: The statements, opinions and data contained in all publications are solely those of the individual author(s) and contributor(s) and not of MDPI and/or the editor(s). MDPI and/or the editor(s) disclaim responsibility for any injury to people or property resulting from any ideas, methods, instructions or products referred to in the content.

MDPI AG
Grosspeteranlage 5
4052 Basel
Switzerland
Tel.: +41 61 683 77 34

Coatings Editorial Office
E-mail: coatings@mdpi.com
www.mdpi.com/journal/coatings



Disclaimer/Publisher's Note: The title and front matter of this reprint are at the discretion of the Guest Editors. The publisher is not responsible for their content or any associated concerns. The statements, opinions and data contained in all individual articles are solely those of the individual Editors and contributors and not of MDPI. MDPI disclaims responsibility for any injury to people or property resulting from any ideas, methods, instructions or products referred to in the content.





Academic Open
Access Publishing

mdpi.com

ISBN 978-3-7258-9110-8